Modeling and Control of Sound and Vibration for Smart Structures

Oliver Janda

Modeling and Control of Sound and Vibration for Smart Structures

Vom Fachbereich
Elektrotechnik und Informationstechnik
der Technischen Universität Darmstadt
zur Erlangung der Würde eines Doktor-Ingenieurs (Dr.-Ing.)
genehmigte Dissertation

von

Dipl.-Ing. Oliver Janda

geboren am 25. Juli 1981 in Miltenberg

Referent:	Prof. Dr.-Ing. Ulrich Konigorski
Korreferent:	Prof. Dr.-Ing. Thilo Bein

Tag der Einreichung:	11. Februar 2014
Tag der mündlichen Prüfung:	5. Mai 2014

D 17

Darmstädter Dissertationen

Bibliografische Information der Deutschen Nationalbibliothek – CIP-Einheitsaufnahme
Die Deutsche Bibliothek verzeichnet diese Publikation in der Deutschen Nationalbibliografie;
detaillierte bibliografische Daten sind im Internet über <http://dnb.ddb.de> abrufbar

Oliver Janda

Modeling and Control of Sound and Vibration for Smart Structures

Elektronische Version:
Bereitgestellt von tuprints, E-Publishing-Service der TU Darmstadt
http://tuprints.ulb.tu-darmstadt.de
tuprints@ulb.tu-darmstadt.de

URL: http://tuprints.ulb.tu-darmstadt.de/id/eprint/4154
URN: urn:nbn:de:tuda-tuprints-41549

Tel. 0551-503664-7 | Fax 0551-3894067
www.sierke-verlag.de

Einbandlayout: Grafik sierke VERLAG Göttingen
Gedruckt auf säure- und chlorfreiem Papier

ISBN 13: 978-3-86844-649-4
1. Auflage 2014

Preface

This thesis is the outcome of my research work carried out in the years from 2009 to 2013 at the Department of Control Systems and Mechatronics at the Technische Universität Darmstadt. The research was integrated within the framework of the LOEWE-Zentrum AdRIA (Adaptronics - Research, Innovation, Application), which is coordinated by the Fraunhofer Institute for Structural Durability and System Reliability (Fraunhofer LBF) and funded by the government of the German federal state of Hesse.

I would like to express my sincere gratitude to Professor Ulrich Konigorski for making this work possible in the first place. I very much cherished our technical discussions which where so fruitful to me. At the same time, he entrusted me with a maximum of freedom concerning my research, which I am also very thankful for. His way of teaching, guiding, and leading is an example to me.

Furthermore, I would like to thank Professor Thilo Bein for his work done as manager of the LOEWE-Zentrum AdRIA. Personally, I am very grateful for his permanent support during more than four years and for being second examiner of my thesis.

The LOEWE-Zentrum provided me with the opportunity to work in a group of young researchers in an exciting project and to benefit from the immense knowledge of the adaptronics experts of the Fraunhofer LBF. Moreover, their international relations made it possible for me to meet well-known researchers whose work has been, and will be, inspiring to me. I am very thankful for my short encounters with Professors Stephen Elliott, André Preumont, Arthur P. Berkhoff, Peter Lancaster, and Robert E. Skelton. I would like to thank Professor Holger Hanselka, former head of Fraunhofer LBF and coordinator of the LOEWE-Zentrum AdRIA, for making all this possible.

My academic and personal life profited a lot by the cooperation with all my fellow colleagues at TU Darmstadt and Fraunhofer LBF. Knowing that their names are to many to mention, I would like to thank Oliver Heuss, Matthias Kurch, Sven Herold, Dirk Mayer, Joachim Bös, Christian Thyes, Johannes Tschesche, and Ying Li at Fraunhofer LBF. I am also indebted to my former colleagues at TU Darmstadt, especially Jan Schlake, Silke Klose, and Marco Münchhof who have known me for a long time and motivated me to start a PhD project in the first place. Most importantly, I would like to thank my buddies Lukas Stein and Eric Lenz for spending with me such a lot of time in offices and laboratories and for the countless discussions on trivial problems and mechatronics.

I very much enjoyed the motivating and amicable working environment at my department. In this context, I would like to thank Corina Fischer, Brigitte Hoppe, and Sandra Schütz of the secretariat. Moreover, I am indebted to Alfred Gross and Alexander Stark and his team for the electrical and mechanical work.

Last but not least, I would like to thank my family, friends, and my love Katja for their whole-hearted support.

Braunschweig, September 2014 *Oliver Janda*

Summary

This thesis presents a contribution to the improvement of modeling and control methodologies for smart structures. It is focused on comfort-compromising, sound- and vibration-related problems, which can be successfully handled by the concepts developed within the interdisciplinary field of adaptronics.

As far as modeling of smart structures is concerned, it is advocated in this thesis to employ theoretical modeling to gather an understanding of the fundamental system properties and of the characteristics that are relevant for control design. Theoretical modeling of a generic smart structure with electromechanical as well as mechanical-acoustical coupling is illustrated at the beginning of this thesis. However, pure theoretical modeling of complex systems generally lacks sufficient accuracy for subsequent control design. For that reason, data-driven modeling is one of the key aspects of this work. A modeling procedure is developed that is capable of identifying models for linear time-invariant systems with many resonances from measurement data along with their associated model uncertainty. A minimum of prior assumptions is needed.

Based on these models and their uncertainty descriptions, a straightforward yet powerful design methodology for multi-input multi-output active vibration control is presented. The resulting control design employs the well-developed machinery of $\mathcal{H}_2$ optimal control, and the resulting control loops are robustly stable with respect to the a-priori identified model uncertainty. This robust optimal design methodology for multi-input multi-output controllers offers both better performance and more degrees of freedom compared to the dominating design of single-input single-output controllers for active vibration control.

These additional degrees of freedom especially pay off when not only vibration amplitudes but also vibration mode shapes in closed-loop are relevant. This is for example the case when acoustic radiation shall be controlled. Active acoustic control with structural measurements and control inputs is known as active structural acoustic control, which is the second key aspect of this work. A powerful tool for describing structure-borne sound radiation is the so-called power transfer matrix. This frequency-dependent matrix allows for the computation of structure-borne sound power from knowledge of structural motion. Here, a novel experimental modeling procedure for power transfer matrices is introduced which does not impose any restrictions on the geometry of the radiating structure or the acoustic environment whatsoever. With the help of this matrix, the robust optimal control design scheme for active vibration control can be extended to the control of structure-borne sound power in a straightforward manner. It is also shown that sound radiation into enclosed spaces can be handled with minor modifications of the control scheme for free-field radiation. All modeling and control design methods presented in this thesis are validated by simulation as well as experimental results.

Kurzfassung

Diese Arbeit leistet einen Beitrag zur Verbesserung der bestehenden Methoden zur Modellierung und Regelung von adaptronischen Systemen. Im Fokus stehen Schall- und Schwingungsprobleme, welche mit den Konzepten der interdisziplinären Forschungsrichtung Adaptronik erfolgreich bearbeitet werden können.

Es wird dabei zunächst theoretische Modellbildung genutzt, um die grundlegenden Systemeigenschaften und auch solche, welche für den Reglerentwurf von Bedeutung sind, herauszuarbeiten. Illustriert wird dieses Vorgehen an einem generischen Demonstrator, welcher sowohl elektromechanische als auch mechanisch-akustische Kopplungen aufweist. Da jedoch eine rein theoretische Modellierung von komplexen Systemen im Allgemeinen nicht die Genauigkeitsanforderungen für einen nachfolgenden Reglerentwurf erfüllt, stellt die experimentelle Modellbildung einen Schwerpunkt dieser Arbeit dar. Es wird dazu ein Verfahren vorgestellt, welches es ermöglicht, Modelle von linearen zeitinvarianten Systemen mit vielen Resonanzen in Verbindung mit der zugehörigen Modellunsicherheit zu identifizieren. Hierzu ist nur ein Minimum an einschränkenden Annahmen notwendig.

Basierend auf diesen Modellen inklusive der Modellunsicherheiten wird eine allgemein anwendbare und leistungsfähige Methodik zum Entwurf von Mehrgrößenreglern zur aktiven Schwingungsdämpfung vorgestellt. Dafür wird auf die ausgereifte Theorie des $\mathcal{H}_2$-optimalen Reglerentwurfs zurückgegriffen und die Regler so entworfen, dass die Regelkreise robuste Stabilität bzgl. der zuvor identifizierten Modellunsicherheiten aufweisen. Dieser robuste und optimale Mehrgrößenentwurf zur Schwingungsdämpfung bietet Vorteile gegenüber dem vorherrschenden Entwurf von Eingrößenreglern in Bezug auf Regelgüte und Anzahl der Freiheitsgrade.

Die zusätzlichen Freiheitsgrade eines Mehrgrößenreglers sind insbesondere dann von Bedeutung, wenn nicht nur die Größe der Schwingungsamplituden, sondern auch die Schwingformen im geschlossenen Regelkreis von Bedeutung sind. Dies ist z.B. dann der Fall, wenn die Schallabstrahlung einer Struktur geregelt werden soll. Geschieht dies ausschließlich anhand von strukturdynamischen Mess- und Stellgrößen, so bezeichnet man dies in der englischen Fachliteratur als active structural acoustic control, welches den zweiten Schwerpunkt dieser Arbeit darstellt. Ein wirksames Werkzeug zur Beschreibung der Schallabstrahlung einer schwingenden Struktur ist die sogenannte Leistungsübertragungsmatrix. Diese frequenzabhängige Matrix ermöglicht die Berechnung der abgestrahlten Schallleistung anhand der Kenntnis der Strukturbewegung. In dieser Arbeit wird ein neuartiges Verfahren zur experimentellen Bestimmung der Leistungsübertragungsmatrix vorgestellt, welches keinerlei Einschränkungen hinsichtlich der Geometrie der Struktur oder des akustischen Umfelds aufweist. Mit Hilfe dieser Matrix ist es möglich, die robuste und optimale Schwingungsregelung auf die Regelung der abgestrahlten Schallleistung zu erweitern. Es wird ebenfalls gezeigt, dass dieses Verfahren zur Regelung der Abstrahlung ins Freifeld mit kleinen Modifikationen auch auf die Regelung des Schalleintrags in einen geschlossenen Raum angewendet werden kann. Sämtliche Modellbildungs- und Reglerentwurfsverfahren, die in dieser Arbeit präsentiert werden, werden durch Simulationen und Experimente validiert.

Contents

Symbols and Acronyms

Symbols

Constants, Parameters

A	area
A_{norm}	normalization factor
c_{ph}	phase velocity
c_0	speed of sound at normal conditions
C	capacitance
D	bending stiffness of plate
$D_{\{\mathrm{S,F}\}}$	damping ratio
E	Young's modulus
f	frequency
h	plate thickness
k	wave number, time index
$l_{\{x,y\}}$	plate length
l_z	cavity height
m	mass, modal mass
M	number of experiments
n	number of elements, number of states
$n_{\{\mathrm{S,F}\},x}$	mode index number
$n_{\{\mathrm{S,P,F}\}}$	number of generalized coordinates
$\mathcal{O}_{\mathcal{K}}$	order of stiffness operator
$\mathcal{O}_{\mathcal{M}}$	order of mass operator
p	number of system outputs
q	number of system inputs

R	universal gas constant
S	surface area
t	time
T_{P}	time period
T_{s}	sampling period
T_0	fluid reference temperature
$V_{\{\mathrm{S,P,F}\}}$	volume
x, y, z	cartesian coordinates
Z_0	specific acoustic impedance
$\varDelta$	Mahalanobi distance
ϵ	permittivity, neighborhood
κ	shear correction factor, isentropic constant
κ^B	controllability index
κ^C	observability index
λ	wave length, eigenvalue
ν	Poisson's ratio
ρ	density of plate material
ρ_0	density of fluid at normal conditions
ω_{c}	coincidence frequency
ω_i	ith eigenfrequency of undamped system

Functions, Operators, Field Variables

B_x	magnetic flux density component
$\mathcal{B}_i$	boundary operator
$\det\{\cdot\}$	matrix determinant
$\mathrm{diag}\{\cdot\}$	vector of diagonal matrix elements
D_x	electric displacement component
$\mathcal{D}$	domain of PDE
$\mathcal{D}_{\{\mathrm{S,F}\}}$	dissipation function
$\mathrm{erf}(\cdot)$	Gaussian error function
E	energy

E_x	electric field component
$\mathrm{E}\{\cdot\}$	expectation operator
F	force per unit area
F_{χ^2}	cummulative distribution function of χ^2 distribution
$\mathcal{F}_{\mathrm{l}}\{\cdot,\cdot\}$	lower linear fractional transformation
$\mathcal{F}_{\mathrm{u}}\{\cdot,\cdot\}$	upper linear fractional transformation
G	Green's function
H_x	magnetic field strength component

$\mathrm{im}\{\cdot\}$	image
$\mathcal{I}_{\{\mathrm{S,F}\}}$	index map
$\Im\{\cdot\}$	imaginary part
$\ker\{\cdot\}$	null space
$\mathcal{K}$	stiffness operator
$\mathcal{L}$	Lagrangian
L_p	sound pressure level
L_P	sound power level
L_v	particle velocity level
m_x	bending moment per unit area
M_x	moment resultant
$\mathcal{M}$	mass operator
p	pressure field
P	sound power
P_i	ith basis function for field variable p
$\Pr(\cdot)$	probability
Q	electric charge per unit volume
Q^tot	total electric charge
$\mathrm{rank}\{\cdot\}$	matrix rank
R_i	ith basis function for field variable Φ
R_{vv}	autocorrelation sequence
R_{vw}	crosscorrelation sequence
$\Re\{\cdot\}$	real part
$\mathrm{span}\{\cdot\}$	span of vector set
$\boldsymbol{S}_{UU}$	auto-spectral density
$\boldsymbol{S}_{YU}$	cross-spectral density
$\mathcal{S}_w$	structural strain operator
U	voltage
v	noise signal, particle velocity
$\mathrm{vec}\{\cdot\}$	vectorization operator
$\mathrm{vech}\{\cdot\}$	vectorization operator for Hermitean matrices
v_x	velocity component
V	volume displacement per unit volume
w	displacement field of plate
W	work
W^c	comparison function
W^e	eigenfunction
W_i	ith basis function for field variable w
$X(\mathrm{j}\omega_n)$	DFT sequence of $x(k)$
Z	impedance
$\mathcal{Z}$	bilinear transform to discrete time
$\gamma(s, x)$	lower incomplete gamma function
γ_{xy}	shear strain
$\Gamma(x)$	gamma function
δ	variational operator
ϵ_x	normal strain
η	modal coordinate, generalized coordinate for w
ν	generalized coordinate for Φ
Π	product of elements
$\rho(\cdot)$	spectral radius
$\sigma(t)$	step function
σ_x	normal stress
Σ	sum of elements
τ_{xy}	shear stress
φ	test function
φ_f	field angle
Φ	electric potential field
Φ_v	velocity potential
$\langle\cdot,\cdot\rangle$	inner product
$*$	convolution
$\otimes$	Kronecker matrix product
$\bigoplus$	direct matrix sum (concatenation of blockdiagonal matrix)
$\|\cdot\|_\mathrm{F}$	Frobenius norm

Vectors, Matrices

$\boldsymbol{A}$	system matrix
$\boldsymbol{B}$	magnetic flux density field vector, input matrix
$\boldsymbol{c}$	elastic material constants
$\boldsymbol{C}$	output matrix
$\boldsymbol{C}_\mathrm{el}$	capacitance matrix
$\boldsymbol{d}$	disturbance input vector
$\boldsymbol{D}$	electric displacement field vector, feedthrough matrix
$\boldsymbol{D}_{\{\mathrm{S,F}\}}$	damping matrix
$\boldsymbol{e}$	piezoelectric constants
$\boldsymbol{E}$	electric field vector,

	disturbance input matrix
$\boldsymbol{F}$	force field, force vector, distburbance feedthrough matrix
$\boldsymbol{Fi}$	Fisher Information Matrix
$\boldsymbol{g}$	Markov parameters
$\boldsymbol{G}$	transfer matrix of parametric model
$\hat{\boldsymbol{G}}$	transfer matrix of non-parametric model
$\boldsymbol{G}_{\mathrm{em}}$	electromechanical coupling matrix
$\boldsymbol{G}_{\mathrm{ma}}$	mechanical-acoustical coupling matrix
$\boldsymbol{H}$	magnetic field vector
$\boldsymbol{I}$	intensity vector
$\mathbf{I}_{(n)}$	Identity matrix (of dimension n)
$\boldsymbol{K}$	stiffness matrix
$\boldsymbol{L}_{\mathrm{A}}$	actuator influence matrix
$\boldsymbol{L}_{\mathrm{S}}$	sensor influence matrix
$\boldsymbol{M}$	mass matrix
$\boldsymbol{p}$	vector of sound pressure measurements
$\boldsymbol{P}$	vector of acoustic basis functions
$\boldsymbol{P}^{\mathrm{dis}}$	matrix of discretized acoustic basis functions
$\boldsymbol{Q}$	vector of total electric charges
$\boldsymbol{S}$	strain tensor
$\boldsymbol{T}$	stress tensor
$\boldsymbol{T}_{\mathrm{E}}^{\mathrm{c}}$	electric field coordinate transformation matrix
$\boldsymbol{T}_{\mathrm{S}}^{\mathrm{c}}$	strain coordinate transformation matrix

$\boldsymbol{u}$	input vector
$\boldsymbol{U}$	vector of voltages
$\boldsymbol{v}$	velocity field vector, eigenvector, noise sequence
$\boldsymbol{V}$	vector of volume displacements, matrix of right eigenvectors
$\boldsymbol{w}$	left eigenvector
$\ddot{\boldsymbol{w}}$	vector of acceleration measurements
$\boldsymbol{W}$	vector of mechanical basis functions, matrix of left eigenvectors
$\boldsymbol{W}^{\mathrm{dis}}$	matrix of discretized mechanical basis functions
$\boldsymbol{x}$	point vector in cartesian space
$\mathbf{0}_{m\times n}$	zero matrix of dimension (m, n)
$\mathbf{1}_{m\times n}$	matrix of ones of dimension (m, n)
$\boldsymbol{\Gamma}_u$	input pattern matrix
$\Delta\boldsymbol{G}$	uncertainty of parametric model
$\Delta\hat{\boldsymbol{G}}$	uncertainty of non-parametric model
$\boldsymbol{\epsilon}$	permittivity constants
$\boldsymbol{\eta}$	vector of generalized coordinates
$\boldsymbol{\Theta}$	parameter vector
σ_{R}	radiation efficiency
$\boldsymbol{\sigma}^2$	covariance matrix
$\boldsymbol{\varphi}$	vector of acoustic generalized coordinates
$\boldsymbol{\Phi}$	modal matrix
$\boldsymbol{\Phi}_{\mathrm{A}}$	actuator modal matrix
$\boldsymbol{\Phi}_{\mathrm{S}}$	sensor modal matrix

Identifiers, Indices

$(\cdot)_{\mathrm{A}}$	actuator
$(\cdot)_{\mathrm{bc}}$	boundary condition
$(\cdot)^{\mathrm{d}}$	dissipative
$(\cdot)_{\mathrm{el}}$	electric
$(\cdot)^{\mathrm{ex}}$	external
$(\cdot)_{\mathrm{F}}$	fluid
$(\cdot)^{\mathrm{g}}$	generalized
$(\cdot)^{\mathrm{H}}$	matrix Hermitian
$(\cdot)_{\mathrm{kin}}$	kinetic
$(\cdot)^{\mathrm{K}}$	Kirchoff

$(\cdot)^{\mathrm{KR}}$	Kirchhoff-Rayleigh
$(\cdot)_{\mathrm{mag}}$	magnetic
$(\cdot)_{\mathrm{mec}}$	mechanic
$(\cdot)_{\mathrm{n}}$	normal direction
$(\cdot)^{\mathrm{nc}}$	non conservative
$(\cdot)_{\mathrm{pot}}$	potential
$(\cdot)_{\mathrm{P}}$	piezo
$(\cdot)_{\mathrm{re}}$	transformation according to (B.2)
$(\cdot)_{\mathrm{Re}}$	transformation according to (B.1)
$(\cdot)^{\mathrm{RM}}$	Reissner-Mindlin

$(\cdot)_{\mathrm{RMS}}$	RMS value
$(\cdot)_{\mathrm{S}}$	structure, sensor
$(\cdot)^{\mathrm{T}}$	matrix transpose
$(\cdot)_{(x,y,z)}$	cartesian coordinate directions
$(\cdot)_0$	initial condition, ambient condition, true value
$\dot{(\cdot)}$	time derivative
$(\cdot)'$	quantity in piezoelectric COS
$(\cdot)^*$	conjugate-complex element

$(\cdot)^+$	Moore-Penrose matrix inverse
$\hat{(\cdot)}$	estimated quantity
$\tilde{(\cdot)}$	phasor quantitiy
$\bar{(\cdot)}$	time-average quantity
$\bar{\bar{(\cdot)}}$	time- and space-average quantity
$(\cdot)^{\sim}$	conjugate system
$(\cdot)_-$	stable spectral factor
$(\cdot)_+$	antistable spectral factor

Acronyms

ARMAX	autoregressive, moving average, exogenous input
ANC	active noise control
ANVC	active noise-vibration control
ASAC	active structural acoustic control
AVC	active vibration control
BIBO	bounded input bouded output
CER	complex exponential representation
COS	coordinate system
CSCN	circular symmetric complex normal
DFT	discrete Fourier transform
DoE	design of experiments
DVF	direct velocity feedback
EVP	eigenvalue problem
FD-ERA	frequency-domain eigensystem realization algorithm
FEM	finite element method
FFT	fast Fourier transform
FIR	finite impulse response
FRF	frequency response function
FSS	feasible systems set
HAC	high-authority control
i.i.d.	independently identically distributed
IFF	integral force feedback

I4C	identification for control
KYP	Kalman-Yakubovich-Popov
l.i.m.	limit in the mean
LAC	low-authority control
LFT	linear fractional transformation
LMFD	left matrix fraction description
LMI	linear matrix inequality
LQR	linear quadratic regulator
LTI	linear time-invariant
MEM	model error modeling
MIMO	multiple input multiple output
MSE	mean-square error
NVH	noise, vibration, and harshness
PCA	principal component analysis
PPF	positive position feedback
PRBS	pseudo-random binary signal
RMS	root mean square
SIMO	single input multiple output
SMI	set membership identification
SNR	signal-to-noise ratio
ODE	ordinary differential equation
PDE	partial differential equation

1 Introduction

This thesis deals with the modeling and control of sound and vibration for smart structures. To this end, the notion of smart structures will be introduced first in this initial chapter. Then, typical problems from the field of noise, vibration, and harshness (NVH) will be illustrated, and it will be shown how they can be treated by the use of smart structures. The introductory chapter closes with the modeling and control design philosophy put forward in this thesis and significant research contributions.

1.1 Smart Structures

For many products, especially those coming from the fields of aerospace or automotive industry, a steadily increasing demand for lightweight design has been observed over the last years. This is due to the omnipresent imperative to produce products from a low amount of construction material for both economic and ecological reasons. At the same time, everlasting pressure to innovate products is put on manufacturers by both customers and competitors. This leads to the aggravating conflict of goals to have high-quality products featuring state-of-the-art technology made from a steadily decreasing amount of natural resources.

An important concept towards the design of highly functional, lightweight mechanical products is that of *smart structures*, which are also termed *adaptive structures*. The key idea is to have a passive, lightweight mechanical structure which is augmented by structurally integrated actuators and sensors that are connected via computer control. The concept of structural integration is the essential difference from mechatronic design, as argued in [101]. To facilitate this, the transducers are made from functional materials that exploit for example piezoelectric, electrostrictive, magnetostrictive, or magnetorheological effects, and can be possibly integrated into the passive material. As such, the design of smart structures is inherently interdisciplinary and requires knowledge from the diverse fields illustrated in Fig. 1.1. Possible applications for smart structures are products where the requirements cannot be met by merely passive structures or when additional functionality is required, e.g. shape control, structural health monitoring, active deployment, or active control of sound and vibration [137].

The origin of smart structures can be seen in the research for active vibration control of space structures that started in the late 70s of the last century. Because of the virtually non-existent atmospheric damping mechanisms in space, the active damping of the structural motion of satellites, space-telescopes, etc. became an increasingly vivid research topic. This is when the first publications on active vibration control of lightweight structures where published, see for example the groundbreaking works of Balas [9, 10, 11, 12] and Meirovitch [133, 134, 135, 136].

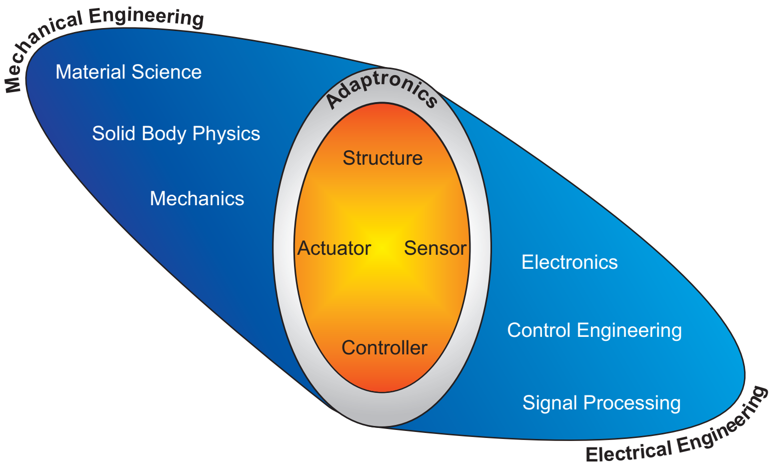

Figure 1.1: Interdisciplinary concept of adaptronics; after Hering & Modler (Eds.) [101].

1.2 Active Control of Noise and Vibration

Sound and vibration problems related to the field of noise, vibration, and harshness (NVH) have received attention by many researches over the last years. The approaches to handle these problems by means of active control can be grouped into the following four areas, according to Fahy [70]: active vibration control (AVC), active noise control (ANC), active noise-vibration control (ANVC), and active structural acoustic control (ASAC). The different approaches are illustrated in Figs. 1.2 to 1.5. In all cases, the structure may be excited by both structural forces and disturbance sound fields. While the goal of AVC is to reduce structural vibration, the other three control approaches search to minimize an acoustic quantity, most importantly structure-borne sound radiation. The approaches differ in the concept of applied actuators and sensors. In ANC, both acoustic sensors (microphones) and actuators (loudspeakers) are located in the acoustic environment to reduce sound levels by destructive interference. In ANVC, only acoustic sensors are used, while sound radiation is influenced by properly applying structural forces. The goal of ASAC is to curb sound radiation by structural transducers exclusively.

The purpose of this thesis is to show how smart structures offer ways of handling NVH-related problems. More specifically, the design of powerful, model-based control algorithms in interaction with sensible actuator and sensor positioning will be highlighted. Only structural transducers will be considered for this purpose. Because of that, ANC and ANVC problems will not be treated.

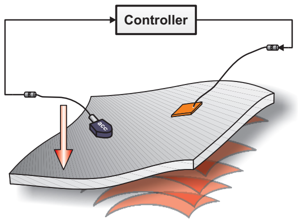

Figure 1.2: AVC.

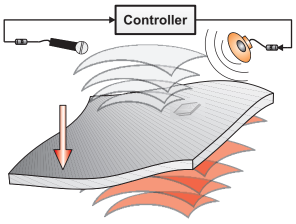

Figure 1.3: ANC.

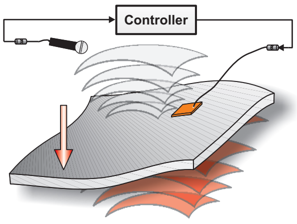

Figure 1.4: ANVC.

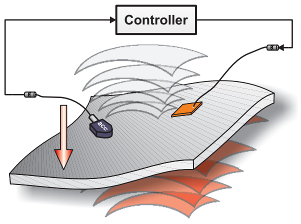

Figure 1.5: ASAC.

Another important classification of control approaches can be made by separating local and global control. The former strives to minimize vibration amplitudes or sound pressures at distinct locations on the structure or in the acoustic field, respectively. For the latter, a global measure of performance is used as control variable. For vibration control, this may be the kinetic, potential, or total energy of the structure. For acoustic control in an enclosure, one usually tries to reduce the overall potential energy of the confined acoustic medium, which is proportional to mean-square sound pressure. This is impractical for sound radiation into unconfined open space and then, energy may be substituted by sound power, see also [65]. As can be inferred from the different control variables, local and global control problems may lead to largely different concepts in terms of actuator-sensor configurations and control algorithms. The focus of this thesis will be almost exclusively on global control approaches for sound and vibration.

1.3 Modeling Philosophy and Acoustic Demonstrator

It will be shown in the later chapters of this thesis how to successfully apply modern, model-based control design methods to AVC and ASAC problems. An essential prerequisite for this is the availability of purposeful models. The most common approaches to the modeling of smart structures are of analytical, numerical, and experimental nature. Analytical models are derived by theoretical means, i.e. considering the system's first principles in form of constitutive, phenomenological, and energy balance equations. Numerical methods, as it is understood here, comprise the wide field of finite element methods (FEMs) and boundary elements methods (BEMs) which spatially discretize the given problem into a large number of small elements whose dynamical behavior are known. Lastly, experimental modeling means calculating a model from measured data only, without considering any underlying physical principles. The most important advantages and drawbacks of these three approaches are summarized in Table 1.1. From these facts, it is obvious that analytical and experimental modeling are complementary in terms of model accuracy and physical insight. This shall be exploited in this thesis.

The system where the modeling and control techniques presented in this thesis will be exemplified is called *acoustic demonstrator* and is depicted in Fig. 1.6. It is essentially a rectangular cavity with five side walls which can be approximately regarded as rigid under the considered loads. On top of the demonstrator, a frame allows for the fixation of flexible plates of varying thickness and material. The plate is clamped inside the frame with interjacent rubber seals. The frame geometry allows for thermal dilation of the plate material in lateral direction. Thus, the boundary conditions of the plate are somewhere in between the theoretical extremes of perfectly clamped and simply supported. The dimensions of the cavity are $(870 \times 620 \times 750)$ mm. The flexible plate which is used throughout this thesis is made of aluminum with a thickness of 4 mm. The demonstrator is supported by four air springs which provide appropriate isolation from ground excitation.
The generic concept of the acoustic demonstrator allows to mockup a variety of fundamental problems of sound and vibration with regard to smart structures. This is illustrated in Fig. 1.7. The flexible plate can be equipped with piezoelectric patches that can serve as actuators as well as sensors due to the inverse and direct piezoelectric effects, respectively. In addition to that,

Table 1.1: Advantages and disadvantages of the different modeling approaches.

Analytical	Numerical	Experimental
Advantages		
Physical insight	General geometries and boundary conditions	Highest possible model accuracy
Concentration on dominant physical effects	Detailed modeling of big systems	Applicable to arbitrary systems
Efficient parameter studies	Model accuracy flexibly adjustable	Offline- and online modeling
Disadvantages		
Solutions only available for a few "classic" geometries and boundary conditions	Low model transparency	No model transparency
Detailed modeling of arbitrary geometries and boundary conditions not possible	Requires additional model reduction techniques	Real system necessary
	Large computation times	Parameter studies require modification of real system
	For high model accuracy, parameter fitting necessary	High instrumentation and measurement effort

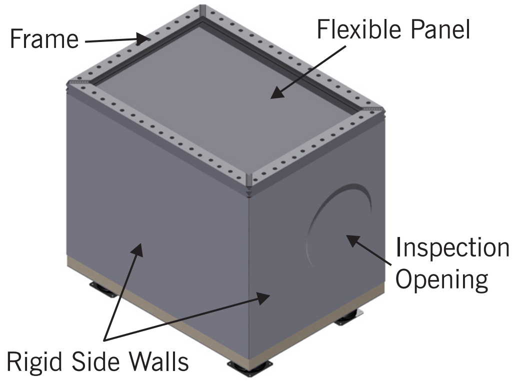

Figure 1.6: Acoustic demonstrator.

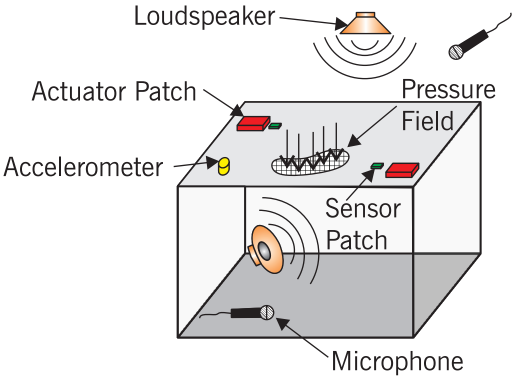

Figure 1.7: Possible applications of acoustic demonstrator.

acceleration can be measured with dedicated sensors at specific locations on the plate, too. We will adopt the term *smart panel* from literature [70] for the combination of the flexible plate with actuators and sensors together with some control algorithm, and this will be the smart structure treated throughout this thesis. The structure may be excited by forces directly acting on the plate, but also by acoustic sources from inside and outside of the cavity. Consequently, the acoustic response outside or inside of the cavity may be relevant, depending on the considered scenario, and can be measured by appropriate acoustical equipment. In addition to that, the frame may be dismounted from the box in order to be able to consider solely the plate dynamics without fluid-structure interaction.

For the modeling of the various possible scenarios that can be simulated with the acoustic demonstrator, the following statements can be made:

- The acoustic demonstrator exhibits complex fluid-structure interaction between the smart panel and the acoustic volumes inside and outside the cavity. These effects, as well as the plate dynamics, have to be incorporated in the model in order to understand the important characteristics of the acoustic demonstrator.
- The piezo patches further introduce electromechanical coupling and modify the mass and stiffness properties of the plate. The principles of this multiphysical coupling have to be modeled, and it must be judged if the mass and stiffness contributions of the patches are significant.

- The principles of acoustic excitation by sources inside and outside the cavity have to be understood.
- The implications of actuator and sensor positioning on the controllability and observability of the system must be made clear.

- For model-based control design, models which are able to quantitatively reproduce the mapping from actuator inputs to sensor signals with high quality are essential.

- For robust control design, some measure of model uncertainty must also be provided.

If one wanted to satisfy all of the above requirements with a single model of the acoustic demonstrator, one would have to create a multiphysics FEM/BEM model with thousands of degrees of freedom whose parameters had to be fitted to real measurement data. This is because a numerical model established from geometry and material data that is solely taken from data sheets cannot be expected to coincide with real measurements. Several imperfections of the real testbed preclude this. First of all, the boundary conditions of the plate would have to be modeled with circumferential rotatory spring and damper elements to emulate the non-ideal plate fixation. The parameters of these elements cannot be measured and have to be adjusted to reproduce the results of an experimental modal analysis. In addition to that, the nominal parameters of the piezoelectric material usually do not sufficiently reproduce the effects of piezoelectric actuation and sensing, because these are also heavily influenced by the properties of the adhesive layer between piezoelectric material and plate. The thickness and material properties of this layer are unknown beforehand and are difficult to identify experimentally. Lastly, the sound field generated by the radiating plate outside the cavity is dependent on the geometry and materials of the room in which the acoustic demonstrator operates. The correct parameters of the acoustic environment are difficult to obtain. It is clear from the above arguments that even with a large-scale numerical model, simplifying assumptions and idealizations would have to be made. This means that not all of the physical quantities and excitation mechanisms were quantitatively reproduced with sufficient accuracy. In addition to that, numerical models offer only a medium degree of physical insight. For that reason, a different modeling philosophy is favored in this thesis.

The first four of the above listed modeling requirements shall be satisfied by an analytical model. Due to the simple geometry of the acoustic demonstrator and several simplifying assumptions, it is possible to create a model which qualitatively reflects all of the distinct features of the real testbed. This allows for profound system analysis as well as systematic development and testing of control algorithms, while providing unsurpassable physical insight. With these results, it is possible to apply the devised control designs in an almost one-to-one manner to the real testbed. The controllers for the real acoustic demonstrator are then based upon experimentally identified models which are able to reproduce the input-output behavior of the actuator-sensor transfer paths with higher accuracy than analytical and numerical models. As will be shown, the experimental modeling technique also allows for the systematic derivation of model uncertainty bounds. With this modeling philosophy, each model is tailored towards its respective purpose.

Based upon these different models, it will be demonstrated how to successfully exploit the abilities of the smart panel to handle several problems of sound and vibration. More specifically, the following scenarios will be treated in this thesis:

1. The excitation of the smart panel by disturbance forces and the reduction of its structural response by means of AVC.
2. The excitation of the acoustic demonstrator by disturbance forces and acoustic sources inside the cavity, and the minimization of emitted sound power outside the cavity by means of ASAC.
3. The excitation of the acoustic demonstrator by disturbance forces and acoustic sources outside the cavity, and the minimization of sound pressure at a specific point inside the cavity by means of ASAC.

The acoustic demonstrator itself does not exhibit low-pass behavior, as will be illustrated in the next chapter. As such, there is no natural limit for the maximum relevant system frequency. Artificial frequency limits will be imposed by appropriate signal processing. In this thesis, we confine the maximum relevant frequency for the modeling and active damping of the smart panel to 500 Hz. Modeling of acoustic radiation and ASAC for the acoustic demonstrator will be done up to 200 Hz. As will be shown in the next chapter, this means that systems with 17 and six modes are treated with the proposed AVC and ASAC methodologies, respectively.

1.4 Contents and Contributions

The contents and workflow of this thesis are depicted in Fig. 1.8. The following two chapters treat the theoretical and experimental modeling problems for the acoustic demonstrator, respectively.

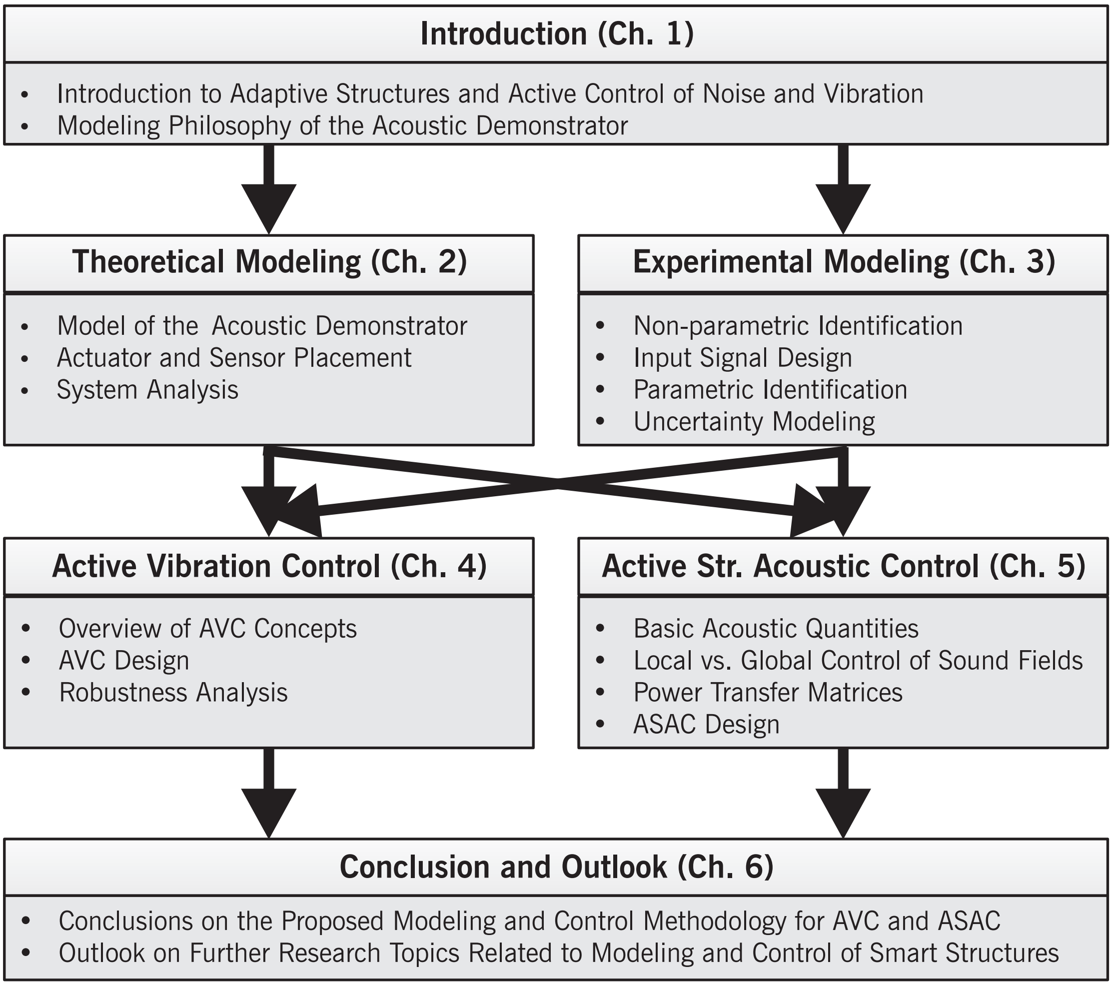

Figure 1.8: Contents and workflow of this thesis.

After that, the AVC and ASAC designs will be developed, where results from both modeling strategies will be required. The last chapter summarizes the results and gives an outlook on further research topics concerned with modeling and control of smart structures that are out of the scope of this thesis.

The significant research contributions that will be presented in the remainder can be summarized as follows:

- In Ch. 2, a theoretical model of the acoustic demonstrator will be derived by means of Hamiltonian mechanics that allows for the incorporation of all types of possible excitation mechanisms as illustrated in Fig. 1.7 by a comprehensive treatment of electromechanical and mechanical-acoustical coupling.

- The experimental modeling technique presented in Ch. 3 provides an improved method to derive accurate, high-order models of linear time-invariant systems together with a reliable estimate of the associated model uncertainty.

- Chapter 4 provides a clear and generally applicable methodology to design robust, high-performance active damping controllers. The robustness analysis is immediately based on the derived model uncertainty description of Ch. 3.

- For ASAC design, a novel experimental modeling technique for power transfer matrices is presented in Ch. 5 that allows for an efficient design of controllers to minimize structure-borne sound power. The modeling technique is solely based on the premise that the acoustic environment may be sufficiently described by linear system theory. For the first time, no further restrictions regarding the geometry of the structure or the acoustic environment are necessary.

Literature reviews on the state-of-the-art of the different topics will be given in the respective chapters.

2 Theoretical Modeling

Theoretical modeling is one possibility to generate mathematical models of systems. It requires the knowledge of the system's first principles and parameters to generate a set of mathematical equations to reproduce and predict its input-output behavior. This chapter presents a complete theoretical modeling procedure for the idealized acoustic demonstrator including electromechanical as well as mechanical-acoustical coupling. At the end of this chapter, this model will be analyzed and the important physical properties will be highlighted. Furthermore, it will be used to facilitate the positioning of actuators and sensors, which is an important step towards successful control system design.

2.1 Motivation

The modeling of technical, biological, and economic systems is an important and diverse discipline. The common goal is to derive a mathematical model of the real system to reproduce and/or predict its input-output behavior. There are two extreme ways which lead down this path. The first one is *theoretical modeling*. It is based on the knowledge of the underlying physical, biological or economical principles, depending on the field of application, which are stated in mathematical form. Also, the parameters which appear in the mathematical equations are assumed to be known. Then, one can derive a so-called *white-box model* displaying both the input-output behavior as well as the system's internal mechanisms. This is what will be done with the acoustic demonstrator in this chapter. However, accurate white-box models of real systems can only be derived for very simple systems which is not true for the acoustic demonstrator. Therefore, some idealizing assumptions are made.

The opposite approach is called *experimental modeling* or *system identification*. It produces a so-called *black-box model* from measured input-output data only. Physical insight is only required for the selection of a model class, e.g. linear or non-linear, and the model order. This approach is able to generate accurate models even for very complex systems but at the same time conceals their internal mechanisms. A black-box approach will be used to facilitate control design for the real acoustic demonstrator in the next chapter. A good compromise which keeps the physical insight of the white-box approach while at the same time increases the model accuracy is to keep the equations of the theoretical modeling approach, but to fit their parameters to measured input-output data by an optimization procedure. This is called gray-box modeling. See [110] for a further elaboration on modeling techniques and [31] for a comprehensive treatment of the gray-box approach.

As can be seen from the above discussion, theoretical and experimental modeling are complementary in terms of physical insight and accuracy. This is why in this chapter, a white-box procedure for the modeling of a smart structure with electromechanical and mechanical-acoustical coupling is presented and carried out on the idealized acoustic demonstrator. The outcome of the modeling procedure is a finite-dimensional, linear time-invariant state space model which facilitates system analysis with the powerful tools of linear system theory. The most important idealizations are the assumptions that the plate has analytic boundary conditions and the other walls of the box are perfectly stiff. The non-trivial model parameters, like the piezoelectric material constants, are taken from data sheets. Due to these and other simplifications, the resulting model does not perfectly match the input-output behavior of the real demonstrator. But this is not really a problem, since the purpose of the theoretical model is somewhat different. It will be used to

- gain insight into the basic physical principles of the vibration of plates as well as the electromechanical and mechanical-acoustical coupling,
- analyze the resulting state space model in terms of system-dynamic properties such as poles, zeros, stability, controllability, and observability,
- facilitate the positioning of actuators and sensors, and
- provide a simulation model to implement, test, and evaluate different control strategies.

It will become evident along the line of this and the next chapter that the theoretical model incorporates all distinct features of the real structure. This allows the development and analysis of control strategies which can, in principal, be applied in an almost one-to-one manner to the real acoustic demonstrator. The main difference is that the theoretical model is set in the continuous time domain while the black-box model of the real system is a discrete-time model. The respective advantages are obvious: the continuous-time model preserves the meaning of the physical parameters, while the discrete-time model allows for efficient controller implementation on digital computer hardware.

Distributed and Lumped Parameter Models

The acoustic demonstrator is a distributed-parameter system since the mass, stiffness, and damping properties of the plate as well as the acoustic volume are spatially distributed. Consequently, the motion of the system is naturally described by partial differential equations (PDEs) leading to a distributed parameter model. Analysis of, and control design for distributed parameter systems are vivid and diverse areas of research. One may consult exemplarily the monographs [13, 52, 57, 74, 116, 128, 163] for a mosaic display of associated problems, methods, and applications.

PDE models may theoretically achieve unsurpassable accuracy and allow insights into the complex dynamics of distributed parameter systems. However, the number of applications to real-world problems is still comparably low because of the much more involved mathematical theory compared to models which are constituted by ordinary differential equations (ODEs). This is why modeling and system analysis is predominantly done with lumped parameter models consisting of a limited set of ODEs which approximate the PDE model in some sense. This approach to distributed parameter systems is termed *early lumping* [163]. Even when the design of a (distributed) control law is directly based on the PDE model, the implementation of the controller will usually require spatial discretization, since distributed actuators and sensors are not available. This approach is known as *late lumping*.

The late lumping approach shall not be a topic of this thesis. Consequently, a lumped-parameter model will be employed for system analysis and control design. One way to do that would be to find the PDEs describing the acoustic demonstrator, and then discretize them by a suitable method. This two-step procedure is tractable, since the PDEs of a plate with analytic boundary conditions and of a fluid volume in a rectangular cavity are readily available from literature. However, a lumped parameter model of the acoustic demonstrator can also directly be derived from energy considerations via the *Assumed Modes method* [46, 158], without explicitly stating the PDEs. This has two obvious advantages: Firstly, the modeling procedure involves only one modeling step and not a modeling step with subsequent discretization. Secondly, the proposed modeling procedure, which will be described in more detail in Sec. 2.3, is also applicable to cases where the underlying PDEs are not available. In addition to that, this direct approach may lead to the same model as the two-step procedure under certain circumstances which are fulfilled in the present case. This will be further explained in Sec. 2.3. Nevertheless, some elements of distributed parameter modeling will prove useful in the following. These elements will be summarized in the next section.

2.2 Elements of Distributed Parameter Modeling

The proposed modeling technique will implicitly make use of certain properties of the distributed parameter system, most importantly its self-adjointness. Thus, the most important properties of self-adjoint systems are briefly recapitulated at the beginning of this section. These will include the different types of boundary conditions and the associated classification of basis functions, as well as the concept of modal coordinates. After that, the basic equations of plate theory and the three-dimensional wave equation will be stated.

2.2.1 Properties of Self-Adjoint Systems and Eigenvalue Problems

Most distributed conservative mechanical systems belong to the class of self-adjoint systems. Important exceptions are gyroscopic systems like rotors or axially translated strings [94]. The vertical dynamics of plates and the dynamics of acoustic volumes in enclosed spaces, however, are known to be self-adjoint problems. Moreover, as will become evident in the following, the governing PDEs of these two phenomena obey the general form

$$\mathcal{M}\left\{\frac{\partial^2 w(\boldsymbol{x},t)}{\partial t^2}\right\} + \mathcal{K}\left\{w(\boldsymbol{x},t)\right\} = F(\boldsymbol{x},t), \quad \boldsymbol{x} \in \mathcal{D}, \tag{2.1}$$

where $w(\boldsymbol{x},t)$ is the continuous variable describing the deflection of the medium from its equilibrium state and depends on spatial coordinates $\boldsymbol{x}$ and time t. The right hand side of the equation contains some space- and time-dependent forcing term denoted by $F(\boldsymbol{x}, t)$. The general PDE (2.1) is defined on some domain $\mathcal{D}$ with boundary $\partial\mathcal{D}$. The mass operator $\mathcal{M}$ and the stiffness operator $\mathcal{K}$ contain only spatial derivatives up to some maximum order which we call the order of the operator. The first important property of self-adjoint systems is that $\mathcal{M}$ and $\mathcal{K}$ are of even order. We denote the order of $\mathcal{M}$ by $\mathcal{O}_{\mathcal{M}}$ and the order of $\mathcal{K}$ by $\mathcal{O}_{\mathcal{K}}$. We generally have $\mathcal{O}_{\mathcal{K}} > \mathcal{O}_{\mathcal{M}}$ [132].

The PDE (2.1) may have infinitely many solutions. In order to have a unique solution, appropriate initial and boundary conditions are necessary which together with the PDE define the *initial/boundary value problem*. The *boundary conditions* can take many different forms and can even depend on the PDE variable $w(\boldsymbol{x}, t)$. However, in many practical applications, they are of the type

$$\mathcal{B}_i \{w(\boldsymbol{x}, t)\} = w_{\mathrm{bc}}(\boldsymbol{x}, t), \quad \boldsymbol{x} \in \partial\mathcal{D}, \quad i = 1, \dots, {}^{\mathcal{O}_{\mathcal{K}}}\!/_{2}, \tag{2.2}$$

with some linear homogeneous spatial operator $\mathcal{B}_i$ for the ith boundary condition and a possibly time-depending term w_{bc} independent of $w(\boldsymbol{x}, t)$. The fact that a total of ${}^{\mathcal{O}_{\mathcal{K}}}\!/_{2}$ boundary conditions are necessary for a well-posed definition of the boundary value problem is also a feature of self-adjoint problems. If the right hand side of (2.2) is equivalent to zero, the boundary condition is termed *homogeneous*. In general, the maximum order of $\mathcal{B}_i$ can be $\mathcal{O}_{\mathcal{K}} - 1$. The boundary conditions of order $0, \dots, {}^{\mathcal{O}_{\mathcal{K}}}\!/_{2} - 1$ are termed *geometric boundary conditions*, whereas the boundary conditions of order ${}^{\mathcal{O}_{\mathcal{K}}}\!/_{2}, \dots, \mathcal{O}_{\mathcal{K}} - 1$ are called *dynamic boundary conditions*. The distinction between these two classes of boundary conditions is essential for the classification of basis functions utilized by discretization methods, see [94]. Any continuous function that is satisfying all the geometric and dynamic boundary conditions and is at least $\mathcal{O}_{\mathcal{K}}$ times differentiable on $\mathcal{D}$ is a *comparison function*. A function that is ${}^{\mathcal{O}_{\mathcal{K}}}\!/_{2}$ times differentiable and satisfies the geometric boundary conditions only is an *admissible function*. Clearly, the set of comparison functions is a subset of the set of admissible functions.

The *initial conditions* state the values of the variable w and its first time derivative at $t = 0$,

$$w_0 := w(\boldsymbol{x}, 0), \quad \dot{w}_0 := \left.\frac{\partial w(\boldsymbol{x}, t)}{\partial t}\right|_{t=0}. \tag{2.3}$$

We can now state a formal definition of a *self-adjoint* operator, see [132], where it is assumed that the boundary conditions do not depend on the variable w: A linear operator $\mathcal{L}$ is called self-adjoint if, for any two comparison functions W_i^{c} and W_j^{c}, we have

$$\langle \mathcal{L}\{W_i^{\mathrm{c}}\}, W_j^{\mathrm{c}} \rangle_{\mathcal{D}} = \langle \mathcal{L}\{W_j^{\mathrm{c}}\}, W_i^{\mathrm{c}} \rangle_{\mathcal{D}}, \tag{2.4}$$

where $\langle f_1(\boldsymbol{x}), f_2(\boldsymbol{x}) \rangle_{\mathcal{D}}$ defines the *inner product* of any two functions defined on the domain $\mathcal{D}$,

$$\langle f_1(\boldsymbol{x}), f_2(\boldsymbol{x}) \rangle_{\mathcal{D}} := \int_{\mathcal{D}} f_1(\boldsymbol{x}) f_2(\boldsymbol{x}) \, \mathrm{d}\mathcal{D}. \tag{2.5}$$

As can be seen from the above equations, self-adjointness involves the notion of symmetry. A problem of the form (2.1) is called self-adjoint, if both the mass- and stiffness operators are self-adjoint.

It is also helpful to introduce the concept of definiteness for operators. A linear operator $\mathcal{L}$ is called *positive definite* if the following inequality holds for every non-zero comparison function W_i^{c},

$$\langle W_i^{\mathrm{c}}, \mathcal{L}\{W_i^{\mathrm{c}}\}\rangle_{\mathcal{D}} > 0. \tag{2.6}$$

If the left hand side of the above inequality can take zero value without W_i^{c} being identically zero, the operator is termed *positive semidefinite*. As pointed out in [132], it is most common that the mass operator is positive definite. Therefore, the definiteness of the problem (2.1) is determined by the stiffness operator $\mathcal{K}$ which can be both positive definite and positive semidefinite.

A solution of the homogeneous PDE (2.1) ($F(\boldsymbol{x},t) \equiv 0$) can be assumed to be of the form $w(\boldsymbol{x},t) = W(\boldsymbol{x})\eta(t)$ with some function W depending on spatial coordinates and some time-dependent function η. The fact that the solution, which depends on both space and time, can be put as a product of two functions with each one depending only on one variable is called the *separation of variables* technique. It is applicable to the solution of homogeneous PDEs with constant coefficients and homogeneous boundary conditions [158]. It is obvious that $W(\boldsymbol{x})$ has to satisfy the boundary conditions while $\eta(t)$ must obey the initial conditions.

One may, for example, assume $w(\boldsymbol{x},t) = W(\boldsymbol{x})\cos(\omega t + \alpha)$. This form of solution is motivated by the fact that undamped mechanical systems perform undamped harmonic oscillations in free motion. When this ansatz is used in (2.1) with zero right hand side, and one requires the resulting expression to be true for all times t, one gets

$$\mathcal{K}\{W\} - \mathcal{M}\{W\}\omega^2 = 0. \tag{2.7}$$

This is the *eigenvalue problem* (EVP) for the PDE. There are in general infinitely many pairs of *eigenvalues* ω_i^2 and *eigenfunctions* W_i^{e} to satisfy the eigenvalue problem. The determination of a system's eigenfunctions and eigenfrequencies is called (theoretical) *modal analysis*.

With the introduced terminology in mind, we state the following properties of self-adjoint eigenvalue problems ([94], [132]):

- The eigenvalues ω_i^2 of positive (semi-)definite eigenvalue problems form an infinite sequence of positive (non-negative) real numbers.
- The eigenfunctions which correspond to the eigenvalues are real-valued functions.
- Any two eigenfunctions W_i^{e} and W_j^{e} associated with two different eigenvalues are orthogonal with respect to the operators $\mathcal{K}$ and $\mathcal{M}$, i.e. $\langle \mathcal{M}\{W_i^{\mathrm{e}}\}, W_j^{\mathrm{e}}\rangle = 0$ and $\langle \mathcal{K}\{W_i^{\mathrm{e}}\}, W_j^{\mathrm{e}}\rangle = 0$.
- Any eigenfunctions associated with a multiple eigenvalue are linearly independent and orthogonal to the remaining eigenfunctions.
- The *expansion theorem* is applicable.

The expansion theorem [94] states that the eigenfunctions constitute a basis for the function space of comparison functions. This means that every function which is continuous in $\mathcal{M}\{w\}$ and $\mathcal{K}\{w\}$

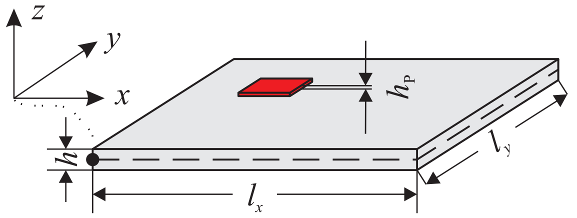

Figure 2.1: Geometric properties of the plate.

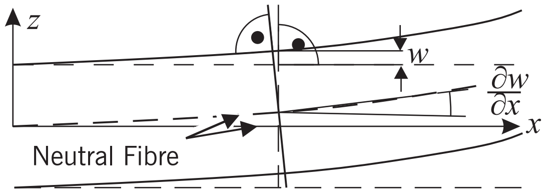

Figure 2.2: Illustration of Kirchhoff's hypothesis.

and satisfies all boundary conditions can be expanded in a uniformly convergent series of the form $W^c(\boldsymbol{x}) = \sum_{i=1}^{\infty} \eta_i W_i^e(\boldsymbol{x})$ with appropriate constants η_i. Therefore, one can think of eigenfunctions as a special subset of comparison functions. The expansion theorem provides the ground for the analytical solution methods for the initial/boundary value problem constituted by (2.1), (2.2), and (2.3). More specifically, the separation of variables technique and the expansion theorem together imply that a natural way to solve such problems is to expand the solution as a superposition of eigenfunctions with time depending coefficients,

$$w(\boldsymbol{x}, t) = \sum_{i=1}^{\infty} W_i^e(\boldsymbol{x})\eta_i(t). \tag{2.8}$$

The coefficients $\eta_i(t)$ which are associated with the eigenfunctions in (2.8) are the *generalized coordinates* or *modal coordinates*. The fact that the expansion theorem is applicable not only implies the existence of a solution. It also implies that the values of the modal coordinates and therefore the whole solution to the initial/boundary value problem is unique. This stems from the basis property of the eigenfunctions. However, the task of finding the eigenfunctions may be futile, especially for systems with irregular geometry.

2.2.2 Elements of Plate Theory

We will now state the PDE which describes the motion of the plate of the acoustic demonstrator and briefly mention the modifications introduced by the existence of bonded piezoceramic patches. The basic geometrical properties of the rectangular plate are shown in Fig. 2.1, where the plate is assumed to be homogeneous and of constant thickness. The coordinate system is placed in the lower left plate corner in the mid-plane of the plate. A single piezoelectric element with thickness h_P is also shown. The polarization direction of the piezoelectric patch is set in negative z-direction. Consequently, the $(1, 2)$-plane of the crystal lattice (see App. A.2) is parallel to the (x, y)-plane of the plate.

The following simplifying assumptions are made ([13], [94])

- The plate has homogeneous material properties and is of constant thickness.
- The plate is subject to: external forces acting normal to the plate and bending moments generated by the piezoelectric elements. The in-plane forces generated by the piezo patches are neglected.

- The plate thickness h is small compared to its lateral extensions l_x and l_y.
- Plate deflections are sufficiently small, so that all equilibrium conditions can be referred to the unperturbed reference state. This together with the previous assumptions ensures the plate equations to become linear and decouples the plate's in-plane and transverse dynamics.
- The thickness of the piezoelectric material is small compared to the plate thickness, $h_{\mathrm{P}} \ll h$, so that constant strain can be assumed within the piezoelectric material. This also implies that the position of the neutral fiber is not altered by the presence of the piezoelectric elements.
- The transverse normal stress is small compared to the other normal stresses in the plate and hence can be neglected.
- A line which is originally normal to the neutral fiber will remain normal to the neutral fiber when the plate is deflected, see Fig. 2.2. This is known as Kirchhoff's hypothesis. It implies that the plate is infinitely stiff in shear. An argument will be given later on that this assumption is satisfied for the plate of the acoustic demonstrator in the considered frequency range.

The main implication of the above statements is that a plane stress state as well as a plane strain state can be assumed. Under these assumptions, the Kirchhoff plate equation for an undamped plate, see [13], can be used to describe the motion of a rectangular plate under external loads,

$$\rho h \frac{\partial^2 w(x,y,t)}{\partial t^2} - \frac{\partial^2 M_x}{\partial x^2} - \frac{\partial^2 M_y}{\partial y^2} - 2\frac{\partial^2 M_{xy}}{\partial x \partial y} = F(x,y,t) + \frac{\partial m_x(x,y,t)}{\partial y} + \frac{\partial m_y(x,y,t)}{\partial x}. \quad (2.9)$$

The plate equation describes the dynamics of the bending wave propagation in the medium. More specifically, it relates the plate's transverse deflection w to the external force distributions and moments over time t. The forces per unit area acting normal to the surface are denoted by F, whereas the moments along the x- and y-axes per unit area are denoted by m_x and m_y, respectively. The density of the plate material is given by ρ. The quantities $M_x(x,y,t)$, $M_y(x,y,t)$, and $M_{xy}(x,y,t)$ are so-called moment resultants,

$$M_x = \int_{-\frac{h}{2}}^{+\frac{h}{2}} \sigma_x z \,\mathrm{d}z, \quad M_y = \int_{-\frac{h}{2}}^{+\frac{h}{2}} \sigma_y z \,\mathrm{d}z, \quad \text{and} \quad M_{xy} = \int_{-\frac{h}{2}}^{+\frac{h}{2}} \tau_{xy} z \,\mathrm{d}z, \quad (2.10)$$

with the two normal stresses σ_x, σ_y, and the shear stress τ_{xy}. All stresses are time-dependent functions of the three coordinates x, y, and z.

The different stresses are related to the strain distribution in the medium by Hooke's law, which in turn can be calculated from the kinematics of plate deformation [94]:

$$\sigma_x = \frac{E}{1-\nu^2}\left(\epsilon_x + \nu\epsilon_y\right) \qquad \sigma_y = \frac{E}{1-\nu^2}\left(\nu\epsilon_x + \epsilon_y\right) \qquad \tau_{xy} = \frac{E}{2(1+\nu)}\gamma_{xy} \quad (2.11\text{a})$$

with

$$\epsilon_x = -z\frac{\partial^2 w}{\partial x^2} \qquad \epsilon_y = -z\frac{\partial^2 w}{\partial y^2} \qquad \gamma_{xy} = -2z\frac{\partial^2 w}{\partial x \partial y}. \quad (2.11\text{b})$$

In the above equations, $\epsilon_{\{x,y\}}$ are the normal strains in x and y-direction, respectively, and γ_{xy} is the shear deformation. Young's modulus is given by E and Poisson's ratio by ν.
When the kinematic relations (2.11b) are used together with Hooke's Law (2.11a) and the moment resultants (2.10), the stiffness operator can be simplified to [94]

$$\mathcal{K} = -\left(\frac{\partial^2 M_x}{\partial x^2} + 2\frac{\partial^2 M_{xy}}{\partial x \partial y} + \frac{\partial^2 M_y}{\partial y^2}\right) = D\nabla^4 w, \tag{2.12}$$

where $\nabla^4 = \frac{\partial^4}{\partial x^4} + 2\frac{\partial^4}{\partial x^2 \partial y^2} + \frac{\partial^4}{\partial y^4}$, and $D = \frac{Eh^3}{12(1-\nu^2)}$ is the bending stiffness of the plate. The mass operator of the plate is simply $\mathcal{M} = \rho h$. Both operators can be shown to be self-adjoint and positive definite.

The PDE (2.9) must be supplied with suitable initial and boundary conditions to be meaningful. The initial conditions specify the plate's position and velocity on every point of the plate area at $t = 0$,

$$w_0 := w(x, y, 0), \tag{2.13a}$$

$$\dot{w}_0 := \dot{w}(x, y, 0). \tag{2.13b}$$

Since there appear fourth order spatial derivatives of the plate deflection w in the plate equation, the boundary conditions can in general contain spatial derivatives up to third order. To completely define the boundary value problem, two boundary conditions are necessary for each edge of the plate.
The most common assumption for the boundary conditions is that the plate is simply supported along all four edges. This amounts to the boundary conditions being

$$\begin{gathered} w(0,y,t) \equiv 0, \qquad w(l_x,y,t) \equiv 0, \qquad w(x,0,t) \equiv 0, \qquad w(x,l_y,t) \equiv 0, \\ \left.\frac{\partial^2 w(x,y,t)}{\partial x^2}\right|_{x=0} \equiv 0, \quad \left.\frac{\partial^2 w(x,y,t)}{\partial x^2}\right|_{x=l_x} \equiv 0, \quad \left.\frac{\partial^2 w(x,y,t)}{\partial y^2}\right|_{y=0} \equiv 0, \quad \left.\frac{\partial^2 w(x,y,t)}{\partial y^2}\right|_{y=l_y} \equiv 0. \end{gathered} \tag{2.14}$$

The first row of (2.14) contains the geometric boundary conditions which simply state that there must be no displacements at the edges of the plate. The second row contains the dynamic boundary conditions which come from the fact the moments at the simply supporting bearings must be zero. The set of boundary conditions for the simply-supported plate is homogeneous.

Although it is impossible to build a perfectly simply-supported plate in reality, it is this special case of plate dynamics which is studied most. The reason for this is that it allows for an analytic solution of the eigenvalue problem. Therefore, we will also adopt these boundary conditions for the analytic model of the acoustic demonstrator. It will be shown in Sec. 2.5 that the boundary conditions of the real plate cannot be captured by any idealized boundary condition, be it a simply-supported boundary or a perfectly clamped boundary.

Since the separation of variables technique and the expansion theorem are applicable for the study of Kirchhoff plate dynamics, a solution can be searched in the form of (2.8). This type of solution is the one which is most suitable for the study of waves in bounded media. It can be interpreted

as a superposition of *standing waves* given by the elements $W_i(x, y)$. In literature, the standing wave solution is also termed *Bernoulli's solution* [94].
Under certain circumstances, it might be advantageous to state the solution as a superposition of *traveling waves*, also known as *d'Alembert's solution*. This is especially the case when unbounded, non-dispersive media are studied. Then, the solution can be efficiently expressed as two waves traveling in opposite direction. Since bending waves in plates are *dispersive*, d'Alemberts solution will not be paid much attention in this thesis. Nevertheless, the traveling wave point of view will be useful for comparing the Kirchhoff plate theory with two more complex theories in the following.

Three Different Plate Theories

The Kirchhoff plate equation is the outcome of the simplest useful plate theory available. It assumes that the in-plane and out-of-plane dynamics are decoupled. Therefore, it suffices to state only the out-of-plane equation (2.9). A model which accounts for coupled dynamics is known as the von Kármán model, see [13]. Furthermore, the rotary inertia of the infinitesimal plate elements is neglected in Kirchhoff theory. A model which allows for noteworthy rotational effects is the Kirchhoff-Rayleigh model. An even more sophisticated theory is the Reissner-Mindlin plate theory that allows for both rotatory effects and shear deformation, see [94].

In order to determine which plate theory is appropriate, it is instructive to examine the different phase velocities of the bending waves given by the plate theories. The phase velocity c_{ph} is the velocity with which an observer must travel along the direction of an harmonic wave of frequency ω to observe a constant phase. It is given by the relation

$$c_{\mathrm{ph}} = \frac{\omega}{k}.$$

The wavenumber k is related to the wavelength λ by $k = \frac{2\pi}{\lambda}$ and represents the periodicity of the wave in space, whereas $\omega = \frac{2\pi}{T_{\mathrm{P}}}$ represents the periodicity in time when T_{P} is the time period. The phase velocities of the Kirchhoff and Kirchhoff-Rayleigh models are given as [94]

$$c_{\mathrm{ph}}^{\mathrm{K}} = \sqrt{\frac{Dk^2}{\rho h}}, \quad c_{\mathrm{ph}}^{\mathrm{KR}} = \sqrt{\frac{Dk^2}{\rho h + \rho h^3 \frac{k^2}{12}}}.$$

The Reissner-Mindlin model describes both bending and shear deformation and has therefore two phase velocities, one for each type of wave. They are implicitly given by the quadratic equation [94]

$$\left(1 - \frac{\left(c_{\mathrm{ph},\{1,2\}}^{\mathrm{RM}}\right)^2}{\kappa^2 c_{\mathrm{S}}^2}\right)\left(\frac{\bar{c}^2}{\left(c_{\mathrm{ph},\{1,2\}}^{\mathrm{RM}}\right)^2} - 1\right) = \frac{12}{h^2 k^2}$$

with $c_{\mathrm{S}} = \sqrt{\frac{E}{2\rho(1+\nu)}}$, $\bar{c} = \lim_{k\to\infty} c_{\mathrm{ph}}^{\mathrm{KR}} = \sqrt{\frac{E}{\rho(1-\nu^2)}}$, and the shear correction factor $\kappa \approx \frac{5}{6}$.

It is clear for all three models that the phase velocity is a function of the wavenumber. This implies that traveling harmonic waves of different wavelengths (and hence different wavenumbers) travel

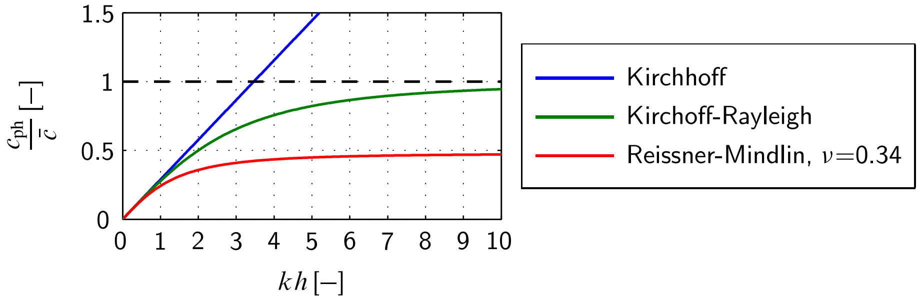

Figure 2.3: Normalized phase velocities of three different plate theories.

with different phase velocities. This can be given a figurative interpretation: Consider an arbitrary waveform at time $t = 0$ as initial condition of the plate surface. This waveform can in general be described as a superposition of harmonic waves by means of spatial Fourier transform. When the plate is released, the different harmonic components will travel with different speeds along the plate and the waveform will disperse, i.e. will lose its initial shape. This is why a plate is called a dispersive medium for bending waves.

In Fig. 2.3, the normalized phase velocities of the three plate theories are displayed over the dimensionless quantity kh. The normalization is taken with respect to the asymptotic value of the phase velocity of the Kirchhoff-Rayleigh model, $\bar{c}$. Only the bending-wave phase velocity of the Reissner-Mindlin theory is shown. The von Kármán theory is not considered here. The Kirchhoff theory implies unbounded phase velocities for increasing bending wave frequencies which is unrealistic and can be attributed to the neglected rotatory inertia. However, all three theories agree reasonably well, as long as the dimensionless quantity kh is smaller than one. Consequently, for a given plate thickness, Kirchhoff plate theory is sufficient if the wave number, and therefore the frequency, is small enough. The relation between the wavenumber k and the bending wave frequency ω of a harmonic wave is given by the medium's *dispersion relation*. In case of the Kirchhoff plate, the dispersion relation is, see [94],

$$\rho h\omega^2 - Dk^4 = 0. \tag{2.15}$$

The maximum relevant frequency of the acoustic demonstrator for modeling and control purposes is set to 500 Hz, as was explained in the last chapter. Then, the above equation can be solved, considering the geometric and material properties of the demonstrator's plate (see Appendix A.1), for the wavenumber which is $k = 22.4\,\mathrm{m}^{-1}$ and $kh = 0.0897 \ll 1$. Thus, it is clear that Kirchhoff plate theory is sufficient for the purpose of describing the plate dynamics of the acoustic demonstrator.

Effects of Piezoelectric Elements

Now that the basic plate dynamics are known to be sufficiently described by (2.9) along with corresponding initial and boundary conditions, the effects of bonded piezoelectric material have to be considered. The effects of piezoelectric patches on the plate dynamics can be separated in

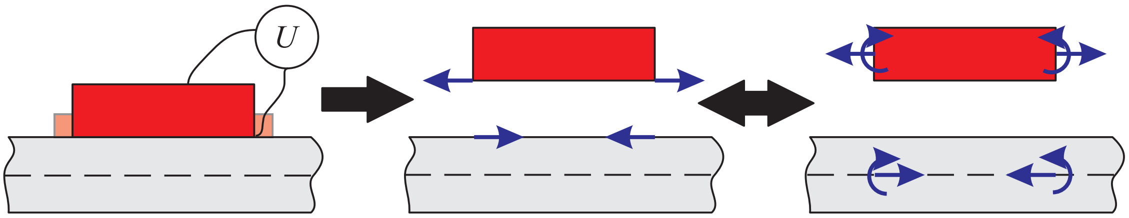

Figure 2.4: Forces and moments generated by the indirect piezoelectric effect.

two groups: passive and active effects. The passive effects are caused by the patches' mass and stiffness contributions alone. The active effects are due to the direct and inverse piezoelectric effects.

The passive effects are included in the moment resultants appearing on the left hand side of the plate equation (2.9). Thus, the expressions (2.10) must be replaced by moment resultants which account for the additional mass and stiffness contributions, see for example [13]. Since only some parts of the plate surface are generally covered with piezoelectric material, the overall mass and stiffness distributions are usually discontinuous. Due to this discontinuity, the required calculation of the spatial derivatives of the moment resultants is impossible, which implies that a classical, or *strong form* solution to the plate equation is not existent. A remedy for this problem is the derivation of the *weak form* of the problem by the use of so-called *test functions*. This procedure is strongly related to the method to be presented in Sec. 2.3 for the finite-dimensional modeling of the acoustic demonstrator. One can consult for example [40] or [67] for a general treatment of partial differential equations.

Bending moments result from the inverse piezoelectric effect when voltages are applied to the actuator patches. Conversely, there will be a measurable electric potential between the electrodes of piezoceramic patches when they are deformed by the plate motion and used as sensor patches. It is assumed throughout this thesis that the amplitude of the applied voltages is small enough for the piezoelectric hysteresis to be negligible. Then, the linearized constitutive equations of piezoelectric material can be used, see App. A.2. If this assumption is not valid, one may either use nonlinear constitutive equations, see e.g. [196], or employ a hysteresis compensation technique, like in [117].
The application of some voltage to the actuator electrodes will result in both normal forces and bending moments due to the shrinkage (or extension, depending on the sign of the electric potential) of the piezoelectric material, see Fig. 2.4. Since Kirchhoff plate theory is applied, the normal forces do not contribute to plate deflection, because in-plane and out-of-plane motion are decoupled. Expressions for the bending moments m_x and m_y appearing on the right hand side of (2.9) for a given voltage $U(t)$ can be found in [13].

2.2.3 Model of the Acoustic Cavity

After the PDE of the plate dynamics has been stated in the last section, we now reproduce the partial differential equation that describes the dynamics of the enclosed acoustic volume of the acoustic demonstrator. This equation is known as the three-dimensional *wave equation*. As in the case of plate theory, several common assumptions are made in the derivation of the three-dimensional wave equation which are stated below [69]:

- The fluid has homogeneous material properties and the fluid properties are direction independent (isotropic).
- The fluid is assumed to obey the Perfect Gas law.
- The fluid is inviscid.
- The process that changes the state of the gas can be described as adiabatic. This, together with the foregoing assumption implies that the process is isentropic.
- The changes of state variables (pressure, temperature, density) are assumed to be small compared to their ambient (undisturbed) values.

Under the above assumptions, the gas dynamics can be described within the framework of linear wave phenomena. As opposed to bending waves in plates, acoustic waves in fluids are *non-dispersive*, i.e. the harmonic wave components propagate with one specific velocity, regardless of their wavelength. Furthermore, acoustic waves are *longitudinal waves*, whereas *bending waves* are a mixture of longitudinal and *transverse waves* [70]. Mathematically, the pressure fluctuation in the fluid can be described by the non-homogeneous, three-dimensional wave equation [69]

$$\frac{1}{c_0^2}\frac{\partial^2 p(x,y,z,t)}{\partial t^2} - \Delta p(x,y,z,t) = \rho_0 \frac{\partial \dot{V}(x,y,z,t)}{\partial t} - \underbrace{\nabla \cdot \boldsymbol{F}(x,y,z,t)}_{=0}, \tag{2.16}$$

where $\Delta = \frac{\partial^2}{\partial x^2} + \frac{\partial^2}{\partial y^2} + \frac{\partial^2}{\partial z^2}$ denotes the Laplace-operator (divergence of the gradient), p is the scalar pressure field in Cartesian coordinates, and c_0 is the wave speed in the fluid. If the medium is air, c_0 corresponds to the speed of sound which is approximately $343\,\mathrm{m\,s^{-1}}$. In general, the speed of sound in a gaseous medium is a function of its absolute temperature, $c_0 = \sqrt{\kappa R T_0}$ with the isentropic constant κ, gas constant R, and absolute temperature T_0 [69].

The applied Cartesian coordinate system which is located in the neutral plane of the plate is shown in Figs. 2.1 and 2.6 on page 26. The z-axis points upwards, and the thickness of the plate is negligible compared to the height l_z of the cavity, $h \ll l_z$. Thus, the z-coordinate within the acoustic volume takes values in the interval $[-l_z, 0]$.

Two types of excitation are possible for the fluid: Volume displacement and external forcing. In acoustics, it is conventional to express the strength of an acoustic source by its rate of change of volume displacement $\dot{V}$ [69]. To clarify this, imagine a loudspeaker. The generated pressure fluctuation (sound) is the stronger, the greater the velocity of the membrane and therefore the rate of change of displaced volume is.

The acoustic forcing term on the right hand side of (2.16) contains the ambient fluid density ρ_0 and the volumetric volume velocity $\dot{V}$ caused by acoustic sources in the fluid. The second term represents the influence of some volumetric force field $\boldsymbol{F}(x,y,z,t)$ acting on the fluid. The operator $\nabla \cdot \boldsymbol{F} = \frac{\partial F_x}{\partial x} + \frac{\partial F_y}{\partial y} + \frac{\partial F_z}{\partial z}$ denotes the divergence of the force field. Excitation by volumetric force fields will not be considered in this thesis and therefore, the corresponding term is deliberately set to zero in the above equation.

An explicit relationship between the pressure field p and the vector field of particle velocity $\boldsymbol{v}(x, y, z, t) = \left(v_x,\ v_y,\ v_z\right)^{\mathrm{T}}$ can be derived [69],

$$\nabla p(x, y, z, t) = -\rho_0 \frac{\partial \boldsymbol{v}(x, y, z, t)}{\partial t}, \tag{2.17}$$

where $\nabla = \left(\frac{\partial}{\partial x}\ \frac{\partial}{\partial y}\ \frac{\partial}{\partial z}\right)^{\mathrm{T}}$ denotes the gradient operator. This is essentially a restatement of Newton's second law of motion.

The PDE (2.16) is only meaningful with corresponding initial and boundary conditions. It contains spatial derivatives up to second order which requires one boundary condition for each subdomain of the boundary, see [132]. In case of an enclosed acoustic volume with rigid walls, the particle velocity perpendicular to a rigid wall must be zero at the boundary. For the acoustic demonstrator, this can be stated as

$$\begin{aligned}
&v_x(0, y, z, t) \equiv 0 \Rightarrow \left.\frac{\partial p(x, y, z, t)}{\partial x}\right|_{x=0} \equiv 0, \quad v_x(l_x, y, z, t) \equiv 0 \Rightarrow \left.\frac{\partial p(x, y, z, t)}{\partial x}\right|_{x=l_x} \equiv 0,\\
&v_y(x, 0, z, t) \equiv 0 \Rightarrow \left.\frac{\partial p(x, y, z, t)}{\partial y}\right|_{y=0} \equiv 0, \quad v_x(x, l_y, z, t) \equiv 0 \Rightarrow \left.\frac{\partial p(x, y, z, t)}{\partial y}\right|_{y=l_y} \equiv 0,\\
&v_z(x, y, -l_z, t) \equiv 0 \Rightarrow \left.\frac{\partial p(x, y, z, t)}{\partial z}\right|_{z=-l_z} \equiv 0,
\end{aligned} \tag{2.18}$$

where (2.17) was taken into account.

Analogously, at the top of the acoustic volume, where fluid is in contact with the flexible plate, the particle velocity in z-direction must be equal to the plate velocity,

$$v_z(x, y, 0, t) = \frac{\partial w(x, y, t)}{\partial t} \Rightarrow \left.\frac{\partial p(x, y, z, t)}{\partial z}\right|_{z=0} = -\rho_0 \frac{\partial^2 w(x, y, t)}{\partial t^2}. \tag{2.19}$$

Equations (2.16), (2.18), and (2.19) along with the initial conditions

$$\begin{aligned}
p_0 &:= p(x, y, z, 0),\\
\dot{p}_0 &:= \dot{p}(x, y, z, 0)
\end{aligned} \tag{2.20}$$

define the complete initial and boundary value problem for the acoustic volume. In contrast to the boundary value problem for the plate, we only have dynamic boundary conditions for the acoustic volume.

The boundary condition (2.19) describes a volumetric force that is prescribed at the boundary $z = 0$. This is a non-homogeneous boundary condition. It precludes the expansion of the solution in a series of eigenfunctions obtained from modal analysis of the homogeneous problem as in (2.8). However, other solution methods, like integral transforms, are still available. Alternatively, the problem may be converted to a new problem with homogeneous boundary conditions. In this new problem, a special forcing term takes care of the non-homogeneity of the original boundary conditions [132]. We will come back to this problem in Sec. 2.3.3.

We assume for now that such a conversion has been carried out and all boundary conditions are rendered homogeneous. In this new problem, there will be the same mass and stiffness operators as in (2.16). With respect to the general formulation (2.1), we have $\mathcal{M} = \frac{1}{c_0^2}$ and $\mathcal{K} = -\Delta$. The mass operator trivially satisfies the conditions for self-adjointness and positive definiteness. However, the stiffness operator is self-adjoint but only positive semidefinite. This can be easily checked by applying the test (2.6) to the comparison function $P(x, y, z) = 1$. The implication of this will be further elaborated on in the following section.

At this point, it is insightful to observe the connection between the plate subsystem and the cavity subsystem in terms of their initial and boundary value problems. It can be seen that the influence of the acoustic volume on the plate appears as a forcing term on the right hand side of (2.9), $F(x, y, t) = p(x, y, 0, t)$ (if no other normal forces are acting on the plate). By contrast, the coupling between the plate and the acoustic volume appears as a non-homogeneous boundary condition (2.19) in the boundary value problem for the three dimensional wave equation (2.16).

2.3 Lumped Parameter Model

The acoustic demonstrator, whose functionality was explained in Sec. 1.3, consists of three major structural elements: the flexible plate in its supporting frame, the piezoelectric elements, and the acoustic cavity. These elements are excitable by three different kinds of inputs: forces acting normal to the plate surface, voltages applied to the actuator patches, and acoustic sources (loudspeakers) inside or outside the fluid volume. The motion of the plate can be measured on several discrete points on the surface with acceleration sensors. Analogously, the sound pressure can be measured at discrete points with microphones. Acceleration sensors, microphones, and loudspeakers are not modeled as structural elements, for simplicity. They are considered as elements of negligible mass and volume. For the white-box model of the acoustic demonstrator, the following additional simplifications are made:

- The plate dynamics can be described by Kirchhoff plate theory.
- The plate is simply supported on all four edges.
- All walls except for the flexible plate are rigid.
- The fluid obeys the assumptions which are stated in Sec. 2.2.3.
- The linearized constitutive equations of piezoelectric material are applicable.

The third statement implies that the walls have infinite acoustic impedance and are therefore perfectly reflecting. Energy dissipation will be considered in the model by introducing modal damping for the plate and the fluid, respectively.

As already explained at the beginning of this section, the lumped-parameter model of the demonstrator will be used to study the important features of the real system and to test the applicability of control concepts. An exact match in terms of input-output behavior between model and real system is not sought. Instead, the white-box model of the acoustic demonstrator has to fulfill the following criteria:

- It should be easily parametrizable,
- contain physically meaningful parameters,
- and display the distinct features of the real system that are important for control design.

It will be illustrated at numerous points in this thesis that the white-box model does indeed capture the characteristic dynamics of the real testbed. The major difference is that the eigenfrequencies of the model are generally lower than that of the real acoustic demonstrator which comes from the idealized boundary conditions of the plate. This will be explained in Sec. 2.5. Besides that, the model truly depicts the following important system features:

- the mode shapes of the plate dynamics and the corresponding observability and controllability properties, see Secs. 2.4 and 2.5,
- the characteristic pole-zero patterns of transfer functions for collocated and non-collocated actuator-sensor-pairs, see Secs. 2.5 and 3.6,
- the structural response due to force and piezoelectric actuation, see Secs. 3.6 and 4.4,
- the characteristic input-output response of modal filters, see Sec. 5.9,
- the sound emission profile of a vibrating plate, see Sec. 5.9,
- and the response of the enclosed fluid volume to excitation by the vibrating plate, see Sec. 5.10.

For the finite-dimensional model of the acoustic demonstrator, it is necessary to discretize the Kirchhoff plate equation (2.9) and the three-dimensional wave equation (2.16) along with their boundary conditions (2.14), (2.18), and (2.19). The outcome of the discretization is a set of ODEs that approximates the weak solution of the problem. As mentioned before, the strong solution is not existent because of the discontinuities caused by the active elements bonded onto the plate. Furthermore, it is shown in App. A.4 that there is another reason that denies the existence of a strong sense solution: As long as the plate is not assumed to be perfectly clamped on all sides, there cannot exist a strong sense solution to the fluid pressure field $p(x, y, z, t)$.

The modeling method which is chosen here is the so-called *Assumed Modes method* [46, 158], as already mentioned in Sec. 2.1. It belongs to the class of *spectral discretization* methods based on variational techniques. The discrete model is derived from *Hamilton's principle* without explicitly making use of the PDEs. It is closely connected to the *Rayleigh-Ritz method*. In fact, the resulting finite-dimensional models of both methods are identical if the same set of basis functions is used. This is shown in [158] which may also be consulted for an overview of spatial and spectral discretization techniques for mechanical structures.

There are two reasons for choosing the Assumed Modes method. Firstly, the finite-dimensional model is produced in a one-step procedure from Hamiltonian mechanics. When using methods that directly operate on the PDEs, like Galerkin's method or the Collocation method, one has to perform a two step process: First derive the PDE by Newtonian or Hamiltonian principles of mechanics and second, discretize the PDE by some suitable method. Since we are not working with the PDEs, the one-step process is preferable. Only the knowledge of the boundary conditions will be required in order to be able to select suitable basis functions for the discretization.

The second reason for selecting this method is that the basis functions need only satisfy the geometric boundary conditions. This is a general advantage over methods that work with comparison functions, like Galerkin's method. One may argue that Galerkin's method and alike are to be expected to show better convergence properties compared to methods that work only with admissible functions [94]. However, it is *not* the primary purpose of the finite-dimensional model to exactly reproduce the dynamics of the infinite-dimensional model, since the PDEs of the idealized acoustic demonstrator are no closer to reality than the finite-dimensional model. It makes therefore no sense to make the error between the dynamics of the PDE and the ODE model as small as possible. In addition to that, if comparison functions are used in the Assumed Modes method, the resulting model is identical to the one derived by Galerkin's method, as pointed out in [94]. Comparison functions will be employed for the modeling process of the plate and fluid dynamics in Sec. 2.3.3.

2.3.1 Literature Review

In the literature, testbeds like the acoustic demonstrator have been considered for fundamental research activities in the field of sound and vibration before, e.g. [149], [179]. Rectangular cavities with a flexible boundary without active elements are considered in textbooks because they are very suitable for illustrating the basic features of mechanical-acoustical coupling ([69], [70]).

The first account of modeling of piezoelectric actuators for control purposes is attributed to Hagood et. al. [95]. Herold [102] explains in his thesis how fluid structure interaction can be captured by finite-element models and how piezoelectric elements can be added a posteriori to order-reduced FEM models for simulation of active systems. He also uses an acoustic demonstrator as an example. In [46] and [193], dynamic models of plates with bonded piezoelectric elements are derived by the same variational technique as is used in this thesis. A connected cavity however, is not considered. A cavity is included in the model of Fang et. al. [72] which is also derived by variational techniques. However, piezo patches and acoustic sources are not present in their model. Cazzolato [43] presents a model of an idealized acoustic demonstrator incorporating all features except for actuator patches. Al-Bassyiouni [3] derives in his thesis a model that incorporates mechanical forces, piezoelectric elements and the coupling of plate and fluid dynamics by Newton's principles of mechanics. Recently, Wang [191] presented a modeling technique for an acoustic cavity with a flexible boundary that is a hybrid of deterministic and stochastic approaches which is especially suitable for medium to high frequencies, where the dynamic behavior of the coupled system is determined by many overlapping modes. Du et. al. [63] present a model that allows for general impedances of the walls containing the fluid, i.e. the walls are not assumed as rigid. However, no plate dynamics of flexible boundaries or actuators and sensors whatsoever are considered.

The following lumped parameter model which includes mechanical, piezoelectric, and acoustic inputs is consequently and completely derived via the Assumed Modes method which employs Hamilton's principle. To the best of the author's knowledge, this model has not been reported in the open literature before.

2.3.2 Lagrange's Equations

The finite-dimensional white-box model of the acoustic demonstrator will now be derived from Hamiltonian mechanics which is a variational formulation of dynamics. The basics of these principles of mechanics can for example be found in [50] and [158].

The extended version of Hamiltonian principle states: *Of all infinitely many paths available to a system between two observed configurations at time instants t_1 and t_2, the system follows that path which achieves*

$$\int_{t_1}^{t_2} \delta\mathcal{L}(t) + \delta W_{\mathrm{nc}}(t)\,\mathrm{d}t = 0. \tag{2.21}$$

In the above equation, the quantity $\mathcal{L}$ is called the *Langrangian* which is constituted by the different forms of energy in the system. In an electromechanical system, one can find four different forms of energy: potential, kinetic, electrical, and magnetic energy. The first two energy forms can be attributed to the mechanics, while the later two belong to the electric domain. In each domain (mechanics and electrics), the two respective forms of energy form a complementary pair. This can for example be seen in undamped harmonic (mechanical or electromagnetic) waves, where the total energy is periodically converted from one form into the other. The Lagrangian is given as the difference of the complementary energies for each domain [50]:

$$\mathcal{L}(t) = E_{\mathrm{kin}}(t) - E_{\mathrm{pot}}(t) + E_{\mathrm{el}}(t) - E_{\mathrm{mag}}(t). \tag{2.22}$$

The addend δW_{nc} in (2.21) represents the virtual work done by non-conservative forces on the system, while the operator δ is the infinitesimal variation operator introduced in calculus of variations [183].

The virtual work of non-conservative forces can be further separated into the part which is done by external non-conservative forces and the part which is due to internal dissipative forces,

$$\delta W_{\mathrm{nc}}(t) = \delta W_{\mathrm{ex}}(t) + \delta W_{\mathrm{d}}(t). \tag{2.23}$$

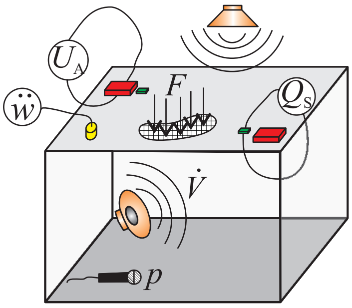

Figure 2.5: Illustration of the acoustic demonstrator.

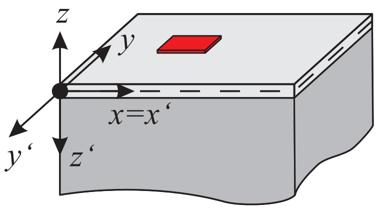

Figure 2.6: Reference and piezoelectric coordinate system.

The acoustic demonstrator model should allow to incorporate three different types of external forces which are illustrated in Fig 2.5: mechanical forces F (per unit area) acting normal on the flexible plate surface, electrical charges Q (per unit volume) acting within the piezoelectric elements which are bonded onto the flexible plate, and the volume displacement velocity $\dot{V}$ (per unit volume) caused by sources of sound within the enclosed fluid. The effects of these external inputs are reflected by the plate deflection w, the electric potential Φ, and the fluid pressure p, respectively. Consequently, δW_{ex} can be further expanded into

$$\delta W_{\mathrm{ex}}(t) = \iint_{A_{\mathrm{S}}} F(x,y,t)\delta w(x,y,t)\,\mathrm{d}A_{\mathrm{S}} - \sum_{i=1}^{n_{\mathrm{P}}} \iiint_{V_{\mathrm{P}_i}} Q_i(x,y,z,t)\delta\Phi_i(x,y,z,t)\,\mathrm{d}V_{\mathrm{P}_i} + \iiint_{V_{\mathrm{F}}} V(x,y,z,t)\delta p(x,y,z,t)\,\mathrm{d}V_{\mathrm{F}}. \tag{2.24}$$

The first term in the above equation refers to the work done by the mechanical load that is acting normal to the surface A_{S} of the plate structure. The second term represents the electrical work done on each of the n_{P} piezoelectric elements with volume V_{P_i}. The scalar field Φ_i is the corresponding electric potential in the ith element. In the last addend, $V(x,y,z,t) = \int_0^t \dot{V}(x,y,z,\tau)\,\mathrm{d}\tau$ denotes the volumetric volume displacement generated by acoustic sources, and p the pressure field in the fluid with volume V_{F}.

The employed coordinate system is shown in Fig. 2.6 and is the same as in Sec. 2.2.2. In addition to that, a second coordinate system with axes x', y', and z' is shown which will be referred to as the coordinate system of the piezoelectric elements. In this coordinate system, the convention is followed that the z-axis is directed in polarization direction. This coordinate system will be useful later on for calculating the energy terms related to the piezo patches.

The negative sign in the term referring to the virtual work of the piezoelectric elements comes from the definition of the electric potential. This can be seen by considering the incremental work done on a charge element Q in an electrical field of strength $\vec{E}$ [47]:

$$\delta W_{\mathrm{el}} = \vec{F}_{\mathrm{el}}\delta\vec{x} = Q\vec{E}\delta\vec{x} = -Q\delta\Phi \quad \text{with} \quad \delta\Phi := -\vec{E}\delta\vec{x}. \tag{2.25}$$

The different forms of energy that appear in the Langrangian (2.22) can be expressed in terms of the field variables $w(x,y,t)$, $\Phi_i(x,y,z,t)$, and $p(x,y,z,t)$. Each field variable is representative for one of the three physical elements that are present in the model of the acoustic demonstrator: the flexible plate, the piezoelectric elements, and the enclosed fluid volume. The dynamics of the fluid volume are governed by the laws of fluid *mechanics* and can therefore be considered as part of the mechanical domain of the model. However, in order to clarify the presentation, we will from now on refer to the acoustic volume as the *acoustic domain* and use the term *mechanical domain* exclusively for the plate dynamics.

The kinetic energy of the system is split between all three domains, i.e. one part refers to the kinetic energy of the flexible structure, one part represents the kinetic energy of the piezoelectric elements, and the third part belongs to the fluid. The same argument applies to the potential energy of the system. The electric and magnetic energy forms are only present in the electric domain. Consequently, (2.22) can be further specified,

$$\mathcal{L} = E_{\mathrm{kin,S}} + E_{\mathrm{kin,P}} + E_{\mathrm{kin,F}} - E_{\mathrm{pot,S}} - E_{\mathrm{pot,P}} - E_{\mathrm{pot,F}} + E_{\mathrm{el,P}} - E_{\mathrm{mag,P}}, \tag{2.26}$$

where the second index indicates the structure (flexible plate), the piezoelectric elements, and fluid, respectively.

The energy terms can be stated in their elementary forms as follows

$$E_{\mathrm{kin,S}} = \frac{1}{2}\rho h \iint_{A_\mathrm{S}} \dot{w}^2 \,\mathrm{d}A_\mathrm{S}, \tag{2.27}$$

$$E_{\mathrm{kin,P}} = \frac{1}{2}\rho_\mathrm{P} \sum_{i=1}^{n_\mathrm{P}} h_{\mathrm{P}_i} \iint_{A_{\mathrm{P}_i}} \dot{w}^2 \,\mathrm{d}A_{\mathrm{P}_i}, \tag{2.28}$$

$$E_{\mathrm{kin,F}} = \frac{1}{2}\rho_0 \iiint_{V_\mathrm{F}} \|\boldsymbol{v}\|_2^2 \,\mathrm{d}V_\mathrm{F}, \tag{2.29}$$

$$E_{\mathrm{pot,S}} = \frac{1}{2} \iiint_{V_\mathrm{S}} \boldsymbol{S}_\mathrm{S}^\mathrm{T} \boldsymbol{T}_\mathrm{S} \,\mathrm{d}V_\mathrm{S}, \tag{2.30}$$

$$E_{\mathrm{pot,P}} = \frac{1}{2} \sum_{i=1}^{n_\mathrm{P}} \iiint_{V_{\mathrm{P}_i}} \boldsymbol{S}_{\mathrm{P}_i}'^\mathrm{T} \boldsymbol{T}_{\mathrm{P}_i}' \,\mathrm{d}V_{\mathrm{P}_i}, \tag{2.31}$$

$$E_{\mathrm{pot,F}} = \frac{1}{2}\frac{1}{\rho_0 c_0^2} \iiint_{V_\mathrm{F}} p^2 \mathrm{d}V_\mathrm{F}, \tag{2.32}$$

$$E_{\mathrm{el,P}} = \frac{1}{2} \sum_{i=1}^{n_\mathrm{P}} \iiint_{V_{\mathrm{P}_i}} \boldsymbol{E}_i'^\mathrm{T} \boldsymbol{D}_i' \,\mathrm{d}V_{\mathrm{P}_i}, \tag{2.33}$$

$$E_{\mathrm{mag,P}} = \frac{1}{2} \sum_{i=1}^{n_\mathrm{P}} \iiint_{V_{\mathrm{P}_i}} \boldsymbol{H}_i'^\mathrm{T} \boldsymbol{B}_i' \,\mathrm{d}V_{\mathrm{P}_i}. \tag{2.34}$$

The newly introduced vector quantities in the above equations are: $\boldsymbol{S} = \left(\epsilon_x, \epsilon_y, \gamma_{xy}\right)^\mathrm{T}$ the vector describing the plane strain state, $\boldsymbol{T} = \left(\sigma_x, \sigma_y, \tau_{xy}\right)^\mathrm{T}$ the vector describing the plane stress state, $\boldsymbol{E} = \left(E_x, E_y, E_z\right)^\mathrm{T}$ the vector field of the electric field strength, $\boldsymbol{D} = \left(D_x, D_y, D_z\right)^\mathrm{T}$ the vector of the electric displacement field, $\boldsymbol{H} = \left(H_x, H_y, H_z\right)^\mathrm{T}$ the vector of the magnetic field strength, and $\boldsymbol{B} = \left(B_x, B_y, B_z\right)^\mathrm{T}$ the vector of the flux density field. All dashed quantities are measured in the piezoelectric coordinate system, and ρ_P denotes the density of the piezoelectric material.
The Kirchhoff plate model is sufficient for the purpose of this thesis to theoretically model the behavior of the flexible structure, as was shown in Sec. 2.2.2. Thus, the kinetic structural energy $E_{\mathrm{kin,S}}$ stems only from transversal motion of the plate. Rotatory motion is neglected.

As mentioned before, all energy quantities can be expressed as integral functions of one of the three field variables $w(x, y, t)$, $\Phi_i(x, y, z, t)$, and $p(x, y, z, t)$. Some of the above energy terms (2.27) to (2.34) are already in this form. The other terms can be rewritten in terms of the respective

field variables as follows:
Equation (2.29) can be expressed in terms of the pressure field by employing (2.17) to give

$$E_{\mathrm{kin,F}}(t) = \frac{1}{2}\frac{1}{\rho_0} \iiint_{V_{\mathrm{F}}} \left\| \nabla \int_0^t p(x,y,z,\tau)\,\mathrm{d}\tau \right\|_2^2 \mathrm{d}V_{\mathrm{F}}. \tag{2.35}$$

The terms for the potential energy of the structure and the piezoelectric elements can be reformulated by making use of the constitutive relations between stress and strain (generalized Hooke's law) in the respective medium. For the structure, this states [87]

$$\boldsymbol{T}_{\mathrm{S}} = \boldsymbol{c}_{\mathrm{S}} \boldsymbol{S}_{\mathrm{S}} \quad \text{with} \quad \boldsymbol{c}_{\mathrm{S}} = \begin{pmatrix} \frac{E}{1-\nu^2} & \frac{E\nu}{1-\nu^2} & 0 \\ \frac{E\nu}{1-\nu^2} & \frac{E}{1-\nu^2} & 0 \\ 0 & 0 & \frac{E}{2(1+\nu)} \end{pmatrix}, \tag{2.36}$$

and consequently

$$E_{\mathrm{pot,S}} = \frac{1}{2} \iiint_{V_{\mathrm{S}}} \boldsymbol{S}_{\mathrm{S}}^{\mathrm{T}} \boldsymbol{c}_{\mathrm{S}} \boldsymbol{S}_{\mathrm{S}}\, \mathrm{d}V_{\mathrm{S}}. \tag{2.37}$$

The potential energy is now fully described by the strain state which is itself a function of the displacement field $w(x,y,t)$, see (2.11b).
For the potential energy of the piezo elements, we employ the linear constitutive equations of piezoelectrics, see App. A.2,

$$\begin{pmatrix} \boldsymbol{D}' \\ \boldsymbol{T}'_{\mathrm{P}} \end{pmatrix} = \begin{pmatrix} \boldsymbol{\epsilon} & \boldsymbol{e} \\ -\boldsymbol{e}^{\mathrm{T}} & \boldsymbol{c}_{\mathrm{P}} \end{pmatrix} \begin{pmatrix} \boldsymbol{E}' \\ \boldsymbol{S}'_{\mathrm{P}} \end{pmatrix} \tag{2.38}$$

and can replace the tension vectors $\boldsymbol{T}_{\mathrm{P},i}$ to give

$$E_{\mathrm{pot,P}} = \underbrace{\frac{1}{2}\sum_{i=1}^{n_{\mathrm{P}}} \iiint_{V_{\mathrm{P}_i}} \boldsymbol{S}_{\mathrm{P}_i}^{\prime\mathrm{T}} \boldsymbol{c}_{\mathrm{P}} \boldsymbol{S}'_{\mathrm{P}_i}\, \mathrm{d}V_{\mathrm{P}_i}}_{=:E_{\mathrm{pot,P,mec}}} - \underbrace{\frac{1}{2}\sum_{i=1}^{n_{\mathrm{P}}} \iiint_{V_{\mathrm{P}_i}} \boldsymbol{S}_{\mathrm{P}_i}^{\prime\mathrm{T}} \boldsymbol{e}^{\mathrm{T}} \boldsymbol{E}'_i\, \mathrm{d}V_{\mathrm{P}_i}}_{=:E_{\mathrm{pot,P,el}}}. \tag{2.39}$$

Since strain in piezoelectric elements cannot only be caused by mechanical stress but also by electric fields, the potential energy of the piezo patches can be split into a part caused by the mechanical load, $E_{\mathrm{pot,P,mech}}$, and one caused by the electrical load, $E_{\mathrm{pot,P,el}}$. In order to finally relate the piezoelectric strain vectors $\boldsymbol{S}_{\mathrm{P},i}$ to the field variable w, it is assumed that the heights of the piezo elements are much smaller that the height of the plate: $h_{\mathrm{P},i} \ll h, \forall i$, as in Sec. 2.2.2. Then, we can also assume that the strains in the piezo elements are constant over their thickness, and thus $\epsilon_{x,\mathrm{P}_i}(x,y,t) = \epsilon_x\left(x,y,\frac{h}{2},t\right)$, $\epsilon_{y,\mathrm{P}_i}(x,y,t) = \epsilon_y\left(x,y,\frac{h}{2},t\right)$, and $\gamma_{xy,\mathrm{P}_i}(x,y,t) = \gamma_{xy}\left(x,y,\frac{h}{2},t\right)$. Now, equations (2.11b) apply again to connect the strain field to the displacement field.
In an analogous way to $E_{\mathrm{pot,P}}$, $E_{\mathrm{el,P}}$ can be expressed in terms of the field variables by considering (2.38),

$$E_{\mathrm{el,P}} = \underbrace{\frac{1}{2}\sum_{i=1}^{n_{\mathrm{P}}} \iiint_{V_{\mathrm{P}_i}} \boldsymbol{E}_i^{\prime\mathrm{T}} \boldsymbol{\epsilon} \boldsymbol{E}'_i\, \mathrm{d}V_{\mathrm{P}_i}}_{=:E_{\mathrm{el,P,el}}} + \underbrace{\frac{1}{2}\sum_{i=1}^{n_{\mathrm{P}}} \iiint_{V_{\mathrm{P}_i}} \boldsymbol{E}_i^{\prime\mathrm{T}} \boldsymbol{e}\, \boldsymbol{S}'_{\mathrm{P}_i}\, \mathrm{d}V_{\mathrm{P}_i}}_{=:E_{\mathrm{el,P,mec}}}. \tag{2.40}$$

It can be easily seen from (2.39) and (2.40) that $E_{\text{pot,P,el}}$ is identical to $E_{\text{el,P,mec}}$ which makes sense, since it represents the mechanical-electrical coupling in the piezoelectric material. The electric field vectors $\boldsymbol{E}_i'$ are connected to the electric potential Φ_i via $\boldsymbol{E}_i' = -\nabla\Phi_i(x', y', z')$, compare (2.25).

The small-signal behavior of piezoelectric material can in most cases be sufficiently described by a capacitive load [196]. The inductance of piezoelectric material is negligible and hence, $E_{\text{mag,P}}$ will not be considered further.

The first step of the discretization process is to express the field variables as functions of a limited set of *generalized coordinates*. Generalized coordinates are defined as coordinates which are linearly independent and thus constitute a minimum-size set of variables to describe the motion of a body [46]. When looking at (2.8), it can be concluded that the modal coordinates are a possible set of generalized coordinates. However, this set is infinite and the eigenfunctions of the system must be known. Since neither the first nor the second statement can be fulfilled in most practical cases, one has to use a finite number of generalized coordinates in combination with appropriate basis functions to discretize the problem and approximate the solution. More precisely: the infinite-dimensional space of the field variable is mapped onto a finite-dimensional space that is spanned by the basis functions. This is the basic idea of all spectral discretization methods [163]. The key idea of the Assumed Modes method is to use this finite-dimensional approximation of the field variables in the variation (2.21) and thereby discretize the energy terms which constitute the Lagrangian. As mentioned before, this is equivalent to the Rayleigh-Ritz method if the same set of basis functions is used [132]. We now introduce the limited set of generalized coordinates and associated basis functions for each of the three field variables,

$$w(x,y,t) = \sum_{i=1}^{n_\text{S}} W_i(x,y)\eta_i(t), \qquad i = 1, \ldots, n_\text{S}, \tag{2.41a}$$

$$\Phi_i(x,y,z,t) = R_i(x,y,z)\nu_i(t), \qquad i = 1, \ldots, n_\text{P}, \tag{2.41b}$$

$$p(x,y,z,t) = \sum_{i=1}^{n_\text{F}} P_i(x,y,z)\dot{\varphi}_i(t), \qquad i = 1, \ldots, n_\text{F}. \tag{2.41c}$$

The numbers n_S and n_F indicate the number of degrees of freedom which are available for the approximation of the respective field variables. For the electric domain, the overall number of degrees of freedom is chosen to be equal to the number of piezoelectric elements because of the following reasoning: Generalized coordinates are, by definition, a minimal set of coordinates. Since the applied voltages U_i to the different patches are mutually independent, it is a natural choice to select the voltages as generalized coordinates, $\nu_i = U_i$, $i = 1, \ldots, n_\text{P}$. Thus, only one generalized coordinate is necessary for each patch.

The choice of the basis functions W_i, R_i, and P_i will be explained later on. In a gyroscopic system, the state of the system may also be explicitly depending on time t and not only implicitly via the generalized coordinates [153]. However, this is not the case for the acoustic demonstrator.

With respect to equations (2.27) to (2.40), it is clear that the Lagrangian becomes now a function of the generalized coordinates and their first order time derivatives only,

$$\mathcal{L} = f(\eta_1, \ldots, \eta_{n_\text{S}}, \nu_1, \ldots, \nu_{n_\text{P}}, \varphi_1, \ldots, \varphi_{n_\text{F}}, \dot{\eta}_1, \ldots, \dot{\eta}_{n_\text{S}}, \dot{\nu}_1, \ldots, \dot{\nu}_{n_\text{P}}, \dot{\varphi}_1, \ldots, \dot{\varphi}_{n_\text{F}}). \tag{2.42}$$

At this stage, it is possible to express (2.21) in terms of the generalized coordinates and to carry out the variation. The derivation involves elementary rules of variational calculus and subsequent partial integration of the terms that contain time derivatives of the variation of the generalized coordinates. After simplification, the resulting expressions finally give the so-called *Lagrange's equations*. The detailed derivation is a standard topic in mechanics and can be looked up in many textbooks, e.g. [46], [94], or [158]. There is one Lagrange equation for each degree of freedom which allows us to group the equations for each domain:

$$\frac{\mathrm{d}}{\mathrm{d}t}\frac{\partial \mathcal{L}}{\partial \dot{\eta}_i} - \frac{\partial \mathcal{L}}{\partial \eta_i} - F^{\mathrm{g,nc}}_{\mathrm{S},i} = 0, \qquad i = 1, \ldots, n_{\mathrm{S}}, \tag{2.43a}$$

$$\frac{\mathrm{d}}{\mathrm{d}t}\frac{\partial \mathcal{L}}{\partial \dot{\nu}_i} - \frac{\partial \mathcal{L}}{\partial \nu_i} - F^{\mathrm{g,nc}}_{\mathrm{P},i} = 0, \qquad i = 1, \ldots, n_{\mathrm{P}}, \tag{2.43b}$$

$$\frac{\mathrm{d}}{\mathrm{d}t}\frac{\partial \mathcal{L}}{\partial \dot{\varphi}_i} - \frac{\partial \mathcal{L}}{\partial \varphi_i} + \frac{\mathrm{d}}{\mathrm{d}t}F^{\mathrm{g,nc}}_{\mathrm{F},i} = 0, \qquad i = 1, \ldots, n_{\mathrm{F}}. \tag{2.43c}$$

The non-standard form of (2.43c) comes from the fact that the field variable p is expressed as a function of the time derivatives of the generalized coordinates φ_i, instead of φ_i directly. This was done to preserve the property of the Lagrangian to contain only the generalized coordinates and their first-order time derivatives in (2.42). Because of this peculiarity, the derivation of (2.43c) is shown in App. A.3.

In the above equations, the quantities $F^{\mathrm{g,nc}}_{\cdot,i}$ represent the generalized forces that are associated with the work of the non-conservative forces. As indicated in (2.23), the non-conservative work, and therefore the generalized forces, can be separated in their dissipative (internal damping) and external parts, $F^{\mathrm{g,nc}}_{\cdot,i} = F^{\mathrm{g,d}}_{\cdot,i} + F^{\mathrm{g,ex}}_{\cdot,i}$. For the mechanical and acoustic domains, the dissipative force is assumed to be expressible by a dissipation function $\mathcal{D}_{\{\mathrm{S,F}\}}$ in the form $F^{\mathrm{g,d}}_{\{\mathrm{S,F}\},i} = -\frac{\partial \mathcal{D}_{\{\mathrm{S,F}\}}}{\partial\{\eta_i,\dot{\varphi}_i\}}$, see for example [153]. Since the electric resistance of the piezoelectric elements is negligible, no energy dissipation is modeled in the electric domain, $\mathcal{D}_{\mathrm{P}} \equiv 0$.

The generalized external forces, which are defined during the process of deriving Lagrange's equations (see Appendices A.3 and A.4), are as follows

$$F^{\mathrm{g,ex}}_{\mathrm{S},i}(t) = \langle F(x,y,t), W_i(x,y)\rangle_{A_{\mathrm{S}}}, \qquad i = 1, \ldots, n_{\mathrm{S}}, \tag{2.44a}$$

$$F^{\mathrm{g,ex}}_{\mathrm{P},i}(t) = -\sum_{k=1}^{n_{\mathrm{P}}}\langle Q_i(x,y,z,t), R_i(x,y,z)\rangle_{V_{\mathrm{P}_i}}, \qquad i = 1, \ldots, n_{\mathrm{P}}, \tag{2.44b}$$

$$F^{\mathrm{g,ex}}_{\mathrm{F},i}(t) = \langle V(x,y,z,t), P_i(x,y,z)\rangle_{V_{\mathrm{F}}}, \qquad i = 1, \ldots, n_{\mathrm{F}}. \tag{2.44c}$$

Since the dissipative generalized forces will from now on be described in terms of their dissipation functions $\mathcal{D}_{\{\mathrm{S,F}\}}$, the upper index ex for the external forces becomes unnecessary and will be dropped from now on.

2.3.3 Basis Functions

It is a common feature of all spectral discretization methods which are based on variational principles that they require the basis functions to be admissible functions [158]. The use of comparison functions is not necessary. The reason for this is that the potential energy term in the Lagrangian contains at most derivatives up to half the order of the stiffness operator. Higher order derivatives do in general not appear. However, if comparison functions are used in the Assumed Modes method, the resulting model will be the same as the model obtained with Galerkin's method which explicitly requires comparison functions [94]. The chosen basis functions are now stated for each domain.

Mechanical Basis Functions

For the flexible plate of the demonstrator model, simply-supported boundary conditions (2.14) are assumed on all edges. These boundary conditions are only a crude approximation of the boundary conditions of the real plate. At the real testbed, the plate is fixed within a metal frame but supported by rubber bands on all edges (see Sec. 1.3). This amounts to the boundary conditions being half-way between simply supported and perfectly clamped. In order to accurately describe the real boundary conditions, one had to assume rotatory stiffness and damping elements which may vary along the plate circumference and may even have nonlinear characteristics. Since it is not our goal to fit the parameters of the analytical model to the real testbed, it is economic to assume simply-supported boundary conditions. The simply-supported boundary has the advantage over the fixed boundary that a closed-form solution is possible for the eigenvalue problem. Only numerical approximations are available for a plate which is fixed on all edges, see e.g. [30]. It is natural that fixed boundaries lead to an overall higher stiffness of the flexible structure than simply-supported boundaries. Consequently, the natural frequencies of the fixed plate will generally be higher than those of the simply-supported plate. It will be shown later on in Sec. 2.5 that the natural frequencies of the real plate will indeed lie in between these two extremes.

The shapes of the eigenfunctions at points which are not close to any boundary are anyway almost unaffected by the choice of boundary conditions, as long as they are identical on all edges, as is pointed out in [177]. The notion "not close" to a boundary means in this context that a point has a distance of more than a third of a wave length from any boundary.

In addition to that, it can be assumed that the eigenfunctions of the plate are not substantially altered by the presence of the bonded piezoelectric elements and the coupled fluid volume. All these arguments support the choice of the eigenfunctions of the simply-supported Kirchhoff plate as mechanical basis functions W_i.

The eigenfunctions of a simply-supported plate are given as [94]

$$W_i^{\mathrm{e,K}} = A_{\mathrm{norm,S},i} \sin\left(\frac{n_{\mathrm{S},x}\pi x}{l_x}\right) \sin\left(\frac{n_{\mathrm{S},y}\pi y}{l_y}\right) =: W_i, \tag{2.45}$$

where $n_{\mathrm{S},x}, n_{\mathrm{S},y} \in \mathbb{N}$ are natural numbers that are associated with the index $i \in \mathbb{N}$ of the eigenfunction via a bijective map

$$\mathcal{I}_{\mathrm{S}} : \mathbb{N} \to \mathbb{N}^2, \quad i \mapsto (n_{\mathrm{S},x}, n_{\mathrm{S},y}). \tag{2.46}$$

The graphs of the eigenfunctions are called *mode shapes*. The numbers $n_{\mathrm{S},x}$ and $n_{\mathrm{S},y}$ have a descriptive interpretation in terms of the mode shapes: It can be seen from (2.45) that $n_{\mathrm{S},x}$ and

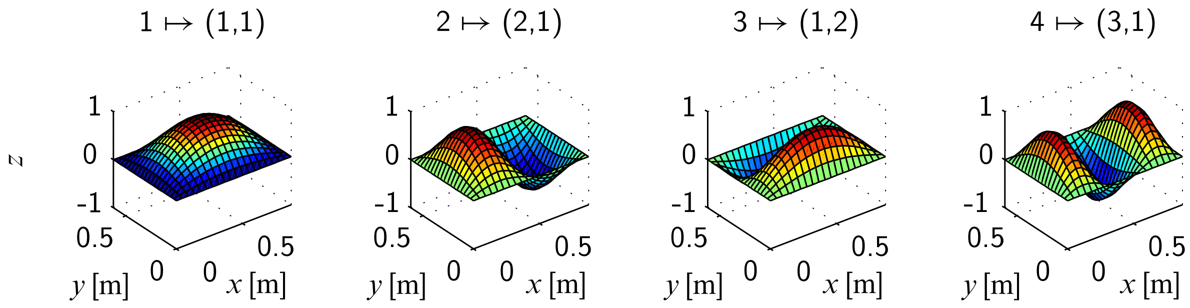

Figure 2.7: First four vibration mode shapes of a simply-supported rectangular plate with $l_x = 870\,\mathrm{mm}$ and $l_y = 620\,\mathrm{mm}$.

$n_{\mathrm{S},y}$ are the numbers of sine half waves of the modes shapes in the x- and y-direction, respectively. Since the eigenfunctions are only defined up to a scaling constant, they can be arbitrarily normalized via the factor $A_{\mathrm{norm,S},i}$. It will be useful to adopt the convention to normalize the eigenfunctions with respect to the mass operator to achieve

$$\iint_{A_{\mathrm{S}}} \mathcal{M}\{W_i^{\mathrm{e}}\} W_j^{\mathrm{e}} \,\mathrm{d}A_{\mathrm{S}} = \delta_{ij}, \quad \forall\{i, j\}, \tag{2.47}$$

where δ_{ij} is equal to one if $i = j$ and zero otherwise. This can be achieved by selecting $A_{\mathrm{norm,S},i} = \frac{2}{\sqrt{\rho h l_x l_y}}$, $\forall i$. The first four normalized mode shapes of a simply-supported plate with dimensions equal to that of the plate of the testbed are shown in Fig. 2.7.

In the finite-dimensional model, the limited subset $W_i^{\mathrm{e},K}$, $i \in \{1, \dots, n_{\mathrm{S}}\}$ of the mutually orthogonal eigenfunctions is used as a basis of the vector space in which the field variable $w(x, y, t)$ is approximated. The basis functions satisfy the geometric and dynamic boundary conditions, i.e. they are comparison functions which generally speeds up convergence.

Electrical Basis Functions

According to (2.41b), the electric potential is expanded in a set of n_{P} basis functions $R_i(x, y, z)$. The small-signal behavior of a piezoelectric patch can be accurately described by the capacitive characteristic of a plate capacitor. Thus, it can be assumed that the electric potential at the top of the ith patch is equal to the applied voltage U_i. From there, potential varies linearly in z-direction to become zero on the ground electrode which is bonded to the plate surface. It is constant in any (x, y)-plane within the patch. The electrical basis functions can therefore be written as

$$R_i(x, y, z) = \begin{cases} \dfrac{1}{h_{\mathrm{P},i}} \left(z - \dfrac{h}{2} \right), & \text{if } (x, y, z) \in V_{\mathrm{P},i}, \\ 0, & \text{else,} \end{cases} \qquad i = 1, \dots, n_{\mathrm{P}}. \tag{2.48}$$

It can be easily verified that the R_i satisfy the required boundary conditions $R_i(x, y, h/2) = 0$ and $R_i(x, y, h/2 + h_{\mathrm{P},i}) = 1$, compare Fig. 2.1. It is obvious that the R_i are mutually orthogonal and therefore also linearly independent.

Since the magnetic field is neglected, the behavior of a piezo element is solely determined by the time-varying electrical field caused by its capacitance. In terms of the electric potential, this can be described by the equation $\Phi_i(x, y, h/2 + h_{\mathrm{P},i}, t) = Q_i(x, y, h/2 + h_{\mathrm{P},i}, t)/C_i$, where C_i is the capacitance of the ith patch. Since the dynamics of the patches are described by *algebraic* equations, the concept of geometric and dynamic boundary conditions does not apply. With the above definition of the electrical basis functions, the electrical generalized forces (2.44b) can be simplified to

$$F^{\mathrm{g}}_{\mathrm{P},i}(t) = -\langle Q_i(x, y, z, t) R_i(x, y, z)\rangle_{V_{\mathrm{P}_i}}, \quad i = 1, \dots, n_{\mathrm{P}}. \tag{2.49}$$

and the ansatz for the electric potential of the ith patch (2.41b) is simply

$$\Phi_i(x, y, z, t) = R_i(x, y, z) U_i(t), \quad i = 1, \dots, n_{\mathrm{P}}. \tag{2.50}$$

Acoustic Basis Functions

As was already mentioned, in the Assumed Modes method, the basis functions need only be admissible functions. Since there are no geometric boundary conditions for the PDE of the acoustic volume, this means that one can choose any set of linearly independent functions as basis functions without consideration of the boundary conditions. However, this is only true if the dynamic boundary conditions are homogeneous. If they are inhomogeneous, i.e. an exogenous force or movement is prescribed at the boundary, the boundary value problem has to be homogenized first. The homogenization process transforms a boundary value problem with inhomogeneous boundary conditions into a problem with homogeneous boundary conditions while at the same introducing an additional forcing term in the PDE. Without homogenization, the exogenous input could not be accounted for in the discretization process.

The inhomogeneity at the boundary between fluid and plate is caused by the requirement that the pressure change in z-direction must be proportional to the plate acceleration, $\frac{\partial p}{\partial z}\big|_{z=0} = -\rho_0 \frac{\partial^2 w}{\partial t^2}$. It is shown in App. A.4 that the inhomogeneous initial/boundary value problem (2.16), (2.18), and (2.19) can be homogenized by adding a forcing term in the distributional sense,

$$\frac{1}{c_0^2}\frac{\partial^2 p(x, y, z, t)}{\partial t^2} - \Delta p(x, y, z, t) = \rho_0 \frac{\partial \dot{V}(x, y, z, t)}{\partial t} - \rho_0 \frac{\partial^2 w}{\partial t^2}\delta(z), \tag{2.51}$$

where $\delta(z)$ represents a three dimensional Dirac function which is located in the plane $z = 0$ that contains the boundary between plate and fluid volume.

Since all the boundary conditions are now homogeneous, a set of basis functions can be easily found. The following set satisfies the new dynamic boundary conditions,

$$P_i = A_{\mathrm{norm,F},i} \cos\left(\frac{n_{\mathrm{F},x}\pi x}{l_x}\right) \cos\left(\frac{n_{\mathrm{F},y}\pi y}{l_y}\right) \cos\left(\frac{n_{\mathrm{F},z}\pi z}{l_z}\right), \quad i = 1, \dots, n_{\mathrm{F}}. \tag{2.52}$$

Analogously to the basis functions for the plate, the index i of the basis function is associated via a bijective map to the indices $n_{\mathrm{F},\cdot}$. The only difference is that the $n_{\mathrm{F},\cdot}$ start from zero,

$$\mathcal{I}_{\mathrm{F}} : \mathbb{N} \to \mathbb{N}_0^3, \quad i \mapsto (n_{\mathrm{F},x}, n_{\mathrm{F},y}, n_{\mathrm{F},z}). \tag{2.53}$$

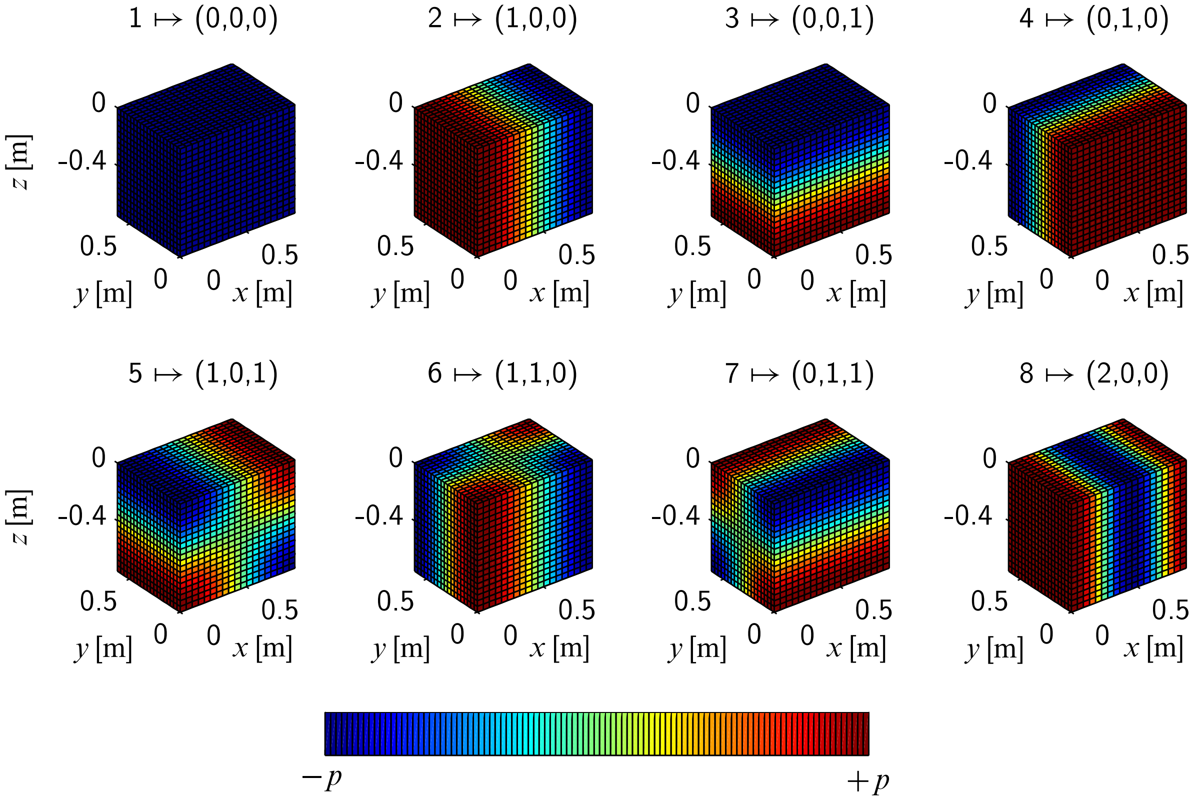

Figure 2.8: First eight vibration mode shapes of the fluid in a rectangular cavity with $l_x = 870\,\text{mm}$, $l_y = 620\,\text{mm}$, and $l_z = 750\,\text{mm}$.

The numbers $n_{\text{F},\cdot}$ represent again the number of harmonic half-waves in the mode shape.
In the case of the fluid, it will show to be advantageous (see App. A.5) to select the normalization factor as

$$A_{\text{norm,F},i} = \begin{cases} 1, & \text{if all } n_{\text{F},\cdot} = 0, \\ A^* \sqrt{\dfrac{l_x l_y l_z \rho_0}{n_{\text{F},x}^2 l_y^2 l_z^2 + n_{\text{F},y}^2 l_x^2 l_z^2 + n_{\text{F},z}^2 l_x^2 l_y^2}}, & \text{else}, \end{cases} \tag{2.54}$$

where

$$A^* = \begin{cases} \dfrac{2\sqrt{2}}{\pi}, & \text{if no } n_{\text{F},\cdot} = 0, \\ \dfrac{2}{\pi}, & \text{if exactly one } n_{\text{F},\cdot} = 0, \\ \dfrac{\sqrt{2}}{\pi}, & \text{if exactly two } n_{\text{F},\cdot} = 0. \end{cases} \tag{2.55}$$

The infinite set of P_i can be shown to be the eigenfunctions of a fluid volume in a rectangular enclosure with rigid walls an all sides, see e.g. [69]. Hence, they form a linearly independent set. The first eight normalized mode shapes are shown in Fig. 2.8.

2.3.4 Discretization of Energy Terms

The energy terms (2.27) to (2.34) have been expressed in terms of the field variables $w(x, y, t)$, $\Phi_i(x, y, z, t)$, and $p(x, y, z, t)$ in Sec. 2.3.2. With the help of the finite-dimensional approximation (2.41), the energy terms and thereby also Lagrange's equations can now be discretized. We will present the discretization process for each energy form separately.

Kinetic Energy of the Structure and the Piezoelectric Elements

Equation (2.27) can be discretized as

$$\begin{aligned} E_{\mathrm{kin,S}} &= \frac{1}{2}\rho h \iint_{A_\mathrm{S}} \dot{w}^2 \,\mathrm{d}A_\mathrm{S} = \frac{1}{2}\rho h \iint_{A_\mathrm{S}} \left(\sum_{i=1}^{n_\mathrm{S}} W_i \dot{\eta}_i\right)^2 \mathrm{d}A_\mathrm{S} = \frac{1}{2}\rho h \iint_{A_\mathrm{S}} \left(\dot{\boldsymbol{\eta}}^\mathrm{T} \boldsymbol{W}\right)^2 \mathrm{d}A_\mathrm{S} \\ \ldots &= \frac{1}{2}\rho h \iint_{A_\mathrm{S}} \dot{\boldsymbol{\eta}}^\mathrm{T} \boldsymbol{W} \boldsymbol{W}^\mathrm{T} \dot{\boldsymbol{\eta}} \,\mathrm{d}A_\mathrm{S} = \frac{1}{2}\dot{\boldsymbol{\eta}}^\mathrm{T} \underbrace{\iint_{A_\mathrm{S}} \boldsymbol{W} \rho h \boldsymbol{W}^\mathrm{T} \,\mathrm{d}A_\mathrm{S}}_{=:\boldsymbol{M}_\mathrm{S}} \dot{\boldsymbol{\eta}} = \frac{1}{2}\dot{\boldsymbol{\eta}}^\mathrm{T} \boldsymbol{M}_\mathrm{S} \dot{\boldsymbol{\eta}}. \end{aligned} \tag{2.56}$$

In the above derivation, the vector notation with vectors $\dot{\boldsymbol{\eta}} = (\dot{\eta}_1, ..., \dot{\eta}_{n_\mathrm{S}})^\mathrm{T}$ and $\boldsymbol{W} = (W_1, ..., W_{n_\mathrm{S}})^\mathrm{T}$ was used. The newly defined matrix $\boldsymbol{M}_\mathrm{S}$ is the mass matrix of the discretized model of the structure.

The kinetic energy of the piezoelectric elements can be analogously derived as

$$E_{\mathrm{kin,P}} = \frac{1}{2}\rho_\mathrm{P} \sum_{i=1}^{n_\mathrm{P}} h_{\mathrm{P}_i} \iint_{A_{\mathrm{P}_i}} \dot{w}^2 \,\mathrm{d}A_{\mathrm{P}_i} = \frac{1}{2}\dot{\boldsymbol{\eta}}^\mathrm{T} \sum_{i=1}^{n_\mathrm{P}} \iint_{A_{\mathrm{P}_i}} \boldsymbol{W}^\mathrm{T} \rho_\mathrm{P} h_{\mathrm{P}_i} \boldsymbol{W} \,\mathrm{d}A_{\mathrm{P}_i} \,\dot{\boldsymbol{\eta}} = \frac{1}{2}\dot{\boldsymbol{\eta}}^\mathrm{T} \boldsymbol{M}_\mathrm{P} \dot{\boldsymbol{\eta}} \tag{2.57}$$

with the piezoelectric mass matrix $\boldsymbol{M}_\mathrm{P}$.

Kinetic Energy of the Fluid Volume

The discretization of the pressure field variable p in (2.35) gives

$$\begin{aligned} E_{\mathrm{kin,F}} &= \frac{1}{2}\frac{1}{\rho_0} \iiint_{V_\mathrm{F}} \left\| \nabla \int_0^t p \,\mathrm{d}\tau \right\|_2^2 \mathrm{d}V_\mathrm{F} = \frac{1}{2}\frac{1}{\rho_0} \iiint_{V_\mathrm{F}} \left\| \nabla \int_0^t \sum_{i=1}^{n_\mathrm{F}} P_i \dot{\varphi}_i \,\mathrm{d}\tau \right\|_2^2 \mathrm{d}V_\mathrm{F} \\ \ldots &= \frac{1}{2}\frac{1}{\rho_0} \iiint_{V_\mathrm{F}} \left\| \nabla \boldsymbol{P}^\mathrm{T} \int_0^t \dot{\boldsymbol{\varphi}} \,\mathrm{d}\tau \right\|_2^2 \mathrm{d}V_\mathrm{F} = \frac{1}{2}\frac{1}{\rho_0} \iiint_{V_\mathrm{F}} \boldsymbol{\varphi}^\mathrm{T}(t) \left(\nabla \boldsymbol{P}^\mathrm{T}\right)^\mathrm{T} \nabla \boldsymbol{P}^\mathrm{T} \boldsymbol{\varphi}(t) \,\mathrm{d}V_\mathrm{F} \\ \ldots &= \frac{1}{2}\boldsymbol{\varphi}^\mathrm{T} \iiint_{V_\mathrm{F}} \left(\nabla \boldsymbol{P}^\mathrm{T}\right)^\mathrm{T} \frac{1}{\rho_0} \nabla \boldsymbol{P}^\mathrm{T} \,\mathrm{d}V_\mathrm{F} \,\boldsymbol{\varphi} = \frac{1}{2}\boldsymbol{\varphi}^\mathrm{T} \boldsymbol{K}_\mathrm{F} \boldsymbol{\varphi}. \end{aligned} \tag{2.58}$$

Here, we use the unusual concept of associating kinetic energy with a stiffness matrix instead of a mass matrix. This is done because the kinetic fluid energy is a function of φ_i and not $\dot{\varphi}_i$. The stiffness matrix of the fluid $\boldsymbol{K}_\mathrm{F}$ is a function of the vector of acoustic basis functions $\boldsymbol{P} = (P_1, \ldots, P_{n_\mathrm{F}})^\mathrm{T}$. It was further assumed, without loss of generality, that the fluid at time $t = 0$ was in its equilibrium state such that $\boldsymbol{\varphi}(0) = (\varphi_1(0), \ldots, \varphi_{n_\mathrm{F}}(0))^\mathrm{T} = \boldsymbol{0}$.

Potential Energy of the Structure and the Piezoelectric Elements

The potential energy which is stored within the flexible structure was given in (2.37) to be

$$E_{\text{pot,S}} = \frac{1}{2} \iiint_{V_\text{S}} \boldsymbol{S}_\text{S}^\text{T} \boldsymbol{c}_\text{S} \boldsymbol{S}_\text{S} \, \mathrm{d}V_\text{S}. \tag{2.59}$$

The interrelationship between the plane strain state $\boldsymbol{S}_\text{S}$ and the plate deflection was shown in (2.11b) and can be compactly rewritten as

$$\boldsymbol{S}_\text{S} = \mathcal{S}_w\{w\} \quad \text{with} \quad \mathcal{S}_w := \left(-z\frac{\partial^2}{\partial x^2}, \, -z\frac{\partial^2}{\partial y^2}, \, -2z\frac{\partial^2}{\partial xy} \right)^\text{T}. \tag{2.60}$$

Using the operator $\mathcal{S}_w$ and the discretization (2.41a) in (2.59), the structural potential energy can be expressed as

$$E_{\text{pot,S}} = \frac{1}{2}\boldsymbol{\eta}^\text{T} \iiint_{V_\text{S}} \mathcal{S}_w \left\{\boldsymbol{W}^\text{T}\right\}^\text{T} \boldsymbol{c}_\text{S} \mathcal{S}_w \left\{\boldsymbol{W}^\text{T}\right\} \, \mathrm{d}V_\text{S} \, \boldsymbol{\eta} = \frac{1}{2}\boldsymbol{\eta}^\text{T} \boldsymbol{K}_\text{S} \boldsymbol{\eta} \tag{2.61}$$

with the structural stiffness matrix $\boldsymbol{K}_\text{S}$.

The potential energy of the piezoelectric elements, measured in the piezoelectric coordinate system, can be calculated by (2.39) as $E_{\text{pot,P}} = E_{\text{pot,P,mec}} - E_{\text{pot,P,el}}$. A coordinate transformation with the transformation matrix $\boldsymbol{T}_\text{S}^\text{c} := \bigoplus\{1, 1, -1\}$ allows for the strain to be expressed in the reference coordinate system, $\boldsymbol{S}_{\text{P},i}' = \boldsymbol{T}_\text{S}^\text{c} \boldsymbol{S}_{\text{P},i}$, compare also Fig. 2.6. Additionally, the strain in each piezo element is assumed to be constant over its thickness (see also Sec. 2.3.2). Thus, we may write $\boldsymbol{S}_{\text{P}_i} = \mathcal{S}_w \{w\} |_{z=h/2}$. Then, the first part of the potential energy reads

$$\begin{aligned} E_{\text{pot,P,mec}} &= \frac{1}{2} \sum_{i=1}^{n_\text{P}} \iiint_{V_{\text{P}_i}} \boldsymbol{S}_{\text{P},i}^\text{T} \underbrace{\boldsymbol{T}_\text{S}^\text{c} \boldsymbol{c}_\text{P} \boldsymbol{T}_\text{S}^\text{c}}_{=\boldsymbol{c}_\text{P}} \boldsymbol{S}_{\text{P},i} \, \mathrm{d}V_{\text{P}_i} \\ \ldots &= \frac{1}{2}\boldsymbol{\eta}^\text{T} \sum_{i=1}^{n_\text{P}} h_{\text{P}_i} \iint_{A_{\text{P}_i}} \mathcal{S}_w \left\{\boldsymbol{W}^\text{T}\right\}^\text{T} \big|_{z=h/2} \boldsymbol{c}_\text{P} \mathcal{S}_w \left\{\boldsymbol{W}^\text{T}\right\} \big|_{z=h/2} \mathrm{d}A_{\text{P}_i} \, \boldsymbol{\eta} = \frac{1}{2}\boldsymbol{\eta}^\text{T} \boldsymbol{K}_\text{P} \boldsymbol{\eta}. \end{aligned} \tag{2.62}$$

Before the electromechanical coupling term is discretized, all quantities will be transformed into the reference coordinate system, too. For that purpose, the transformation matrix $\boldsymbol{T}_\text{E}^\text{c} := \bigoplus\{1, -1, -1\}$ is defined that relates the electric field strength in both coordinate systems, i.e. $\boldsymbol{E}_i' = \boldsymbol{T}_\text{E}^\text{c} \boldsymbol{E}_i$. Now, the coupling term can be expanded as

$$\begin{aligned} E_{\text{pot,P,el}} &= \frac{1}{2} \sum_{i=1}^{n_\text{P}} \iiint_{V_{\text{P}_i}} \boldsymbol{S}_{\text{P}_i}^\text{T} \boldsymbol{T}_\text{S}^\text{c} \boldsymbol{e}^\text{T} \boldsymbol{T}_\text{E}^\text{c} \boldsymbol{E}_i \, \mathrm{d}V_{\text{P}_i} = -\frac{1}{2} \sum_{i=1}^{n_\text{P}} \iiint_{V_{\text{P}_i}} \mathcal{S}_w \{w\}^\text{T} \big|_{z=h/2} \boldsymbol{T}_\text{S}^\text{c} \boldsymbol{e}^\text{T} \boldsymbol{T}_\text{E}^\text{c} \nabla \Phi_i \, \mathrm{d}V_{\text{P}_i} \\ \ldots &= -\frac{1}{2}\boldsymbol{\eta}^\text{T} \sum_{i=1}^{n_\text{P}} \iiint_{V_{\text{P}_i}} \mathcal{S}_w \left\{\boldsymbol{W}^\text{T}\right\}^\text{T} \big|_{z=h/2} \boldsymbol{T}_\text{S}^\text{c} \boldsymbol{e}^\text{T} \boldsymbol{T}_\text{E}^\text{c} \nabla R_i \, \mathrm{d}V_{\text{P}_i} \, U_i = -\frac{1}{2}\boldsymbol{\eta}^\text{T} \sum_{i=1}^{n_\text{P}} \boldsymbol{G}_\text{em}^{(:,i)} U_i \\ \ldots &= -\frac{1}{2}\boldsymbol{\eta}^\text{T} \boldsymbol{G}_\text{em} \boldsymbol{U}, \end{aligned} \tag{2.63}$$

with $\boldsymbol{G}_\text{em}^{(:,i)}$ being the ith column of the electromechanical coupling matrix, and $\boldsymbol{U} = (U_1, ..., U_{n_\text{P}})^\text{T}$.

Potential Energy of the Fluid Volume

The potential energy of the fluid volume was given in (2.32) to be

$$E_{\mathrm{pot,F}} = \frac{1}{2}\frac{1}{\rho_0 c_0^2} \iiint_{V_{\mathrm{F}}} p^2 \mathrm{d}V_{\mathrm{F}} \tag{2.64}$$

which can be discretized as

$$E_{\mathrm{pot,F}} = \frac{1}{2}\frac{1}{\rho_0 c_0^2} \iiint_{V_{\mathrm{F}}} \left(\dot{\boldsymbol{\varphi}}^{\mathrm{T}} \boldsymbol{P}\right)^2 \,\mathrm{d}V_{\mathrm{F}} = \frac{1}{2}\dot{\boldsymbol{\varphi}}^{\mathrm{T}} \iiint_{V_{\mathrm{F}}} \boldsymbol{P} \frac{1}{\rho_0 c_0^2} \boldsymbol{P}^{\mathrm{T}} \,\mathrm{d}V_{\mathrm{F}}\, \dot{\boldsymbol{\varphi}} = \frac{1}{2}\dot{\boldsymbol{\varphi}}^{\mathrm{T}} \boldsymbol{M}_{\mathrm{F}} \dot{\boldsymbol{\varphi}}. \tag{2.65}$$

With an argument analogous to the kinetic fluid energy, we associate the potential energy with a mass matrix because it is a function of the time derivative of the generalized coordinates.

Electric Energy of the Piezoelectric Elements

Similar to the potential energy of the piezoelectric elements, the electric energy stored within the piezo patches consists of two parts: a pure electrical part and one coming from the electromechanical coupling. The electric part reads (see also (2.40))

$$\begin{aligned}
E_{\mathrm{el,P,el}} &= \frac{1}{2}\sum_{i=1}^{n_{\mathrm{P}}} \iiint_{V_{\mathrm{P}_i}} \boldsymbol{E}_i'^{\mathrm{T}} \boldsymbol{\epsilon} \boldsymbol{E}_i' \,\mathrm{d}V_{\mathrm{P}_i} = \frac{1}{2}\sum_{i=1}^{n_{\mathrm{P}}} \iiint_{V_{\mathrm{P}_i}} \boldsymbol{E}_i^{\mathrm{T}} \underbrace{\boldsymbol{T}_{\mathrm{E}}^{\mathrm{c}} \boldsymbol{\epsilon}_{\mathrm{P}} \boldsymbol{T}_{\mathrm{E}}^{\mathrm{c}}}_{=\boldsymbol{\epsilon}_{\mathrm{P}}} \boldsymbol{E}_i \,\mathrm{d}V_{\mathrm{P}_i} \\
\ldots &= \frac{1}{2}\sum_{i=1}^{n_{\mathrm{P}}} \iiint_{V_{\mathrm{P}_i}} (\nabla \Phi_i)^{\mathrm{T}} \boldsymbol{\epsilon}_{\mathrm{P}} \nabla \Phi_i \,\mathrm{d}V_{\mathrm{P}_i} = \frac{1}{2}\sum_{i=1}^{n_{\mathrm{P}}} U_i \iiint_{V_{\mathrm{P}_i}} (\nabla R_i)^{\mathrm{T}} \boldsymbol{\epsilon}_{\mathrm{P}} \nabla R_i \,\mathrm{d}V_{\mathrm{P}_i}\, U_i \\
\ldots &= \frac{1}{2}\sum_{i=1}^{n_{\mathrm{P}}} U_i C_{\mathrm{el},i} U_i = \frac{1}{2}\boldsymbol{U}^{\mathrm{T}} \boldsymbol{C}_{\mathrm{el}} \boldsymbol{U}
\end{aligned} \tag{2.66}$$

with $C_{\mathrm{el},i}$ being the ith diagonal element of the diagonal capacitance matrix $\boldsymbol{C}_{\mathrm{el}}$.

As already pointed out, the cross-coupling term $E_{\mathrm{el,P,mec}}$ is identical to $E_{\mathrm{pot,P,el}}$ and reads in discretized form

$$E_{\mathrm{el,P,mec}} = -\frac{1}{2}\boldsymbol{U}^{\mathrm{T}} \boldsymbol{G}_{\mathrm{em}}^{\mathrm{T}} \boldsymbol{\eta}. \tag{2.67}$$

Some of the presented mass, stiffness, coupling and capacitance matrices can by further simplified, for example by taking into account the special normalization of the basis functions. These simplifications are presented in App. A.5.

2.3.5 Equations of the Lumped Parameter Model

The discretized energy terms can now be used to express the Lagrangian (2.26) in terms of the generalized coordinates as

$$\begin{aligned}\mathcal{L} = & E_{\mathrm{kin,S}} + E_{\mathrm{kin,P}} + E_{\mathrm{kin,F}} - E_{\mathrm{pot,S}} - E_{\mathrm{pot,P,mec}} + E_{\mathrm{pot,P,el}} - E_{\mathrm{pot,F}} \\ & + E_{\mathrm{el,P,el}} + E_{\mathrm{el,P,mec}} \\ = & \frac{1}{2}\dot{\boldsymbol{\eta}}^{\mathrm{T}}\boldsymbol{M}_{\mathrm{S}}\dot{\boldsymbol{\eta}} + \frac{1}{2}\dot{\boldsymbol{\eta}}^{\mathrm{T}}\boldsymbol{M}_{\mathrm{P}}\dot{\boldsymbol{\eta}} + \frac{1}{2}\boldsymbol{\varphi}^{\mathrm{T}}\boldsymbol{K}_{\mathrm{F}}\boldsymbol{\varphi} - \frac{1}{2}\boldsymbol{\eta}^{\mathrm{T}}\boldsymbol{K}_{\mathrm{S}}\boldsymbol{\eta} - \frac{1}{2}\boldsymbol{\eta}^{\mathrm{T}}\boldsymbol{K}_{\mathrm{P}}\boldsymbol{\eta} - \frac{1}{2}\boldsymbol{\eta}^{\mathrm{T}}\boldsymbol{G}_{\mathrm{em}}\boldsymbol{U} - \frac{1}{2}\dot{\boldsymbol{\varphi}}^{\mathrm{T}}\boldsymbol{M}_{\mathrm{F}}\dot{\boldsymbol{\varphi}} \\ & + \frac{1}{2}\boldsymbol{U}^{\mathrm{T}}\boldsymbol{C}_{\mathrm{el}}\boldsymbol{U} - \frac{1}{2}\boldsymbol{U}^{\mathrm{T}}\boldsymbol{G}_{\mathrm{em}}^{\mathrm{T}}\boldsymbol{\eta}.\end{aligned} \tag{2.68}$$

Using the above expression in the Lagrange equations (2.43), we finally get the discretized equations of motion for each of the three domains.

Structural Equations of Motion

The first n_{S} equations given by (2.43a) can be collected in vector form as

$$\left[\frac{\mathrm{d}}{\mathrm{d}t}\frac{\partial}{\partial\dot{\boldsymbol{\eta}}}\left(\frac{1}{2}\dot{\boldsymbol{\eta}}^{\mathrm{T}}\left(\boldsymbol{M}_{\mathrm{S}}+\boldsymbol{M}_{\mathrm{P}}\right)\dot{\boldsymbol{\eta}}\right)+\frac{\partial\mathcal{D}_{\mathrm{S}}}{\partial\dot{\boldsymbol{\eta}}}-\frac{\partial}{\partial\boldsymbol{\eta}}\left(-\frac{1}{2}\boldsymbol{\eta}^{\mathrm{T}}\left(\boldsymbol{K}_{\mathrm{S}}+\boldsymbol{K}_{\mathrm{P}}\right)\boldsymbol{\eta}-\boldsymbol{\eta}^{\mathrm{T}}\boldsymbol{G}_{\mathrm{em}}\boldsymbol{U}\right)\right]^{\mathrm{T}}=\boldsymbol{F}_{\mathrm{S}}^{\mathrm{g}}. \tag{2.69}$$

The idea of the structural dissipation function $\mathcal{D}_{\mathrm{S}}$ is to introduce viscous damping. To this end, we select it as $\mathcal{D}_{\mathrm{S}} = \frac{1}{2}\dot{\boldsymbol{\eta}}\boldsymbol{D}_{\mathrm{S}}\dot{\boldsymbol{\eta}}$ with $\boldsymbol{D}_{\mathrm{S}} = 2D_{\mathrm{S}} \bigoplus_{i=1}^{n_{\mathrm{S}}} m_{\mathrm{S},i}\,\omega_{\mathrm{S},i}$. Here, D_{S} is the selected damping ratio of the structure, and $\omega_{\mathrm{S},i}$ are the eigenfrequencies of the simply-supported plate alone, i.e. without piezoelectric elements. These are used here for simplicity because it will be shown in Sec. 2.5 that the eigenfrequencies of the structure are not much altered by the presence of the piezoelectric elements. The modal masses $m_{\mathrm{S},i}$ are the diagonal elements of $\boldsymbol{M}_{\mathrm{S}}$ which have been normalized to one for all $i = 1, \ldots, n_{\mathrm{S}}$, see App. A.5. Thus, $\boldsymbol{D}_{\mathrm{S}} = 2D_{\mathrm{S}} \bigoplus_{i=1}^{n_{\mathrm{S}}} \omega_{\mathrm{S},i}$. The $\omega_{\mathrm{S},i}$ can be calculated from the plate properties as [94]

$$\omega_{\mathrm{S},i} = \sqrt{\frac{D}{\rho h}}\pi^2\left[\left(\frac{n_{\mathrm{S},x}}{l_x}\right)^2+\left(\frac{n_{\mathrm{S},y}}{l_y}\right)^2\right]. \tag{2.70}$$

Furthermore, we stack all generalized structural forces defined in (2.44a) to build up the vector $\boldsymbol{F}_{\mathrm{S}}^{\mathrm{g}}$. By noting that in general, for some symmetric $\boldsymbol{M}$, $\frac{\partial}{\partial\boldsymbol{\eta}}\boldsymbol{\eta}^{\mathrm{T}}\boldsymbol{M}\boldsymbol{\eta} = 2\boldsymbol{\eta}^{\mathrm{T}}\boldsymbol{M}$, the equations of motion can now be derived from (2.69) to be

$$\left(\boldsymbol{M}_{\mathrm{S}}+\boldsymbol{M}_{\mathrm{P}}\right)\ddot{\boldsymbol{\eta}}+\boldsymbol{D}_{\mathrm{S}}\dot{\boldsymbol{\eta}}+\left(\boldsymbol{K}_{\mathrm{S}}+\boldsymbol{K}_{\mathrm{P}}\right)\boldsymbol{\eta}=\boldsymbol{F}_{\mathrm{S}}^{\mathrm{g}}-\boldsymbol{G}_{\mathrm{em}}\boldsymbol{U}. \tag{2.71}$$

At this stage, it is appropriate to include the coupling between the flexible structure and the enclosed acoustic volume into the equations of motion of the flexible structure. This coupling was already shown to appear as a non-homogeneous boundary condition in the equations of the fluid volume. For the flexible structure however, the coupling appears as a forcing term. This can be easily seen be recognizing the fact that F in (2.9) includes the pressure distribution acting on the structure from *both* sides of the plate. This means that we have the acoustic pressure acting from underneath and the disturbance and control forces acting on top of the plate. Thus, we can split up the pressure distribution F (force per unit area) acting on the plate as $F(x, y, t) = p(x, y, 0, t) + F'(x, y, t)$, where p is the acoustic pressure and F' denotes all other forcing terms. Consequently, we can also separate the generalized forces in an analogous manner and write $F^{\mathrm{g}}_{\mathrm{S},i} = \langle \dot{\boldsymbol{\varphi}}^{\mathrm{T}} \boldsymbol{P}\,|_{z=0}, W_i \rangle_{A_{\mathrm{S}}} + F'^{\mathrm{g}}_{\mathrm{S},i}$, $i = 1, \ldots, n_{\mathrm{S}}$. With the definition of the mechanical-acoustical coupling matrix $\boldsymbol{G}_{\mathrm{ma}}$ in A.4, this can be summarized as $\boldsymbol{F}^{\mathrm{g}}_{\mathrm{S}} = \boldsymbol{G}_{\mathrm{ma}}\dot{\boldsymbol{\varphi}} + \boldsymbol{F}'^{\mathrm{g}}_{\mathrm{S}}$. The final version of the equations of motion of the plate is then

$$(\boldsymbol{M}_{\mathrm{S}} + \boldsymbol{M}_{\mathrm{P}})\,\ddot{\boldsymbol{\eta}} + \boldsymbol{D}_{\mathrm{S}}\dot{\boldsymbol{\eta}} + (\boldsymbol{K}_{\mathrm{S}} + \boldsymbol{K}_{\mathrm{P}})\,\boldsymbol{\eta} = \boldsymbol{F}'^{\mathrm{g}}_{\mathrm{S}} + \boldsymbol{G}_{\mathrm{ma}}\dot{\boldsymbol{\varphi}} - \boldsymbol{G}_{\mathrm{em}}\boldsymbol{U}. \tag{2.72}$$

To avoid cluttering, $\boldsymbol{F}'^{\mathrm{g}}_{\mathrm{S}}$ will now be renamed to $\boldsymbol{F}^{\mathrm{g}}_{\mathrm{S}}$. Hence, $\boldsymbol{F}^{\mathrm{g}}_{\mathrm{S}}$ denotes from now on the vector of generalized mechanical forces acting on the plate, apart from the acoustic pressure.

Piezoelectric Equations of Motion

The n_{P} stacked equations for the piezoelectric elements are derived with the help of (2.43b) as

$$\begin{aligned} -\left[\frac{\partial}{\partial \boldsymbol{U}}\left(-\boldsymbol{U}^{\mathrm{T}}\boldsymbol{G}^{\mathrm{T}}_{\mathrm{em}}\boldsymbol{\eta} + \frac{1}{2}\boldsymbol{U}^{\mathrm{T}}\boldsymbol{C}_{\mathrm{el}}\boldsymbol{U}\right)\right]^{\mathrm{T}} &= \boldsymbol{F}^{\mathrm{g}}_{\mathrm{P}}, \\ \boldsymbol{G}^{\mathrm{T}}_{\mathrm{em}}\boldsymbol{\eta} - \boldsymbol{C}_{\mathrm{el}}\boldsymbol{U} &= \boldsymbol{F}^{\mathrm{g}}_{\mathrm{P}}. \end{aligned} \tag{2.73}$$

The ith generalized electric force $F^{\mathrm{g}}_{\mathrm{P}_i}$ was given by the inner product of the charge density (per unit volume) Q_i and the ith basis function R_i as $F^{\mathrm{g}}_{\mathrm{P}_i} = -\langle Q_i, R_i \rangle_{V_{\mathrm{P}_i}}$ in (2.49). Since the piezo elements are modeled as plate capacitors, the total charge $Q^{\mathrm{tot}}_i = \iiint_{V_{P_i}} Q_i \,\mathrm{d}V_{P_i}$ within the patch volume is concentrated on the upper and lower surface and zero within,

$$\begin{aligned} F^{\mathrm{g}}_{\mathrm{P}_i} &= -\iiint_{V_{\mathrm{P}_i}} Q_i R_i \,\mathrm{d}V_{\mathrm{P}_i} = -\iiint_{V_{\mathrm{P}_i}} \left[\frac{Q^{\mathrm{tot}}_i}{A_{\mathrm{P}_i}}\delta\left(z - \frac{h}{2} - h_{\mathrm{P}_i}\right) - \frac{Q^{\mathrm{tot}}_i}{A_{\mathrm{P}_i}}\delta\left(z - \frac{h}{2}\right)\right] R_i \,\mathrm{d}V_{\mathrm{P}_i} \\ \ldots &= -\frac{Q^{\mathrm{tot}}_i}{A_{\mathrm{P}_i}} \iint_{A_{\mathrm{P}_i}} R_i\left(\frac{h}{2} + h_{\mathrm{P}_i}\right) - R_i\left(\frac{h}{2}\right) \mathrm{d}A_{\mathrm{P}_i} = -\frac{Q^{\mathrm{tot}}_i}{A_{\mathrm{P}_i}} \iint_{A_{\mathrm{P}_i}} 1 - 0 \,\mathrm{d}A_{\mathrm{P}_i} = -Q^{\mathrm{tot}}_i. \end{aligned} \tag{2.74}$$

Thus, the ith generalized electric force is equal to the negative value of the total charge of the ith patch, and we may write

$$\boldsymbol{C}_{\mathrm{el}}\boldsymbol{U} - \boldsymbol{G}^{\mathrm{T}}_{\mathrm{em}}\boldsymbol{\eta} = \boldsymbol{Q}, \tag{2.75}$$

with $\boldsymbol{Q} = \left(Q^{\mathrm{tot}}_1, \ldots, Q^{\mathrm{tot}}_{n_{\mathrm{P}}}\right)^{\mathrm{T}}$.

Acoustic Equations of Motion

The equations of motion which govern the dynamics of the acoustic fluid volume are given by the evaluation of (2.43c) together with (2.68) and result in

$$\left[\frac{\mathrm{d}}{\mathrm{d}t}\frac{\partial}{\partial \dot{\boldsymbol{\varphi}}}\left(-\frac{1}{2}\dot{\boldsymbol{\varphi}}^{\mathrm{T}}\boldsymbol{M}_{\mathrm{F}}\dot{\boldsymbol{\varphi}}\right) + \frac{\partial \mathcal{D}_{\mathrm{F}}}{\partial \dot{\boldsymbol{\varphi}}} - \frac{\partial}{\partial \boldsymbol{\varphi}}\left(\frac{1}{2}\boldsymbol{\varphi}^{\mathrm{T}}\boldsymbol{K}_{\mathrm{F}}\boldsymbol{\varphi}\right)\right]^{\mathrm{T}} = -\frac{\mathrm{d}}{\mathrm{d}t}\boldsymbol{F}^{\mathrm{g}}_{\mathrm{F}} \tag{2.76}$$

with some $\mathcal{D}_\mathrm{F} = -\frac{1}{2}\dot{\boldsymbol{\varphi}}^\mathrm{T}\boldsymbol{D}_\mathrm{F}\dot{\boldsymbol{\varphi}}$. Carrying out the derivation gives

$$\boldsymbol{M}_\mathrm{F}\ddot{\boldsymbol{\varphi}} + \boldsymbol{D}_\mathrm{F}\dot{\boldsymbol{\varphi}} + \boldsymbol{K}_\mathrm{F}\boldsymbol{\varphi} = \frac{\mathrm{d}}{\mathrm{d}t}\boldsymbol{F}_\mathrm{F}^\mathrm{g}. \tag{2.77}$$

The purpose of the dissipation function $\mathcal{D}_\mathrm{F}$ is to introduce damping that is proportional to the pressure amplitude which is the simplest reasonable dissipation model. The pressure-proportional damping can be achieved by selecting $\boldsymbol{D}_\mathrm{F} = 2D_\mathrm{F}\bigoplus_{i=1}^{n_\mathrm{F}} m_{\mathrm{F},i}\,\omega_{\mathrm{F},i}$. The constant D_F denotes the desired modal damping ratio for the fluid, and $\omega_{\mathrm{F},i}$ are the eigenfrequencies of the fluid volume bounded by a rectangular box with rigid walls on all sides. These eigenfrequencies are given as [69]

$$\omega_{\mathrm{F},i} = c_0^2\left[\left(\frac{n_{\mathrm{F},x}\pi}{l_x}\right)^2 + \left(\frac{n_{\mathrm{F},y}\pi}{l_y}\right)^2 + \left(\frac{n_{\mathrm{F},z}\pi}{l_z}\right)^2\right]. \tag{2.78}$$

Since the first modal mass $m_{\mathrm{F},1}$ is equal to $V_\mathrm{F}/\left(\rho_0 c_0^2\right)$ (see App. A.5), and $\omega_{\mathrm{F},1} = 0$, the first element of the diagonal matrix $\boldsymbol{D}_\mathrm{F}$ is zero. Due to the normalization of the other modal masses, $m_{\mathrm{F},i} = 1/\omega_{\mathrm{F},i}^2$, $i = 2, \ldots, n_\mathrm{F}$, the remainder of the fluid damping matrix reads $\boldsymbol{D}_{\mathrm{F},i} = 2D_\mathrm{F}/\omega_{\mathrm{F},i}$, $i = 2, \ldots, n_\mathrm{F}$.

The forcing term on the right hand side of (2.77) can be split into two parts: One is due to the excitation by acoustic sources inside the fluid volume, and the other one originates from the mechanical-acoustical coupling of the fluid with the flexible plate structure, $F_{\mathrm{F},i}^\mathrm{g} = \langle V, P_i\rangle_{V_\mathrm{F}} - \boldsymbol{\eta}^\mathrm{T}\boldsymbol{G}_\mathrm{ma}^{(:,i)}$. See App. A.4 for the definition of the mechanical-acoustical coupling matrix $\boldsymbol{G}_\mathrm{ma}$. Thus, we finally have

$$\boldsymbol{M}_\mathrm{F}\ddot{\boldsymbol{\varphi}} + \boldsymbol{D}_\mathrm{F}\dot{\boldsymbol{\varphi}} + \boldsymbol{K}_\mathrm{F}\boldsymbol{\varphi} = \underbrace{\langle \dot{V}, \boldsymbol{P}\rangle_{V_\mathrm{F}} - \boldsymbol{G}_\mathrm{ma}^\mathrm{T}\dot{\boldsymbol{\eta}}}_{=\dot{\boldsymbol{F}}_\mathrm{F}^\mathrm{g}}. \tag{2.79}$$

Separation of Actuator and Sensor Patches

As already explained in Sec. 2.2.2, the piezoelectric elements can be used as sensors by exploiting the piezoelectric effect, or as actuators by making use of the inverse piezoelectric effect. Thus, the total number of piezo patches n_P can be split up in $n_\mathrm{P} = n_\mathrm{P,A} + n_\mathrm{P,S}$, where $n_\mathrm{P,A}$ and $n_\mathrm{P,S}$ denote the number of actuator and sensor patches, respectively. It is therefore possible to split up the electromechanical coupling matrix, where each column represents one patch. Without loss of generality, it is now assumed that the first $n_\mathrm{P,A}$ columns of $\boldsymbol{G}_\mathrm{em}$ correspond to the actuator patches. The equations of motion of the plate can then be rewritten,

$$\left(\boldsymbol{M}_\mathrm{S} + \boldsymbol{M}_\mathrm{P}\right)\ddot{\boldsymbol{\eta}} + \boldsymbol{D}_\mathrm{S}\dot{\boldsymbol{\eta}} + \left(\boldsymbol{K}_\mathrm{S} + \boldsymbol{K}_\mathrm{P}\right)\dot{\boldsymbol{\eta}} = \boldsymbol{F}_\mathrm{S}^\mathrm{g} + \boldsymbol{G}_\mathrm{ma}\dot{\boldsymbol{\varphi}} - \begin{pmatrix}\boldsymbol{G}_\mathrm{em,A} & \boldsymbol{G}_\mathrm{em,S}\end{pmatrix}\begin{pmatrix}\boldsymbol{U}_\mathrm{A}\\ \boldsymbol{U}_\mathrm{S}\end{pmatrix}. \tag{2.80}$$

In a similar manner, one can reformulate the piezoelectric equations as

$$\begin{pmatrix}\boldsymbol{C}_\mathrm{el,A} & \boldsymbol{0}\\ \boldsymbol{0} & \boldsymbol{C}_\mathrm{el,S}\end{pmatrix}\begin{pmatrix}\boldsymbol{U}_\mathrm{A}\\ \boldsymbol{U}_\mathrm{S}\end{pmatrix} - \begin{pmatrix}\boldsymbol{G}_\mathrm{em,A}^\mathrm{T}\\ \boldsymbol{G}_\mathrm{em,S}^\mathrm{T}\end{pmatrix}\boldsymbol{\eta} = \begin{pmatrix}\boldsymbol{Q}_\mathrm{A}\\ \boldsymbol{Q}_\mathrm{S}\end{pmatrix}. \tag{2.81}$$

The elements of $\boldsymbol{Q}_\mathrm{A}$ and $\boldsymbol{Q}_\mathrm{S}$ are the total charges introduced in (2.75) which are generated within the patches by some externally applied voltage, see Sec. 2.3.2. Hence, for the sensor patches, these quantities are zero (see also [193]) and thus, $\boldsymbol{U}_\mathrm{S} = \boldsymbol{C}_\mathrm{el,S}^{-1}\boldsymbol{G}_\mathrm{em,S}^\mathrm{T}\boldsymbol{\eta}$. This is introduced in (2.80) to give

$$\underbrace{(\boldsymbol{M}_\mathrm{S} + \boldsymbol{M}_\mathrm{P})}_{=:\tilde{\boldsymbol{M}}_\mathrm{S}}\ddot{\boldsymbol{\eta}} + \boldsymbol{D}_\mathrm{S}\dot{\boldsymbol{\eta}} + \underbrace{\left(\boldsymbol{K}_\mathrm{S} + \boldsymbol{K}_\mathrm{P} + \boldsymbol{G}_\mathrm{em,S}\boldsymbol{C}_\mathrm{el,S}^{-1}\boldsymbol{G}_\mathrm{em,S}^\mathrm{T}\right)}_{=:\tilde{\boldsymbol{K}}_\mathrm{S}}\boldsymbol{\eta} = \boldsymbol{F}_\mathrm{S}^\mathrm{g} + \boldsymbol{G}_\mathrm{ma}\dot{\boldsymbol{\varphi}} - \boldsymbol{G}_\mathrm{em,A}\boldsymbol{U}_\mathrm{A}. \tag{2.82}$$

It can be concluded that the piezoelectric effect of the sensor patches creates an additional stiffness term. Since $\boldsymbol{C}_\mathrm{el,S}^{-1}$ is diagonal with positive entries, the additional term $\boldsymbol{G}_\mathrm{em,S}\boldsymbol{C}_\mathrm{el,S}^{-1}\boldsymbol{G}_\mathrm{em,S}^\mathrm{T}$ is symmetric and positive definite, as can be expected.

Matrix Representations

For quick reference, all relevant equations are finally summarized in first and second order matrix form. To this end, (2.79) and (2.82) are combined to give

$$\begin{pmatrix} \tilde{\boldsymbol{M}}_\mathrm{S} & \boldsymbol{0} \\ \boldsymbol{0} & \boldsymbol{M}_\mathrm{F} \end{pmatrix}\begin{pmatrix} \ddot{\boldsymbol{\eta}} \\ \ddot{\boldsymbol{\varphi}} \end{pmatrix} + \begin{pmatrix} \boldsymbol{D}_\mathrm{S} & -\boldsymbol{G}_\mathrm{ma} \\ \boldsymbol{G}_\mathrm{ma}^\mathrm{T} & \boldsymbol{D}_\mathrm{F} \end{pmatrix}\begin{pmatrix} \dot{\boldsymbol{\eta}} \\ \dot{\boldsymbol{\varphi}} \end{pmatrix} + \begin{pmatrix} \tilde{\boldsymbol{K}}_\mathrm{S} & \boldsymbol{0} \\ \boldsymbol{0} & \boldsymbol{K}_\mathrm{F} \end{pmatrix}\begin{pmatrix} \boldsymbol{\eta} \\ \boldsymbol{\varphi} \end{pmatrix} = \begin{pmatrix} \mathbf{I} & -\boldsymbol{G}_\mathrm{em,A} & \boldsymbol{0} \\ \boldsymbol{0} & \boldsymbol{0} & \mathbf{I} \end{pmatrix}\begin{pmatrix} \boldsymbol{F}_\mathrm{S}^\mathrm{g} \\ \boldsymbol{U}_\mathrm{A} \\ \dot{\boldsymbol{F}}_\mathrm{F}^\mathrm{g} \end{pmatrix}. \tag{2.83}$$

Alternatively, it is possible to summarize all system equations in a state space model (first-order matrix equation) as

$$\begin{pmatrix} \dot{\boldsymbol{\eta}} \\ \dot{\boldsymbol{\varphi}} \\ \ddot{\boldsymbol{\eta}} \\ \ddot{\boldsymbol{\varphi}} \end{pmatrix} = \begin{pmatrix} \boldsymbol{0} & \boldsymbol{0} & \mathbf{I} & \boldsymbol{0} \\ \boldsymbol{0} & \boldsymbol{0} & \boldsymbol{0} & \mathbf{I} \\ -\tilde{\boldsymbol{M}}_\mathrm{S}^{-1}\tilde{\boldsymbol{K}}_\mathrm{S} & \boldsymbol{0} & -\tilde{\boldsymbol{M}}_\mathrm{S}^{-1}\boldsymbol{D}_\mathrm{S} & \tilde{\boldsymbol{M}}_\mathrm{S}^{-1}\boldsymbol{G}_\mathrm{ma} \\ \boldsymbol{0} & -\boldsymbol{M}_\mathrm{F}^{-1}\boldsymbol{K}_\mathrm{F} & -\boldsymbol{M}_\mathrm{F}^{-1}\boldsymbol{G}_\mathrm{ma}^\mathrm{T} & -\boldsymbol{M}_\mathrm{F}^{-1}\boldsymbol{D}_\mathrm{F} \end{pmatrix}\begin{pmatrix} \boldsymbol{\eta} \\ \boldsymbol{\varphi} \\ \dot{\boldsymbol{\eta}} \\ \dot{\boldsymbol{\varphi}} \end{pmatrix} + \begin{pmatrix} \boldsymbol{0} & \boldsymbol{0} & \boldsymbol{0} \\ \boldsymbol{0} & \boldsymbol{0} & \boldsymbol{0} \\ \tilde{\boldsymbol{M}}_\mathrm{S}^{-1} & -\tilde{\boldsymbol{M}}_\mathrm{S}^{-1}\boldsymbol{G}_\mathrm{em,A} & \boldsymbol{0} \\ \boldsymbol{0} & \boldsymbol{0} & \boldsymbol{M}_\mathrm{F}^{-1} \end{pmatrix}\begin{pmatrix} \boldsymbol{F}_\mathrm{S}^\mathrm{g} \\ \boldsymbol{U}_\mathrm{A} \\ \dot{\boldsymbol{F}}_\mathrm{F}^\mathrm{g} \end{pmatrix}. \tag{2.84}$$

The approximated values of the field variables w and p, and the voltages at the sensor patches $\boldsymbol{U}_\mathrm{S}$, can then be recovered by using the following output equation for the state space model

$$\begin{pmatrix} w \\ \boldsymbol{U}_\mathrm{S} \\ p \end{pmatrix} = \begin{pmatrix} \boldsymbol{W}^\mathrm{T} & \boldsymbol{0} & \boldsymbol{0} & \boldsymbol{0} \\ \boldsymbol{C}_\mathrm{el,S}^{-1}\boldsymbol{G}_\mathrm{em,S}^\mathrm{T} & \boldsymbol{0} & \boldsymbol{0} & \boldsymbol{0} \\ \boldsymbol{0} & \boldsymbol{0} & \boldsymbol{0} & \boldsymbol{P}^\mathrm{T} \end{pmatrix}\begin{pmatrix} \boldsymbol{\eta} \\ \boldsymbol{\varphi} \\ \dot{\boldsymbol{\eta}} \\ \dot{\boldsymbol{\varphi}} \end{pmatrix}. \tag{2.85}$$

The analytical model of the acoustic demonstrator is now complete. In a last step, we introduce two minor modifications. First, for simplicity, we assume that the structural forces acting on the plate are point forces exclusively. Analogously, it is assumed that the sources of sound within the fluid volume can be accurately modeled as point sources. Then, the calculation of the respective generalized structural and acoustic forces can be simplified, compare (2.44a) and (2.44c),

$$F_{\mathrm{S},i}^\mathrm{g}(t) \overset{\text{point forces}}{=} \sum_{k=1}^{n_\mathrm{forces}} F_k(t) W_i(x_k, y_k), \qquad i = 1, \dots, n_\mathrm{S} \tag{2.86a}$$

$$F_{\mathrm{F},i}^\mathrm{g}(t) \overset{\text{point sources}}{=} \sum_{k=1}^{n_\mathrm{sources}} V_k(t) P_i(x_k, y_k, z_k) \qquad i = 1, \dots, n_\mathrm{F}. \tag{2.86b}$$

In the above equations, $W_i(x_k, y_k)$ and $P_i(x_k, y_k, z_k)$ indicate that the ith basis function is evaluated at the position of the kth point force F_k or kth point source of strength V_k, respectively. Second, for the simulation of a practical control loop, it is justified to assume that the movement of the plate structure is detected via a set of acceleration sensors whose signals shall be collected in the vector $\ddot{\boldsymbol{w}}$. The real-time measurement of the complete displacement field w would be to complex. For the same reason, it is also assumed that the acoustic pressure is detected via a set of microphones at a finite number of discrete locations. These measurements are collected in the vector $\boldsymbol{p}$. For compact notation, we introduce the following four matrices

$$\boldsymbol{W}^{\mathrm{dis}}_{\{\mathrm{force},\mathrm{sensor}\}} := \begin{pmatrix} W_1(x_1, y_1) & \dots & W_{n_{\mathrm{S}}}(x_1, y_1) \\ \vdots & & \vdots \\ W_1(x_{n_{\{\mathrm{forces},\mathrm{sensors}\}}}, y_{n_{\{\mathrm{forces},\mathrm{sensors}\}}}) & \dots & W_{n_{\mathrm{S}}}(x_{n_{\{\mathrm{forces},\mathrm{sensors}\}}}, y_{n_{\{\mathrm{forces},\mathrm{sensors}\}}}) \end{pmatrix}, \tag{2.87a}$$

$$\boldsymbol{P}^{\mathrm{dis}}_{\{\mathrm{source},\mathrm{sensor}\}} := \begin{pmatrix} P_1(x_1, y_1, z_1) & \dots & P_{n_{\mathrm{F}}}(x_1, y_1, z_1) \\ \vdots & & \vdots \\ P_1(x_{n_{\{\mathrm{sources},\mathrm{sensors}\}}}, y_{n_{\{\mathrm{so.},\mathrm{se.}\}}}, z_{n_{\{\mathrm{so.},\mathrm{se.}\}}}) & \dots & P_{n_{\mathrm{F}}}(x_{n_{\{\mathrm{so.},\mathrm{se.}\}}}, y_{n_{\{\mathrm{so.},\mathrm{se.}\}}}, z_{n_{\{\mathrm{so.},\mathrm{se.}\}}}) \end{pmatrix}, \tag{2.87b}$$

where n_{sensors} refers to the number of acceleration sensors in (2.87a) and to the number of microphones in (2.87b), respectively. We now have the following simple expressions for the generalized forces

$$\boldsymbol{F}^{\mathrm{g}}_{\mathrm{S}} = \left(\boldsymbol{W}^{\mathrm{dis}}_{\mathrm{force}}\right)^{\mathrm{T}} \boldsymbol{F}, \quad \boldsymbol{F} = \left(F_1, \dots, F_{n_{\mathrm{forces}}}\right)^{\mathrm{T}}, \tag{2.88a}$$

$$\dot{\boldsymbol{F}}^{\mathrm{g}}_{\mathrm{F}} = \left(\boldsymbol{P}^{\mathrm{dis}}_{\mathrm{source}}\right)^{\mathrm{T}} \dot{\boldsymbol{V}}, \quad \dot{\boldsymbol{V}} = \left(\dot{V}_1, \dots, \dot{V}_{n_{\mathrm{sources}}}\right)^{\mathrm{T}}. \tag{2.88b}$$

Thus, one can replace the input vector $\left(\left(\boldsymbol{F}^{\mathrm{g}}_{\mathrm{S}}\right)^{\mathrm{T}}, \boldsymbol{U}^{\mathrm{T}}_{\mathrm{A}}, \left(\dot{\boldsymbol{F}}^{\mathrm{g}}_{\mathrm{F}}\right)^{\mathrm{T}}\right)^{\mathrm{T}}$ in (2.84) by $\left(\boldsymbol{F}^{\mathrm{T}}, \boldsymbol{U}^{\mathrm{T}}_{\mathrm{A}}, \dot{\boldsymbol{V}}^{\mathrm{T}}\right)^{\mathrm{T}}$ by an obvious modification of the input matrix.

With the new sensor outputs $\ddot{\boldsymbol{w}}$ and $\boldsymbol{p}$, the output equation (2.85) can be modified to

$$\begin{aligned} \begin{pmatrix} \ddot{\boldsymbol{w}} \\ \boldsymbol{U}_{\mathrm{S}} \\ \boldsymbol{p} \end{pmatrix} &= \begin{pmatrix} -\boldsymbol{W}^{\mathrm{dis}}_{\mathrm{sensor}} \tilde{\boldsymbol{M}}_{\mathrm{S}}^{-1} \tilde{\boldsymbol{K}}_{\mathrm{S}} & \boldsymbol{0} & -\boldsymbol{W}^{\mathrm{dis}}_{\mathrm{sensor}} \tilde{\boldsymbol{M}}_{\mathrm{S}}^{-1} \boldsymbol{D}_{\mathrm{S}} & \boldsymbol{W}^{\mathrm{dis}}_{\mathrm{sensor}} \tilde{\boldsymbol{M}}_{\mathrm{S}}^{-1} \boldsymbol{G}_{\mathrm{ma}} \\ \boldsymbol{C}_{\mathrm{el}} \boldsymbol{G}^{\mathrm{T}}_{\mathrm{em,S}} & \boldsymbol{0} & \boldsymbol{0} & \boldsymbol{0} \\ \boldsymbol{0} & \boldsymbol{0} & \boldsymbol{0} & \boldsymbol{P}^{\mathrm{dis}}_{\mathrm{sensor}} \end{pmatrix} \begin{pmatrix} \boldsymbol{\eta} \\ \boldsymbol{\varphi} \\ \dot{\boldsymbol{\eta}} \\ \dot{\boldsymbol{\varphi}} \end{pmatrix} \\ &+ \begin{pmatrix} \boldsymbol{W}^{\mathrm{dis}}_{\mathrm{sensor}} \tilde{\boldsymbol{M}}_{\mathrm{S}}^{-1} \left(\boldsymbol{W}^{\mathrm{dis}}_{\mathrm{force}}\right)^{\mathrm{T}} & -\boldsymbol{W}^{\mathrm{dis}}_{\mathrm{sensor}} \tilde{\boldsymbol{M}}_{\mathrm{S}}^{-1} \boldsymbol{G}_{\mathrm{em,A}} & \boldsymbol{0} \\ \boldsymbol{0} & \boldsymbol{0} & \boldsymbol{0} \\ \boldsymbol{0} & \boldsymbol{0} & \boldsymbol{0} \end{pmatrix} \begin{pmatrix} \boldsymbol{F} \\ \boldsymbol{U}_{\mathrm{A}} \\ \dot{\boldsymbol{V}} \end{pmatrix}. \end{aligned} \tag{2.89}$$

In contrast to (2.85), there appears a feedthrough term in the new output equation because of the acceleration measurements.

2.4 Actuator and Sensor Placement

Most often in control system design, the states of the plant that can be measured – and therefore the information that can be made available to the control algorithm – are predetermined. The same holds true for the inputs of the plant to be controlled. Thus, the choice of a control strategy and its parameters are the only degrees of freedom a control engineer has to achieve a certain goal. This is not true for adaptronic systems. Here, the mechanical structure, the actuators and sensors, and the controller can be simultaneously designed to achieve the best possible performance under given design constraints.

In this thesis, the mechanical structure, i.e. the plate or the acoustic demonstrator, is assumed to be given. Thus, the optimization of the actuators and sensors as well as the controller are left as design variables. The optimal selection of sensor information and control inputs has achieved a lot of attention in the literature and can be regarded as a discipline of its own. However, actuator and sensor placement is not regarded as a main topic of this thesis and will therefore be treated shortly. The body of this section is structured as follows: First, the goals of an intelligent actuator and sensor placement are listed. Second, the most important concepts and ideas that have been developed are mentioned. Finally, a simple but generally applicable procedure for the selection of control inputs and sensor outputs for active control of flexible structures is demonstrated on the plate of the acoustic demonstrator. It will be shown in Ch. 4 that this design scheme will prove very effective for the system at hand.

2.4.1 Goals

The information which can be provided to the control algorithm and the plant inputs that can be manipulated by the actuators are of decisive importance. A system that is “ill-designed” by careless actuator and sensor selection can in general not be fixed by any possible control algorithm. This is for example illustrated in [168]. The important questions that have to be answered are:

- What are the best quantities to measure and what are the best inputs to manipulate?
- What kinds of actuators and sensors are suitable?
- How many actuators and sensors are needed to achieve the design goals?
- What are the best positions to place the actuators and sensors?
- What is the optimal geometry of actuators and sensors?

The answers to these questions depend on how the system performance is measured, i.e. how the selected performance metric looks like. The achievable value of this metric is influenced by the control algorithm which is in turn based on the available system inputs and outputs. Thus, the optimal actuator and sensor configuration may in turn depend on the chosen control algorithm. As pointed out by Herold [102] for example, there is a difference in the optimal positioning of actuators and sensors for modal and non-modal control schemes.

Regarding the first two questions, we confine ourselves to piezoelectric patches as actuators that exert moments on the plate. As sensors, piezo patches and acceleration sensors are suggesting themselves. The former are essentially strain sensors, and the strain is in turn determined by the plate deflection. Thus, the main difference between piezo patches and accelerometers is that the measured quantities are related by two time derivatives. For control of structural vibration and structure-borne sound, velocity is the important quantity, and so neither sensor type has a principal advantage. From a practical point of view, accelerometers are easier to apply and usually come with integrated charge amplifiers. Taking all this into account, accelerometers are chosen as sensors for active damping as well as control of sound radiation in this thesis. However, it is not claimed that this decision is the best option under all possible circumstances.

The last question which has been raised is relevant when using smart materials that can be shaped. In principle, the size and form of the piezo patches is free and can be optimized, but this topic will not be pursued here. However, the shaping of actuators and sensors is especially important for modal actuation and sensing concepts, e.g. [107], [112], [180]. In the works of this thesis, actuator patches of dimension $(50 \times 50 \times 0.5)$ mm will be used throughout.

2.4.2 Literature Review

The most popular concepts for the input and output selection of smart structures shall be shortly presented. As was mentioned before, in an optimal design procedure, the plant inputs and outputs as well as the control algorithm and its parameters would have to be designed in a holistic procedure to achieve specified performance goals. However, this problem is seldom dealt with in this way because of the immense mathematical difficulties. In general, an optimization procedure that starts with a certain control configuration would have to carry out an automated control design, evaluate closed-loop performance, calculate the gradient of the non-linear performance surface, adjust the actuator and sensor positions, and so forth. This may be a very involved process. Thus, efforts have been made to simplify this optimization procedure. First results have been reported for the special cases of $\mathcal{H}_\infty$ ([90], [104]) and LQR control [144], where the optimal controller parameters are explicitly parametrized by the actuator and sensor locations. Li et. al. [119] propose a holistic optimization strategy that combines actuator and sensor placement with covariance optimal control.

If one is not willing to take the effort and pursue this “ideal” path, it is possible to pursue other more manageable strategies. The common idea to all these near-optimal strategies is that a cost function is minimized that depends only on the plant and not on the controller. A good cost function is expected to correlate with the performance metric of the closed-loop system, i.e. if the cost function is minimized, it should be expected that the closed-loop performance metric also results in a small value.

Many different cost functions are imaginable. For sensor positioning for example, the minimization of information entropy was proposed ([91], [150]). For actuation of flexible structures, many cost functions have been put forward which are based on the modal description of this class of systems. Bin et. al. [29] and Herold [102] propose procedures to maximize an index which is based on the modal forces that can be achieved with given actuator locations. The optimal positions are found via iterative numerical optimization methods. Similar methods have for example been proposed by [58] and [98]. In [77], a procedure is proposed which poses less computational effort. There, actuators are allocated at all possible locations on the structure. Then, for every actuator and every mode, a placement index is calculated which is based on some norm of the transfer function of that single mode. Based on these indices, some actuators with low indices are discarded and new placement indices are calculated for the remaining actuators. Then, the procedure starts anew.

Other methods construct cost functions based on observability and controllability measures from control theory. Some of these measures are of geometric type, i.e. they evaluate how the system eigenvectors correlate to the range space of the system input matrix. The measures of Litz [121] and Lückel & Müller [126] are of that type. Others are energy based, i.e. they evaluate how much a system state can be perturbed with a given energy budget. Benninger [22], Günnewig [91], and Leleu et. al. [118] propose such measures which are based on controllability gramians and are closely connected to the work of Moore [143]. All controllability measures can in principal be expressed by mechanical modal quantities. The expressions of the measures of Litz, Lückel & Müller, and Benninger in terms of eigenfrequencies, mode shapes, and damping ratios can be found in [93] and [148], see also App. A.7.

In general, the maximization of controllability measures of some targeted modes ensures that these modes can be excited with a minimum of control energy. Analogously, the maximization of observability measures says that the modes have a large influence on the sensor signals. However, in the control of distributed parameter systems, it is often desirable to minimize the excitation and the observability of modes that should not be influenced by the controller. Therefore, a compromise has to be sought between the controllability and observability of the modes within and outside the control loop bandwidth. This issue is elaborated on in several publications, e.g. [37], [38], [93], and [99].

The reader is referred to the review papers [92] and [184] for a more comprehensive overview.

2.4.3 Placement for Active Damping of the Smart Panel

Five fundamental questions have been raised in Sec. 2.4.1 regarding actuator and sensor placement. The first two and the last one have been answered for the plate with active elements[1] within the context of this thesis. The remaining questions that shall be answered are: How many actuators and sensors are needed, and where is the best location to apply them? The answers will be exemplarily given for the active damping of the smart panel, which is the topic of Ch. 4.

To simplify the problem, we optimize the system's input and output properties regardless of a specific control algorithm. We only make the assumption that the control algorithm is not modal, i.e. we do not want to influence a specific mode or a set of modes by a specific input. That would impose the additional requirement on the columns of $\boldsymbol{G}_{\mathrm{em,A}}$ in (2.83) to be as orthogonal as possible [102].

Regarding the number of actuators, we follow the intuitive argument given by Elliott in [65]. There, it is argued that the minimum number of required control inputs is equal to the maximum number of excited modes at single frequency. The number of substantially excited modes at a single frequency is measured by the so-called *modal overlap*. This quantity is equal to the average

---

[1] The term *smart panel* is often used in the literature for a plate with active elements.

number of resonances per frequency multiplied by the modal bandwidth. For plates in general, the average number of resonances per frequency, also called *modal density*, is constant over frequency [65]. For the plate of the acoustic demonstrator, the modal density is approximately $35.4\,\mathrm{kHz}^{-1}$. The 3 dB modal bandwidth of the ith resonance is approximately given by $2D_i\omega_i$ [145]. Assuming a constant damping ratio for all modes, $D_i = D = 1\,\%$, this leads to a linearly increasing modal overlap. The target bandwidth of the controller for active damping is 400 Hz. At this frequency, the value of the modal overlap can be calculated to be 1.78. Thus, a minimum of two actuators is required to achieve a significant control performance. However, better control authority and smaller control inputs per actuator can be expected if more actuators are applied. Therefore, a total number of four actuators will be used. Since analogous arguments can be put forward for the selection of the number of sensors, also four sensors will be applied.

When searching for appropriate locations for the actuators, it is insightful to have a look at the mode shapes of the modes to be controlled. This is made clear by recalling (A.34),

$$\boldsymbol{G}_{\mathrm{em,A}}^{(:,i)} = e_{31}\frac{h}{2}\iint_{A_{\mathrm{P}_i}} \left(\frac{\partial^2 W_1}{\partial x^2} + \frac{\partial^2 W_1}{\partial y^2}, \ldots, \frac{\partial^2 W_{n_\mathrm{S}}}{\partial x^2} + \frac{\partial^2 W_{n_\mathrm{S}}}{\partial y^2}\right)^{\mathrm{T}} \mathrm{d}A_{\mathrm{P}_i}, \tag{2.90}$$

where $\boldsymbol{G}_{\mathrm{em,A}}^{(:,i)}$ is the ith column of the electromechanical coupling matrix referring to ith actuator patch. This matrix is also the input matrix of the plate system when excited by the control voltages $\boldsymbol{U}_{\mathrm{A}}$, compare (2.83). The degree of controllability of the nth mode is thus determined by the quantity $\frac{\partial^2 W_n}{\partial x^2} + \frac{\partial^2 W_n}{\partial y^2}$. For a simply supported plate with eigenfunctions given by (2.45), this expression is equal to $-\pi^2\left(n_{\mathrm{S},x}^2/l_x^2 + n_{\mathrm{S},y}^2/l_y^2\right) W_n(x,y)$. Thus, the sum of modal curvatures is proportional to the mode shape function itself.

When actuators shall be positioned to control several modes, the absolute values of the relevant mode shape functions should be multiplied when searching for suitable locations. This ensures that the value of the corresponding "controllability surface" has zero value at those points where at least one mode is uncontrollable. There are twelve resonances in the frequency range up to 400 Hz for the simply-supported plate as well as for the real testbed, compare Table 2.1 on page 51. The left side of Fig. 2.9 shows the result of the multiplication of the first twelve bending mode shapes of the theoretical model. It can be seen that the result is point symmetric, and there are four global maxima. In addition to that, eight local maxima, four at the long edges and four at the short edges, can be distinguished. The local maxima at the long edges have a slighter higher value than those at the short edges.

The multiplication of the mode shapes has the disadvantage that the slope of the surface near the maxima becomes quite large. This means that when this procedure was to be applied to the real testbed, a very small grid would have to be used when measuring the mode shapes by experimental modal analysis. This is even more critical when the second order numerical differentiations of the measured mode shapes have to be carried out to determine the modal curvatures. For that reason, the result of the multiplicative superposition is compared with that of the additive superposition. This is shown on the right side of Fig. 2.9. It can be seen that the slope is less steep, and the positions of the maxima, and therefore the possible actuator locations, are identical. Thus, only additive superpositions are shown for the experimental results in Fig. 2.10. The left part of this figure shows the superposition of the modal curvatures, while the right hand side shows the

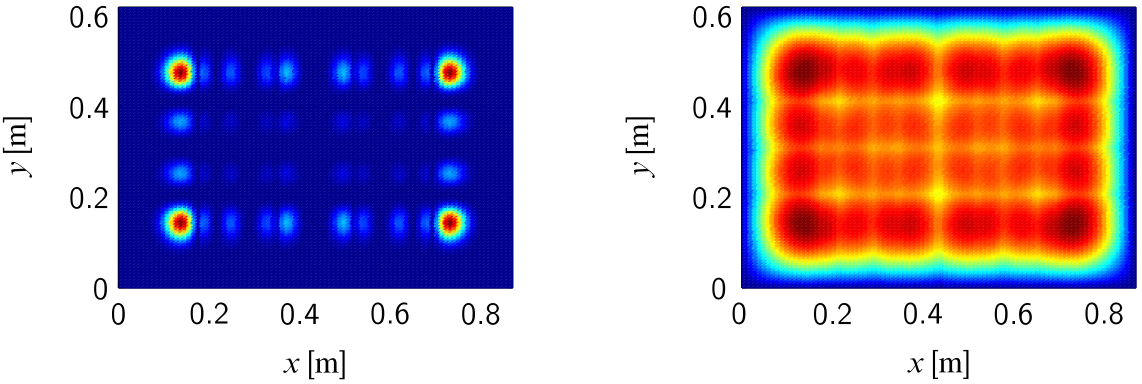

Figure 2.9: Superposition of the magnitudes of the first twelve mode shapes of the theoretical plate model, left: multiplicative; right: additive.

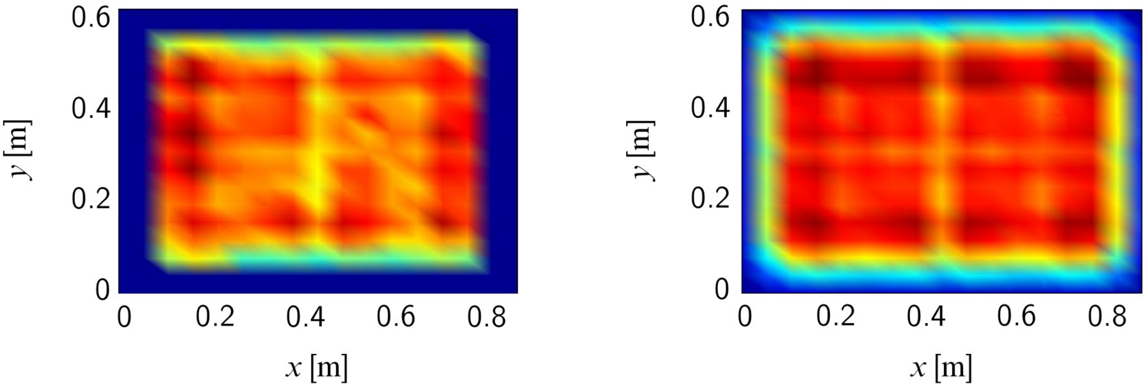

Figure 2.10: Additive superposition of magnitudes of the first twelve experimental modal quantities, left: modal curvatures; right: mode shapes.

superposition of the mode shapes themselves. It is difficult to recognize the maxima in the plot of the curvatures, because it is distorted by the second-order numerical differentiations. The additive superposition of the mode shapes, however, matches the result of the theoretical model very well.
According to Figs. 2.9 and 2.10, there are twelve possible transducer locations indicated by the global and local maxima. The prominent positions at the four corners have an equal value which is higher than those of the other eight locations. This might suggest the idea that the four corners are the best possible choice for the four actuators in terms of control performance. However, this is misleading because of the following argument: At some specific corner, there are modes which are well controllable and some which are less controllable. Because of the symmetry of the mode shapes, all four corners are equivalent in terms of controllability, i.e. the situation is the same at every corner. For high control performance, it is advisable to place some actuators at points that allow good controllability of other modes, compared to the corner positions, although the overall controllability at these points may be lower.

In order to select the appropriate actuator positions out of the twelve possible locations, a controllability measure is employed. This will serve as an easily applicable substitute measure for the closed-loop performance. In this thesis, the measure of Lückel & Müller [126] is used, which is a quantification of Gilbert's controllability criterion, because of its intuitive appeal and low computational cost. The controllability index of a system's ith mathematical eigenmode is given by

$$\kappa_i^{B} = \frac{\boldsymbol{w}_i^{\mathrm{T}} \boldsymbol{B}\boldsymbol{B}^{\mathrm{T}} \boldsymbol{w}_i^{*}}{\boldsymbol{w}_i^{\mathrm{T}} \boldsymbol{w}_i^{*}}, \quad i = 1, \ldots, n, \tag{2.91}$$

where $\boldsymbol{B}$ is the input matrix of the system's state space model of size n, $\boldsymbol{w}_i$ is the system's ith left eigenvector and the star superscript indicates the conjugate operation. Obviously, when the ith left eigenvector lies within the left null space of the input matrix, the ith mode is uncontrollable, and the controllability index is zero. When the system is a flexible mechanical structure with modal damping, the state space model can be stated in terms of structural mode shapes, eigenfrequencies and damping ratios[129]. In this case, the controllability indices can also be expressed in mechanical quantities, as demonstrated in [148] and App. A.7,

$$\kappa_i^{B} = \boldsymbol{G}_{\mathrm{em,A}}^{(i,:)} \left(\boldsymbol{G}_{\mathrm{em,A}}^{(i,:)}\right)^{\mathrm{T}} \frac{1}{1+\omega_i^2}, \quad i = 1, \ldots, {}^{n}\!/_{2}. \tag{2.92}$$

Only one half of the controllability indices must be calculated, because all system eigenvalues appear in conjugate-complex pairs.

For a given actuator configuration, the controllability indices can be computed by the above equation, and a total controllability index is formed by multiplication of the indices of each mode, $\kappa_{\mathrm{tot}}^{B} = \prod_{i=1}^{n/2} \kappa_i^{B}$. There are two reasons why a multiplicative superposition of modal controllability indices is preferable to an additive superposition. First, it is a desirable property that the overall controllability index $\kappa_{\mathrm{tot}}^{B}$ is zero when one targeted mode is uncontrollable with the current actuator configuration. Second, with multiplicative superposition, the overall index can be alternatively stated as $\kappa_{\mathrm{tot}}^{B} = \Pi_{i=1}^{n/2} \boldsymbol{G}_{\mathrm{em,A}}^{(i,:)} \left(\boldsymbol{G}_{\mathrm{em,A}}^{(i,:)}\right)^{\mathrm{T}} \Pi_{i=1}^{n/2} \frac{1}{1+\omega_i^2}$. Now, it becomes obvious that the ranking of different actuator configurations for a fixed set of modes is not influenced by the values of the system eigenfrequencies. With additive superposition, the overall index would be dominated by the first few terms, because the contributions of the higher modes tend rapidly to zero due the vanishing terms ${}^{1}\!/_{1+\omega_i^2}$.

Calculations show that placing two actuators at global maxima and two at local maxima at the long edges increases the total controllability index by 38 % as compared to having all four actuators at the global maxima. This is the actuator configuration which is realized at the testbed and which will be used for simulations throughout this thesis. Due to the symmetry of the problem, it is irrelevant which of the global maxima and the local maxima at the long edges are selected.

Once the placement of the actuators has been done, the placement of the sensors turns out to be the dual problem. Accelerometers shall be mounted on top of the plate to detect the plate motion at discrete locations. The observability index of Lückel & Müller for this case is given as (see App. A.7)

$$\kappa_i^{C} = \left(\boldsymbol{W}_{\mathrm{sensor}}^{\mathrm{dis}(:,i)}\right)^{\mathrm{T}} \boldsymbol{W}_{\mathrm{sensor}}^{\mathrm{dis}(:,i)} \frac{1}{1+\omega_i^2} \quad i = 1, \ldots, {}^{n}\!/_{2}. \tag{2.93}$$

Since the mode shapes and the shape functions of the sum of the modal curvatures are identical up to the scaling constant $-\pi^2 \left({}^{n_{\mathrm{s},x}^2}\!/_{l_x^2} + {}^{n_{\mathrm{s},y}^2}\!/_{l_y^2}\right)$, and the integration in (2.90) takes place over a small area of the plate, the optimization of the observability index results in the same positions as

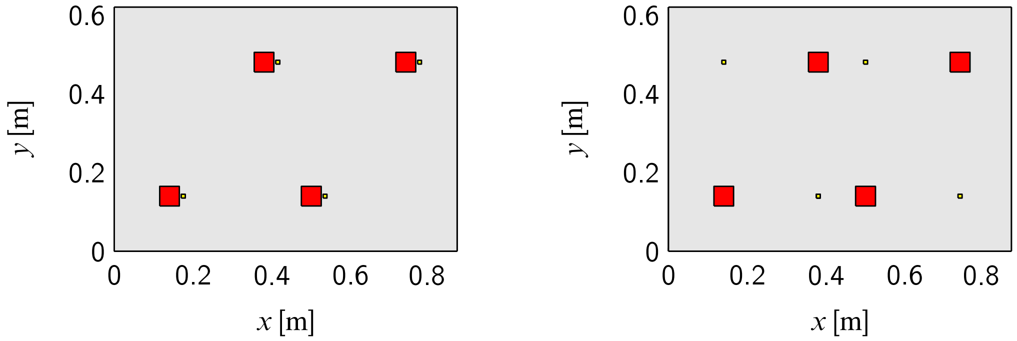

Figure 2.11: Placement of actuator patches (big squares) and accelerometers (small squares) for active damping. Left: Selected configuration for active damping; right: alternative configuration with the same controllability and observability indices.

the controllability index. Thus, a good choice for the sensor locations is to place two sensors at the corners (global maxima) and two at the local maxima at the long edges of the plate, as was for the actuators. Every such placement will result in the same value of the observability index, i.e. the two configurations shown in Fig. 2.11 should be equal in performance.

However, it is advantageous to place the sensors at the same locations as the actuators, because this will help to prevent non-minimum phase zeros to appear in the transfer function from the actuators to the sensors. This will be explained in the next section. For that reason, the accelerometers will be mounted nearly collocated to the actuators, as shown on the left side of Fig. 2.11. The normal distance of one accelerometer to the nearest edge of an actuator patch is 10 mm.

2.5 System Analysis

In the last sections, a complete lumped-parameter model of the idealized acoustic demonstrator with actuators and sensors was derived. In this section, this model will be used to work out and analyze the characteristic features of this system and to show their implications for control design. Because of several simplifying assumptions during the theoretical modeling process, the input-output behavior of the analytic model does not perfectly match that of the real system. However, the analytic model reveals very valuable information about the real system. It does so by qualitatively displaying essential features of the real system that are indispensable for successful control design, most importantly its qualitative pole-zero configuration and deduced properties like stability, controllability, and observability. The connection of these system-theoretic properties to mechanical properties, like mode shape functions, will also be shown. This could not be done with a black-box model.

2.5.1 Pole-Zero Configuration

A system's pole-zero configuration reveals many of the important system features to the control engineer, because essential properties, like stability and controllability for example, can be immediately derived. The acoustic demonstrator white-box model shows a pole-zero map that qualitatively also applies to the real testbed. The most important system properties which can be derived from the pole-zero configuration will now be shortly elaborated on.

System Poles

The poles determine the eigenbehavior of a system, most importantly its stability. Since we are dealing with linear time-invariant systems, the common stability definitions BIBO[2]-stability and asymptotic stability are equivalent. Thus, we will just speak of stability in the following.
The acoustic demonstrator model is comprised of the two subsystems plate and cavity. It is obvious that the plate with bonded piezo-patches constitutes a stable system. Formally, the positive-definiteness of the mass- and stiffness operators in the Kirchhoff plate equation (2.9) ensures all system poles to be purely imaginary with non-zero magnitude. This property is unaffected by the discretization process, apart from numerical errors. By introduction of a positive definite damping matrix, the system is made stable.
Table 2.1 lists the first twelve eigenfrequencies of a simply-supported plate, a clamped plate, and the plate which is used in the testbed along with the mode shape numbers $n_{\mathrm{S},x}$ and $n_{\mathrm{S},y}$. All plates have the same dimensions and material properties, see App. A.1. The eigenfrequencies of the simply-supported plate have been calculated by (2.70). For the clamped plate, the approximation given in [30] was used. The eigenfrequencies of the real plate where determined by experimental modal analysis. The important information is that the eigenfrequencies of the real plate consequently lie in between those of the plates with the extremal theoretical boundary conditions. This confirms the conjecture that no simple analytical boundary condition can be used to accurately describe the plate dynamics of the real testbed. Furthermore, it can be seen that the mode shapes corresponding to the last two eigenfrequencies of the simply-supported plate are swapped compared to those of the clamped and real plate. This is possible, since the corresponding eigenfrequencies are very close.

The stiffness-operator of the PDE (2.16) which governs the undamped fluid dynamics of the acoustic volume is positive-semidefinite, while the mass-operator is positive definite. Thus, there are two eigenvalues located at the origin of the complex plane. This means that a constant volume displacement V leads to a pressure amplitude p which is constant over time. This pressure field is also spatially constant, compare Fig. 2.8. Furthermore, the fluid subsystem without damping also has an infinite number of purely imaginary eigenvalues.

The important question is now how the pole configuration of the combined plate-cavity system looks like. It is clear that the system poles of the complete system will not be identical to the conjunction of the poles of the two subsystems. The location of the poles will be altered due to the coupling between the two subsystems. As it is shown in Appendix A.6, the combined system (2.83) with $\boldsymbol{\eta}$ and $\boldsymbol{\varphi}$ as model outputs has all its poles in the open left half of the complex plane, apart from two eigenvalues at the origin. However, we are not interested in $\boldsymbol{\varphi}$ but the physically meaning output p which is in turn determined by $\dot{\boldsymbol{\varphi}}$, as can be seen by the modal expansion

---

[2] *B*ounded *I*nput *B*ounded *O*utput

Table 2.1: Eigenfrequencies of a simply-supported and a clamped plate in comparison with those of the plate of the testbed in Hz. The last column shows the mode shape numbers. Numbers in curly brackets refer to the real and clamped plate.

Nr.	simply supported	real	clamped	$(n_{\mathrm{S},x}, n_{\mathrm{S},y})$
1	38.5	58.6	72.5	(1, 1)
2	77.4	97.3	117.4	(2, 1)
3	115.2	145.9	173.8	(1, 2)
4	142.3	161.3	192.1	(3, 1)
5	154.1	181.2	215.5	(2, 2)
6	219.0	242.4	285.8	(3, 2)
7	233.1	249.5	294.6	(4, 1)
8	242.9	276.3	327.3	(1, 3)
9	281.8	312.8	368.1	(2, 3)
10	309.8	329.2	385.0	(4, 2)
11	346.7	363.4	423.7	(3, 3) {5, 1}
12	349.9	373.8	435.6	(5, 1) {3, 3}

(2.41c). Thus, any model with output p, like (2.85), has only one pole at the origin. The other pole is unobservable. The remaining integrator is responsible for the fact that for the combined system, a constant volume displacement V also leads to a temporally constant pressure amplitude. In addition to that, it is shown in the Appendix that the remaining system poles all appear in conjugate-complex pairs. Summing up, the combined system has $2(n_{\mathrm{S}} + n_{\mathrm{F}})$ system poles of which two are equal to zero. All other poles are stable conjugate pairs.

Controllability and Observability

The principles of controllability of the acoustic demonstrator are easily grasped by considering the theoretical developments so far. It was shown that it is natural to think of the system at hand as a superposition of modes, where each mode represents a weakly damped second-order system. Therefore, a system is completely controllable if and only if[3] all modes can be excited by the available actuators.

The plate subsystem is completely controllable from the mechanical input $F(x, y, t)$ iff all generalized forces defined in (2.44a) are non-zero. This means that the pressure distribution must not be orthogonal to any mode shape function. Moreover, the plate subsystem is completely controllable by the piezoelectric actuators iff not all patches are positioned in such a way that their surface centers are on the nodal lines of one mechanical basis function W_i. That would cause a complete row of the electromechanical coupling matrix $\boldsymbol{G}_{\mathrm{em}}$ to become zero, and the corresponding mode would be uncontrollable.

Furthermore, the coupled plate-cavity system is completely controllable from the actuators that act on the plate, i.e. the external forces $F(x, y, t)$ or applied voltages $\boldsymbol{U}_{\mathrm{A}}(t)$, iff the plate is com-

---

[3] The abbreviation "iff" will be used in the following.

pletely controllable by that source and the mechanical-acoustical coupling matrix $\boldsymbol{G}_{\mathrm{ma}}$ does not have a zero column. This can be concluded by inspection of (2.83). On the other hand, the coupled system is completely controllable from acoustic sources iff the distribution of the volume velocity is not orthogonal to any acoustic basis function, compare (2.44c), and $\boldsymbol{G}_{\mathrm{ma}}$ has no row identical to the zero vector.

The observability of the plate subsystem and the coupled system by different collections of sensors can be analyzed in an analogous manner. The plate subsystem is completely observable by accelerometers iff the matrix $\boldsymbol{W}^{\mathrm{dis}}_{\mathrm{sensor}}$ has no zero column, i.e. not all accelerometers are positioned on the nodal lines of one mechanical basis function. Furthermore, the plate is completely observable by piezoelectric sensors iff not all centers of the patches lie on the nodal lines of one W_i.

The modes of the coupled system are completely observable by accelerometers or piezoelectrical sensors iff the plate is completely observable and $\boldsymbol{G}_{\mathrm{ma}}$ has no zero column. Finally, the modes of the coupled system are completely observable by microphones within the fluid volume iff the cavity subsystem is completely observable, i. e. $\boldsymbol{P}^{\mathrm{dis}}_{\mathrm{sensor}}$ has no zero column, and $\boldsymbol{G}_{\mathrm{ma}}$ has no zero row.

As was already mentioned, the coupled system does not only have conjugate-complex system poles, where each pair corresponds to one mode, but also has two poles identical to zero. To calculate the pressure distribution $p(x, y, z, t)$, the variables of $\boldsymbol{\varphi}$ must be differentiated with respect to time. It can be shown that this generates an invariant zero at the origin of the complex plane whose state direction is identical to eigenvector of one integrator pole. Thus, this pole is made unobservable.

Since theoretically, distributed parameter systems have infinitely many modes, there will definitely be unobservable and/or uncontrollable modes when a limited number of actuators and sensors are used. Nevertheless, it will be assumed in the following that the modes of the considered system which lie in the bandwidth of the control loop are observable and controllable. This is assured by a sensible placement of the actuators and sensors, see Sec. 2.4.3.

System Zeros

The plate subsystem is assumed to be completely controllable and observable. Thus, the set of transmission zeros is identical to the set of invariant zeros. The number of transmission zeros for the considered case with four actuator patches and four accelerometers, see Fig. 2.11, is equal to the number of poles, since the feedthrough matrix has full rank [54]. Since the number of system inputs is equal to the number of system outputs, i.e. the system is square, the set of transmission zeros is also identical to the set of system zeros.

The placement of the sensors nearly collocated to the actuators will ensure that all transmission zeros will appear in conjugate-complex minimum-phase pairs, at least up to a certain frequency. This can be made clear by the following argument: The input matrix of the plate system excited by the actuator patches is $-\boldsymbol{G}_{\mathrm{em,A}}$, and the output equation for discrete displacement sensing would be $\boldsymbol{w} = \boldsymbol{W}^{\mathrm{dis}}_{\mathrm{sensor}}\boldsymbol{\eta}$, compare (2.82) and (2.87a). The (i, j) th element of $\boldsymbol{G}_{\mathrm{em,A}}$ is given by

$e_{31}\frac{h}{2}\iint_{A_{\mathrm{P}_j}} \frac{\partial^2 W_i}{\partial x^2} + \frac{\partial^2 W_i}{\partial y^2}\,\mathrm{d}A_{\mathrm{P}_j}$ which can be simplified to $-e_{31}\frac{h}{2}\pi^2\left(n_{\mathrm{S},x}^2/l_x^2 + n_{\mathrm{S},y}^2/l_y^2\right)\iint_{A_{\mathrm{P}_j}} W_i\,\mathrm{d}A_{\mathrm{P},j}$ for the simply-supported plate. It is now assumed that all patches have the same area A_{P} which is so small that the following conditions are satisfied: $\sqrt{A_{\mathrm{P}}} \ll l_x/n_{\mathrm{S},x}$ and $\sqrt{A_{\mathrm{P}}} \ll l_y/n_{\mathrm{S},y}$. Then, the function W_i under the integral is approximately constant and the (i, j) th element of $\boldsymbol{G}_{\mathrm{em,A}}$ can be approximated by $-e_{31}\frac{h}{2}\pi^2\left(n_{\mathrm{S},x}^2/l_x^2 + n_{\mathrm{S},y}^2/l_y^2\right) A_{\mathrm{P}} W_i(x_{\mathrm{P}_j}, y_{\mathrm{P}_j}) = k_i W_i(x_{\mathrm{P}_j}, y_{\mathrm{P}_j})$ with some constant k_i for the ith mode. Thus, the system's input and output matrix are approximately related by $\boldsymbol{G}_{\mathrm{em,A}} = \bigoplus\{k_1, \ldots, k_{n_{\mathrm{S}}}\}\left(\boldsymbol{W}_{\mathrm{sensor}}^{\mathrm{dis}}\right)^{\mathrm{T}}$. Now, suppose that a static output feedback of the type $\boldsymbol{U}_{\mathrm{A}} = -g\mathbf{I}\,\boldsymbol{w}$ is applied. The closed-loop equation of the autonomous system is then $\boldsymbol{M}_{\mathrm{S}}\ddot{\boldsymbol{\eta}} + \boldsymbol{D}_{\mathrm{S}}\dot{\boldsymbol{\eta}} + \boldsymbol{K}_{\mathrm{S}}\boldsymbol{\eta} - g\bigoplus\{k_1, \ldots, k_{n_{\mathrm{S}}}\}\left(\boldsymbol{W}_{\mathrm{sensor}}^{\mathrm{dis}}\right)^{\mathrm{T}}\boldsymbol{W}_{\mathrm{sensor}}^{\mathrm{dis}}\boldsymbol{\eta} = \mathbf{0}$. The matrix $\left(\boldsymbol{W}_{\mathrm{sensor}}^{\mathrm{dis}}\right)^{\mathrm{T}}\boldsymbol{W}_{\mathrm{sensor}}^{\mathrm{dis}}$ is symmetric and positive definite. The matrix $g\bigoplus\{k_1, \ldots, k_{n_{\mathrm{S}}}\}\left(\boldsymbol{W}_{\mathrm{sensor}}^{\mathrm{dis}}\right)^{\mathrm{T}}\boldsymbol{W}_{\mathrm{sensor}}^{\mathrm{dis}}$ is negative definite because all k_i are negative. Furthermore, it is still symmetric if all k_i are equal and approximately symmetric if the k_i do not differ to much in their magnitude. This implies that the term $-g\bigoplus\{k_1, ..., k_{n_{\mathrm{S}}}\}\left(\boldsymbol{W}_{\mathrm{sensor}}^{\mathrm{dis}}\right)^{\mathrm{T}}\boldsymbol{W}_{\mathrm{sensor}}^{\mathrm{dis}}$ can be interpreted as an additional stiffness matrix to $\boldsymbol{K}_{\mathrm{S}}$. Thus, the controlled system behaves like the original system but with additional stiffness elements whose magnitudes are controlled by the control gain g, i.e. the control loop is passive. This means that the closed-loop poles will always be stable conjugate-complex pairs. When g goes to infinity, the closed-loop poles will be identical to the transmission zeros of the open-loop system [54]. This implies the final result that the transmission zeros of the plate with discrete displacement sensing are all minimum-phase conjugate-complex pairs under the above assumptions. This also holds true for the plate with acceleration sensing, but additional zeros do appear at the origin which are, in fact, blocking zeros. However, the assumptions which have been made to derive this result will surely be invalidated at high frequencies.

A computation of the transmission zeros in the frequency range up to 500 Hz for the two actuator-sensor configurations shown in Fig. 2.11 shows that the left configuration has only one pair of non-minimum phase zeros at 459 Hz. The configuration on the right side has non-minimum phase zeros at 47 Hz, 100 Hz, 194 Hz, and 386 Hz which all lie in the bandwidth of the controller which would have a very detrimental effect on the achievable control performance [168].

As already mentioned, the white-box model of the complete acoustic demonstrator is observable except for one pole at the origin. Thus, the model has one output decoupling zero which can be eliminated from the model.

Calculations show that if the coupled system has the same inputs and outputs as the plate system, then it can be expected that all transmission zeros appear as minimum-phase conjugate-complex pairs up to a certain frequency which is not much different from that of the isolated plate system. For example, the first non minimum-phase zero of the coupled system containing $n_{\mathrm{S}} = 17$ plate modes and $n_{\mathrm{F}} = 13$ cavity modes appears at 458.7 Hz, whereas the first non minimum-phase zero for the plate subsystem appears at 458.8 Hz. This may be attributed to the fact that the mechanical-acoustical coupling causes additional dynamics but does very little alter the existing plate dynamics, i.e. vibration mode shapes and corresponding eigenfrequencies. The effects generated by the coupling of the different physical domains shall now be further illustrated.

2.5.2 Coupling of Physical Domains

During the modeling process, the elements of the acoustic demonstrator have been grouped into three domains: the mechanical, the electrical, and the acoustic domain. The mechanical domain represents the plate dynamics, whereas the acoustic domain comprises the enclosed fluid. The electrical domain is made up of the diverse piezoelectric elements that can be used as sensors as well as actuators. Due to the physical setup, there is an immediate connection between the piezo patches and the plate. Moreover, the plate is in direct contact with the fluid. The piezo elements interact with the fluid only indirectly via the structural dynamics. The effects of the electro-mechanical and the mechanical-acoustical coupling shall now be highlighted.

Electromechanical Coupling

The properties of a plate with bonded piezoelectric elements are different from that of a plate without piezo patches. These differences stem from the modified mass and stiffness distribution caused by the additional elements. These were termed passive effects in Sec. 2.2.2. In addition to that, the piezo elements which are used as sensors introduce an additional stiffness term which comes from the piezoelectric effect, compare (2.82). The magnitude of these effects shall be examined. In Fig. 2.11, the actuator configuration which will be used for the active damping of the plate, see Ch. 4, was already shown. Four piezo elements with dimensions 50 mm × 50 mm × 0.5 mm are applied at appropriate locations, according to the statements in Sec. 2.4.3. No sensor patches are used. Instead, for the control loop, the plate motion is measured with accelerometers which are assumed to be massless. They are indicated by the small squares next to the actuator patches.

The eigenfrequencies of the simply-supported plate with piezo elements were computed and compared with those shown in the second column of Table 2.1. The result was that the eigenfrequencies were shifted by a small amount, where some increased and others decreased. Thus, one cannot make a statement on whether the additional stiffness or the additional mass is dominant. However, no eigenfrequency was changed by more than 0.40 %. The change of the mode shapes is also negligible. As a consequence, the additional mass and stiffness terms caused by the piezo elements will be neglected in future simulations. More importantly, the result implies that the task of actuator placement can be simplified in a way, because the mass and stiffness properties of the actuators need not be taken into account.

Mechanical-Acoustical Coupling

The fluid-structure interaction between the flexible plate and the adjacent enclosed volume of gas will now be shortly analyzed. The mechanical-acoustical coupling has some influence on the vibration mode shapes and the corresponding eigenfrequencies, similar to the electromechanical coupling. The eigenfrequencies and mode shapes of the undamped coupled system can be computed as explained in App. A.6. Table 2.2 shows the first 15 eigenfrequencies, along with those of the plate and the acoustic volume (in a rigid rectangular containment) in the same frequency range. It appears that the eigenfrequencies of the coupled system are almost identical to the uni-

Table 2.2: First 15 eigenfrequencies of the undamped coupled plate-cavity system along with the eigenfrequencies of the plate and the fluid separated in Hz.

Nr.	coupled	plate	cavity
0			0
1	41.8	38.5	
2	76.8	77.4	
3	114.7	115.2	
4	142.0	142.3	
5	153.7	154.1	
6	197.5		197.1
7	218.7	219.0	
8	229.0		228.7
9	233.1	233.1	
10	244.1	242.9	
11	277.2		276.6
12	281.2	281.8	
13	303.8		301.9
14	309.3	309.8	
15	340.3		339.7

fication of the sets of eigenfrequencies of the separated subsystems. Figure 2.12 shows the first eight discretized eigenforms of the undamped system. The eigenforms corresponding to the sixth and eights resonance frequency are dominated by the fluid dynamics, whereas the others are dominated by the plate motion.

2.6 Chapter Summary

A theoretical model has been provided in this chapter. The purpose of this white-box model is to gain insight into the prominent physical principles of the acoustic demonstrator. The governing PDEs comprising the plate and fluid dynamics have been stated from available literature, and it was also shown that Kirchhoff plate theory is sufficient to describe the dynamical behavior of the plate within the considered frequency range.

The bulk of this chapter was considered with the development of a lumped-parameter model of the acoustic demonstrator whose complexity is easily scalable by the number of basis functions and is therefore easy to simulate on computer. This model was derived without explicitly making use of the PDEs, but it is argued that the lumped-parameter model is identical to the one which can be derived by discretizing the PDEs by Galerkin's method. This model allows for the excitation of the acoustic demonstrator by concentrated and distributed forces on the plate surface, piezo patches on the plate surface, and acoustic sources within the acoustic volume. Given some specific excitation, the model calculates the pressure distribution within the acoustic volume as well as the normal displacement of the plate surface. In addition to that, sensor outputs of accelerometers,

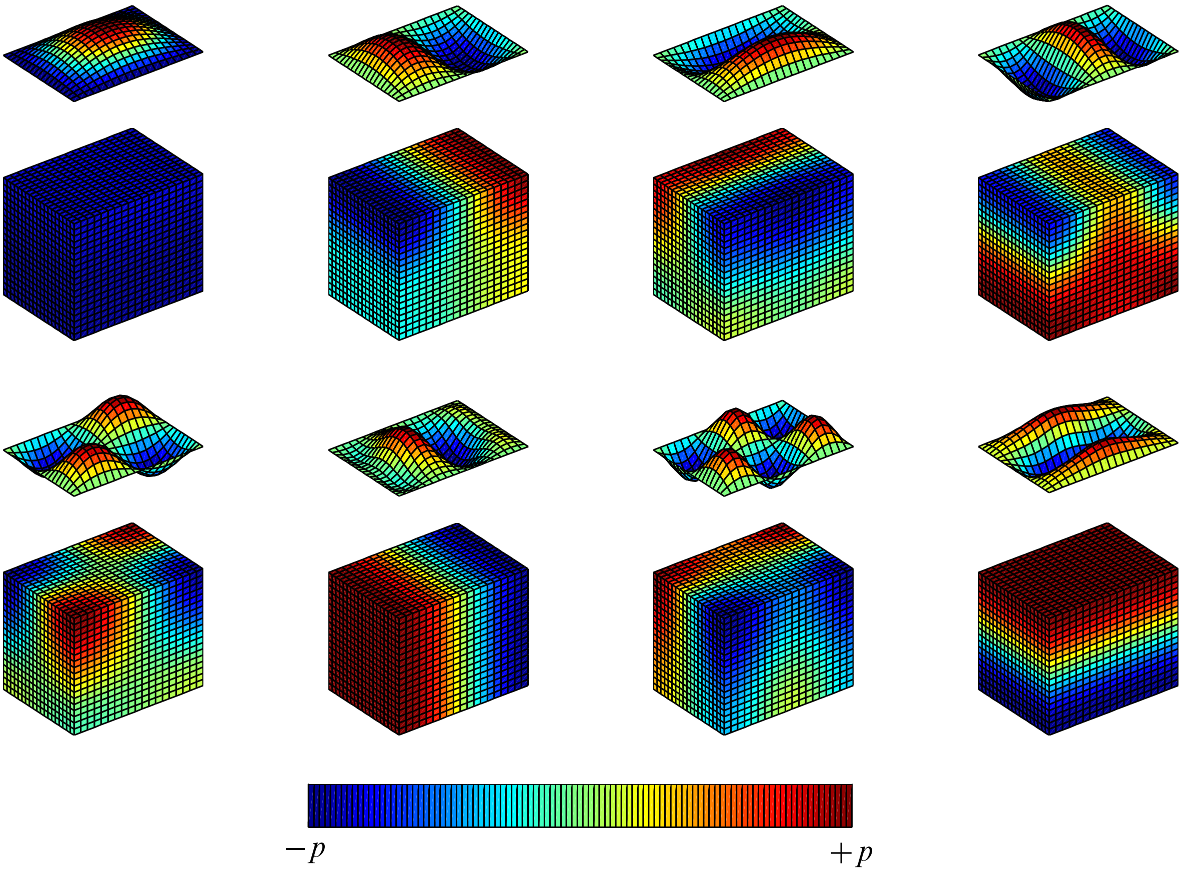

Figure 2.12: First eight eigenforms of the undamped coupled system.

piezo patches, and microphones can be simulated. For simplicity, proportional damping has been introduced separately for the plate and cavity subsystems. The coupled system however, does not preserve this property. Further properties of the coupled plate-cavity system, like eigenfrequencies and eigenforms, have been examined.

After having given a short literature review on actuator and sensor placement, a simple methodology for that problem has been presented and exemplified on the placement of actuators for active damping of the plate.

3 Experimental Modeling

Experimental modeling techniques derive mathematical models of systems from measurement data. This chapter presents an experimental modeling procedure for high-order, linear time-invariant systems which is capable of estimating a nominal model along with its corresponding uncertainty description solely from measurement data with a minimum of prior assumptions. The uncertainty description is in a form which can be immediately applied in standard robust control techniques. The procedure is exemplified on the modeling of the plate with force and piezoelectric actuators, and acceleration sensors. Some remarks on the design of suitable excitation signals to minimize model uncertainty will also be given.

3.1 Motivation and Identification Setup

Experimental modeling, or system identification, of systems is almost always necessary for model-based control design, since accurate white-box models are hard to obtain even for systems of medium complexity [110]. Therefore, an identification procedure will be put forward in this chapter which can handle high order, linear time-invariant systems which are typical for flexible mechanical structures.
Even the most sophisticated identification method cannot provide a perfect model. Every model comes with an associated model error. Since no exact representation of the model error is available, this model error leads to a model uncertainty. There are two kinds of model errors and therefore model uncertainty (see for example [110] or [123]): bias and variance errors.

Bias errors in any estimation procedure cannot, per definition, be removed by increasing the amount of available information, i.e. measurement data, because the sources of the bias errors are inherent in the estimation algorithm. Bias errors may appear in system identification, for example, when a linear system model is fitted to a process which behaves nonlinear. Even if the system's input-output behavior can be described by a linear model, bias errors are relevant if the order of the linear model is too small. In both cases, the bias errors are due to undermodeling, i.e. the true system cannot be represented by any candidate model within the selected model set. It is important to note that the latter example is often deliberately accepted, because moderate model orders are advantageous for system analysis and model-based control design. Bias errors may also be caused by the selected estimation algorithm itself, i.e. the algorithm is not bias free for the given system identification setup. The identification setup is defined by the signal path from the excitation signals to the measurement signals including

- the system to be identified,
- actuator and sensor dynamics,

- signal-processing elements, e.g. sample & hold devices, quantizers,
- and points in the signal path where noise having certain characteristics is injected.

Especially the points in the signal path where noise influences the measurements are critical for the choice of a bias-free estimation algorithm. This led to the development of algorithms which can handle noise on the input signals, the output signals, or both, see for example [152]. As argued in [147], quantization effects can be modeled as a white noise injection if the quantization steps are much smaller than the signal amplitudes.
Variance errors, as opposed to bias errors, asymptotically disappear when the amount of information regarding the system to be identified tends to infinity. However, the speed with which the variance errors disappear also depends on the selected estimation algorithm [152].

Here, the problem of identifying a model of the smart panel is considered as an example for the proposed identification procedure. As a consequence of the above arguments, any experimentally identified linear time-invariant model of the smart panel will be prone to model errors, and the most important sources of error will be

- the nonlinear behavior of the piezoelectric actuator material,
- the undermodeling error due to the infinite-dimensional nature of the flexible structure,
- and the measurement noise of the sensors.

This has important implications for control design, since performance and robustness generally impose diametrical requirements on the control-loop specifications [168]. For that reason, it is desirable to have accurate information on the uncertainty of the model on which the control design is based. In this chapter, an identification procedure which tries to feature this for high-order, linear time-invariant systems is proposed.

The model of the smart panel will be used to facilitate the design of a controller to achieve active damping of the flexible plate in the next chapter. The identification setup is shown in Fig. 3.1. The plate is equipped with four actuator patches and four nearly collocated accelerometers, where the positions have been determined according to the guidelines given in Sec. 2.4.3. In addition to that, an electromagnetic shaker is mounted at a position which allows to excite all modes of the plate within the target bandwidth of 500 Hz. This shaker generates a disturbance point force which can be measured with a force sensor. A fifth accelerometer is positioned at the point of disturbance injection for analysis purposes. Thus, the overall system to be identified has five inputs and six outputs, where only four inputs and four outputs will be used in the control loop.
The purpose of the experimentally identified model is to accurately describe the input-output behavior of the plant to be controlled. This plant has four piezo patches as inputs and four nearly-collocated accelerometers as outputs and is indicated by the solid lines in Fig. 3.1 as the main identification path. This path includes not only the smart panel but also the necessary signal conditioning devices, i.e. the piezo amplifier and the analog filters. Since the amplifiers do not exhibit

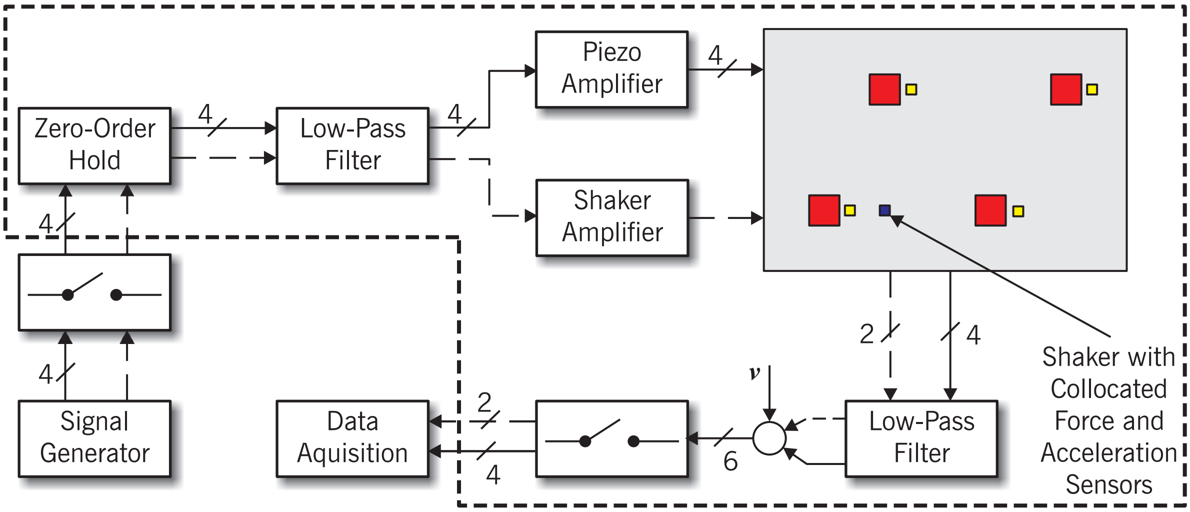

Figure 3.1: System identification setup for the smart panel with four actuators and four sensors. The disturbance path from the point force, generated by the shaker, to the collocated force and acceleration sensors is indicated by the dashed arrows.

sufficient low-pass characteristics, additional low-pass filters, so-called reconstruction filters [65], are necessary to limit the bandwidth of the actuator signals.

The inputs to the main identification path are piecewise constant due to the zero-order hold device of the signal generator. For that reason, it is natural to identify a discrete-time model. Identifying a continuous-time model for the given setup would cause bias errors in the estimated frequency response, as is shown in [152]. These errors decrease with decreasing sampling time T_s. However, it is not advantageous to work with a high sampling rate, since the resulting discrete-time controller has, in general, the same high sampling frequency as the underlying model. These high sampling frequencies are especially critical, in terms of computational effort, in combination with high model orders, as is the case here. Thus, a discrete-time model with a moderate sampling rate of $T_s = 0.6\,\text{ms}$ will be identified. This equals a sampling rate of $1.666\,\text{kHz}$. In order to avoid frequency aliasing, the corner frequencies of all low-pass filters are set to 600 Hz. All filters are Cauer filters of sixth order.

Two remarks have to be made regarding the assumptions on the noise. Since the sampled output of the signal generator is taken as system input, it can be assumed to be perfectly known, i.e. it is noise free. If in addition to that, all subsystems in the signal path from the zero-order hold to the anti-aliasing filters are linear time-invariant, then all noise injections along this path can be represented by a single noise injection $\boldsymbol{v}$ just before the output sampling.

3.2 Literature Review

Research on the topic of uncertainty modeling from measurement data has generated a rich body of works over the last two decades, and the whole field has been termed *robust identification* or *identification for control* (I4C). The purpose of this paragraph is to introduce the main ideas which can be found in the literature and to show how the identification method which is applied in this thesis is connected to existing works. By now, several books exclusively devoted to this topic have appeared, namely the works by Chen & Gu [45], Codrons [48], Garulli [76], Milanese [138], Smith [169], Sánchez-Peña [170], Tøffner-Clausen [181], and Veres [188]. Survey papers on the subject have been published by Gevers [78] and Hjalmarsson [105].

It is difficult to find suitable criteria to systematically categorize the work which has been done in the field of I4C. The main reason for this is that all works taken together give a mosaic display, i.e. lots of different ideas have been developed to solve many different specialized problems. In addition to that, many I4C schemes consist of several steps, where it is often possible to carry out a specific step by different algorithms. The only agreement in the literature is that I4C approaches can be split up in two broad groups: deterministic and stochastic methods. Deterministic methods give so-called hard error bounds, whereas stochastic methods give soft error bounds. For hard error bounds, the true plant is definitely contained within the identified model set, given that some underlying assumptions are satisfied. Soft error bounds come with a certain probability.

The key ideas behind deterministic methods, which are also termed *Set Membership Identification* (SMI) methods, can be summarized as follows: Given time- or frequency-domain measurement data, those plant models are looked for which could have possibly generated the observed data. To render this set bounded, assumptions have to made regarding the class of models. So far, SMI methods have only been developed for linear time-invariant systems. In addition to that, a bound on the measurement noise in some suitable norm, i.e. $\|v(k)\| \leq v_{\max}$, must be given. Thus, the noise is assumed unknown but bounded. Moreover, most works on SMI further assume that the plant exhibits some degree of stability, i.e. the system's impulse response $g(k)$ has an envelope $|g(k)| \leq M\rho^{-k}$, where M and ρ are also given. All models that satisfy the required assumptions and cannot be falsified by the observed measurement data form the *Feasible Systems Set* (FSS). However, the FSS can, in general, not be described in a form which is suitable for standard robust control design algorithms. Thus, the challenge in SMI methods is to tightly overbound the FSS with a suitable model set description which can be employed in robust control design. For general linear time-invariant parametric model structures, e.g. ARMAX or state space models, this may lead to optimization problems which may be practically intractable. Because of that, parametric model descriptions are often limited to models which are linearly parametrized, most importantly FIR models. Generalized basis functions, such as Laguerre or Kautz functions, are also possible. An early publication in this flavor is for example the paper by Wahlberg & Ljung [189]. Further works on deterministic I4C methods can for example be found in [88], [103], [139], [140], [171], and [185].

The intrinsic drawback of the deterministic approach is that the size of the FSS, and therefore model uncertainty, is largely determined by the a priori assumptions, most importantly by the bound on the noise. Since it is impossible to give a tight bound on the measurement noise *a priori*, it is often suggested to start with an "educated guess", and then iteratively adjust the bounds such that the FSS is small but not empty [56]. Other publications give methods to *estimate* the a priori information from a posteriori measurement data. As argued by Douma [59], both approaches question the hard bounds delivered by the I4C procedures, since they are derived from uncertain prior assumptions. Thus, deterministic I4C methods do, in fact, also calculate soft error bounds, unless overly conservative prior assumptions are made.

Stochastic I4C methods start from the more realistic assumption that statements with 100 % probability cannot be made for any experimental modeling technique. Thus, these methods are explicitly based on a stochastic paradigm to derive soft error bounds. In fact, stochastic methods where developed from basic statistical confidence tests which have always been employed in system identification. Consider, for example, the well-known prediction error framework in system identification. The key idea is to minimize the difference between the one-step ahead prediction of the model and the measured system output for some identification data set: $\min_{\boldsymbol{\theta}} \sum y(k) - \hat{y}(k|k-1)$, where $\hat{y}(k|k-1)$ is the output of the model which is parametrized by the parameter vector $\boldsymbol{\theta}$. It is shown by Ljung in [123] that the covariance matrix of the model parameters $\boldsymbol{\theta}$ is asymptotically (in data length) zero-mean normally distributed under mild assumptions and can be easily calculated — as long as the true system is within the chosen model set. This means that high-order models may have to be used in order to calculate the confidence intervals of the model parameters $\boldsymbol{\theta}$. Even if this is satisfied, the covariance matrix of the model parameters defines a model set which cannot be immediately handled by standard algorithms for robust control, because these usually require the uncertainty to be defined in the frequency domain. Thus, confidence intervals for the frequency response must be calculated by Gaussian error propagation calculation (first order approximation) from the covariances of the model parameters. By now, robustness tests have been developed which directly employ the model set as defined by the prediction error framework if undermodeling is negligible. See [80] and [81] for the SISO case and [14] for an extension to MIMO systems.

Nevertheless, reduced order models are often favorable for control design and cannot be avoided for distributed parameter systems at all. Thus, classical prediction error identification lacks the tools to connect system identification with robust control design, because it cannot handle bias errors. In order to better cope with the demands of robust model-based control design, more sophisticated stochastic I4C methods have been developed, the two most popular ones being termed *Stochastic Embedding* and *Model Error Modeling*.

Stochastic Embedding has been proposed by Goodwin and coworkers, see [84, 85]. Whereas the prediction error methods perform identification in the time domain, stochastic embedding is set in the frequency domain. As we have already seen, the main drawback of the classical prediction error framework is that it cannot handle bias errors which are most often caused by undermodeling. The key idea behind stochastic embedding is that the undermodeling error, which is clearly a deterministic error, is described by a stationary stochastic process. The parameters of this stochastic process are estimated from measurement data. For any given system, only one instance of this process will be relevant, since it is deterministic. However, this trick allows one to handle undermodeling and noise errors in a common (stochastic) framework, as argued by Tøffner-Clausen [181]. With the help of this approach, the covariance analysis of the prediction error framework can be extended to cases in which undermodeling is present, as also shown by Bombois [32]. However, as also stated in [181], the stochastic embedding approach requires linearly parametrized (FIR-type) models and cannot be immediately applied to MIMO systems. Suitable extensions seem not to be available today.

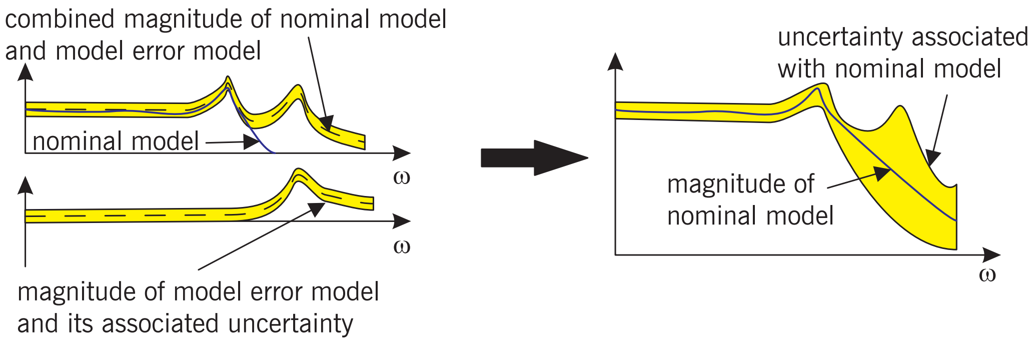

Figure 3.2: Workflow of model error modeling.

Model Error Modeling (MEM) has been proposed by Ljung and coworkers in a series of publications [122, 124, 159, 160]. The advantage of MEM is that it is not restricted to SISO systems nor linearly parametrized models. In fact, it is a method to provide model error bounds in non-parametric form for any parametric model derived by *any* identification algorithm. The workflow of MEM is as follows: Given any parametric model, a residual sequence $r(k) = y(k) - \hat{y}(k)$ is calculated from a validation data set. Then, a parametric model, the so-called model error model, is identified via prediction error methods which maps the input sequence $u(k)$ to the residual sequence $r(k)$ as well as possible. “As well as possible” means in this context that the model order of the model error model is chosen very high such that the undermodeling error is negligible. Then, the classical residual analysis of the prediction error framework becomes applicable to the model error model. This means that confidence bounds on the parameters of the model error model and its frequency response can be easily derived. In those frequency ranges where no undermodeling is present in the nominal model, the uncertainty of the model error model will be due only to variance (noise) errors. Thus, the magnitude of the model error model will be close to zero. In those frequency ranges where undermodeling errors are present, the magnitude of the model error model is expected to become significantly different from zero. In a final step, the FRFs of the nominal model and the model error model together with its associated uncertainty description are inspected in a Bode diagram. Of course, there is no guarantee that the FRF of the nominal model will lie in the uncertainty region of the model error model. In fact, it is expected to lie outside at those frequencies where undermodeling is present. The final uncertainty region associated with the nominal model is constructed by extending the uncertainty region of the model error model to symmetrically bound the nominal FRF. The procedure is illustrated in Fig. 3.2.

A drawback of this method is the usage of a high-order parametric model error model whose computation may be expensive or even ill-conditioned. Furthermore, the only purpose of the parametric model error model is to compute non-parametric uncertainty regions in the frequency domain. Thus, it may be argued that a non-parametric model error model, obtained by some FRF estimator, may be more appropriate, as is for example outlined in [175].

Summing up, MEM is a two-step procedure: First, a parametric nominal model is identified and second, a non-parametric model error model (or alternatively, a high-order parametric model) is employed to construct the uncertainty description for the nominal model a posteriori.

A more elegant way of performing I4C with a two-step procedure is to swap these two basic steps: Identify a non-parametric model first and then, based on that, a parametric nominal model. The first account of this approach is attributed to Bayard [17, 18, 19, 20]. It consists of the following steps:

1. Collect time-domain input-output data and transform to frequency domain via DFT.
2. Estimate a non-parametric model and its associated uncertainty description from the statistical properties of the employed FRF estimator.
3. Compute a parametric nominal model based on the FRF data.
4. Calculate an uncertainty description associated with the parametric model based on the uncertainty of the non-parametric model.

The identification procedure which will be applied in this thesis will also employ these four basic steps. However, the algorithms to implement these steps will differ from the original works by Bayard.

More specifically, in the second step, a FRF estimator is used in the original publications which is a SISO FRF estimator. MIMO plants are treated by performing several SIMO identification experiments. Moreover, the statistical estimator properties are derived for the special case of sinusoidal Schroeder phased [152] input signals only. The FRF estimator which is used in this thesis is a MISO estimator and its statistical properties are stated for arbitrary periodic input signals. This allows for the proper treatment of multi-input plants and more freedom in the choice of the excitation signal. In addition to that, it is assumed by Bayard that the measurement noise sequences on the output channels are mutually statistically independent. We will relax that assumption and show the implications on the resulting model uncertainty.

In the third step, a nonlinear optimization technique was originally proposed to fit a state space model to the FRF data via fixed-point iteration. In this thesis, the problem is formulated as a least squares problem, allowing for a one-step solution. This is especially beneficial for high order systems, as they appear in the modeling of flexible structures.

Also the fourth step is solved differently in this thesis. Bayard focuses on the maximum singular value of the model uncertainty transfer matrix, $\bar{\sigma}\{\Delta \boldsymbol{G}\}$, whereas in this thesis, the uncertainty in every transfer function is calculated. This leads to a more detailed model uncertainty description, allowing for less conservative robust stability tests, like μ-analysis. The detailed description of the proposed identification procedure can be found in the next sections.

It should finally be mentioned that it is of course also possible to replace the non-parametric intermediate model of step 2 by a linearly parametrized model, like it can be done with model error modeling. Important works in this flavor are for example [55], [96], and [97].

In order to prevent confusion with the notation of the various models and uncertainty descriptions in the following sections, Table 3.1 states in advance the declarations which will be used.

Table 3.1: Notations of models and uncertainty descriptions appearing in the experimental modeling procedure.

	true model	non-parametric (intermediate) model	parametric (final) model
model	$\boldsymbol{G}_0$	$\hat{\boldsymbol{G}}$	$\boldsymbol{G}$
uncertainty description	—	$\Delta\hat{\boldsymbol{G}}$	$\Delta\boldsymbol{G}$

3.3 Non-Parametric Identification

In this section, the identification of the non-parametric intermediate model is described. The attribute “intermediate” means that the final parametric model, which will be employed for control design, will be based on this non-parametric model. There are two major advantages to this two-step procedure:

First, the computational effort of calculating a final parametric model is reduced, because the parametric model will be based on FRF data and not on time-domain data. The amount of FRF data is usually several times smaller than the amount of underlying time-domain data, because the time-domain data set is usually formed by concatenating time-sequences from several repeated experiments. Furthermore, the amount of informative FRF data is naturally smaller by a factor of two compared to the time-domain data of a single experiment because of the symmetry of the DFT of (real valued) time-domain data sequences. The calculation of FRF data itself via FFT is computationally cheap, even for large data sets.

Second, the statistical properties of many FRF estimators are well known and can be employed to calculate the uncertainty of the non-parametric intermediate model, which is intuitive and suitable for standard robust stability tests.

A non-parametric, discrete-time MIMO LTI system model with p outputs, q inputs and sampling time T_s shall be identified from experimental data. M sets of time domain data, each of length $2N$, are collected by applying input signals[1] $\boldsymbol{u}_m(k) \in \mathbb{R}^q$ and measuring the corresponding output data $\boldsymbol{y}_m(k) \in \mathbb{R}^p$ with $k = 0, \dots, 2N-1$ and $m = 1, \dots, M$.

For the system at hand, the system inputs are the voltages applied to the piezo patches and the signal driving the electromagnetic shaker. The output channels are the force sensor output and the accelerometer signals, compare Fig. 3.1. For the uncertainty modeling of the plant used in the subsequent control design, only the four actuator voltages and the four collocated acceleration signals are required. The additional inputs and outputs, indicated by the dashed lines in Fig. 3.1, are discarded. They only serve for test and analysis purposes.

The design of the excitation signal is the most important part in the planning of identification experiments. The quality of the resulting model stands and falls with the properties of the excitation input sequence. General considerations on suitable input signal and experiment design can for example be found in [110] and [152]. Some specific remarks on the resulting model uncertainty will be later given in Sec. 3.4.

For now, only the following general assumptions on the input signals are made: The q-channel

---

[1] Note that the factor T_s will be dropped in arguments like $u(kT_\mathrm{s})$ for ease of notation.

input signal $\boldsymbol{u}_m(k)$ is either periodic or time limited. In the periodic case, an integer-multiple of periods of steady-state data is recorded. In the time-limited case, the record must not be stopped until the output signal has (approximately) decayed to zero. Consequently, the DFT spectra of the input and output signals

$$\boldsymbol{U}_m(\mathrm{j}\omega_n) = T_\mathrm{s} \sum_{k=0}^{2N-1} \boldsymbol{u}_m(k) \mathrm{e}^{-\mathrm{j}\omega_n k T_\mathrm{s}}, \tag{3.1a}$$

$$\boldsymbol{Y}_m(\mathrm{j}\omega_n) = T_\mathrm{s} \sum_{k=0}^{2N-1} \boldsymbol{y}_m(k) \mathrm{e}^{-\mathrm{j}\omega_n k T_\mathrm{s}}, \tag{3.1b}$$

are free of leakage effects, with $\omega_n = n\frac{\pi}{NT_\mathrm{s}}$, $n = 0, \dots, N-1$, and $m = 1, \dots, M$. Moreover, it is assumed that aliasing effects are prevented by proper signal conditioning.
Then, the following input-output relationship holds when output noise is present

$$\boldsymbol{Y}(\mathrm{j}\omega_n) = \boldsymbol{G}_0\left(\mathrm{e}^{\mathrm{j}\omega_n}\right) \boldsymbol{U}(\mathrm{j}\omega_n) + \boldsymbol{V}(\mathrm{j}\omega_n), \tag{3.2}$$

with $\boldsymbol{V}(\mathrm{j}\omega_n)$ being the DFT sequence of the output measurement noise $\boldsymbol{v}(k) \in \mathbb{R}^p$.
Estimates of the cross- and autopower spectra of the input and output signals can be derived from the M experiments by

$$\hat{\boldsymbol{S}}_{UU}(\mathrm{j}\omega_n) = \frac{1}{M} \sum_{m=1}^{M} \boldsymbol{U}_m(\mathrm{j}\omega_n) \boldsymbol{U}_m^\mathrm{H}(\mathrm{j}\omega_n) \tag{3.3a}$$

$$\hat{\boldsymbol{S}}_{YU}(\mathrm{j}\omega_n) = \frac{1}{M} \sum_{m=1}^{M} \boldsymbol{Y}_m(\mathrm{j}\omega_n) \boldsymbol{U}_m^\mathrm{H}(\mathrm{j}\omega_n). \tag{3.3b}$$

These estimates are known as periodograms which are known to be asymptotically unbiased [115].

The so-called H_1 estimate [187] of the FRF is then given as

$$\hat{\boldsymbol{G}}\left(\mathrm{e}^{\mathrm{j}\omega_n}\right) = \hat{\boldsymbol{S}}_{YU}(\mathrm{j}\omega_n) \hat{\boldsymbol{S}}_{UU}^{-1}(\mathrm{j}\omega_n). \tag{3.4}$$

It can be seen from the last equation that in order to extract $\hat{\boldsymbol{G}}\left(\mathrm{e}^{\mathrm{j}\omega_n}\right) \in \mathbb{R}^{p \times q}$ from data, $\hat{\boldsymbol{S}}_{UU}$ has to be regular. Therefore, at least q different experiments with linear independent input signals are needed.

With (3.4), we have a non-parametric nominal model. We now compute its confidence interval at each frequency point ω_n. The following assumptions for the noise are made: The DFT sequence $\boldsymbol{V}(\mathrm{j}\omega_n)$ satisfies

$$\mathrm{E}\{\boldsymbol{V}(\mathrm{j}\omega_n)\} = \boldsymbol{0}, \qquad \mathrm{E}\{\boldsymbol{V}(\mathrm{j}\omega_n)\boldsymbol{V}^\mathrm{T}(\mathrm{j}\omega_n)\} = \boldsymbol{0}, \qquad \mathrm{E}\{\boldsymbol{V}(\mathrm{j}\omega_n)\boldsymbol{V}^\mathrm{H}(\mathrm{j}\omega_n)\} = \boldsymbol{\sigma}_V^2(\mathrm{j}\omega_n), \tag{3.5}$$

where $\boldsymbol{\sigma}_V^2(\mathrm{j}\omega_n)$ is the covariance matrix of the DFT noise sequence. Higher order moments are zero. This amounts to $\boldsymbol{V}(\mathrm{j}\omega_n)$ being zero-mean, circular symmetric complex normally (CSCN) distributed. In addition to that, the Fourier coefficients of the noise sequence are assumed to be

independent of each other. The last assumption has the important implication that all frequency samples $\omega_0, \dots, \omega_N$ can be treated separately for statistical analysis.
It has been proven by Brillinger (see [35], Theorem 4.4.1) that the above assumptions are asymptotically satisfied for a wide class of time-domain probability density functions of the noise sequence $\boldsymbol{v}(k)$. More specifically, Theorem 14.25 in [152] states that a sufficient condition for this is that the noise $\boldsymbol{v}(k)$ is generated by passing zero-mean white noise $\boldsymbol{e}(k)$ through a stable transfer matrix, i.e. $\boldsymbol{v}(k) = \boldsymbol{G}_v \boldsymbol{e}(k)$. Considerations on a finite number of samples can be found in [164]. Furthermore, we make the common assumption that the noise is independent and identically distributed (i.i.d.) over the M different experiments and independent of the input.

If this holds, it can be shown that the H_1 estimator is unbiased and its covariance $\boldsymbol{\sigma}^2_{\hat{G}} \in \mathbb{R}^{pq \times pq}$ is given by

$$\begin{aligned} \boldsymbol{\sigma}^2_{\hat{G}}(\mathrm{j}\omega_n) &= \mathrm{E}\left\{ \mathrm{vec}\left\{ \hat{\boldsymbol{G}}\left(\mathrm{e}^{\mathrm{j}\omega_n}\right) - \mathrm{E}\left\{ \hat{\boldsymbol{G}}\left(\mathrm{e}^{\mathrm{j}\omega_n}\right)\right\}\right\} \left(\mathrm{vec}\left\{ \hat{\boldsymbol{G}}\left(\mathrm{e}^{\mathrm{j}\omega_n}\right) - \mathrm{E}\left\{ \hat{\boldsymbol{G}}\left(\mathrm{e}^{\mathrm{j}\omega_n}\right)\right\}\right\}\right)^{\mathrm{H}} \right\} \\ &= \frac{1}{M} \hat{\boldsymbol{S}}_{UU}^{-\mathrm{T}}(\mathrm{j}\omega_n) \otimes \boldsymbol{\sigma}^2_V(\mathrm{j}\omega_n), \end{aligned} \tag{3.6}$$

where $\otimes$ denotes Kronecker product, and the vec$\{\cdot\}$ operator symbolizes concatenation of matrix columns.
The true noise covariance matrix in the above equation is unknown. However, an unbiased estimate of $\boldsymbol{\sigma}^2_V$ can be used which is given in [187] as

$$\hat{\boldsymbol{\sigma}}^2_V(\mathrm{j}\omega_n) = \frac{M}{M-q} \left(\hat{\boldsymbol{S}}_{YY}(\mathrm{j}\omega_n) - \hat{\boldsymbol{S}}_{YU}(\mathrm{j}\omega_n) \hat{\boldsymbol{S}}_{UU}^{-1}(\mathrm{j}\omega_n) \hat{\boldsymbol{S}}_{UY}(\mathrm{j}\omega_n) \right), \tag{3.7}$$

where $\hat{\boldsymbol{S}}_{YY}$ and $\hat{\boldsymbol{S}}_{UY}$ can be calculated in analogy to (3.3a) and (3.3b).

In addition to being unbiased, the H_1 estimator has several more favorable properties under the given assumptions. Namely, it is:

- unbiased, i.e. $\mathrm{E}\{\hat{\boldsymbol{G}}\} = \boldsymbol{G}_0$,
- consistent in the mean square sense, i.e. $\underset{M \to \infty}{\mathrm{l.\,i.\,m.}}\, \hat{\boldsymbol{G}} = \boldsymbol{G}_0$,
- efficient, i.e. $\boldsymbol{\sigma}^2_{\hat{G}} \leq v^2_{\hat{\boldsymbol{G}}}$, where $v^2_{\hat{\boldsymbol{G}}}$ is the covariance matrix of *any* other estimator[2].
- CSCN distributed, i.e. $\hat{\boldsymbol{G}} \in \mathcal{CN}^{pq}\left(\boldsymbol{G}_0, \boldsymbol{\sigma}^2_{\hat{G}}, \boldsymbol{0}\right)$,

where the notation $\mathcal{CN}^{n_\theta}\left(\boldsymbol{E}, \boldsymbol{\Gamma}, \boldsymbol{C}\right)$ in general stands for complex normal distributions of n_θ elements with mean $\boldsymbol{E}$, covariance matrix $\boldsymbol{\Gamma}$, and relation matrix $\boldsymbol{C}$.
The properties mentioned above are well known in the literature. However, explicit proofs are

---

[2] The matrix notation $\boldsymbol{A} \geq \boldsymbol{B}$ is used to indicate that the matrix $\boldsymbol{A} - \boldsymbol{B}$ is positive semi-definite throughout this thesis.

scarce, especially for the MIMO case. The proof of unbiasedness and the derivation of the covariance expression (3.6) can for example be found in [192]. In [187], the properties of the MIMO H_1 estimator are derived by showing that it is a special case of a more generalized total least squares problem. Since the estimation of the non-parametric model $\hat{\boldsymbol{G}}$ is an integral part of the identification procedure presented in this thesis, all proofs of the listed estimator properties are derived anew in App. B.2.

The covariance matrix $\boldsymbol{\sigma}^2_{\hat{G}}(\mathrm{j}\omega_n)$ gives complete information on auto- and covariances of the estimated frequency responses of the transfer matrix $\hat{\boldsymbol{G}}(\mathrm{e}^{\mathrm{j}\omega_n})$. The variances of the individual SISO transfer functions $\hat{G}_{ij}$, $i = 1, \dots, p$, $j = 1, \dots, q$ of $\hat{\boldsymbol{G}}$ can be found on the diagonal of $\boldsymbol{\sigma}^2_{\hat{G}}$ and will be termed $\sigma^2_{\hat{G},ij}$ with

$$\sigma^2_{\hat{G},ij}(\mathrm{j}\omega_n) = \mathrm{E}\left\{\left|\hat{G}_{ij}(\mathrm{j}\omega_n) - \mathrm{E}\{\hat{G}_{ij}(\mathrm{j}\omega_n)\}\right|^2\right\}. \tag{3.8}$$

Due to the properties of the CSCN distribution [7], the respective real and imaginary parts are normally distributed with variances

$$\sigma^2_{\Re,ij}(\mathrm{j}\omega_n) = \sigma^2_{\Im,ij}(\mathrm{j}\omega_n) = \frac{1}{2}\sigma^2_{\hat{G}_{ij}}(\mathrm{j}\omega_n). \tag{3.9}$$

These variances will now be employed to construct confidence intervals for every transfer function $\hat{G}_{ij}(\mathrm{e}^{\mathrm{j}\omega_n})$ at every DFT frequency ω_n. These confidence intervals will be interpreted as additive model uncertainty descriptions for the purpose of robust control design. An additive uncertainty description for some transfer function $\hat{G}_{ij}$ states that

$$G_{0,ij}\left(\mathrm{e}^{\mathrm{j}\omega_n}\right) \in \hat{G}_{ij}\left(\mathrm{e}^{\mathrm{j}\omega_n}\right) + \Delta\hat{G}_{ij}\left(\mathrm{e}^{\mathrm{j}\omega_n}\right), \tag{3.10}$$

where the possible values of $\Delta\hat{G}_{ij}$ are bounded in some way. We choose the bounds to be

$$\Delta\hat{G}_{ij,\max}\left(\mathrm{e}^{\mathrm{j}\omega_n}\right) := \frac{1}{\sqrt{2}}n(\alpha)\sigma_{\hat{G}_{ij}}(\mathrm{j}\omega_n)(1+\mathrm{j}), \tag{3.11}$$

where $n(\alpha)$ is a real number that is determined by the desired confidence level α. The uncertain quantity $\Delta\hat{G}_{ij}$ can be any complex number where the absolute value, taken separately for the real and imaginary part, takes at most the value of the real or imaginary part of $\Delta\hat{G}_{ij,\max}$.
The greater the desired confidence level, the greater becomes the uncertainty region. For $n = 2$ for example, the real part of the true model is contained within the real part of the uncertain model with a probability of $\alpha = 95.5\,\%$ by virtue of the normal distribution. The same holds true for the imaginary part. The rationale behind equations (3.9) to (3.11) is illustrated in Fig. 3.3. At a certain frequency, the value of the (i,j)th frequency response of the non-parametric model is determined by (3.4). The uncertainties of the corresponding real and imaginary parts are derived by equations (3.6) and (3.11) which define a square box with center $\hat{G}_{ij}$. Since the real and imaginary part of one estimated transfer function are jointly normally distributed and uncorrelated [7], they are statistically independent. Thus, the probability that the true model $G_{0,ij}$ is contained within the uncertainty region of the non-parametric model, that is statement (3.10), holds with probability α^2.

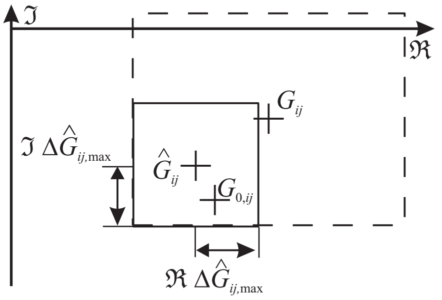

Figure 3.3: Frequency responses of different models from the jth input to the ith output in the complex plane at a certain frequency. $G_{0,ij}$: true model; $\hat{G}_{ij}$: non-parametric model; G_{ij}: parametric model. Solid square: uncertainty region of non-parametric model; dashed rectangle: uncertainty description of parametric model.

The elements $\Delta\hat{G}_{ij,\max}$ taken together define an uncertain complex matrix $\Delta\hat{\boldsymbol{G}}$ where, again, the absolute value of each entry, taken separately for the real and imaginary parts, is allowed to take at most the value defined in (3.11).

The obvious question is now the following: Given that statement (3.10) is true with the user-selected probability α^2 for every element $i = 1, \dots, p$, $j = 1, \dots, q$. Then, what is the joint probability that (3.10) is true for every element $\hat{G}_{ij}$ *simultaneously*? The answer can be given in an exact and an approximate way.

Since the estimate $\hat{\boldsymbol{G}}$ is CSCN distributed, it's probability density function is completely determined by two quantities: expected value $\mathrm{E}\{\hat{\boldsymbol{G}}\}$ and covariance matrix $\boldsymbol{\sigma}^2_{\hat{G}}$. The true values of expected value and covariance are unknown but can be replaced by their unbiased estimates which are given by equations (3.4) to (3.7). The multidimensional probability density function $p(\boldsymbol{\theta})$ of all estimated variables

$$\hat{\boldsymbol{\theta}} := \left(\Re\{\hat{G}_{11}\}, \dots, \Re\{\hat{G}_{pq}\}, \Im\{\hat{G}_{11}\}, \dots, \Im\{\hat{G}_{pq}\}\right)^{\mathrm{T}} = \left(\mathrm{vec}^{\mathrm{T}}\left\{\Re\{\hat{\boldsymbol{G}}\}\right\}, \mathrm{vec}^{\mathrm{T}}\left\{\Im\{\hat{\boldsymbol{G}}\}\right\}\right)^{\mathrm{T}}$$

is known to be [68]

$$p(\boldsymbol{\theta}) = \frac{1}{(2\pi)^{pq}\sqrt{\det\boldsymbol{\Gamma}}}\mathrm{e}^{-\frac{1}{2}\left(\boldsymbol{\theta}-\mathrm{E}\{\boldsymbol{\theta}\}\right)^{\mathrm{T}}\boldsymbol{\Gamma}^{-1}\left(\boldsymbol{\theta}-\mathrm{E}\{\boldsymbol{\theta}\}\right)} \tag{3.12}$$

with the modified, real-valued covariance matrix

$$\boldsymbol{\Gamma} = \frac{1}{2}\begin{pmatrix} \Re\{\boldsymbol{\sigma}^2_{\hat{G}}\} & -\Im\{\boldsymbol{\sigma}^2_{\hat{G}}\} \\ \Im\{\boldsymbol{\sigma}^2_{\hat{G}}\} & \Re\{\boldsymbol{\sigma}^2_{\hat{G}}\} \end{pmatrix}. \tag{3.13}$$

Once the probability density function has been determined, the joint probability could theoretically be calculated by multidimensional integration. More specifically, the joint probability α^* is

$$\alpha^* := \Pr\left(\boldsymbol{G}_0 \in \hat{\boldsymbol{G}} + \Delta\hat{\boldsymbol{G}}\right) = \int_{\boldsymbol{\theta}_{\min}}^{\boldsymbol{\theta}_{\max}} p(\boldsymbol{\theta})\,\mathrm{d}\boldsymbol{\theta}, \tag{3.14}$$

where the limits of integration are given by

$$\boldsymbol{\theta}_{\{\max,\min\}} = \left(\mathrm{vec}^{\mathrm{T}}\left\{\Re\{\hat{\boldsymbol{G}} \pm \Delta\hat{\boldsymbol{G}}_{\max}\}\right\}, \mathrm{vec}^{\mathrm{T}}\left\{\Im\{\hat{\boldsymbol{G}} \pm \Delta\hat{\boldsymbol{G}}_{\max}\}\right\}\right)^{\mathrm{T}}. \tag{3.15}$$

It must be made clear, however, that (3.14) is a $(2pq)$-dimensional integral which has to be evaluated numerically. This is often computationally infeasible.
Fortunately, it is easy to provide a lower bound on α^* by making use of Bonferroni's inequality [68]. It makes a statement on the minimum joint probability of events when the probabilities of each single event are known. It states for the case at hand that

$$\alpha^* \geq 1 - pq\left(1 - \alpha^2\right). \tag{3.16}$$

Assume, for example, a system with four inputs and four outputs using $n(\alpha) = 3$ standard deviations ($\alpha = 99.7\,\%$). One can calculate that the value of α^* is at least 90.4 %. Thus, three standard deviations provide a reasonable value of confidence for determining the model uncertainty region.

The reader is reminded that statements (3.10), (3.14), and (3.16) are valid for each frequency sample $\omega_0, \ldots, \omega_N$ separately. No information is available in between two DFT sampling frequencies. Consider an extreme case when very few sampling points are available such that the continuous frequency response cannot be sufficiently approximated by interpolation. Then, the estimate $\hat{\boldsymbol{G}}\left(\mathrm{e}^{\mathrm{j}\omega_n}\right)$ is practically useless, even if the confidence level of each sampling point is high. For that reason, a sufficient number of DFT points must be provided. The number of sufficient points clearly depends on the smoothness of the plant's frequency response in the considered frequency range.
It is hard to quantify the number of sufficient frequency samples, mainly because of the following dilemma: Mathematically, any two estimates $\hat{\boldsymbol{G}}\left(\mathrm{e}^{\mathrm{j}\omega_1}\right)$ and $\hat{\boldsymbol{G}}\left(\mathrm{e}^{\mathrm{j}\omega_2}\right)$ at different frequencies ω_1 and ω_2 are asymptotically statistically independent, because this is an important DFT property (see also the assumptions on the noise). Thus, theoretically, the probability that the true frequency response is contained within $\hat{\boldsymbol{G}}\left(\mathrm{e}^{\mathrm{j}\omega_n}\right) + \Delta\hat{\boldsymbol{G}}\left(\mathrm{e}^{\mathrm{j}\omega_n}\right)$ at all $N+1$ frequency samples *simultaneously* is simply $(\alpha^*)^{N+1}$. This quantity tends towards zero very fast, indicating that the more DFT points are used, the less trustworthy the FRF estimate becomes. This is clearly a contradiction to engineering intuition: One might expect that the more DFT points are available, the better the overall information should be. The solution to this contradiction is that no information on the smoothness of the FRF of the plant is used by the estimation algorithm (3.4). Thus, anything could happen to the continuous FRF in between sampling points, leading to an overall confidence level of zero. On the contrary, the FRF of every LTI system is known to be a continuous function, apart from singularities on the imaginary axis. Hence, if infinitely many DFT samples were available, the continuous FRF could be reconstructed to arbitrary precision.

One possible approach to incorporate knowledge of FRF smoothness in the estimation procedure is to assume that the plant which is to be identified has a certain degree of stability which can be quantified by the decay rate of its impulse response: $|g(k)| \leq M\rho^{-k}$. If parameters M and ρ are known, it can be shown that the derivative of $G(\mathrm{e}^{\mathrm{j}\omega})$ on the unit disk can be uniformly bounded from above by

$$\left|\frac{\mathrm{d}G(\mathrm{e}^{\mathrm{j}\omega})}{\mathrm{d}\omega}\right| \leq \frac{T_{\mathrm{s}}M\rho}{(1-\rho^2)}. \tag{3.17}$$

This bound is derived by Bayard in [17] and employed to compute a *continuous* uncertainty description with prescribed confidence level for the whole frequency range. However, the same au-

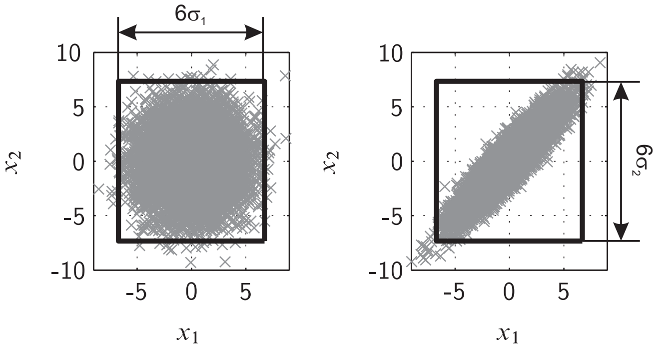

Figure 3.4: Two zero-mean normally distributed, real-valued random variables.
Left: $\boldsymbol{\sigma}^2$=[5 0; 0 6]; right: $\boldsymbol{\sigma}^2$=[5 5; 5 6].

thor states in a later publication [20] that this approach leads to overly conservative results, and instead advocates for "engineering intuition" in choosing a sufficiently dense frequency grid. Similar observations are stated by another author in [55].
On top of that, it is advantageous to have as many frequency sampling points as can be tolerated under the given experimental conditions, because important properties of the estimator are only asymptotically (in data length) satisfied. Thus, a dense frequency grid will be used throughout this thesis.

In the construction of the additive frequency-wise uncertainty description (3.11), only the variances of $\hat{\boldsymbol{G}}$, i.e. the diagonal elements of $\boldsymbol{\sigma}^2_{\hat{G}}$, have been taken into account. This may lead to an uncertainty region that is unnecessary large if the contribution of the covariance information is significant. This is illustrated for the case of two correlated real-valued quantities in Fig. 3.4. In order to reduce conservatism of the uncertainty description, it is desirable to reduce the off-diagonal entries of the covariance matrix (3.6) and thus make $\boldsymbol{\sigma}^2_{\hat{G}}$ diagonal in the ideal case. This is achieved when both $\boldsymbol{S}_{UU}$ and $\boldsymbol{\sigma}^2_V$ are diagonal. Diagonality of $\boldsymbol{\sigma}^2_V$ implies that the measurement noise on the p measurement channels is uncorrelated. This may or may not be the case, depending on the measurement equipment. Nevertheless, $\boldsymbol{\sigma}^2_{\hat{G}}$ will at least have block-diagonal structure if $\boldsymbol{S}_{UU}$ is diagonal. This can be achieved by proper design of the input signals and will be further specified in the next section.
Alternatively, if covariance information is significant and cannot be reduced, a way to calculate the model uncertainty region by taking into account the complete information contained in $\boldsymbol{\sigma}^2_{\hat{G}}$ is treated in App. B.3.

3.4 Input Signal Design

The design of input signals which are used to excite the system that is to be identified has a major impact on the identification process and the quality of the resulting model. Input signals may be evaluated and optimized by various criteria, most importantly:

1. the duration of the excitation and therefore the overall time to collect the measurement data,

2. the peak value which is important to obey actuator and sensor limits and ensure linear system behavior,
3. the waveforms and frequency content which are required to be generated by the given signal generator equipment,
4. the implications on the quality of the resulting model.

The first aspect can be easily exemplified for linear systems: Exciting a system with simple harmonic signals, one at time, can give the same information as exciting the system with all frequencies of interest simultaneously. However, the overall measurement time and the algorithms to manipulate the data may differ significantly. Thus, to save measurement time, a broadband signal which covers the complete considered frequency range of the system should be employed. For the system at hand, this means spanning a range from 10 Hz to 500 Hz. Frequencies below 10 Hz are not amenable for identification, since very low frequencies can neither be excited by the elastically mounted shaker nor measured with piezoelectric accelerometers. Frequencies above 500 Hz should not be excited by the input signal to avoid excitation of modes outside the considered bandwidth, because that could deteriorate the quality of the finite-dimensional model.

The second aspect always plays an important role in input signal design. In the present problem, the identification of the smart panel, the maximum peak voltage which could be applied to the piezo actuators, according their specifications, is $+500\,\mathrm{V}$. Negative voltages, i.e. against direction of polarization, can only be tolerated up to about $-150\,\mathrm{V}$ without premature wear of the piezoelectric material [176]. Since symmetric operation around a stationary point is desired, one could, for example, have an input signal oscillating with an amplitude of 250 V around a constant value of $+250\,\mathrm{V}$. This type of excitation causes two problems: Firstly, the DC voltage pre-stresses the plate which may alter its behavior compared to its unforced state. Secondly, the large amplitude would result in nonlinear system behavior due to the piezoelectric hysteresis.

On top of that, exciting a piezo patch with an amplitude of 250 V at 500 Hz requires a mean apparent output power of the piezo amplifier of 13 W per channel[3]. This is already at the limit of most medium-range piezo amplifiers. Thus, in order to prevent nonlinear actuator behavior and pre-stressing of the plate, a zero-mean excitation signal with an amplitude of 30 V was found to be sufficient for identification.

The last and most important aspect of input signal design is the impact on the resulting model quality. Model quality can be quantified in terms of model confidence. The confidence in the identified model is high if the uncertainty of the model parameters is low. Thus, the influence of the DFT input sequence $\boldsymbol{U}(\mathrm{j}\omega_n) \in \mathbb{C}^q$ on the covariance matrix of model parameters $\boldsymbol{\sigma}^2_{\hat{G}}$ provides vital information on important properties of input signals. First of all, the relationship (3.6),

$$\boldsymbol{\sigma}^2_{\hat{G}}(\mathrm{j}\omega_n) = \frac{1}{M}\hat{\boldsymbol{S}}^{-\mathrm{T}}_{UU}(\mathrm{j}\omega_n) \otimes \boldsymbol{\sigma}^2_V(\mathrm{j}\omega_n),$$

---

[3] The capacity of a piezo patch can be approximated by 130 nF in large signal operation.

shows that the autopower spectrum of the input signal must be invertible at all frequencies which requires $\hat{\boldsymbol{S}}_{UU} = \frac{1}{M}\sum_{m=1}^{M} \boldsymbol{U}_m \boldsymbol{U}_m^{\mathrm{H}} \in \mathbb{C}^{q\times q}$ to be of full rank. This is equivalent to saying that the number of experiments M must not be less that the number of inputs q, and that $\operatorname{span}\{\boldsymbol{U}_1, ..., \boldsymbol{U}_M\} = \mathbb{C}^q$. This minimum requirement is known as the concept of *persistent excitation* in the literature on system identification, see for example [110].

On top of that, it is evident that the model uncertainty is inversely proportional to the input power which means that "small" model uncertainty requires "large" input power. The size of the matrix $\boldsymbol{\sigma}^2_{\hat{G}}$ can for example be measured by the value of its determinant. Since

$$\det \boldsymbol{\sigma}^2_{\hat{G}} = \frac{1}{M^{pq}} \left(\det \hat{\boldsymbol{S}}_{UU}^{-\mathrm{T}}\right)^p \left(\det \boldsymbol{\sigma}_V^2\right)^q = \frac{1}{M^{pq}} \frac{\left(\det \boldsymbol{\sigma}_V^2\right)^q}{\left(\det \hat{\boldsymbol{S}}_{UU}\right)^p}, \tag{3.18}$$

minimization of the determinant of $\boldsymbol{\sigma}^2_{\hat{G}}$ means maximizing the determinant of $\hat{\boldsymbol{S}}_{UU}$.

Since the H_1 estimator is efficient, its covariance matrix equals the inverse of the Fisher information matrix $\boldsymbol{Fi}$. Minimization of $\det \boldsymbol{\sigma}^2_{\hat{G}}$ therefore equals maximizing $\det \boldsymbol{Fi}$, which is known as *D-optimal* design in the field of design of experiments (DoE) [8].

Now, suppose that a single-channel, broadband excitation signal $u(k)$ with desirable peak values and waveform has been selected. The sequence $u(k)$ shall contain $2N$ samples in order to produce $N+1$ informative DFT samples, as before. We further assume that q experiments are carried out, which is the minimum number of experiments to determine a model, and that $u(k)$ is used to excite the system inputs in a certain pattern. Then, the overall input sequence $\boldsymbol{u}_{\mathrm{tot}} \in \mathbb{R}^{2Nq\times q}$ for the complete measurement can be written as

$$\boldsymbol{u}_{\mathrm{tot}} = \left(\begin{array}{ccc} u_1^1(0) & \dots & u_q^1(0) \\ \vdots & & \vdots \\ u_1^1(2N-1) & \dots & u_q^1(2N-1) \\ \hline \vdots & & \vdots \\ \hline u_1^q(0) & \dots & u_q^q(0) \\ \vdots & & \vdots \\ u_1^q(2N-1) & \dots & u_q^q(2N-1) \end{array}\right) = \boldsymbol{\Gamma}_q \otimes \begin{pmatrix} u(0) \\ \vdots \\ u(2N-1) \end{pmatrix}, \tag{3.19}$$

where $u_i^j(k)$ represents the kth input sample on the ith channel for the jth experiment. The $(q \times q)$-dimensional matrix $\boldsymbol{\Gamma}_q$ contains only elements drawn from the set $\{-1, 0, 1\}$. If the input channels are excited one after another in q SIMO experiments, then $\boldsymbol{\Gamma}_q$ equals the identity matrix. However, it is intuitively clear that exciting all system inputs simultaneously can give a higher value of input power than exciting each input sequentially. It is argued in [89] that $\det \hat{\boldsymbol{S}}_{UU}$ is maximized when $\boldsymbol{\Gamma}_q$ equals a Hadamard matrix, i.e. a symmetric matrix containing only entries -1 and 1 with orthogonal rows. A Hadamard matrix is only existent for $q = 2$ or modulo $(q, 4) = 0$. If the number of system inputs does not satisfy these conditions, then the qth principal minor of the Hadamard matrix of next possible size may be used to obtain a near optimal excitation pattern. For the identification of the smart panel, there are five inputs: four voltages driving the piezo amplifier and one for driving the amplifier of the shaker. Thus, $\boldsymbol{\Gamma}_q$ is chosen to be equal to the first five rows

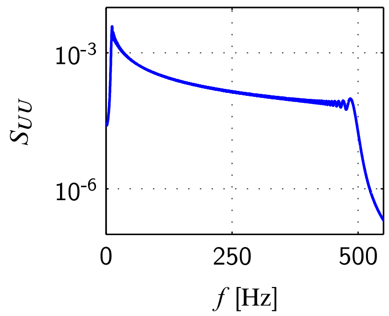

Figure 3.5: Autopower spectrum of the swept sine input sequence.

and columns of a Hadamard matrix of dimension eight,

$$\boldsymbol{\Gamma}_q = \begin{pmatrix} 1 & 1 & 1 & 1 & 1 \\ 1 & -1 & 1 & -1 & 1 \\ 1 & 1 & -1 & -1 & 1 \\ 1 & -1 & -1 & 1 & 1 \\ 1 & 1 & 1 & 1 & -1 \end{pmatrix}. \tag{3.20}$$

This implies that the mutual angle between two arbitrary columns equals 78°, except for the first and last column which span only an angle of 53°.

For the input sequence $u(k)$, there are numerous possibilities and the best choice depends on the actual system to be identified and the measurement equipment. The most popular general purpose signals are swept sine, Schroeder-phased multisine, pseudo-random binary signal (PRBS), and random noise [152]. In the area of structural dynamics, pulse-impact testing is also very common. For the smart panel, it is important to have an excitation signal whose bandwidth can be easily and accurately specified to lie in between the desired values. For that reason, only swept sine and Schroeder multisine are suitable from the above listed signals. A logarithmically swept sine is selected with a continuous frequency spectrum from $f_0 = 10\,\text{Hz}$ to $f_1 = 500\,\text{Hz}$ and a duration of $t_1 = 6\,\text{s}$,

$$u(k) = \hat{u} \cdot \sin\left(2\pi f_0 \left(\frac{f_1}{f_0}\right)^{\frac{kT_s}{t_1}} k\right), \quad k = 0, \ldots, \frac{t_1}{T_s}, \tag{3.21}$$

with $\hat{u}$ being the amplitude of the swept sine. For excitation with piezoelectric patches, $\hat{u}$ is chosen in such a way that 30 to 40 V are applied to the patches. For shaker excitation, the amplitude is selected to excite the plate with a force of approximately 1 N.

An extra time of 0.5 s is added to the swept sine in order to wait for the sensor signals to die out. The logarithmic acceleration increases the signal power in the low frequency range where the signal-to-noise ratio (SNR) is typically low when employing piezoelectric sensors, see Fig.3.5.

The topic of optimal input design for the identification of multi-input systems has been further investigated by Gevers et. al. [82] who show that MIMO experiments improve identification results significantly almost always, and are never less informative than SIMO experiments.

Currently, research in that field is concerned with the question of how to optimally design excitation signals when some maximum level of allowed model uncertainty is given. Works dealing with that problem are for example [79] and [105].

3.5 Parametric Identification

So far, by applying carefully designed excitation signals, high quality, non-parametric frequency-domain models (3.4) and corresponding uncertainty descriptions (3.11) can be identified. It was further shown that describing model uncertainty by additive perturbation turns out to be quite natural when the uncertainty description is gathered from (co-)variance information. The model uncertainty can be interpreted as a square box for every transfer function at every single frequency, compare Fig. 3.3.

A parametric model is required for model-based control design. There are many algorithms available that compute parametric models from time- or frequency-domain data. An overview of parametric modeling methods can be found in the books [110], [113], and [123]. However, the problem at hand poses some special requirements on the identification algorithm, namely:

- It should be able to deal with high-order systems,
- allow for weighted optimization,
- handle MIMO model structures,
- make use of available FRF data.

The first point is essential, since the system at hand is infinite-dimensional and will have to be approximated by a high-order finite-dimensional model. Although most parametric identification algorithms can, in theory, handle models of arbitrary order, it is well known that many algorithms suffer from numerical difficulties and/or excessive computation times when the model order increases. See for example [39] for a showcase of this issue.
The second aspect is closely related to the first one: Since the model can at most capture the behavior of the real system in a limited frequency range, it is natural that certain frequency ranges are more important than others. Thus, the modeling procedure should provide the possibility for frequency weighting of the model mismatch.
The third aspect applies to non-parametric as well as parametric identification: There is a difference between the following two procedures:

1. Identify all elements of a transfer matrix by performing SISO experiments and then building the transfer matrix by concatenation of the individual elements.
2. Identify the transfer matrix row- or column-wise by performing MISO or SIMO experiments, respectively, or even entirely by MIMO experiments.

These procedures are only theoretically equivalent in the noise free case. In practice however, there may be large differences in the results because of the following reasons:

1. No model matches real input-output data perfectly. The model is a result of an optimization problem. The optimality criterion which is minimized is different for SISO, MISO, SIMO, or MIMO experiments.
   Especially for SISO experiments, it is a common phenomenon [168] that the system poles can be identified very well, but eigenvectors and zeros are usually of low quality. This is because eigenvectors and multivariable zeros are determined by the interactions of the elements of the transfer matrix which are poorly captured by SISO experiments.
2. It has already been pointed out in the last section that model uncertainty decreases with increasing power of the excitation signal. This clearly speaks in favor of performing multi-input experiments whenever possible.

The last point in the list of algorithm requirements is important for economic as well as aesthetic reasons. Since FRF data has already been computed from time-domain measurements to compute the non-parametric model, it is natural to reuse this data as input for the parametric modeling procedure as well. Computing the parametric model from time series would introduce an unnecessary step back in the modeling workflow. In addition to that, the amount of FRF data is generally smaller than the underlying time data. This is beneficial in terms of computational cost.

In this thesis, the *Frequency-Domain Eigensystem Realization Algorithm* (FD-ERA), which has been developed by Juang and coworkers [113], is used. The algorithm consists of three major steps:

1. Take the FRF data (3.4) as input and fit a left matrix fraction description (LMFD)[4] $\boldsymbol{G}(z) = \boldsymbol{M}^{-1}(z)\boldsymbol{N}(z)$ via weighted least-squares optimization.
2. Compute the system's Markov parameters $\boldsymbol{g}(k)$ from $\boldsymbol{M}(z)$ and $\boldsymbol{N}(z)$.
3. Compute a state space model of desired order from the Markov parameters by employing the Eigensystem Realization Algorithm or one of its variants.

The FD-ERA algorithm is a MISO algorithm, i.e. it identifies the transfer matrix $\boldsymbol{G}(z)$ row-wise. Thus, processing MIMO and MISO data gives identical results. This also holds true for the non-parametric model, since the H_1 estimator (3.4) can be stated as

$$\hat{\boldsymbol{G}}^{(i,:)}(\mathrm{e}^{\mathrm{j}\omega_n}) = \hat{\boldsymbol{S}}_{YU}^{(i,:)}(\mathrm{j}\omega_n)\hat{\boldsymbol{S}}_{UU}^{-1}(\mathrm{j}\omega_n), \quad i = 1, \ldots, p. \tag{3.22}$$

Thus, the complete identification procedure is a MISO algorithm.

---

[4] This model structure is also known as ARX model.

The outcome of the parametric modeling step is a discrete-time state space model of the form

$$\begin{aligned}
\boldsymbol{x}(k+1) &= \boldsymbol{A}\boldsymbol{x}(k) &&+\boldsymbol{B}\boldsymbol{u}(k) &&+\boldsymbol{E}\boldsymbol{d}(k)\\
\boldsymbol{y}(k) &= \boldsymbol{C}\boldsymbol{x}(k) &&+\boldsymbol{D}\boldsymbol{u}(k) &&+\boldsymbol{F}\boldsymbol{d}(k)\\
\tilde{\boldsymbol{y}}(k) &= \tilde{\boldsymbol{C}}\boldsymbol{x}(k) &&+\tilde{\boldsymbol{D}}\boldsymbol{u}(k) &&+\tilde{\boldsymbol{F}}\boldsymbol{d}(k)
\end{aligned} \tag{3.23}$$

of order n. The algorithm ensures that (3.23) is a minimal realization[5]. This state space system may be compactly represented in terms of its transfer matrix as

$$\boldsymbol{G}(z) = \left[\begin{array}{c|cc} \boldsymbol{A} & \boldsymbol{B} & \boldsymbol{E} \\ \hline \boldsymbol{C} & \boldsymbol{D} & \boldsymbol{F} \\ \tilde{\boldsymbol{C}} & \tilde{\boldsymbol{D}} & \tilde{\boldsymbol{F}} \end{array}\right]. \tag{3.24}$$

In the above system, $\boldsymbol{u}(k) \in \mathbb{R}^{n_\mathrm{P}}$ is the vector of voltages at the output of the D/A converter driving the piezo amplifier. The vector $\boldsymbol{d}(k) \in \mathbb{R}^{n_\mathrm{forces}}$ collects the actual disturbance point forces acting on the plate, i.e. those measured by the force sensors. In the experimental setup described in Sec. 3.1, we have $n_\mathrm{P} = 4$ and $n_\mathrm{forces} = 1$. The outputs $\boldsymbol{y}(k) \in \mathbb{R}^{n_\mathrm{sensors}}$ are the sensor signals which are used within the control loop. These are the outputs of the four accelerometers located next to the actuator patches. There is one additional accelerometer collocated to the disturbance force and its output appears as $\tilde{\boldsymbol{y}}(k)$. With the collocated measurement of disturbance force and acceleration, the mechanical admittance at this point can be determined.

The disturbance input $\boldsymbol{d}(k)$ is a sampled version of the low-pass filtered continuous output of the force sensor, see Fig. 3.1. As such, it does not satisfy the property of being piecewise constant, as it is implicitly assumed in a discrete-time model. Thus, the model of the transfer paths from $\boldsymbol{d}$ to $\boldsymbol{y}$ and $\tilde{\boldsymbol{y}}$ comes with systematic errors. These errors imply that the identified discrete-time transfer functions do not match their continuous-time counterparts after zero-order-hold discretization. In addition to that, the identified discrete-time model does depend on the transfer functions of the low-pass filters and the shaker amplifier, which is clearly not the case for the true transfer behavior of the disturbance input. For more technical details, one may consult [152].
However, as also pointed out in [152], this systematic identification error is usually small and decreases with increasing sampling frequency. More importantly, the disturbance transfer path of the model is not utilized in control design but only used for simulation purposes. As such, this conceptual weakness is not significant.

Once a parametric model of the system to be controlled is available, an uncertainty description $\Delta\boldsymbol{G}(\mathrm{e}^{\mathrm{j}\omega_n})$ of the FRF of $\boldsymbol{G}(z)$ may be computed. This uncertainty description must incorporate $\Delta\hat{\boldsymbol{G}}(\mathrm{e}^{\mathrm{j}\omega_n})$ and also account for the differences between the non-parametric model $\hat{\boldsymbol{G}}(z)$ and the parametric model $\boldsymbol{G}(z)$. These differences are inevitable in practice, because extremely high model orders would have to be used to perfectly fit the FRF data. More importantly, moderate model orders are desired to alleviate numerical difficulties in the subsequent computation of the controller. Usually, the limitation of the model order leads to negligence of high frequency dynamics, because the limited set of model parameters is used to fit the FRF data as well as possible

---

[5] Alternatively, one may directly compose a canonical state space model from the LMFD which is not necessarily minimal, see [113] for details.

in the desired control loop bandwidth. The model will therefore be fairly inaccurate above the control loop bandwidth which increases the danger of spillover effects.

An intuitive idea for computing $\Delta \boldsymbol{G}$ is to incorporate the differences of the non-parametric and the parametric model by extending the uncertainty region (3.11) by the amount of the model mismatch,

$$\Delta G_{ij,\max} := \left(\left|\Re\left\{G_{ij} - \hat{G}_{ij}\right\}\right| + \Re\left\{\Delta\hat{G}_{ij,\max}\right\}\right) + \mathrm{j}\left(\left|\Im\left\{G_{ij} - \hat{G}_{ij}\right\}\right| + \Im\left\{\Delta\hat{G}_{ij,\max}\right\}\right), \tag{3.25}$$

for all transfer functions $i = 1, \ldots, p$, $j = 1, \ldots, q$, and all frequencies $\omega_n = 0, \ldots, \frac{(N-1)\pi}{NT_\mathrm{s}}$. This is also illustrated by the dashed box in Fig. 3.3. As a consequence, the uncertainty of one element $G_{ij}(\mathrm{e}^{\mathrm{j}\omega_n})$ can be interpreted as a rectangular box which touches the uncertainty region of $\hat{G}_{ij}(\mathrm{e}^{\mathrm{j}\omega_n})$ at two of its boundaries. All elements of (3.25) taken together define the additive uncertainty description $\Delta\boldsymbol{G}_{\max}(\mathrm{e}^{\mathrm{j}\omega_n})$ of the parametric model. Thus, there exists some $\Delta\boldsymbol{G}\left(\mathrm{e}^{\mathrm{j}\omega_n}\right)$ such that

$$\boldsymbol{G}_0\left(\mathrm{e}^{\mathrm{j}\omega_n}\right) = \boldsymbol{G}\left(\mathrm{e}^{\mathrm{j}\omega_n}\right) + \Delta\boldsymbol{G}\left(\mathrm{e}^{\mathrm{j}\omega_n}\right), \tag{3.26}$$

where the values of the uncertain matrix $\Delta\boldsymbol{G}$ are bounded by $\Delta\boldsymbol{G}_{\max}$. The probability of the last equation to hold is greater than α^* at each frequency sample ω_n.

The last two equations define an additive uncertainty description for the parametric model $\boldsymbol{G}$ which overbounds the uncertainty of the non-parametric model. Every overbounding procedure necessarily introduces conservatism in the model uncertainty description. The additive uncertainty formulation turned out to be quite natural for the non-parametric model $\Delta\hat{\boldsymbol{G}}$, because its uncertainty was derived from parameter (co-)variance information. However, it must be questioned if an additive uncertainty formulation is also a good choice for the parametric model. Even if the answer was positive, it is not sure that the additive uncertainty given by (3.25) is optimal.

However, this question is not at the focus of this thesis, because an uncertainty description for the parametric model is actually not necessary for robustness analysis which can be explained as follows: Suppose, some controller $\boldsymbol{K}$ is given and the closed loop shall be tested for robust stability. Then, it is sufficient to perform this test for the loop given by the controller $\boldsymbol{K}$ and the uncertain non-parametric model, $\hat{\boldsymbol{G}} + \Delta\hat{\boldsymbol{G}}$. The parametric model $\boldsymbol{G}$ might be required to actually calculate the controller beforehand, but its uncertainty description is not required for *a posteriori* robustness analysis. Things are different if one wants to do robust synthesis, i.e. design a controller which is known *a priori* to robustly stabilize the plant. Then, a parametric model together with its uncertainty description must be known. Robust controller synthesis can for example be done by μ-synthesis via DK-iteration [168]. However, this significantly increases computational complexity, especially for high-order systems. Since it is easy to calculate a robustly stabilizing controller with the design scheme presented in Ch. 4, robust synthesis shall not be an issue here. Nevertheless, some remarks on uncertainty overbounding are given in App. B.4.

3.6 Examples

This section gives some examples to illustrate the identification procedure described in Secs. 3.3 to 3.5. First, simulation results are given which are derived by employing the identification procedure to the theoretical plate model of Ch. 2. Then, experimental results from the smart plate testbed are shown.

3.6.1 Simulation Results

The theoretical plate model with the actuator and sensor placement shown in Fig. 3.1 is simulated. For reference, the inputs and outputs of the system shall be enumerated according to (3.24). The model contains all 17 plate modes in the frequency range up to 500 Hz. The identification procedure is geared towards discrete-time systems. For that reason, the model is discretized using the zero-order hold technique with a sampling time equal to that of the real testbed, $T_\mathrm{s} = 0.6\,\mathrm{ms}$. To simulate the real identification experiment, continuous-time low-pass filters are added at the system inputs and outputs before discretization. The filters are sixth-order Cauer filters which closely resemble those of the real testbed.

The four piezoelectric patches are excited with the swept sine signal (3.21) with an amplitude of 40 V. For force excitation, the amplitude $\hat{u}$ is chosen to be 1 N. The five sensor signals give the accelerations near the patches and at the location of the point force.

The influence of certain aspects of experiment design on the identification result shall be illustrated. The quality of the non-parametric identification is represented by the covariance matrix $\boldsymbol{\sigma}^2_{\hat{G}}$. However, the entries of this matrix cannot be intuitively assessed. To this end, it is more insightful to look at the estimated FRFs $\hat{G}_{ij}$ in the bode diagram together with the confidence bounds on magnitude and/or phase. The variances of $|\hat{G}_{ij}|$ and $\angle\hat{G}_{ij}$ can be approximately calculated from the variance of the complex number $\hat{G}_{ij}$ by error propagation, see App. B.5.

Influence of Measurement Noise Strength

For this simulation, $M = 10$ SIMO experiments are performed, i.e. each of the five inputs is excited twice, but only one at a time. Normally distributed random numbers are added to the output signals to simulate measurement noise. The noise is white and independent over the different measurement channels. Figure 3.6 shows the output of the accelerometer which is collocated to the point force when excited by the force. Two different magnitudes of the noise are simulated. The magnitude of the corresponding estimated FRF together with a $3\,\sigma$ confidence bound is shown in Fig. 3.7.

For the case of low noise amplitude, a very good estimation of the FRF is possible that almost coincides with the true FRF. Regions of model uncertainty appear only below 10 Hz and above 500 Hz where the input power is low, compare Fig. 3.5. In case of large noise, the quality of the estimated FRF is low and the model uncertainty is high, except for the resonance peaks where the SNR is high.

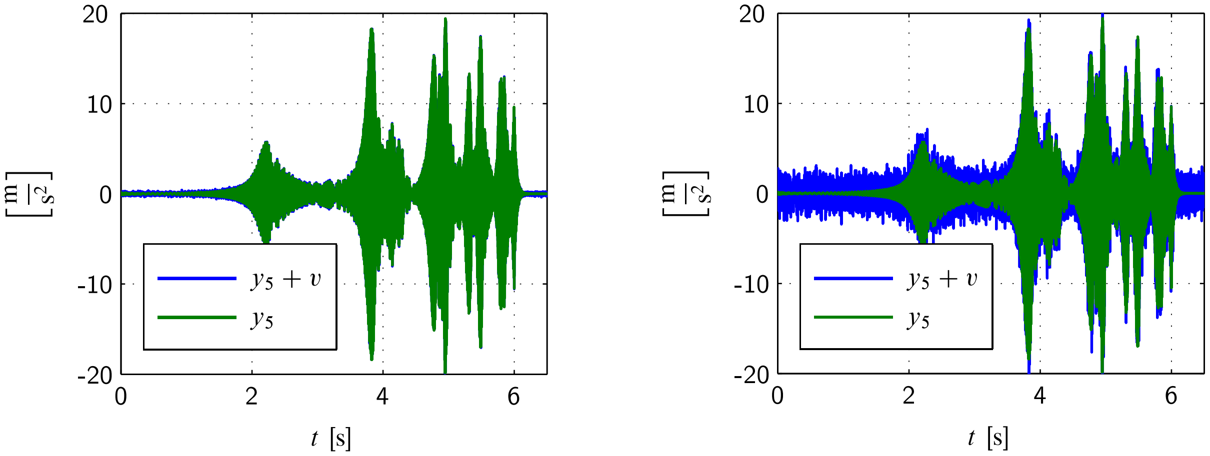

Figure 3.6: Acceleration at the location where the point force excites the structure. Left: $\sigma_v^2 = 0.01\,{}^{m}/_{s^2}$; Right: $\sigma_v^2 = 1\,{}^{m}/_{s^2}$.

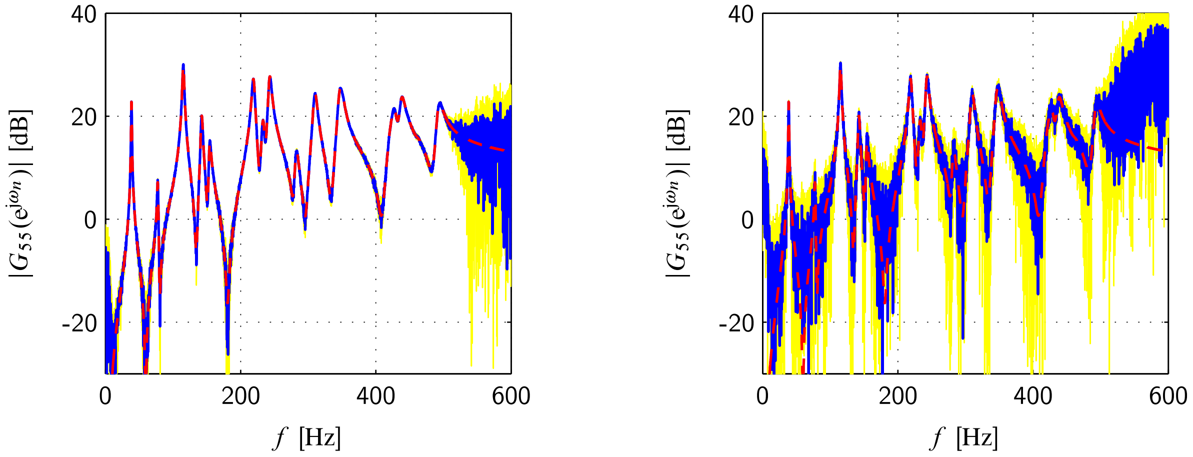

Figure 3.7: Modulus of frequency response from point force to collocated acceleration together with $3\,\sigma$ confidence bound (shaded area). Left: $\sigma_v^2 = 0.01\,{}^{m}/_{s^2}$; Right: $\sigma_v^2 = 1\,{}^{m}/_{s^2}$. Dashed line: Frequency response of true system $G_{0,55}(e^{j\omega_n})$.

In any case, it can be observed at frequencies well above 500 Hz that the true model will lie outside the confidence interval. This is because (3.6) can give reliable results only in those frequency ranges where the input power is significantly different from zero. Outside the frequency range of the swept sine input, the inversion of the input power matrix $\hat{\boldsymbol{S}}_{UU}$ does not lead to trustworthy estimates of $\boldsymbol{\sigma}_{\hat{G}}^2$.

Influence of Measurement Noise Characteristics

In the last paragraph, white noise was added to the simulated measurements. White noise actually represents the "ideal" noise for the H_1 estimator, because the time sequence $v(k)$ is perfectly uncorrelated. Thus, it can be easily shown that the DFT sequence $V(j\omega_n)$ is also uncorrelated, see App. B.6. This is one of the major assumptions on which the analysis of the estimator characteris-

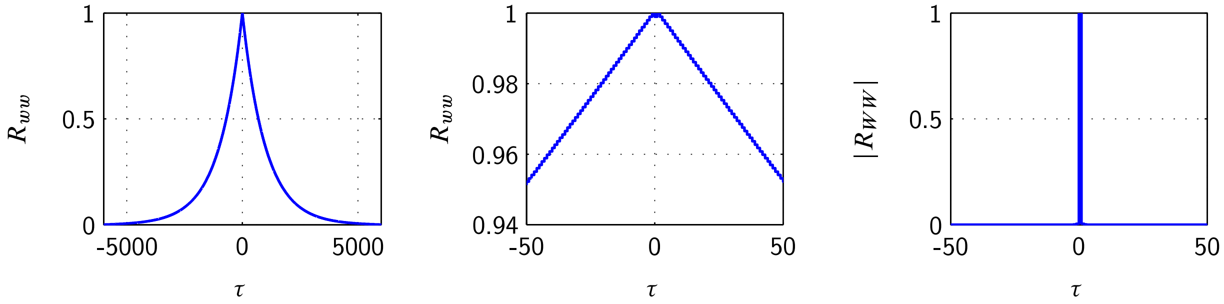

Figure 3.8: Left: Normalized autocorrelation sequence of $w(k)$, full scale; Middle: Normalized autocorrelation sequence of $w(k)$, zoomed; Right: Normalized modulus of the autocorrelation sequence of $W(\mathrm{j}\omega_n)$.

tics is built, see Sec. 3.3. With this property, it is possible to do the statistical calculations for each frequency sample ω_n separately.

As also mentioned in Sec. 3.3, uncorrelatedness of the DFT noise sequence is asymptotically satisfied for all noise sequences that can be represented as passing white noise through a stable transfer function. To this end, red noise is considered as an illustrative example of a "non-ideal" noise. As stated in App. B.6, the autocorrelation function $R_{ww}(\tau)$ of red noise is given by

$$R_{ww}(\tau) = \sigma_v^2 \, \sigma(\tau - 1) * \sigma(-\tau + 1), \tag{3.27}$$

where $\sigma(\tau)$ is the step function and the $*$ operator denotes convolution. The function $\sigma(\tau - 1)$ represents the impulse response of a discrete-time integrator $H(z) = \frac{T_\mathrm{s}}{z-1}$. Since this transfer function is not stable, its impulse response does not decay and therefore, the autocorrelation sequence R_{ww} is unbounded for all τ. For that reason, a stabilized version of the transfer function, $H(z) = \frac{T_\mathrm{s}}{(1+\epsilon)z-1}$ with $\epsilon = 1 \cdot 10^{-3}$, is used in the following. Its impulse response decays after approximately 5000 samples. Figure 3.8 shows the autocorrelation sequence of red noise which was produced by passing white noise through the modified transfer function. It can be seen that the time sequence $w(k)$ is correlated over a time sequence that equals the duration of the impulse response of $H(z)$. By contrast, the DFT sequence $W(\mathrm{j}\omega_n)$ is almost perfectly uncorrelated. To produce the right figure, the relationship (B.76) was used with $N = 100$ time samples of $w(k)$. This exemplifies the decorrelation property of the discrete Fourier transform.

Influence of Excitation Pattern and Number of Experiments

The minimum number of experiments to successfully identify a MIMO system equals the number of system inputs q. It was already argued in Sec. 3.4 that the following two guidelines generally apply to input signal design:

- Excite all q system inputs simultaneously if possible.
- Maximize the degree of linear independence of the input sequences over q identification experiments.

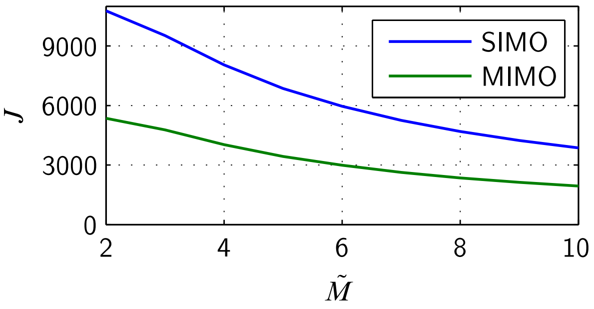

Figure 3.9: Sum of variances over all transfer functions and frequencies in the range from 10 Hz to 500 Hz.

As an example, consider the case of q SIMO experiments. In every experiment, one input is excited with a suitable input sequence $\boldsymbol{u}(k) \in \mathbb{R}^{2N}$. The other inputs are zero. Then, the input sequences of all q experiments can be compactly written as

$$\boldsymbol{u}^i(k) = \boldsymbol{e}_i \otimes \boldsymbol{u}(k), \quad i = 1, \dots, q, \tag{3.28}$$

with $\boldsymbol{e}_i$ being the ith column of the identity matrix of dimension q. Then, the input sequences of the different experiments are orthogonal to each other,

$$\langle \boldsymbol{u}^i(k), \boldsymbol{u}^j(k) \rangle = 0, \quad \text{for } i \neq j. \tag{3.29}$$

For MIMO experiments, the columns of a Hadamard matrix may be used instead of unit vectors,

$$\boldsymbol{u}^i(k) = \boldsymbol{\Gamma}_q^{(:,i)} \otimes \boldsymbol{u}(k), \quad i = 1, \dots, q. \tag{3.30}$$

This does not lead to orthogonal input sequences, unless a Hadamard matrix of dimension q exists. In the present case with five inputs, there does not exist a Hadamard matrix of that dimension and therefore, the input sequences are not orthogonal, as already pointed out in Sec. 3.4. However, it can be expected that this drawback it outweighed by the fact that all inputs are excited simultaneously and thus, more energy is transferred into the system. This is indeed the case, as illustrated in Fig. 3.9. There, the following criterion is plotted over the number of experiments $\tilde{M} = {}^{M}\!/_{q}$,

$$J = \sum_{i=1}^{p} \sum_{j=1}^{q} \sum_{\omega_n \in \Omega} \sigma^2_{\hat{G}_{ij}}(\mathrm{j}\omega_n), \tag{3.31}$$

where Ω indicates the relevant frequency range from 10 Hz to 500 Hz. It can be seen that the overall variance is reduced by approximately 50 % in the MIMO case.

Influence of Undermodeling

The second step of the identification procedure consists of fitting a parametric model $\boldsymbol{G}$ to the estimated FRF $\hat{\boldsymbol{G}}$. Since the frequency response of this parametric model does in general not perfectly match the underlying FRF, additional modeling errors are introduced. These are caused by two effects:

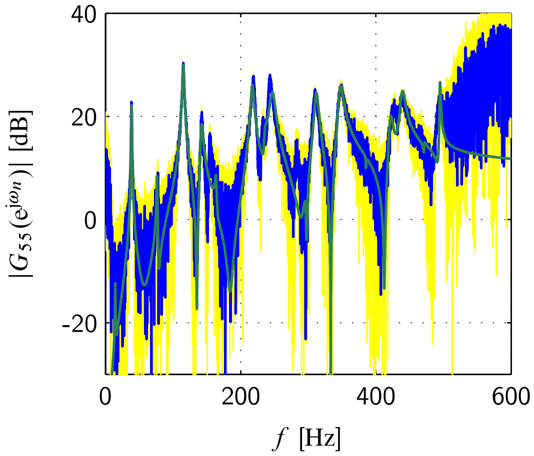

Figure 3.10: Extended uncertainty region (shaded area) of the parametric model (green), together with the FRF estimate (blue).

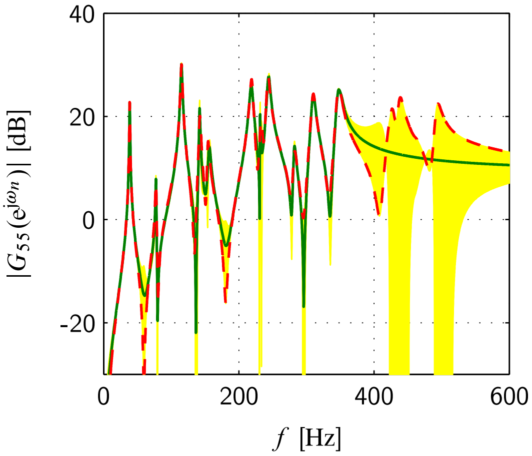

Figure 3.11: Uncertainty region (shaded area) of the parametric model, together with the magnitude of the true model (dashed).

1. The non-parametric FRF model is distorted by measurement noise on the time signals, leading to a noisy FRF curve. This cannot, and should not, be fitted by a parametric model of moderate degree.
2. Even in the noise-free case, moderate model orders are desirable and thus undermodeling errors are often deliberately accepted.

These two effects shall be illustrated by simulation examples. In the first case, the FRF matrix with large noise amplitude, whose (5,5) element is displayed on the right side of Fig. 3.7, is fitted by a parametric model of order 34. This is also the true model order, since 17 plate modes are contained in the simulation model. For robust stability analysis, the modeling errors of the parametric model with respect to the non-parametric model are incorporated as in (3.25). For illustration, an uncertainty region of the parametric model is formed which symmetrically bounds the magnitude of G_{ij} and incorporates the uncertainty region of $|\hat{G}_{ij}|$. This is shown in Fig. 3.10 for the (5,5) element of the transfer matrix. It can be seen that the uncertainty region of the parametric model is considerably enlarged due to the differences between non-parametric and parametric model.

The second effect is illustrated in Fig. 3.11. Here, no noise was added. Consequently, the estimated FRF matrix is nearly identical to the FRF of the true system. This noise-free FRF matrix $\hat{\boldsymbol{G}}$ shall be fitted by a parametric model of order 24, which is smaller than that of the true model. Thus, some of the system dynamics cannot be captured. For that reason, only the FRF matrix up to 400 Hz, containing the first twelve resonance frequencies, is fitted. Since there is no noise present, the uncertainty region of the parametric model is nearly zero at low and medium frequencies where the available system poles are used to fit the resonances. At high frequencies, the uncertainty stems solely from the differences between non-parametric and parametric model.

In a final example, noise errors and undermodeling errors shall be combined. To that end, the noisy FRF matrix with $\sigma_v^2 = 0.01\,{}^{m}/_{s^2}$ is fitted with a model of order 26 in the frequency range up to 500 Hz. This allows to capture only 13 out of 17 modes of the system. Thus, both moderate

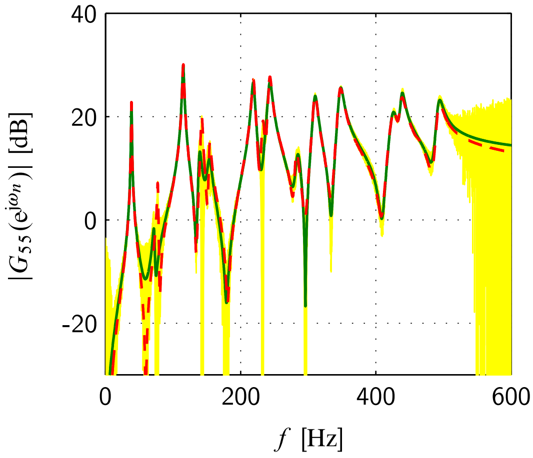

Figure 3.12: Uncertainty region (shaded area) of the parametric model, together with the magnitude of the true model (dashed).

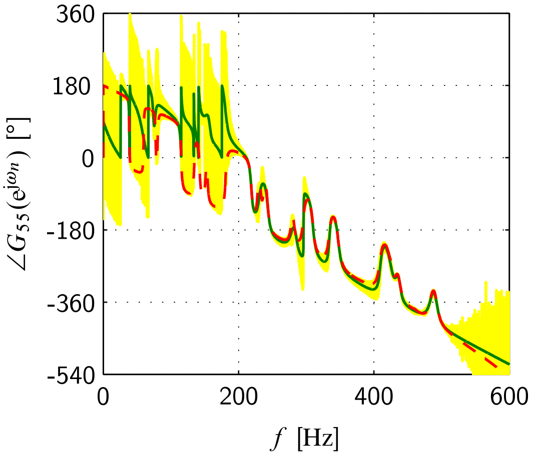

Figure 3.13: Uncertainty region (shaded area) of the parametric model, together with the phase of the true model (dashed).

noise and undermodeling errors are present in the parametric model. The results are shown for the frequency response of G_{55} in Figs. 3.12 and 3.13. In the magnitude plot, four resonances are not included in the parametric model which are located at 78, 143, 155, and 233 Hz. Undermodeling and noise leads to moderate uncertainty regions in the frequency range where the system was excited by the input signals and to large uncertainty below 10 Hz and above 500 Hz. The phase plot in Fig. 3.13 shows similar results. Up to 200 Hz, the missed-out resonances lead to maximum phase uncertainty of $\pm 180°$. Most importantly, the true model FRF is contained within the estimated model uncertainty over the complete considered frequency range which demonstrates the validity of the proposed approach.

3.6.2 Experimental Results

Now, measurement results from the smart panel testbed are presented. The experimental setup is identical to the simulated experiment. Figures 3.14 and 3.15 show pictures of the plate with piezo patches and the shaker which is mounted on the backside of the panel. The four actuator patches can be seen, which are placed as discussed in Sec. 2.4.3. There is one accelerometer nearly collocated to every actuator and one collocated to the shaker driving point. The disturbance force which is generated by the shaker can be measured by a force transducer.

The input signal is the logarithmically swept sine signal (3.21) with an amplitude of 30 V and $f_0 = 20$ Hz. Due to the elastic mounting of the shaker, the shaker force cannot be directly prescribed but only the input voltage to the shaker amplifier. It is adjusted such that the actual shaker force is approximately 1 N. The input scheme is chosen according to the first five columns of a Hadamard matrix of dimension eight. Figure 3.16 shows the shaker force when the structure is excited with all five system inputs simultaneously in phase, i.e. the input scheme is taken from the first column of the Hadamard matrix (3.20). Figure 3.17 shows the resulting driving point acceleration. The

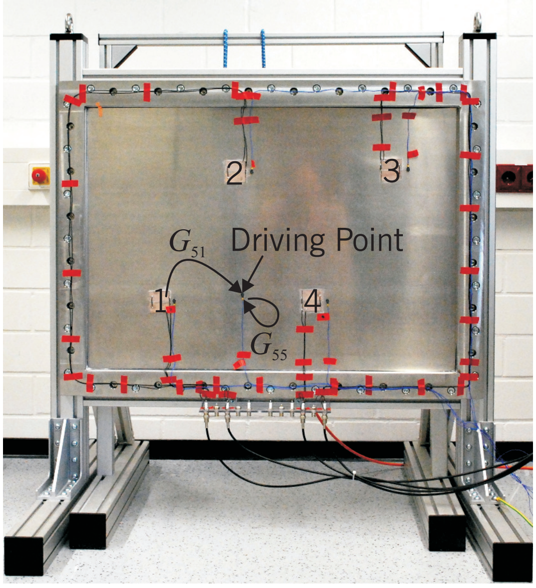

Figure 3.14: Smart panel testbed with four piezo patches and five accelerometers with indicated shaker driving point.

Figure 3.15: Backside of smart panel testbed showing the electromagnetic shaker and force sensor.

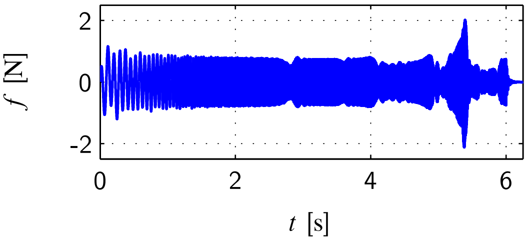

Figure 3.16: Shaker force when exciting the structure with all inputs simultaneously in phase.

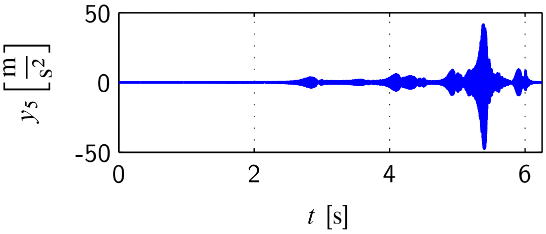

Figure 3.17: Driving point acceleration when exciting the structure according to Fig. 3.16.

overall experiment is repeated nine times to reduce the influence of measurement noise, i.e. $\tilde{M} = 9$, which reduces the standard deviations of the entries of $\hat{\boldsymbol{G}}\left(\mathrm{e}^{\mathrm{j}\omega_n}\right)$ to a third of their initial values, compare (3.6).

Some results of the non-parametric modeling step are presented in Figs 3.18 and 3.19. The first shows the estimated FRF from the disturbance force to the collocated driving-point accelerometer. The second displays the magnitude of the FRF from the voltage applied to the first piezo patch to the same accelerometer. All FRFs are of very good quality as can be seen from the associated uncertainty regions which are almost only visible outside the excitation bandwidth of 20 to 500 Hz.

A stable parametric model $\boldsymbol{G}(z)$ of order $n = 200$ was fitted to the FRF data which was subsequently reduced to order 100 by balanced truncation. A model order of 100 is reasonable, since the minimum model order can be calculated as follows: The considered frequency range up to 500 Hz contains the first 17 bending modes of the plate which implies a model of order $17 \cdot 2 = 34$. In

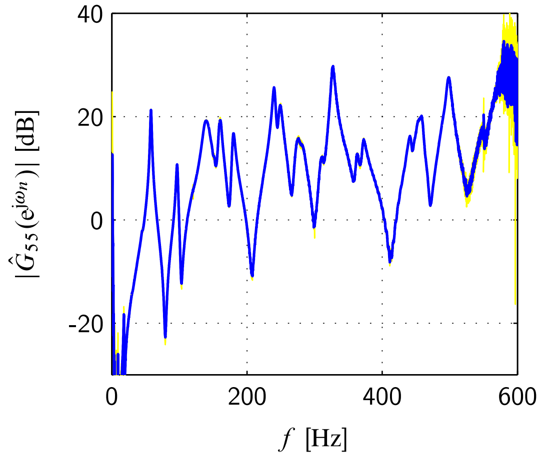

Figure 3.18: FRF magnitude from disturbance force to collocated accelerometer with associated uncertainty region (shaded area).

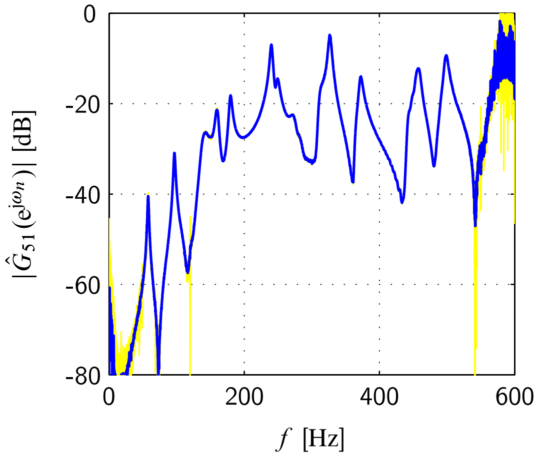

Figure 3.19: FRF magnitude from first piezo patch to driving-point accelerometer with associated uncertainty region (shaded area).

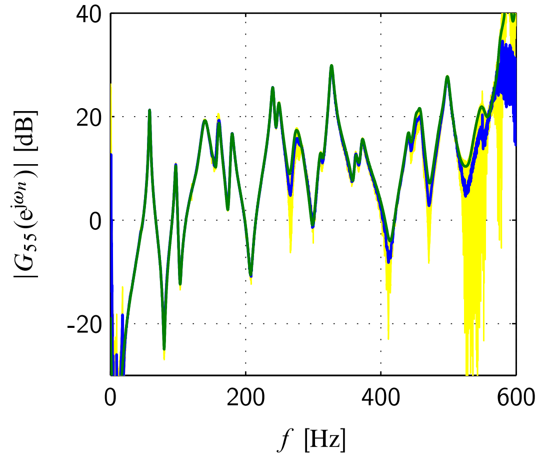

Figure 3.20: FRF magnitude of parametric model (green) with associated uncertainty region (shaded area) from disturbance force to collocated accelerometer, together with the non-parametric model (blue).

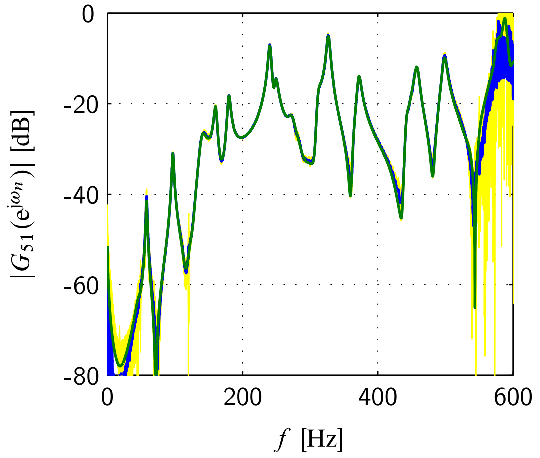

Figure 3.21: FRF magnitude of parametric model (green) with associated uncertainty region (shaded area) from first piezo patch to driving-point accelerometer, together with the non-parametric model (blue).

addition to that, the analog low-pass filters of order six are present at the inputs and the outputs of the transfer paths from the four piezo patches to all five acceleration sensors. This increases the necessary model order by $(4+5)\cdot 6 = 54$. Thus, the total theoretical minimum of the model order is $34+54 = 88$. The FRFs of the parametric model are shown in Figs. 3.20 and 3.21 for the same transfer paths as in Figs. 3.18 and 3.19. The model uncertainty region is enlarged to symmetrically bound the FRF magnitude values of $G_{55}(e^{j\omega_n})$ and $G_{51}(e^{j\omega_n})$ and include the uncertainty regions of the associated non-parametric models.

3.7 Chapter Summary

An experimental modeling method was provided in this chapter to generate parametric models of LTI systems together with an estimation of the associated model uncertainty. The identification procedure consists of two steps. The first step estimates a non-parametric FRF model and employs the statistical properties of the FRF estimator to generate an uncertainty description for the non-parametric model. In the second step, a state space model is calculated to match the estimated FRF, and the model uncertainty description is suitably adjusted to be in line with the parametric model. The distinct features of the presented approach are that it can handle models of high order ($n > 100$) and does not involve computationally expensive optimization techniques, like alternative I4C approaches of which a survey was also given in this chapter. Furthermore, the estimated uncertainty description is in a form which is compatible with established robustness analysis tests and is therefore immediately applicable to robust control design. Simulation as well as experimental results were presented for the identification of a smart panel with force and piezoelectrical inputs, and acceleration outputs. In addition to that, it was shown how different aspects of input signal design affect the resulting model uncertainty and how this uncertainty can be reduced by thoughtful experiment design.

4 Active Vibration Control

Vibration damping by means of active control is the topic of this chapter. Numerous control concepts of varying complexity have been devised for this purpose, and a short summary of common active vibration control concepts will be given. Based on that, it will be argued why a multiple-input multiple-output control concept is favored in this thesis. The $\mathcal{H}_2$ optimal control design methodology will be applied to compute a control algorithm which is able to significantly damp about three times as many modes as there are available actuators. Furthermore, the controller will be shown to robustly stabilize the plant, where the plant uncertainty description which was derived in the last chapter will be employed. Further topics will be the selection of the weighting functions for the optimal control problem and the difference between local and global control approaches. The proposed control design scheme will be illustrated by both simulation and experimental results.

4.1 Introduction

Active damping of structural vibration may be seen as the nucleus from which all the research in the field of smart structures flourished. As already pointed out in Sec. 1.1, active vibration damping of large space structures ignited research in this field in the late 70s and early 80s of the last century. An overview of the various active vibration control (AVC) concepts which have been developed since then may be gathered by consulting the monographs [42, 46, 75, 77, 114, 131, 154, 156].

The various concepts presented there may be categorized from a control point of view by the following attributes: adaptive or non-adaptive, feedforward, feedback or some combination thereof, SISO and MIMO structures, model-based or non-model based, structurally stable or not. Furthermore, certain control concepts are especially designed for certain actuator-sensor pairings, e.g. for the combination of a force actuator and a displacement sensor; others are more generally applicable. The reason for this is that certain actuator-sensor combinations lead to specific root-locus properties of the (theoretical) structural transfer function [154]. This implies that these controllers are designed based upon a gray-box model, or are non-model based but implicitly assume that the real structure also exhibits the same characteristic properties as some theoretical model. Consequently, a quasi-continuous time-sampling must be ensured when implementing such a controller on digital hardware. Furthermore, some control concepts additionally assume that modal quantities are available which requires the implementation of a modal filtering scheme or a special state observer; and for both possibilities, several design methods do exist, too.

We will only be concerned with non-adaptive control algorithms in this thesis to limit its focus. However, controllers which can adapt to time-varying disturbances and/or changes in plant dynamics may achieve excellent performance, and various successful applications are reported, see for example the monographs [46, 65, 130].

4.2 Overview of AVC Concepts

This section gives an overview of the most common (non-adaptive) AVC concepts, without seeking completeness. The control concepts will be subdivided into two groups: collocated and non-collocated control configurations. These are also the main categories which are employed by Preumont in [154]. To this end, the notion of *collocation* shall be introduced first.

4.2.1 Classification of AVC Schemes

Collocation is closely related to the concept of *passivity*. This interrelation is not always established in the literature. To illustrate what passivity means, imagine a single point force on an arbitrary structure where velocity is measured at the same point. Since actuator and sensor are located at the same point on the structure, they are collocated. However, there is more to this actuator-sensor configuration than the mere geometrical aspect. Force and velocity are dual quantities in the sense that their product equals power. Put in other words, the transfer function between force and velocity in a linear system is a (structural) rational point impedance function. Point impedance functions[1] are known to be *positive real*. Positive realness for linear time-invariant systems is equivalent to saying that they are passive. It is a well-known fact from linear system theory that the feedback interconnection of a positive real system with another strictly positive real system is asymptotically stable. This implies that any strictly positive real control algorithm will lead to a structurally stable control loop. In case that the plant transfer function is itself strictly positive real, a positive real controller suffices. One may consult for example [36] for further details on passive systems.

For a positive real transfer function, its argument never exceeds $[-\frac{\pi}{2}, \frac{\pi}{2}]$. Thus, its locus is confined to two quadrants of the complex s-plane, which is the key property of a positive real function.
In practice, one rarely has an ideal velocity sensor. Accelerometers or strain sensors are far more practical. In addition to that, although voice-coil inertial actuators may be modeled as point forces under certain circumstances, piezoelectric patches are more common. Thus, even when actuator and sensor are still located at the same position, the measured quantities are most often no longer dual, and the transfer function is no longer positive real. Nevertheless, the key property of a positive real transfer function may still be satisfied, albeit in a limited frequency range.
To see this, it is recalled that transfer functions of vibratory mechanical systems are usually characterized by conjugate-complex pairs of poles and zeros, apart from poles or zeros at the origin, see Sec. 2.5. Thus, it is mandatory for a positive real transfer function that the pairs of poles and zeros alternate with frequency. This is known as the *interlacing property* [154]. When the ideal velocity sensor is substituted by an ideal accelerometer for example, this property is retained, but now, the transfer function's argument lies in the interval $[0, \pi]$. When the ideal point force actuator is replaced by a patch actuator, the interlacing property will definitely be violated at some (usually high) frequency, i.e. the plant will have two resonance frequencies in a row without an intermittent

---

[1] In an electrical analogy, one may speak of a one-port impedance function.

anti-resonance or vice versa. Nevertheless, the interlacing property can be expected to be still satisfied in the low frequency range. Low in this context means that the length of the bending waves is much smaller than the patch dimensions, see [70] for further details. Non-negligible actuator and/or sensor dynamics usually further lower the frequency where the interlacing property is first violated. In accordance with [154], we will call a transfer path collocated if the interlacing property is satisfied in the relevant frequency range. Exemplary plots of collocated and non-collocated transfer paths of the smart plate testbed are given in Figs. 3.20 and 3.21, respectively.

There exist some popular vibration control concepts which explicitly build upon the properties of collocated actuator-sensor pairs. These inherently decentralized concepts will be summarized as collocated control concepts and shall now be shortly presented. All controllers in this category assume that the plant can be described by an undamped second order LTI system in modal form,

$$\ddot{\eta}_i + \omega_i^2 \eta_i = \boldsymbol{\Phi}_{\mathrm{A},i}^{\mathrm{T}} \boldsymbol{f}, \quad i = 1, \dots, \infty, \tag{4.1}$$

where $\boldsymbol{\Phi}_{\mathrm{A},i}$ denotes the ith row of the modal actuator influence matrix, and $\boldsymbol{f}$ are the control forces. The employed sensor types differ for the various collocated controllers. For practical application, it is argued that the interlacing property is retained when the system exhibits light modal damping, and so do the stability properties of the control loop. One may consult [154] for further details.

The first control concept to be introduced is the *positive position feedback* (PPF). Its controller transfer function is of the form $K(s) = {}^{-g}/_{(s^2+2D\omega s+\omega^2)}$. The damping D of this second-order filter is typically chosen rather high (0.5 to 0.7), and the frequency ω is the eigenfrequency of the mode to be targeted by the controller. The controller gain g is positive, resulting in a positive feedback of the measured structural displacement. The control loop is stable under the stated assumptions as long as the static open-loop gain is smaller than one.
If more than one mode has to be targeted by AVC, one may use one PPF control loop for each mode. The actuators and sensors of the different loops are usually placed at the anti-nodes of the respective mode shapes. Alternatively, one may employ modal filtering to use modal displacements as controller inputs. This allows for the computation of modal control forces by several parallel second order filters. These modal forces are subsequently transformed into a possibly smaller number of physical controller outputs. Modal PPF control has for example been demonstrated by Herold [102]. The general three-step procedure of modal filtering, modal control algorithm, and back-transformation to physical coordinates has been termed *independent modal space control* (IMSC) by Meirovitch [131].

A control algorithm which is capable of targeting more than one mode with a single actuator-sensor pair without IMSC is the lead controller, i.e. $K(s) = g\frac{s+z}{s+p}$ with $p \gg z$. Assuming that a displacement sensor is used, all modes in the interval $[z, p]$ are damped by the controller, albeit with smaller effect than with several PPF controllers. In case of negligible actuator and sensor dynamics, the control loop is structurally stable. It must be mentioned that the controller has no low-pass behavior at high frequencies, therefore the structure itself must exhibit sufficient roll-off to reduce spillover and ensure practical stability.

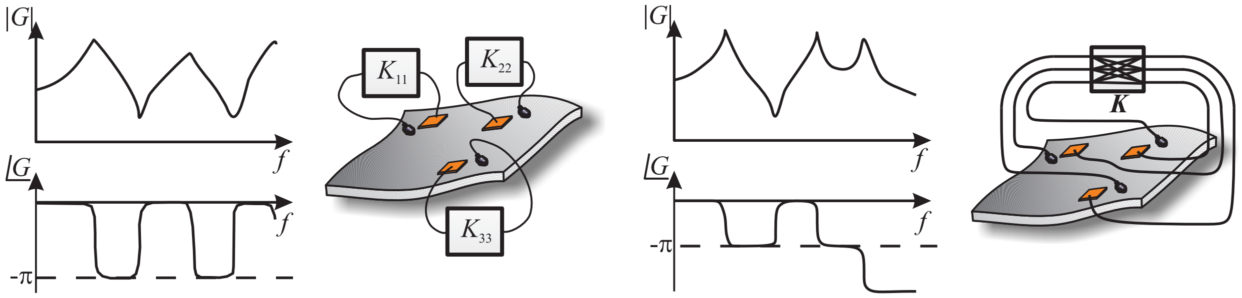

Figure 4.1: Illustration of LAC (left) and HAC (right).

In case that this is satisfied, one may theoretically also damp all structural resonances by *direct velocity feedback* (DVF). In case that acceleration is measured, the controller transfer function reads $K(s) = {}^{g}/_{s}$. This controller is, in theory, stable for any non-negative value of the control gain g.

The above concepts build upon the interlacing property and on the fact that the first eigenfrequency is lower than the frequency of the first anti-resonance. This is ensured by the assumed actuator-sensor configurations. If one has a force sensor and a displacement actuator however, the sequence of alternating poles and zeros starts with a pair of zeros. This actuator-sensor configuration is frequently encountered in truss structures with active elements, see [154] for an example. In this case, one may use the *integral force feedback* (IFF) controller, $K(s) = {}^{g}/_{s}$, which is also structurally stable.

All of the above concepts are non-model based, albeit relying on theoretical properties of special collocated transfer functions of linear vibratory systems. Their mere purpose is active damping, i.e. relocation of closed-loop pole pairs without deliberately altering eigenfrequencies or vibration mode shapes, which are reflected by closed-loop eigenvectors. The control structure is decentralized, since several SISO control loops are often placed on the same structure. Cross-talk effects are either handled via heuristic tuning guidelines or completely ignored during control design [154]. This kind of non model-based SISO control is also termed *low-authority control* (LAC) in literature. Opposed to that, *high-authority control* (HAC) principally allows also for reassignment of eigenfrequencies and/or vibratory mode shapes by making use of MIMO control. In a control context, this can be interpreted as eigenstructure assignment. Since the controller transfer matrix is now fully occupied, it also connects sensor signals with non-collocated actuators. Thus, HAC schemes are non-collocated control designs and always model-based. The concepts of LAC and HAC are illustrated in Fig. 4.1.

The HAC concepts which have been successfully applied to smart structures are well known from linear control theory. With increasing maturity of optimal control design theories, like LQG, $\mathcal{H}_2$, and $\mathcal{H}_\infty$, these methods have found applications which are described in specialized textbooks, like [42, 46, 77, 114, 131, 154, 156].

Direct pole-placement design is also reported. For MIMO design, not only the closed-loop eigenvalues but also so-called parameter vectors have to be assigned to uniquely determine a state-feedback law. The parameter vectors allow for a systematic modification of system eigenvectors, see for example [161]. However, this technique is of rather low significance for control of flexible structures. The reason for this is that the direct selection of closed-loop poles and parameter vectors by the designer is only sensible for low-order systems. For a system with $n \approx 50 \ldots 200$ poles, which is a reasonable size for a flexible structure model, selection of pole locations and parameter vectors will become confusing, especially when there is high modal overlap. Moreover, the system eigenvectors will not allow for a physical interpretation when a black-box model is used. This further complicates the selection of sensible parameter vectors. Junkins and Kim [114] propose to shape the set of closed-loop eigenvectors to maximize its orthogonality and give according instructions. This is known to generally improve accuracy of pole placement with respect to model errors. However, robust control design can be incorporated in a more specific and accurate way if the model uncertainty is (approximately) known. This is the case in this thesis, due to the concepts illustrated in Ch. 3. In addition to that, only a subset of poles – say the pole pairs of the first five to ten modes – may be focused for active damping. The other poles should preferably not be moved to reduce control spillover which endangers stability. Thus, their open-loop and closed-loop locations are intuitively chosen to be equal. It is a well-known phenomenon that placement of all system eigenvalues to specific locations may easily lead to excessive control gains for high-order systems. Thus, it has been proposed to assign only a subset of poles to specific locations, and assign the remaining poles to lie in a specified area. This strategy is known as partial pole placement, see [53]. One may then for example use the non-uniqueness of the resulting state-feedback matrix to minimize its norm, and thereby reduce control gains. But then, one may as well formulate the complete control design as a norm-minimization problem right from the start, unless a clear reason for explicit pole-placement is given. These are the reasons why pole-placement shall not be a topic in this thesis.

High-authority control will be treated exclusively in this chapter from now on, because of the following advantages over LAC:

1. HAC schemes do not necessarily rely on the theoretic system properties of vibratory systems with little or no modal damping. Thus, they can be used in combination with black-box models that have been identified from measurement data and which cannot be expected to exhibit these theoretical properties. This is especially the case when a black-box model also incorporates non-structural elements, like analog filters or actuator and sensor dynamics. If this is not the case, these elements have to be modeled separately in order to compute the complete plant model. This increases modeling effort and generally decreases modeling accuracy when forming the plant model from several submodels, as opposed to identifying the plant model directly [152]. More importantly, black-box models generally achieve higher accuracy of a system's input-output mapping compared to white and gray-box models, which is *the* requirement relevant for high performance control.
2. In the same line of thought, it can be put forward that quasi-continuous time sampling is not required for high authority model-based control. The sampling time of the plant model, which is usually identical to that of the resulting controller, may be chosen by the designer. This allows to account for specific computational requirements. In addition to that, lower sampling rates do reduce computational effort which may allow for the selection of cheaper digital hardware.

3. By definition, HAC makes far-reaching modification of system properties possible. This may or may not be relevant for active vibration damping, depending on the specific application, but will definitely prove necessary for the control of structure-borne sound. This is because sound radiation does not only depend on the vibration amplitude, but even more on the vibration mode shape. This will be illustrated in the next chapter.

4. Lastly, HAC allows for significant damping of a number of modes which exceeds the number of actuators as well as the number of sensors. This is not possible with non-modal PPF control. Even with IMSC techniques, one necessarily has at least as many sensors as relevant modes to implement modal filtering. Lead control and DVF do only theoretically achieve significant damping of many modes. In practice, one always has to add additional low pass filters to limit the control bandwidth and achieve enough roll-off at high frequencies. Furthermore, piezoelectric accelerometers are often used as sensors which exhibit large measurement uncertainty at low frequencies. Thus, the control-loop bandwidth also has to be limited by high-pass filters in this low-frequency range. The additional filters do strongly compromise the theoretic stability and performance properties of simple LAC schemes for real setups.

4.2.2 Literature Review on HAC for Active Damping

Besides the monographs [42, 46, 77, 114, 131, 154, 156], which have already been mentioned and contain predominantly simulation examples, there exist a number of papers presenting successful experimental applications of HAC. Many of these papers do not consider model uncertainty, i.e. robust stability of the control loop is not an issue there. Exemplary publications would be the works by Charon [44] and Sethi & Song [166] which both apply LQG theory to their examples. The publications by Crassidis et. al. [51] and Rao et. al. threat their problems with $\mathcal{H}_\infty$ methods.
A number of works can be found where some kind of model uncertainty is considered during control design and thus, robust stability is (theoretically) ensured. In many cases however, the assumed model uncertainty cannot be considered appropriate. This is the case when undermodeling errors are considered as the only contributor to model uncertainty. More specifically, the model uncertainty description is generated from the difference between the non-parametric and parametric plant models, or between a full-order and a reduced-order model. The respective first model is treated as being free of errors. Works in this line of thought are [142, 151] which demonstrate how a minimax LQG controller can be designed to achieve active damping. The same concept, but with different optimization criteria, is presented by Du et. al. [62] for mixed $\mathcal{H}_2/\mathcal{H}_\infty$ control and by Xie et. al. [195] for $\mathcal{H}_\infty$ control. In the publications mentioned so far, uncertainty is considered in non-parametric form, i.e. by frequency-domain bounds. In the publication [109], parametric uncertainty is employed, but the uncertainty intervals of the model parameters are arbitrarily chosen, and no explanations are given on how to derive these bounds for a real setup.

This motivates again the overall concept of this thesis: Firstly, a model should be identified where the identification procedure also allows for the computation of reasonable model uncertainty bounds. These bounds account for both deterministic and stochastic model errors. Secondly, a robustly stabilizing controller is designed which specifically takes into account the identified model

uncertainty. There should be no need for ad-hoc uncertainty descriptions.
In the next section, it will be shown how an optimal design problem for the calculation of a high-authority controller can be deduced from an appropriate statement of the AVC problem.

4.3 Active Vibration Control Design

Before elaborating on the control design methodology to achieve active damping, a precise statement on the problem to be treated is necessary.

4.3.1 Specification of the AVC Problem

The problem of active vibration control, as it is interpreted in this thesis, shall be paraphrased as follows:

The AVC problem consists of finding and implementing a control algorithm which reduces the overall dynamic response of a flexible structure due to external disturbances. The actuators and sensors are located on the structure at suitably chosen positions, whereas the disturbance is assumed to be broadband, but its spectral density and point of attack are unknown.

We want to comment on some of the aspects of the above statement. The term *dynamic response* alludes to the fact that static deflection due to disturbance forces is not considered as something which should be targeted by active control. This is an important issue in position control of smart structures, but is not considered here, since our focus is on reduction of vibration and noise harassment. This is in accordance with the choice of piezoelectric accelerometers as sensors which cannot detect low-frequency motion.
The preset adjective *overall* represents the aim of global control, as opposed to local control, see also Sec. 1.2. Local control may be important when a fragile device is mounted on a confined area of a supporting structure, or if vibration levels shall be reduced at links or connections to other machinery parts. This field of application is also termed *vibration isolation* [75, 154] and may result in totally different control strategies.
In the examples presented in this thesis, the positioning of actuators and sensors is assumed to be possible at arbitrary locations on the structure. This may not be the case for a real-world design problem of a smart structure. However, the freedom in the assignment of transducer positions reflects the inherent pretense of smart structures to be the outcome of an integrated system design approach. Although control algorithm and transducer locations are not explicitly simultaneously designed in this thesis, the interrelations have been highlighted in Sec. 2.4 where suitable positions for AVC have been selected.
The last important aspects of the above definition are the assumptions on the disturbance. Postulation of a broadband disturbance is relevant for the choice of control algorithm. When the structure is excited by some broadband disturbance, its response is dominated by those modal quantities which are associated with the structural resonances that are significantly excited by the

disturbance. Consequently, reduction of vibration levels can be achieved by reduction of structural resonances, i.e. augmenting the damping of resonance peaks. In a control context, this can be interpreted as moving the conjugate-complex pole pairs within the disturbance frequency range to regions of higher damping. One must be aware that increasing the damping of resonances generally also leads to increased damping of the system's anti-resonances. This is because the anti-resonances are determined by the zeros of the elements of the system's transfer matrix which change under feedback control, as opposed to the invariant zeros of the system. Thus, if the disturbance was narrowband and its frequency spectrum was close to an anti-resonance, active damping may well lead, at specific locations, to higher vibration levels as compared to the uncontrolled system. In this case, disturbance cancellation will give better results. This may be implemented via some kind of disturbance observer when the location of the disturbance is known. However, this is rarely the case. When the disturbance location and frequency are unknown, one may resort to the adaptive disturbance cancellation schemes presented by Elliott [65] or Widrow & Walach [194].

4.3.2 Control Design Methodology

The AVC problem must now be translated into a mathematical form. To this end, assume that the plant to be controlled can be described by a nth-order discrete-time state space model

$$\begin{aligned} \boldsymbol{x}(k+1) &= \boldsymbol{A}\boldsymbol{x}(k) + \boldsymbol{B}\boldsymbol{u}(k) + \boldsymbol{E}\boldsymbol{d}(k) \\ \boldsymbol{y}(k) &= \boldsymbol{C}\boldsymbol{x}(x) + \boldsymbol{D}\boldsymbol{u}(k) + \boldsymbol{F}\boldsymbol{d}(k), \end{aligned} \tag{4.2}$$

where $\boldsymbol{u} \in \mathbb{R}^q$ are the control inputs, and $\boldsymbol{y} \in \mathbb{R}^p$ are the sensor signals, see also the system description (3.23). In this chapter, the AVC methodology will be demonstrated for the problem of actively damping the smart panel which was presented in the last chapter. Structure-fluid interaction will not be considered here, but in Ch. 5. Thus, $\boldsymbol{u}$ are the voltages applied to the $q = 4$ actuator patches, and $\boldsymbol{y}$ are the outputs of the $p = 4$ nearly collocated accelerometers of the setup shown in Fig. 3.1. The disturbance $\boldsymbol{d}$ acts on the system via the matrices $\boldsymbol{E}$ and $\boldsymbol{F}$. The plant model does not only contain the structural dynamics, but also the actuator and sensor dynamics, including amplifiers as well as the dynamic behavior of the reconstruction and anti-aliasing filters, compare Fig. 3.1. For future reference, we will denote the transfer function from $\boldsymbol{u}$ to $\boldsymbol{y}$ with $\boldsymbol{G}$, i.e.

$$\boldsymbol{G} = \left[\begin{array}{c|c} \boldsymbol{A} & \boldsymbol{B} \\ \hline \boldsymbol{C} & \boldsymbol{D} \end{array}\right]. \tag{4.3}$$

As stated in the above definition of the AVC problem, the matrices $\boldsymbol{E}$ and $\boldsymbol{F}$ are unknown, as well as the vector $\boldsymbol{d}$. In order to reflect this in control design, it is proposed to replace the unknown excitation term $\boldsymbol{E}\boldsymbol{d}$ by an exogenous input $\boldsymbol{B}_w\boldsymbol{w}_1$. The variable $\boldsymbol{w}_1$ is assumed as a vector sequence of independent and uncorrelated, zero-mean white noise processes of unit intensity. If some knowledge is available on how the disturbance acts on the system, it can be utilized in the construction of the matrix $\boldsymbol{B}_w$. For a continuous-time mechanical system of the form (2.84) for

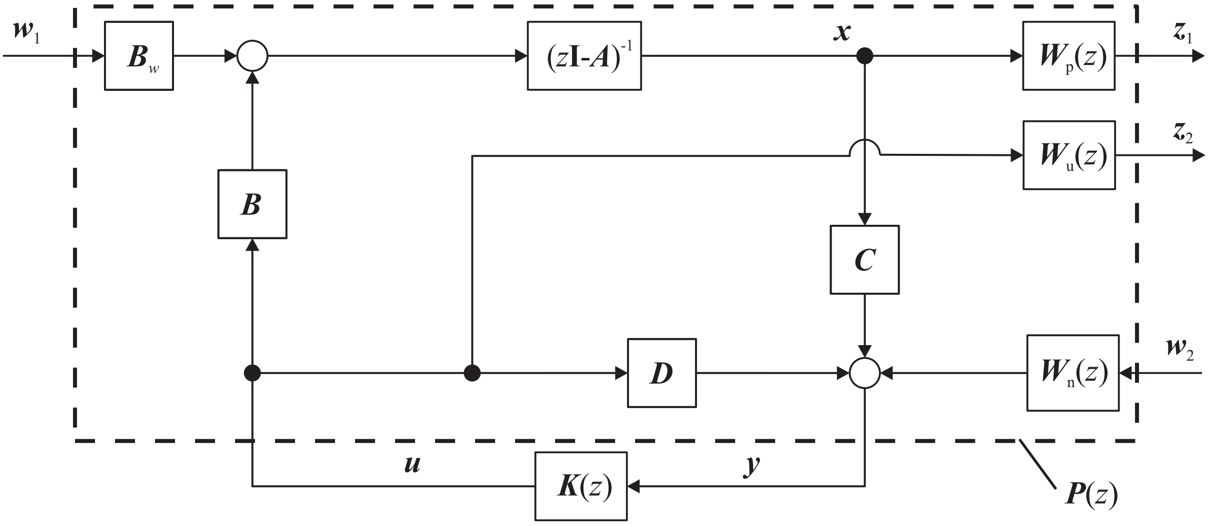

Figure 4.2: Control loop with generalized plant $\boldsymbol{P}(z)$ and controller $\boldsymbol{K}(z)$ for AVC design.

example, it is clear that the upper half of the input matrix must equal zero, irrespective of the specific disturbance. In case that no knowledge is available on the disturbance input, one may set $\boldsymbol{B}_w$ to unity. Since the feedthrough term $\boldsymbol{Fd}$ cannot be influenced by a change of system poles, it will be discarded. A graphical representation of these ideas is shown in Fig. 4.2, where the generalized plant $\boldsymbol{P}(z)$ is shown for which the controller $\boldsymbol{K}(z)$ shall be designed.

For many applications, it is more realistic to assume that some knowledge on the frequency content of the disturbance is available, instead of knowledge on its point of attack. Then, one may include this knowledge in an additional filter which is placed before $\boldsymbol{B}_w$ and appropriately modifies the frequency content of the white noise sequence $\boldsymbol{w}_1$.

The figure of the generalized plant shows three more weighting functions, each with a specific purpose, that have to be chosen by the designer. The most important weight is $\boldsymbol{W}_\mathrm{p}$ which we will refer to as the performance weight. Its input is the system's state vector $\boldsymbol{x}$ and its output is the control (or performance) variable $\boldsymbol{z}_1$. The purpose of the controller shall be to minimize the influence of the exogenous input $\boldsymbol{w}_1$ on $\boldsymbol{z}_1$. In order to prevent excessive control effort in achieving this goal, the effort weight $\boldsymbol{W}_\mathrm{u}$ forms an additional control variable $\boldsymbol{z}_2$ which shall be kept small, too. In almost any real control loop, one has to deal with measurement noise. The influence of noise on the measurement vector $\boldsymbol{y}$ is reflected by the presence of the noise weight $\boldsymbol{W}_\mathrm{n}$ which may be used to model the noise characteristics by filtering the sequence $\boldsymbol{w}_2$ that has the same properties as $\boldsymbol{w}_1$. Here, $\boldsymbol{W}_\mathrm{n}$ is chosen to be constant, i.e. the measurement noise is assumed to be white and uncorrelated over time.

Now, it must be specified what minimizing the influence of $\boldsymbol{w}_1$ on $\boldsymbol{z}_1$ means. Assuming that the exogenous input $\boldsymbol{w}_1$ is indeed a white noise vector sequence as mentioned above, we require the controller $\boldsymbol{K}(z)$ to minimize the RMS value of $\boldsymbol{z}_1$. It is a result from linear system theory that the RMS output value of a LTI system to an independent and uncorrelated, zero-mean white noise sequence of unit intensity is identical to the $\mathcal{H}_2$ norm of its transfer function [162, 197], i.e.

$$\mathrm{RMS}\,\boldsymbol{z}_1(k) = \sqrt{\mathrm{E}\left\{\boldsymbol{z}_1(k)^{\mathrm{T}}\boldsymbol{z}_1(k)\right\}} \overset{\boldsymbol{w}_1}{=} \left\|\boldsymbol{T}_{z_1 w_1}(\mathrm{e}^{\mathrm{j}\omega})\right\|_2 = \sqrt{\frac{1}{2\pi}\mathrm{tr}\int_{-\pi}^{\pi} \boldsymbol{T}_{z_1 w_1}^{\mathrm{H}}(\mathrm{e}^{\mathrm{j}\omega})\boldsymbol{T}_{z_1 w_1}(\mathrm{e}^{\mathrm{j}\omega})\,\mathrm{d}\omega}, \tag{4.4}$$

where $\boldsymbol{T}_{z_1 w_1}$ denotes the closed-loop transfer matrix from $\boldsymbol{w}_1$ to $\boldsymbol{z}_1$. It was assumed for the first equality that $\boldsymbol{z}_1$ is wide-sense stationary, which is ensured if $\boldsymbol{w}_1$ has the stated properties. Thus, it follows from the above framework that applying $\mathcal{H}_2$ optimal control theory to the problem of AVC is quite natural. For a practical design however, it is necessary to include also the input $\boldsymbol{w}_2$ and the output $\boldsymbol{z}_2$ of the generalized plant. The controller should therefore not minimize the norm $\|\boldsymbol{T}_{z_1 w_1}\|_2$, but that of the complete generalized plant in closed loop, i.e.

$$\boldsymbol{K}(z) = \arg\min \|\boldsymbol{T}_{zw}\|_2\,, \quad \text{s.t. } \boldsymbol{K}(z) \text{ internally stabilizing,} \tag{4.5}$$

with

$$\boldsymbol{T}_{zw} = \begin{pmatrix} \boldsymbol{T}_{z1w1} & \boldsymbol{T}_{z1w2} \\ \boldsymbol{T}_{z2w1} & \boldsymbol{T}_{z2w2} \end{pmatrix} = \mathcal{F}_{\mathrm{l}}\left\{\boldsymbol{P}(z), \boldsymbol{K}(z)\right\}, \tag{4.6}$$

where $\mathcal{F}_{\mathrm{l}}\{\cdot,\cdot\}$ denotes lower linear fractional transformation (LFT) of two transfer functions, see for example [168, 197]. For further reference, the following subsystems of the generalized plant are introduced,

$$\boldsymbol{P}_{zw}(z) = \begin{bmatrix} \boldsymbol{W}_{\mathrm{p}}(z)\,(z\mathbf{I}-\boldsymbol{A})^{-1}\boldsymbol{B}_w & \mathbf{0} \\ \mathbf{0} & \mathbf{0} \end{bmatrix}, \tag{4.7}$$

$$\boldsymbol{P}_{yw}(z) = \begin{bmatrix} \boldsymbol{C}(z\mathbf{I}-\boldsymbol{A})^{-1}\boldsymbol{B}_w & \boldsymbol{W}_{\mathrm{n}}(z) \end{bmatrix}, \tag{4.8}$$

$$\boldsymbol{P}_{zu}(z) = \begin{bmatrix} \boldsymbol{W}_{\mathrm{p}}(z)\,(z\mathbf{I}-\boldsymbol{A})^{-1}\boldsymbol{B} \\ \boldsymbol{W}_{\mathrm{u}}(z) \end{bmatrix}, \tag{4.9}$$

$$\boldsymbol{P}_{yu}(z) = \boldsymbol{C}(z\mathbf{I}-\boldsymbol{A})^{-1}\boldsymbol{B} + \boldsymbol{D}. \tag{4.10}$$

We will now elaborate on the choice of the different weighting functions. As already mentioned, the noise weight $\boldsymbol{W}_{\mathrm{n}}$ can be used to reflect knowledge of the measurement noise in the generalized plant. When it is assumed to be a white noise sequence with the same characteristics as $\boldsymbol{w}_1$, one may set $\boldsymbol{W}_{\mathrm{n}} = \mathbf{I}W_{\mathrm{n}}$ with the real-valued scalar W_{n}. If in addition to that, $\boldsymbol{B}_w$ is chosen to be unity, it is natural to have $W_{\mathrm{n}} \ll 1$ in order to weight the relative importance of the exogenous inputs $\boldsymbol{w}_1$ and $\boldsymbol{w}_2$ for the optimality criterion $\|\boldsymbol{T}_{zw}\|_2$.

The weighting of the control effort serves three purposes:

1. Keep the control gain below a certain bound within the desired controller bandwidth.
2. Penalize controller action above the considered control-loop bandwidth to avoid spillover effects.
3. Reduce controller action in frequency bands where model uncertainty is high to enhance robust stability.

The last point is relevant at very low frequencies due to the piezoelectric measurement principle, and at high frequencies that are not excited during identification experiments, as pointed out in

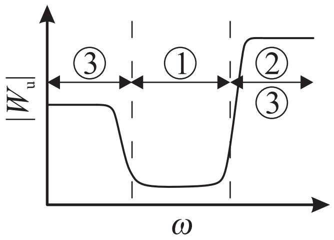

Figure 4.3: Characteristic of W_u.

the last chapter. Since all actuators in a control loop are usually of the same type, one may set $\boldsymbol{W}_\mathrm{u}(z) = \mathbf{I}W_\mathrm{u}(z)$. Considering the above requirements, one can see that a reasonable choice for the weighting function W_u would be a bandstop filter, see Fig. 4.3. This can be realized by a scalar transfer function of the form

$$W_\mathrm{u}(z) = \mathcal{Z}_{T_\mathrm{s}}\left\{\frac{(1+T_{\mathrm{D}1}s)^{n_1}(1+T_{\mathrm{D}2}s)^{n_2}}{(1+T_1 s)^{n_1}(1+T_2 s)^{n_2}}k\right\}, \tag{4.11}$$

with $\infty > T_1 > T_{\mathrm{D}1} > T_{\mathrm{D}2} > T_2 > 0$, and $\{n_1, n_2\} \in \mathbb{N}$. The operator $\mathcal{Z}$ realizes the discrete-time transfer function $W_\mathrm{u}(z)$ from the continuous filter design via bilinear transformation with sampling time T_s. The desired penalization of low-frequency controller action can be specified via the parameter k up to frequency $1/T_1$. The lower and upper margins of the controller bandwidth can be set with the constants $T_{\mathrm{D}1}$ and $T_{\mathrm{D}2}$, while the magnitude of W_u in this region can be adjusted by n_1. The starting frequency and magnitude of the penalization of controller action above the control bandwidth is set via T_2 and n_2, respectively.

The most important, but also least intuitive part is the choice of the performance weight. We shall consider for the moment the state space description of a continuous-time mechanical system with n modes and proportional damping which can be generally written as

$$\begin{pmatrix}\dot{\boldsymbol{\eta}}\\ \ddot{\boldsymbol{\eta}}\end{pmatrix} = \begin{pmatrix}\mathbf{0} & \mathbf{I}\\ -\bigoplus_{i=1}^n \omega_i^2 & -2\bigoplus_{i=1}^n D_i\omega_i\end{pmatrix}\begin{pmatrix}\boldsymbol{\eta}\\ \dot{\boldsymbol{\eta}}\end{pmatrix} + \begin{pmatrix}\mathbf{0}\\ \boldsymbol{\Phi}_\mathrm{A}^\mathrm{T}\end{pmatrix}\boldsymbol{f}, \tag{4.12}$$

see also App. A.7. Then, $\boldsymbol{W}_\mathrm{p}$ may be chosen to reflect the kinetic and/or potential energy of the system which are represented by the modal deflections and velocities in the state vector $\boldsymbol{x} = (\boldsymbol{\eta}^\mathrm{T}, \dot{\boldsymbol{\eta}}^\mathrm{T})^\mathrm{T}$. In fact, it is easily verified that $E_\mathrm{kin} = \frac{1}{2}\dot{\boldsymbol{\eta}}^\mathrm{T}\dot{\boldsymbol{\eta}}$, and $E_\mathrm{pot} = \frac{1}{2}\boldsymbol{\eta}^\mathrm{T}\boldsymbol{\Omega}^2\boldsymbol{\eta}$ with $\boldsymbol{\Omega} = \bigoplus_{i=1}^n \omega_i$. However, the states of an identified discrete-time black-box model generally preclude a physical interpretation in terms of displacements, velocities, etc. In case that such a model exclusively presents structural dynamics, i.e. signal processing or transducer dynamics etc. are not included, it is possible to transform the $2n$ dimensional discrete-time model (4.2) with arbitrary state basis into the form (4.12) by an algorithm which has been proposed by Alvin and coworkers in [5, 6]. One may then select $\boldsymbol{W}_\mathrm{p}$ for the resulting continuous-time generalized plant $\boldsymbol{P}(s)$, and then discretize again. The drawbacks of this approach are the inelegant workflow and that the algorithm will produce significant errors when the discrete-time model does not exactly match the sampled input-output sequence of a model of the form (4.12). Alternatively, one may directly identify a gray-box model with structure (4.12), as shown by Cavallo et. al. in [41]. This procedure also comes with two drawbacks. Firstly, it requires continuous-time sampling, and secondly, the accuracy of black-box identification cannot be achieved by gray-box modeling, as also illustrated by the authors of [41] in their presented example. Nevertheless, one appeal of continuous-time design is that analytical solutions to $\mathcal{H}_2$ and $\mathcal{H}_\infty$ AVC problems for systems of the form (4.12) could recently be produced, see [42]. Since the problems considered in this thesis are of moderate size, computation time is not an issue, and having analytical formulas is thus not regarded as a strong argument.

It will now be shown how to find a performance weight for the state vector $\boldsymbol{x}$ given in an arbitrary state basis of the discrete-time model. They key idea is that although the states do not have a physical interpretation, the model will have conjugate-complex poles with frequencies corresponding to the eigenfrequencies of the structure. It is usually not hard to separate the structural eigenfrequencies from other eigenfrequencies of the model, for example those contributed by actuator and sensor resonances, which should generally lie outside the control bandwidth, anyway.

To begin with, the state space description of $\boldsymbol{G}$ is transformed into a block-diagonal modal form via the state-transformation matrix $\boldsymbol{T}$ such that $\boldsymbol{x} = \boldsymbol{T}\tilde{\boldsymbol{x}}$, and the transformed system matrix $\tilde{\boldsymbol{A}} = \boldsymbol{T}^{-1}\boldsymbol{A}\boldsymbol{T}$ takes the form $\tilde{\boldsymbol{A}} = \bigoplus\{\tilde{\boldsymbol{A}}_1, \dots, \tilde{\boldsymbol{A}}_k, \tilde{\boldsymbol{A}}_0\}$ with each

$$\tilde{\boldsymbol{A}}_i = \begin{pmatrix} \sigma_i & \kappa_i \\ -\kappa_i & \sigma_i \end{pmatrix}, \quad i = 1, \dots, k \tag{4.13}$$

showing the real and imaginary parts of a pair of conjugate complex eigenvalues $\sigma_i \pm \mathrm{j}\kappa_i$ that belong to one targeted resonance. The submatrix $\tilde{\boldsymbol{A}}_0 \in \mathbb{R}^{r\times r}$ contains all real poles of the system and those conjugate complex system poles that correspond to modes which are not targeted by the controller. We will set the size of the performance weight to $\tilde{\boldsymbol{W}}_\mathrm{p} \in \mathbb{C}^{k\times n}$ with $n = 2k + r$. Thus, the vector $\boldsymbol{z}_1$ will contain one element for each targeted resonance.

We further want to specify $\tilde{\boldsymbol{W}}_\mathrm{p} = \tilde{\boldsymbol{W}}_\mathrm{p2}\tilde{\boldsymbol{W}}_\mathrm{p1}$ with $\tilde{\boldsymbol{W}}_\mathrm{p2} = \bigoplus_{i=1}^{k} w_i$. The reason for this separation of the performance weight is that the k elements w_i can be easily chosen by the designer to weight the relative importance of the targeted modes. The other part of the weighting matrix reflects the relative weighting of the two system states associated with one resonance relatively to each other. The first ideas would be to weight only one state, or both states equally, i.e. $\tilde{\boldsymbol{W}}_\mathrm{p1} = (\mathbf{I}_k \otimes \mathbf{1}_{1\times 2},\ \mathbf{0}_{k\times r})$. This is practicable, but tends to produce disparate values for the w_i. A more homogenous distribution of these modal weights can be achieved by a modified relative weighting for the pairs of system states.

To this end, we have the following reasoning for a different choice of $\tilde{\boldsymbol{W}}_\mathrm{p1}$. Assume that the transformed system is excited with the same harmonic signal on each input channel, i.e. $\boldsymbol{u}(k) = (\hat{u}, \dots, \hat{u})^\mathrm{T}\sin(\omega_i k T_\mathrm{s})$, where $\omega_i = \sqrt{\sigma_i^2 + \kappa_i^2}$ is the eigenfrequency of the ith mode. Consequently, the states $\tilde{x}_{i1}$ and $\tilde{x}_{i2}$ of the subsystem $\tilde{\boldsymbol{A}}_i$ will also oscillate harmonically with time, each with amplitude $\hat{x}_{ij}$, $j = \{1, 2\}$. Then, we want the relative weighting of the states $\tilde{x}_{i1}$ and $\tilde{x}_{i2}$ to be equal to $\hat{x}_{i2}/\hat{x}_{i1}$. This proposition implies that for the transformed system, if we applied a weighting $\tilde{\boldsymbol{W}}_\mathrm{p1} = \bigoplus(\tilde{\boldsymbol{W}}_\mathrm{p1,1}, \dots, \tilde{\boldsymbol{W}}_\mathrm{p1,k}, \mathbf{0})$ with $\tilde{\boldsymbol{W}}_{\mathrm{p1},i} = ({}^{\hat{x}_{i2}}/_{\hat{x}_{i1}}\ 1)$, the state variables $\tilde{x}_{ij}$, $j = \{1, 2\}$ would contribute with equal amplitude to the performance variable $\tilde{z}_i = {}^{\hat{x}_{i2}}/_{\hat{x}_{i1}}\,\tilde{x}_{i1} + \tilde{x}_{i2}$ when the system was excited at ith resonance. The ratio $\hat{x}_{i2}/\hat{x}_{i1}$ at resonance frequency ω_i is for each subsystem $\tilde{\boldsymbol{A}}_i$ equal to

$$\frac{\hat{x}_{i2}}{\hat{x}_{i1}} = \left|\frac{\kappa_i \Sigma_{i_1} + \sigma_i \Sigma_{i_2} - e^{\mathrm{j}\omega_i T_\mathrm{s}} \Sigma_{i_2}}{\sigma_i \Sigma_{i_1} - \kappa_i \Sigma_{i_2} - e^{\mathrm{j}\omega_i T_\mathrm{s}} \Sigma_{i_1}}\right|, \tag{4.14}$$

with $\Sigma_{i_m, m=1,2} = \sum_{l=1}^{q} \tilde{\boldsymbol{B}}^{(i_m,l)}$, $i_1 = 2i - 1$, $i_2 = 2i$, and $\tilde{\boldsymbol{B}} = \boldsymbol{T}^{-1}\boldsymbol{B}$. A proof for the ratio (4.14) is given in App. C.1.

The weighting matrix $\tilde{\boldsymbol{W}}_{\mathrm{p1}}$ for the transformed system can now be calculated. The overall performance weight which can be applied to the original system (4.2) is then given by $\boldsymbol{W}_{\mathrm{p}} = \tilde{\boldsymbol{W}}_{\mathrm{p2}}\tilde{\boldsymbol{W}}_{\mathrm{p1}}\boldsymbol{T}^{-1}$.

Lastly, it must be mentioned that using $\boldsymbol{W}_{\mathrm{p}} = \boldsymbol{C}$, i.e. simply weighting the sensor outputs, is generally not a viable option for active damping. This is because minimization of sensor outputs can also be achieved by making vibration mode shapes unobservable at the sensor locations. Such a modification of closed-loop vibration mode shapes leads to an unreduced vibration amplitude on the complete surface apart from the sensor locations. However, this phenomenon usually appears only for inauspicious actuator-sensor configurations and low weighting of control effort.

With the above choices for the weighting functions and the disturbance input matrix, the generalized plant is completely defined. Now, one needs to solve the optimization problem (4.5). The different kinds of $\mathcal{H}_2$ optimal control design problems may be separated into regular and singular ones. We have the following definition of a regular discrete-time $\mathcal{H}_2$ problem (see also Definition 2.2.6 in [162]):

A discrete-time $\mathcal{H}_2$ problem is called regular iff the generalized plant $\boldsymbol{P}(z)$ shown in Fig. 4.2 satisfies the following conditions:

- *The pair $(\boldsymbol{A}, \boldsymbol{B})$ is stabilizable.*
- *The pair $(\boldsymbol{C}, \boldsymbol{A})$ is detectable.*
- *The subsystem $\boldsymbol{P}_{zu}$ is left invertible and has no invariant zeros on the unit circle.*
- *The subsystem $\boldsymbol{P}_{yw}$ is right invertible and has no invariant zeros on the unit circle.*

The first two statements of the above definition are fundamental for the design of any feedback controller, and are trivially satisfied in case that the considered system is stable. It is obvious that the smart panel is an inherently stable mechanical system. The experimentally identified model for this system is also a stable minimal realization.

Regarding the requirements on $\boldsymbol{P}_{zu}$, one can see from (4.9) that this transfer matrix is of dimension $(k + q) \times q$, and therefore has a maximum rank of q. If $\boldsymbol{W}_{\mathrm{u}}$ is chosen as proposed above, one can see that $\boldsymbol{P}_{zu}$ has full column normal rank and is therefore left invertible. An analogous statement can be made for the right invertibility of the subsystem $\boldsymbol{P}_{yw}$ as given by (4.8).

Since the continuous transfer function (4.11) has no zeros or poles on the imaginary axis, $\boldsymbol{W}_{\mathrm{u}}(z)$ will not have zeros or poles on the unit circle, either. Thus, $\boldsymbol{P}_{zu}$ does not have transmission zeros on the unit circle. When the system matrix $\boldsymbol{A}$ is stable, there cannot be any pole zero cancellations on the unit circle. This means that if $\boldsymbol{P}_{zu}$ does not have transmission zeros on the unit circle, it cannot have invariant zeros there, either. With a similar reasoning, it can be argued that $\boldsymbol{P}_{yw}$ has no invariant zeros at all if $\boldsymbol{W}_{\mathrm{n}}$ is chosen as proposed above. Thus, the defined $\mathcal{H}_2$ problem satisfies the regularity conditions.

Regular problems are known to always have a unique solution, see Theorem 6.7.4 in [162]. In case that no measurement noise is incorporated in the generalized plant, i.e. $\boldsymbol{W}_\mathrm{n} = \boldsymbol{0}$, the problem may become singular for certain choices of $\boldsymbol{B}_w$. This implies that the weight $\boldsymbol{W}_\mathrm{n}$ also serves as a regularizing element.
If the problem is singular, existence and uniqueness of an $\mathcal{H}_2$ optimal controller are not ensured and depend on structural properties of certain subsystems of $\boldsymbol{P}$, see [162] for further details. These properties would have to be guaranteed by an identification algorithm when using the AVC methodology with a black-box model. This difficulty shall be avoided in this thesis, because it will be demonstrated later on in Sec. 4.4 by a simulation example that the performance loss due to the ensured regularity is small.

The computation of continuous-time $\mathcal{H}_2$ optimal controllers for regular problems is a standard topic in the optimal control literature. Since the $\mathcal{H}_2$-norm is not invariant under bilinear transformation, as opposed to the $\mathcal{H}_\infty$-norm, specific algorithms have been developed for the discrete-time case, see for example [162, 197]. As already mentioned, a unique optimal controller always exists for regular $\mathcal{H}_2$ problems. A less well-known fact is that there exist unique solutions for each of the two sets of proper and strictly-proper controllers. This means that there exist a unique proper controller and a unique strictly proper controller that generally do not achieve the same minimum value γ of $\|\boldsymbol{T}_{zw}\|_2$. One naturally has $\gamma_\mathrm{p} \leq \gamma_\mathrm{sp}$, where γ_p and γ_sp denote the achieved $\mathcal{H}_2$-norms for the proper and strictly proper controller, respectively[2].
This difference in performance is usually of inferior importance compared to the advantage of having a strictly proper controller. A strictly proper control algorithm is easier to implement on series or near-series hardware, since the computation of the control output can be stretched over one complete sampling period. This allows for an implementation on ASIC or FPGA hardware with a lower number of logic circuits. Indeed, the controller which is to be presented in the experimental example of this section has been successfully converted to fixed-point arithmetic FPGA hardware without loss of performance compared to a floating-point rapid-control-prototyping platform [111]. For completeness and reference, the basic equations for the calculation of a strictly proper controller for regular, discrete-time $\mathcal{H}_2$ problems are reported from [162] in App. C.2.

4.3.3 Robustness Analysis

After computation of the controller, robust stability of the control loop with respect to the identified model uncertainty of Ch. 3 has to be tested. In case that the test result is negative, more conservative weights should be used for control design. More specifically, one may increase the control effort weight at those frequencies where the robust stability condition is violated. In addition to that, one can reduce the magnitude of the entries w_i of $\tilde{\boldsymbol{W}}_{p2}$ for different targeted modes.

The uncertainty description $\Delta \boldsymbol{G}(\mathrm{e}^{\mathrm{j}\omega_n})$ derived in Ch. 3 is in non-parametric form, i.e. it is given in the form of frequency-dependent bounds on the plant's frequency response. There are two common robust stability tests for this kind of model uncertainty: small-gain theorem and μ-analysis.

---

[2] For continuous-time problems, one always has $\gamma_\mathrm{p} = \gamma_\mathrm{sp}$.

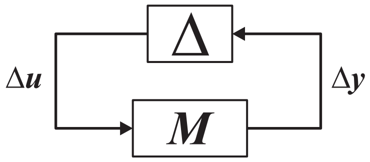

Figure 4.4: $M\Delta$-structure.

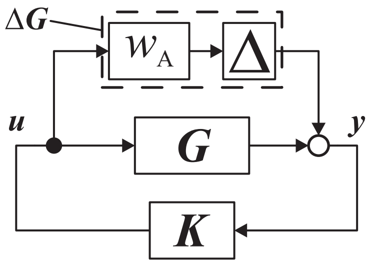

Figure 4.5: Closed loop with normalized additive uncertainty.

The application of both procedures to the closed loop made up by the uncertain model and the controller will now be demonstrated.

For both tests, the uncertain closed loop is transformed into the so-called $M\Delta$-structure [168] shown in Fig. 4.4. The uncertain transfer matrix Δ of the $M\Delta$-structure represents the set of all stable transfer matrices with $\|\Delta(\mathrm{e}^{\mathrm{j}\omega})\|_\infty = \sup_\omega \bar{\sigma}(\Delta(\mathrm{e}^{\mathrm{j}\omega})) \leq 1$, where $\bar{\sigma}$ denotes the largest singular value. All certain blocks are absorbed into M, and it is assumed that M is stable which is equivalent to saying that the system is nominally stable. It is necessary to normalize the uncertain matrix ΔG to conform with the definition of the $M\Delta$ structure. This can be done by a real-valued scalar function $w_\mathrm{A}(\mathrm{e}^{\mathrm{j}\omega_n})$ such that $\Delta(\mathrm{e}^{\mathrm{j}\omega_n}) = \Delta G(\mathrm{e}^{\mathrm{j}\omega_n}) / w_\mathrm{A}(\mathrm{e}^{\mathrm{j}\omega_n})$ with $\|\Delta G / w_\mathrm{A}\|_\infty = \|\Delta G\|_\infty / w_\mathrm{A} \leq 1$ for all possible ΔG, as shown in Fig. 4.5. The resulting frequency-dependent, normalized uncertainty matrix $\Delta(\mathrm{e}^{\mathrm{j}\omega_n})$ is fully populated, since ΔG is, and will be termed Δ_f in the following.

Obviously, the calculation of the uncertainty normalization function $w_\mathrm{A}(\mathrm{e}^{\mathrm{j}\omega_n})$ involves the computation of the maximum singular value of the uncertain matrix $\Delta G(\mathrm{e}^{\mathrm{j}\omega_n})$ over the complete unit circle. This is not an easy task. To illustrate the problem, consider the following (2×2) example at one single frequency,

$$\Delta G = \begin{pmatrix} r_{11} + \mathrm{j}i_{11} & r_{12} + \mathrm{j}i_{12} \\ r_{21} + \mathrm{j}i_{21} & r_{22} + \mathrm{j}i_{22} \end{pmatrix}. \tag{4.15}$$

In the above matrix, every real and imaginary entry is bounded by its associated interval, i.e. $r_{kl} \in \pm r_{kl,\max}$, and $i_{kl} \in \pm i_{kl,\max}$. This is why ΔG may be termed a frequency-dependent complex interval matrix. The boundary values of the symmetric intervals are given by the matrix $\Delta G_\max$ as defined in (3.25). Since the infinity-norm is a convex function of the matrix entries, its maximum is known to be reached at one of the vertices of ΔG. Thus, one has

$$\|\Delta G\|_\infty = \max \left\| \begin{pmatrix} \pm r_{11,\max} \pm \mathrm{j}i_{11,\max} & \pm r_{12,\max} \pm \mathrm{j}i_{12,\max} \\ \pm r_{21,\max} \pm \mathrm{j}i_{21,\max} & \pm r_{22,\max} \pm \mathrm{j}i_{22,\max} \end{pmatrix} \right\|_\infty . \tag{4.16}$$

The maximum operator in the above equation means taking the maximum value over all $2^8 = 4^4 = 256$ possible sign combinations. Generally, one has 4^{pq} combinations for $\Delta G \in \mathbb{C}^{p \times q}$. For the case at hand, i.e. the active damping of the smart panel with $q = 4$ actuators and $p = 4$ sensors, that would result in approximately 4.3 billion combinations at every frequency sample ω_n. Just recently, a more elaborated method has been proposed by Ahn [2] which requires only

2^{p^2+3p-2} instead of 4^{p^2} tests for a square ($p \times p$) matrix. For the present example, this still amounts to about 67 million norm evaluations per frequency.

Robustness Test via Small-Gain Theorem

The following simple approach is proposed to circumvent this problem. It is assumed that every entry of the uncertain matrix $\Delta\boldsymbol{G}$ takes its maximum allowed value, i.e. the uncertain matrix $\Delta\boldsymbol{G}$ is replaced by the certain matrix $\Delta\boldsymbol{G}_{\max}$. The additive uncertainty weight w_{A} shall then be given by the Frobenius norm of $\Delta\boldsymbol{G}_{\max}$,

$$w_{\mathrm{A}}(\mathrm{e}^{\mathrm{j}\omega_n}) = \|\Delta\boldsymbol{G}_{\max}(\mathrm{e}^{\mathrm{j}\omega_n})\|_{\mathrm{F}} = \sqrt{\sum_{i=1}^{p}\sum_{j=1}^{q} |\Delta G_{\max,ij}(\mathrm{e}^{\mathrm{j}\omega_n})|^2}. \tag{4.17}$$

This ensures that $\|\Delta\boldsymbol{G}_{\max} \,/\, w_{\mathrm{A}}\|_\infty \leq 1$, because the maximum singular value of a matrix is known to be bounded from above by its Frobenius norm, since it also holds $\|\boldsymbol{A}\|_{\mathrm{F}} = \sqrt{\sum_i \sigma_i^2(\boldsymbol{A})}$ for any complex-valued $\boldsymbol{A}$ [168]. In addition to that, it surely holds $\|\Delta\boldsymbol{G}\|_{\mathrm{F}} \leq \|\Delta\boldsymbol{G}_{\max}\|_{\mathrm{F}}$, since the Frobenius norm of $\Delta\boldsymbol{G}$ is bound to decrease if its entries differ in any allowed way from $\Delta\boldsymbol{G}_{\max}$. All in all, the choice (4.17) guarantees $\|\Delta_{\mathrm{f}}\|_\infty \leq 1$, as required.

It can then be concluded from Figs. 4.4 and 4.5 that the system $\boldsymbol{M}$ of the $\boldsymbol{M}\Delta$-structure, which is associated with the fully occupied uncertainty matrix Δ_{f}, is given by

$$\boldsymbol{M}_{\mathrm{f}} = w_{\mathrm{A}}\boldsymbol{K}(\mathbf{I} - \boldsymbol{G}\boldsymbol{K})^{-1}. \tag{4.18}$$

The small-gain theorem [64, 168] now states that the closed-loop system with fully occupied uncertainty Δ_{f} is robustly stable if and only if $\|\boldsymbol{M}_{\mathrm{f}}\|_\infty < 1$. It must be remarked at this point that the necessity of the small-gain condition only holds if $\|\Delta_{\mathrm{f}}\|_\infty$ may indeed reach the value one. Since our proposed normalization procedure for $\Delta\boldsymbol{G}$ is conservative, we have $\|\Delta_{\mathrm{f}}\|_\infty < 1$, and the small-gain condition is in fact only sufficient.

Robustness Test via μ-Analysis

Since the small-gain theorem gives only a sufficient condition for our considered application, one may want to make a less conservative robustness analysis when the small-gain test fails. This can be done by μ-analysis which provides a necessary and sufficient condition in the case of a block-diagonal uncertainty matrix Δ.

To this end, the system description containing the transfer matrix $\boldsymbol{G}$ and the unnormalized, fully populated uncertainty matrix $\Delta\boldsymbol{G}$ is transformed into a constant matrix $\tilde{\boldsymbol{M}}$ and a diagonal uncertainty matrix $\tilde{\Delta}_{\mathrm{d}}(\mathrm{e}^{\mathrm{j}\omega_n}) = \bigoplus\{\mathrm{vec}\,\Delta\boldsymbol{G}(\mathrm{e}^{\mathrm{j}\omega_n})\}$ such that the input-output behavior of the structure $\boldsymbol{G} + \Delta\boldsymbol{G}$ is equivalent to the one of $\mathcal{F}_{\mathrm{u}}(\tilde{\boldsymbol{M}}, \tilde{\Delta}_{\mathrm{d}})$, where $\mathcal{F}_{\mathrm{u}}(\cdot,\cdot)$ denotes the upper LFT of two transfer matrices. The matrix $\tilde{\boldsymbol{M}}$ has the following structure for a general $\boldsymbol{G} \in \mathbb{C}^{p\times q}$,

$$\tilde{\boldsymbol{M}}(\mathrm{e}^{\mathrm{j}\omega_n}) = \begin{pmatrix} \mathbf{0}_{pq\times pq} & \mathbf{I}_q \otimes \mathbf{1}_{p\times 1} \\ \mathbf{1}_{1\times q} \otimes \mathbf{I}_p & \boldsymbol{G}(\mathrm{e}^{\mathrm{j}\omega_n}) \end{pmatrix}. \tag{4.19}$$

The equivalence of $\boldsymbol{G} + \Delta\boldsymbol{G}$ and $\mathcal{F}_\mathrm{u}\{\tilde{\boldsymbol{M}}, \tilde{\Delta}_\mathrm{d}\}$ can be verified by considering that the general upper LFT of two matrices $\boldsymbol{M} = \begin{pmatrix} \boldsymbol{M}_{11} & \boldsymbol{M}_{12} \\ \boldsymbol{M}_{21} & \boldsymbol{M}_{22} \end{pmatrix}$ and Δ is given by $\mathcal{F}_\mathrm{u}(\boldsymbol{M}, \Delta) = \boldsymbol{M}_{22} + \boldsymbol{M}_{21}\Delta(\mathbf{I} - \boldsymbol{M}_{11}\Delta)^{-1}\boldsymbol{M}_{12}$, see for example [168].

By contrast to the fully populated uncertainty matrix Δ_f used with the small-gain theorem, the diagonal matrix $\tilde{\Delta}_\mathrm{d} = \boldsymbol{W}_\mathrm{A}\Delta_\mathrm{d}$ can be easily normalized such that $\|\Delta_\mathrm{d}\|_\infty \leq 1$ by dividing each element by its maximum absolute value. We therefore set the uncertainty normalization matrix to

$$\boldsymbol{W}_\mathrm{A}(\mathrm{e}^{\mathrm{j}\omega_n}) = \left|\tilde{\Delta}_{\mathrm{d,max}}(\mathrm{e}^{\mathrm{j}\omega_n})\right| = \bigoplus \left|\mathrm{vec}\,\Delta\boldsymbol{G}_{\mathrm{max}}(\mathrm{e}^{\mathrm{j}\omega_n})\right|. \tag{4.20}$$

Since the weighting matrix $\boldsymbol{W}_\mathrm{A}$ is a certain matrix, it must be absorbed into the $\tilde{\boldsymbol{M}}$ structure. This can be done by changing the lower-left block in (4.19) to

$$\tilde{\boldsymbol{M}}_{21} = (\mathbf{1}_{1\times q} \otimes \mathbf{I}_p)\boldsymbol{W}_\mathrm{A}. \tag{4.21}$$

In order to finally arrive at the $\boldsymbol{M}\Delta$-structure shown in Fig. 4.4, $\tilde{\boldsymbol{M}}$ and controller $\boldsymbol{K}$ are absorbed into $\boldsymbol{M}_\mathrm{d}$ by $\boldsymbol{M}_\mathrm{d} = \mathcal{F}_\mathrm{l}\{\tilde{\boldsymbol{M}}, \boldsymbol{K}\}$.

The overall closed-loop system $\mathcal{F}_\mathrm{u}(\boldsymbol{M}_\mathrm{d}, \Delta_\mathrm{d})$ is robustly stable iff the structured singular value μ of $\boldsymbol{M}_\mathrm{d}$ with respect to the uncertainty structure Δ_d is smaller than one on the unit circle, i.e.

$$\mu_{\Delta_\mathrm{d}}\left(\boldsymbol{M}_\mathrm{d}(\mathrm{e}^{\mathrm{j}\omega})\right) < 1 \;\forall\; \omega \in [-\pi, \pi]. \tag{4.22}$$

In general, the function $\mu_\Delta(\boldsymbol{M})$ for some block-diagonal uncertainty Δ with all blocks being complex is given by

$$\mu_\Delta\left(\boldsymbol{M}(\mathrm{e}^{\mathrm{j}\omega})\right) = \max_{\Delta, \bar{\sigma}(\Delta)\leq 1} \rho\left(\boldsymbol{M}(\mathrm{e}^{\mathrm{j}\omega})\Delta(\mathrm{e}^{\mathrm{j}\omega})\right), \tag{4.23}$$

where $\rho(\cdot)$ denotes spectral radius of a matrix. In case that the structured uncertainty Δ contains also real-valued blocks, the general definition of μ must be applied, which is more complex than (4.23) [168]. But even in the case considered here, the evaluation of (4.23) is a non-convex optimization problem[3]. However, it can be shown that a frequency-wise upper bound on μ can be computed by solving a convex optimization problem [168]. Algorithms for the computation of lower bounds also exist. With the help of these bounds, the structured singular value can be iteratively computed to the desired accuracy. One may consult [64] and [197] for details on the calculation of the structured singular value μ.

If the structured singular value is computed with sufficient accuracy, it is clear that μ-analysis is less conservative than the small-gain procedure for the case at hand, since no conservatism is introduced during uncertainty normalization. Thus, one can expect $\mu_{\Delta_\mathrm{d}}(\boldsymbol{M}_\mathrm{d}(\mathrm{e}^{\mathrm{j}\omega_n})) < \bar{\sigma}(\boldsymbol{M}_\mathrm{f}(\mathrm{e}^{\mathrm{j}\omega_n})) \;\forall\; \omega \in [-\pi, \pi]$. This will be verified for the experimental example to be presented in Sec. 4.4.
The reader is reminded that a full uncertainty matrix may be viewed as a block-diagonal matrix with only one block. Thus, μ-analysis treats small-gain theory as a special case. Indeed, one can show that for a fully populated, complex Δ_f, it holds $\mu_{\Delta_\mathrm{f}}(\boldsymbol{M}) = \bar{\sigma}(\boldsymbol{M})$ [168].

---

[3] Maximization can only be a convex optimization problem if the function is concave which $\rho(\cdot)$ clearly is not.

It was already pointed out in Sec. 3.5 that robustness analysis can be done for the parametric model $\boldsymbol{G}$ and its associated uncertainty description $\Delta\boldsymbol{G}$, as well as for the non-parametric model together with its uncertainty, $\hat{\boldsymbol{G}}$ and $\Delta\hat{\boldsymbol{G}}$. The uncertainty of the parametric model is computed from the uncertainty of the non-parametric model by an overbounding procedure. This introduces conservatism in the uncertainty description and consequently leads to conservative results for robustness analysis. For that reason, it is recommended to test robustness of the control loop which is made up by the controller $\boldsymbol{K}$ and the non-parametric model. This will also be exemplified with experimental results in the next section.

4.4 Examples

This section illustrates certain aspects of the proposed active damping methodology by simulation and experimental examples. The experimental verification will be done for the smart panel testbed for which identification results were shown at the end of the last chapter. The simulation results will be shown first.

4.4.1 Simulation Results

Active damping of the smart panel configuration shown in Fig. 3.1 is considered. A simulation model which contains all 17 plate bending modes up to 500 Hz is employed for control design. The modal damping ratio of all modes is set to 1 %. The goal of AVC is to actively damp the first 12 modes which span the frequency range up to 400 Hz. Four actuator patches and the same number of nearly collocated accelerometers are used in the control loop. For validation purposes, the plate will be excited by a point force which is able to excite all 17 bending modes, as also indicated in Fig. 3.1. The well-known formulae for calculating a continuous-time, strictly proper $\mathcal{H}_2$ optimal controller are utilized [162, 197].

The noise weight is set to $\mathbf{I}W_{\mathrm{n}}$ with $W_{\mathrm{n}} = 0.1$, while the vector sequences $\boldsymbol{w}_1$ and $\boldsymbol{w}_2$ are white and of unit intensity, as mentioned in Sec. 4.3.2. The disturbance influence matrix is set to unity. The parameters of the control effort weight are chosen to penalize low and high frequency controller action, because these are the regions where model uncertainty is typically high, compare Sec. 3.6.2. In addition to that, controller action above 400 Hz must be minimized to prevent spillover effects. The magnitude of the utilized control effort weight is displayed in Fig. 4.6.
The performance weight is selected as explained in Sec. 4.3.2 by applying (4.14). The modes to be damped are weighted relatively to each other by the matrix $\tilde{\boldsymbol{W}}_{\mathrm{p},2}$ which is simply taken as $\bigoplus\{3\ \mathbf{1}_{1\times 11}\}$. The performance of this non-physical weighting is compared with energy-based weighting in Fig. 4.7. There, the magnitude of the transfer function from the disturbance point force to the collocated accelerometer, $T_{a1,f1}$, is shown. For the energy-based design, the weighting of the modal velocities is chosen such that the RMS value of the performance variables $\boldsymbol{z}_1$ equals that of the kinetic energy contributed by the first twelve modes. The control effort weight shown in Fig. 4.6 is scaled for energy-based weighting such that the same peak value of control

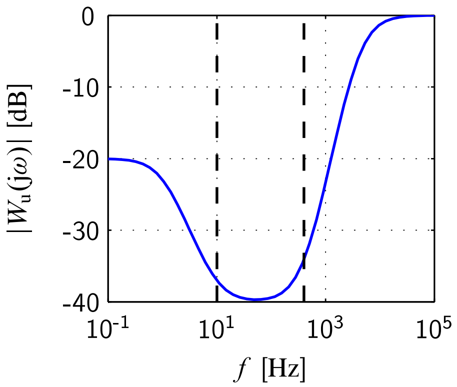

Figure 4.6: Magnitude of control effort weight. The frequency range from 10 Hz to 400 Hz is indicated by vertical lines.

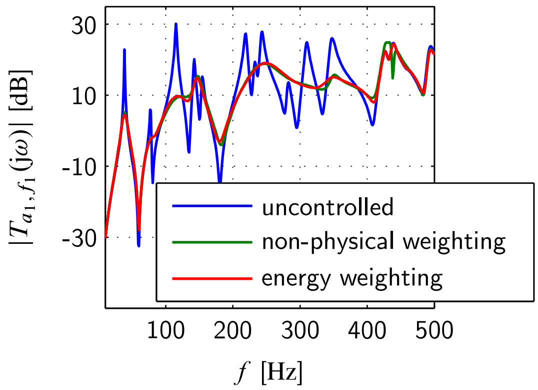

Figure 4.7: Control performance for non-physical and energy-based performance weighting.

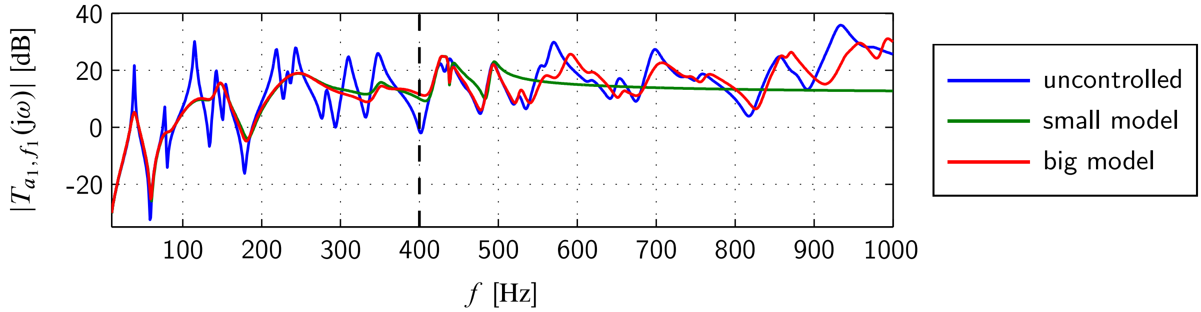

Figure 4.8: Performance of the controller based upon the small model with 17 modes when interacting with the big model with 36 modes.

effort is reached for both designs, which is 139 V for a disturbance of 1 N. Obviously, the proposed method for the selection of W_p is able to produce almost identical performance results as with energy-based weighting, but for models with arbitrary state basis.

Another important point to look at is the robustness of the control design to unmodeled dynamics. To this end, the strictly proper controller which has been designed based upon the 500 Hz model is tested with a 1000 Hz model containing 36 modes. Thus, the big model contains 19 extra modes which were not taken into account during control design. The results are displayed in Fig. 4.8. led dynamics. To this end, the strictly proper controller which has been designed based upon the 500 Hz model is tested with a 1000 Hz model containing 36 modes. Thus, the big model contains 19 extra modes which were not taken into account during control design. The results are displayed in Fig. 4.8. One can see that the performance predicted by the small model almost coincides with the achieved performance for the big model below 500 Hz. In addition to that, no significant amplification of modes above 500 Hz can be found compared to the uncontrolled system. If the penalization of high frequency controller action was increased, the curves of the uncontrolled and

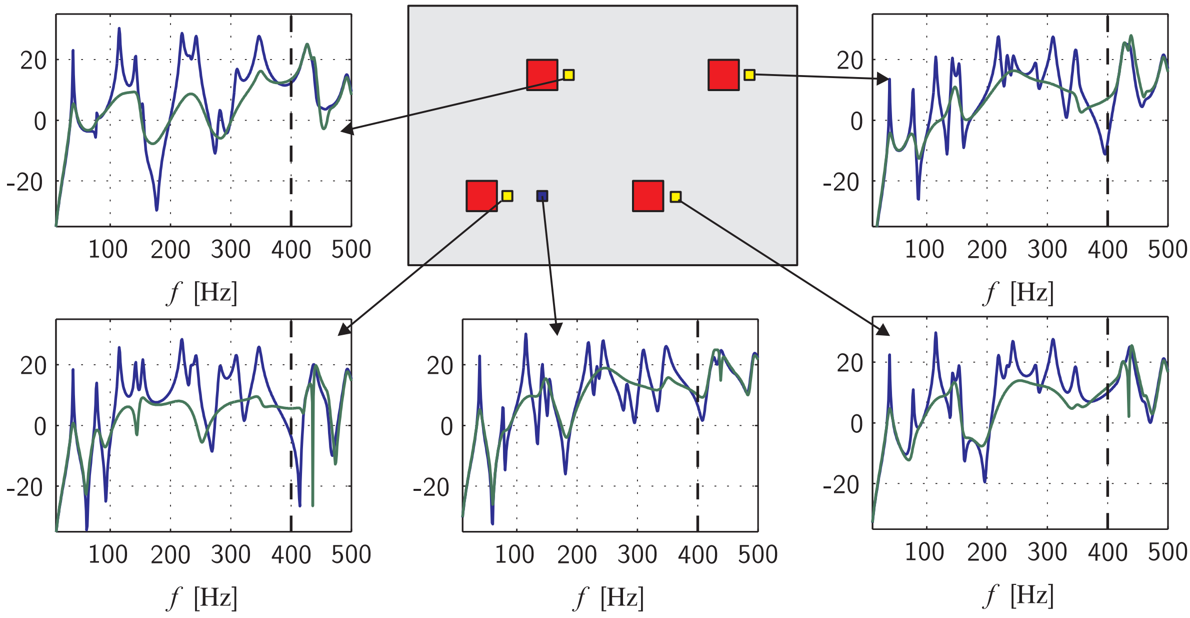

Figure 4.9: Magnitudes of transfer functions from disturbance force to the four accelerometers which are used in the control loop and the one collocated to the disturbance (simulation); ordinate values in dB.

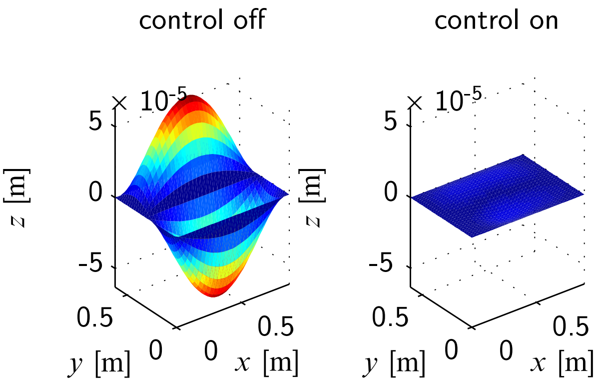

Figure 4.10: Vibration mode shape at 115 Hz.

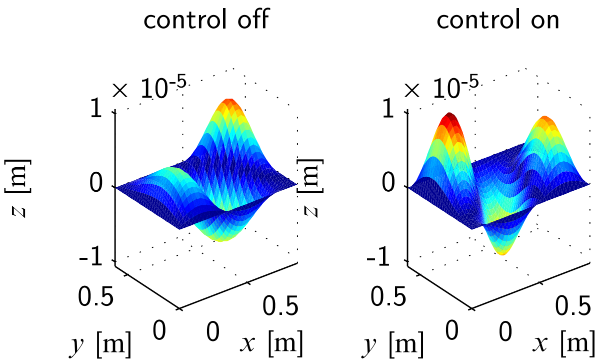

Figure 4.11: Vibration mode shape at 148 Hz.

controlled big system would draw near in this frequency range. For lower penalization, the loop would become unstable with the big model.

The global impact of the designed control loop can be judged from the plots shown in Fig. 4.9, where the transfer functions from the disturbance force to all five accelerometers are shown. All targeted resonances are significantly damped.

Further insights can be gathered by looking at the vibration mode shapes at the eigenfrequencies of the undamped, uncontrolled system. Figure 4.10 shows the vibration mode shapes for the third eigenfrequency at 115 Hz for the uncontrolled and controlled state at the time instant of their respective maximum deflections. A reduction of the vibration peak value from 63 µm to 5 µm is achieved when the structure is excited by a point force of 1 N. The third resonance is the frequency where the greatest relative amount of peak-level reduction is achieved in the targeted frequency

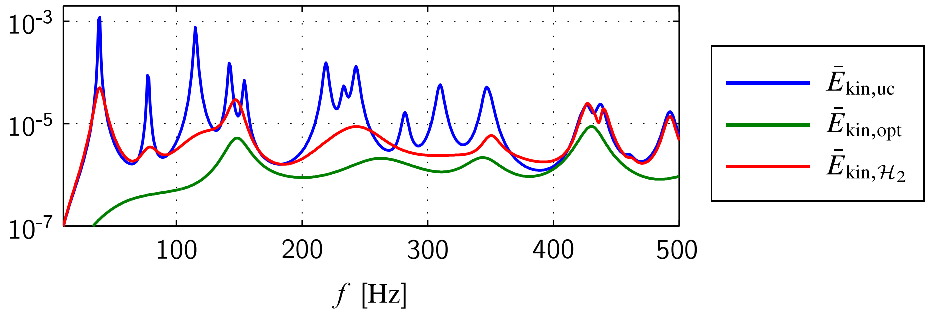

Figure 4.12: Time-average kinetic energy in uncontrolled state and for controlled system; ordinate values in Joule.

band. The greatest absolute amount of peak-level reduction is achieved for the first resonance from 374 µm to 48 µm.
As already mentioned, it may well happen for a narrow-band or harmonic disturbance to be amplified by the controller. This can for example be observed when looking at the different plots of Fig. 4.9 in the vicinity of 176 Hz. There, an increase in vibration levels is indicated for some transfer paths. When looking at the peak vibration level of the complete surface however, it is found that the biggest relative amplification of harmonic disturbances would be observed at 148 Hz. At this frequency, the peak vibration level would slightly rise from 9 µm to 11 µm under control. This vibration mode shape is displayed in Fig. 4.11.

The presented controller has been designed without employing any knowledge of the location and frequency spectrum of the disturbance. The only design parameters were the targeted frequency range of the system and the limitation of control effort. It is interesting to compare the performance of this controller with a theoretical optimum. In this case, the theoretical optimum shall be characterized by a controller which is designed to specifically cancel out a monofrequent disturbance with known frequency and known point of attack. The optimum control voltages for this case can be easily calculated at every single frequency as shown in App. C.4. There, phasor notation is used for compact notation which is introduced in App. C.3. Figure 4.12 shows the time-average kinetic energy of the 500 Hz plate model with and without control. The $\mathcal{H}_2$ optimal controller is compared with the frequency-wise optimal control voltages to minimize kinetic energy. Here, the performance loss due to low information on the disturbance characteristics is obvious. Nevertheless, if some information on the disturbance is available, it can be included into the generalized plant to further reduce this discrepancy.

Lastly, some remarks on singular $\mathcal{H}_2$ control are in order. It was already pointed out in Sec. 4.3.2 that the presence of the measurement noise weight $\boldsymbol{W}_{\mathrm{n}}$ also serves to regularize the control design problem. When it is set to zero, the $\mathcal{H}_2$ problem becomes singular[4]. One can show by checking the existence and uniqueness conditions given in [162] that a strictly proper optimal controller does not exist in this case. However, a proper, unique $\mathcal{H}_2$ optimal controller does exist, and it can be calculated by solving two linear matrix inequality (LMI) problems. The performances of

---

[4] The continuous-time $\mathcal{H}_2$ problem will always become singular when the noise weight is set to zero. This is due to the different existence conditions compared to the discrete-time case, see [162].

Table 4.1: Parameters of the control effort weight W_u, compare (4.11).

Parameter	f_1	$f_{\mathrm{D}1}$	$f_{\mathrm{D}2}$	f_2	n_1	n_2
Value	0.1 Hz	10 Hz	400 Hz	4000 Hz	1	1

Table 4.2: Parameters of the performance weight $\tilde{\boldsymbol{W}}_{\mathrm{p}2}$, compare Sec. 4.3.2.

i	1	2	3	4	5	6	7	8	9	10	11	12	13	14	15
$\tilde{W}_{\mathrm{p}2}^{(i,i)}$	8	8	2	6	6	2	3	2	12	12	1	5	6	5	5

the singular and the regular controllers can be compared by looking at their achieved closed-loop norms. The regular controller achieves $\|\boldsymbol{T}_{zw}\|_2 = 5.02$, but this generalized plant is comprised of the inputs $\boldsymbol{w}_1$ and $\boldsymbol{w}_2$. When the sensor noise input $\boldsymbol{w}_2$ is dropped, on gets $\|\boldsymbol{T}_{zw1}\|_2 = 4.64$. The singular controller achieves a performance of $\|\boldsymbol{T}_{zw1}\|_2 = 4.50$, which is an improvement of 3 % compared to the regular controller. Not surprisingly, the plots shown in Fig. 4.9 for the regular controller almost coincide with those of the singular controller. Because of the low performance gain, compared to the tricky existence conditions and increased computational effort, singular $\mathcal{H}_2$ control is not further considered in this thesis.

4.4.2 Experimental Results

Finally, experimental results will be shown for the active damping of the smart panel testbed which has already been introduced in the last chapter. The goal of AVC will be the same here as for the simulation examples. The real testbed also exhibits 17 resonances up to 500 Hz of which the first twelve are contained in the frequency band from zero to 400 Hz. These will be targeted by AVC with the same setup for actuators, sensors, and disturbance force as in the simulations, see also Figs. 3.14 and 3.15.

The model $\boldsymbol{G}(\mathrm{e}^{\mathrm{j}\omega_n})$ for the transfer paths from the actuators to the sensor outputs which has been presented in the last chapter will be employed for control design. It also incorporates the dynamics of actuators, sensors, amplifiers, and low-pass filters, compare Fig. 3.1. Robust stability of the control loop will be checked via both small-gain theorem and μ-analysis for the identified uncertainty $\Delta\boldsymbol{G}(\mathrm{e}^{\mathrm{j}\omega_n})$.

Since the problem is set in the discrete time domain, the formulae presented in App. C.2 will be used for controller computation. As already mentioned in the last chapter, the cut-off frequencies of the reconstruction and anti-aliasing filters are set to 600 Hz, and the sampling rate is $T_\mathrm{s} = 0.6\,\mathrm{ms}$.

The parametrization of the different weighting functions is done exactly the same way as in the simulation examples. The noise weight is again set to $\boldsymbol{W}_\mathrm{n} = \mathbf{I}W_\mathrm{n}$ with $W_\mathrm{n} = 0.1$. The parameters of the control effort and performance weights are given in Tables 4.1 and 4.2, respectively. The time constants of (4.11) are computed from the frequencies given in Table 4.1 by $T = {}^{1}\!/_{2\pi f}$. The performance weight $\tilde{\boldsymbol{W}}_{\mathrm{p}2}$ is of dimension (15×15) and not (12×12), as could be expected. This is due to the fact that the black-box model contains three extra "mathematical modes" in the targeted

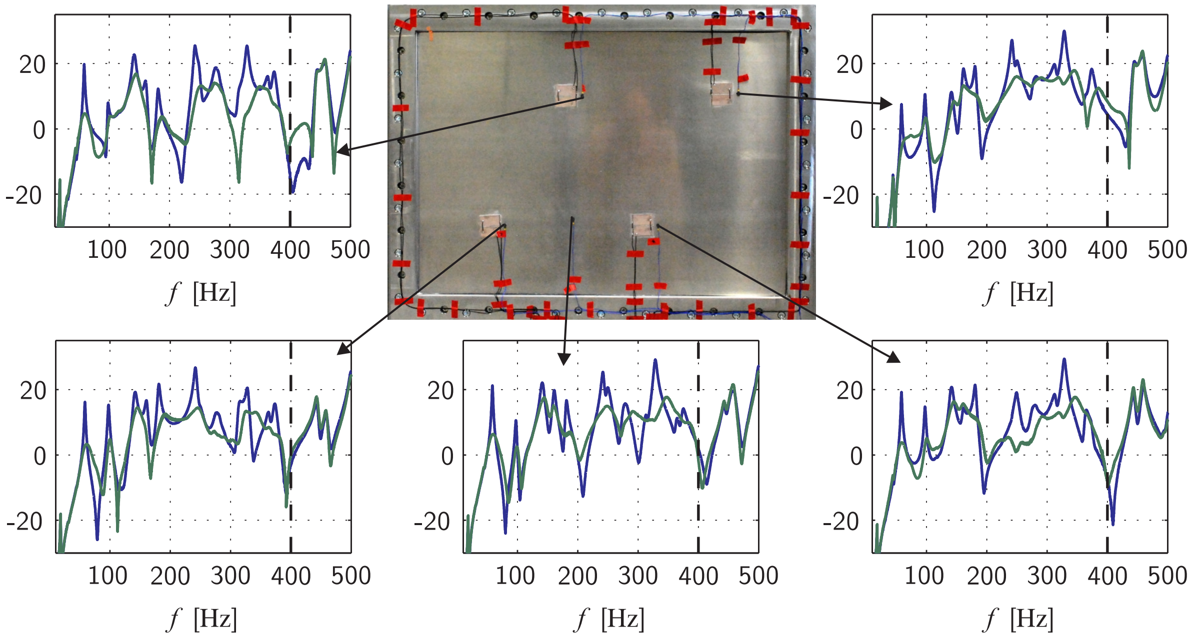

Figure 4.13: Magnitudes of transfer functions from disturbance force to the four accelerometers which are used in the control loop and the one collocated to the disturbance (experiment); ordinate values in dB.

frequency band in order to better fit the measured FRFs of the real testbed. These mathematical modes have no direct interpretation in terms of the twelve "physical" modes of the plate, but have to be considered for control design based upon the identified model. The parameters of $\tilde{\boldsymbol{W}}_{\mathrm{p}2}$ have been found by trial-and-error in order to ensure high performance while maintaining robust stability. Nevertheless, it is sensible to argue that the finding of these numbers is still less cumbersome than searching for appropriate pole locations in a pole-placement design, given alone the fact that one then needs to select two parameters per pole pair and not only one.
Considering the size of the identified plant model $\boldsymbol{G}(z)$ of $n = 100$, compare Sec. 3.6.2, and the order of W_{u}, the generalized plant $\boldsymbol{P}(z)$ has 108 states. This is also the size of the resulting controller $\boldsymbol{K}(z)$. With the help of frequency-weighted balanced truncation [146, 197], the controller can be reduced to order 40 without noticeable loss of performance.

The performance of this controller shall now be illustrated. In analogy to Fig. 4.9, figure 4.13 shows the magnitudes of the transfer functions from the disturbance to the five accelerometers which are placed on the panel. By comparing the curves for the uncontrolled system in the two figures, one can again recognize that the simulation model approximates well both the magnitude and the qualitative curve shape of the real system. Just the resonances are generally lower because of the simplified plate boundary condition in the simulation model, as pointed out in Sec. 2.5.
The greatest peak value of the transfer functions from disturbance to the four control outputs is 38.6 dB and is reached at first resonance. This implies that a harmonic disturbance with this frequency and amplitude 1 N leads to a maximum patch voltage of 85.4 V.

With the help of a laser scanning vibrometer, the plate surface is scanned at $N = 81$ points located on a regular 9×9 grid. With this data, the surface motion can be reconstructed for both

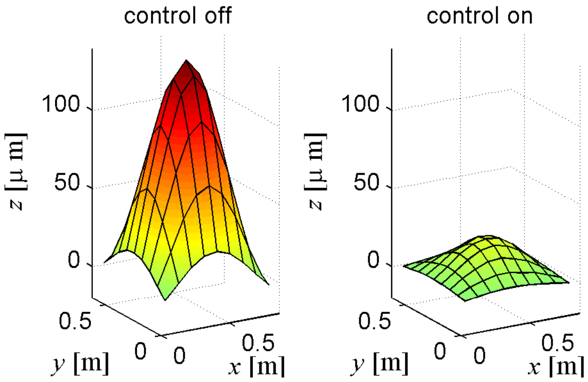

Figure 4.14: Vibration mode shape at first resonance.

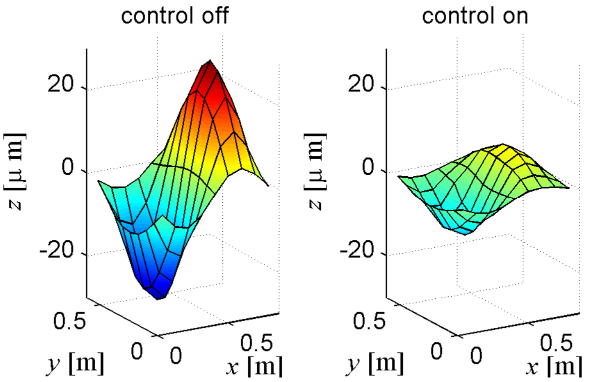

Figure 4.15: Vibration mode shape at second resonance.

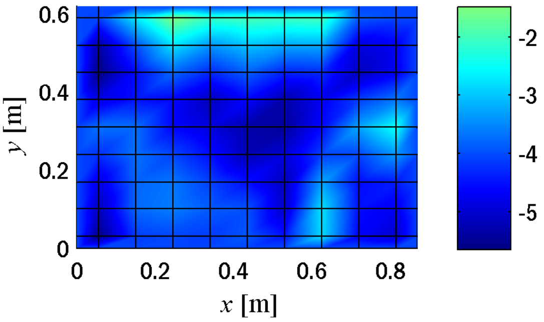

Figure 4.16: Surface plot of the performance measures (4.24) in dB.

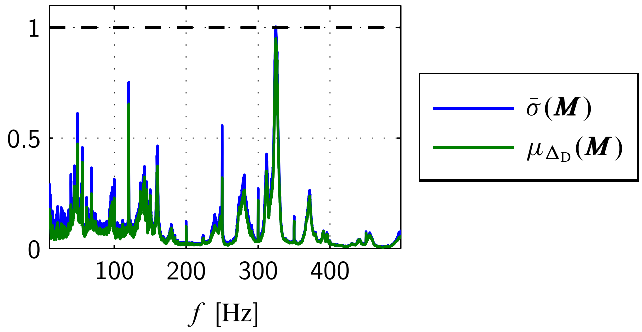

Figure 4.17: Results of robust stability analysis.

the uncontrolled and controlled system. The open- and closed-loop vibration mode shapes for the first two resonances are displayed at the time instant of their respective maximum deflection in Figs. 4.14 and 4.15.

The frequency response from the disturbance force to the deflection at the ith discretization point shall be denoted by $H_{\mathrm{uc},i}$ for the uncontrolled and by $H_{\mathrm{c},i}$ for the controlled system. To get an overall impression of the achieved vibration reduction in the frequency band up to 400 Hz, the following measures are defined,

$$J_i = 20\lg\frac{\sum\limits_{\omega_n\in\Omega}\left|H_{\mathrm{c},i}(\mathrm{e}^{\mathrm{j}\omega_n})\right|}{\sum\limits_{\omega_n\in\Omega}\left|H_{\mathrm{uc},i}(\mathrm{e}^{\mathrm{j}\omega_n})\right|},\quad i = 1,\dots,N, \tag{4.24}$$

where Ω is the set of 1521 equidistant DFT samples within the interval from 20 Hz to 400 Hz. The values J_i are plotted in Fig. 4.16 and show that, apart from a small area at the upper boundary, reductions between 3.5 dB and 5.5 dB are achieved on average over the targeted frequency band.

Robust stability of the non-parametric model $\hat{\boldsymbol{G}}(\mathrm{e}^{\mathrm{j}\omega_n})$ with respect to its additive, non-parametric uncertainty $\Delta\hat{\boldsymbol{G}}(\mathrm{e}^{\mathrm{j}\omega_n})$ is checked with the two tests presented in Sec. 4.3.3. The resulting (structured) singular values are shown in Fig. 4.17 in the frequency range from 10 Hz to 500 Hz.

Theoretically, the trajectories of $\bar{\sigma}(\boldsymbol{M}_\mathrm{f}(\mathrm{e}^{\mathrm{j}\omega}))$ and $\mu_{\Delta_\mathrm{d}}(\boldsymbol{M}_\mathrm{d}(\mathrm{e}^{\mathrm{j}\omega}))$ would have to be calculated on the complete unit circle. This is not possible for two reasons. Firstly, the values of the frequency response of $\boldsymbol{M}$ are only available at discrete frequency samples, since they are computed via DFT from discrete-time signals. For that reason, the spacing of the frequency samples is chosen rather dense to be 0.16 Hz, in order to accurately reconstruct the singular value curves. Secondly, the identified model uncertainty is only reliable in the frequency range where the system has been sufficiently excited during the identification experiments, which was in the range from 20 Hz to 500 Hz, see 3.6.2. Nevertheless, this robust stability analysis is considered reliable because of the limitation of the closed-loop bandwidth by appropriate penalization of control effort.

One can see from the presented plots that the closed loop can be expected to be robustly stable, since the maximum of the structured singular value is 0.95 which is smaller than one, as required. For the plot of the greatest singular value of $\boldsymbol{M}_\mathrm{f}$, the maximum in the considered frequency range is 1.00. As expected, the curve of the structured singular value is slightly below that of the maximum singular value at all frequencies, which implies that this robustness test is less conservative. When the above computations are done with the frequency response of the parametric model $\boldsymbol{G}$ and its associated uncertainty $\Delta\boldsymbol{G}$, one gets the maxima 1.07 and 1.13 for μ-analysis and small-gain theorem, respectively. This exemplifies the conservatism of the uncertainty description of the parametric model.

4.5 Chapter Summary

This chapter was devoted to the presentation of an intuitive and effective design methodology for AVC. After having stated the predominant existing AVC concepts and their categorization into LAC and HAC designs, the assets of MIMO high-authority control were pointed out. The most important feature of HAC is the possibility to effectively damp more modes than there are available actuators and sensors. Then, the AVC problem, as it is interpreted in this thesis, was stated, and the design scheme was explained. At the heart of the concept is the generalized plant which allows to intuitively include knowledge of the disturbance spectrum and/or location, if available. The plant contains three weighting functions. For the performance weight, a new design was proposed which allows for a relatively easy parametrization. In addition to that, it was shown that the presented generalized plant leads to a regular $\mathcal{H}_2$ optimization problem which trivializes the existence and uniqueness conditions for the optimal controller. It was further explained how to utilize the uncertainty descriptions of the non-parametric and parametric models which were derived in the last chapter for robustness analysis. This analysis was performed with two different tests, which are complementary in terms of accuracy and computational effort. Finally, the control design methodology and its important aspects were illustrated by simulation and experimental results.

5 Active Structural Acoustic Control

This chapter deals with the control of structure-borne sound by means of active structural acoustic control. In the bulk of this chapter, an exterior acoustic problem is considered, i.e. it is assumed that the sound is radiated into arbitrary, possibly unbounded space such that the influence of the fluid on the structure is negligible. The best-studied example for this situation is the sound radiation of a planar structure into free space. This will be the starting point for introducing the concepts of local and global control of structure-borne sound fields, whereas the latter will be the focus of this chapter. To this end, a novel procedure for the experimental modeling of power transfer matrices will be provided, which permits the usage of effective optimal control techniques to explicitly minimize the emitted time-average sound power. At the end of this chapter, an interior acoustic problem, i.e. the sound transmission into enclosed spaces, is considered and suitable modifications for control design are given.

5.1 Basic Acoustic Quantities

We consider a flexible vibrating body in a linear acoustic environment in harmonic vibration with angular frequency ω. The fluid properties shall be homogeneous with density ρ_0. For ease of notation, the complex exponential representation, or phasor notation, of harmonic functions is applied, see App. C.3. It is assumed that there are no other noise sources present. Then, the complex sound pressure amplitude $\tilde{p}$ at any point $\boldsymbol{x}$ in space is given by [100]

$$\tilde{p}(\boldsymbol{x}, \omega) = \iint_S G(\boldsymbol{x}, \boldsymbol{x}_\mathrm{S}, \omega)\, \dot{\tilde{w}}(\boldsymbol{x}_\mathrm{S}, \omega)\, \mathrm{d}S, \tag{5.1}$$

where $\dot{\tilde{w}}(\boldsymbol{x}, t)$ denotes the surface velocity field of the vibrating body with surface area S, and $\boldsymbol{x}_\mathrm{S}$ denotes some location on S. The term G is known as *Green's function* and depends on the geometry of the vibrating body, the fluid properties, and the acoustic environment. Its value is equal to the complex sound pressure amplitude at point $\boldsymbol{x}$ caused by an acoustic monopole of unit strength at location $\boldsymbol{x}_\mathrm{S}$ vibrating with frequency ω. Alternatively, in a control context, $G(\boldsymbol{x}, \boldsymbol{x}_\mathrm{S}, \omega)$ may be seen as the frequency response of the transfer function from $\boldsymbol{x}_\mathrm{S}$ to $\boldsymbol{x}$ at frequency ω.

Assuming that a pressure field $p(\boldsymbol{x}, t)$ of arbitrary time-dependence is known, the particle velocity field $\boldsymbol{v}(\boldsymbol{x}, t) = (v_x, v_y, v_z)^\mathrm{T}$ can be calculated from the relationship (2.17),

$$\nabla p(\boldsymbol{x}, t) = -\rho_0 \frac{\partial \boldsymbol{v}(\boldsymbol{x}, t)}{\partial t}. \tag{5.2}$$

In terms of harmonic quantities, $\tilde{p}(\boldsymbol{x}, \omega) = \hat{p}(\boldsymbol{x}, \omega)\, \mathrm{e}^{\mathrm{j}\varphi(\boldsymbol{x}, \omega)}$, we have

$$\nabla \tilde{p}(\boldsymbol{x}, \omega) = -\rho_0\, \mathrm{j}\, \omega \tilde{\boldsymbol{v}}(\boldsymbol{x}, \omega), \tag{5.3}$$

with

$$\nabla \tilde{p}(\boldsymbol{x},\omega) = \left(\frac{\partial \hat{p}(\boldsymbol{x},\omega)}{\partial \boldsymbol{x}}\right)^{\mathrm{T}} \mathrm{e}^{\mathrm{j}\varphi} + \mathrm{j}\,\hat{p}(\boldsymbol{x},\omega)\mathrm{e}^{\mathrm{j}\varphi}\left(\frac{\partial \varphi}{\partial \boldsymbol{x}}\right)^{\mathrm{T}}. \tag{5.4}$$

In analogy to electrical network theory, an acoustic impedance can be defined which relates harmonic oscillations of pressure and particle velocity at a single point of an acoustic field,

$$Z(\boldsymbol{x},\omega) = \frac{\tilde{p}(\boldsymbol{x},\omega)}{\tilde{v}(\boldsymbol{x},\omega)}. \tag{5.5}$$

In a plane wave sound field, the impedance is known to be real and only dependent on the fluid properties, $Z_0 = \rho_0 c_0$, where c_0 denotes the speed of sound [69]. The quantity Z_0 is known as the *specific acoustic impedance*. In general, a real-valued acoustic point impedance implies that pressure and particle velocity are in phase.

For arbitrary sound fields, the relative phase between the phasors of pressure and particle velocity is termed *field angle* φ_{f},

$$\varphi_{\mathrm{f}}(\boldsymbol{x},\omega) = \angle\left\{\tilde{p}(\boldsymbol{x},\omega), \tilde{v}(\boldsymbol{x},\omega)\right\}. \tag{5.6}$$

The product of the two acoustic quantities pressure and particle velocity gives the energy of the sound field per unit area. This quantity is known as *sound intensity*,

$$\boldsymbol{I}(\boldsymbol{x},t) = p(\boldsymbol{x},t)\boldsymbol{v}(\boldsymbol{x},t), \tag{5.7}$$

and its time-average in the case of harmonic time dependence is given as

$$\bar{\boldsymbol{I}}(\boldsymbol{x}) = \frac{1}{2}\Re\left\{\tilde{p}(\boldsymbol{x})\tilde{\boldsymbol{v}}^{*}(\boldsymbol{x})\right\}. \tag{5.8}$$

The integral of the normal component of the intensity, $I_{\mathrm{n}} = p v_{\mathrm{n}}$, over any closed surface A including the sound sources gives the emitted *sound power*,

$$P(t) = \oint\!\!\!\oint_A I_{\mathrm{n}}(\boldsymbol{x},t)\,\mathrm{d}A. \tag{5.9}$$

Its time average is bound to be non-negative and is given by

$$\bar{P} = \oint\!\!\!\oint_A \bar{I}_{\mathrm{n}}(\boldsymbol{x})\,\mathrm{d}A. \tag{5.10}$$

5.2 Sound Radiation of a Baffled Planar Structure into Free Space

The Green's function appearing in (5.1) is hard to determine in practice. It may be derived for given acoustic boundary conditions by the *Kirchhoff-Helmholtz integral equations* [70]. However, these are in general only solvable by numerical means. There exist very few situations that allow

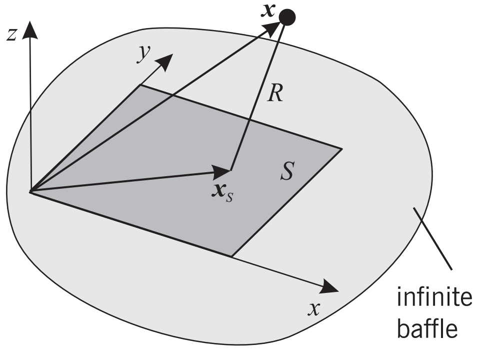

Figure 5.1: A baffled planar structure for which Rayleigh's integral formula applies.

for an analytic solution. The most important one is the case of a planar structure in an infinite baffle radiating into free space, see Fig. 5.1. Then, the *Rayleigh integral* applies [70],

$$\tilde{p}(\boldsymbol{x},\omega) = \frac{\mathrm{j}\omega\rho_0}{2\pi}\iint_S \frac{\tilde{\dot{w}}(\boldsymbol{x},\omega)\mathrm{e}^{-\mathrm{j}k\boldsymbol{R}}}{R}\,\mathrm{d}S, \tag{5.11}$$

where k denotes the acoustic wave number, $k = \frac{\omega}{c_0}$. The scalar R is given by the distance between the location $\boldsymbol{x}$ where the pressure is evaluated, and some point $\boldsymbol{x}_\mathrm{S}$ on the structural surface,

$$R = \|\boldsymbol{x} - \boldsymbol{x}_\mathrm{S}\|_2. \tag{5.12}$$

Comparison with (5.1) shows that in this case

$$G(\boldsymbol{x},\boldsymbol{x}_\mathrm{S},\omega) = \frac{\mathrm{j}\omega\rho_0}{2\pi R}\mathrm{e}^{-\mathrm{j}k\boldsymbol{R}}. \tag{5.13}$$

Although Green's function is known in this special case, the integral (5.11) is not analytically solvable for arbitrary geometries S and/or observer points $\boldsymbol{x}$.

Assuming that the vibrating body admits a description in modal form, its velocity profile may be expanded as

$$\tilde{\dot{w}}(x,y,\omega) = \sum_{i=1}^{\infty} \tilde{\dot{\eta}}_i(\omega) W_i(x,y), \tag{5.14}$$

with $\dot{\eta}_i(t)$ being the ith modal velocity and $W_i(x,y)$ the corresponding mode shape. For the case of a simply-supported rectangular plate, the mutually orthogonal mode shapes are given as

$$W_i = A_{\mathrm{norm,S},i}\sin\left(\frac{n_{\mathrm{S},x}\pi x}{l_x}\right)\sin\left(\frac{n_{\mathrm{S},y}\pi y}{l_y}\right), \tag{5.15}$$

compare (2.45). In practice, only a finite number of n_S structural modes is considered. For compactness of notation, the modal amplitudes and mode shapes may be collected in the column vectors $\boldsymbol{\eta} = (\eta_1, \ldots, \eta_{n_\mathrm{S}})^\mathrm{T}$ and $\boldsymbol{W} = (W_1, \ldots, W_{n_\mathrm{S}})^\mathrm{T}$. It is mentioned that the Rayleigh integral is not analytically solvable for the mode shapes (5.15), but approximations for the case $R \gg \{l_x, l_y\}$ exist [70].

The energy of a vibrating structure in stationary motion can be measured by its time- and space-average squared velocity,

$$\overline{\overline{\dot{w}^2}} = \frac{1}{S} \iint_S \left(\frac{1}{T} \int_0^T \dot{w}^2(x, y, t)\, \mathrm{d}t \right) \mathrm{d}S, \tag{5.16}$$

where T is a suitable period of time. More precisely, $\overline{\overline{\dot{w}^2}}$ is proportional to the total energy which is stored in an undamped Kirchhoff plate in harmonic motion with frequency ω. This can be seen as follows. In an undamped flexible structure, kinetic and potential energy are periodically converted into each other with frequency 2ω. Their time average values are identical and equal to one half of the total energy, which is constant, i.e. $E_{\mathrm{tot}}(t) = \bar{E}_{\mathrm{tot}} = \bar{E}_{\mathrm{pot}} + \bar{E}_{\mathrm{kin}} = 2\bar{E}_{\mathrm{kin}}$. The kinetic energy consists of a translatory and a rotatory term, of which only the translatory term is present in Kirchhoff plate theory, thus one has with (2.27)

$$\bar{E}_{\mathrm{tot}} = 2\bar{E}_{\mathrm{trans}} = 2\frac{1}{T} \int_0^T \left(\frac{1}{2}\rho h \iint_S \dot{w}(x, y, t)^2\, \mathrm{d}S \right) \mathrm{d}t = \underbrace{\rho h S}_{=m}\, \overline{\overline{\dot{w}^2}}, \tag{5.17}$$

where m is the plate mass.

The ability of a structure to radiate sound can be judged by its *radiation efficiency*. This quantity is given by the time-average emitted sound power relative to its area, average mean-square velocity, and specific acoustic impedance,

$$\sigma_{\mathrm{R}} = \frac{\bar{P}}{S\overline{\overline{\dot{w}^2}} Z_0}. \tag{5.18}$$

It must be mentioned that the radiation efficiency is not an efficiency measure in a strict sense, i.e. its value is not per definition limited to the interval [0, 1]. However, it actually is below or very close to one in most practical applications [70].

Any sound-emitting structure suffers from energy drain due to radiation loss. For harmonic motion, this can be measured by the *radiation loss factor* which is defined as $\eta_{\mathrm{R}} = \bar{P}/\bar{E}_{\mathrm{tot}}\omega$ [70]. For the undamped Kirchhoff plate, this can be written as

$$\eta_{\mathrm{R}}(\omega) = \frac{\bar{P}(\omega)}{\bar{E}_{\mathrm{tot}}(\omega)\omega} \overset{\text{Kirchhoff}}{=} \frac{\rho_0}{\rho} \frac{c_0}{h\omega} \sigma_{\mathrm{R}}, \tag{5.19}$$

in view of equations (5.17) and (5.18). The radiation loss factor can be expected to be at most $1 \cdot 10^{-3}$ for engineering structures vibrating in air [70]. For the plate of the acoustic demonstrator vibrating at first resonance, the radiation loss factor is approximately $3 \cdot 10^{-10}$.

Some simulation results of a baffled plate are presented in App. D.1 to illustrate the stated interrelations of the above acoustic quantities.

5.3 Local and Global Control of Free Space Sound Fields

Large differences exist between local and global control of sound and vibration as far as measurement techniques and control paradigms are concerned, as already mentioned in Sec. 1.2. These

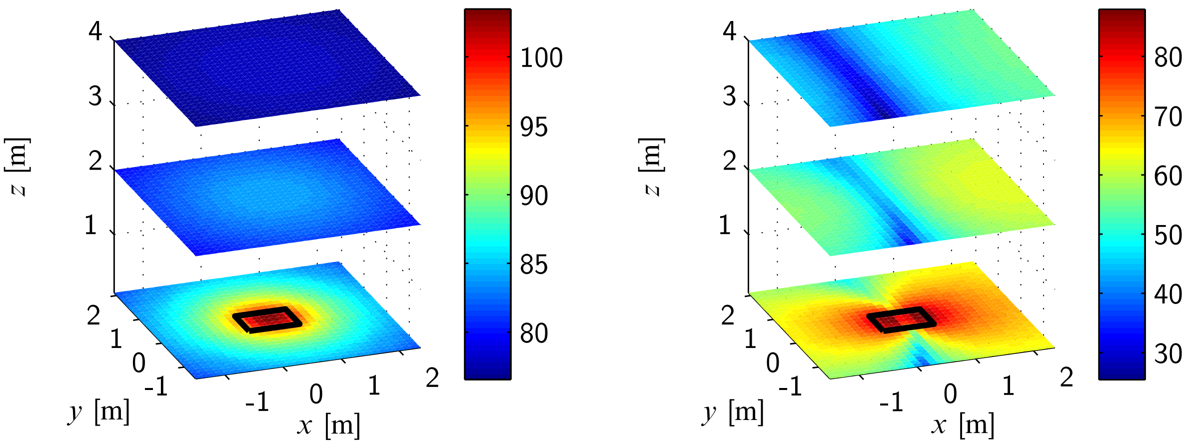

Figure 5.2: Uncontrolled sound pressure level (in dB) when the plate is excited at first (left) and second (right) resonance frequency.

differences shall now be further illuminated by a simulation example. The plate configuration shown in Fig. 3.1 is simulated when excited at the shaker position by a harmonic point force with amplitude 1 N. The force oscillates with either first or second plate resonance frequency. The goal of local sound field control shall be minimizing the RMS sound pressure at a specific location in the field. Opposed to that, global control shall be concerned with minimizing the emitted time-average sound power.

Assuming that the location and frequency spectrum of the disturbance excitation are known, the optimal control voltages for the piezo actuators can be calculated for both cases, see App. D.2. It is also shown there that local control of free-field radiation can, under certain circumstances, be perfectly achieved in theory. This is the case for the simulation example to be presented.

Figure 5.2 shows the uncontrolled sound pressure level[1] when the plate is excited at its first and second resonance frequency, respectively. The underlying model contains 17 modes and all modes where incorporated in the calculation of the resulting sound field. Minor differences can be seen compared to Fig. D.6 where only the respective resonant eigenmodes are incorporated.

For local control of the point with coordinates $[1.56, 1.00, 4.00]$ m, perfect cancellation can be achieved for the given simulation model and actuator configuration. This results in narrow zones of quiet, as can be seen in Fig. 5.3. An overall reduction of sound pressure is also achieved, but it is not of the same magnitude and homogeneity as that which is caused by global control, compare Fig. 5.4. These differences can also be seen when the emitted time-average sound powers for the two control strategies are calculated, see Fig. 5.5. Lastly, Fig. 5.6 shows the sound pressure level at the point which is targeted by local control when the global control scheme is used. For local control, the value is minus infinity at all shown frequencies.

This simulation example helps to highlight the respective advantages and drawbacks of the local and global control schemes. The reduction of sound pressure is the intuitive candidate for a control objective, since this is the physical quantity which is actually perceived by human ear. However,

---

[1] For details regarding the calculation of acoustic levels, see App. D.1.

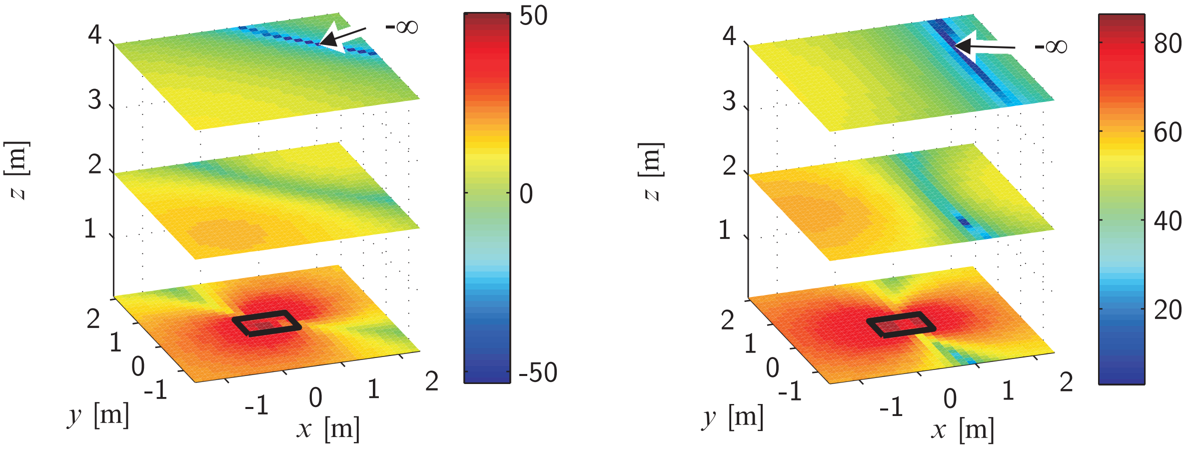

Figure 5.3: Sound pressure level (in dB) when the plate is locally optimal controlled at first (left) and second (right) resonance frequency.

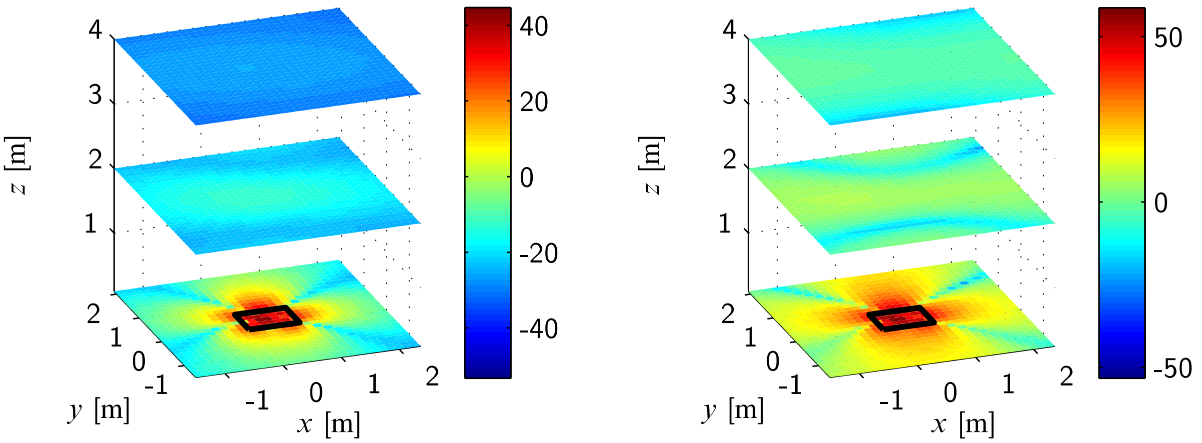

Figure 5.4: Sound pressure level (in dB) when the plate is globally optimal controlled at first (left) and second (right) resonance frequency.

if the location of the subject which is to be protected from noise harassment relative to the sound emitting structure is unknown or time-variant, local non-adaptive control fails to serve its purpose. In case that the subject's location could be tracked, adaptive control schemes can be successful, but this comes with additional complexity for both control and tracking. More importantly, the sound pressure field is subject to both the sound emitter and the acoustic environment. The acoustic environment of a sound emitting device may for example be changed by putting it in a room with different geometry or wall material. Acoustic boundary conditions may also frequently change by opening windows and doors, or by moving objects in a room. These changes may indeed cause instability in local control schemes [27].

A structure's emitted sound power, on the other hand, is independent of the acoustic environment as long as reflected waves have a negligible effect on the structure itself. This is usually satisfied for engineering structures vibrating in air. Thus, global sound power control offers the possibility to reduce noise on a spatially average level, regardless of the acoustic environment, but without

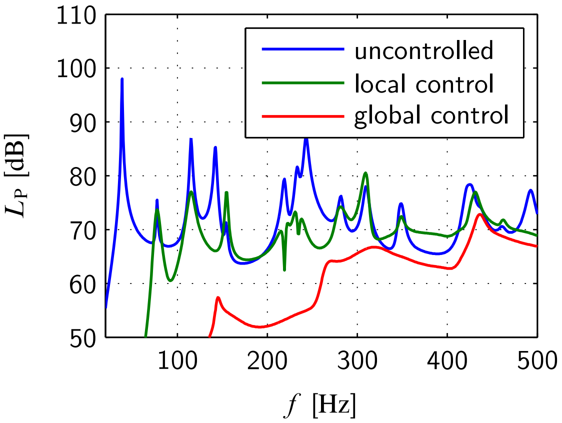

Figure 5.5: Sound power level $L_P = 10\lg\left(\bar{P}/P_0\right)$ in uncontrolled state, and for local and global control. $P_0 = p_0 v_0 \cdot 1\,\mathrm{m}^2$, see also App. D.1.

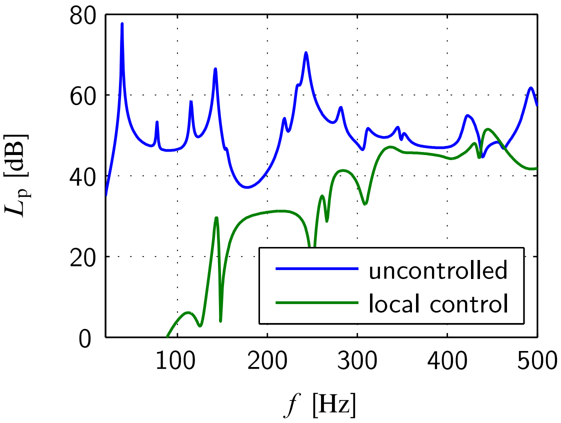

Figure 5.6: Sound pressure level at point $[1.56, 1.00, 4.00]\,\mathrm{m}$ in uncontrolled state and for global control.

achieving the same extremal levels as local control.

The focus of this chapter shall be global control of sound power, because of its more general applicability. An instrument termed *power transfer matrix* will be essential in establishing the connection between structural dynamics and emitted sound power.

5.4 Power Transfer Matrices

5.4.1 Spectral and Spatial Discretization of Baffled Structures

The time-average structure-borne sound power may be determined by integrating sound intensity over any surface enclosing the vibrating structure. In the case of a baffled planar structure, this surface may be selected as the surface of the structure, $S = A$. Then, the normal fluid particle velocity is identical to the surface velocity, $v_n \equiv \dot{w}$. The emitted sound power can then be calculated by combining equations (5.14), (5.11), (5.8), and (5.10) to give [70]

$$\bar{P}(\omega) = \dot{\boldsymbol{\eta}}^{\mathrm{H}}(\omega)\boldsymbol{\Pi}(\omega)\dot{\boldsymbol{\eta}}(\omega). \tag{5.20}$$

The $(n_S \times n_S)$ dimensional matrix $\boldsymbol{\Pi}(\omega)$ is the *power transfer matrix*. For the case at hand, it is given by

$$\boldsymbol{\Pi}(\omega) = \frac{\omega\rho_0}{4\pi}\int_0^{l_x}\int_0^{l_y}\int_0^{l_x}\int_0^{l_y}\boldsymbol{W}(x,y)\frac{\sin(kR)}{R}\boldsymbol{W}(x',y')^{\mathrm{T}}\,\mathrm{d}y'\,\mathrm{d}x'\,\mathrm{d}y\,\mathrm{d}x. \tag{5.21}$$

This quadruple integral is in general not analytically solvable, and may even pose a burden for numerical solution.

For that reason, a second possibility for calculating power transfer matrices of baffled planar structures is presented in [70] that does not involve the solution of quadruple integrals. There, the structure is not spectrally but spatially discretized. This means that the structure is not approximated by a finite number n_S of mode shapes but by a finite number $n_\mathrm{e} \gg n_\mathrm{S}$ of structural elements. Each element of area A_e is assumed to be rigid. It is argued that if the element dimensions are much smaller than both the structural and acoustic wavelengths, this approximation is justified. By collecting the velocities of the structural elements in the vector $\dot{\boldsymbol{w}}_\mathrm{e} = (\dot{w}_{\mathrm{e},1} \; \dots \; , \dot{w}_{\mathrm{e},n_\mathrm{e}})^\mathrm{T}$, the time-average sound power may also be expressed as

$$\bar{P}(\omega) = \dot{\tilde{\boldsymbol{w}}}_\mathrm{e}^\mathrm{H}(\omega)\boldsymbol{R}(\omega)\dot{\tilde{\boldsymbol{w}}}_\mathrm{e}(\omega), \tag{5.22}$$

with

$$\boldsymbol{R}(\omega) = \frac{\omega^2 \rho_0 A_\mathrm{e}^2}{4\pi c_0} \begin{pmatrix} 1 & \frac{\sin(kR_{12})}{kR_{12}} & \dots & \frac{\sin(kR_{1n_\mathrm{e}})}{kR_{1n_\mathrm{e}}} \\ \frac{\sin(kR_{21})}{kR_{21}} & 1 & \dots & \dots \\ \vdots & \vdots & \ddots & \vdots \\ \frac{\sin(kR_{n_\mathrm{e}1})}{kR_{n_\mathrm{e}1}} & \dots & \dots & 1 \end{pmatrix}. \tag{5.23}$$

The matrix $\boldsymbol{R} \in \mathbb{R}^{n_\mathrm{e} \times n_\mathrm{e}}$ is termed *radiation resistance matrix* in [70]. The scalars R_{ij} represent the center distance between the elements i and j.

With the help of modal expansion, the velocities of the elements can be related to the modal velocities by

$$\dot{\boldsymbol{w}}_\mathrm{e} = \boldsymbol{W}_\mathrm{e}^\mathrm{dis}\dot{\boldsymbol{\eta}}, \tag{5.24}$$

with the matrix of mode shape functions evaluated at the centers of the elements,

$$\boldsymbol{W}_\mathrm{e}^\mathrm{dis} = \begin{pmatrix} W_1(x_1, y_1) & \dots & W_{n_\mathrm{S}}(x_1, y_1) \\ \vdots & & \vdots \\ W_1(x_{n_\mathrm{e}}, y_{n_\mathrm{e}}) & \dots & W_{n_\mathrm{S}}(x_{n_\mathrm{e}}, y_{n_\mathrm{e}}) \end{pmatrix}. \tag{5.25}$$

Inserting (5.24) in (5.22) gives

$$\bar{P} = \dot{\tilde{\boldsymbol{\eta}}}^\mathrm{H} \left(\boldsymbol{W}_\mathrm{e}^\mathrm{dis}\right)^\mathrm{H} \boldsymbol{R}\boldsymbol{W}_\mathrm{e}^\mathrm{dis}\dot{\tilde{\boldsymbol{\eta}}}, \tag{5.26}$$

and thus $(\boldsymbol{W}_\mathrm{e}^\mathrm{dis})^\mathrm{H}\boldsymbol{R}\boldsymbol{W}_\mathrm{e}^\mathrm{dis} = \boldsymbol{\Pi}$, by comparison with (5.20). Obviously, the acoustic power can be expressed in different sets of variables, e.g. $\dot{\boldsymbol{\eta}}$ or $\dot{\boldsymbol{w}}_\mathrm{e}$, associated with matrices of suitable dimensions.

5.4.2 General Properties of Power Transfer Matrices

The last relationships shall now be put in a more general context. Linear physical systems are most suitably described by a set of effort variables $\boldsymbol{q}_\mathrm{E}(t)$ and flux variables $\boldsymbol{q}_\mathrm{F}(t)$ in a minimal coordinate system. In acoustics, sound pressures are usually interpreted as the effort variables, and particle velocities are flux variables. The scalar product of both sets is the instantaneous power of the system, $P(t) = \boldsymbol{q}_\mathrm{E}^\mathrm{T}(t)\boldsymbol{q}_\mathrm{F}(t)$. For harmonic time dependence, the time-average power is given as $\bar{P} = \frac{1}{2}\Re\{\tilde{\boldsymbol{q}}_\mathrm{E}^\mathrm{H}\tilde{\boldsymbol{q}}_\mathrm{F}\}$. The effort variables are related to the flux variables by an impedance matrix $\boldsymbol{Z}$, $\tilde{\boldsymbol{q}}_\mathrm{E} = \boldsymbol{Z}\tilde{\boldsymbol{q}}_\mathrm{F}$. In linear acoustics, the impedance matrix is known to be symmetric in general, which is known as the concept of *acoustic reciprocity* [69]. Thus, time-average power may also be written as $\bar{P} = \frac{1}{2}\Re\{\tilde{\boldsymbol{q}}_{\mathrm{F}}^{\mathrm{H}}\boldsymbol{Z}^*\tilde{\boldsymbol{q}}_{\mathrm{F}}\}$. This means that the power may be expressed as a quadratic form of flux variables. Analogously, one can express $\bar{P}$ in terms of effort variables with the help of the admittance matrix $\boldsymbol{Z}^{-1}$. It is concluded that the power is generally expressed as a quadratic form of flux or effort variables. For that reason, it will not be further distinguished between effort and flux variables in the following.

Any complex matrix $\boldsymbol{Z}$ may be expressed as the sum of its Hermitian and anti-Hermitian part,

$$\boldsymbol{Z} = \frac{1}{2}\left(\boldsymbol{Z} + \boldsymbol{Z}^{\mathrm{H}}\right) + \frac{1}{2}\left(\boldsymbol{Z} - \boldsymbol{Z}^{\mathrm{H}}\right). \tag{5.27}$$

Since impedance matrices are usually symmetric, this may be reformulated as

$$\boldsymbol{Z}^* = \frac{1}{2}\left(\boldsymbol{Z} + \boldsymbol{Z}^*\right) + \frac{1}{2}\left(\boldsymbol{Z}^* - \boldsymbol{Z}\right). \tag{5.28}$$

Only the Hermitian part of a matrix contributes to the real part of the value of its quadratic form, thus

$$\begin{aligned}\bar{P} &= \frac{1}{2}\Re\left\{\tilde{\boldsymbol{q}}^{\mathrm{H}}\boldsymbol{Z}^*\tilde{\boldsymbol{q}}\right\}\\ &= \frac{1}{4}\tilde{\boldsymbol{q}}^{\mathrm{H}}\left(\boldsymbol{Z} + \boldsymbol{Z}^*\right)\tilde{\boldsymbol{q}}\\ &= \tilde{\boldsymbol{q}}^{\mathrm{H}}\boldsymbol{\Pi}\tilde{\boldsymbol{q}}\end{aligned} \tag{5.29}$$

with the real-valued, symmetric matrix $\boldsymbol{\Pi} = \frac{1}{4}(\boldsymbol{Z} + \boldsymbol{Z}^*)$. The power transfer matrix is also bound to be positive definite, since the time-average power is non-negative and only zero in the case of $\tilde{\boldsymbol{q}} = \boldsymbol{0}$.

Assume now that a minimal set of variables $\tilde{\boldsymbol{q}}_1$ that completely, or sufficiently, describes the state of the system is found, and the power may be expressed as $\bar{P} = \tilde{\boldsymbol{q}}_1^{\mathrm{H}}\boldsymbol{\Pi}\tilde{\boldsymbol{q}}_1$. Then, the power may be equivalently expressed in terms of another set of variables $\tilde{\boldsymbol{q}}_2$ which is an injective linear function of $\tilde{\boldsymbol{q}}_1$, $\tilde{\boldsymbol{q}}_2 = \boldsymbol{T}\tilde{\boldsymbol{q}}_1$. The injective property ensures the existence of a left inverse $\boldsymbol{T}^+$ of the transformation matrix $\boldsymbol{T}$, such that $\tilde{\boldsymbol{q}}_1 = \boldsymbol{T}^+\tilde{\boldsymbol{q}}_2$. The time-average power is then given as $\bar{P} = \tilde{\boldsymbol{q}}_2^{\mathrm{H}}\left(\boldsymbol{T}^+\right)^{\mathrm{H}}\boldsymbol{\Pi}\boldsymbol{T}^+\tilde{\boldsymbol{q}}_2 = \tilde{\boldsymbol{q}}_2^{\mathrm{H}}\boldsymbol{\Pi}_T\tilde{\boldsymbol{q}}_2$. This is the abstract background of the relationship between the expressions (5.20) and (5.22) for the acoustic power. Since these two are merely related by the (non-regular) change of coordinates (5.24), we will term every matrix a power transfer matrix (PTM) which represents the power of a linear system by means of a quadratic form. Although the PTM derived in (5.29) is real, this is not the case for general complex-valued transformation matrices $\boldsymbol{T}$. Hence, we will not restrict power transfer matrices to be real in the following. Nevertheless, they can be assumed to be Hermitian.

The purpose of some PTM is to enable the calculation of time-average emitted power from a set of variables $\boldsymbol{q}$. It is especially appealing to calculate the acoustic quantity $\bar{P}$ from structural measurements only, like in (5.20) and (5.22). This shall be the focus of this chapter and therefore, we will term $\boldsymbol{q}$ the set of *structural variables* from now on.

Power transfer matrices are usually fully occupied, compare (5.21) and (5.23). This implies that the structural variables do not contribute to time-average power independently. A set of new variables $\boldsymbol{z}$ which do so may be found by eigenvalue decomposition of the Hermitian PTM,

$\boldsymbol{\Pi} = \boldsymbol{V}^{\mathrm{H}}\boldsymbol{\Lambda}\boldsymbol{V}$. The sought set of variables is then given by $\boldsymbol{z} = \boldsymbol{V}\boldsymbol{q}$. The application of this concept to the acoustic PTM of a baffled plate is shown in App. D.3.

5.4.3 Motivation and Literature Review

From the stated properties of PTMs, it becomes clear that these may serve as acoustic models to bridge the gap between structural dynamics on the one hand and structure-borne sound power on the other hand. Having an accurate acoustic model is essential for successful ASAC design, since in an ASAC control loop, all sensors and actuators are located on the structure, while the control variables are non-measured acoustic quantities, see Sec. 1.2.

In the bulk of available literature, PTMs for analysis purposes and global control design are derived from Rayleigh's integral formula, and interesting insights can be gathered from the resulting theoretical considerations and simulation examples, see for example [15, 16, 23, 24, 33, 66, 172, 190]. Analytically derived PTMs have also been used in experiments, although the underlying assumptions of Rayleigh's integral formula are hardly satisfied for a real structure. Good results are reported for example in [83], where the sound radiated from a rectangular plate in a (finite) baffle is controlled in an anechoic chamber. Nevertheless, one must expect severe performance degradations when a control design based on an analytically derived PTM is applied to a structure of arbitrary geometry in a non-ideal acoustic environment.

To this end, it is proposed in this thesis to experimentally identify a structure's PTM from measurement data. Experimental modeling of PTMs has, to the author's knowledge, only been considered by Berkhoff and coworkers in the publications [25, 26, 28]. In these publications, it is assumed that the structure radiates under free-field conditions, which requires experiments to be carried out in an anechoic chamber. In this thesis, an experimental modeling procedure for PTMs is presented which does not rely on any assumptions on the structure's geometry or acoustic boundary conditions whatsoever, apart from the linearity of the acoustic environment. Thus, it offers a wider applicability of high-performance ASAC design.

5.5 Direct Identification of Power Transfer Matrices

Theoretically, one could calculate both the pressure and velocity fields from the relationships (5.1) and (5.2) if the Green's function of the given acoustic problem was known. However, as already mentioned, analytic solutions exist only in rare cases. In practice, solutions have to be found by means of extensive numerical calculations by making use of finite element method (FEM) or boundary element method (BEM) techniques. Even in this case, the computer simulations have to be matched with real measurement data, since the model parameters, especially material parameters, are most often not known with sufficient accuracy. In addition to that, complete knowledge of the acoustic field may not even be necessary. An estimate of the total emitted power may be sufficient in many cases, like in global acoustic control as it is defined in this thesis.

For that reason, experimental modeling of power transfer matrices is a viable option for characterizing structure-born sound fields. One approach, which will be termed the direct approach here, is to directly estimate the parameters of some PTM $\boldsymbol{\Pi}(\omega) = (p_{ij}(\omega)) \in \mathbb{C}^{n \times n}$. It is assumed that measurements of a set of structural variables $\tilde{\boldsymbol{q}}(\omega) \in \mathbb{C}^n$ and time-average power $\bar{P}(\omega)$ at some frequency ω are given. The quadratic form $\bar{P}(\omega) = \tilde{\boldsymbol{q}}^{\mathrm{H}}(\omega)\boldsymbol{\Pi}(\omega)\tilde{\boldsymbol{q}}(\omega)$ may be expanded as

$$\begin{aligned}
\bar{P} &= \tilde{\boldsymbol{q}}^{\mathrm{H}}\boldsymbol{\Pi}\tilde{\boldsymbol{q}} \\
&= \sum_{i=1}^{n}\sum_{j=1}^{n} \tilde{q}_i^* p_{ij}\tilde{q}_j \\
&= \sum_{i=1}^{n} |\tilde{q}_i|^2 p_{ii} + \sum_{i,j=1,i<j}^{n} 2\,\Re\left\{\tilde{q}_i^* p_{ij}\tilde{q}_j\right\}.
\end{aligned} \tag{5.30}$$

The first term on the right hand side of the last equation represents the autopower of the chosen variables q_i, and the second term represents the cross-coupling between some coordinates q_i and $q_j, i \neq j$. Only the lower triangular part of $\boldsymbol{\Pi}$ is considered unknown, since $\boldsymbol{\Pi}$ is Hermitian. The unknown parameters can be stacked in a vector by the operation $\boldsymbol{p} = \mathrm{vech}\{\boldsymbol{\Pi}\}$, where this operator works like the $\mathrm{vec}\{\cdot\}$ operator but takes only the lower triangular part of a Hermitian matrix. The vector $\boldsymbol{p}$ contains $\frac{n}{2}(n+1)$ complex numbers and shall be estimated by the least-squares method. Since the entries are complex apart from the diagonal elements of $\boldsymbol{\Pi}$, the actual number of unknown parameters is n^2.

The minimization problem shall be put in the form $\min_{\boldsymbol{x}_{\mathrm{LS}}}. \|\boldsymbol{A}_{\mathrm{LS}}\boldsymbol{x}_{\mathrm{LS}} - \boldsymbol{b}_{\mathrm{LS}}\|_2^2$ with the regressor matrix $\boldsymbol{A}_{\mathrm{LS}}$ and the observation vector $\boldsymbol{b}_{\mathrm{LS}}$. To determine these quantities, assume that at a certain frequency ω, $M \geq n^2$ observations are taken. More specifically, M vectors $(\tilde{\boldsymbol{q}}_1, \ldots, \tilde{\boldsymbol{q}}_M) = \tilde{\boldsymbol{Q}}$ must be given along with associated power measurements $(\bar{P}_1, \ldots, \bar{P}_M)^{\mathrm{T}} = \boldsymbol{P}$. In matrix form, this states

$$\boldsymbol{P} = \mathrm{diag}\left\{\tilde{\boldsymbol{Q}}^{\mathrm{H}}\boldsymbol{\Pi}\tilde{\boldsymbol{Q}}\right\}. \tag{5.31}$$

With the help of some binary matrices $\boldsymbol{T}_1$ and $\boldsymbol{T}_2$, this can be rewritten as (see App. D.4)

$$\boldsymbol{P} = \boldsymbol{T}_1\left(\tilde{\boldsymbol{Q}}^{\mathrm{T}} \otimes \tilde{\boldsymbol{Q}}^{\mathrm{H}}\right)\boldsymbol{T}_2\,\mathrm{vech}\{\boldsymbol{\Pi}\}. \tag{5.32}$$

This system of equations with complex numbers can be reformulated in terms of real numbers[2] as

$$\begin{pmatrix}\boldsymbol{P}\\ \boldsymbol{0}\end{pmatrix} = \left[\boldsymbol{T}_1\left(\tilde{\boldsymbol{Q}}^{\mathrm{T}} \otimes \tilde{\boldsymbol{Q}}^{\mathrm{H}}\right)\boldsymbol{T}_2\right]_{\mathrm{Re}}\boldsymbol{p}_{\mathrm{re}}. \tag{5.33}$$

This implies the identities

$$\boldsymbol{A}_{\mathrm{LS}} = \left[\boldsymbol{T}_1\left(\tilde{\boldsymbol{Q}}^{\mathrm{T}} \otimes \tilde{\boldsymbol{Q}}^{\mathrm{H}}\right)\boldsymbol{T}_2\right]_{\mathrm{Re}}, \quad \boldsymbol{x}_{\mathrm{LS}} = \boldsymbol{p}_{\mathrm{re}}, \quad \text{and} \quad \boldsymbol{b}_{\mathrm{LS}} = \boldsymbol{P}_{\mathrm{re}}. \tag{5.34}$$

This least-squares problem is solved by

$$\boldsymbol{p}_{\mathrm{re}} = \boldsymbol{A}_{\mathrm{LS}}^{+}\boldsymbol{b}_{\mathrm{LS}}. \tag{5.35}$$

---

[2] For the definition of the Re and re operators, see App. B.1

For a meaningful solution, it must be assumed that $\boldsymbol{A}_{\mathrm{LS}}$ has full column rank. However, this is not a trivial task because of the complex structure of $\boldsymbol{A}_{\mathrm{LS}}$. Moreover, the direct approach comes with a number of significant drawbacks, which can be summarized as follows:

1. The least-squares problem (5.35) is linear in the sound power measurements $\bar{P}$ but nonlinear (quadratic) in the structural variables. Thus, it is not obvious how to select $\tilde{\boldsymbol{Q}}$ such that $\boldsymbol{A}_{\mathrm{LS}}$ has full column rank.
2. The variable sets $\tilde{\boldsymbol{q}}_i$ consist of structural quantities which describe the motion of the sound-emitting mechanical structure. As such, the sets $\tilde{\boldsymbol{q}}_i$ cannot be directly prescribed. In practice, one can only prescribe the forces acting on the structure and then *measure* the resulting structural variables simultaneously to the sound power. As such, both the input data $\tilde{\boldsymbol{q}}_i$ and the output data $\bar{P}_i$ of the estimation problem are generally affected by noise, which means that estimation of power transfer matrices is an *errors-in-variables problem*. This is not taken into account by this simple approach and may significantly increase the bias error of (5.35).
3. The relationship (5.35) holds for every single frequency ω. Since the structural variables enter nonlinearly in the estimation problem, it is not possible to sweep through the frequency range of interest, but one must excite every frequency one at a time. This unduly increases the required measurement time to collect the required data.
4. There exists nothing like a “sound power sensor”. Each of the numerous sound power measurement methods *calculates* the emitted sound power from the in situ measurable quantities sound pressure and/or particle velocity. The direct approach does not make use of this fact. For an overview of sound power measurement methods, see [100].

In order to circumvent these drawbacks, an indirect approach for estimating power transfer matrices is now presented.

5.6 Indirect Identification of Power Transfer Matrices

All of the disadvantages mentioned for the direct method can be avoided by an indirect approach to PTM modeling. The prominent idea is to appreciate the fact that the physical quantity sound power is never directly measured but can always be calculated from sound pressure and normal particle velocity at a sufficient number of points on a closed measurement surface. This can be expressed as (compare (5.8) and (5.10))

$$\bar{P}(\omega) = \frac{1}{2} \oiint_A \Re\left\{\tilde{p}(\boldsymbol{x},\omega)\tilde{v}_{\mathrm{n}}^*(\boldsymbol{x},\omega)\right\} \mathrm{d}A \approx \frac{1}{2}\sum_{i=1}^{n_{\mathrm{A}}} \Re\left\{\tilde{p}_i(\boldsymbol{x},\omega)\tilde{v}_{\mathrm{n},i}^*(\boldsymbol{x},\omega)\right\} A_i, \tag{5.36}$$

where A_i represents the fraction of the measurement surface A which is associated with the measurement point i. For simplicity, it will be assumed that the measurement surface is split up into n_{A}

segments of equal area A_{el}. This results in the following estimation formula for the sound power,

$$\hat{\bar{P}}(\omega) = \frac{1}{2} A_{\mathrm{el}} \sum_{i=1}^{n_{\mathrm{A}}} \Re\left\{\tilde{p}_i(\boldsymbol{x},\omega)\tilde{v}^*_{\mathrm{n},i}(\boldsymbol{x},\omega)\right\}. \tag{5.37}$$

Since we will only be concerned with the velocity component normal to the measurement surface, the index n in v_{n} is dropped from now on.

The pressure and velocity fields are each linearly related to the velocity profile $\dot{w}$ of the sound-emitting structure. This is implied by (5.1) and (5.2). In addition to that, it is assumed that the structural variables $\boldsymbol{q}$ are also linearly related to $\dot{w}$. For $\boldsymbol{q} = \dot{\boldsymbol{\eta}}$ for example, we have $\dot{w}(\boldsymbol{x},t) = \boldsymbol{W}^{\mathrm{T}}(\boldsymbol{x})\dot{\boldsymbol{\eta}}(t)$, where $\boldsymbol{W}^{\mathrm{T}}(\boldsymbol{x}) = (W_1(\boldsymbol{x}), \ldots, W_{n_{\mathrm{S}}}(\boldsymbol{x}))$ contains the structural mode shape functions. Summing up, it can be concluded that there must exist frequency response matrices that relate the structural variables to the two basic acoustic variables at the n_{A} measurement points,

$$\begin{aligned} \tilde{\boldsymbol{p}}(\omega) &= \boldsymbol{G}_{\mathrm{p}}(\mathrm{j}\omega)\tilde{\boldsymbol{q}}(\omega), &\quad \text{with} \quad \tilde{\boldsymbol{p}} &= (\tilde{p}_1, \ldots, \tilde{p}_{n_{\mathrm{A}}})^{\mathrm{T}}, \quad \text{and} \\ \tilde{\boldsymbol{v}}(\omega) &= \boldsymbol{G}_{\mathrm{v}}(\mathrm{j}\omega)\tilde{\boldsymbol{q}}(\omega), &\quad \text{with} \quad \tilde{\boldsymbol{v}} &= (\tilde{v}_1, \ldots, \tilde{v}_{n_{\mathrm{A}}})^{\mathrm{T}}. \end{aligned} \tag{5.38}$$

With the help of these frequency responses, (5.37) can be rewritten as

$$\begin{aligned} \hat{\bar{P}}(\omega) &= \frac{1}{2} A_{\mathrm{el}} \Re\left\{\tilde{\boldsymbol{p}}(\omega)^{\mathrm{T}}\tilde{\boldsymbol{v}}(\omega)^*\right\} \\ &= \frac{1}{2} A_{\mathrm{el}} \Re\left\{\tilde{\boldsymbol{p}}^{\mathrm{H}}(\omega)\tilde{\boldsymbol{v}}(\omega)\right\} \\ &= \frac{1}{2} A_{\mathrm{el}} \Re\left\{\tilde{\boldsymbol{q}}^{\mathrm{H}}(\omega)\boldsymbol{G}_{\mathrm{p}}^{\mathrm{H}}(\mathrm{j}\omega)\boldsymbol{G}_{\mathrm{v}}(\mathrm{j}\omega)\tilde{\boldsymbol{q}}(\omega)\right\}. \end{aligned} \tag{5.39}$$

Only the Hermitian part of $\boldsymbol{G}_{\mathrm{p}}^{\mathrm{H}}\boldsymbol{G}_{\mathrm{v}}$ contributes to the real part of the quadratic form on the right hand side. Thus,

$$\begin{aligned} \hat{\bar{P}}(\omega) &= \frac{1}{2} A_{\mathrm{el}} \tilde{\boldsymbol{q}}^{\mathrm{H}}(\omega) \, \frac{1}{2} \left(\boldsymbol{G}_{\mathrm{p}}(\mathrm{j}\omega)^{\mathrm{H}}\boldsymbol{G}_{\mathrm{v}}(\mathrm{j}\omega) + \boldsymbol{G}_{\mathrm{v}}(\mathrm{j}\omega)^{\mathrm{H}}\boldsymbol{G}_{\mathrm{p}}(\mathrm{j}\omega)\right) \tilde{\boldsymbol{q}}(\omega) \\ &= \frac{1}{4} A_{\mathrm{el}} \tilde{\boldsymbol{q}}^{\mathrm{H}}(\omega) \left(\hat{\boldsymbol{\Xi}}^{\mathrm{H}}(\mathrm{j}\omega) + \hat{\boldsymbol{\Xi}}(\mathrm{j}\omega)\right) \tilde{\boldsymbol{q}}(\omega), \end{aligned} \tag{5.40}$$

with $\hat{\boldsymbol{\Xi}}(\mathrm{j}\omega) := \boldsymbol{G}_{\mathrm{v}}^{\mathrm{H}}(\mathrm{j}\omega)\boldsymbol{G}_{\mathrm{p}}(\mathrm{j}\omega)$. It follows that an estimation of the PTM is given by

$$\hat{\boldsymbol{\Pi}}(\omega) = \frac{1}{4} A_{\mathrm{el}} \left(\hat{\boldsymbol{\Xi}}(\mathrm{j}\omega) + \hat{\boldsymbol{\Xi}}^{\mathrm{H}}(\mathrm{j}\omega)\right). \tag{5.41}$$

Obviously, this matrix is Hermitian, but not necessarily real symmetric.

5.6.1 Estimation of Acoustic Frequency Responses

The first essential step in the estimation of the PTM is to accurately determine the frequency responses of $\boldsymbol{G}_{\mathrm{p}}(\mathrm{j}\omega)$ and $\boldsymbol{G}_{\mathrm{v}}(\mathrm{j}\omega)$. At a real testbed, it can be expected that the signal acquisition is done with digital hardware and therefore, the input and output signals are given as sampled data sequences $\boldsymbol{q}(k)$, $\boldsymbol{p}(k)$, and $\boldsymbol{v}(k)$ with sampling time T_{s}. The lengths of the time-domain sequences are assumed to be $2N$ in order to result in $N+1$ informative DFT samples, without loss of generality. It is assumed that the measurement sequences are appropriately chosen to prevent leakage effects. If, in addition to that, all sequences are suitably filtered to prevent aliasing effects, it can be shown that the estimated FRFs match that of the continuous-time frequency responses at the sampling frequencies in the noise-free case [152], i.e.

$$\boldsymbol{G}_{\mathrm{p}}\left(\mathrm{e}^{\mathrm{j}\omega_n}\right) = \boldsymbol{G}_{\mathrm{p}}(\mathrm{j}\omega_n) \quad \text{and} \quad \boldsymbol{G}_{\mathrm{v}}\left(\mathrm{e}^{\mathrm{j}\omega_n}\right) = \boldsymbol{G}_{\mathrm{v}}(\mathrm{j}\omega_n), \tag{5.42}$$

at the DFT frequencies $\omega_n = n\frac{\pi}{NT_{\mathrm{s}}}, n = 0, \dots, N-1$. The parameter T_{s} in the exponential $\mathrm{e}^{\mathrm{j}\omega T_{\mathrm{s}}}$ is dropped again for ease of notation. Proper anti-alias filtering will be assumed in the following.

The two acoustic transfer matrices each have n_{S} inputs and n_{A} outputs. The identification of the corresponding FRFs consequently requires at least n_{S} experiments with persistently exciting inputs. More precisely, $M \geq n_{\mathrm{S}}$ measurements have to be recorded with input data

$$\boldsymbol{U}_{\text{time}} = \begin{pmatrix} \boldsymbol{q}_{1,0} & \cdots & \boldsymbol{q}_{M,0} \\ \vdots & & \vdots \\ \boldsymbol{q}_{1,2N-1} & \cdots & \boldsymbol{q}_{M,2N-1} \end{pmatrix} = (\boldsymbol{q}_1, \dots, \boldsymbol{q}_M), \quad \boldsymbol{q}_i \in \mathbb{R}^{2N \times n_{\mathrm{S}}}, \tag{5.43}$$

and output data $\boldsymbol{Y}_{\text{time}} = (\boldsymbol{p}_1, \dots, \boldsymbol{p}_M)$, or $\boldsymbol{Y}_{\text{time}} = (\boldsymbol{v}_1, \dots, \boldsymbol{v}_M)$. All $\boldsymbol{p}_i$ and $\boldsymbol{v}_i$ are of dimension $2N \times n_{\mathrm{A}}$. Since the procedure is identical for both acoustic transfer matrices, we will not further distinguish between $\boldsymbol{G}_{\mathrm{p}}$ and $\boldsymbol{G}_{\mathrm{v}}$ in the remainder of this section.

Both the structural variables and the acoustic variables are in general affected by noise. This renders the estimation of $\boldsymbol{G}$ an *errors-in-variables* problem. Special care must be taken to guarantee unbiased estimates in this case. To this end, the following is assumed:

- The number of experiments is an integer multiple of the number of inputs, $M = \tilde{M} n_{\mathrm{S}}$, with $\tilde{M} \in \mathbb{N}$.
- The input sequences are periodically repeated after n_{S} experiments, i.e. $\boldsymbol{q}_i = \boldsymbol{q}_{i+n_{\mathrm{S}}}$.
- The DFT sequences of all time signals are free of leakage effects.

The last point can be achieved by ensuring that the system is at rest at the beginning of each experiment and that the input and output signals both have died out at the end of the measurement. As pointed out in [187] and [192], unbiased FRF estimates can then be achieved with the so-called *errors-in-variables estimator*

$$\hat{\boldsymbol{G}}\left(\mathrm{e}^{\mathrm{j}\omega_n}\right) = \left(\frac{1}{\tilde{M}} \sum_{\tilde{m}=1}^{\tilde{M}} \tilde{\boldsymbol{Y}}_{\tilde{m}}(\mathrm{j}\omega_n)\right) \left(\frac{1}{\tilde{M}} \sum_{\tilde{m}=1}^{\tilde{M}} \tilde{\boldsymbol{U}}_{\tilde{m}}(\mathrm{j}\omega_n)\right)^{-1}. \tag{5.44}$$

In the above equation, the matrices $\tilde{\boldsymbol{U}}_{\tilde{m}}$ are constructed as follows. First, take the DFT of (5.43) along its columns and consider only the first $N+1$ informative rows of the resulting matrix, which is of dimension $(N+1) \times \tilde{M} n_{\mathrm{S}}^2$,

$$\boldsymbol{U}_{\mathrm{DFT}} = \begin{pmatrix} \boldsymbol{q}_{1,\omega_0} & \cdots & \boldsymbol{q}_{M,\omega_0} \\ \vdots & & \vdots \\ \boldsymbol{q}_{1,\omega_N} & \cdots & \boldsymbol{q}_{M,\omega_N} \end{pmatrix}. \tag{5.45}$$

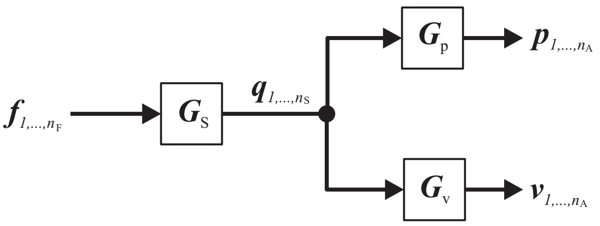

Figure 5.7: Transfer paths from disturbance forces to acoustical quantities.

Now, for each frequency sample ω_k, take the elements of the kth row of $\boldsymbol{U}_{\mathrm{DFT}}$ and fill the columns of a $n_S \times \tilde{M} n_S$ dimensional matrix $\tilde{\boldsymbol{U}}(\mathrm{j}\omega_k)$. This matrix can be separated into $\tilde{M}$ quadratic blocks of dimension $n_S \times n_S$,

$$\begin{aligned}\tilde{\boldsymbol{U}}(\mathrm{j}\omega_k) &= \left(\begin{array}{ccc|c|ccc} q_1^1(\mathrm{j}\omega_k) & \dots & q_{n_S}^1(\mathrm{j}\omega_k) & \dots & q^1_{(\tilde{M}-1)n_S+1}(\mathrm{j}\omega_k) & \dots & q^1_{\tilde{M}n_S}(\mathrm{j}\omega_k) \\ \vdots & & \vdots & \dots & \vdots & & \vdots \\ q_1^{n_S}(\mathrm{j}\omega_k) & \dots & q_{n_S}^{n_S}(\mathrm{j}\omega_k) & \dots & q^{n_S}_{(\tilde{M}-1)n_S+1}(\mathrm{j}\omega_k) & \dots & q^{n_S}_{\tilde{M}n_S}(\mathrm{j}\omega_k) \end{array}\right) \\ &= \left(\tilde{\boldsymbol{U}}_1, \dots, \tilde{\boldsymbol{U}}_{\tilde{M}}\right),\end{aligned} \tag{5.46}$$

where $q_i^j(\mathrm{j}\omega_k)$ denotes the jth element of $\boldsymbol{q}_{i,\omega_k}$. The matrices $\tilde{\boldsymbol{Y}}_{\tilde{m}}$ are defined analogously.

In order to ensure that the inversion on the right hand side of (5.44) is possible at every frequency sample, the matrices $1/\tilde{M} \sum_{\tilde{m}=1}^{\tilde{M}} \tilde{\boldsymbol{U}}_{\tilde{m}}(\mathrm{j}\omega_n)$ must be regular. Since the excitation scheme is periodically repeated after n_S experiments, all addends $\tilde{\boldsymbol{U}}_{\tilde{m}}$ are identical up to the additive noise on the inputs. Thus, only the first block $\tilde{\boldsymbol{U}}_1(\mathrm{j}\omega_n)$ is considered in the following.

The major difficulty lies in the fact that the input quantities $\boldsymbol{q}$ cannot be prescribed but only indirectly influenced via some structural transfer matrix $\boldsymbol{G}_S$. It relates the n_F structural excitations $\boldsymbol{f}$ to the n_S structural variables $\boldsymbol{q}$. This is illustrated in Fig. 5.7. The vector $\boldsymbol{f}$ contains the inputs that are available for the identification process, which may be forces, moments, or voltages applied to actuators. We may write $\tilde{\boldsymbol{U}}_1(\mathrm{j}\omega_n) = \boldsymbol{G}_S(\mathrm{e}^{\mathrm{j}\omega_n})\tilde{\boldsymbol{F}}_1(\mathrm{j}\omega_n)$ when no noise is present, where

$$\tilde{\boldsymbol{F}}_1(\mathrm{j}\omega_n) = \begin{pmatrix} f_1^1(\mathrm{j}\omega_n) & \dots & f_{n_S}^1(\mathrm{j}\omega_n) \\ \vdots & & \vdots \\ f_1^{n_F}(\mathrm{j}\omega_n) & \dots & f_{n_S}^{n_F}(\mathrm{j}\omega_n) \end{pmatrix}, \quad n = 0, \dots, N. \tag{5.47}$$

A necessary condition for the regularity of $\tilde{\boldsymbol{U}}_1(\mathrm{j}\omega_n)$ is that $\boldsymbol{G}_S(\mathrm{e}^{\mathrm{j}\omega_n})$ is of full row rank, which implies $n_F \geq n_S$. A sufficient condition is that both $\boldsymbol{G}_S$ and $\tilde{\boldsymbol{F}}_1$ are injective in the considered frequency range, which means that $\tilde{\boldsymbol{U}}_1$ becomes injective and thus also regular. This may only be achieved if $n_S = n_F$, since $\boldsymbol{G}_S \in \mathbb{C}^{n_S \times n_F}$ and $\tilde{\boldsymbol{F}} \in \mathbb{C}^{n_F \times n_S}$.

If the excitation inputs $\boldsymbol{f}$ are voltages which are applied to actuators that excite the structure, it can be assumed that these are perfectly known, i.e. not affected by noise. In this case, the transfer matrix $\boldsymbol{G}_S$ represents the combined dynamics of the structure and the actuators. Since it is required by the errors-in-variables estimator that the input scheme is periodically repeated after n_S experiments, one necessarily has $\tilde{\boldsymbol{F}}_{\tilde{m}}(\mathrm{j}\omega_n) = \tilde{\boldsymbol{F}}_{\tilde{n}}(\mathrm{j}\omega_n), \forall\, \tilde{m}, \tilde{n} \in \{1, \dots, \tilde{M}\}$ at every frequency sample ω_n.

For control design and simulation purposes, a model of $\boldsymbol{G}_\mathrm{S}$ is generally also desired. For the experimental modeling of $\boldsymbol{G}_\mathrm{S}$, at least n_F experiments have to be performed. Thus, in case $n_\mathrm{F} > n_\mathrm{S}$, $\boldsymbol{G}_\mathrm{S}$ cannot be identified from the same data set which is used to identify $\boldsymbol{G}_\mathrm{p}$ and $\boldsymbol{G}_\mathrm{v}$. For that reason, if both the structural and the acoustic transfer matrices have to be identified, it is natural to choose $n_\mathrm{F} = n_\mathrm{S}$ in order to reduce experimental effort. This will be assumed in the following, and we require that $\boldsymbol{G}_\mathrm{S}(\mathrm{e}^{\mathrm{j}\omega_n})$ is regular in the considered frequency range, which may be assured by proper actuator and sensor placement.

5.6.2 Selection of Structural Variables

For acoustic radiation, the motion of the sound-emitting structure, i.e. its complete surface information, is generally relevant, compare (5.1). Since complete measurement is generally not a viable option, the structural dynamics must be described by a finite number of variables $\boldsymbol{q}$. Two natural choices exist for these structural variables:

1. Physical quantities measured at discrete locations of the structure, like accelerations or displacements. This leads to a spatial discretization of the structure.
2. Modal quantities calculated by linear combination of physical quantities, which is termed spectral discretization.

The respective advantages and drawbacks of these two choices shall be highlighted.

The first important aspect is the effort that must be taken to measure the structural quantities in real time. Choosing $\boldsymbol{q}(t) = \boldsymbol{w}(t) = (w(\boldsymbol{x}_1, t), \dots, w(\boldsymbol{x}_{n_\mathrm{sensors}}, t))^\mathrm{T}$, or some time-derivative of $\boldsymbol{w}$, requires setting up a sensor grid on the structure. The number of sensors n_sensors must be high enough to prevent spatial aliasing in the considered frequency range $[\Omega_\mathrm{min}, \Omega_\mathrm{max}]$ [154]. Accelerometers will be most suitable in most cases, giving $\boldsymbol{q} = \ddot{\boldsymbol{w}}$. However, capacitive or inductive displacement sensors may also be possible.

Letting $\boldsymbol{q} = \boldsymbol{\eta}$ or some time derivative of $\boldsymbol{\eta}$ involves linear combination of physical quantities to transform them into modal quantities, $\boldsymbol{\eta} = \boldsymbol{T}\boldsymbol{w}$. The calculation of the static transformation matrix $\boldsymbol{T}$ requires knowledge of some of the structure's modal parameters. There are two common procedures to derive $\boldsymbol{T}$. One requires knowledge of the values of the structural mode shape functions (or eigenfunctions) at the sensor locations ([107], [174]). The other method relies on the eigenfrequencies and modal damping ratios of the considered modes [155]. The transformation matrix is always of full row rank, i.e. the number of sensors cannot be less than the number of modal quantities.

The advantage of the modal approach is that the number of structural quantities n_S may be reduced compared to the physical approach. This is because the structural dynamics in a given frequency range $[\Omega_\mathrm{min}, \Omega_\mathrm{max}]$ can often be well approximated by the modal quantities associated with the eigenfrequencies ω_i with $\Omega_\mathrm{min} < \omega_i < \Omega_\mathrm{max}$, if the modal overlap is not to high. The number of relevant eigenfrequencies ω_i is usually smaller than the number of sensors required for the physical approach. However, the number of sensors required to extract the modal quantities with high confidence is not necessarily smaller than the number of sensors required for spatial discretization. The disadvantage of the modal approach is that (partial) knowledge of modal parameters is necessary, which is not the case for the physical approach. We will assume $\Omega_{\min} = 0$ in the sequel, without loss of generality.

The number of structural variables has a direct influence on the number of experiments which have to be carried out in order to identify the acoustic transfer functions. Since the number of inputs in $\boldsymbol{G}_{\mathrm{p}}$ and $\boldsymbol{G}_{\mathrm{v}}$ is n_{S}, at least n_{S} experiments have to be done. If the acoustic quantities $\boldsymbol{p}$ and $\boldsymbol{v}$ can be measured simultaneously on the measurement surface A, the minimum number of measurements is n_{S}. However, this would require n_{A} sound intensity probes which is very costly.
If the sound intensity measurements are carried out in an anechoic chamber for example, sound intensity can be calculated from sound pressure measurements only [69]. Thus, only n_{S} measurements with n_{A} microphones are necessary, which is more realistic. However, if an idealized acoustic environment is not available, one has to resort to measuring sound pressure and particle velocity simultaneously. Assuming that only one sound intensity probe is available, each of the n_{S} measurements has to be repeated n_{A} times while the probe is moved from one grid point to the next. This significantly increases measurement time. Thus, depending on the measurement equipment, having a low number of structural variables may be critical.

5.6.3 Influence of Discretization and Approximation Errors

The sound pressure generated by a vibrating structure at some location in space depends on the structure's velocity profile, compare (5.11). The same holds true for the particle velocity. Since the surface profile can only be approximated by a finite number of measured structural variables, a discretization error will occur. The effects of this error on the estimated acoustic frequency responses shall now be exemplified for $\boldsymbol{G}_{\mathrm{p}}$ and $\boldsymbol{q} = \dot{\boldsymbol{\eta}}$. Analogue considerations can be made for the spatial discretization $\boldsymbol{q} = \dot{\boldsymbol{w}}$.

The complex pressure $\tilde{p}(x_k, \omega) := \tilde{p}_k(\omega)$ at some measurement location x_k on the discretized acoustic measurement surface A is considered. Its value depends on the infinitely many modal velocities,

$$\tilde{p}_k(\omega) = \underbrace{\left(G_{p_k\dot{\eta}_1}(\mathrm{e}^{\mathrm{j}\omega}), \ldots, G_{p_k\dot{\eta}_\infty}(\mathrm{e}^{\mathrm{j}\omega})\right)}_{=\boldsymbol{G}_{\mathrm{p},\infty}^{(k,:)}} \begin{pmatrix} \dot{\tilde{\eta}}_1(\omega) \\ \vdots \\ \dot{\tilde{\eta}}_\infty(\omega) \end{pmatrix}. \tag{5.48}$$

The modal velocities are in turn generated by exciting the structure via n_{S} forces,

$$\begin{pmatrix} \dot{\tilde{\eta}}_1(\omega) \\ \vdots \\ \dot{\tilde{\eta}}_\infty(\omega) \end{pmatrix} = \underbrace{\begin{pmatrix} G_{\dot{\eta}_1 f_1}(\mathrm{e}^{\mathrm{j}\omega}) & \ldots & G_{\dot{\eta}_1 f_{n_{\mathrm{S}}}}(\mathrm{e}^{\mathrm{j}\omega}) \\ \vdots & & \vdots \\ G_{\dot{\eta}_\infty f_1}(\mathrm{e}^{\mathrm{j}\omega}) & \ldots & G_{\dot{\eta}_\infty f_{n_{\mathrm{S}}}}(\mathrm{e}^{\mathrm{j}\omega}) \end{pmatrix}}_{=\boldsymbol{G}_{\mathrm{S},\infty}} \begin{pmatrix} \tilde{f}_1(\omega) \\ \vdots \\ \tilde{f}_{n_{\mathrm{S}}}(\omega) \end{pmatrix} = \begin{pmatrix} \boldsymbol{G}_{\mathrm{S}} \\ \boldsymbol{G}_{\mathrm{S,r}} \end{pmatrix} \tilde{\boldsymbol{f}}, \tag{5.49}$$

where the first n_{S} rows of $\boldsymbol{G}_{\mathrm{S},\infty}$ constitute the square structural transfer matrix $\boldsymbol{G}_{\mathrm{S}}$, and the remaining rows form the residual part of $\boldsymbol{G}_{\mathrm{S},\infty}$. In Sec. 5.6.1, it was assumed that $\boldsymbol{G}_{\mathrm{S}}(\mathrm{e}^{\mathrm{j}\omega})$ is regular in the considered frequency range Ω. This implies that $\boldsymbol{G}_\mathrm{S}(z)$ has full normal rank and no transmission zeros on the unit circle in Ω. Here, spectral discretization is employed such that the outputs of $\boldsymbol{G}_\mathrm{S}$ are modal velocities. Then, it is easily shown (see App. D.5) that $\boldsymbol{G}_\mathrm{S}(z)$ does only have transmission zeros at $z = 1$, which stem from the differentiation of the modal displacements $\boldsymbol{\eta}$, and zeros inside the unit circle at frequencies well above Ω for sufficiently small sampling time T_s. Thus, regularity of $\boldsymbol{G}_\mathrm{S}(\mathrm{e}^{\mathrm{j}\omega})$ in $]0, 2\pi[$ is ensured if the first n_S modes can be excited by the actuators.

Due to the assumed regularity of $\boldsymbol{G}_\mathrm{S}$, the first n_S rows of $\boldsymbol{G}_{\mathrm{S},\infty}$ are linearly independent in $]0, 2\pi[$. This implies that these first rows constitute a basis for the row space of $\boldsymbol{G}_{\mathrm{S},\infty}$. In that case, the infinitely many rows of $\boldsymbol{G}_{\mathrm{S,r}}$ can be uniquely written as linear combinations of the first n_S rows,

$$\boldsymbol{G}_{\mathrm{S},\infty}(\mathrm{e}^{\mathrm{j}\omega}) = \begin{pmatrix} \boldsymbol{G}_{\dot\eta_1}(\mathrm{e}^{\mathrm{j}\omega}) \\ \vdots \\ \boldsymbol{G}_{\dot\eta_{n_\mathrm{S}}}(\mathrm{e}^{\mathrm{j}\omega}) \\ \sum_{i=1}^{n_\mathrm{S}} e_{(n_\mathrm{S}+1),i}(\mathrm{j}\omega)\, \boldsymbol{G}_{\dot\eta_i}(\mathrm{e}^{\mathrm{j}\omega}) \\ \vdots \\ \sum_{i=1}^{n_\mathrm{S}} e_{\infty,i}(\mathrm{j}\omega)\, \boldsymbol{G}_{\dot\eta_i}(\mathrm{e}^{\mathrm{j}\omega}) \end{pmatrix} \quad \text{with} \quad \omega \in \Omega, \tag{5.50}$$

where $\boldsymbol{G}_{\dot\eta_i} := \boldsymbol{G}_\mathrm{S}^{(i,:)}$. The coefficients $e_{i,j}(\mathrm{j}\omega)$ are functions of the positions of the excitation forces $\boldsymbol{f}$ and can therefore be influenced by the designer. Using the above result in (5.48) gives

$$\begin{aligned} \tilde{p}_k =& G_{p_k\dot\eta_1}\boldsymbol{G}_{\dot\eta_1}\tilde{\boldsymbol{f}} + \cdots + G_{p_k\dot\eta_{n_\mathrm{S}}}\boldsymbol{G}_{\dot\eta_{n_\mathrm{S}}}\tilde{\boldsymbol{f}} \\ &+ G_{p_k\dot\eta_{n_\mathrm{S}+1}}\sum_{i=1}^{n_\mathrm{S}} e_{(n_\mathrm{S}+1),i}\boldsymbol{G}_{\dot\eta_i}\tilde{\boldsymbol{f}} + \cdots + G_{p_k\dot\eta_\infty}\sum_{i=1}^{n_\mathrm{S}} e_{\infty,i}\boldsymbol{G}_{\dot\eta_i}\tilde{\boldsymbol{f}}, \end{aligned} \tag{5.51}$$

which is equivalent to

$$\begin{aligned} \tilde{p}_k =& G_{p_k\dot\eta_1}\dot{\tilde{\eta}}_1 + \cdots + G_{p_k\dot\eta_{n_\mathrm{S}}}\dot{\tilde{\eta}}_{n_\mathrm{S}} \\ &+ G_{p_k\dot\eta_{n_\mathrm{S}+1}}\sum_{i=1}^{n_\mathrm{S}} e_{(n_\mathrm{S}+1),i}\dot{\tilde{\eta}}_i + \cdots + G_{p_k\dot\eta_\infty}\sum_{i=1}^{n_\mathrm{S}} e_{\infty,i}\dot{\tilde{\eta}}_i. \end{aligned} \tag{5.52}$$

Collecting the modal velocity terms results in

$$\tilde{p}_k = \underbrace{\left(G_{p_k\dot\eta_1} + \sum_{i=n_\mathrm{S}+1}^{\infty} e_{i,1}G_{p_k\dot\eta_i} \right)}_{=:\tilde{G}_{p_k\dot\eta_1}} \dot{\tilde{\eta}}_1 + \cdots + \underbrace{\left(G_{p_k\dot\eta_{n_\mathrm{S}}} + \sum_{i=n_\mathrm{S}+1}^{\infty} e_{i,n_\mathrm{S}}G_{p_k\dot\eta_i} \right)}_{=:\tilde{G}_{p_k\dot\eta_{n_\mathrm{S}}}} \dot{\tilde{\eta}}_{n_\mathrm{S}}. \tag{5.53}$$

The last equation reveals the influence of the spectral discretization. Assuming that the first n_S modal velocities and p_k could be measured without error, the estimated frequency response would be $\boldsymbol{G}_{p_k} = (\tilde{G}_{p_k\dot\eta_1}, \ldots, \tilde{G}_{p_k\dot\eta_{n_\mathrm{S}}})$. Each element $\tilde{G}_{p_k\dot\eta_m}$ differs from the true FRF $G_{p_k\dot\eta_m}$ by an error term,

$$\tilde{G}_{p_k\dot\eta_m} = G_{p_k\dot\eta_m} + e_m, \quad \text{with} \quad e_m := \sum_{i=n_\mathrm{S}+1}^{\infty} e_{i,m}G_{p_k\dot\eta_i}, \quad m = 1, \ldots, n_\mathrm{S}. \tag{5.54}$$

The error coefficients $e_{i,j}$ are the same for every $p_k, k = 1, \dots, n_\mathrm{A}$.

The important point is that although the error terms may cause significant deviations between the true and the estimated frequency response functions, the estimated FRFs do allow for the correct calculation of the sound pressure caused by the inputs $f_i, i = 1, \dots, n_\mathrm{S}$ on the acoustical measurement surface . When the structure is excited by other inputs than those which were used to produce the identification data sets, the error terms $e_m, m = 1, \dots, n_\mathrm{S}$ will lead to a systematic error in the calculation of p_k. Thus, the following guidelines can be provided:

- The inputs $\boldsymbol{f}$ which are used to excite the structure to generate the data sets for identification of the acoustic frequency responses $\boldsymbol{G}_\mathrm{p}$ and $\boldsymbol{G}_\mathrm{v}$ should in general be identical to those excitations which will occur during normal operation of the system.
  Consequently, if the disturbance forces acting on the structure during normal operation can be reproduced, they should be included in the identification experiment.
  The actuator inputs which are used in the control loop should also be included in the acoustic identification experiment. This has the additional advantage that the structural plant model for control design and the acoustic models can be extracted from the same measurement data set.
- In addition to that, the influence of the error terms should be minimized by cautious actuator placement whenever possible. In case of modal velocities as structural variables, the actuators are positioned such that the modal velocities $\dot\eta_1, \dots, \dot\eta_{n_\mathrm{S}}$ can be sufficiently excited, but the first few adjacent modal velocities $\dot\eta_{n_\mathrm{S}+1}, \dot\eta_{n_\mathrm{S}+2}, \dots$ are of low controllability. A good compromise between these conflicting requirements can be found by suitable strategies for actuator placement, see for example [93, 99]. The actuator placement procedure for the experimental setup which is used in this thesis is illustrated in App. D.6.

Suitable actuator placement tends to reduce the magnitude of the rows adjacent to $\boldsymbol{G}_{\dot\eta_{n_\mathrm{S}}}$, and thus also the error coefficients $e_{i,j}(\mathrm{j}\omega)$ in the considered frequency range $[0, \Omega_\mathrm{max}]$. Moreover, if the modal density is not to high and the modal velocities are available without error, it can be assumed that the first n_S rows of (5.50) are dominant in $[0, \Omega_\mathrm{max}]$, i.e. the rows $n_\mathrm{S} + 1$ to infinity can be discarded with moderate error.

In practice however, the extraction of the modal quantities from physical measurements may come with a non-negligible error. The transformation matrix $\boldsymbol{T}$ is of dimension $(n_\mathrm{S} \times n_\mathrm{sensors})$, where n_sensors is the number of sensors on the structure. There exist two natural limits for the reconstruction of modal quantities:

- The number of reconstructed modal velocities is at most equal to the number of sensors, i.e. $n_\mathrm{S} \leq n_\mathrm{sensors}$. If this is not satisfied, the column space of $\boldsymbol{T}$ cannot span the complete vector space of modal velocities anymore. In practice, the quality of the reconstruction may deteriorate significantly when the number of modal quantities tends towards n_sensors.
- For a regular sensor array, the grid geometry must allow for the spatial reconstruction of the eigenfunction $W_i(\boldsymbol{x})$ of the corresponding modal quantity $\eta_i(t)$. More specifically, Shannon's

theorem must be satisfied for the spatial discretization of the eigenfunctions associated with the modal quantities which are significantly excited during the measurement experiment. If this is not satisfied, the dominant contributors $W_i(\boldsymbol{x})$ to the velocity profile $\dot{w}(\boldsymbol{x}, t)$ cannot be separated, and aliasing effects occur. This precludes the correct reconstruction of the associated modal velocities $\dot{\eta}_i(t)$.

Significant errors in the reconstruction of the modal quantities will deteriorate modal decoupling. This can be mathematically stated as

$$\boldsymbol{G}_{\mathrm{S}} = \boldsymbol{T}\,\boldsymbol{G}_{\dot{w}f} = (\boldsymbol{T}_0 + \boldsymbol{T}_{\mathrm{e}})\,\boldsymbol{G}_{\dot{w}f} = \boldsymbol{G}_{\mathrm{S},0} + \boldsymbol{G}_{\mathrm{S,e}}, \tag{5.55}$$

where $\boldsymbol{T}_0$ denotes the error-free transformation matrix and $\boldsymbol{T}_{\mathrm{e}}$ the error term. Due to the structural error transfer function $\boldsymbol{G}_{\mathrm{S,e}}$, negligence of the rows with index greater that n_{S} in (5.50) may not be justified anymore. This in turn implies an increased magnitude of the error coefficients and aggravates the problem of identifying the acoustic frequency responses.

Summing up, it is concluded that in order to reduce the effect of the error terms in (5.54), the following is important:

1. The magnitude of the error coefficients $e_{i,j}(\mathrm{j}\omega),\ 0 \leq \omega \leq \Omega_{\max}$ should be minimized by sensible actuator positioning whenever possible.

2. Proper reconstruction of the modal quantities also reduces the influence of the error terms by increasing the magnitude of the first n_{S} rows of (5.50) compared to the rows $n_{\mathrm{S}} + 1$ to infinity in the considered frequency range. This may be achieved by having $n_{\mathrm{S}} < {}^{n_{\mathrm{sensors}}}/_{2}$ and by ensuring that the structure is not excited at frequencies above $\Omega_{\max}$ during the measurements.

Analogue arguments can be put forward for the spatial discretization, $\boldsymbol{q} = \dot{\boldsymbol{w}}$, by considering an infinite number of surface point velocities, instead of infinitely many modal velocities. In that case, the structural transfer function can be written as the cascade of some transfer function from excitation forces to modal velocities followed by a matrix containing the eigenfunctions evaluated at the sensor points, compare (5.24),

$$\underbrace{\begin{pmatrix} \dot{w}_1 \\ \vdots \\ \dot{w}_{n_{\mathrm{sensors}}} \end{pmatrix}}_{=\dot{\boldsymbol{w}}} = \underbrace{\begin{pmatrix} W_1(\boldsymbol{x}_1) & \dots & W_\infty(\boldsymbol{x}_1) \\ \vdots & & \vdots \\ W_1(\boldsymbol{x}_{n_{\mathrm{sensors}}}) & \dots & W_\infty(\boldsymbol{x}_{n_{\mathrm{sensors}}}) \end{pmatrix}}_{=\boldsymbol{W}_\infty^{\mathrm{dis}}} \underbrace{\begin{pmatrix} G_{\dot{\eta}_1 f_1} & \dots & G_{\dot{\eta}_1 f_{n_{\mathrm{S}}}} \\ \vdots & & \vdots \\ G_{\dot{\eta}_\infty f_1} & \dots & G_{\dot{\eta}_\infty f_{n_{\mathrm{S}}}} \end{pmatrix}}_{=\boldsymbol{G}_{\dot{\eta}f,\infty}} \underbrace{\begin{pmatrix} f_1 \\ \vdots \\ f_{n_{\mathrm{S}}} \end{pmatrix}}_{=\boldsymbol{f}}, \tag{5.56}$$

and $\boldsymbol{G}_{\mathrm{S},\infty} = \boldsymbol{W}_\infty^{\mathrm{dis}} \boldsymbol{G}_{\dot{\eta}f,\infty}$. Further comments on the regularity of $\boldsymbol{G}_{\mathrm{S}}$ in this case can be found in App. D.5.

5.6.4 Positive-Definiteness Property

Once the acoustical frequency responses $\boldsymbol{G}_\mathrm{p}(\mathrm{e}^{\mathrm{j}\omega_n})$ and $\boldsymbol{G}_\mathrm{v}(\mathrm{e}^{\mathrm{j}\omega_n})$ have been estimated via the errors-in-variables estimator (5.44), the artificial frequency response $\hat{\boldsymbol{\Xi}} = \boldsymbol{G}_\mathrm{v}^{\mathrm{H}}\boldsymbol{G}_\mathrm{p}$ can be formed, from which the estimate of the PTM (5.41) is finally derived.
However, it cannot be expected that this estimate $\hat{\boldsymbol{\Pi}}(\omega_n)$ is positive definite, which is an important characteristic of any PTM, as explained in Sec. 5.4.2. This is mainly due to the following two reasons:

- The estimated PTM cannot be positive definite when negative mean values of the acoustic power are measured. Negative mean powers are mainly caused by two reasons:
  - According to (5.37), the estimated mean power is the sum of n_A mean intensity measurements. The mean sound intensity on some arbitrary point on the measurement surface is not sign-definite, i.e. can be positive, negative, or zero. It is just the sum of all intensity measurements which must be positive for an infinite number of measurement points. If the measurement grid on the surface A is to coarse, the sound power estimate is of low quality and can even become negative.
  - Measurement errors may wrongly indicate negative mean intensity measurements if the absolute value of the intensity is small. The reason for this is that the relative phase angles between p and v cannot be properly determined for low SNR ratios. To examine this in more detail, the relationship (5.37) is considered again. The sign of the mean intensity is given by

    $$\operatorname{sgn}\left\{\bar{I}(\boldsymbol{x})\right\} = \operatorname{sgn}\left\{\cos\varphi_\mathrm{f}(\boldsymbol{x})\right\}. \tag{5.57}$$

    Positive mean intensity implies that the field angle must not exceed ±90°. It is a well-known fact in linear acoustics that the field angle approaches 90° when the normal distance to some vibrating surface tends to zero under free-field conditions [69]. This also holds approximately true under non-free-field conditions, since the acoustic field very close to the sound emitting structure is not much altered by reflected waves [177].
    The dilemma is that measurements of sound intensity close to the surface of the sound-emitting structure are highly desirable because of the good SNR of $p(\boldsymbol{x},t)$ and $v(\boldsymbol{x},t)$, and the small measurement surface A. It is shown in [71] that small measurement errors in φ_f will lead to large relative errors in sound intensity when the absolute value of the field angle is close to ninety degrees,

    $$e_{\bar{I}} = \frac{\bar{I} - \bar{I}_0}{\bar{I}_0} = \cos(\varphi_\mathrm{e}) - \tan(\varphi_\mathrm{f})\sin(\varphi_\mathrm{e}) - 1, \tag{5.58}$$

    where $\bar{I}_0$ is the true mean intensity, and φ_e is the field angle error. The relationship (5.58) is plotted for different values of φ_e in Fig. 5.8.
- Even if no negative mean powers are measured during the identification experiments, the estimated PTM cannot be expected to be positive definite. This is illustrated by the following

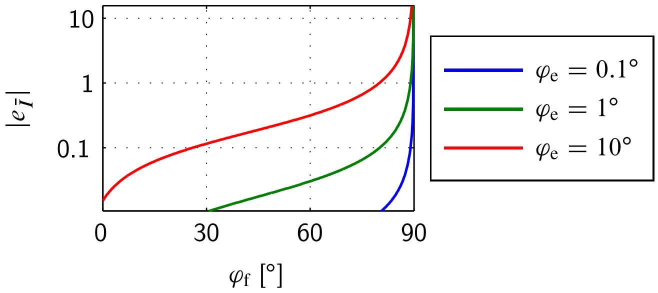

Figure 5.8: Magnitude of relative intensity error for different values of field angle error φ_{e}.

gedankenexperiment.

If the estimated FRFs $\boldsymbol{G}_{\mathrm{p}}(\mathrm{e}^{\mathrm{j}\omega_n})$ and $\boldsymbol{G}_{\mathrm{v}}(\mathrm{e}^{\mathrm{j}\omega_n})$ were identical to their true values, i.e. the discretization error were zero, the estimated PTM would be positive definite. However, as pointed out in Sec. 5.6.3, this is never the case for a finite number of structural variables. Nevertheless, the FRFs allow for the correct calculation of the pressures and particle velocities on the measurement surface for fixed disturbance input locations.

Performing n_{S} experiments with linearly independent inputs $(\tilde{\boldsymbol{f}}_1(\omega), \dots, \tilde{\boldsymbol{f}}_{n_{\mathrm{S}}}(\omega))$ results in the same number of linear independent structural variables $(\tilde{\boldsymbol{q}}_1(\omega), \dots, \tilde{\boldsymbol{q}}_{n_{\mathrm{S}}}(\omega))$ and the corresponding values for sound pressure and particle velocity. Since these are correct, the calculated mean sound powers $\bar{P}_1, \dots, \bar{P}_{n_{\mathrm{S}}}$ according to (5.40) and (5.41) are also correct and thus necessarily positive. Although the n_{S} vectors $\tilde{\boldsymbol{q}}_i(\omega)$ constitute a basis of $\mathbb{C}^{n_{\mathrm{S}}}$, $\bar{P}_i = \tilde{\boldsymbol{q}}_i^{\mathrm{H}} \hat{\boldsymbol{\Pi}} \tilde{\boldsymbol{q}}_i > 0, i = 1, \dots, n_{\mathrm{S}}$ is not a sufficient condition for $\hat{\boldsymbol{\Pi}}(\omega)$ to be positive definite [178]. For that reason, the discretization error may well lead to an indefinite estimate of the PTM $\hat{\boldsymbol{\Pi}}$.

To ensure a positive definite model of the PTM, appropriate modifications on its estimate have to be carried out. This issue will be dealt with in Sec. 5.7.

In addition to that, a parametric model of the PTM will be necessary for model-based control design, which can be computed from a parametric model $\boldsymbol{\Xi}(z)$ of $\hat{\boldsymbol{\Xi}}(\mathrm{e}^{\mathrm{j}\omega_n})$. This could in turn be computed from parametric models of $\boldsymbol{G}_{\mathrm{p}}$ and $\boldsymbol{G}_{\mathrm{v}}$, but fitting the frequency responses of the acoustic transfer functions would result in a parametric model with n_{S} inputs and n_{A} outputs, where typically $n_{\mathrm{A}} \gg n_{\mathrm{S}}$. It is more economical to compute a non-parametric model $\hat{\boldsymbol{\Xi}}(\mathrm{e}^{\mathrm{j}\omega_n})$ from the acoustic FRFs and then fit the frequency response of $\hat{\boldsymbol{\Xi}}$, which results in a model of dimension $(n_{\mathrm{S}} \times n_{\mathrm{S}})$.

5.6.5 Parametric Modeling of Acoustic Transfer Functions

The non-parametric model of the artificial frequency response matrix $\hat{\boldsymbol{\Xi}}(\mathrm{e}^{\mathrm{j}\omega_n})$ shall now be replaced by a parametric model $\boldsymbol{\Xi}(z)$. This can be accomplished by fitting the parameters of a multiple-input multiple-output model such that its frequency responses match those of the estimated FRFs. However, it is illusive to achieve this perfectly. The estimated FRFs can never be exactly matched mainly because of the following reasons:

- The estimated FRFs are generally distorted by noise. This results in noisy frequency response curves which should not (and cannot) be perfectly matched by parametric models of moderate order.
- Even in the noise-free case, models of very high order would be necessary to achieve a perfect matching. This is undesirable because of the resulting computational effort and numerical complications.
- The non-parametric model may be distorted by nonlinearities which cannot be reproduced by linear models of arbitrary order.

Having this notion of imperfectness in mind, it is clear that the criterion

$$J_{\boldsymbol{\Xi}} = \sum_{\omega_n \in \Omega} \sum_{i=1}^{n_\mathrm{S}} \sum_{j=1}^{n_\mathrm{S}} \left| \hat{\boldsymbol{\Xi}}_{ij}(\mathrm{e}^{\mathrm{j}\omega_n}) - \boldsymbol{\Xi}_{ij}(\mathrm{e}^{\mathrm{j}\omega_n}) \right|^2 = \left\| \mathrm{vec}\left\{ \hat{\boldsymbol{\Xi}}_{\Omega} - \boldsymbol{\Xi}_{\Omega} \right\} \right\|_2^2 \tag{5.59}$$

with $\boldsymbol{\Xi}_{\Omega} = (\boldsymbol{\Xi}\,(\mathrm{e}^{\mathrm{j}\omega_1}), \ldots, \boldsymbol{\Xi}\,(\mathrm{e}^{\mathrm{j}\omega_N}))$ cannot be brought to zero. The set $\Omega = (\omega_1 \ldots, \omega_N)$ shall contain the samples in the frequency domain of interest.

The purpose of the parametric model $\boldsymbol{\Xi}$ is to compute a parametric model of the PTM, and with this matrix reproduce the sound power measurements as well as possible from the structural variables $\boldsymbol{q}$. The problem with the above criterion is that one does not know a-priori what frequency ranges and which input-output channels are critical for reproducing the sound power measurements. Thus, it is proposed to use the discrepancy between the reconstructed sound powers of the non-parametric and parametric models as objective function,

$$J_{\bar{P}} = \sum_{\omega_n \in \Omega} \sum_{m=1}^{M} \left(\hat{\bar{P}}_m(\omega_n) - \bar{P}_m(\omega_n) \right)^2, \tag{5.60}$$

with M being the number of sound power measurements. The quantities $\hat{\bar{P}}_m$ and $\bar{P}_m$ are given by using the non-parametric PTM $\hat{\boldsymbol{\Pi}}$ and the parametric PTM $\boldsymbol{\Pi}$ in (5.31), respectively. Since $\hat{\boldsymbol{\Pi}}$ is computed from $\boldsymbol{G}_\mathrm{p}$ and $\boldsymbol{G}_\mathrm{v}$, which in turn accurately reproduce $\boldsymbol{p}$ and $\boldsymbol{v}$ from the structural variables $\boldsymbol{q}$ for the measurement data sets, the sound powers $\hat{\bar{P}}_m$ are almost identical to the measured sound powers, which are given by the relationship (5.37). This is why the same notation $\hat{\bar{P}}_m$ is used here.

As explained in Sec. 5.6.1, one necessarily has $M \geq n_\mathrm{S}$. The function (5.60) can be rewritten in terms of $\Delta\boldsymbol{\Xi}_{\Omega} := \hat{\boldsymbol{\Xi}}_{\Omega} - \boldsymbol{\Xi}_{\Omega}$ with the help of $\boldsymbol{P}(\omega) = (\bar{P}_1(\omega_n), \ldots, \bar{P}_M(\omega_n))^\mathrm{T}$ as

$$\begin{aligned} J_{\bar{P}} &= \sum_{\omega_n \in \Omega} \left\| \hat{\boldsymbol{P}}(\omega_n) - \boldsymbol{P}(\omega_n) \right\|_2^2 \\ &= \sum_{\omega_n \in \Omega} \left\| \mathrm{diag}\left\{ \boldsymbol{Q}^\mathrm{H} \hat{\boldsymbol{\Pi}}\, \boldsymbol{Q} - \boldsymbol{Q}^\mathrm{H} \boldsymbol{\Pi} \boldsymbol{Q} \right\} \right\|_2^2 \quad \text{(see (5.31))} \\ &= \sum_{\omega_n \in \Omega} \left\| \mathrm{diag}\left\{ \boldsymbol{Q}^\mathrm{H} \left[\hat{\boldsymbol{\Pi}} - \boldsymbol{\Pi} \right] \boldsymbol{Q} \right\} \right\|_2^2 . \end{aligned}$$

This can be further expanded as

$$
\begin{aligned}
J_{\bar{P}} &= \sum_{\omega_n \in \Omega} \left\| \mathrm{diag} \left\{ \boldsymbol{Q}^{\mathrm{H}} \left[\frac{1}{4} A_{\mathrm{el}} \left(\hat{\boldsymbol{\Xi}} + \hat{\boldsymbol{\Xi}}^{\mathrm{H}} \right) - \frac{1}{4} A_{\mathrm{el}} \left(\boldsymbol{\Xi} + \boldsymbol{\Xi}^{\mathrm{H}} \right) \right] \boldsymbol{Q} \right\} \right\|_2^2 \quad \text{(see (5.41))} \\
&= \frac{1}{16} A_{\mathrm{el}}^2 \sum_{\omega_n \in \Omega} \left\| \mathrm{diag} \left\{ \boldsymbol{Q}^{\mathrm{H}} \left[\hat{\boldsymbol{\Xi}} - \boldsymbol{\Xi} + \hat{\boldsymbol{\Xi}}^{\mathrm{H}} - \boldsymbol{\Xi}^{\mathrm{H}} \right] \boldsymbol{Q} \right\} \right\|_2^2 \\
&= \frac{1}{16} A_{\mathrm{el}}^2 \sum_{\omega_n \in \Omega} \left\| \mathrm{diag} \left\{ \boldsymbol{Q}^{\mathrm{H}} \left[\Delta \boldsymbol{\Xi} + \Delta \boldsymbol{\Xi}^{\mathrm{H}} \right] \boldsymbol{Q} \right\} \right\|_2^2 \\
&= \frac{1}{16} A_{\mathrm{el}}^2 \sum_{\omega_n \in \Omega} \left\| \mathrm{diag} \left\{ \boldsymbol{Q}^{\mathrm{H}} \Delta \boldsymbol{\Xi} \boldsymbol{Q} \right\} + \mathrm{diag} \left\{ \boldsymbol{Q}^{\mathrm{H}} \Delta \boldsymbol{\Xi} \boldsymbol{Q} \right\}^{\mathrm{H}} \right\|_2^2 \\
&= \frac{1}{4} A_{\mathrm{el}}^2 \sum_{\omega_n \in \Omega} \left\| \Re \left\{ \mathrm{diag} \left\{ \boldsymbol{Q}^{\mathrm{H}} \Delta \boldsymbol{\Xi} \boldsymbol{Q} \right\} \right\} \right\|_2^2 \\
&= \frac{1}{4} A_{\mathrm{el}}^2 \sum_{\omega_n \in \Omega} \left\| \Re \left\{ \underbrace{\boldsymbol{T}_1 \left(\boldsymbol{Q}^{\mathrm{T}}(\omega_n) \otimes \boldsymbol{Q}^{\mathrm{H}}(\omega_n) \right)}_{=:\boldsymbol{W}_n} \mathrm{vec}\, \Delta \boldsymbol{\Xi}\, (\omega_n) \right\} \right\|_2^2 \quad \text{(see (D.16)).}
\end{aligned}
\tag{5.61}
$$

Defining $\boldsymbol{e} := \mathrm{vec}\{\Delta \boldsymbol{\Xi}_{\Omega}\}$ and $\boldsymbol{W} := \bigoplus_{n=1}^{N} \boldsymbol{W}_n$, the final result is

$$
J_{\bar{P}} = \frac{1}{4} A_{\mathrm{el}}^2 \left\| \Re \left\{ \boldsymbol{W} \boldsymbol{e} \right\} \right\|_2^2 . \tag{5.62}
$$

The task is now to find a parametric model $\boldsymbol{\Xi}\,(z)$ which minimizes (5.62). The error vector $\boldsymbol{e}$ is linear in the FRF of the model $\boldsymbol{\Xi}\,(\mathrm{e}^{\mathrm{j}\omega_n})$. The model FRF itself, however, is usually a nonlinear function of the model parameters. This renders the modeling problem nonconvex, which requires iterative optimization techniques. More specifically, minimizing (5.62) with respect to the model parameters is a nonlinear weighted least-squares problem. Good initial values for the optimization procedure can be generated by simplifying $J_{\bar{P}}$ such that it becomes convex in the model parameters and solving the resulting ordinary least-squares problem. The parametric modeling procedure is further explained in App. D.7.

5.7 Enforcing Positive Definiteness of Power Transfer Matrices

It was explained in Sec. 5.6.4 that the frequency response of the identified parametric PTM model, $\boldsymbol{\Pi}\,(\omega_n) = \frac{1}{4} A_{\mathrm{el}} (\boldsymbol{\Xi}\,(\mathrm{e}^{\mathrm{j}\omega_n}) + \boldsymbol{\Xi}^{\mathrm{H}}(\mathrm{e}^{\mathrm{j}\omega_n}))$, cannot be expected to be positive definite at all frequencies. Consequently, this property must be enforced in a subsequent step by adjusting the parametric model $\boldsymbol{\Xi}\,(z)$ without sacrificing to much accuracy of the PTM model. For a state space representation of $\boldsymbol{\Xi}$, it will be shown shortly that manipulating all four constituent matrices is of course an option, but leads to a non-convex optimization problem. In order to end up with a convex problem, only a subset of the state space matrices must be taken as optimization variables.

Before elaborating on the mathematical details, it is insightful to look at two extreme situations in which the parametric PTM model may be calculated from the artificial system $\boldsymbol{\Xi}\,(z)$.

In the first case, the sound-emitting structure radiates into free field, and the surface for sound intensity measurement A shall be identical to the structural surface S. Then, the normal particle velocity component is identical to the structural velocity, $v(\boldsymbol{x}, t) = \dot{w}(\boldsymbol{x}, t)$. This makes it possible to choose the structural variables $\boldsymbol{q}$ such that $\boldsymbol{G}_{\mathrm{v}}(z)$ is constant. For $\boldsymbol{q} = \dot{\boldsymbol{\eta}}$ for example, one has $\boldsymbol{G}_{\mathrm{v}} = \boldsymbol{W}_{\mathrm{e}}^{\mathrm{dis}}$, compare (5.24). If the variables $\boldsymbol{q}$ are proportional to structural acceleration or displacement, $\boldsymbol{G}_{\mathrm{v}}$ does only have poles or zeros at $z = 1$. The same holds true for the conjugate system[3] $\boldsymbol{G}_{\mathrm{v}}^{\sim}(z)$, having frequency response $\boldsymbol{G}_{\mathrm{v}}^{\mathrm{H}}(\mathrm{e}^{\mathrm{j}\omega_n})$. Since $\boldsymbol{G}_{\mathrm{p}}(z)$ is inherently stable, it follows that $\boldsymbol{\Xi}(z) = \boldsymbol{G}_{\mathrm{v}}^{\sim}(z)\boldsymbol{G}_{\mathrm{p}}(z)$ cannot have poles outside the unit circle, i.e. is stable in the sense of Lyapunov. This, together with the requirement

$$\boldsymbol{\Pi}(\omega) > \mathbf{0} \Leftrightarrow \boldsymbol{\Xi}\left(\mathrm{e}^{\mathrm{j}\omega}\right) + \boldsymbol{\Xi}^{\mathrm{H}}\left(\mathrm{e}^{\mathrm{j}\omega}\right) > \mathbf{0}, \quad \forall \omega \in [-\pi, \pi], \tag{5.63}$$

is equivalent to saying that $\boldsymbol{\Xi}(z)$ must be *strictly positive real* [197], which reflects the passivity property of $\boldsymbol{\Xi}$ in case $S = A$.

In the other extreme case, the intensity measurement surface A is located infinitely far from the structure. Then, every structure-borne sound field can be described by plane waves. This implies that at any point $\boldsymbol{x}$ on A, the acoustic point impedance is Z_0, which means that pressure and normal particle velocity are related by $\tilde{p}(\boldsymbol{x}, \omega) = Z_0 \tilde{v}(\boldsymbol{x}, \omega)$. Thus, $\boldsymbol{G}_{\mathrm{p}}(z) = Z_0 \boldsymbol{G}_{\mathrm{v}}(z)$, and $\boldsymbol{\Xi}(z) = \frac{1}{Z_0}\boldsymbol{G}_{\mathrm{p}}^{\sim}(z)\boldsymbol{G}_{\mathrm{p}}(z)$. Since $\boldsymbol{G}_{\mathrm{p}} \in \mathbb{C}^{n_{\mathrm{A}} \times n_{\mathrm{S}}}$ can be assumed to be of full column rank, one has $\boldsymbol{\Xi}(\mathrm{e}^{\mathrm{j}\omega}) > \mathbf{0}$, and consequently also $\boldsymbol{\Pi}(\mathrm{e}^{\mathrm{j}\omega}) > \mathbf{0}$. This shows that the positive-definiteness property of the PTM is automatically satisfied when $\boldsymbol{\Xi}$ is evaluated at an infinite distance from the sound source.

At any realistic distance, it must be expected that the estimated PTM is neither positive definite, nor is $\boldsymbol{\Xi}(z)$ Lyapunov stable.

The requirement (5.63) involves the computation of the eigenvalues of the PTM on a continuous frequency grid, which is not practically tractable. An equivalent test for positive definiteness can be found by applying the celebrated Kalman-Yakubovich-Popov (KYP) lemma. The main result can be stated, following the publication by Rantzer [157]:

KYP lemma: *Given matrices* $\boldsymbol{A} \in \mathbb{R}^{n \times n}$, $\boldsymbol{B} \in \mathbb{R}^{n \times q}$, $\boldsymbol{M} = \boldsymbol{M}^{\mathrm{T}} \in \mathbb{R}^{(n+q)\times(n+q)}$, *with* $\det\{\mathrm{e}^{\mathrm{j}\omega} - A\} \neq 0$ *for* $\omega \in \mathbb{R}$, *the following two statements are equivalent:*

1.
$$\begin{bmatrix} \left(\mathrm{e}^{\mathrm{j}\omega}\mathbf{I} - \boldsymbol{A}\right)^{-1}\boldsymbol{B} \\ \mathbf{I}_q \end{bmatrix}^{\mathrm{H}} \boldsymbol{M} \begin{bmatrix} \left(\mathrm{e}^{\mathrm{j}\omega}\mathbf{I} - \boldsymbol{A}\right)^{-1}\boldsymbol{B} \\ \mathbf{I}_q \end{bmatrix} > \mathbf{0}, \qquad \forall \omega \in \mathbb{R}.$$

2. *There exists a symmetric matrix* $\boldsymbol{P} \in \mathbb{R}^{n \times n}$ *such that*

$$\boldsymbol{M} + \begin{bmatrix} \boldsymbol{P} - \boldsymbol{A}^{\mathrm{T}}\boldsymbol{P}\boldsymbol{A} & -\boldsymbol{A}^{\mathrm{T}}\boldsymbol{P}\boldsymbol{B} \\ -\boldsymbol{B}^{\mathrm{T}}\boldsymbol{P}\boldsymbol{A} & -\boldsymbol{B}^{\mathrm{T}}\boldsymbol{P}\boldsymbol{B} \end{bmatrix} > \mathbf{0}.$$

---

[3] The conjugate system $\boldsymbol{G}^{\sim}(z)$ to a given system $\boldsymbol{G}(z)$ has frequency response $\boldsymbol{G}^{\mathrm{H}}(\mathrm{e}^{\mathrm{j}\omega})$ and is given by $\boldsymbol{G}^{\mathrm{T}}(1/z)$.

With the state space representation $\boldsymbol{\Xi}(z) = \boldsymbol{C}(z\mathbf{I} - \boldsymbol{A})^{-1}\boldsymbol{B} + \boldsymbol{D}$, it can be readily verified that this result is applicable to the problem of checking (5.63) by selecting

$$\boldsymbol{M} = \begin{pmatrix} \mathbf{0} & \boldsymbol{C}^{\mathrm{T}} \\ \boldsymbol{C} & \boldsymbol{D} + \boldsymbol{D}^{\mathrm{T}} \end{pmatrix}. \tag{5.64}$$

More precisely, (5.63) holds iff there exists a symmetric matrix $\boldsymbol{P}$ such that

$$\begin{pmatrix} \boldsymbol{P} - \boldsymbol{A}^{\mathrm{T}}\boldsymbol{P}\boldsymbol{A} & \boldsymbol{C}^{\mathrm{T}} - \boldsymbol{A}^{\mathrm{T}}\boldsymbol{P}\boldsymbol{B} \\ \boldsymbol{C} - \boldsymbol{B}^{\mathrm{T}}\boldsymbol{P}\boldsymbol{A} & \boldsymbol{D} + \boldsymbol{D}^{\mathrm{T}} - \boldsymbol{B}^{\mathrm{T}}\boldsymbol{P}\boldsymbol{B} \end{pmatrix} > \mathbf{0}. \tag{5.65}$$

This requirement is affine in the matrix parameters $\boldsymbol{P}$, $\boldsymbol{C}$, and $\boldsymbol{D}$. We pose the following constrained optimization problem:

$$\begin{aligned} \min_{\boldsymbol{P},\boldsymbol{C},\boldsymbol{D}} \quad & J = \|\Re\{\boldsymbol{W}\boldsymbol{e}\}\|_2^2 \\ \text{s. t.} \quad & (5.65). \end{aligned} \tag{5.66}$$

The error vector $\boldsymbol{e} = \operatorname{vec}\{\hat{\boldsymbol{\Xi}}_{\Omega} - \boldsymbol{\Xi}_{\Omega}\}$ is affine in the state space matrices $\boldsymbol{C}$ and $\boldsymbol{D}$, which implies that $J(\boldsymbol{C}, \boldsymbol{D})$ is a convex function. Together with the convex constraint (5.65), the optimization problem becomes convex and can be solved by suitable optimization algorithms, see for example [34]. It it assumed in the following that the parametric model $\boldsymbol{\Xi}(z)$ has no poles on the unit circle, such that the KYP lemma is applicable.

In order to properly pose the problem (5.66), the function $J(\boldsymbol{C}, \boldsymbol{D})$ is expanded as follows. Define the matrix

$$\boldsymbol{H} := \begin{bmatrix} \left(\mathrm{e}^{\mathrm{j}\omega_1 T_{\mathrm{s}}}\mathbf{I} - \boldsymbol{A}\right)^{-1}\boldsymbol{B} & \dots & \left(\mathrm{e}^{\mathrm{j}\omega_N T_{\mathrm{s}}}\mathbf{I} - \boldsymbol{A}\right)^{-1}\boldsymbol{B} \\ \mathbf{I}_{n_{\mathrm{S}}} & \dots & \mathbf{I}_{n_{\mathrm{S}}} \end{bmatrix} \tag{5.67}$$

with the frequency set of interest $\Omega = \{\omega_1, \dots, \omega_N\}$ and the corresponding FRF values of the non-parametric model, $\hat{\boldsymbol{\Xi}}_{\Omega} = (\hat{\boldsymbol{\Xi}}(\mathrm{e}^{\mathrm{j}\omega_1 T_{\mathrm{s}}}), \dots, \hat{\boldsymbol{\Xi}}(\mathrm{e}^{\mathrm{j}\omega_N T_{\mathrm{s}}}))$. Now, set $\boldsymbol{K} = \Re\{\boldsymbol{W}(\boldsymbol{H}^{\mathrm{T}} \otimes \mathbf{I}_{n_{\mathrm{S}}})\}$ and $\boldsymbol{l} = \Re\{\boldsymbol{W}\operatorname{vec}\hat{\boldsymbol{\Xi}}_{\Omega}\}$. Then, we have for the weighted error vector

$$\Re\{\boldsymbol{W}\boldsymbol{e}\} = \Re\left\{\boldsymbol{W}\operatorname{vec}\left\{\hat{\boldsymbol{\Xi}}_{\Omega} - \boldsymbol{\Xi}_{\Omega}\right\}\right\} = \boldsymbol{l} - \boldsymbol{K}\boldsymbol{x}, \tag{5.68}$$

where $\boldsymbol{x} = \operatorname{vec}(\boldsymbol{C}\ \ \boldsymbol{D})$ contains the state space matrices to be optimized. Thus, the objective function is given by

$$J = \|\Re\{\boldsymbol{W}\boldsymbol{e}\}\|_2^2 = \boldsymbol{x}^{\mathrm{T}}\boldsymbol{K}^{\mathrm{T}}\boldsymbol{K}\boldsymbol{x} - 2\boldsymbol{l}^{\mathrm{T}}\boldsymbol{K}\boldsymbol{x} + \boldsymbol{l}^{\mathrm{T}}\boldsymbol{l}. \tag{5.69}$$

This formulation can be used to implement the objective function J subject to the constraint (5.65).

It is readily deduced that (5.63) holds if and only if it holds for the dual system of $\boldsymbol{\Xi}(z)$ with transfer function $\boldsymbol{B}^{\mathrm{T}}(z\mathbf{I} - \boldsymbol{A}^{\mathrm{T}})^{-1}\boldsymbol{C}^{\mathrm{T}} + \boldsymbol{D}^{\mathrm{T}}$. This allows us to give an alternative test for the positive definiteness property of the PTM,

$$\begin{pmatrix} \boldsymbol{P} - \boldsymbol{A}\boldsymbol{P}\boldsymbol{A}^{\mathrm{T}} & \boldsymbol{B} - \boldsymbol{A}\boldsymbol{P}\boldsymbol{C}^{\mathrm{T}} \\ \boldsymbol{B}^{\mathrm{T}} - \boldsymbol{C}\boldsymbol{P}\boldsymbol{A}^{\mathrm{T}} & \boldsymbol{D} + \boldsymbol{D}^{\mathrm{T}} - \boldsymbol{C}\boldsymbol{P}\boldsymbol{C}^{\mathrm{T}} \end{pmatrix} > \mathbf{0}. \tag{5.70}$$

This formulation is affine in the parameters $\boldsymbol{P}$, $\boldsymbol{B}$, and $\boldsymbol{D}$, and consequently, one can pose the dual problem

$$\begin{aligned} \min_{\boldsymbol{P},\boldsymbol{B},\boldsymbol{D}} \quad & J = \|\Re\{\boldsymbol{W}\boldsymbol{e}\}\|_2^2 \\ & \text{s. t.} \quad (5.70). \end{aligned} \tag{5.71}$$

A formulation analog to (5.69) for the dual problem can be easily found.

The optimization problems (5.66) and (5.71) are both convex, but do in general not share the same minimum. Surely, degrees of freedom exist for posing these optimization problems, because the input-output mapping of $\boldsymbol{\Xi}(z)$ is invariant under regular state transformation. This immediately raises the question which state space coordinate system to choose before solving (5.66) or (5.71) in order to improve the numerical conditioning of the problem.

To this end, one might guess that it is helpful to put the state space model for $\boldsymbol{\Xi}$ into controllable canonical form for problem (5.66). The argument would be that the input matrix $\boldsymbol{B}$ is predetermined, containing only ones and zeros at certain positions. The information on the system's specific input-output behavior is only stored in the optimization variables $\boldsymbol{C}$ and $\boldsymbol{D}$. However, this canonical form also imposes heavy constraints on the system matrix $\boldsymbol{A}$ by enforcing integrator chains of certain lengths given by the system's controllability indices. This unduly reduces the amount by which the system's input-output behavior can be modified by altering the optimization variables. Arguments following the same line of thought can be put forward for problem (5.71) in observable canonical form. Simulation results show that satisfying results can be obtained by using a real-valued modal state space form, in which there is no interconnection of system states apart from that of the conjugate-complex pole pairs.

5.8 Control Design

The results of the last sections are readily applicable for optimal control design to minimize the emitted mean sound power of a vibrating structure. To this end, a state space model of the structure to be controlled shall be given by $\boldsymbol{G}(z) = \boldsymbol{C}(z\mathbf{I}-\boldsymbol{A})^{-1}\boldsymbol{B}+\boldsymbol{D}$. The system $\boldsymbol{G}$ maps the n_u control inputs to the n_{sensors} sensor outputs, i. e. $\boldsymbol{y}_{\text{s}}(z) = \boldsymbol{G}(z)\boldsymbol{u}(z)$. As pointed out in Sec. 5.6.3, the inputs of $\boldsymbol{G}$ should be a subset of the inputs of $\boldsymbol{G}_{\text{S}}(z)$.

We now consider the generalized plant $\boldsymbol{P}(z)$ shown in Fig. 5.9. It is further assumed that the structural variables $\boldsymbol{q}$ are formed by processing the sensor outputs $\boldsymbol{y}_{\text{S}}$ by a static filter $\boldsymbol{T}$, as is done in modal filtering. The input matrix $\boldsymbol{B}_w$ represents the influence of the disturbance forces $\boldsymbol{w}_1$ on the structure. Since it is generally unknown, it will be set to unity in the following, i.e. $\boldsymbol{B}_w = \mathbf{I}_n$, where n is the model order of $\boldsymbol{G}$. If some knowledge is present on how the disturbances act on the structure, it may be included here. In case that the frequency spectrum of the disturbance is known, one may add a suitably designed filter preceding $\boldsymbol{B}_w$, and let $\boldsymbol{w}_1$ enter this filter.

The critical issue is to find a performance weight $\boldsymbol{W}_{\text{p}}$ to weight the structural variables $\boldsymbol{q}$ such that the output of $\boldsymbol{W}_{\text{p}}$, $\boldsymbol{z}_1$, suitably represents the controlled output sound power. This is achieved by spectral decomposition of the parametric model of the PTM, $\boldsymbol{\Pi}(z)$, which was first proposed by

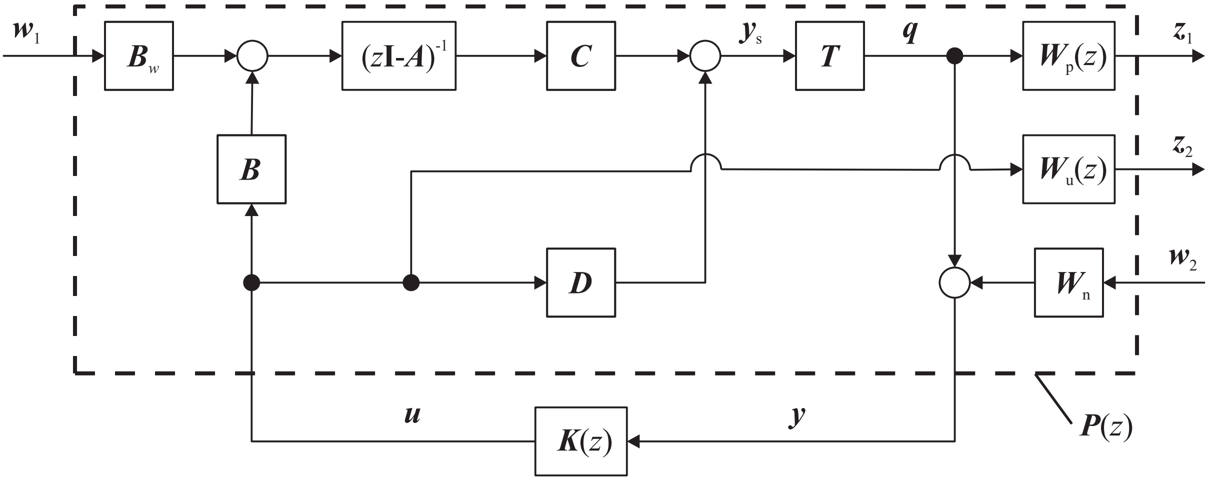

Figure 5.9: Control loop with generalized plant $\boldsymbol{P}(z)$ and controller $\boldsymbol{K}(z)$ for ASAC design.

Baumann in [15]. The spectral decomposition has the form $\boldsymbol{\Pi}(z) = \boldsymbol{F}_+(z)\boldsymbol{F}_-(z)$, where $\boldsymbol{F}_-$ is minimum phase, and $\boldsymbol{F}_+$ has all poles and zeros outside the unit disc. More specifically, $\boldsymbol{F}_-$ and $\boldsymbol{F}_+$ are conjugate transfer matrix pairs, which implies $\boldsymbol{F}_+(\mathrm{e}^{\mathrm{j}\omega}) = \boldsymbol{F}_-(\mathrm{e}^{\mathrm{j}\omega})^{\mathrm{H}}$.

Spectral decomposition can be performed directly in the discrete time domain, but is more common for continuous-time transfer functions. The characteristic properties of the spectral factors' pole-zero patterns are retained under bilinear transformation. Thus, it is also possible to perform the spectral decomposition for the continuous-time counterpart $\boldsymbol{\Pi}(s)$ of the PTM, and then transform back its spectral factors via bilinear transformation. One may consult [73] for details on an algorithm for continuous-time spectral factorization and [182] for a discrete-time counterpart. It is also shown in the second publication that $\boldsymbol{\Xi}(\mathrm{e}^{\mathrm{j}\omega}) + \boldsymbol{\Xi}^{\mathrm{H}}(\mathrm{e}^{\mathrm{j}\omega}) > \mathbf{0},\ \forall\omega \in [-\pi, \pi]$ is a sufficient condition for the spectral factors to exist. Letting $\boldsymbol{W}_{\mathrm{p}}(z) = \boldsymbol{F}_-(z)$ leads to

$$\bar{P}(\omega) = \boldsymbol{q}^{\mathrm{H}}(\omega)\boldsymbol{\Pi}(\omega)\boldsymbol{q}(\omega) = \boldsymbol{q}^{\mathrm{H}}\boldsymbol{F}_-(\mathrm{e}^{\mathrm{j}\omega})^{\mathrm{H}}\boldsymbol{F}_-(\mathrm{e}^{\mathrm{j}\omega})\boldsymbol{q}(\omega) = \boldsymbol{z}_1(\omega)^{\mathrm{H}}\boldsymbol{z}_1(\omega). \qquad (5.72)$$

The transfer matrix $\boldsymbol{W}_{\mathrm{u}}(z)$ is used to limit the control effort in exactly the same way as in active vibration control, see Sec. 4.3.2. Also similarly, the constant noise weighting matrix $\boldsymbol{W}_{\mathrm{n}} = \mathbf{I}_{n_{\mathrm{S}}} W_{\mathrm{n}}$ is used to model the influence of measurement noise on the structural variables and to regularize the control design problem.

The goal of ASAC design is to find a controller $\boldsymbol{K}(z)$ which minimizes the magnitude of the transfer path from disturbances $\boldsymbol{w}_1$ to emitted mean sound power $\bar{P}$. We want to quantify this magnitude as follows: Assuming that the n time sequences $\boldsymbol{w}_1(k) = (w_{1,1}(k), \ldots, w_{1,n}(k))^{\mathrm{T}}$ are mutually uncorrelated, and each sequence is a white noise random process of unit intensity, we want to minimize $\bar{P}$. To this end, we establish the relationship between the RMS value of the performance variables $\boldsymbol{z}_1(k)$ and $\bar{P}$ with the help of Parseval's theorem,

$$\mathrm{RMS}\,\boldsymbol{z}_1(k) = \sqrt{\mathrm{E}\left\{\boldsymbol{z}_1^{\mathrm{T}}(k)\boldsymbol{z}_1(k)\right\}} = \sqrt{\mathrm{E}\left\{\frac{1}{2\pi}\int_{-\pi}^{\pi} \underbrace{\boldsymbol{z}_1^{\mathrm{H}}(\mathrm{e}^{\mathrm{j}\omega})\boldsymbol{z}_1(\mathrm{e}^{\mathrm{j}\omega})}_{=\bar{P}(\omega)}\,\mathrm{d}\omega\right\}}. \qquad (5.73)$$

For the first equality, it was assumed that $z_1(k)$ is wide-sense stationary, which is ensured if $\boldsymbol{w}_1$ has the stated properties. Thus, minimizing the RMS value of z_1 means minimizing the frequency-average emitted mean sound power. Let the closed-loop transfer matrix from $\boldsymbol{w}_1$ to z_1 be denoted by $\boldsymbol{T}_{z_1 w_1}$. Then, it further holds

$$\begin{aligned}\mathrm{RMS}\, z_1(k) &= \sqrt{\mathrm{E}\left\{\frac{1}{2\pi}\int_{-\pi}^{\pi} \boldsymbol{w}_1^{\mathrm{H}} \boldsymbol{T}_{z_1 w_1}^{\mathrm{H}} \boldsymbol{T}_{z_1 w_1} \boldsymbol{w}_1 \,\mathrm{d}\omega\right\}} \\ &= \sqrt{\frac{1}{2\pi}\int_{-\pi}^{\pi} \mathrm{tr}\left\{\boldsymbol{T}_{z_1 w_1}^{\mathrm{H}} \boldsymbol{T}_{z_1 w_1}\right\} \mathrm{d}\omega} \\ &= \left\| \boldsymbol{T}_{z_1 w_1}(z) \right\|_2 .\end{aligned} \tag{5.74}$$

This shows that the RMS value of z_1 is minimized by a controller which minimizes the $\mathcal{H}_2$ norm of the disturbance transfer path. In a practical design, a controller is sought which minimizes the norm of the transfer matrix from both input sets $\boldsymbol{w}_1$ and $\boldsymbol{w}_2$ to both output sets z_1 and z_2.

In order to ensure regularity of the $\mathcal{H}_2$ problem, the same restrictions on the weights $\boldsymbol{W}_\mathrm{u}$ and $\boldsymbol{W}_\mathrm{n}$ apply as in Sec. 4.3.2. In fact, acoustic control design can be treated exactly the same way as the vibration control design presented in the last chapter but with a different performance weight $\boldsymbol{W}_\mathrm{p}$. Robustness analysis can also be done analogously.

5.9 Examples

As in the last two chapters, the proposed design methodology for global ASAC control shall be illustrated and validated by simulation as well as experimental results.

5.9.1 Simulation Results

The presented methodology for ASAC design shall be illustrated on the acoustic demonstrator model shown in Fig. 5.10. The model incorporates all plate and cavity modes up to 500 Hz. For control design, the plate-cavity system is considered in the frequency range from zero up to 200 Hz. This frequency band incorporates five lightly damped resonance frequencies which are dominated by the plate dynamics, compare Table 2.2. The modal damping ratios of the plate subsystem are all set to $D_\mathrm{S} = 1\,\%$. The two additional complex pole pairs at zero and 197 Hz do not cause pronounced resonances, since the modal damping ratio of the fluid subsystem is set to $D_\mathrm{F} = 10\,\%$. This is in accordance with the real testbed, where acoustic insulation material covers the inside of the cavity and thus largely flattens out the acoustic resonances. Thus, five modal accelerations will serve as structural variables to approximate the dynamical behavior of the acoustic demonstrator in the selected frequency range.

The plate is assumed to be set in an infinite baffle such that Rayleigh's integral formula can be applied to calculate free space radiation. Four actuator patches are positioned as outlined in App. D.6, following the guidelines given in Sec. 5.6.3. Thirteen accelerometers are distributed on the

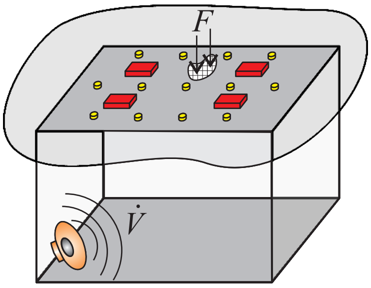

Figure 5.10: Acoustic demonstrator in an infinite baffle with structural and acoustical disturbance excitation.

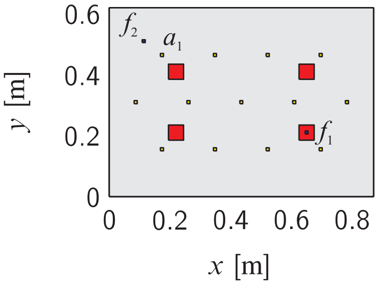

Figure 5.11: Actuator and sensor positioning for ASAC. Additional point forces for identification (lower right) and valididation (upper left) are also indicated.

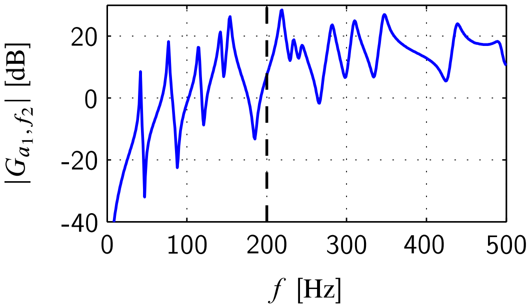

Figure 5.12: Magnitude of frequency response from validation force to first accelerometer.

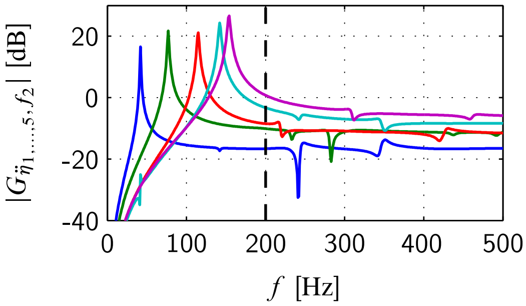

Figure 5.13: Magnitude of frequency response from validation force to the five modal filter outputs.

plate surface to measure the input signals to the five modal filters, whose design is explained in App. D.8. The plate can be excited by both distributed forces on the plate and acoustic disturbances within the enclosure.

The actuators and sensors are also shown to scale in Fig. 5.11. There, two additional point forces are indicated. The first is located at the center of the lower right patch and will serve as an input for the identification experiments, in addition to the four actuators, since five inputs are required. The second point force will not be used for identification experiments, but later on for validation of the identified model.

To illustrate the efficacy of modal filtering, Fig. 5.12 shows the frequency response from the validation force f_2 to the first accelerometer indicated by a_1 in Fig. 5.11. The five dominant resonances in the frequency range up to 200 Hz can be recognized, as well as several more resonance frequencies up to 500 Hz. Figure 5.13 shows the modal filter outputs for the same input. As can be seen, the coupled plate-cavity system can be well approximated by the five selected modes in the considered frequency range. Nevertheless, perfect modal decoupling cannot be achieved, since the coupled system does not satisfy the assumption of Caughey damping.

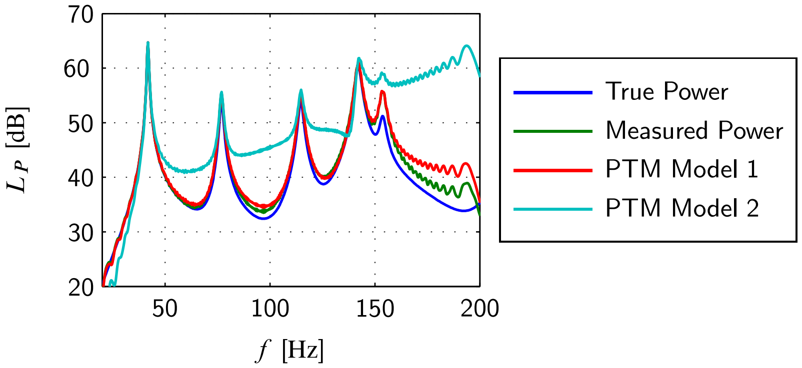

Figure 5.14: Sound power level determined via simulated measurement and two PTM models.

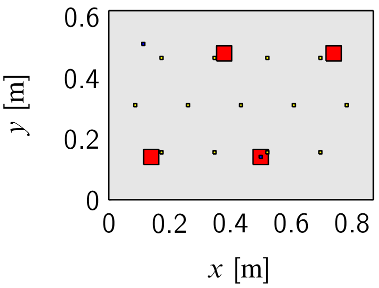

Figure 5.15: Actuator configuration to identify PTM model 2.

Influence of Actuator Positioning on Discretization Error

The first step in the process of experimental PTM modeling is to identify the acoustic FRFs $\boldsymbol{G}_\text{p}$ and $\boldsymbol{G}_\text{v}$. To this end, 60 points are defined on a regular plane grid very close to the plate surface such that $\boldsymbol{G}_\text{v}$ can be approximated by a constant transfer matrix, as pointed out in Sec. 5.7. At these points, measurement of sound intensity is simulated.

Similarly to the FRF measurement examples in Ch. 3, the plate is excited with a swept sine signal from 10 Hz up to 200 Hz via the four actuators and the point force f_1 in order to extract the frequency responses from the outputs of the five modal filters to the intensity measurement points. From the simulated outputs of the modal filters and the pressure and particle velocity data, $\boldsymbol{G}_\text{p}(\text{e}^{\text{j}\omega_n})$ and $\boldsymbol{G}_\text{v}(\text{e}^{\text{j}\omega_n})$, and thus also $\hat{\boldsymbol{\Pi}}(\omega_n)$ can be calculated. Then, one can calculate the time-average sound power from both the intensity measurements (via (5.37)) and from the identified PTM model with the equality $\bar{P}(\omega_n) = \tilde{\boldsymbol{q}}^\text{H}(\omega_n)\hat{\boldsymbol{\Pi}}(\omega_n)\tilde{\boldsymbol{q}}(\omega_n)$.

To illustrate the validity of this approach, a validation experiment is performed where the plate is excited with a swept sine signal at the force input f_2, which was not used in the identification experiments. The first curve in Fig. 5.14 shows the true value of the emitted sound power, as calculated by the analytical solutions (5.20) and (5.21). The next two curves show the resulting power estimates as obtained by intensity measurement on the 60 discretization points and by the non-parametric PTM model. The small differences between the two curves are caused by the fact that $\boldsymbol{G}_\text{p}$ and $\boldsymbol{G}_\text{v}$ do not match their theoretical values, because of the discretization error. Nevertheless, if the validation experiment was performed with one of the inputs which were used during the identification, the two curves would match despite the discretization error.

To show the influence of actuator positioning, the identification and validation experiments are repeated with the alternative actuator configuration shown in Fig. 5.15. There, the actuator positions are chosen as those which were used for active vibration damping in the last chapter. The point force f_1 is again pinned to the center of the lower right patch. The position of the validation force f_2 is unchanged. One can see from the result of the validation experiment that this actuator setup results in a PTM model of lower accuracy, because modes number six and higher are highly excited during the identification experiments and are thus flawing the acoustic FRFs, see Fig. 5.14.

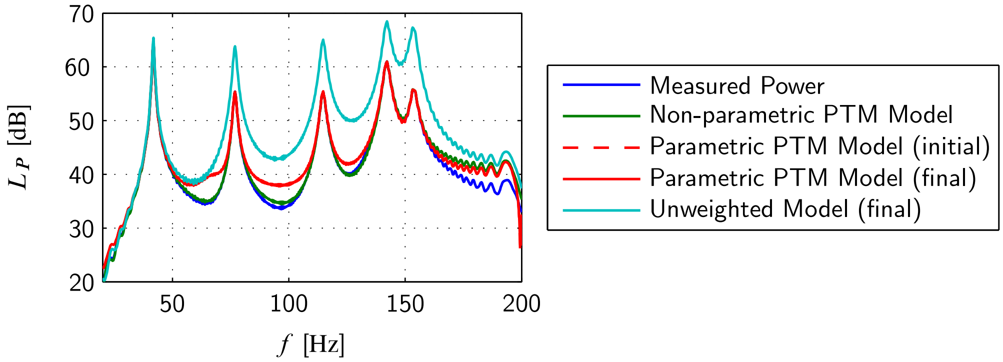

Figure 5.16: Results of parametric PTM modeling.

Parametric PTM Modeling and Post-Optimization

The non-parametric model $\hat{\boldsymbol{\Xi}}\,(\mathrm{e}^{\mathrm{j}\omega_n})$ is now fitted with a fifth order ARX model by the procedure outlined in App. D.7. To this end, the FRF of $\hat{\boldsymbol{\Xi}}$ from 20 Hz to 200 Hz is taken at 587 equidistant frequency samples. The weighting matrix $\boldsymbol{W}$ is formed from the frequency-domain modal acceleration data which was gathered during the five identification experiments, according to equations (5.61) and (5.62). The results are shown in Fig. 5.16. There, the first two curves are the same as the second and third curves of Fig. 5.14, namely the sound power reconstructed from the simulated sound intensity measurement and from the non-parametric PTM model, respectively. The initial values for the parametric PTM model are very good such that no significant improvement is achieved by iterative optimization. For comparison, the resulting final parametric PTM model is shown when an unweighted cost function is employed, i.e. $\|\Re\,\boldsymbol{e}\,\|_2^2$ is minimized instead of $\|\Re\{\boldsymbol{W}\boldsymbol{e}\}\|_2^2$. It can be seen that the quality of the PTM model is poor, since the modeling error is not tuned towards good reconstruction of the emitted sound power.

Although the reconstruction of the emitted sound power via the parametric PTM model is good for both the identification and validation data sets, the FRF of the PTM model is not positive definite at all frequencies. This implies that for arbitrary excitations, negative mean sound powers may be computed from the PTM model, which is not physically possible. This problem can be coped with by the post-optimization procedure outlined in Sec. 5.7. Both variants, i.e. the optimization over state space matrices $\boldsymbol{B}$ and $\boldsymbol{D}$ as well as the pair $\boldsymbol{C}$ and $\boldsymbol{D}$, are performed and the cost function J is evaluated for the same frequency grid as was done for the parametric modeling step. The state-space model of $\boldsymbol{\Xi}\,(z)$ was transformed into a real-valued modal form before optimization. The results of the validation experiments with the corrected models are shown in Fig. 5.17. It can be seen that the quality of both corrected models is very similar. Differences can be seen in the eigenvalue plots of the parametric models, which are shown in Fig. 5.18. Major corrections are made by the post-optimization procedure in the low frequency range, where one eigenvalue of the uncorrected parametric model takes relatively large negative values. The eigenvalues of both corrected models are positive for all frequencies. The first corrected model which was modified over the parameter set $\{\boldsymbol{C}, \boldsymbol{D}\}$ has one very big eigenvalue at about 200 Hz, whereas the second model, which has modified $\boldsymbol{B}$ and $\boldsymbol{D}$ matrices, shows a smaller spread of eigenvalues. For the

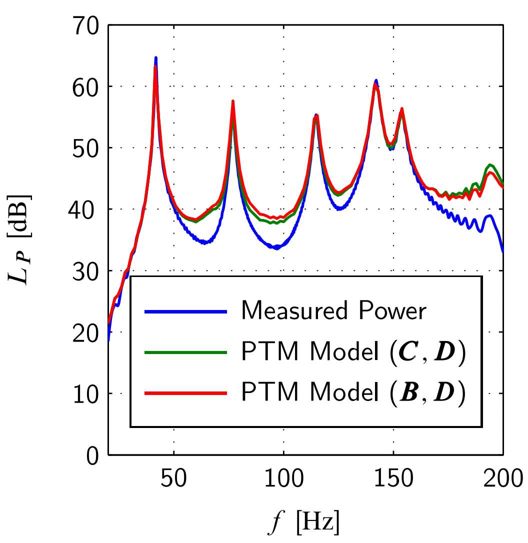

Figure 5.17: Reconstructed sound powers after post-optimization to ensure postive-definiteness.

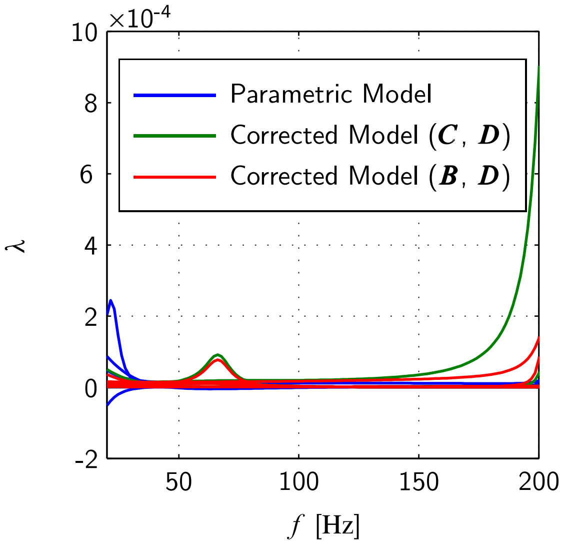

Figure 5.18: Eigenvalues of parametric PTM models.

further simulation examples, this second model is chosen for numerical reasons, since the values of the cost function J are very similar for both models.

Control Design

For control design, the corrected, positive definite model of the PTM is decomposed into the factors $\boldsymbol{F}_{-}(z)$ and $\boldsymbol{F}_{+}(z)$, as explained in Sec. 5.8, where the stable spectral factor serves as performance weight $\boldsymbol{W}_{\mathrm{p}}$. As already mentioned, PTMs are not diagonal in general. Nevertheless, the identified PTM is diagonally dominant in the sense that the diagonal elements are about one decade greater in magnitude than the off-diagonal elements. This also leads to a diagonally dominant performance weight. Figure 5.19 shows the magnitude of the five diagonal elements of $\boldsymbol{W}_{\mathrm{p}}$ in the relevant frequency range, and Fig. 5.20 shows the magnitude of the selected control effort weight $\boldsymbol{W}_{\mathrm{u}}$.

An $\mathcal{H}_2$ optimal controller is designed for the plant $\boldsymbol{TG}(z)$, which has the four actuator voltages as inputs and the five modal accelerations as outputs. The disturbance inputs are assumed to be unknown. To validate controller efficiency, two experiments are simulated. In the first one, the plate is excited via the control force f_2, as indicated in Fig. 5.11. In the second experiment, the plate is excited via some point sound source, which is positioned in the lower left corner of the cavity at coordinates [5 cm, 5 cm, −70 cm], see also Fig. 5.10. The resulting emitted sound powers for both excitations are shown for controller switched on and off in Fig. 5.21. The amplitude of the point force was 1 N, while the volume velocity of the sound source was set to 1 $\mathrm{cm}^3\,\mathrm{s}^{-1}$ to achieve a similar peak sound power. Since the acoustic wavelength at 200 Hz is still approximately 1.7 m, which is about twice the plate length, the plate is approximately excited by a uniform pressure

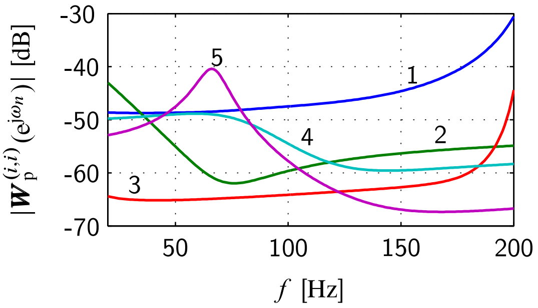

Figure 5.19: Magnitude of the diagonal elements of the performance weight $\boldsymbol{W}_{\mathrm{p}}$.

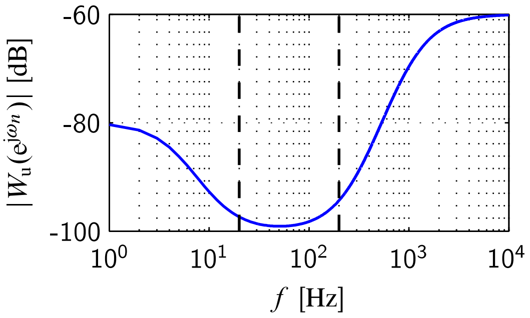

Figure 5.20: Magnitude of the control effort weight W_{u}.

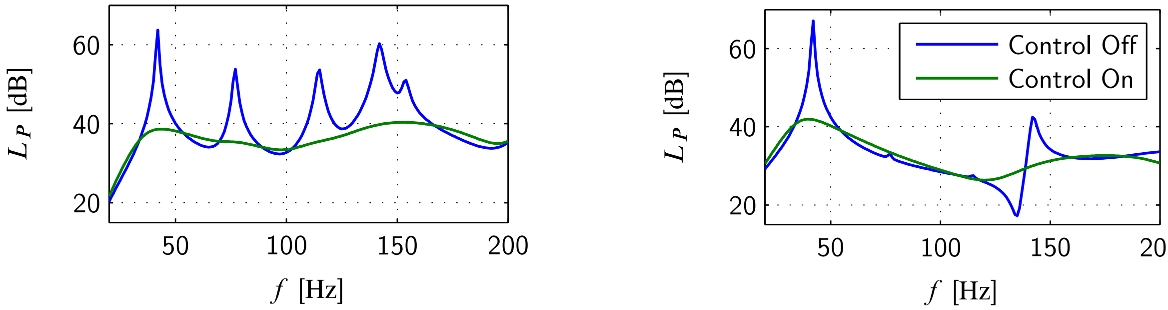

Figure 5.21: Effect of acoustic control when point force f_2 (left) or sound source (right) excites the system.

distribution. This explains why only mode shapes with net volume displacement, like the (1,1) mode and the (3,1) mode, are significantly excited.

5.9.2 Experimental Results

The experimental setup is similar to the simulated system of the last section and is shown in Fig. 5.22. The piezo patches indicated by the numbers one to four are used as actuators in the control loop and are positioned in the same way as in the simulation example, see also App. D.6. Thirteen accelerometers are employed to extract the first five modal accelerations of the coupled system, as before. The fifth patch is used as the additional input which is necessary to identify the acoustic FRFs. The reason for replacing the point force f_1 of the simulation example by a patch actuator is the following: An electromagnetic shaker which generates a point force has to be flexibly mounted such that the plate dynamics are not altered by the presence of the shaker. This is cumbersome to realize when the shaker is mounted inside the cavity. Mounting the shaker on top of the plate by a gibbet would be possible, but its noise and mere presence on the plate surface impedes the sound intensity measurement.

The measurement grid for intensity measurement is of dimension 9×7, thus resulting in 63 measurement points, and is set in a plane 7 cm above the plate surface. By contrast to the simulation

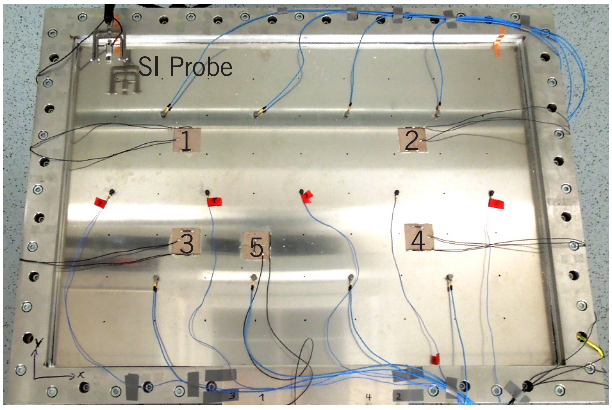

Figure 5.22: Experimental ASAC setup with five piezo patches and 13 accelerometers.

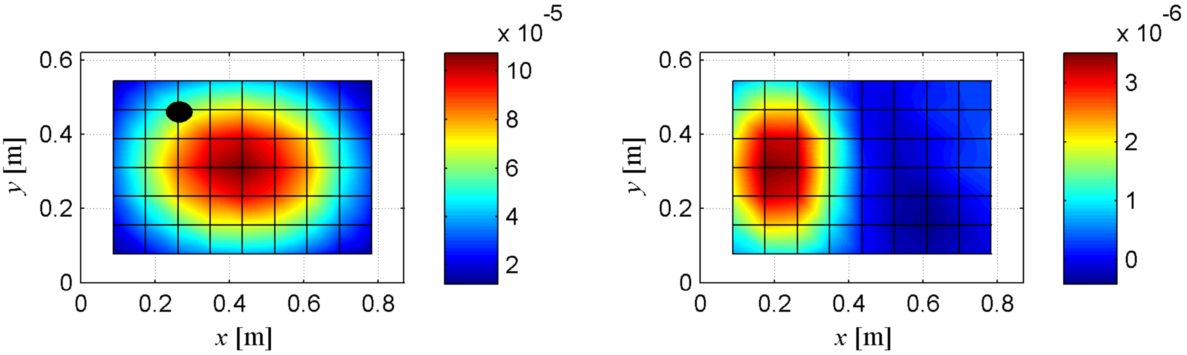

Figure 5.23: Time-average normal intensity at first resonance 60.8 Hz (left), and second resonance 97.3 Hz (right) in W/m^2. The measurement point #20 is indicated in the left plot.

example, the plate does not radiate into free space, but the acoustic demonstrator is placed in a normal laboratory room with dimensions $(8 \times 7 \times 3.5)$ m without any acoustical treatment.

As pointed out in Sec. 5.6.4, the distance of the measurement surface from the structure is a critical issue. A compromise must be sought between the stochastic measurement errors caused by the SNR, and deterministic errors due to phase mismatch between pressure and particle velocity. The chosen distance equals approximately 4 % of the acoustic wavelength at 200 Hz. This small distance implies that the field angle on the measurement surface can be expected to be greater than 80°. This, in turn, requires the field angle measurement error to be smaller than 1° in order to avoid significant errors due to phase mismatch, compare Fig. 5.8.
To illustrate the sound intensity measurement, Fig. 5.23 shows the time-average normal intensity on the measurement surface at the first and second resonance frequencies of the plate-cavity system when it is excited by all five inputs simultaneously in phase with an amplitude of 60 V. For the 20th measurement point, as indicated in the left plot of Fig. 5.23, the field angle is shown exemplarily in Fig. 5.24. There, it can be seen that φ_{f} indeed takes values close to 90° in the relevant frequency range. This affirms the unfavorable relation between the active intensity, given by the real part of the intensity phasor, and the so-called reactive (or quadrature) intensity, given by the imaginary part, i.e. $\bar{I}_{\mathrm{react}} = \frac{1}{2}\Im\{\tilde{p}\tilde{v}^*\}$. These quantities are shown in Fig. 5.25 and illustrate the ne-

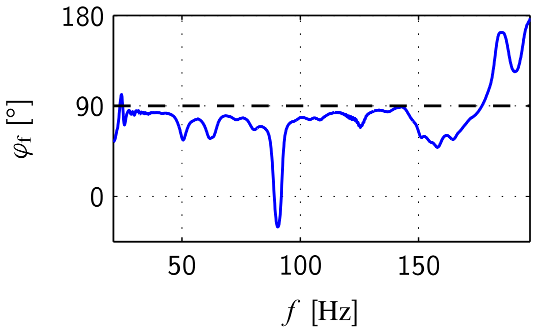

Figure 5.24: Field angle at measurement point #20.

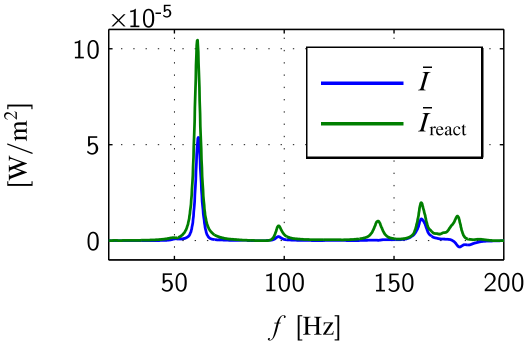

Figure 5.25: Active and reactive time-average intensity at point #20.

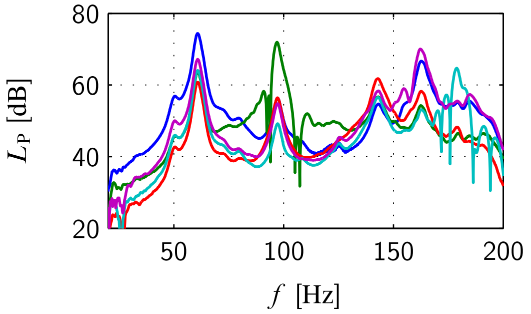

Figure 5.26: Sound power measurements from the five identification experiments.

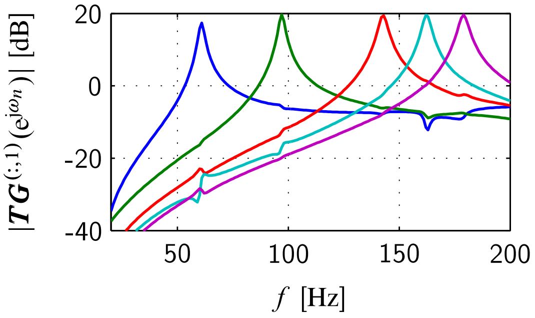

Figure 5.27: Magnitudes of frequency responses from the first piezo patch to the five modal accelerations.

cessity of accurate measurement equipment. Five identification experiments are performed where the inputs are excited according to a Hadamard scheme, as explained in Sec. 3.4. The resulting sound powers, which can be calculated from the intensities at the 63 grid points, are shown in Fig. 5.26. Two of the measurement curves are interrupted at some frequencies. This is where slightly negative sound powers are computed, due to measurement errors.

As in the simulation example, the structural model $\boldsymbol{TG}(z)$ denotes the transfer function from the first four actuator patches to the five outputs of the modal filters. The measured FRFs are fitted with a 7th order ARX model with $T_\mathrm{s} = 0.6\,\mathrm{ms}$, and the resulting frequency response of $\boldsymbol{TG}$ from the first input to all modal outputs is displayed in Fig. 5.27. The quality of the modal separation is similar for the other four inputs, and all sensor signals are low-pass filtered above 200 Hz in order to limit the plant bandwidth.

The first step of parametric PTM modeling is to find initial values for the model, which are subsequently improved by iterative optimization. The model is chosen as a 3rd order ARX model with the same sampling time as $\boldsymbol{G}$. The results of the modeling steps are shown exemplarily for the measured and reconstructed sound powers of the first identification experiment on the left side of Fig. 5.28. In this case, significant improvement is achieved by the iterative optimization

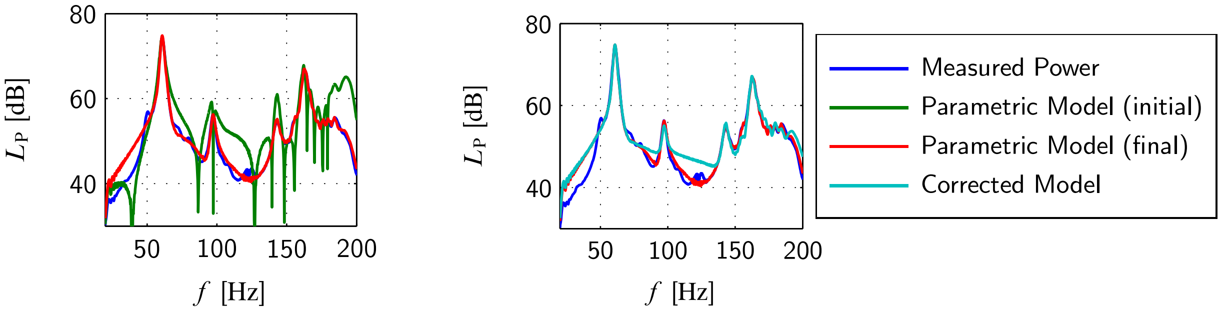

Figure 5.28: Measured and reconstructed sound powers for the first identification experiment via different PTM models.

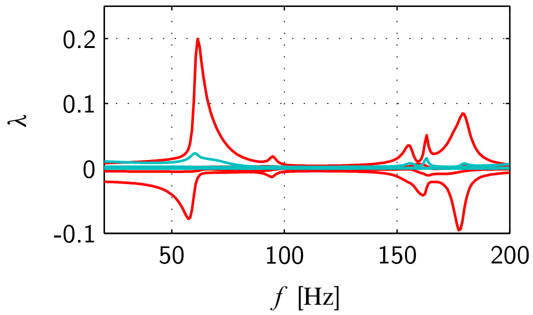

Figure 5.29: Eigenvalues of final parametric and corrected PTM model (same color code as in Fig. 5.28).

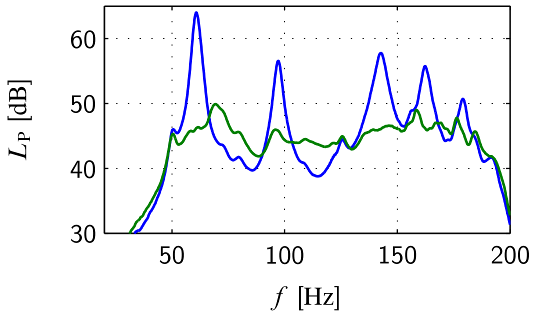

Figure 5.30: Sound power level with and without control when exciting the structure with the fifth piezo patch.

algorithm. The right part of the figure shows the reconstructed sound power as computed by the corrected model, which has a positive-definite frequency response for all frequencies. The corresponding eigenvalues of the (final) parametric model and the corrected model are plotted in Fig. 5.29. Significant changes are made by the post-optimization procedure, without sacrificing much of the model accuracy.

The performance of the 40th order controller whose design is based upon the corrected PTM model can be seen in Fig. 5.30. There, the structure is excited by the fifth piezo patch, while patches one to four are used in the control loop. For this measurement, the disturbance amplitude is chosen to 60 V, and the maximum resulting control voltage is 107 V. Significant reduction of sound power level is achieved in the targeted frequency band. In the vicinity of the first resonance for example, a reduction of 14 dB is achieved, which implies that the peak power value reaches only about 4 % of its original value.
An alternative validation example with a loudspeaker excitation, like in the simulation studies of the last section, can however not be done. The reason for this is that the inside of the real testbed is covered with sound-insulating material which exhibits a strong damping effect that cannot be described by a Caughey-damping model. Consequently, the coupled plate-cavity system has complex mode shapes, and satisfactory modal filter design cannot be achieved by evaluating the undamped mode shapes at the sensor positions. Instead, the fitting procedure outlined in App. D.8 is used.

With this method, satisfying results can be achieved for the system inputs which are used in the fitting process, i.e. the five piezo patches, as shown in Fig. 5.27. When the system is excited with a loudspeaker from inside the cavity however, the separation property of the modal filters strongly deteriorates. This leads in turn to non-satisfactory control results. This problem could be solved by directly employing the sensor signals as structural quantities, without modal filtering. The drawback would be an increased number of structural quantities and thus measurement experiments, as explained in Sec. 5.6.2.

5.10 Sound Transmission into Enclosed Spaces

So far, sound radiation has been considered into undefined space, i.e. acoustic boundary conditions were not relevant, because it was assumed that reflected sound waves either have no influence on the structure-borne radiation or are not reflected at all, like in free space. Now, the case shall be considered where sound waves interact with the acoustic boundaries of a defined geometry and may be able to excite resonances of the enclosed fluid. In this case, some other measure for global performance than time-average sound power is considered more appropriate. Since the fluid volume is now of finite extension, it is natural to measure global performance by some kind of time-average total energy. Acoustic pressure is the physical quantity which is relevant for acoustic cognition. Thus, it is usually argued that the time-average total potential energy of a fluid volume is the best-suited performance measure [100, 145],

$$\bar{E}_{\text{pot}} = \frac{1}{T} \int_0^T \frac{1}{2} \frac{1}{\rho_0 c_0^2} \iiint_V p^2(\boldsymbol{x}, t) \, \mathrm{d}V \, \mathrm{d}t \tag{5.75}$$

for some suitable time period T, compare also (2.32).

For harmonic time dependence, this can be alternatively written in phasor notation as

$$\begin{aligned} \bar{E}_{\text{pot}} &= \frac{1}{4} \frac{1}{\rho_0 c_0^2} \iiint_V |\tilde{p}(\boldsymbol{x}, \omega)|^2 \, \mathrm{d}V \\ &\approx \frac{1}{4} \frac{1}{\rho_0 c_0^2} V_{\text{el}} \sum_{i=1}^{n_{\text{A}}} |\tilde{p}_i(\boldsymbol{x}, \omega)|^2 \\ &= \frac{1}{4} \frac{1}{\rho_0 c_0^2} V_{\text{el}} \, \tilde{\boldsymbol{p}}^{\text{H}} \tilde{\boldsymbol{p}} \\ &= \frac{1}{4} \frac{1}{\rho_0 c_0^2} V_{\text{el}} \, \tilde{\boldsymbol{q}}^{\text{H}} \boldsymbol{G}_{\text{p}}^{\text{H}} \boldsymbol{G}_{\text{p}} \tilde{\boldsymbol{q}} . \end{aligned} \tag{5.76}$$

In the above derivation, it was assumed, without loss of generality, that the acoustic volume is discretized into n_{A} volume elements of identical size V_{el}. In case that the acoustic environment is linear, there exist transfer matrices $\boldsymbol{G}_{\text{p}}$ from the n_{S} structural variables $\boldsymbol{q}$ to the n_{A} pressure measurement points $\tilde{p}_i$, which are collected in the vector $\tilde{\boldsymbol{p}} = (\tilde{p}_1, \ldots, \tilde{p}_{n_{\text{A}}})^{\text{T}}$. Assuming that $\boldsymbol{G}_{\text{p}}$ has full column rank, the associated energy transfer matrix $V_{\text{el}}/4\rho_0 c_0^2 \boldsymbol{G}_{\text{p}}^{\text{H}} \boldsymbol{G}_{\text{p}}$ is positive definite, and its stable spectral factor is given by $\sqrt{V_{\text{el}}/4\rho_0 c_0^2} \boldsymbol{G}_{\text{p}}$. Thus, the ASAC methodology of this chapter can be immediately applied for global control of enclosed sound fields.

Table 5.1: Mode index numbers of the acoustical basis functions.

i	1	2	3	4	5	6	7	8	9	10	11	12	13
$n_{x,i}$	0	1	0	0	1	1	0	2	1	2	0	2	1
$n_{y,i}$	0	0	0	1	0	1	1	0	1	0	0	1	0
$n_{z,i}$	0	0	1	0	1	0	1	0	1	1	2	0	2

We will treat sound transmission into the cavity of the acoustic demonstrator as an example problem and will focus on the frequency range up to 500 Hz. The pressure distribution inside the cavity can be approximated in this frequency range by the modal expansion $p(\boldsymbol{x}, t) = \boldsymbol{P}^{\mathrm{T}}(\boldsymbol{x})\dot{\boldsymbol{\varphi}}(t)$, see (2.85). The vector $\boldsymbol{P}$ contains the acoustic basis functions according to (2.52). In other words, the pressure distribution is approximated by a limited number of standing waves which are given by the elements P_i of $\boldsymbol{P}$. Table 5.1 shows the mode index numbers of the 13 basis functions which are incorporated in the acoustic demonstrator model up to 500 Hz. The trace wavelengths of each three-dimensional wave are given by the numbers $\lambda_{x,i} = {}^{2l_x}/_{n_{x,i}}$, $\lambda_{y,i} = {}^{2l_y}/_{n_{y,i}}$, and $\lambda_{z,i} = {}^{2l_z}/_{n_{z,i}}$, where the cavity is of dimension $(l_x \times l_y \times l_z)$. Since the maximum appearing index number is two, the trace wavelengths are never smaller than the associated cavity dimension. Thus, it can be expected that local pressure reduction at a specific point inside the cavity also has a global effect, as long as the point is not located on a nodal line of some mode shape function. For that reason, only local control will be considered in the following.

The following specific local control problem shall be studied. The plate configuration is the same as shown in Fig. 3.1, i.e. there are four actuator patches with nearly collocated accelerometers. A point force allows to directly excite the structure. In addition to that, the plate may be disturbed by an acoustic source outside the cavity, as illustrated in Fig. 2.5. For simplicity, it is assumed that the source generates plane waves normally incident on the structure. The modeling of this additional input is explained in App. D.9.

The goal is to design an $\mathcal{H}_2$ optimal controller to minimize the sound pressure p at the coordinates $[0.77, 0.10, -0.65]$ m inside the cavity. This means that a microphone is placed in the lower right corner with a distance of 10 cm to all nearby walls. The generalized plant is set up as in Sec. 4.3.2 for AVC design with the control variable $z = p$. As in all control designs of this thesis, the disturbance inputs are assumed to be unknown.

Simulation Results

The dynamic behavior of the coupled plate-cavity system is described by the simulation model (2.84) with state vector $(\boldsymbol{\eta}^{\mathrm{T}}\ \boldsymbol{\varphi}^{\mathrm{T}}\ \dot{\boldsymbol{\eta}}^{\mathrm{T}}\ \dot{\boldsymbol{\varphi}}^{\mathrm{T}})^{\mathrm{T}}$. The correct input matrix of the state space model which represents the influence of the disturbance point force and the sound wave excitation on the acoustic demonstrator is deliberately not employed for control design. However, the definition of the interior ASAC problem implies that the system is not excited by sources inside the cavity, only via forces acting directly or indirectly on the plate. Thus, the disturbance influence matrix is set in accordance with the state vector to $\boldsymbol{B}_w = (\mathbf{0}_{n_\mathrm{S}\times n_\mathrm{S}}\ \mathbf{0}_{n_\mathrm{S}\times n_\mathrm{F}}\ \mathbf{I}_{n_\mathrm{S}}\ \mathbf{0}_{n_\mathrm{S}\times n_\mathrm{F}})^{\mathrm{T}}$.

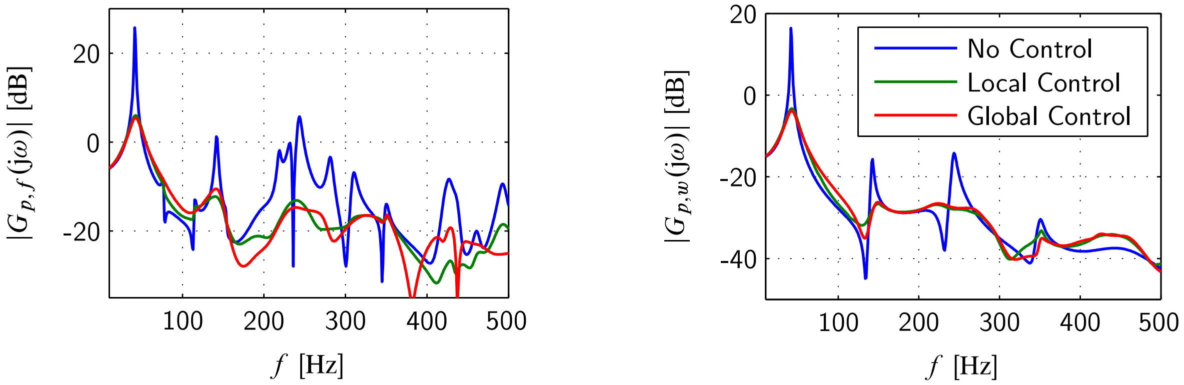

Figure 5.31: Control performance for the ASAC interior problem for point-force excitation (left) and plane wave excitation (right).

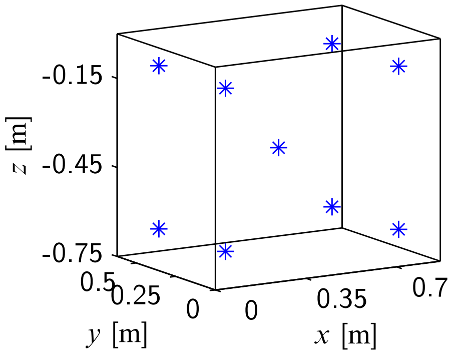

Figure 5.32: Location of nine virtual microphones for approximate global control.

The efficacy of the designed controller can be seen in the first two curves of Fig. 5.31, where the open- and closed-loop behaviors are shown for both the point force and the plane wave excitation. As already seen in the simulation example of the last section, only mode shapes with net volume displacement can be excited by the acoustical disturbance.

For comparison, a third simulation result is shown where not only the output of one virtual microphone is taken as control variable, but also eight additional microphones which are located as shown in Fig. 5.32. This control strategy may be interpreted as an approximate global control design. As can be seen, the differences to local control at one microphone position are not significant. Analytical expressions for optimal harmonic local and global control of this problem can be easily derived in analogy to App. D.2.

To show the global effect of the local control strategy, Fig. 5.33 shows the plate deflection and cavity pressure distribution with and without control when the system is excited by the point force at first resonance. Each snapshot is taken when the respective maximum pressure level is reached inside the cavity. Figure 5.34 shows the same information for second resonance.

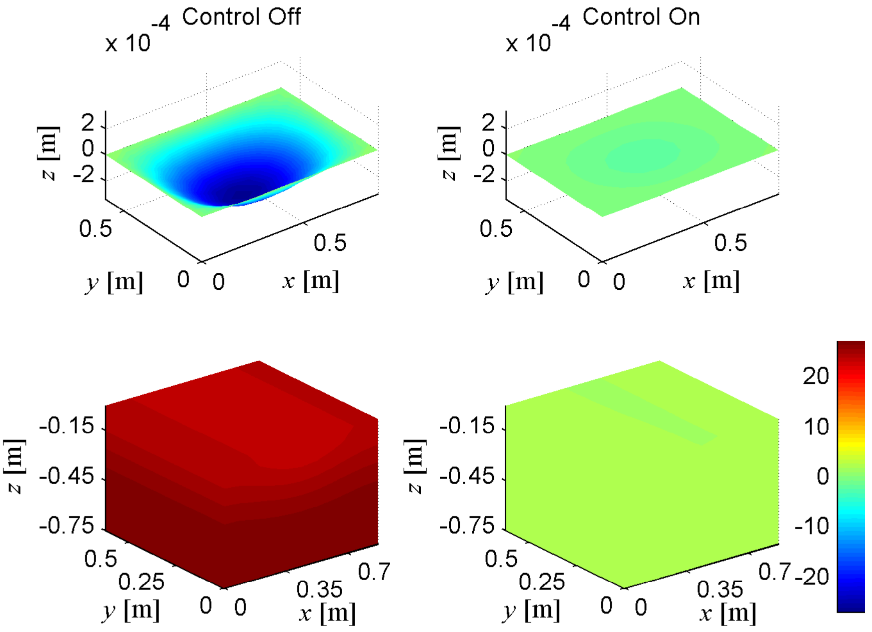

Figure 5.33: Effect of interior ASAC on plate deflection and pressure distribution at first resonance when the system is excited by a point force. Pressure units in Pa.

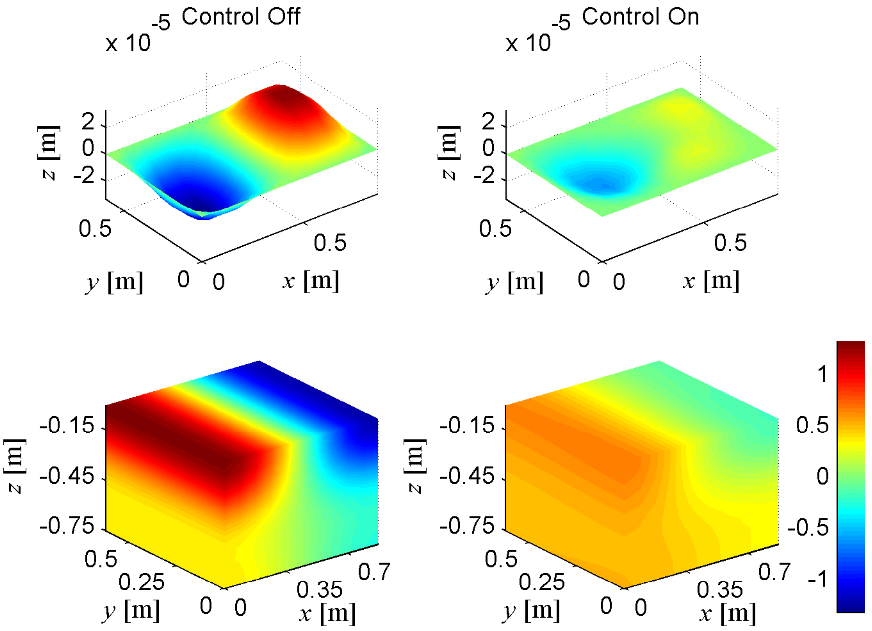

Figure 5.34: Effect of interior ASAC on plate deflection and pressure distribution at second resonance when the system is excited by a point force. Pressure units in Pa.

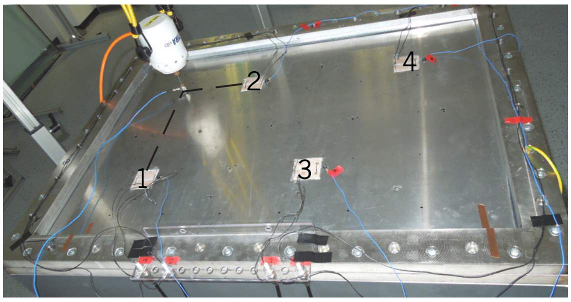

Figure 5.35: Experimental setup for the interior ASAC problem.

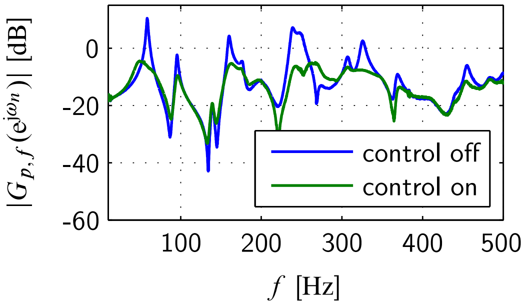

Figure 5.36: Performance of local ASAC controller.

Experimental Results

The presented simulation examples are now validated with experimental results. To that end, the smart panel which was used for AVC, as depicted in Fig. 3.14, is mounted on top of the acoustic demonstrator. An electromagnetic shaker attached on the topside of the panel emulates the point disturbance, see Fig. 5.35. For practical reasons, the shaker position was changed compared to the simulation example. Nevertheless, this new excitation position also allows to excite all panel modes from zero to 500 Hz, compare Sec. 2.4.

The determination of the disturbance influence matrix $\boldsymbol{B}_w$ is more difficult here than for the simulation example. The reason for this is that the identified black-box model of the acoustic demonstrator does not allow for a separation of its state-vector into components that are associated with the plate and fluid dynamics, as was possible for the simulation model. Simply setting $\boldsymbol{B}_w = \mathbf{I}$ leads to unsatisfactory results, because this implies that the acoustic demonstrator may be possibly excited by any kind of structural or acoustic source inside and outside the cavity. This necessarily leads to very conservative controllers.

For practical applications where the input matrix of the disturbance is unknown, the following procedure is proposed to handle this problem. In a first step, the positions where the structural modes in the targeted frequency band can be simultaneously excited are determined by superposition of the corresponding mode shapes, compare Sec. 2.4. Then, the shaker is used to excite at these positions and the resulting sensor signals are recorded. After that, the structure is excited with the actuator inputs. Both data sets are combined to identify a black-box model for the acoustic demonstrator of the following structure

$$\boldsymbol{G}(z) = \left[\begin{array}{c|cc} \boldsymbol{A} & \boldsymbol{B} & \boldsymbol{E} \\ \hline \boldsymbol{C} & \boldsymbol{D} & \boldsymbol{F} \end{array}\right]. \tag{5.77}$$

In the above equation, the matrices $\boldsymbol{E}$ and $\boldsymbol{F}$ represent the input and feedthrough matrices for the shaker inputs, respectively. An orthonormal basis for the span of $\boldsymbol{E}$ can then be used as disturbance input matrix $\boldsymbol{B}_w$.

The performance of the resulting $\mathcal{H}_2$ optimal controller which was designed with these guidelines is shown in Fig. 5.36. There, the magnitude of the transfer function from the disturbance force to the microphone inside the cavity is shown for the controlled and uncontrolled case. Significant reductions are achieved, especially at first resonance, where the magnitude of the transfer function is reduced by 15 dB.

5.11 Chapter Summary

Influencing structure-borne sound by means of ASAC has been studied in this chapter. The focus was on global reduction of sound emission and was exemplified on the minimization of time-average sound power emitted by the plate of the acoustic demonstrator. The differences to local control where illustrated for the classical problem of sound radiation of a baffled plate, which also served to introduce the basic properties of structure-borne sound fields. Based on this problem, the concept of power transfer matrices was introduced, which allow for the calculation of time-average emitted power given certain structural variables that sufficiently describe the structural dynamics. At the heart of this chapter was a novel identification method for power transfer matrices that does not rely on any assumptions regarding the structure's geometry or the boundary conditions of the linear acoustic environment and should thus improve the applicability of ASAC to real-world problems. The influence of the discretized representation of structural dynamics on the non-parametric modeling step as well as the problems faced during parametric modeling have been pointed out in detail. It was shown that by some suitable factorization, the PTM model can immediately be employed in optimal control design to specifically reduce the emitted sound power. How interior acoustical problems can be treated with the proposed ASAC methodology has also been explained at the end of this chapter. The modeling and control results for both the interior and exterior problems have been illustrated with simulations as well as experiments.

6 Conclusion and Outlook

Adaptive structures may enable the system engineer to fulfill requirements for mechanical systems which cannot be satisfied by passive designs under given material and weight restrictions. In most applications, the reduction of vibration and noise caused by a flexible mechanical system is at the focus of intelligent system design. To this end, the provision of a generic, yet effective design procedure for the reduction of vibration levels and emitted sound power of adaptive structures is at the heart of this thesis.

The modeling of adaptive structures is indispensable to understand their characteristic physical effects and for advanced, model-based control design. Physical insight to the system behavior is best achieved by theoretical modeling. This approach is demonstrated for the acoustic demonstrator, which exhibits both electromechanical and mechanical-acoustic coupling. The outcome of this modeling procedure is a continuous-time white-box model, which transparently displays important system features, like stability, controllability, observability, and the properties of collocated transfer paths. These findings are invaluable for the subsequent development of control strategies. For model-based control design however, accurate input-output mapping of the system's transfer paths is of paramount importance. Because of that, a black-box modeling strategy is utilized, which is able to handle high-order systems ($n \leq 300$). One of the main contributions of this thesis is the improvement of this identification procedure in order to provide a non-conservative, yet reliable estimate of model uncertainty for LTI systems. It is further pointed out how the identification result is affected by input signal design, and how correlated measurement noise influences the model uncertainty estimate. Discrete-time modeling enables the designer to choose less demanding sampling periods, which significantly reduces obstacles when porting the control algorithms to low-cost hardware.

Although simple and effective control algorithms exist for active damping, the advantages of MIMO HAC are pointed out. The efficacy of the proposed AVC design is demonstrated on the active damping of a smart panel, where the number of damped modes is considerably higher than the number of sensors. Robust stability of the designed control loop can be readily checked by well-known stability tests, since the derived model uncertainty is already in a suitable form.

Compared to AVC, ASAC design is a more demanding problem, since sound radiation does not only depend on vibration levels, but also on vibration mode shapes. Structure-borne sound power is often a suitable choice as control variable for problems where radiation takes place into free space, but it is not available for direct feedback. To cope with this problem, a novel modeling procedure for power transfer matrices is presented. With the help of these matrices, it is possible to estimate the emitted sound power solely from structural sensor information. This modeling procedure does not depend on special acoustic measurement environments, like anechoic chambers. By applying spectral decomposition, a weighting filter for the sensor signals can be calculated which allows for the application of optimal control design methodologies. Furthermore, it is shown how to modify the proposed ASAC design to handle sound radiation into enclosed spaces.

Outlook

Improvement of modeling and control strategies for adaptive structures will allow for enhanced control performance and extended applicability. As far as experimental modeling is concerned, it seems natural to seek for an extension of I4C methods for subclasses of nonlinear systems. With such methods, it would for example be possible to handle hysteresis effects not only by compensation, but by treating it as a model error of a linear model. The same could be possible for friction and stiction effects. A first idea for the modeling of systems with nonlinearities as uncertain linear systems has been put forward by Ljung in [125].

Even for (sufficiently) linear systems, it is possible to further enhance control performance by appreciating the fact that the modeling and control problems are inseparably intertwined. It has long been recognized that the optimal model for control design in turn depends on the controller. The reader might consult [78] and [167] for insightful treatments of this fundamental issue. A logical consequence is that identification and control should practically be done in a repeating sequence. This involves the closed-loop identification of an improved plant model in iteration $n + 1$, where the loop has been closed with the model-based controller of the previous step n. This approach is known as *iterative identification and control* in literature, and the basic ideas and first successful applications can be found in [4]. However, the convergence behavior of these techniques is not yet sufficiently understood.

In order to combine uncertainty modeling and iterative identification, it is necessary to be able to identify unbiased plant estimates from closed-loop data, and to derive accurate expressions for the estimator variance. Depending on the specific control loop setup and the available loop signals, this requires additional computational effort and more advanced algorithms. As pointed out by Goodwin in [86], the issue of closed-loop identification has been a topic for over five decades by now. One of the most intriguing problems of closed-loop identification is that the identified model may not be stabilized by the controller, although the real closed-loop is stable. It can even be shown that this is guaranteed to happen for certain measurement setups and non-minimum phase controllers, see [48]. Further issues of closed-loop identification are for example treated in [1, 21, 82, 106, 141, 165, 186].

Improvement of control performance can also be achieved by more advanced control algorithms. It is self-evident that the effect of disturbance rejection can be severely limited when the frequency spectrum and the point of attack is unknown. The impact of the resulting controller is then far from its theoretical optimum, which can be calculated when the disturbance is known. The performance of the presented controllers for AVC and ASAC could be improved by adding an adaptive disturbance rejection algorithm. Adaptive controllers allow for the tracking of time-varying disturbances. For narrow-band disturbance excitations, near-optimal control performance can be achieved. For broadband disturbances however, adaptive disturbance cancellation is known to suffer from slow convergence and low performance, as pointed out by Widrow & Walach in [194]. As such, the advantages and disadvantages of adaptive disturbance cancellation are complementary to those of non-adaptive control, e.g. active damping, since these are suitable for reducing the effects of broadband excitation. Model uncertainty can possibly be handled by performing adaption in the frequency-domain [65]. These and other arguments speak in favor of combining these two techniques in future works to achieve high-performance, robust control.

A Appendix to Theoretical Modeling

A.1 Geometry and Material Parameters of the Acoustic Demonstrator Model

Table A.1: Geometry properties.

Parameter Name	Symbol	Value	Unit
Cavity length in x-direction	l_x	870	mm
Cavity length in y-direction	l_y	620	mm
Cavity length in z-direction	l_z	750	mm
Plate thickness	h	4	mm
Area of square actuator patches	A_P	2500	mm^2
Thickness of actuator patches	h_P	0.5	mm

Table A.2: Material properties of plate and fluid. Nominal fluid conditions are given by $T_0 = 20\,°\mathrm{C}$ and $p_0 = 1013\,\mathrm{hPa}$.

Parameter Name	Symbol	Value	Unit
Young's modulus of the plate	E	$70 \cdot 10^3$	$\mathrm{N/mm}^2$
Poisson's ratio of plate material	ν	0.34	–
Density of plate material	ρ	2700	$\mathrm{kg/m}^3$
Speed of sound at nominal conditions	c_0	343	$\mathrm{m\,s}^{-1}$
Density of air at nominal conditions	ρ_0	1.20	$\mathrm{kg/m}^3$

Table A.3: Material properties of the piezoelectric material.

Parameter Name	Symbol	Value	Unit
Compliance in (1,1)-direction	s_{11}	$16.2 \cdot 10^{-6}$	mm^2/N
Compliance in (1,2)-direction	s_{12}	$-4.84 \cdot 10^{-6}$	mm^2/N
Compliance in (6,6)-direction	s_{66}	$42.0 \cdot 10^{-6}$	mm^2/N
Piezoelectric charge constant in (1,3)-direction	d_{31}	$-154 \cdot 10^{-12}$	$\mathrm{C\,N}^{-1}$
Permittivity in (3,3)-direction	ϵ_{33}	$12,0 \cdot 10^{-9}$	$\mathrm{F\,m}^{-1}$
Density	ρ_P	7760	$\mathrm{kg/m}^3$

A.2 Linear Constitutive Equations of Piezoelectrics

For quick reference, the linearized constitutive equations of piezoelectric material are shortly summarized, see also [101]. A detailed description and the general nonlinear equations can for example be found in [196].

There are four relevant quantities that describe the state of the piezoelectric material: strain $\boldsymbol{S}$, stress $\boldsymbol{T}$, field strength $\boldsymbol{E}$, and electric displacement $\boldsymbol{D}$. The mechanical quantities have in general six components each, while the electric quantities appear in three coordinate directions. This can be summarized as

$$\boldsymbol{S} = \begin{pmatrix} S_1 \\ S_2 \\ S_3 \\ S_4 \\ S_5 \\ S_6 \end{pmatrix} = \begin{pmatrix} \epsilon_1 \\ \epsilon_2 \\ \epsilon_3 \\ \gamma_{23} \\ \gamma_{13} \\ \gamma_{12} \end{pmatrix}, \quad \boldsymbol{T} = \begin{pmatrix} T_1 \\ T_2 \\ T_3 \\ T_4 \\ T_5 \\ T_6 \end{pmatrix} = \begin{pmatrix} \sigma_1 \\ \sigma_2 \\ \sigma_3 \\ \tau_{23} \\ \tau_{13} \\ \tau_{12} \end{pmatrix}, \quad \boldsymbol{E} = \begin{pmatrix} E_1 \\ E_2 \\ E_3 \end{pmatrix}, \quad \boldsymbol{D} = \begin{pmatrix} D_1 \\ D_2 \\ D_3 \end{pmatrix}. \tag{A.1}$$

According to the IEEE standard [108], the coordinate axes are labeled as 1, 2, and 3, while the 3-axis points in the direction of polarization. In Sec. 2.3, the notation x', y', and z' is used instead. There are two common forms of matrix equations that display the interrelationship of the four quantities. Assuming that the electrical field and the mechanical strain are predetermined, the corresponding electrical displacement and mechanical stress can be calculated by

$$\begin{pmatrix} \boldsymbol{D} \\ \boldsymbol{T} \end{pmatrix} = \begin{pmatrix} \boldsymbol{\epsilon} & \boldsymbol{e} \\ -\boldsymbol{e}^{\mathrm{T}} & \boldsymbol{c}_{\mathrm{P}} \end{pmatrix} \begin{pmatrix} \boldsymbol{E} \\ \boldsymbol{S} \end{pmatrix}. \tag{A.2}$$

The matrices of material constants have the following structure, assuming that the material properties are isotropic in the (1,2)-plane:

$$\boldsymbol{\epsilon} = \begin{pmatrix} \epsilon_{11} & 0 & 0 \\ 0 & \epsilon_{11} & 0 \\ 0 & 0 & \epsilon_{33} \end{pmatrix}, \quad \boldsymbol{e}^{\mathrm{T}} = \begin{pmatrix} 0 & 0 & e_{31} \\ 0 & 0 & e_{31} \\ 0 & 0 & e_{33} \\ 0 & e_{15} & 0 \\ e_{15} & 0 & 0 \\ 0 & 0 & 0 \end{pmatrix}, \quad \boldsymbol{c}_{\mathrm{P}} = \begin{pmatrix} c_{11} & c_{12} & c_{13} & 0 & 0 & 0 \\ c_{12} & c_{11} & c_{13} & 0 & 0 & 0 \\ c_{13} & c_{13} & c_{33} & 0 & 0 & 0 \\ 0 & 0 & 0 & c_{44} & 0 & 0 \\ 0 & 0 & 0 & 0 & c_{44} & 0 \\ 0 & 0 & 0 & 0 & 0 & c_{66} \end{pmatrix}.$$

If, on the other hand, the stress is known and the strain shall be calculated, then the following equation is useful,

$$\begin{pmatrix} \boldsymbol{S} \\ \boldsymbol{D} \end{pmatrix} = \begin{pmatrix} \boldsymbol{s}_{\mathrm{P}} & \boldsymbol{d}^{\mathrm{T}} \\ \boldsymbol{d} & \boldsymbol{\epsilon}' \end{pmatrix} \begin{pmatrix} \boldsymbol{T} \\ \boldsymbol{E} \end{pmatrix}, \tag{A.3}$$

with the following matrices of material constants:

$$\boldsymbol{s}_{\mathrm{P}} = \begin{pmatrix} s_{11} & s_{12} & s_{13} & 0 & 0 & 0 \\ s_{12} & s_{11} & s_{13} & 0 & 0 & 0 \\ s_{13} & s_{13} & s_{33} & 0 & 0 & 0 \\ 0 & 0 & 0 & s_{44} & 0 & 0 \\ 0 & 0 & 0 & 0 & s_{44} & 0 \\ 0 & 0 & 0 & 0 & 0 & s_{66} \end{pmatrix}, \quad \boldsymbol{d}^{\mathrm{T}} = \begin{pmatrix} 0 & 0 & d_{31} \\ 0 & 0 & d_{31} \\ 0 & 0 & d_{33} \\ 0 & d_{15} & 0 \\ d_{15} & 0 & 0 \\ 0 & 0 & 0 \end{pmatrix}, \quad \boldsymbol{\epsilon}' = \begin{pmatrix} \epsilon'_{11} & 0 & 0 \\ 0 & \epsilon'_{11} & 0 \\ 0 & 0 & \epsilon'_{33} \end{pmatrix}.$$

The material constants that appear in the two matrix equations are interrelated by the following equalities,

$$\boldsymbol{s}_{\mathrm{P}} = \boldsymbol{c}_{\mathrm{P}}^{-1}; \quad \boldsymbol{d} = \boldsymbol{e}\,\boldsymbol{c}_{\mathrm{P}}^{-1}; \quad \boldsymbol{\epsilon}' = \boldsymbol{\epsilon} + \boldsymbol{e}\,\boldsymbol{c}_{\mathrm{P}}^{-1}\,\boldsymbol{e}^{\mathrm{T}}. \tag{A.4}$$

A.3 Derivation of Lagrange's Equations for the Acoustic Domain

The virtual work of the external acoustic forces can be expressed as

$$\delta W_{\mathrm{ex,F}}(t) = \iiint_{V_{\mathrm{F}}} V(x,y,z,t)\delta p(x,y,z,t)\,\mathrm{d}V_{\mathrm{F}}, \tag{A.5}$$

where the acoustic pressure field p is discretized via the set of acoustic basis functions P_i into n_{F} generalized coordinates,

$$p(x,y,z,t) = \sum_{i=1}^{n_{\mathrm{F}}} P_i(x,y,z)\dot{\varphi}_i(t). \tag{A.6}$$

The discretized work of the external forces can now be restated as

$$\delta W_{\mathrm{ex,F}} = \iiint_{V_{\mathrm{F}}} V\delta\left(\sum_{i=1}^{n_{\mathrm{F}}} P_i\dot{\varphi}_i\right)\mathrm{d}V_{\mathrm{F}} = \sum_{i=1}^{n_{\mathrm{F}}} \underbrace{\iiint_{V_{\mathrm{F}}} VP_i\,\mathrm{d}V_{\mathrm{F}}}_{=:F_{\mathrm{F},i}^{\mathrm{g,ex}}}\ \delta\dot{\varphi}_i \tag{A.7}$$

with the ith generalized external acoustic force $F_{\mathrm{F},i}^{\mathrm{g,ex}}$.
The virtual work of the dissipative force $F_{\mathrm{F}}^{\mathrm{d}}$ can be analogously stated as

$$\delta W_{\mathrm{d,F}} = \iiint_{V_{\mathrm{F}}} F_{\mathrm{F}}^{\mathrm{d}}\delta p\,\mathrm{d}V_{\mathrm{F}} = \sum_{i=1}^{n_{\mathrm{F}}} \underbrace{\iiint_{V_{\mathrm{F}}} F_{\mathrm{F}}^{\mathrm{d}}P_i\,\mathrm{d}V_{\mathrm{F}}}_{=:F_{\mathrm{F},i}^{\mathrm{g,d}}}\ \delta\dot{\varphi}_i = \sum_{i=1}^{n_{\mathrm{F}}} F_{\mathrm{F},i}^{\mathrm{g,d}}\delta\dot{\varphi}_i. \tag{A.8}$$

The expressions for the virtual works are now used in (2.21) and give

$$\int_{t_1}^{t_2}\left(\delta\mathcal{L} + \sum_{i=1}^{n_{\mathrm{F}}} F_{\mathrm{F},i}^{\mathrm{g,ex}}\delta\dot{\varphi}_i + \sum_{i=1}^{n_{\mathrm{F}}} F_{\mathrm{F},i}^{\mathrm{g,d}}\delta\dot{\varphi}_i\right)\mathrm{d}t = 0. \tag{A.9}$$

Since the Lagrangian $\mathcal{L}$ is a function of φ_i and $\dot{\varphi}_i$, carrying out the variation gives

$$\int_{t_1}^{t_2}\left(\sum_{i=1}^{n_{\mathrm{F}}}\frac{\partial\mathcal{L}}{\partial\varphi_i}\delta\varphi_i + \sum_{i=1}^{n_{\mathrm{F}}}\frac{\partial\mathcal{L}}{\partial\dot{\varphi}_i}\delta\dot{\varphi}_i + \sum_{i=1}^{n_{\mathrm{F}}} F_{\mathrm{F},i}^{\mathrm{g,ex}}\delta\dot{\varphi}_i + \sum_{i=1}^{n_{\mathrm{F}}} F_{\mathrm{F},i}^{\mathrm{g,d}}\delta\dot{\varphi}_i\right)\mathrm{d}t = 0. \tag{A.10}$$

The variational operator commutes with every linear differential operator, so this can be rewritten as

$$\sum_{i=1}^{n_{\mathrm{F}}}\int_{t_1}^{t_2}\left(\frac{\partial\mathcal{L}}{\partial\varphi_i}\delta\varphi_i + \frac{\partial\mathcal{L}}{\partial\dot{\varphi}_i}\frac{\mathrm{d}}{\mathrm{d}t}\delta\varphi_i + F_{\mathrm{F},i}^{\mathrm{g,ex}}\frac{\mathrm{d}}{\mathrm{d}t}\delta\varphi_i + F_{\mathrm{F},i}^{\mathrm{g,d}}\frac{\mathrm{d}}{\mathrm{d}t}\delta\varphi_i\right)\mathrm{d}t = 0. \tag{A.11}$$

The last three terms in the integral are now integrated by parts,

$$\begin{aligned}\sum_{i=1}^{n_{\mathrm{F}}}\Bigg(\int_{t_1}^{t_2}\frac{\partial\mathcal{L}}{\partial\varphi_i}\delta\varphi_i\,\mathrm{d}t + \left[\frac{\partial\mathcal{L}}{\partial\dot{\varphi}_i}\delta\varphi_i\right]_{t_1}^{t_2} - \int_{t_1}^{t_2}\frac{\mathrm{d}}{\mathrm{d}t}\frac{\partial\mathcal{L}}{\partial\dot{\varphi}_i}\delta\varphi_i\,\mathrm{d}t + \left[F_{\mathrm{F},i}^{\mathrm{g,ex}}\delta\varphi_i\right]_{t_1}^{t_2} - \int_{t_1}^{t_2}\frac{\mathrm{d}F_{\mathrm{F},i}^{\mathrm{g,ex}}}{\mathrm{d}t}\delta\varphi_i\,\mathrm{d}t \\ + \left[F_{\mathrm{F},i}^{\mathrm{g,d}}\delta\varphi_i\right]_{t_1}^{t_2} - \int_{t_1}^{t_2}\frac{\mathrm{d}F_{\mathrm{F},i}^{\mathrm{g,d}}}{\mathrm{d}t}\delta\varphi_i\,\mathrm{d}t\Bigg) = 0.\end{aligned} \tag{A.12}$$

The evaluation of the terms in brackets results in zero, because the variation is carried out in between time instants t_1 and t_2 and is zero at the boundaries,

$$\sum_{i=1}^{n_\mathrm{F}} \int_{t_1}^{t_2} \left(\frac{\partial \mathcal{L}}{\partial \varphi_i} \delta\varphi_i - \frac{\mathrm{d}}{\mathrm{d}t} \frac{\partial \mathcal{L}}{\partial \dot{\varphi}_i} \delta\varphi_i - \frac{\mathrm{d}F_{\mathrm{F},i}^{\mathrm{g,ex}}}{\mathrm{d}t} \delta\varphi_i - \frac{\mathrm{d}F_{\mathrm{F},i}^{\mathrm{g,d}}}{\mathrm{d}t} \delta\varphi_i \right) \mathrm{d}t = 0. \tag{A.13}$$

Since all n_F variations of the generalized coordinates φ_i are arbitrary and mutually independent, one may set all but one equal to zero [46],

$$\int_{t_1}^{t_2} \left(\frac{\partial \mathcal{L}}{\partial \varphi_i} - \frac{\mathrm{d}}{\mathrm{d}t} \frac{\partial \mathcal{L}}{\partial \dot{\varphi}_i} - \frac{\mathrm{d}F_{\mathrm{F},i}^{\mathrm{g,ex}}}{\mathrm{d}t} - \frac{\mathrm{d}F_{\mathrm{F},i}^{\mathrm{g,d}}}{\mathrm{d}t} \right) \delta\varphi_i \mathrm{d}t = 0. \tag{A.14}$$

In addition to that, since the variation is arbitrary but non-zero, the left hand side is only zero if the integrand is zero,

$$\frac{\partial \mathcal{L}}{\partial \varphi_i} - \frac{\mathrm{d}}{\mathrm{d}t} \frac{\partial \mathcal{L}}{\partial \dot{\varphi}_i} - \frac{\mathrm{d}F_{\mathrm{F},i}^{\mathrm{g,ex}}}{\mathrm{d}t} - \frac{\mathrm{d}F_{\mathrm{F},i}^{\mathrm{g,d}}}{\mathrm{d}t} = 0. \tag{A.15}$$

This can be rearranged to give the result (2.43c),

$$\frac{\mathrm{d}}{\mathrm{d}t} \frac{\partial \mathcal{L}}{\partial \dot{\varphi}_i} - \frac{\partial \mathcal{L}}{\partial \varphi_i} + \frac{\mathrm{d}F_{\mathrm{F},i}^{\mathrm{g,nc}}}{\mathrm{d}t} = 0. \tag{A.16}$$

The Lagrangian equations for the other two domains can be derived analogously and result in the standard forms (2.43a) and (2.43b).

A.4 Homogenization of the Acoustic Boundary Value Problem

This section is split into two parts. In the first one, it is shown that no homogenization function in the classical sense can be found to transform the inhomogeneous boundary value problem of the enclosed acoustic volume into a homogeneous one. An insightful physical interpretation is also given. In the second part, the homogenization is carried out with the help of generalized functions, so called distributions.

Proof of the Non-Existence of a Classic Homogenization Function

The boundary value problem of the acoustic volume which is stated in equations (2.16), (2.18), and (2.19) is non-homogeneous, because of the boundary condition $\frac{\partial p}{\partial z}\big|_{z=0} = -\rho_0 \frac{\partial^2 w}{\partial t^2}$. This boundary condition represents the impact of the plate motion on the fluid dynamics.

The classical approach ([94], [132]) for the homogenization of problems with inhomogeneous boundary conditions is to have the ansatz

$$p(x, y, z, t) = \tilde{p}(x, y, z, t) + h(t)\hat{p}(x, y, z), \tag{A.17}$$

where $\tilde{p}$ is chosen to satisfy the problem with homogenous boundary conditions. For the acoustic volume, this means that the pressure gradient of $\tilde{p}$ normal to the boundary is zero everywhere on

the boundary. The task is to find a function $\hat{p}$ such that the overall solution $p = \tilde{p} + h\hat{p}$ satisfies the original boundary conditions.
Using the ansatz (A.17) in the boundary conditions (2.18) for the x and y directions results in

$$\underbrace{\left.\frac{\partial \tilde{p}}{\partial x}\right|_{x=\{0,l_x\}}}_{=0} + \underbrace{\left.\frac{\partial \hat{p}}{\partial x}\frac{\partial^2 w}{\partial t^2}\right|_{x=\{0,l_x\}}}_{\equiv 0} + \hat{p}\left.\frac{\partial^3 w}{\partial x \partial t^2}\right|_{x=\{0,l_x\}} \overset{!}{\equiv} 0, \tag{A.18a}$$

$$\underbrace{\left.\frac{\partial \tilde{p}}{\partial y}\right|_{y=\{0,l_y\}}}_{=0} + \underbrace{\left.\frac{\partial \hat{p}}{\partial y}\frac{\partial^2 w}{\partial t^2}\right|_{y=\{0,l_y\}}}_{\equiv 0} + \hat{p}\left.\frac{\partial^3 w}{\partial y \partial t^2}\right|_{y=\{0,l_y\}} \overset{!}{\equiv} 0, \tag{A.18b}$$

where the first terms in the above equations are identical to zero because of the construction of $\tilde{p}$, and the second terms are identical to zero because of the boundary conditions of the plate, see (2.14). Thus, it can be concluded that $\hat{p}$ has to satisfy

$$\hat{p}\big|_{x=\{0,l_x\}} \overset{!}{\equiv} 0, \quad \text{and} \quad \hat{p}\big|_{y=\{0,l_y\}} \overset{!}{\equiv} 0. \tag{A.19}$$

The remaining boundary conditions in (2.18) and (2.19), which correspond to the z coordinate, result in

$$\underbrace{\left.\frac{\partial \tilde{p}}{\partial z}\right|_{z=-l_z}}_{=0} + \left.\frac{\partial \hat{p}}{\partial z}\right|_{z=-l_z}\frac{\partial^2 w}{\partial t^2} \overset{!}{\equiv} 0, \tag{A.20a}$$

$$\underbrace{\left.\frac{\partial \tilde{p}}{\partial z}\right|_{z=0}}_{=0} + \left.\frac{\partial \hat{p}}{\partial z}\right|_{z=0}\frac{\partial^2 w}{\partial t^2} \overset{!}{\equiv} -\rho_0\frac{\partial^2 w}{\partial t^2}. \tag{A.20b}$$

$$\tag{A.20c}$$

From these equations, it is clear that $\hat{p}$ also has to satisfy

$$\left.\frac{\partial \hat{p}}{\partial z}\right|_{z=-l_z} \overset{!}{\equiv} 0, \quad \text{and} \quad \left.\frac{\partial \hat{p}}{\partial z}\right|_{z=0} \overset{!}{\equiv} -\rho_0. \tag{A.21}$$

At this point, it can already be concluded that there does not exist any function (in the classical sense) that is able to satisfy the requirements (A.19) and (A.21) simultaneously. At the coordinate origin for example, the homogenization function $\hat{p}(0,0,0)$ is required to have zero value but negative slope in z-direction. Thus, the value of $p(0,0,-\epsilon)$ for some sufficiently small positive number ϵ must be positive. By contrast, it is also required that $p(0,0,z) \equiv 0$ for $-l_z \leq z \leq 0$, which is a contradiction to the former statement.

Now, it is mathematically clear that no classical homogenization function can be found for the acoustic boundary value problem. Furthermore, a physical explanation shall also be given:
If we assume for now that the fluid dynamics satisfy the requirements of a potential flow, then there exists a velocity potential Φ_v such that $\boldsymbol{v} = -\nabla\Phi_v$, where $\boldsymbol{v}$ is the particle velocity field. Because of the relationship (2.17), the pressure field is related to the velocity potential by $p = -\rho_0\frac{\partial \Phi_v}{\partial t}$.

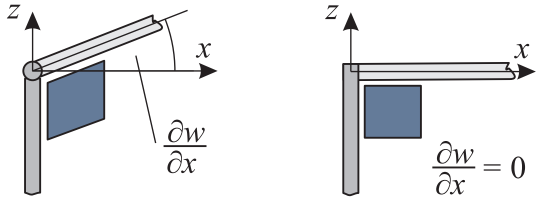

Figure A.1: Fluid element at the edge of the plate with simply-supported boundary (left) and clamped boundary (right).

Thus, it is easy to see that the boundary conditions for p and Φ_v are identical, except for the constant $-\rho_0$. Consequently, requirements (A.19) and (A.21) apply also to the velocity potential when an ansatz like (A.17) is used for Φ_v. This means that a suitable $\hat{\Phi}_v$ cannot be found.

Another implication is that a potential of the form $\Phi_v = \tilde{\Phi}_v + h\hat{\Phi}_v$ cannot be found, because no potential of *any* form can exist. This is because the boundary conditions for the velocity field (2.18) and (2.19) violate the integrability condition [173] $\frac{\partial v_x}{\partial z} \overset{!}{=} \frac{\partial v_z}{\partial x}$ at all points where the fluid boundary coincides with the plate boundary. The non-existence of a velocity potential in turn implies that the fluid flow is not vortex free, which means that some fluid elements undergo shear deformation, see for example [173]. This shear deformation takes place at the edges of the plate. The reason for this is that at the simply-supported boundary, the slope of the plate normal to the boundary is not identical to zero. The fluid elements immediately underneath the plate are necessarily sheared when the plate is deflected. This is not the case for a plate which is clamped at all edges, see Fig. A.1. The only way to homogenize the problem is to resort to generalized functions, also called distributions.

Homogenization with Distributions

Here, we show that the boundary value problem consisting of the PDE

$$\frac{1}{c_0^2}\frac{\partial^2 p}{\partial t^2} - \Delta p = -\rho_0 \frac{\partial^2 w}{\partial t^2}\delta(z) \tag{A.22}$$

and the homogeneous boundary conditions

$$\left.\frac{\partial p}{\partial x}\right|_{x=\{0,l_x\}} = \left.\frac{\partial p}{\partial y}\right|_{y=\{0,l_y\}} = \left.\frac{\partial p}{\partial z}\right|_{z=\{0,-l_z\}} \equiv 0 \tag{A.23}$$

is, in the weak sense, equivalent to the problem

$$\frac{1}{c_0^2}\frac{\partial^2 p}{\partial t^2} - \Delta p = 0 \tag{A.24}$$

with inhomogeneous boundary conditions

$$\left.\frac{\partial p}{\partial x}\right|_{x=\{0,l_x\}} = \left.\frac{\partial p}{\partial y}\right|_{y=\{0,l_y\}} = \left.\frac{\partial p}{\partial z}\right|_{z=-l_z} \equiv 0, \quad \text{and} \quad \left.\frac{\partial p}{\partial z}\right|_{z=0} = -\rho_0 \frac{\partial^2 w}{\partial t^2}. \tag{A.25}$$

The additional forcing terms that stem from acoustic sources and external volumetric forces in (2.16) are dropped in this section to streamline the presentation.

First, we search for the weak form of the solution to (A.22), (A.23) by multiplying with some test function φ and integrating over the domain of the PDE,

$$\frac{1}{c_0^2}\iiint_{V_\mathrm{F}} \frac{\partial^2 p}{\partial t^2}\varphi \,\mathrm{d}V_\mathrm{F} - \iiint_{V_\mathrm{F}} \Delta p\varphi \,\mathrm{d}V_\mathrm{F} = -\rho_0 \iiint_{V_\mathrm{F}} \frac{\partial^2 w}{\partial t^2}\varphi\delta(z)\,\mathrm{d}V_\mathrm{F}. \tag{A.26}$$

Applying Green's formula to the second term on the left hand side and making use of the sifting property of the Dirac function gives

$$\frac{1}{c_0^2}\iiint_{V_\mathrm{F}} \frac{\partial^2 p}{\partial t^2}\varphi \,\mathrm{d}V_\mathrm{F} - \underbrace{\iint_{\partial V_\mathrm{F}} (\nabla p)^\mathrm{T}\vec{n}\varphi \,\mathrm{d}\partial V_\mathrm{F}}_{\overset{!}{=}0} + \iiint_{V_\mathrm{F}} (\nabla p)^\mathrm{T}\nabla\varphi \,\mathrm{d}V_\mathrm{F} = -\rho_0 \iint_{A_\mathrm{S}} \frac{\partial^2 w}{\partial t^2}\varphi\big|_{z=0}\,\mathrm{d}A_\mathrm{S}. \tag{A.27}$$

We say that p is a weak solution to (A.27) if it satisfies the equation for all φ from a suitable class of functions. We can state the requirements on this class of test functions from the last equation: Because of the third term on the left hand side, all φ must have a first order partial derivative in the weak sense for all three coordinates x, y, and z. This means that all test functions must belong to the Sobolev space H^1 [67].

To ensure that a strong solution, if it existed, was compatible with the formulation of the weak solution, the integral over the boundary must vanish. This could be achieved by demanding that the test functions are zero at the complete boundary. However, this would also cause the excitation term on the right hand side to vanish. Thus, we only demand that the test functions are zero at the rigid walls. Then, the weak solution of p must satisfy the boundary condition $\frac{\partial p}{\partial z}\big|_{z=0} \equiv 0$ which causes the boundary integral to vanish completely. This must be kept in mind when selecting appropriate basis functions for the discretization procedure. It is obvious that the basis functions (2.52) satisfy this requirement.

We now consider the PDE (A.24) of the original problem for the same class of test functions. Assuming that an analytic (strong sense) solution to (A.24), (A.25) exists, one may integrate over V_F and apply again Green's formula to the second term, which results in

$$\frac{1}{c_0^2}\iiint_{V_\mathrm{F}} \frac{\partial^2 p}{\partial t^2}\varphi \,\mathrm{d}V_\mathrm{F} - \iint_{\partial V_\mathrm{F}} (\nabla p)^\mathrm{T}\vec{n}\varphi \,\mathrm{d}\partial V_\mathrm{F} + \iiint_{V_\mathrm{F}} (\nabla p)^\mathrm{T}\nabla\varphi \,\mathrm{d}V_\mathrm{F} = 0. \tag{A.28}$$

The area of integration of the second term can be reduced to A_S, because the test functions are zero at the rigid walls. We may now rewrite the last equation as

$$\frac{1}{c_0^2}\iiint_{V_\mathrm{F}} \frac{\partial^2 p}{\partial t^2}\varphi \,\mathrm{d}V_\mathrm{F} + \iiint_{V_\mathrm{F}} (\nabla p)^\mathrm{T}\nabla\varphi \,\mathrm{d}V_\mathrm{F} = \iint_{A_\mathrm{S}} (\nabla p)^\mathrm{T}\vec{n}\varphi\big|_{z=0}\,\mathrm{d}A_\mathrm{S}. \tag{A.29}$$

Finally, we can simplify $(\nabla p)^\mathrm{T}\vec{n}\varphi\big|_{z=0}$ by $\frac{\partial p}{\partial z}\varphi\big|_{z=0}$, which must be equal to $-\rho_0\frac{\partial^2 w}{\partial t^2}\varphi|_{z=0}$. Now, it is obvious that (A.27) formally equals (A.29). Since we used the same class of test functions for both problems, every weak sense solution to (A.27) also satisfies (A.29).

A consequence of the replacement of the problem (A.24), (A.25) by (A.22), (A.23) is that the generalized acoustic forces defined in (A.7) have to be modified. The distributional forcing term can be interpreted as an additional acoustic source at the boundary of strength $\dot{V}_{\mathrm{bc}} = -\frac{\partial w}{\partial t}\delta(z)$. Thus, the modified generalized forces read

$$\begin{aligned} F^{\mathrm{g,ex}}_{\mathrm{F},i} &= \langle V, P_i\rangle_{V_{\mathrm{F}}} + \langle V_{\mathrm{bc}}, P_i\rangle_{V_{\mathrm{F}}} = \langle V, P_i\rangle_{V_{\mathrm{F}}} - \iiint_{V_{\mathrm{F}}} w\delta(z) P_i \,\mathrm{d}V_{\mathrm{F}} = \\ \ldots &= \langle V, P_i\rangle_{V_{\mathrm{F}}} - \iint_{A_{\mathrm{S}}} wP_i|_{z=0} \,\mathrm{d}A_{\mathrm{S}} = \langle V, P_i\rangle_{V_{\mathrm{F}}} - \boldsymbol{\eta}^{\mathrm{T}} \iint_{A_{\mathrm{S}}} \boldsymbol{W} P_i|_{z=0} \,\mathrm{d}A_{\mathrm{S}} \\ \ldots &= \langle V, P_i\rangle_{V_{\mathrm{F}}} - \boldsymbol{\eta}^{\mathrm{T}} \boldsymbol{G}^{(:,i)}_{\mathrm{ma}}, \end{aligned} \tag{A.30}$$

where $\boldsymbol{G}^{(:,i)}_{\mathrm{ma}}$ denotes as the ith column of the mechanical-acoustical coupling matrix.

A.5 Simplification of the Matrices of the Lumped Parameter Model

Some of the matrices which are derived in Sec. 2.3.4 can be further simplified. These simplifications will now be shown.

The mechanical basis functions constitute an orthogonal set over the domain of the plate, i.e. $\langle W_i, W_j\rangle_{A_{\mathrm{S}}} = \delta_{ij}$. Thus, the mass matrix of the structure is bound to be diagonal. In addition to that, due to the normalization of the mechanical basis functions (2.47), the mass matrix of the structure, $\boldsymbol{M}_{\mathrm{S}} = \iint_{A_{\mathrm{S}}} \boldsymbol{W} \rho h \boldsymbol{W}^{\mathrm{T}} \,\mathrm{d}A_{\mathrm{S}}$, is simply equal to the identity matrix of dimension n_{S}, $\boldsymbol{M}_{\mathrm{S}} = \mathbf{I}_{n_{\mathrm{S}}}$.

The basis functions W_i do not only constitute a orthogonal set. They are known to be the eigenfunctions of the simply supported rectangular plate. In general, the discretization of an undamped continuous system with its eigenfunctions as basis functions results in an infinite dimensional discrete system, where the generalized coordinates are identical to the modal coordinates [94]. The outcome is an infinite set of decoupled modal equations of the form $m^{\mathrm{g}}_{\mathrm{S},i}\ddot{\eta}_i + k^{\mathrm{g}}_{\mathrm{S},i}\eta_i = F^{\mathrm{g}}_{\mathrm{S},i}$. The eigenfrequencies of the structure are given by $\omega_{\mathrm{S},i} = \sqrt{k^{\mathrm{g}}_{\mathrm{S},i}/m^{\mathrm{g}}_{\mathrm{S},i}}$. The generalized masses (or modal masses) $m^{\mathrm{g}}_{\mathrm{S},i}$ are the diagonal elements of $\boldsymbol{M}_{\mathrm{S}}$. Since all generalized masses have been normalized to one, the generalized stiffnesses $k^{\mathrm{g}}_{\mathrm{S},i}$ are equal to the squares of the eigenfrequencies, $k^{\mathrm{g}}_{\mathrm{S},i} = \omega^2_{\mathrm{S},i}$. Consequently, the stiffness matrix of the structure is diagonal with the squares of the eigenfrequencies as elements, $\boldsymbol{K}_{\mathrm{S}} = \bigoplus_{i=1}^{n_{\mathrm{S}}} w^2_{\mathrm{S},i}$.

With a similar argument, one can show that with the help of the normalization (2.54) and (2.55), the stiffness matrix of the fluid reduces to

$$\boldsymbol{K}_{\mathrm{F}} = \iiint_{V_{\mathrm{F}}} \left(\nabla \boldsymbol{P}^{\mathrm{T}}\right)^{\mathrm{T}} \frac{1}{\rho_0} \nabla \boldsymbol{P}^{\mathrm{T}} \,\mathrm{d}V_{\mathrm{F}} = \begin{pmatrix} 0 & \mathbf{0} \\ \mathbf{0} & \mathbf{I}_{n_{\mathrm{S}}-1} \end{pmatrix}. \tag{A.31}$$

Obviously, the stiffness matrix is positive semidefinite. This is a direct consequence of the fact that the stiffness operator of the wave equation is only positive semidefinite, too (compare Sec. 2.2.3).

The value of the stiffness operator is zero for any constant comparison function. Analogously, the first entry of the diagonal stiffness matrix is also zero because the first basis function P_1 is also constant.

Since the modal stiffnesses of the fluid except for the first one are normalized to one, the corresponding modal masses of the fluid must be equal to $m_{\mathrm{F},i}^{\mathrm{g}} = 1/\omega_{\mathrm{F},i}^2$, $i = 2, \ldots, n_\mathrm{F}$. The first entry of $\boldsymbol{M}_\mathrm{F}$ can be calculated in a straightforward manner from (2.65) to be $m_{\mathrm{F},1}^{\mathrm{g}} = l_x l_y l_z / \left(\rho_0 c_0^2\right)$.

A simplification of the electromechanical coupling matrix can be carried out as follows. As illustrated in Sec. 2.3.4, each column of $\boldsymbol{G}_\mathrm{em}$ can be calculated separately, where the ith column is given by

$$\boldsymbol{G}_{\mathrm{em}}^{(:,i)} = \iiint_{V_{\mathrm{P}_i}} \mathcal{S}_w \left\{\boldsymbol{W}^\mathrm{T}\right\}^\mathrm{T} \Big|_{z=h/2} \boldsymbol{T}_\mathrm{S}^\mathrm{c} \boldsymbol{e}^\mathrm{T} \boldsymbol{T}_\mathrm{E}^\mathrm{c} \nabla R_i \, \mathrm{d}V_{\mathrm{P}_i}. \tag{A.32}$$

Inserting the definitions of the coordinate transformation matrices and the electrical basis functions results in

$$\boldsymbol{G}_{\mathrm{em}}^{(:,i)} = -\frac{e_{31}}{h_{\mathrm{P}_i}} \iiint_{V_{\mathrm{P}_i}} \mathcal{S}_w \left\{\boldsymbol{W}^\mathrm{T}\right\}^\mathrm{T} \Big|_{z=h/2} \begin{pmatrix} 1 & 1 & 0 \end{pmatrix}^\mathrm{T} \mathrm{d}V_{\mathrm{P}_i}. \tag{A.33}$$

Carrying out the operation $\mathcal{S}_w$ and integration in z-direction finally gives

$$\boldsymbol{G}_{\mathrm{em}}^{(:,i)} = e_{31} \frac{h}{2} \iint_{A_{\mathrm{P}_i}} \left(\frac{\partial^2 W_1}{\partial x^2} + \frac{\partial^2 W_1}{\partial y^2}, \ldots, \frac{\partial^2 W_{n_\mathrm{S}}}{\partial x^2} + \frac{\partial^2 W_{n_\mathrm{S}}}{\partial y^2} \right)^\mathrm{T} \mathrm{d}A_{\mathrm{P}_i}. \tag{A.34}$$

Equation (A.34) highlights the physical effect of the piezoceramic actuators and sensors. It can be seen that the electromechanical effect is proportional to the curvature (second order spatial derivative) of the surface. It is known from elasticity theory that the curvature of a flexible structure is proportional to the applied bending moments. Thus, the piezoelectric actuators can be regarded as devices which can exert bending moments on the structure. And analogously, the piezoelectric sensors produce a signal which is proportional to the applied moment.

The electrical capacitance matrix defined in (2.66) is diagonal by construction. As expected, its diagonal elements turn out to be the capacitances of plate capacitors having dimensions equal to that of the piezoelectric patch,

$$\begin{aligned} \boldsymbol{C}_\mathrm{el} &= \bigoplus_{i=1}^{n_\mathrm{P}} \left\{ \iiint_{V_{\mathrm{P}_i}} \left(\nabla R_i\right)^\mathrm{T} \boldsymbol{\epsilon} \nabla R_i \, \mathrm{d}V_{\mathrm{P}_i} \right\} = \bigoplus_{i=1}^{n_\mathrm{P}} \left\{ \iiint_{V_{\mathrm{P}_i}} \frac{1}{h_{\mathrm{P}_i}^2} \epsilon_{33} \, \mathrm{d}V_{\mathrm{P}_i} \right\} \\ \ldots &= \bigoplus_{i=1}^{n_\mathrm{P}} \left\{ \frac{1}{h_{\mathrm{P}_i}^2} \epsilon_{33} A_{\mathrm{P}_i} h_{\mathrm{P}_i} \right\} = \bigoplus_{i=1}^{n_\mathrm{P}} \left\{ \frac{\epsilon_{33} A_{\mathrm{P}_i}}{h_{\mathrm{P}_i}} \right\}. \end{aligned} \tag{A.35}$$

A.6 Eigenvalue Analysis of the Combined Plate-Cavity System

The homogeneous equation of motion of the white-box model of the acoustic demonstrator given by (2.83) shall be restated in its general form as

$$\boldsymbol{M}\ddot{\boldsymbol{x}} + \boldsymbol{D}\dot{\boldsymbol{x}} + \boldsymbol{K}\boldsymbol{x} = \boldsymbol{0}. \tag{A.36}$$

The corresponding quadratic eigenvalue problem is therefore given by

$$\left(\boldsymbol{M}\lambda^2 + \boldsymbol{D}\lambda + \boldsymbol{K}\right)\boldsymbol{v} = \boldsymbol{0} \tag{A.37}$$

with eigenvalues λ and corresponding eigenvectors $\boldsymbol{v}$. The eigenvalues are identical to the system poles. Multiplying from the left with some arbitrary row vector $\tilde{\boldsymbol{v}}^{\mathrm{T}}$ gives

$$\tilde{\boldsymbol{v}}^{\mathrm{T}}\boldsymbol{M}\boldsymbol{v}\lambda^2 + \tilde{\boldsymbol{v}}^{\mathrm{T}}\boldsymbol{D}\boldsymbol{v}\lambda + \tilde{\boldsymbol{v}}^{\mathrm{T}}\boldsymbol{K}\boldsymbol{v} = 0. \tag{A.38}$$

Every solution to the eigenvalue problem (A.37) satisfies the above equation for *any* $\tilde{\boldsymbol{v}}^{\mathrm{T}}$. Thus, it also satisfies (A.38) for the special case $\tilde{\boldsymbol{v}}^{\mathrm{T}} = \boldsymbol{v}^{\mathrm{T}}$. We know that $\boldsymbol{v}^{\mathrm{T}}\boldsymbol{M}\boldsymbol{v} > 0$ for any $\boldsymbol{v}$, because $\boldsymbol{M} = \bigoplus\{\tilde{\boldsymbol{M}}_{\mathrm{S}},\ \boldsymbol{M}_{\mathrm{F}}\}$ is positive definite, see also App. A.5. With an analogous argument, one can verify that $\boldsymbol{v}^{\mathrm{T}}\boldsymbol{K}\boldsymbol{v} \geq 0$ for some arbitrary $\boldsymbol{v}$. The definiteness of the second term in (A.38) can be checked by straightforward calculation,

$$\boldsymbol{v}^{\mathrm{T}}\boldsymbol{D}\boldsymbol{v} = \begin{pmatrix}\boldsymbol{v}_1^{\mathrm{T}} & \boldsymbol{v}_2^{\mathrm{T}}\end{pmatrix}\begin{pmatrix}\boldsymbol{D}_{\mathrm{S}} & -\boldsymbol{G}_{\mathrm{ma}} \\ \boldsymbol{G}_{\mathrm{ma}}^{\mathrm{T}} & \boldsymbol{D}_{\mathrm{F}}\end{pmatrix}\begin{pmatrix}\boldsymbol{v}_1 \\ \boldsymbol{v}_2\end{pmatrix} = \boldsymbol{v}_1^{\mathrm{T}}\boldsymbol{D}_{\mathrm{S}}\boldsymbol{v}_1 + \underbrace{\boldsymbol{v}_2^{\mathrm{T}}\boldsymbol{G}_{\mathrm{ma}}^{\mathrm{T}}\boldsymbol{v}_1 - \boldsymbol{v}_1^{\mathrm{T}}\boldsymbol{G}_{\mathrm{ma}}\boldsymbol{v}_2}_{=0} + \boldsymbol{v}_2^{\mathrm{T}}\boldsymbol{D}_{\mathrm{F}}\boldsymbol{v}_2. \tag{A.39}$$

Since both $\boldsymbol{D}_{\mathrm{S}}$ and $\boldsymbol{D}_{\mathrm{F}}$ are positive definite by construction, one can conclude that $\boldsymbol{v}^{\mathrm{T}}\boldsymbol{D}\boldsymbol{v} > 0,\ \forall \boldsymbol{v}$. By letting $\tilde{\boldsymbol{v}}^{\mathrm{T}} = \boldsymbol{v}^{\mathrm{T}}$ in (A.38), there must be some $\boldsymbol{v}$ such that $\boldsymbol{v}^{\mathrm{T}}\boldsymbol{K}\boldsymbol{v} = 0$. To achieve this, $\boldsymbol{v}$ must either belong to the left or right null space of $\boldsymbol{K}$. Because of the specific structure of $\boldsymbol{K} = \bigoplus\{\tilde{\boldsymbol{K}}_{\mathrm{S}}, \boldsymbol{K}_{\mathrm{F}}\}$ with $\tilde{\boldsymbol{K}}_{\mathrm{S}}$ being regular and $\boldsymbol{K}_{\mathrm{F}}$ being diagonal and rank deficient by one, both subspaces are identical and of dimension one. A basis for $\ker \boldsymbol{K}$ is given by $(0, \dots, 0, 1, 0, \dots, 0)^{\mathrm{T}}$ where the one is the $(n_{\mathrm{S}} + 1)$th entry.

Now suppose that $\boldsymbol{v}$ is indeed of the form $(0, \dots, 0, c, 0, \dots, 0)^{\mathrm{T}}$ with some arbitrary non-zero real constant c, then $\lambda_1 = 0$ is a solution to (A.38). It must now be checked if this is also a solution to the original eigenvalue problem. The solution $\lambda_1 = 0$ is an eigenvalue if and only if it satisfies the condition $\det\{\boldsymbol{M}\lambda_1^2 + \boldsymbol{D}\lambda_1 + \boldsymbol{K}\} = 0$ and the corresponding eigenvector satisfies the underlying assumption $\boldsymbol{v} \in \ker \boldsymbol{K}$. The first part can be easily verified, since $\det \boldsymbol{K} = 0$ is a true statement. The resulting eigenvector satisfies $\boldsymbol{K}\boldsymbol{v} = 0$. Therefore, $\lambda_1 = 0$ is indeed a system pole. The second solution to (A.38) for the case that $\boldsymbol{v}^{\mathrm{T}}\boldsymbol{K}\boldsymbol{v} = 0$ is given by $\lambda_2 = -\frac{\boldsymbol{v}^{\mathrm{T}}\boldsymbol{D}\boldsymbol{v}}{\boldsymbol{v}^{\mathrm{T}}\boldsymbol{M}\boldsymbol{v}}$. Obviously, λ_2 is independent of the length of $\boldsymbol{v}$ and can be simplified to $\lambda_2 = -\frac{\boldsymbol{D}_{\mathrm{F},1}}{\boldsymbol{M}_{\mathrm{F},1}} = 0$. Thus, the system described by (A.36) has two eigenvalues equal to zero.

If all remaining solutions to (A.38) with $\boldsymbol{v}^{\mathrm{T}}\boldsymbol{K}\boldsymbol{v} > 0$ are conjugate complex, then λ_1 and λ_2 must be the only real eigenvalues. This is the case if the discriminant of (A.38) is negative. This means that

$$\left(\boldsymbol{v}^{\mathrm{T}}\boldsymbol{D}\boldsymbol{v}\right)^2 - 4\boldsymbol{v}^{\mathrm{T}}\boldsymbol{M}\boldsymbol{v}\boldsymbol{v}^{\mathrm{T}}\boldsymbol{K}\boldsymbol{v} \overset{!}{<} 0. \tag{A.40}$$

It can be shown that the above is a true statement under two reasonable assumptions: Firstly, the influence of the presence of the piezoelectric elements on the plate dynamics is negligible, i.e. $\tilde{\boldsymbol{M}}_{\mathrm{S}} \approx \boldsymbol{M}_{\mathrm{S}}$ and $\tilde{\boldsymbol{K}}_{\mathrm{S}} \approx \boldsymbol{K}_{\mathrm{S}}$. Secondly, the modal damping ratios of the structure and the fluid, D_{S} and D_{F}, are smaller than one. Both conditions are fulfilled by the model parameters which are used in this thesis, see also Sec. 2.5. In addition to that, all conjugate complex poles are stable, since all coefficients of the second order polynomial (A.38) are positive. This result is due to Hurwitz, see for example [127].

In a last step, the eigenfrequencies and eigenvectors of the undamped coupled system shall be computed. To this end, we neglect the damping matrices in (2.83) and set the excitation forces to zero. This results in

$$\begin{pmatrix} \tilde{\boldsymbol{M}}_{\mathrm{S}} & \boldsymbol{0} \\ \boldsymbol{G}_{\mathrm{ma}}^{\mathrm{T}} & \boldsymbol{M}_{\mathrm{F}} \end{pmatrix} \begin{pmatrix} \ddot{\boldsymbol{\eta}} \\ \ddot{\boldsymbol{\varphi}} \end{pmatrix} + \begin{pmatrix} \tilde{\boldsymbol{K}}_{\mathrm{S}} & -\boldsymbol{G}_{\mathrm{ma}} \\ \boldsymbol{0} & \boldsymbol{K}_{\mathrm{F}} \end{pmatrix} \begin{pmatrix} \boldsymbol{\eta} \\ \dot{\boldsymbol{\varphi}} \end{pmatrix} = \boldsymbol{0}. \tag{A.41}$$

The solution to this eigenvalue problem has the squares of the eigenfrequencies $\omega_i, i = 1, \dots, n_{\mathrm{S}} + n_{\mathrm{F}}$ as eigenvalues. The eigenvectors of the form $\left(\boldsymbol{\eta}^{\mathrm{T}} \; \dot{\boldsymbol{\varphi}}^{\mathrm{T}}\right)^{\mathrm{T}}$ contain the corresponding modal amplitudes of the plate deflection and pressure amplitude. It must be kept in mind that these eigenvectors are different from those of the damped system, because the system (2.83) does not satisfy the condition of Caughey damping [129].

A.7 Expression of the Structural Indices of Lückel & Müller in Terms of Modal Quantities

Consider a lumped-parameter model of a lightly damped flexible structure of the form

$$\boldsymbol{M}\ddot{\boldsymbol{x}} + \boldsymbol{D}\dot{\boldsymbol{x}} + \boldsymbol{K}\boldsymbol{x} = \boldsymbol{L}_{\mathrm{A}}\boldsymbol{f}, \tag{A.42}$$

where $\boldsymbol{D}$ satisfies the property of Caughey damping [129], and $\boldsymbol{L}_{\mathrm{A}}$ has dimensions $^{n}\!/_{2} \times n_{\mathrm{A}}$. Via modal transformation with the mechanical modal matrix $\boldsymbol{\Phi}$, this can be rewritten in a decoupled form as

$$\ddot{\boldsymbol{\eta}} + 2\bigoplus_{i=1}^{n/2}\{D_i\omega_i\}\,\dot{\boldsymbol{\eta}} + \bigoplus_{i=1}^{n/2}\omega_i^2\boldsymbol{\eta} = \boldsymbol{\Phi}^{\mathrm{T}}\boldsymbol{L}_{\mathrm{A}}\boldsymbol{f}, \tag{A.43}$$

or equivalently

$$\begin{pmatrix} \dot{\boldsymbol{\eta}} \\ \ddot{\boldsymbol{\eta}} \end{pmatrix} = \begin{pmatrix} \boldsymbol{0} & \mathbf{I} \\ -\bigoplus_{i=1}^{n/2}\omega_i^2 & -2\bigoplus_{i=1}^{n/2}D_i\omega_i \end{pmatrix} \begin{pmatrix} \boldsymbol{\eta} \\ \dot{\boldsymbol{\eta}} \end{pmatrix} + \begin{pmatrix} \boldsymbol{0} \\ \boldsymbol{\Phi}_{\mathrm{A}}^{\mathrm{T}} \end{pmatrix} \boldsymbol{f}, \tag{A.44}$$

with $\boldsymbol{x} = \boldsymbol{\Phi}\boldsymbol{\eta}$, and $\boldsymbol{\Phi}_{\mathrm{A}} = \boldsymbol{L}_{\mathrm{A}}^{\mathrm{T}}\boldsymbol{\Phi}$. The system of first order ODEs (A.44) is the dynamics equation of the corresponding state space model.

The controllability index of Lückel & Müller for the ith eigenmode of a general state space system is given by [126]

$$\kappa_i^B = \frac{\boldsymbol{w}_i^{\mathrm{T}}\boldsymbol{B}\boldsymbol{B}^{\mathrm{T}}\boldsymbol{w}_i^*}{\boldsymbol{w}_i^{\mathrm{T}}\boldsymbol{w}_i^*}, \quad i = 1, \dots, n. \tag{A.45}$$

The purpose of this section is to sketch a calculation which shows that (A.45) can be equivalently expressed by

$$\kappa_i^B = \left(\boldsymbol{\Phi}_{\mathrm{A}}^{(:,i)}\right)^{\mathrm{T}}\boldsymbol{\Phi}_{\mathrm{A}}^{(:,i)}\frac{1}{1+\omega_i^2}, \quad i = 1, \dots, {}^{n}\!/_{2}, \tag{A.46}$$

when dealing with a state space model of the form (A.44). Only one half of the indices has to be calculated, since the system does exclusively have pairs of conjugate-complex eigenvalues.
To begin with, it can be verified that the system matrix of the state space model (A.44) has the right-eigenvector matrix

$$\boldsymbol{V} = \begin{pmatrix} \mathbf{I} & \mathbf{I} \\ \bigoplus_{i=1}^{n/2} \left\{ -D_i + \sqrt{D_i^2 - 1}\,\omega_i \right\} & \bigoplus_{i=1}^{n/2} \left\{ -D_i - \sqrt{D_i^2 - 1}\,\omega_i \right\} \end{pmatrix} \tag{A.47}$$

and the left-eigenvector matrix

$$\boldsymbol{W} = \frac{1}{2} \begin{pmatrix} \bigoplus_{\mathrm{i}=1}^{n/2} \left\{ \frac{\mathrm{D_i} + \sqrt{\mathrm{D_i^2} - 1}}{\sqrt{\mathrm{D_i^2} - 1}} \right\} & -\bigoplus_{\mathrm{i}=1}^{n/2} \left\{ \frac{\mathrm{D_i} - \sqrt{\mathrm{D_i^2} - 1}}{\sqrt{\mathrm{D_i^2} - 1}} \right\} \\ \bigoplus_{i=1}^{n/2} \left\{ \frac{1}{\omega_i \sqrt{D_i^2 - 1}} \right\} & -\bigoplus_{i=1}^{n/2} \left\{ \frac{1}{\omega_i \sqrt{D_i^2 - 1}} \right\} \end{pmatrix}, \tag{A.48}$$

when the ordering of the set of eigenvalues is $\{\lambda_1, \ldots, \lambda_{n/2}, \lambda_1^*, \ldots, \lambda_{n/2}^*\}$. Using the ith left eigenvector in (A.45) results in

$$\kappa_i^B = \sum_{j=1}^{n_\mathrm{A}} \left(\boldsymbol{\Phi}_\mathrm{A}^{(j,i)} \right)^2 \frac{\left(\frac{1}{\sqrt{D_i^2 - 1}} \right)^*}{\left(\frac{D_i + \sqrt{D_i^2 - 1}}{\sqrt{D_i^2 - 1}} \right)^* \omega_i^2 D_i + \left(\frac{D_i + \sqrt{D_i^2 - 1}}{\sqrt{D_i^2 - 1}} \right)^* \omega_i^2 \sqrt{D_i^2 - 1} + \left(\frac{1}{\sqrt{D_i^2 - 1}} \right)^*}. \tag{A.49}$$

After several elemental manipulations, the right factor of this equation collapses to $1/(1 + \omega_i^2)$, and thus

$$\kappa_i^B = \sum_{j=1}^{n_\mathrm{A}} \left(\boldsymbol{\Phi}_\mathrm{A}^{(j,i)} \right)^2 \frac{1}{1 + \omega_i^2}, \tag{A.50}$$

and we have result (A.46). Obviously, the controllability index of Lückel & Müller is independent of the modal damping ratio D_i.

Now, the motion of the plate with piezoelectric actuators described by (2.82) is considered. When the structural modifications caused by the piezoelectric elements are neglected, this set of equations reduces to

$$\boldsymbol{M}_\mathrm{S} \ddot{\boldsymbol{\eta}} + \boldsymbol{D}_\mathrm{S} \dot{\boldsymbol{\eta}} + \boldsymbol{K}_\mathrm{S} \boldsymbol{\eta} = -\boldsymbol{G}_{\mathrm{em,A}} \boldsymbol{U}_\mathrm{A}. \tag{A.51}$$

According to App. A.5, the matrices $\boldsymbol{M}_\mathrm{S}$, $\boldsymbol{D}_\mathrm{S}$ and $\boldsymbol{K}_\mathrm{S}$ are already in the form of (A.43), and $-\boldsymbol{G}_{\mathrm{em,A}}$ corresponds to $\boldsymbol{\Phi}_\mathrm{A}^\mathrm{T}$. Then, result (2.92) follows immediately from (A.46).

The representation of the observability index defined by Lückel & Müller,

$$\kappa_i^C = \frac{\left(\boldsymbol{v}_i^* \right)^\mathrm{T} \boldsymbol{C}^\mathrm{T} \boldsymbol{C} \boldsymbol{v}_i}{\boldsymbol{v}_i^\mathrm{T} \boldsymbol{v}_i^*}, \tag{A.52}$$

in modal quantities can be analogously derived and results in

$$\kappa_i^C = \left(\boldsymbol{\Phi}_\mathrm{S}^{(:,i)} \right)^\mathrm{T} \boldsymbol{\Phi}_\mathrm{S}^{(:,i)} \frac{1}{1 + \omega_i^2}, \tag{A.53}$$

where it was assumed that the output equation of the state space model (A.44) is of the form

$$\boldsymbol{y} = \begin{pmatrix} \boldsymbol{\Phi}_{\mathrm{S}} & \boldsymbol{0} \end{pmatrix} \begin{pmatrix} \boldsymbol{\eta} \\ \dot{\boldsymbol{\eta}} \end{pmatrix}. \tag{A.54}$$

In the special case of displacement sensing at discrete locations, $\boldsymbol{\Phi}_{\mathrm{S}}$ would be equal to $\boldsymbol{W}^{\mathrm{dis}}_{\mathrm{sensor}}$ from (2.87a). It can be assumed that those locations which are optimal for displacement sensing are also optimal for acceleration sensing. Thus, (A.53) can also be used for the optimization of accelerometer locations.

B Appendix to Experimental Modeling

B.1 Isomorphism Between Complex and Real Matrices

Here, two bijective maps are introduced which allow to express properties of complex-valued signals as properties of corresponding real-valued signals. These transformations will be useful in the following to proof the properties of the H_1 estimator. The material is taken from Sec. 13.8 in [152].

For any complex-valued matrix $\boldsymbol{A}$, define a corresponding real-valued matrix $\boldsymbol{A}_{\mathrm{Re}}$ by the bijective map

$$\mathrm{Re} : M(m,n,\mathbb{C}) \to M(2m,2n,\mathbb{R}), \boldsymbol{A} \mapsto \boldsymbol{A}_{\mathrm{Re}} = \begin{pmatrix} \Re\boldsymbol{A} & -\Im\boldsymbol{A} \\ \Im\boldsymbol{A} & \Re\boldsymbol{A} \end{pmatrix}, \tag{B.1}$$

where $M(m,n,\mathbb{K})$ denotes the set of matrices of dimension $m \times n$ over the field $\mathbb{K}$.

Furthermore, we define a second isomorphism

$$\mathrm{re} : M(m,n,\mathbb{C}) \to M(2m,n,\mathbb{R}),\ \boldsymbol{A} \mapsto \boldsymbol{A}_{\mathrm{re}} = \begin{pmatrix} \Re\boldsymbol{A} \\ \Im\boldsymbol{A} \end{pmatrix}. \tag{B.2}$$

The following properties of these maps will be useful in the following:

$$\boldsymbol{A} = \boldsymbol{B}^{\mathrm{H}} \Leftrightarrow \boldsymbol{A}_{\mathrm{Re}} = \boldsymbol{B}_{\mathrm{Re}}^{\mathrm{T}} \tag{B.3a}$$

$$\boldsymbol{A} = \boldsymbol{B}^{-1} \Leftrightarrow \boldsymbol{A}_{\mathrm{Re}} = \boldsymbol{B}_{\mathrm{Re}}^{-1} \tag{B.3b}$$

$$\boldsymbol{A} = \boldsymbol{B}\boldsymbol{X} \Leftrightarrow \boldsymbol{A}_{\mathrm{re}} = \boldsymbol{B}_{\mathrm{Re}}\boldsymbol{X}_{\mathrm{re}} \tag{B.3c}$$

$$\boldsymbol{A} = \boldsymbol{B}\boldsymbol{C} \Leftrightarrow \boldsymbol{A}_{\mathrm{Re}} = \boldsymbol{B}_{\mathrm{Re}}\boldsymbol{C}_{\mathrm{Re}} \tag{B.3d}$$

B.2 Properties of the H_1 Estimator

The H_1 estimator for frequency response functions from DFT data was given in (3.4) as

$$\hat{\boldsymbol{G}}\left(\mathrm{e}^{\mathrm{j}\omega_n}\right) = \left(\frac{1}{M}\sum_{m=1}^{M} \boldsymbol{Y}_m(\mathrm{j}\omega_n)\boldsymbol{U}_m^{\mathrm{H}}(\mathrm{j}\omega_n)\right)\left(\frac{1}{M}\sum_{m=1}^{M} \boldsymbol{U}_m(\mathrm{j}\omega_n)\boldsymbol{U}_m^{\mathrm{H}}(\mathrm{j}\omega_n)\right)^{-1}, \tag{B.4}$$

where it was also argued that at least $M \geq q$ experiments with suitably designed excitation signals are necessary to ensure invertibility of the second factor on the right hand side. For ease of notation and without loss of generality, one can assume that the total number of experiments M is an integer multiple of the number of system inputs q, i.e. $M = q\tilde{M}$. Then, the estimator equation can be rewritten as

$$\hat{\boldsymbol{G}}\left(\mathrm{e}^{\mathrm{j}\omega_n}\right) = \left(\frac{1}{\tilde{M}}\sum_{\tilde{m}=1}^{\tilde{M}} \tilde{\boldsymbol{Y}}_{\tilde{m}}\tilde{\boldsymbol{U}}_{\tilde{m}}^{\mathrm{H}}(\mathrm{j}\omega_n)\right)\left(\frac{1}{\tilde{M}}\sum_{\tilde{m}=1}^{\tilde{M}} \tilde{\boldsymbol{U}}_{\tilde{m}}\tilde{\boldsymbol{U}}_{\tilde{m}}^{\mathrm{H}}(\mathrm{j}\omega_n)\right)^{-1} \tag{B.5}$$

with

$$\tilde{\boldsymbol{Y}}_{\tilde{m}}\tilde{\boldsymbol{U}}_{\tilde{m}}^{\mathrm{H}} := \frac{1}{q}\sum_{m=1}^{q} \boldsymbol{Y}_{(\tilde{m}-1)q+m}\boldsymbol{U}_{(\tilde{m}-1)q+m}^{\mathrm{H}} \quad \text{and} \quad \tilde{\boldsymbol{U}}_{\tilde{m}}\tilde{\boldsymbol{U}}_{\tilde{m}}^{\mathrm{H}} := \frac{1}{q}\sum_{m=1}^{q} \boldsymbol{U}_{(\tilde{m}-1)q+m}\boldsymbol{U}_{(\tilde{m}-1)q+m}^{\mathrm{H}}. \tag{B.6}$$

It is also assumed for simplicity that the input signal sequence is periodically repeated after q experiments, which means that $\tilde{\boldsymbol{U}}_i\tilde{\boldsymbol{U}}_i^{\mathrm{H}} = \tilde{\boldsymbol{U}}_j\tilde{\boldsymbol{U}}_j^{\mathrm{H}}\ \forall\{i,j\} = 1,\dots,\tilde{m}$. This further simplifies (B.5) to

$$\hat{\boldsymbol{G}}\left(\mathrm{e}^{\mathrm{j}\omega_n}\right) = \underbrace{\left(\frac{1}{\tilde{M}}\sum_{\tilde{m}=1}^{\tilde{M}} \tilde{\boldsymbol{Y}}_{\tilde{m}}(\mathrm{j}\omega_n)\tilde{\boldsymbol{U}}_{\tilde{m}}^{\mathrm{H}}(\mathrm{j}\omega_n)\right)}_{=\hat{\boldsymbol{S}}_{YU}}\Bigg(\underbrace{\tilde{U}(\mathrm{j}\omega_n)\tilde{\boldsymbol{U}}^{\mathrm{H}}(\mathrm{j}\omega_n)}_{=:\boldsymbol{S}_{UU}}\Bigg)^{-1}, \tag{B.7}$$

which is the form that will be used in the following. However, these assumptions do not affect the validity of the proofs.

B.2.1 Unbiasedness

The input signal sequence $\boldsymbol{u}_m(k)$ is assumed to be perfectly known, whereas the output signals are distorted by zero-mean additive noise, i.e. $\boldsymbol{y}_m(k) = \boldsymbol{y}_{0,m}(k) + \boldsymbol{v}_m(k)$. It is assumed that precautions are taken to avoid leakage errors in the DFT sequences of $\boldsymbol{u}_m$ and $\boldsymbol{y}_{0,m}$, as explained in Sec. 3.3. Then, the DFT output sequences read

$$\boldsymbol{Y}_m(\mathrm{j}\omega_n) = \boldsymbol{Y}_{0,m}(\mathrm{j}\omega_n) + \boldsymbol{V}_m(\mathrm{j}\omega_n), \quad \text{with} \quad \boldsymbol{Y}_{0,m}(\mathrm{j}\omega_n) = \boldsymbol{G}_0(\mathrm{e}^{\mathrm{j}\omega_n})\boldsymbol{U}_m(\mathrm{j}\omega_n), \tag{B.8}$$

where $\boldsymbol{G}_0\left(\mathrm{e}^{\mathrm{j}\omega_n}\right)$ represents the FRF of the true plant to be identified. Using these expressions in (B.6) and (B.7) gives

$$\begin{aligned}\hat{\boldsymbol{G}} &= \left(\frac{1}{\tilde{M}}\sum_{\tilde{m}=1}^{\tilde{M}} \tilde{\boldsymbol{Y}}_{0,\tilde{m}}\tilde{\boldsymbol{U}}_{\tilde{m}}^{\mathrm{H}} + \tilde{\boldsymbol{V}}_{\tilde{m}}\tilde{\boldsymbol{U}}_{\tilde{m}}^{\mathrm{H}}\right)\boldsymbol{S}_{UU}^{-1} \\ &= \left(\frac{1}{\tilde{M}}\sum_{\tilde{m}=1}^{\tilde{M}} \tilde{\boldsymbol{Y}}_{0,\tilde{m}}\tilde{\boldsymbol{U}}_{\tilde{m}}^{\mathrm{H}}\right)\boldsymbol{S}_{UU}^{-1} + \left(\frac{1}{\tilde{M}}\sum_{\tilde{m}=1}^{\tilde{M}} \tilde{\boldsymbol{V}}_{\tilde{m}}\tilde{\boldsymbol{U}}_{\tilde{m}}^{\mathrm{H}}\right)\boldsymbol{S}_{UU}^{-1} \\ &= \boldsymbol{G}_0 + \left(\frac{1}{\tilde{M}}\sum_{\tilde{m}=1}^{\tilde{M}} \tilde{\boldsymbol{V}}_{\tilde{m}}\tilde{\boldsymbol{U}}_{\tilde{m}}^{\mathrm{H}}\right)\boldsymbol{S}_{UU}^{-1}.\end{aligned} \tag{B.9}$$

Taking the expected value finally gives

$$\mathrm{E}\left\{\hat{\boldsymbol{G}}\right\} = \boldsymbol{G}_0 + \left(\frac{1}{\tilde{M}}\sum_{\tilde{m}=1}^{\tilde{M}} \underbrace{\mathrm{E}\left\{\tilde{\boldsymbol{V}}_{\tilde{m}}\boldsymbol{U}_{\tilde{m}}^{\mathrm{H}}\right\}}_{=\boldsymbol{0}}\right)\boldsymbol{S}_{UU}^{-1} = \boldsymbol{G}_0, \tag{B.10}$$

since $\mathrm{E}\{\boldsymbol{V}\} = \boldsymbol{0}$ (according to (3.5)), and the noise is assumed to be independent of the input.

B.2.2 Circular Symmetric Complex Normal Distribution

It is known that the following operations do preserve the CSCN distribution of a random vector $\boldsymbol{z} \in \mathcal{CN}^n\left(\boldsymbol{\mu}, \boldsymbol{\sigma}_z^2, \mathbf{0}\right)$ [7]:

- affine transformation, i.e. $\boldsymbol{A}\boldsymbol{z}+\boldsymbol{b} \in \mathcal{CN}^m\left(\boldsymbol{A}\boldsymbol{\mu}+\boldsymbol{b}, \boldsymbol{A}\boldsymbol{\sigma}_z^2\boldsymbol{A}^{\mathrm{H}}, \mathbf{0}\right)$ for some non-random $\boldsymbol{A} \in \mathbb{C}^{m\times n}$ and $\boldsymbol{b} \in \mathbb{C}^m$,
- linear combination of mutually independent CSCN variables $\boldsymbol{z}_1 \in \mathcal{CN}^n\left(\boldsymbol{\mu}_1, \boldsymbol{\sigma}_{z_1}^2, \mathbf{0}\right)$ and $\boldsymbol{z}_2 \in \mathcal{CN}^n\left(\boldsymbol{\mu}_2, \boldsymbol{\sigma}_{z_2}^2, \mathbf{0}\right)$, i.e. $a\boldsymbol{z}_1 + b\boldsymbol{z}_2 \in \mathcal{CN}^n\left(a\boldsymbol{\mu}_1 + b\boldsymbol{\mu}_2, a^2\boldsymbol{\sigma}_{z_1}^2 + b^2\boldsymbol{\sigma}_{z_2}^2, \mathbf{0}\right)$ with $a, b \in \mathbb{R}$.

In view of (B.9), it can be concluded that $\hat{\boldsymbol{G}}\left(\mathrm{e}^{\mathrm{j}\omega_n}\right)$ is influenced by the CSCN distributed noise $\boldsymbol{V}_m(\mathrm{j}\omega_n)$ only via these distribution-preserving operations. Thus, the estimate of $\hat{\boldsymbol{G}}\left(\mathrm{e}^{\mathrm{j}\omega_n}\right)$ is also CSCN distributed.

B.2.3 Noise Covariance Matrix

The covariance matrix of the sensor noise is defined as

$$\boldsymbol{\sigma}_V^2(\mathrm{j}\omega_n) = \mathrm{E}\left\{\left(\boldsymbol{V}(\mathrm{j}\omega_n) - \mathrm{E}\{\boldsymbol{V}(\mathrm{j}\omega_n)\}\right)\left(\boldsymbol{V}(\mathrm{j}\omega_n) - \mathrm{E}\{\boldsymbol{V}(\mathrm{j}\omega_n)\}\right)^{\mathrm{H}}\right\} = \mathrm{E}\left\{\boldsymbol{V}(\mathrm{j}\omega_n)\boldsymbol{V}^{\mathrm{H}}(\mathrm{j}\omega_n)\right\}, \tag{B.11}$$

because $\mathrm{E}\{\boldsymbol{V}(\mathrm{j}\omega_n)\} = \mathbf{0}$. In addition to that, we have

$$\boldsymbol{V}(\mathrm{j}\omega_n) = \boldsymbol{Y}(\mathrm{j}\omega_n) - \boldsymbol{Y}_0(\mathrm{j}\omega_n) = \boldsymbol{Y}(\mathrm{j}\omega_n) - \boldsymbol{G}_0\boldsymbol{U}(\mathrm{j}\omega_n). \tag{B.12}$$

Since the estimator is bias free, we can determine the true plant response as the average of an infinite number of experiments, i.e. $\boldsymbol{G}_0 = \mathrm{E}\{\hat{\boldsymbol{G}}\} = \mathrm{E}\{\hat{\boldsymbol{S}}_{YU}\boldsymbol{S}_{UU}^{-1}\} = \mathrm{E}\{\hat{\boldsymbol{S}}_{YU}\}\boldsymbol{S}_{UU}^{-1}$, with $\mathrm{E}\{\hat{\boldsymbol{S}}_{YU}\} = \lim_{\tilde{M}\to\infty}\frac{1}{\tilde{M}}\sum_{\tilde{m}=1}^{\tilde{M}}\tilde{\boldsymbol{Y}}_{\tilde{m}}\tilde{\boldsymbol{U}}_{\tilde{m}}^{\mathrm{H}} =: \boldsymbol{S}_{YU}$, since the sensor noise is i.i.d over different experiments and independent of the input. Using this in (B.11) and (B.12) gives

$$\begin{aligned}\boldsymbol{\sigma}_V^2 &= \mathrm{E}\left\{\left(\boldsymbol{Y} - \boldsymbol{S}_{YU}\boldsymbol{S}_{UU}^{-1}\boldsymbol{U}\right)\left(\boldsymbol{Y} - \boldsymbol{S}_{YU}\boldsymbol{S}_{UU}^{-1}\boldsymbol{U}\right)^{\mathrm{H}}\right\} \\ &= \mathrm{E}\left\{\boldsymbol{Y}\boldsymbol{Y}^{\mathrm{H}} - \boldsymbol{Y}\boldsymbol{U}^{\mathrm{H}}\boldsymbol{S}_{UU}^{-\mathrm{H}}\boldsymbol{S}_{YU}^{\mathrm{H}} - \boldsymbol{S}_{YU}\boldsymbol{S}_{UU}^{-1}\boldsymbol{U}\boldsymbol{Y}^{\mathrm{H}} + \boldsymbol{S}_{YU}\boldsymbol{S}_{UU}^{-1}\boldsymbol{U}\boldsymbol{U}^{\mathrm{H}}\boldsymbol{S}_{UU}^{-\mathrm{H}}\boldsymbol{S}_{YU}^{\mathrm{H}}\right\}.\end{aligned} \tag{B.13}$$

Since $\mathrm{E}\{\boldsymbol{Y}\boldsymbol{U}^{\mathrm{H}}\} = \lim_{\tilde{M}\to\infty}\frac{1}{\tilde{M}}\sum_{m=1}^{\tilde{M}}\tilde{\boldsymbol{Y}}\tilde{\boldsymbol{U}}^{\mathrm{H}} = \boldsymbol{S}_{YU}$ and analog arguments hold for $\mathrm{E}\{\boldsymbol{Y}\boldsymbol{Y}^{\mathrm{H}}\}$, $\mathrm{E}\{\boldsymbol{U}\boldsymbol{Y}^{\mathrm{H}}\}$, and $\mathrm{E}\{\boldsymbol{U}\boldsymbol{U}^{\mathrm{H}}\}$, the above equation is equal to

$$\begin{aligned}\boldsymbol{\sigma}_V^2 &= \left(\boldsymbol{S}_{YY} - \boldsymbol{S}_{YU}\boldsymbol{S}_{UU}^{-\mathrm{H}}\boldsymbol{S}_{YU}^{\mathrm{H}} - \boldsymbol{S}_{YU}\boldsymbol{S}_{UU}^{-1}\boldsymbol{S}_{UY} + \boldsymbol{S}_{YU}\boldsymbol{S}_{UU}^{-1}\boldsymbol{S}_{UU}\boldsymbol{S}_{UU}^{-\mathrm{H}}\boldsymbol{S}_{YU}^{\mathrm{H}}\right) \\ &= \left(\boldsymbol{S}_{YY} - \boldsymbol{S}_{YU}\boldsymbol{S}_{UU}^{-1}\boldsymbol{S}_{UY}\right).\end{aligned} \tag{B.14}$$

The asymptotic estimates of the cross- and autopower spectra are not available, but it is intuitive to use their finite-sample estimates to derive an estimator for the noise covariance matrix,

$$\hat{\boldsymbol{\sigma}}_V^2 = \left(\hat{\boldsymbol{S}}_{YY} - \hat{\boldsymbol{S}}_{YU}\boldsymbol{S}_{UU}^{-1}\hat{\boldsymbol{S}}_{UY}\right). \tag{B.15}$$

This estimator is only asymptotically bias free, because the power spectra themselves are also estimated. It is argued by Verboven [187] that using a scaling term $\tilde{M}/\tilde{M}-1$ leads to an unbiased estimate of $\boldsymbol{\sigma}_V^2$.

B.2.4 Estimator Covariance Matrix

With the help of the noise covariance $\boldsymbol{\sigma}_V^2$, the covariance of the estimated elements $\hat{\boldsymbol{G}}\left(\mathrm{e}^{\mathrm{j}\omega_n}\right)$ can be calculated. The estimated quantities are stacked in a column vector such that

$$\boldsymbol{\sigma}_{\hat{G}}^2(\mathrm{j}\omega_n) = \mathrm{E}\left\{\operatorname{vec}\left\{\hat{\boldsymbol{G}}\left(\mathrm{e}^{\mathrm{j}\omega_n}\right) - \mathrm{E}\left\{\hat{\boldsymbol{G}}\left(\mathrm{e}^{\mathrm{j}\omega_n}\right)\right\}\right\}\left(\operatorname{vec}\left\{\hat{\boldsymbol{G}}\left(\mathrm{e}^{\mathrm{j}\omega_n}\right) - \mathrm{E}\left\{\hat{\boldsymbol{G}}\left(\mathrm{e}^{\mathrm{j}\omega_n}\right)\right\}\right\}\right)^{\mathrm{H}}\right\}. \tag{B.16}$$

Due to the unbiasedness of the estimator, this gives

$$\boldsymbol{\sigma}_{\hat{G}}^2(\mathrm{j}\omega_n) = \mathrm{E}\left\{\operatorname{vec}\left\{\hat{\boldsymbol{G}}\left(\mathrm{e}^{\mathrm{j}\omega_n}\right) - \boldsymbol{G}_0\right\}\left(\operatorname{vec}\left\{\hat{\boldsymbol{G}}\left(\mathrm{e}^{\mathrm{j}\omega_n}\right) - \boldsymbol{G}_0\right\}\right)^{\mathrm{H}}\right\}. \tag{B.17}$$

In view of (B.9), this is equal to

$$\boldsymbol{\sigma}_{\hat{G}}^2 = \mathrm{E}\left\{\operatorname{vec}\left\{\left(\frac{1}{\tilde{M}}\sum_{\tilde{m}=1}^{\tilde{M}}\tilde{\boldsymbol{V}}_{\tilde{m}}\tilde{\boldsymbol{U}}_{\tilde{m}}^{\mathrm{H}}\right)\boldsymbol{S}_{UU}^{-1}\right\}\left(\operatorname{vec}\left\{\left(\frac{1}{\tilde{M}}\sum_{\tilde{m}=1}^{\tilde{M}}\tilde{\boldsymbol{V}}_{\tilde{m}}\tilde{\boldsymbol{U}}_{\tilde{m}}^{\mathrm{H}}\right)\boldsymbol{S}_{UU}^{-1}\right\}\right)^{\mathrm{H}}\right\}. \tag{B.18}$$

With the help of the identity $\operatorname{vec}\{\boldsymbol{ACB}\} = \left(\boldsymbol{B}^{\mathrm{T}} \otimes \boldsymbol{A}\right)\operatorname{vec}\boldsymbol{C}$, this can be rewritten as

$$\boldsymbol{\sigma}_{\hat{G}}^2 = \left(\boldsymbol{S}_{UU}^{-\mathrm{T}} \otimes \mathbf{I}\right)\mathrm{E}\left\{\operatorname{vec}\left\{\frac{1}{\tilde{M}}\sum_{\tilde{m}=1}^{\tilde{M}}\tilde{\boldsymbol{V}}_{\tilde{m}}\tilde{\boldsymbol{U}}_{\tilde{m}}^{\mathrm{H}}\right\}\left(\operatorname{vec}\left\{\frac{1}{\tilde{M}}\sum_{\tilde{m}=1}^{\tilde{M}}\tilde{\boldsymbol{V}}_{\tilde{m}}\tilde{\boldsymbol{U}}_{\tilde{m}}^{\mathrm{H}}\right\}\right)^{\mathrm{H}}\right\}\left(\boldsymbol{S}_{UU}^{-\mathrm{T}} \otimes \mathbf{I}\right)^{\mathrm{H}}. \tag{B.19}$$

Under the assumption that the measurement noise is i.i.d. over different experiments and uncorrelated with the input, it can be shown by straightforward manipulations that the expected value in the above equation is equal to $1/\tilde{M}q\ \boldsymbol{S}_{UU}^{*} \otimes \boldsymbol{\sigma}_V^2$, where $*$ denotes taking the conjugate-complex element of every entry. Then,

$$\begin{aligned}
\boldsymbol{\sigma}_{\hat{G}}^2 &= \frac{1}{\tilde{M}q}\left(\boldsymbol{S}_{UU}^{-\mathrm{T}} \otimes \mathbf{I}\right)\left(\boldsymbol{S}_{UU}^{*} \otimes \boldsymbol{\sigma}_V^2\right)\left(\boldsymbol{S}_{UU}^{-*} \otimes \mathbf{I}\right) \\
&= \frac{1}{\tilde{M}q}\left[\left(\boldsymbol{S}_{UU}^{-\mathrm{T}}\boldsymbol{S}_{UU}^{*}\right) \otimes \boldsymbol{\sigma}_V^2\right]\left(\boldsymbol{S}_{UU}^{-*} \otimes \mathbf{I}\right) \\
&= \frac{1}{\tilde{M}q}\boldsymbol{S}_{UU}^{-\mathrm{T}}\boldsymbol{S}_{UU}^{*}\boldsymbol{S}_{UU}^{-*} \otimes \boldsymbol{\sigma}_V^2 \\
&= \frac{1}{\tilde{M}q}\boldsymbol{S}_{UU}^{-\mathrm{T}} \otimes \boldsymbol{\sigma}_V^2,
\end{aligned} \tag{B.20}$$

which is the result presented in (3.6). In practice, an estimate of $\boldsymbol{\sigma}_{\hat{G}}^2$ is given by using $\hat{\boldsymbol{\sigma}}_V^2$ instead of $\boldsymbol{\sigma}_V^2$ in the above equation. The expected value of this estimate is

$$\mathrm{E}\left\{\hat{\boldsymbol{\sigma}}_{\hat{G}}^2\right\} = \frac{1}{\tilde{M}q}\boldsymbol{S}_{UU}^{-T} \otimes \mathrm{E}\left\{\hat{\boldsymbol{\sigma}}_V^2\right\}. \tag{B.21}$$

This shows that the covariance estimate of the estimated transfer functions is unbiased if an unbiased estimate for $\boldsymbol{\sigma}_V^2$ is used.

B.2.5 Convergence and Consistency

An estimator is consistent if it converges to the true value for an infinite amount of observation data, i.e. $\tilde{M} \to \infty$. Here, convergence and consistency are understood in the mean square sense, see for example [152] for further details. Precisely stated, we require

$$\underset{\tilde{M}\to\infty}{\text{l. i. m.}}\ \hat{\boldsymbol{G}}\left(\mathrm{e}^{\mathrm{j}\omega_n}\right) \overset{!}{=} \boldsymbol{G}_0\left(\mathrm{e}^{\mathrm{j}\omega_n}\right) \Leftrightarrow \lim_{\tilde{M}\to\infty} \mathrm{E}\left\{\left|\hat{\boldsymbol{G}}\left(\mathrm{e}^{\mathrm{j}\omega_n}\right) - \boldsymbol{G}_0\left(\mathrm{e}^{\mathrm{j}\omega_n}\right)\right|^2\right\} \overset{!}{=} \mathbf{0}, \tag{B.22}$$

where all operations are taken element wise. As before, we can treat every frequency sample ω_n separately, because the DFT noise samples $\boldsymbol{V}(\mathrm{j}\omega_n)$ are assumed to be independent, see Sec. 3.3. Then, considering again (B.9), we may write

$$\lim_{\tilde{M}\to\infty} \mathrm{E}\left\{\left|\left(\frac{1}{\tilde{M}}\sum_{\tilde{m}=1}^{\tilde{M}} \tilde{\boldsymbol{V}}_{\tilde{m}}\tilde{\boldsymbol{U}}_{\tilde{m}}^{\mathrm{H}}\right)\boldsymbol{S}_{UU}^{-1}\right|^2\right\} \overset{!}{=} \mathbf{0}. \tag{B.23}$$

The left hand side is equal to

$$\lim_{\tilde{M}\to\infty} \frac{1}{\tilde{M}^2}\mathrm{E}\left\{\left|\underbrace{\left(\sum_{\tilde{m}=1}^{\tilde{M}} \tilde{\boldsymbol{V}}_{\tilde{m}}\tilde{\boldsymbol{U}}_{\tilde{m}}^{\mathrm{H}}\right)\boldsymbol{S}_{UU}^{-1}}_{=:\boldsymbol{X}}\right|^2\right\}. \tag{B.24}$$

We now consider the (i,j)th element of the matrix $\boldsymbol{X}$, which is determined by the ith row of $\sum_{\tilde{m}=1}^{\tilde{M}} \tilde{\boldsymbol{V}}_{\tilde{m}}\tilde{\boldsymbol{U}}_{\tilde{m}}^{\mathrm{H}}$ and the jth column of $\boldsymbol{S}_{UU}^{-1}$,

$$\begin{aligned} \boldsymbol{X}^{(i,j)} &= \sum_{\tilde{m}=1}^{\tilde{M}} \left(\tilde{V}_{\tilde{m}}^{i}\left(\tilde{U}_{\tilde{m}}^{1}\right)^{*}, \ldots, \tilde{V}_{\tilde{m}}^{i}\left(\tilde{U}_{\tilde{m}}^{q}\right)^{*}\right)\boldsymbol{S}_{UU}^{-1\,(:,j)} \\ &= \boldsymbol{S}_{UU}^{-\mathrm{T}\,(j,:)} \underbrace{\begin{pmatrix} \sum_{\tilde{m}=1}^{\tilde{M}} \tilde{V}_{\tilde{m}}^{i}\left(\tilde{U}_{\tilde{m}}^{1}\right)^{*} \\ \vdots \\ \sum_{\tilde{m}=1}^{\tilde{M}} \tilde{V}_{\tilde{m}}^{i}\left(\tilde{U}_{\tilde{m}}^{q}\right)^{*} \end{pmatrix}}_{=:\boldsymbol{Z}^{i}}, \end{aligned} \tag{B.25}$$

where $\tilde{V}_{\tilde{m}}^{i}\left(\tilde{U}_{\tilde{m}}^{k}\right)^{*}$ is the (i,k)th element of the matrix $\tilde{\boldsymbol{V}}_{\tilde{m}}\tilde{\boldsymbol{U}}_{\tilde{m}}^{\mathrm{H}}$. Due to the CSCN distribution of the noise, we have $V^{i} \in \mathcal{CN}\left(0, \boldsymbol{\sigma}_{V}^{2\,(i,i)}, 0\right)$. Furthermore,

$$\begin{aligned} V^{i}\left(U^{k}\right)^{*} &\in \mathcal{CN}\left(0, \left|U^{k}\right|^{2}\boldsymbol{\sigma}_{V}^{2\,(i,i)}, 0\right), \\ \sum_{m=1}^{q} V_{m}^{i}\left(U_{m}^{k}\right)^{*} &\in \mathcal{CN}\left(0, \sum_{m=1}^{q}\left|U_{m}^{k}\right|^{2}\boldsymbol{\sigma}_{V}^{2\,(i,i)}, 0\right), \\ \sum_{\tilde{m}=1}^{\tilde{M}} \tilde{V}_{\tilde{m}}^{i}\left(\tilde{U}_{\tilde{m}}^{k}\right)^{*} &\in \mathcal{CN}\left(0, \frac{\tilde{M}}{q^{2}}\sum_{m=1}^{q}\left|U_{m}^{k}\right|^{2}\boldsymbol{\sigma}_{V}^{2\,(i,i)}, 0\right). \end{aligned} \tag{B.26}$$

Consequently, the vector $\boldsymbol{Z}^i \in \mathcal{CN}^q\left(\boldsymbol{0}, \boldsymbol{\sigma}^2_{Z^i}, \boldsymbol{0}\right)$, where the (k, l)th element of $\boldsymbol{\sigma}^2_{Z^i}$ is given by

$$\boldsymbol{\sigma}^{2\,(k,l)}_{Z^i} = \frac{\tilde{M}}{q^2} \sum_{m=1}^{q} U_m^k \left(U_m^l\right)^* \boldsymbol{\sigma}^{2\,(i,i)}_V = \frac{\tilde{M}}{q^2} \boldsymbol{S}^{(k,l)}_{UU} \boldsymbol{\sigma}^{2\,(i,i)}_V. \tag{B.27}$$

This implies that $\boldsymbol{X}^{(i,j)} \in \mathcal{CN}\left(0, \sigma^2_{X^{(i,j)}}, 0\right)$, with $\sigma^2_{X^{(i,j)}} = \boldsymbol{S}^{-\mathrm{T}\,(j,:)}_{UU} \boldsymbol{\sigma}^2_{Z^i} \boldsymbol{S}^{-*\,(:,j)}_{UU}$.
Since $\boldsymbol{X}^{(i,j)}$ is CSCN distributed, it follows that the normalized distribution of its magnitude squared, i.e. $\left|\boldsymbol{X}^{(i,j)}\right|^2 2/\sigma^2_{X^{(i,j)}}$, is χ^2_2 distributed, which is a χ^2 distribution with two degrees of freedom [68]. Since the expected value of a χ^2_2 distributed variable is 2, if finally follows

$$\mathrm{E}\left\{\left|\boldsymbol{X}^{(i,j)}\right|^2 \frac{2}{\sigma^2_{X^{(i,j)}}}\right\} = 2 \Leftrightarrow \mathrm{E}\left\{\left|\boldsymbol{X}^{(i,j)}\right|^2\right\} = \sigma^2_{X^{(i,j)}}. \tag{B.28}$$

With this knowledge, it holds for every element in (B.24)

$$\begin{aligned}
\lim_{\tilde{M}\to\infty} \frac{1}{\tilde{M}^2} \mathrm{E}\left\{\left|\boldsymbol{X}^{(i,j)}\right|^2\right\} &= \lim_{\tilde{M}\to\infty} \frac{1}{\tilde{M}^2} \sigma^2_{X^{(i,j)}} \\
&= \lim_{\tilde{M}\to\infty} \frac{1}{\tilde{M}^2} \boldsymbol{S}^{-\mathrm{T}\,(j,:)}_{UU} \frac{\tilde{M}}{q^2} \boldsymbol{S}_{UU} \boldsymbol{\sigma}^{2\,(i,i)}_V \boldsymbol{S}^{-*\,(:,j)}_{UU} \\
&= \lim_{\tilde{M}\to\infty} \frac{1}{\tilde{M} q^2} \boldsymbol{\sigma}^{2\,(i,i)}_V \boldsymbol{S}^{-\mathrm{T}\,(j,:)}_{UU} \boldsymbol{S}_{UU} \boldsymbol{S}^{-*\,(:,j)}_{UU}.
\end{aligned} \tag{B.29}$$

This limit is zero, because the variance of the noise is assumed to be bounded and the scalar $\boldsymbol{S}^{-\mathrm{T}\,(j,:)}_{UU} \boldsymbol{S}_{UU} \boldsymbol{S}^{-*\,(:,j)}_{UU}$ is also bounded if $\boldsymbol{S}_{UU}$ is invertible. Thus, (B.24) is indeed identical to zero for every element, and the H_1 estimator is consistent.

B.2.6 Efficiency

We assume a general estimator which takes observation vectors $\boldsymbol{z}$ as inputs and produces an estimate $\hat{\boldsymbol{\theta}}$ of the vector of true parameter values $\boldsymbol{\theta}_0$. Such an estimator is termed efficient if its mean-square error (MSE) reaches the Cramér-Rao bound, which provides a lower limit on the achievable MSE if the probability density function of the measurements $f_{\boldsymbol{z}}(\boldsymbol{z}, \boldsymbol{\theta}_0)$ and the true values $\boldsymbol{\theta}_0$ are known. The MSE of an estimator is defined as

$$\mathrm{MSE}\left(\hat{\boldsymbol{\theta}}\right) = \boldsymbol{\sigma}^2_\theta + \boldsymbol{b}_\theta \boldsymbol{b}_\theta^{\mathrm{T}}, \tag{B.30}$$

with $\boldsymbol{\sigma}^2_\theta$ being the covariance matrix and $\boldsymbol{b}_\theta$ being the bias vector. Under some weak technical assumptions [152], the Cramér-Rao bound states

$$\mathrm{MSE}\left(\hat{\boldsymbol{\theta}}\right) \geq \left(\mathbf{I} + \frac{\partial \boldsymbol{b}_\theta}{\partial \boldsymbol{\theta}_0}\right) \boldsymbol{Fi}^+ \left(\mathbf{I} + \frac{\partial \boldsymbol{b}_\theta}{\partial \boldsymbol{\theta}_0}\right)^{\mathrm{H}}, \tag{B.31}$$

where $\boldsymbol{Fi}^+$ denotes the Moore-Penrose inverse of the *Fisher information matrix*. For an unbiased estimator, this statement reduces to $\boldsymbol{\sigma}^2_\theta \geq \boldsymbol{Fi}^+$. Consequently, an unbiased estimator is efficient if this inequality becomes an equality. The Fisher information matrix itself is defined as

$$\boldsymbol{Fi} = -\mathrm{E}\left\{\frac{\partial^2 \ln f_{\boldsymbol{z}}}{\partial \boldsymbol{\theta}_0^2}\right\}. \tag{B.32}$$

The following proof shows that the H_1 estimator is efficient under the stated assumptions. The maps introduced in App. B.1 are used to transform complex matrices into real ones.

The measurement noise vector $\boldsymbol{V}(\mathrm{j}\omega_n)$ is assumed to be CSCN distributed, as stated in (3.5), which may be compactly written as

$$\boldsymbol{V}(\mathrm{j}\omega_n) \in \mathcal{CN}^p\left(\mathbf{0}, \boldsymbol{\sigma}_V^2(\mathrm{j}\omega_n), \mathbf{0}\right). \tag{B.33}$$

Since $\boldsymbol{Y}_m(\mathrm{j}\omega_n) = \boldsymbol{Y}_{0,m}(\mathrm{j}\omega_n) + \boldsymbol{V}_m(\mathrm{j}\omega_n) = \boldsymbol{G}_0(\mathrm{e}^{\mathrm{j}\omega_n})\boldsymbol{U}_m(\mathrm{j}\omega_n) + \boldsymbol{V}_m(\mathrm{j}\omega_n)$, it follows that

$$\boldsymbol{Y}_m(\mathrm{j}\omega_n) \in \mathcal{CN}^p\left(\boldsymbol{Y}_{0,m}, \boldsymbol{\sigma}_V^2(\mathrm{j}\omega_n), \mathbf{0}\right). \tag{B.34}$$

This CSCN distribution may be equivalently expressed as a normal distribution of the real-valued elements of the vector $\boldsymbol{Y}_{m,\mathrm{re}}$ as [7]

$$\boldsymbol{Y}_{m,\mathrm{re}} \in \mathcal{N}^{2p}\left(\boldsymbol{Y}_{0,m,\mathrm{re}}, \frac{1}{2}\boldsymbol{\sigma}_{V,\mathrm{Re}}^2\right). \tag{B.35}$$

At least q experiments are necessary to estimate all elements of the transfer matrix $\boldsymbol{G}_0$, where the measurement data may be stacked as $\tilde{\boldsymbol{Y}} = (\boldsymbol{Y}_1, \ldots, \boldsymbol{Y}_M)$, with $M = \tilde{M}q,\ \tilde{M} \in \mathbb{N}$.
Since the noise is independent over different experiments, the distribution of such a data set can be expressed as

$$\left(\operatorname{vec}\tilde{\boldsymbol{Y}}\right)_{\mathrm{re}} \in \mathcal{N}^{2Mp}\Bigg(\underbrace{\left(\operatorname{vec}\tilde{\boldsymbol{Y}}_{\mathbf{0}}\right)_{\mathrm{re}}}_{=:\tilde{\boldsymbol{\mu}}_{\mathrm{re}}}, \underbrace{\frac{1}{2}\left(\mathbf{I}_M \otimes \boldsymbol{\sigma}_V^2\right)_{\mathrm{Re}}}_{=:\tilde{\boldsymbol{\Gamma}}_{\mathrm{Re}}}\Bigg). \tag{B.36}$$

With reference to the general case, we have $\boldsymbol{z} = \operatorname{vec}\tilde{\boldsymbol{Y}}$ and $\boldsymbol{\theta}_0 = \operatorname{vec}\boldsymbol{G}_0$. The probability density function of this multivariate normal distribution is [68]

$$f_{\boldsymbol{z}} = \frac{1}{(2\pi)^{pq}\sqrt{\det\tilde{\boldsymbol{\Gamma}}_{\mathrm{Re}}}}\mathrm{e}^{-\frac{1}{2}(\boldsymbol{z}_{\mathrm{re}}-\tilde{\boldsymbol{\mu}}_{\mathrm{re}})^{\mathrm{T}}\tilde{\boldsymbol{\Gamma}}_{\mathrm{Re}}^{-1}(\boldsymbol{z}_{\mathrm{re}}-\tilde{\boldsymbol{\mu}}_{\mathrm{re}})}, \tag{B.37}$$

which further gives

$$\ln f_{\boldsymbol{z}} = \ln\frac{1}{(2\pi)^{pq}\sqrt{\det\tilde{\boldsymbol{\Gamma}}_{\mathrm{Re}}}} - \frac{1}{2}\left(\boldsymbol{z}_{\mathrm{re}} - \tilde{\boldsymbol{\mu}}_{\mathrm{re}}\right)^{\mathrm{T}}\tilde{\boldsymbol{\Gamma}}_{\mathrm{Re}}^{-1}\left(\boldsymbol{z}_{\mathrm{re}} - \tilde{\boldsymbol{\mu}}_{\mathrm{re}}\right). \tag{B.38}$$

This function is now used to evaluate (B.32) as

$$\begin{aligned}
\frac{\partial^2 \ln f_{\boldsymbol{z}}}{\partial\boldsymbol{\theta}_{0,\mathrm{re}}^2} &= -\frac{1}{2}\frac{\partial^2}{\partial\boldsymbol{\theta}_{0,\mathrm{re}}^2}\left(\left(\boldsymbol{z}_{\mathrm{re}} - \tilde{\boldsymbol{\mu}}_{\mathrm{re}}\right)^{\mathrm{T}}\tilde{\boldsymbol{\Gamma}}_{\mathrm{Re}}^{-1}\left(\boldsymbol{z}_{\mathrm{re}} - \tilde{\boldsymbol{\mu}}_{\mathrm{re}}\right)\right)\\
&= -\frac{1}{2}\frac{\partial^2}{\partial\boldsymbol{\theta}_{0,\mathrm{re}}^2}\left[\left((\boldsymbol{z} - \tilde{\boldsymbol{\mu}})_{\mathrm{re}}\right)^{\mathrm{T}}\tilde{\boldsymbol{\Gamma}}_{\mathrm{Re}}^{-1}\left(\boldsymbol{z} - \tilde{\boldsymbol{\mu}}\right)_{\mathrm{re}}\right]\\
&= -\frac{1}{2}\frac{\partial^2}{\partial\boldsymbol{\theta}_{0,\mathrm{re}}^2}\left[\left(\left(\operatorname{vec}\tilde{\boldsymbol{Y}} - \operatorname{vec}\left\{\boldsymbol{G}_0\tilde{\boldsymbol{U}}\right\}\right)_{\mathrm{re}}\right)^{\mathrm{T}}\tilde{\boldsymbol{\Gamma}}_{\mathrm{Re}}^{-1}\left(\operatorname{vec}\tilde{\boldsymbol{Y}} - \operatorname{vec}\left\{\boldsymbol{G}_0\tilde{\boldsymbol{U}}\right\}\right)_{\mathrm{re}}\right],
\end{aligned} \tag{B.39}$$

with $\tilde{\boldsymbol{U}} = (\boldsymbol{U}_1, \ldots, \boldsymbol{U}_M)$. Using the identity $\operatorname{vec}\{\boldsymbol{ACB}\} = (\boldsymbol{B}^{\mathrm{T}} \otimes \boldsymbol{A})\operatorname{vec}\boldsymbol{C}$, this can be further modified to

$$\frac{\partial^2 \ln f_{\boldsymbol{z}}}{\partial \boldsymbol{\theta}_{0,\mathrm{re}}^2} = -\frac{1}{2}\frac{\partial^2}{\partial \boldsymbol{\theta}_{0,\mathrm{re}}^2}\left[\left(\left(\operatorname{vec}\tilde{\boldsymbol{Y}} - \left(\tilde{\boldsymbol{U}}^{\mathrm{T}} \otimes \mathbf{I}\right)\operatorname{vec}\boldsymbol{G}_0\right)_{\mathrm{re}}\right)^{\mathrm{T}} \tilde{\boldsymbol{\Gamma}}_{\mathrm{Re}}^{-1}\left(\operatorname{vec}\tilde{\boldsymbol{Y}} - \left(\tilde{\boldsymbol{U}}^{\mathrm{T}} \otimes \mathbf{I}\right)\operatorname{vec}\boldsymbol{G}_0\right)_{\mathrm{re}}\right]. \tag{B.40}$$

Since $\tilde{\boldsymbol{\Gamma}}_{\mathrm{Re}}$ is symmetric due to property (B.3a), there exists a decomposition of the form $\boldsymbol{P}^{\mathrm{T}}\boldsymbol{P} = \tilde{\boldsymbol{\Gamma}}_{\mathrm{Re}}$. This together with property (B.3c) leads to

$$\begin{aligned}\frac{\partial^2 \ln f_{\boldsymbol{z}}}{\partial \boldsymbol{\theta}_{0,\mathrm{re}}^2} &= -\frac{1}{2}\frac{\partial^2}{\partial \boldsymbol{\theta}_{0,\mathrm{re}}^2}\left[\left(\left(\operatorname{vec}\tilde{\boldsymbol{Y}}\right)_{\mathrm{re}} - \left(\tilde{\boldsymbol{U}}^{\mathrm{T}}\otimes\mathbf{I}\right)_{\mathrm{Re}}\boldsymbol{\theta}_{0,\mathrm{re}}\right)^{\mathrm{T}}\boldsymbol{P}^{-1}\boldsymbol{P}^{-\mathrm{T}}\left(\left(\operatorname{vec}\tilde{\boldsymbol{Y}}\right)_{\mathrm{re}} - \left(\tilde{\boldsymbol{U}}^{\mathrm{T}}\otimes\mathbf{I}\right)_{\mathrm{Re}}\boldsymbol{\theta}_{0,\mathrm{re}}\right)\right] \\ &= -\frac{1}{2}\frac{\partial^2}{\partial \boldsymbol{\theta}_{0,\mathrm{re}}^2}\left(\boldsymbol{g}(\boldsymbol{z},\boldsymbol{\theta}_{0,\mathrm{re}})^{\mathrm{T}}\boldsymbol{g}(\boldsymbol{z},\boldsymbol{\theta}_{0,\mathrm{re}})\right),\end{aligned} \tag{B.41}$$

with the $(2Mp)$-dimensional vector $\boldsymbol{g} = \boldsymbol{P}^{-\mathrm{T}}\left(\left(\operatorname{vec}\tilde{\boldsymbol{Y}}\right)_{\mathrm{re}} - \left(\tilde{\boldsymbol{U}}^{\mathrm{T}} \otimes \mathbf{I}\right)_{\mathrm{Re}}\boldsymbol{\theta}_{0,\mathrm{re}}\right)$.

Taking the second order derivative gives (see for example [152], Sec. 13.9.1)

$$\frac{\partial^2 \boldsymbol{g}^{\mathrm{T}}\boldsymbol{g}}{\partial \boldsymbol{\theta}_{0,\mathrm{re}}^2} = 2\left(\frac{\partial \boldsymbol{g}}{\partial \boldsymbol{\theta}_{0,\mathrm{re}}}\right)^{\mathrm{T}}\left(\frac{\partial \boldsymbol{g}}{\partial \boldsymbol{\theta}_{0,\mathrm{re}}}\right) + 2\sum_{k=1}^{2Mp} g_k \frac{\partial^2 g_k}{\partial \boldsymbol{\theta}_{0,\mathrm{re}}^2}. \tag{B.42}$$

Since

$$\frac{\partial \boldsymbol{g}}{\partial \boldsymbol{\theta}_{0,\mathrm{re}}} = -\boldsymbol{P}^{-\mathrm{T}}\left(\tilde{\boldsymbol{U}}^{\mathrm{T}} \otimes \mathbf{I}\right)_{\mathrm{Re}} \tag{B.43}$$

and

$$\frac{\partial^2 \boldsymbol{g}}{\partial \boldsymbol{\theta}_{0,\mathrm{re}}^2} = \mathbf{0}, \tag{B.44}$$

it follows that all terms of the sum in (B.42) are zero. Thus,

$$\begin{aligned}\frac{\partial^2 \ln f_{\boldsymbol{z}}}{\partial \boldsymbol{\theta}_{0,\mathrm{re}}^2} &= -\left(-\boldsymbol{P}^{-\mathrm{T}}\left(\tilde{\boldsymbol{U}}^{\mathrm{T}} \otimes \mathbf{I}\right)_{\mathrm{Re}}\right)^{\mathrm{T}}\left(-\boldsymbol{P}^{-\mathrm{T}}\left(\tilde{\boldsymbol{U}}^{\mathrm{T}} \otimes \mathbf{I}\right)_{\mathrm{Re}}\right) \\ &= -\left(\left(\tilde{\boldsymbol{U}}^{\mathrm{T}} \otimes \mathbf{I}\right)_{\mathrm{Re}}\right)^{\mathrm{T}}\boldsymbol{P}^{-1}\boldsymbol{P}^{-\mathrm{T}}\left(\tilde{\boldsymbol{U}}^{\mathrm{T}} \otimes \mathbf{I}\right)_{\mathrm{Re}} \\ &= -\left(\left(\tilde{\boldsymbol{U}}^{\mathrm{T}} \otimes \mathbf{I}\right)_{\mathrm{Re}}\right)^{\mathrm{T}}\tilde{\boldsymbol{\Gamma}}_{\mathrm{Re}}^{-1}\left(\tilde{\boldsymbol{U}}^{\mathrm{T}} \otimes \mathbf{I}\right)_{\mathrm{Re}},\end{aligned} \tag{B.45}$$

and we finally have

$$\boldsymbol{Fi} = \left(\left(\tilde{\boldsymbol{U}}^{\mathrm{T}} \otimes \mathbf{I}\right)_{\mathrm{Re}}\right)^{\mathrm{T}}\tilde{\boldsymbol{\Gamma}}_{\mathrm{Re}}^{-1}\left(\tilde{\boldsymbol{U}}^{\mathrm{T}} \otimes \mathbf{I}\right)_{\mathrm{Re}}. \tag{B.46}$$

The term $(\tilde{\boldsymbol{U}}^{\mathrm{T}} \otimes \mathbf{I})_{\mathrm{Re}}$ is of dimension $(2Mp) \times (2pq)$ and has full column rank, due to the assumptions on the excitation $\tilde{\boldsymbol{U}}$. For every matrix, it holds that $\operatorname{rank}\{\boldsymbol{A}^{\mathrm{T}}\boldsymbol{A}\} = \operatorname{rank}\boldsymbol{A}$. Thus, the Fisher information matrix, which is of dimension $(2pq) \times (2pq)$, is regular,

$$\begin{aligned}\boldsymbol{Fi}^{+} &= \boldsymbol{Fi}^{-1} \\ &= \left(\left(\tilde{\boldsymbol{U}}^{\mathrm{T}} \otimes \mathbf{I}\right)_{\mathrm{Re}}\right)^{-1}\tilde{\boldsymbol{\Gamma}}_{\mathrm{Re}}\left(\left(\tilde{\boldsymbol{U}}^{\mathrm{T}} \otimes \mathbf{I}\right)_{\mathrm{Re}}\right)^{-\mathrm{T}} \\ &= \frac{1}{2}\left(\left(\tilde{\boldsymbol{U}}^{\mathrm{T}} \otimes \mathbf{I}\right)_{\mathrm{Re}}\right)^{-1}\left(\mathbf{I}_M \otimes \boldsymbol{\sigma}_V^2\right)_{\mathrm{Re}}\left(\left(\tilde{\boldsymbol{U}}^{\mathrm{T}} \otimes \mathbf{I}\right)_{\mathrm{Re}}\right)^{-\mathrm{T}}.\end{aligned} \tag{B.47}$$

With the help of property (B.3b), this can be rewritten as

$$
\begin{aligned}
\boldsymbol{Fi}^{+} &= \frac{1}{2}\left(\tilde{\boldsymbol{U}}^{\mathrm{T}}\otimes\mathbf{I}\right)_{\mathrm{Re}}^{-1}\left(\mathbf{I}_M\otimes\boldsymbol{\sigma}_V^2\right)_{\mathrm{Re}}\left(\left(\tilde{\boldsymbol{U}}^{\mathrm{T}}\otimes\mathbf{I}\right)_{\mathrm{Re}}^{-1}\right)^{\mathrm{T}} \\
&= \frac{1}{2}\left(\tilde{\boldsymbol{U}}^{-\mathrm{T}}\otimes\mathbf{I}\right)_{\mathrm{Re}}\left(\mathbf{I}_M\otimes\boldsymbol{\sigma}_V^2\right)_{\mathrm{Re}}\left(\left(\tilde{\boldsymbol{U}}^{-\mathrm{T}}\otimes\mathbf{I}\right)_{\mathrm{Re}}\right)^{\mathrm{T}} \\
&= \frac{1}{2}\left[\left(\tilde{\boldsymbol{U}}^{-\mathrm{T}}\otimes\mathbf{I}\right)\left(\mathbf{I}_M\otimes\boldsymbol{\sigma}_V^2\right)\right]_{\mathrm{Re}}\left(\left(\tilde{\boldsymbol{U}}^{-\mathrm{T}}\otimes\mathbf{I}\right)_{\mathrm{Re}}\right)^{\mathrm{T}} \qquad \text{(Property (B.3d))} \\
&= \frac{1}{2}\left(\tilde{\boldsymbol{U}}^{-\mathrm{T}}\otimes\boldsymbol{\sigma}_V^2\right)_{\mathrm{Re}}\left(\left(\tilde{\boldsymbol{U}}^{-\mathrm{T}}\otimes\mathbf{I}\right)_{\mathrm{Re}}\right)^{\mathrm{T}} \\
&= \frac{1}{2}\left(\tilde{\boldsymbol{U}}^{-\mathrm{T}}\otimes\boldsymbol{\sigma}_V^2\right)_{\mathrm{Re}}\left(\left(\tilde{\boldsymbol{U}}^{-\mathrm{T}}\right)^{\mathrm{H}}\otimes\mathbf{I}\right)_{\mathrm{Re}} \qquad \text{(Property (B.3a))} \\
&= \frac{1}{2}\left(\tilde{\boldsymbol{U}}^{-\mathrm{T}}\otimes\boldsymbol{\sigma}_V^2\right)_{\mathrm{Re}}\left(\tilde{\boldsymbol{U}}^{-*}\otimes\mathbf{I}\right)_{\mathrm{Re}} \\
&= \frac{1}{2}\left[\left(\tilde{\boldsymbol{U}}^{-\mathrm{T}}\otimes\boldsymbol{\sigma}_V^2\right)\left(\tilde{\boldsymbol{U}}^{-*}\otimes\mathbf{I}\right)\right]_{\mathrm{Re}} \qquad \text{(Property (B.3b))} \\
&= \frac{1}{2}\left[\left(\tilde{\boldsymbol{U}}^{*}\tilde{\boldsymbol{U}}^{\mathrm{T}}\right)^{-1}\otimes\boldsymbol{\sigma}_V^2\right]_{\mathrm{Re}} \\
&= \frac{1}{2}\left[\left(\left(\tilde{\boldsymbol{U}}^{\mathrm{H}}\right)^{\mathrm{T}}\tilde{\boldsymbol{U}}^{\mathrm{T}}\right)^{-1}\otimes\boldsymbol{\sigma}_V^2\right]_{\mathrm{Re}} \\
&= \frac{1}{2}\left[\left(\tilde{\boldsymbol{U}}\tilde{\boldsymbol{U}}^{\mathrm{H}}\right)^{-\mathrm{T}}\otimes\boldsymbol{\sigma}_V^2\right]_{\mathrm{Re}} .
\end{aligned}
\tag{B.48}
$$

Assuming that the excitation scheme is repeated after q experiments, the term $\tilde{\boldsymbol{U}}\tilde{\boldsymbol{U}}^{\mathrm{H}}$ is equal to $\boldsymbol{S}_{UU}$ as defined in (B.7) multiplied by $M = \tilde{M}q$,

$$
\boldsymbol{Fi}^{+} = \frac{1}{2}\frac{1}{\tilde{M}q}\left(\boldsymbol{S}_{UU}^{-\mathrm{T}}\otimes\boldsymbol{\sigma}_V^2\right)_{\mathrm{Re}} . \tag{B.49}
$$

The covariance matrix of the estimator was shown in Sec. B.2.4 to be $\boldsymbol{\sigma}_{\hat{G}}^2 = \frac{1}{\tilde{M}q}\boldsymbol{S}_{UU}^{-\mathrm{T}}\otimes\boldsymbol{\sigma}_V^2$, which means that

$$
\hat{\boldsymbol{\theta}} \in \mathcal{CN}^{pq}\left(\boldsymbol{\theta}_0, \boldsymbol{\sigma}_{\hat{G}}^2, \mathbf{0}\right) , \tag{B.50}
$$

where $\hat{\boldsymbol{\theta}} = \operatorname{vec}\hat{\boldsymbol{G}}$. This CSCN distribution is equivalent to the normal distribution of the real-valued vector $\hat{\boldsymbol{\theta}}_{\mathrm{re}}$ [7],

$$
\hat{\boldsymbol{\theta}}_{\mathrm{re}} \in \mathcal{N}^{2pq}\left(\boldsymbol{\theta}_{0,\mathrm{re}}, \frac{1}{2}\boldsymbol{\sigma}_{\hat{G},\mathrm{Re}}^2\right) . \tag{B.51}
$$

Thus,

$$
\boldsymbol{\sigma}_{\hat{\theta}_{\mathrm{re}}}^2 = \frac{1}{2}\frac{1}{\tilde{M}q}\left(\boldsymbol{S}_{UU}^{-\mathrm{T}}\otimes\boldsymbol{\sigma}_V^2\right)_{\mathrm{Re}} , \tag{B.52}
$$

which equals (B.49). This shows that the covariance matrix of the estimator equals the Cramér-Rao bound and the estimator is therefore efficient.

B.3 Estimating Model Uncertainty from Covariance Information

In Sec 3.3, an additive model uncertainty description is derived from the diagonal elements of the covariance matrix $\boldsymbol{\sigma}^2_{\hat{G}}$ of the estimated FRFs. This uncertainty information can be interpreted as a square box centered at the nominal FRF value for every transfer function $\hat{G}_{ij}(\mathrm{e}^{\mathrm{j}\omega_n})$ at every frequency sample ω_n, see Fig. 3.3.

At a single frequency, a total number of pq elements are estimated, namely the elements of the parameter vector $\hat{\boldsymbol{\theta}}(\mathrm{e}^{\mathrm{j}\omega_n}) := \left(\hat{G}_{11}(\mathrm{e}^{\mathrm{j}\omega_n}), \dots, \hat{G}_{pq}(\mathrm{e}^{\mathrm{j}\omega_n})\right)^{\mathrm{T}}$. The standard deviations of these pq elements can be interpreted to define a hyper-parallelepiped in $\mathbb{C}^{pq}$, where the lengths l_{ij} of the semi-axes are given by

$$l_{ij} = \Delta\hat{G}_{ij,\max} = \frac{1}{\sqrt{2}} n(\alpha)\sigma_{\hat{G}_{ij}}(1+\mathrm{j}), \quad i = 1, \dots, p, \quad j = 1, \dots, q, \tag{B.53}$$

see also (3.11). The model uncertainty region then reads $\mathrm{vec}\{\Delta\hat{\boldsymbol{G}}_{\max}\} = \left(l_{11}, \dots, l_{pq}\right)^{\mathrm{T}}$. The probability that the FRF of the true system $\boldsymbol{G}_0$ is contained within this hyper-parallelepiped is at least α^*, by virtue of Bonferroni's inequality, compare (3.16).

If the off-diagonal elements of $\boldsymbol{\sigma}^2_{\hat{G}}$ are small compared to the diagonal elements, it is reasonable to compute the model uncertainty solely from the matrix' diagonal elements $\sigma^2_{\hat{G}_{ij}}$. Diagonal structure of $\boldsymbol{\sigma}^2_{\hat{G}}$ is ensured if the measurement noise is uncorrelated over the different measurement channels and if the excitation signal is suitably chosen, see Sec. 3.4. There may be cases where it is not possible to fulfill this, for example if the input sequences for the system inputs cannot be freely designed during the identification experiment due to operational limits of the plant. Then, it is advisable to make use of the complete covariance information to compute the semi-axes of the hyper-parallelepiped (B.53).

To see how this can be done, consider again the multivariate CSCN-distributed vector $\boldsymbol{\theta}$ of length pq. It can be transformed into a zero-mean vector $\boldsymbol{z} \in \mathbb{C}^{pq}$ of uncorrelated variables with all variances equal to one by the transformation [68],

$$\boldsymbol{z} = \boldsymbol{\Gamma}^{-\mathrm{H}}(\boldsymbol{\theta} - \mathrm{E}\{\boldsymbol{\theta}\}), \quad \text{with} \quad \boldsymbol{\sigma}^2_{\hat{G}} = \boldsymbol{\Gamma}^{\mathrm{H}}\boldsymbol{\Gamma}. \tag{B.54}$$

The Cholesky decomposition of the covariance matrix is always possible if no element of the vector $\boldsymbol{\theta}$ has variance equal to zero, which will be assumed in the following. We now consider twice the sum of squares of these normalized variables $\boldsymbol{z}$,

$$2\sum_{i=1}^{pq} |z_i|^2 = 2\boldsymbol{z}^{\mathrm{H}}\boldsymbol{z} = 2(\boldsymbol{\theta} - \mathrm{E}\{\boldsymbol{\theta}\})^{\mathrm{H}}(\boldsymbol{\sigma}^2_{\hat{G}})^{-1}(\boldsymbol{\theta} - \mathrm{E}\{\boldsymbol{\theta}\}) \in \chi^2_{2pq}. \tag{B.55}$$

Taking twice the inner product of the normalized variables $\boldsymbol{z}$ gives a new random variable which is χ^2 distributed with $2pq$ degrees of freedom. Its value is a positive real scalar which is – with probability α' – less than the squared *Mahalanobis distance* Δ ([7], [68]),

$$\Pr\left(2\boldsymbol{z}^{\mathrm{H}}\boldsymbol{z} \le \Delta^2(\alpha')\right) = \alpha', \tag{B.56}$$

where $\Delta(\alpha')$ is a strictly increasing function of α'. More precisely, $\Delta(\alpha')$ is given by the square root of the inverse cumulative probability density function of the χ^2 distribution with $2pq$ degrees of freedom. The above equation is equal to saying that

$$(\boldsymbol{\theta} - \mathrm{E}\{\boldsymbol{\theta}\})^{\mathrm{H}} \frac{2(\boldsymbol{\sigma}^2_{\hat{G}})^{-1}}{\Delta^2} (\boldsymbol{\theta} - \mathrm{E}\{\boldsymbol{\theta}\}) \leq 1 \tag{B.57}$$

is true with some prescribed probability α'. The above statement implies that for an unbiased estimator, $\mathrm{E}\{\boldsymbol{\theta}\} = \boldsymbol{\theta}_0 = \mathrm{vec}\{\boldsymbol{G}_0\}$, the true values $\boldsymbol{\theta}_0$ are contained with probability α' within the hyper-ellipsoid defined by making (B.57) an equality. This ellipsoid is characterized by the lengths of its semi-axes and their orientation. The lengths of the semi-axes are given by $l'_{ij} = (\lambda'_k)^{-1/2}$, $k = 1, \ldots, pq$, where λ'_k are the eigenvalues of the matrix $2(\boldsymbol{\sigma}^2_{\hat{G}})^{-1}/\Delta^2$. The directions of the semi-axes are given be the eigenvectors of $2(\boldsymbol{\sigma}^2_{\hat{G}})^{-1}/\Delta^2$, which are equal to the eigenvectors of $\boldsymbol{\sigma}^2_{\hat{G}}$. With the help of the eigenvalue decomposition of the covariance matrix, $\boldsymbol{\sigma}^2_{\hat{G}} = \boldsymbol{V}\boldsymbol{\Lambda}\boldsymbol{V}^{\mathrm{H}}$, the lengths of the semi-axes can also be expressed as

$$l'_{ij} = (\lambda'_k)^{-\frac{1}{2}} = \frac{1}{\sqrt{2}}\Delta\sqrt{\lambda_k}\ (1 + \mathrm{j}), \quad \text{with} \quad \boldsymbol{\Lambda} = \bigoplus_{k=1}^{pq} \lambda_k. \tag{B.58}$$

This type of analysis which employs ellipsoidal confidence regions is also called *principal component analysis* (PCA) in the area of multivariate statistics. However, common uncertainty descriptions for transfer functions, like additive or multiplicative uncertainty, do not represent ellipsoids but parallelepipeds in parameter space. Thus, it is suggesting to overbound the ellipsoidal uncertainty region defined by (B.57) by an parallelepiped with identical semi-axes. This naturally leads to an uncertainty region which is bigger than that of the ellipsoid. Equivalently, it can be said that the probability α'' that the true FRF is contained within this parallelepiped is greater than α'. This new uncertainty region is given by $\mathrm{vec}\{\Delta\hat{\boldsymbol{G}}_{\max}\} = \boldsymbol{V}\left(l'_{11}, \ldots, l'_{pq}\right)^{\mathrm{T}}$ with the unitary eigenvector matrix $\boldsymbol{V}$. Comparison of equations (B.53) and (B.58) shows that number of standard deviations $n(\alpha)$ has been replaced by the Mahalanobis distance and the diagonal elements of $\sigma^2_{\hat{G}}$ by its eigenvalues.

The idea is illustrated in Fig. B.1 for two real-valued variables. In both parts of this figure, the purple box, which is defined through the semi-axes of the $\alpha' = 95\,\%$ confidence ellipsoid contains approximately $\alpha'' = 97\,\%$ of all samples. The corresponding Mahalanobis distance is $\Delta = 5.99$. The green box represents the uncertainty region which is defined by the diagonal elements of the covariance matrix. When the axes lengths of the green box are set to $n = \sqrt{\Delta}$ times the standard deviations of x_1 and x_2, respectively, it coincides with the purple box in case of uncorrelated variables. This means that in the left part of the figure, $\alpha^* = \alpha''$ with identical uncertainty region. In case of strongly correlated variables, however, it can be seen that the parallelepiped which is defined by the complete covariance information gives a more appropriate uncertainty region.

In case of uncorrelated variables, we have $\boldsymbol{\sigma}^2_{\hat{G}} = \bigoplus_{k=1}^{pq} \sigma^2_{\hat{G}_k}$, and thus $\boldsymbol{V} = \mathbf{I}$ and $\boldsymbol{\Lambda} = \boldsymbol{\sigma}^2_{\hat{G}}$. This implies that $l'_{ij} = 1/\sqrt{2}\ \Delta(\alpha')\ \sigma_{\hat{G}_{ij}}\ (1 + \mathrm{j})$. Comparison with (B.53) shows that the uncertainty regions which are derived by the two described methods are identical iff $\Delta(\alpha') = n(\alpha)$.
As already mentioned, the function $\Delta^2(\alpha')$ is given by the inverse of the cumulative distribution

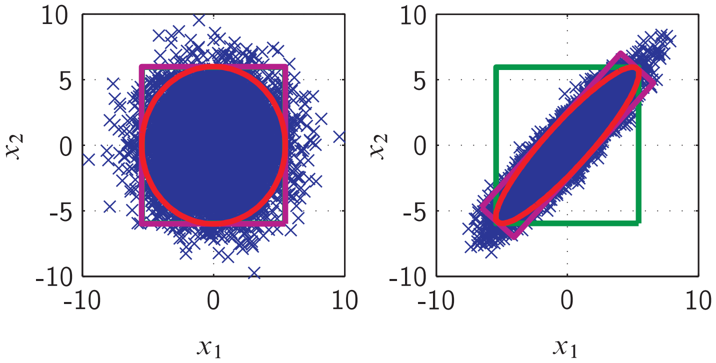

Figure B.1: 10^4 samples of two real-valued normally distributed variables x_1 and x_2. Red: Confidence ellipsoid containing 95 % of all samples. Purple: Parallelepiped with semi-axes identical to that of the ellipsoid. Green: Parallelepiped with axes lengths equal to 2.45 times the standard deviation of x_1 and x_2, respectively. The purple and green boxes coincide in the left picture. Left: $\boldsymbol{\sigma}^2 = [5\ 0;\ 0\ 6]$; Right: $\boldsymbol{\sigma}^2 = [5\ 5;\ 5\ 6]$.

function $F_{\chi^2_{2pq}}(\Delta^2)$ of the χ^2 distribution with $2pq$ degrees of freedom, see for example [68],

$$\alpha' = F_{\chi^2_{2pq}}\left(\Delta^2\right) = \frac{\gamma\left(pq, \frac{1}{2}\Delta^2\right)}{\Gamma(pq)}, \tag{B.59}$$

where $\gamma(pq, \frac{1}{2}\Delta^2)$ is the lower incomplete Gamma function, which can be computed by

$$\gamma\left(pq, \frac{1}{2}\Delta^2\right) = \int_0^{\frac{1}{2}\Delta^2} t^{pq-1}\mathrm{e}^{-t}\mathrm{d}t. \tag{B.60}$$

$\Gamma(pq)$ represents the (complete) Gamma function, which can be easily evaluated if its parameter is a positive integer, $\Gamma(pq) = (pq-1)!$.
The function $n(\alpha)$ equals the inverse function of $\alpha = \operatorname{erf}\left(\frac{n}{\sqrt{2}}\right)$ with the Gaussian error function

$$\operatorname{erf}\left(\frac{n}{\sqrt{2}}\right) = \frac{2}{\sqrt{\pi}}\int_0^{\frac{n}{\sqrt{2}}} \mathrm{e}^{-t^2}\mathrm{d}t. \tag{B.61}$$

These expressions allow for a numerical solution for the value of α' such that $\Delta(\alpha') = n(\alpha)$ if α is given, or vice versa.

B.4 Uncertainty Overbounding

Here, some remarks are given concerning the problem of finding an uncertainty description $\Delta\boldsymbol{G}$ for the parametric model $\boldsymbol{G}$, by overbounding the uncertainty of the non-parametric model $\hat{\boldsymbol{G}}$. There exist a number of well-established formulations for the model uncertainty, for example in additive, multiplicative, and coprime form. Additive and multiplicative descriptions can both be formulated in feedforward or feedback form. In addition to that, multiplicative uncertainty can be

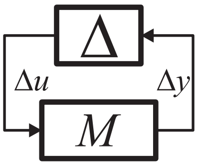

Figure B.2: $M\,\Delta$-structure.

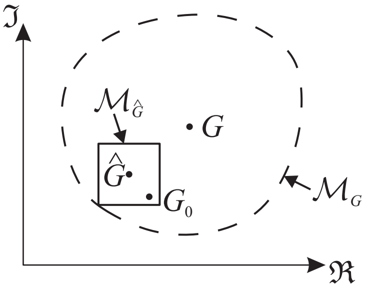

Figure B.3: Illustration of uncertainty overbounding.

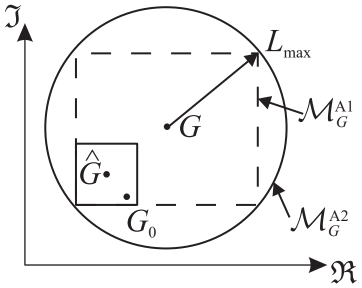

Figure B.4: Additive and circular uncertainty overbounding.

put at the model input or at the model output. For a survey of these formulations, see for example [168]. For simplicity and illustrative purposes, only SISO systems shall be considered here.

Robust stability of some uncertain system can be checked with the *Small Gain theorem*. To this end, the uncertain feedback loop is transformed into the so-called $M\Delta$-structure, see Fig. B.2. The block Δ in this feedback loop is uncertain but bounded by $\|\Delta(\mathrm{e}^{\mathrm{j}\omega})\|_\infty \leq 1$ on the unit circle. The loop is robustly stable iff $\|M(\mathrm{e}^{\mathrm{j}\omega})\|_\infty = \|W(\mathrm{e}^{\mathrm{j}\omega})\; M_0(\mathrm{e}^{\mathrm{j}\omega})\|_\infty \leq 1 \;\forall\; \omega \in [-\pi, \pi]$, see [64]. For SISO systems, this is equivalent to $\max|W(\mathrm{e}^{\mathrm{j}\omega})|\;|M_0(\mathrm{e}^{\mathrm{j}\omega})| \leq 1$ on the unit circle. The transfer function W is a weighting function which is used to normalize the model uncertainty, i.e. $\Delta G(\mathrm{e}^{\mathrm{j}\omega}) = W(\mathrm{e}^{\mathrm{j}\omega})\Delta(\mathrm{e}^{\mathrm{j}\omega})$. The transfer function M_0 depends on the layout of the control loop and on the uncertainty structure. Due to the uncertainty normalization, the weighting must satisfy $|W(\mathrm{e}^{\mathrm{j}\omega})| = \max|\Delta G(\mathrm{e}^{\mathrm{j}\omega})|$ on the unit circle.

For every frequency, the true plant G_0 is considered to lie in a bounded region $\mathcal{M}_G$ of the complex plane, see Fig. B.3. The region $\mathcal{M}_G$ is defined by the nominal model G and its perturbation ΔG. In case of additive uncertainty for example, the uncertainty region is given by $\mathcal{M}_G = G + \Delta G$, where ΔG is bounded.

Now, the problem of uncertainty overbounding is considered. The uncertainty region of the non-parametric model is represented by the square region $\mathcal{M}_{\hat{G}}$ in Fig. B.3. Obviously, $\mathcal{M}_G$ must satisfy $\mathcal{M}_{\hat{G}} \subseteq \mathcal{M}_G$. The uncertainty region $\mathcal{M}_G$ is defined by two constituents: The uncertainty structure, e.g. additive or multiplicative, and the corresponding bounded model uncertainty ΔG. In order to reduce conservatism in $\mathcal{M}_G$, it is generally desirable to have a “tight” overbound.

It might seem to speak against intuition that “tight” in this context does not necessarily mean to have a $\mathcal{M}_G$ with minimal area. In fact, according to the Small Gain theorem, a small value of the weighting function is desired. Since $|W| = \max|\Delta G|$ on the unit circle, $\max|\Delta G|$ should be minimized subject to the constraint $\mathcal{M}_{\hat{G}} \subseteq \mathcal{M}_G$. In case of an additive uncertainty structure, $\mathcal{M}_G = G + \Delta G$, the scalar $\max|\Delta G|$ can be directly interpreted as the greatest distance $L_{\max}$ between the nominal model G and the boundary of $\mathcal{M}_G$. This is illustrated in Fig. B.4. The uncertainty area $\mathcal{M}_G^{A1}$ is given by bounding ΔG as in (3.25),

$$\Delta G_{ij,\max} := \left(\left|\Re\left\{G_{ij} - \hat{G}_{ij}\right\}\right| + \Re\left\{\Delta\hat{G}_{ij,\max}\right\}\right) + \mathrm{j}\left(\left|\Im\left\{G_{ij} - \hat{G}_{ij}\right\}\right| + \Im\left\{\Delta\hat{G}_{ij,\max}\right\}\right). \tag{B.62}$$

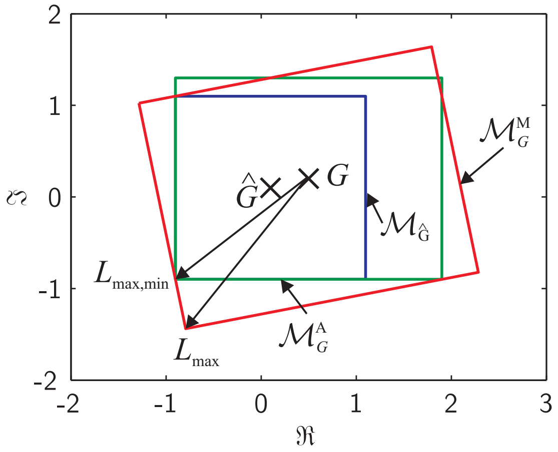

Figure B.5: Non-parametric model $\hat{G}$ with its associated uncertainty $\mathcal{M}_{\hat{G}}$. This area is overbounded by $\mathcal{M}_G^{\mathrm{A}}$ (parametric model with additive uncertainty) and $\mathcal{M}_G^{\mathrm{M}}$ (parametric model with multiplicative uncertainty).

The uncertainty region $\mathcal{M}_G^{A2}$ is given by requiring $|\Delta G| \leq \max_{\tilde{G}\in\mathcal{M}_{\hat{G}}} |\tilde{G} - G|$. Both uncertainty descriptions yield the same stability margin according to the Small Gain theorem, although $\mathcal{M}_G^{A1} \subset \mathcal{M}_G^{A2}$. Thus, the optimal bounding function of the model uncertainty ΔG is not unique for a given uncertainty structure. For the additive uncertainty description, (3.25) is one of the optimal solutions.

Furthermore, the choice of the uncertainty structure is critical, which shall now be exemplified. To this end, additive and multiplicative uncertainty structures in feedforward form shall be compared. In case of multiplicative uncertainty, the uncertainty region in the complex plane is given by $\mathcal{M}_G^{\mathrm{M}} = G(1 + \Delta G^{\mathrm{M}})$. It is assumed that the real and imaginary parts of ΔG^{M} are symmetrically bounded as before, i.e. $\Re\,\Delta G^{\mathrm{M}} \in [-\Re\,\Delta G^{\mathrm{M}}_{\mathrm{max}}, \Re\,\Delta G^{\mathrm{M}}_{\mathrm{max}}]$ and $\Im\,\Delta G^{\mathrm{M}} \in [-\Im\,\Delta G^{\mathrm{M}}_{\mathrm{max}}, \Im\,\Delta G^{\mathrm{M}}_{\mathrm{max}}]$. Then, $\mathcal{M}_G^{\mathrm{M}}$ also defines a rectangular area in the complex plane. However, its axes are in general no longer aligned with the coordinate axes, but rotated by an angle equal to $\angle G$, see Fig. B.5. It is now required to determine $\Re\Delta G^{\mathrm{M}}_{\mathrm{max}}$ and $\Im\Delta G^{\mathrm{M}}_{\mathrm{max}}$ such that the resulting uncertainty region is of minimal area but satisfies $\mathcal{M}_{\hat{G}} \subseteq \mathcal{M}_G^{\mathrm{M}}$. It can be shown that the optimal values can be evaluated as

$$\begin{aligned}\Re\,\Delta G^{\mathrm{M}}_{\mathrm{max}} &= \frac{1}{|G|^2} \max_{\tilde{G}\in\mathcal{M}_{\hat{G}}} \left|\Re G\,\Re\left\{\tilde{G} - G\right\} + \Im G\,\Im\{\tilde{G} - G\}\right|, \\ \Im\,\Delta G^{\mathrm{M}}_{\mathrm{max}} &= \frac{1}{|G|^2} \max_{\tilde{G}\in\mathcal{M}_{\hat{G}}} \left|\Re G\,\Im\left\{\tilde{G} - G\right\} - \Im G\,\Re\{\tilde{G} - G\}\right|.\end{aligned} \tag{B.63}$$

Due to the convexity of the above problem, it is sufficient to evaluate only the four corners of $\mathcal{M}_{\hat{G}}$. The lengths of the principal semi-axes of the area defined by $\mathcal{M}_G^{\mathrm{M}}$ are given by $2|G|\Re\,\Delta G^{\mathrm{M}}_{\mathrm{max}}$ and $2|G|\Im\,\Delta G^{\mathrm{M}}_{\mathrm{max}}$. Consequently, the uncertainty area is $4|G|^2\Re\,\Delta G^{\mathrm{M}}_{\mathrm{max}}\,\Im\,\Delta G^{\mathrm{M}}_{\mathrm{max}}$. The maximum distance of the uncertain parametric model from its nominal value shall be termed L_{max} and is evaluated as

$$\begin{aligned}L_{\mathrm{max}} &= \sqrt{\left(|G|\,\Re\,\Delta G^{\mathrm{M}}_{\mathrm{max}}\right)^2 + \left(|G|\,\Im\,\Delta G^{\mathrm{M}}_{\mathrm{max}}\right)^2} \\ &= |G||\Delta G^{\mathrm{M}}_{\mathrm{max}}|.\end{aligned} \tag{B.64}$$

This distance cannot be smaller than the distance between G and the furthest corner of $\mathcal{M}_{\hat{G}}$, $L_{\text{max,min}} \leq L_{\text{max}}$. Otherwise, $\mathcal{M}_{\hat{G}}$ would not be included in $\mathcal{M}_G$. The value of $L_{\text{max,min}}$ is equal to

$$\begin{aligned} L_{\text{max,min}} &= \sqrt{\left(|\Re\{G-\hat{G}\}| + \Re\,\Delta\hat{G}_{\text{max}}\right)^2 + \left(|\Im\{G-\hat{G}\}| + \Im\,\Delta\hat{G}_{\text{max}}\right)^2} \\ &= |\Delta G^{\text{A}}_{\text{max}}|, \end{aligned} \tag{B.65}$$

where $\Delta G^{\text{A}}_{\text{max}}$ defines the limits of the additive model uncertainty ΔG^{A} according to (B.62). The weights for both uncertainty structures are given by

$$\begin{aligned} W^{\text{M}} &= \max|\Delta G^{\text{M}}| = |\Delta G^{\text{M}}_{\text{max}}|, \\ W^{\text{A}} &= \max|\Delta G^{\text{A}}| = |\Delta G^{\text{A}}_{\text{max}}|. \end{aligned} \tag{B.66}$$

The stability margin according to the Small Gain theorem is determined by the two factors $|W|$ and $|M_0|$. A standard control loop with controller $K(z)$ and negative feedback is assumed. For the additive uncertainty structure, we then have (see [168]) $M^{\text{A}}_0(z){=}K(z)\,(1+G(z)K(z))^{-1}$. The multiplicative uncertainty structure gives $M^{\text{M}}_0(z) = K(z)\,(1+G(z)K(z))^{-1}\,G(z)$. The ratio of the stability margins achieved by the multiplicative and additive uncertainty structures is thus given by

$$\frac{|M^{\text{M}}|}{|M^{\text{A}}|} = \frac{|W^{\text{M}}M^{\text{M}}_0|}{|W^{\text{A}}M^{\text{A}}_0|} = \frac{|W^{\text{M}}G|}{|W^{\text{A}}|} = \frac{W^{\text{M}}|G|}{W^{\text{A}}} = \frac{|\Delta G^{\text{M}}_{\text{max}}|\,|G|}{|\Delta G^{\text{A}}_{\text{max}}|} = \frac{L_{\text{max}}}{L_{\text{max,min}}} \geq 1, \tag{B.67}$$

where the last expression holds for all $\omega \in [-\pi, \pi]$. This is a formal proof of the following plausible argument: An optimal uncertainty overbounding $\mathcal{M}_G(\mathrm{e}^{\mathrm{j}\omega}) \supseteq \mathcal{M}_{\hat{G}}(\mathrm{e}^{\mathrm{j}\omega})$ is characterized by the fact that $L_{\text{max}}(\mathrm{e}^{\mathrm{j}\omega}) = L_{\text{max,min}}(\mathrm{e}^{\mathrm{j}\omega})\ \forall\,\omega \in [-\pi, \pi]$. Similar proofs can most probably also be given for the additive and multiplicative uncertainty structures in feedback form and for coprime factor uncertainty. Then, it could be concluded that the overbounding strategy (3.25) is indeed an optimal solution for SISO systems if standard uncertainty structures are used. Further comments on more advanced model uncertainty structures, like ν-Gap, can for example be found in the works by Douma ([59], [60], [61]).

B.5 Calculation of the Variances of FRF Magnitude and Phase

Assume the covariance matrix $\boldsymbol{\sigma}^2_{x}$ of some real-valued random vector $\boldsymbol{x}$ with mean $\boldsymbol{\mu}$ is given. Then, with the help of Taylor series expansion, the covariance matrix of some function $f(\boldsymbol{x})$ can be approximately calculated by [152]

$$\boldsymbol{\sigma}^2_{f(\boldsymbol{x})} \approx \left.\frac{\partial f(\boldsymbol{x})}{\partial \boldsymbol{x}}\right|_{\boldsymbol{x}=\boldsymbol{\mu}} \boldsymbol{\sigma}^2_{x} \left(\left.\frac{\partial f(\boldsymbol{x})}{\partial \boldsymbol{x}}\right|_{\boldsymbol{x}=\boldsymbol{\mu}}\right)^{\text{T}}. \tag{B.68}$$

Here, the modulus of some estimated transfer function $\hat{G}_{ij} = \Re\,\hat{G}_{ij} + \mathrm{j}\,\Im\,\hat{G}_{ij}$ is considered. As shown in Sec. 3.3, the real and imaginary parts are uncorrelated and have equal variance, $\sigma^2_{\Re,ij} = \sigma^2_{\Im,ij} =: \sigma^2_{ij}$. Thus, we have $\boldsymbol{x} = (x_1, x_2)^{\text{T}}$, where x_1 is the random variable representing the real part of $\hat{G}_{ij}$ and x_2 the imaginary part of $\hat{G}_{ij}$. The expected values of these variables are the values of the true FRF, $\boldsymbol{\mu} = (\Re\, G_0, \Im\, G_0)^{\mathrm{T}}$. Since these are unknown, they are substituted by their estimates, $\boldsymbol{\mu} \approx (\Re\, \hat{G}_{ij}, \Im\, \hat{G}_{ij})^{\mathrm{T}}$. The function of the variables is $f(\boldsymbol{x}) = \sqrt{x_1^2 + x_2^2}$. Applying (B.68) gives $\sigma^2_{|\hat{G}_{ij}|} \approx \sigma^2_{ij}$.

For the variance of the phase $\angle\hat{G}_{ij}$, the function is $\arctan\left(\frac{\Im\, \hat{G}_{ij}}{\Re\, \hat{G}_{ij}}\right)$, and (B.68) gives $\sigma^2_{\angle\hat{G}_{ij}} \approx \frac{\sigma^2_{ij}}{|\hat{G}_{ij}|^2}$. However, it must be noted that the quantities $|\hat{G}_{ij}|$ and $\angle\hat{G}_{ij}$ are no longer normally distributed.

B.6 Noise Characteristics

Here, some important characteristics of white noise and filtered white noise, which are employed in Sec. 3.6, are summarized.

White Noise

It is assumed that the zero-mean noise sequence $v(k)$ is white, i.e. perfectly uncorrelated, and stationary. The value of its DFT sequence $V(\mathrm{j}\omega_n)$ is given by

$$V(\mathrm{j}\omega_n) = T_{\mathrm{s}} \sum_{k=0}^{N-1} v(k) \mathrm{e}^{-\mathrm{j}\omega_n k T_{\mathrm{s}}} = \sum_{k=0}^{N-1} v(k) W_N^{k,n}, \quad \text{with} \quad W_N^{k,n} = T_{\mathrm{s}} \mathrm{e}^{-\mathrm{j}\omega_n k T_{\mathrm{s}}}. \tag{B.69}$$

For reference, it is defined $\bar{W}_N^{k,n} := \left(W_N^{k,n}\right)^*$. Then, it holds that

$$\begin{aligned}
\mathrm{E}\left\{V^*(\mathrm{j}\omega_m) V(\mathrm{j}\omega_n)\right\} &= \mathrm{E}\left\{\sum_{k=0}^{N-1} v(k) \bar{W}_N^{k,m} \sum_{l=0}^{N-1} v(l) W_N^{l,n}\right\} \\
&= \mathrm{E}\left\{v(0) \bar{W}_N^{0,m} \sum_{l=0}^{N-1} v(l) W_N^{l,n} + \ldots + v(N-1) \bar{W}_N^{N-1,m} \sum_{l=0}^{N-1} v(l) W_N^{l,n}\right\} \\
&= \mathrm{E}\left\{v^2(0)\right\} \bar{W}_N^{0,m} W_N^{0,n} + \mathrm{E}\left\{v(0)v(1)\right\} \bar{W}_N^{0,m} W_N^{1,n} + \ldots \\
&\quad + \mathrm{E}\left\{v^2(N-1)\right\} \bar{W}_N^{N-1,m} W_N^{N-1,n} \\
&= \mathrm{E}\left\{v^2(0)\right\} \bar{W}_N^{0,m} W_N^{0,n} + \mathrm{E}\left\{v^2(1)\right\} \bar{W}_N^{1,m} W_N^{1,n} + \ldots \\
&\quad + \mathrm{E}\left\{v^2(N-1)\right\} \bar{W}_N^{N-1,m} W_N^{N-1,n},
\end{aligned} \tag{B.70}$$

because $\mathrm{E}\{v(k)v(l)\} = 0$ for $k \neq l$. Since the noise is i.i.d., it also holds $\mathrm{E}\{v^2(0)\} = \mathrm{E}\{v^2(1)\} = \ldots = \mathrm{E}\{v^2(N-1)\}$, which implies

$$\mathrm{E}\left\{V^*(\mathrm{j}\omega_m) V(\mathrm{j}\omega_n)\right\} = \mathrm{E}\left\{v^2(0)\right\} \underbrace{\sum_{k=0}^{N-1} \bar{W}_N^{k,m} W_N^{k,n}}_{=:W_{m,n,N}}. \tag{B.71}$$

It can be shown that $W_{m,n,N} = 0$ for $m \neq n$ and arbitrary N. Thus, $\mathrm{E}\{V^*(\mathrm{j}\omega_m)V(\mathrm{j}\omega_n)\} = 0$ for two different DFT samples ω_m and ω_n.

On the other hand, it holds

$$\begin{aligned}\mathrm{E}\left\{V^*(\mathrm{j}\omega_m)\right\}\ \mathrm{E}\left\{V(\mathrm{j}\omega_n)\right\} &= \mathrm{E}\left\{\sum_{k=0}^{N-1} v(k)\bar{W}_N^{k,m}\right\}\ \mathrm{E}\left\{\sum_{l=0}^{N-1} v(l)W_N^{l,n}\right\} \\ &= \sum_{k=0}^{N-1} \mathrm{E}\left\{v(k)\right\} \bar{W}_N^{k,m} \sum_{l=0}^{N-1} \mathrm{E}\left\{v(l)\right\} W_N^{l,n} \\ &= 0,\end{aligned} \tag{B.72}$$

since $\mathrm{E}\{v(k)\} = 0\ \forall\, k$.

Thus, it is clear that $\mathrm{E}\{V^*(\mathrm{j}\omega_m)V(\mathrm{j}\omega_n)\}$ is identical to $\mathrm{E}\{V^*(\mathrm{j}\omega_m)\}\ \mathrm{E}\{V(\mathrm{j}\omega_n)\}$ for any two different frequency samples ω_m and ω_n, and the DFT sequence of the noise is therefore uncorrelated.

Filtered White Noise

Colored noise can be thought of as passing white noise through an LTI transfer function. More specifically, the inverse $\mathcal{Z}$-transform of $w(z) = H(z)v(z)$ is a colored noise time sequence. The autopower spectrum of filtered white noise has the form [115]

$$S_{ww}(\mathrm{j}\omega_n) = \sigma_v^2\, |H(\mathrm{e}^{\mathrm{j}\omega_n})|^2. \tag{B.73}$$

As an example, consider red noise which can be produced by letting $H(z)$ be a discrete-time integrator. This implies that the intensity of red noise decreases as $^1/_{f^2}$.
The autocorrelation function of filtered white noise is [115]

$$R_{ww}(\tau) = \sigma_v^2\ h(\tau) * h(-\tau), \tag{B.74}$$

where $h(\tau)$ denotes the impulse response of $H(z)$. In the case of red-noise, the impulse response equals a step function with unit time delay.
For some correlated time sequence, its discrete Fourier transform is generally also correlated. The autocorrelation function of a N-point DFT sequence can be calculated as follows,

$$\begin{aligned}R_{WW}(n, n+\tau) &= \mathrm{E}\left\{W^*(\mathrm{j}\omega_n)W(\mathrm{j}\omega_{n+\tau})\right\} \\ &= \mathrm{E}\left\{w^2(0)\right\} \bar{W}_N^{0,n} W_N^{0,n+\tau} + \mathrm{E}\left\{w(0)w(1)\right\} \bar{W}_N^{0,n} W_N^{1,n+\tau} + \ldots \\ &\quad + \mathrm{E}\left\{w^2(N-1)\right\} \bar{W}_N^{N-1,n} W_N^{N-1,n+\tau} \qquad \text{(compare (B.70))} \\ &= \sum_{k=0}^{N-1}\sum_{l=0}^{N-1} \mathrm{E}\left\{w(k)w(l)\right\} \bar{W}_N^{k,n} W_N^{l,n+\tau} \\ &= \sum_{k=0}^{N-1}\sum_{l=0}^{N-1} R_{ww}(l-k)\ \bar{W}_N^{k,n} W_N^{l,n+\tau}.\end{aligned} \tag{B.75}$$

In the above analysis, it was assumed that the noise process $w(k)$ is stationary, such that the value of the time-domain correlation sequence $R_{ww}(k, l) = \mathrm{E}\{w(k)w(l)\}$ depends only on the time shift $\tau = l - k$. Furthermore, if $w(k)$ is stationary, then also its DFT sequence $W(\mathrm{j}\omega_n)$ is stationary, and one can set $n = 0$ without loss of generality. This allows to simplify the last result since $\omega_0 = 0$, and thus finally

$$R_{WW}(\tau) = T_\mathrm{s} \sum_{k=0}^{N-1} \sum_{l=0}^{N-1} R_{ww}(l - k)\; W_N^{l,\tau}. \tag{B.76}$$

C Appendix to Active Vibration Control

C.1 Amplitude Ratio of Two State Variables Associated with a Pole Pair at Resonance

Here, we give a constructive proof for the relationship (4.14) giving the amplitude ratio of two harmonically oscillating state variables associated with a pole pair at resonance. To begin with, it is assumed that the system is given in real-valued block-diagonal form, as in (4.13). Then, each of the subsystems can be described by two coupled difference equations,

$$\begin{pmatrix} \tilde{x}_{i1}(k+1) \\ \tilde{x}_{i2}(k+1) \end{pmatrix} = \begin{pmatrix} \sigma_i & \kappa_i \\ -\kappa_i & \sigma_i \end{pmatrix} \begin{pmatrix} \tilde{x}_{i1}(k) \\ \tilde{x}_{i2}(k) \end{pmatrix} + \begin{pmatrix} \tilde{\boldsymbol{b}}_{i1}^{\mathrm{T}} \\ \tilde{\boldsymbol{b}}_{i2}^{\mathrm{T}} \end{pmatrix} \boldsymbol{u}(k), \tag{C.1}$$

with $\tilde{\boldsymbol{b}}_{im,m=1,2}^{\mathrm{T}} \in \mathbb{R}^{(1\times q)}$, and where the states are also taken as the subsystem's outputs. Its transfer function is then calculated via z-Transform and setting initial conditions to zero,

$$\boldsymbol{G}(z) = \frac{1}{\kappa_i^2 + \sigma_i^2 - 2\sigma_i z + z^2} \begin{pmatrix} z-\sigma_i & \kappa_i \\ -\kappa_i & z-\sigma_i \end{pmatrix} \begin{pmatrix} \tilde{\boldsymbol{b}}_{i1}^{\mathrm{T}} \\ \tilde{\boldsymbol{b}}_{i2}^{\mathrm{T}} \end{pmatrix}. \tag{C.2}$$

The ratio of the z-transformed state-variables for any input is then

$$\frac{\tilde{x}_{i2}(z)}{\tilde{x}_{i1}(z)} = \frac{\left[-\kappa_i \tilde{\boldsymbol{b}}_{i1}^{\mathrm{T}} + (z-\sigma_i)\tilde{\boldsymbol{b}}_{i2}^{\mathrm{T}}\right]\boldsymbol{u}(z)}{\left[(z-\sigma_i)\tilde{\boldsymbol{b}}_{i1}^{\mathrm{T}} + \kappa_i \tilde{\boldsymbol{b}}_{i2}^{\mathrm{T}}\right]\boldsymbol{u}(z)}. \tag{C.3}$$

If the input is of the form $(1, \dots, 1)^{\mathrm{T}} u(z)$, one has

$$\frac{\tilde{x}_{i2}(z)}{\tilde{x}_{i1}(z)} = \frac{\kappa_i \sum_{l=1}^{q} \tilde{\boldsymbol{b}}_{i1,l}^{\mathrm{T}} + \sigma_i \sum_{l=1}^{q} \tilde{\boldsymbol{b}}_{i2,l}^{\mathrm{T}} - z \sum_{l=1}^{q} \tilde{\boldsymbol{b}}_{i2,l}^{\mathrm{T}}}{\sigma_i \sum_{l=1}^{q} \tilde{\boldsymbol{b}}_{i1,l}^{\mathrm{T}} - \kappa_i \sum_{l=1}^{q} \tilde{\boldsymbol{b}}_{i2,l}^{\mathrm{T}} - z \sum_{l=1}^{q} \tilde{\boldsymbol{b}}_{i2,l}^{\mathrm{T}}}. \tag{C.4}$$

The term on the right hand side can be interpreted as a transfer function from $\tilde{x}_{i1}(z)$ to $\tilde{x}_{i2}(z)$. The result (4.14) follows then by taking into account that the input and therefore also $\tilde{x}_{i1}$ are harmonic, i.e. letting $z = \mathrm{e}^{\mathrm{j}\omega T_{\mathrm{s}}}$ in the artificial transfer function.

C.2 Calculation of an Optimal Controller for Regular $\mathcal{H}_2$ Problems

The following results are taken from the monograph by Saberi et. al. [162]. To begin with, it is assumed that the generalized plant $\tilde{\boldsymbol{P}}(z)$ can be represented as

$$\tilde{\boldsymbol{P}}(z) = \begin{pmatrix} \tilde{\boldsymbol{P}}_{zw}(z) & \tilde{\boldsymbol{P}}_{zu}(z) \\ \tilde{\boldsymbol{P}}_{yw}(z) & \tilde{\boldsymbol{P}}_{yu}(z) \end{pmatrix} = \left[\begin{array}{c|cc} \boldsymbol{A} & \boldsymbol{B}_1 & \boldsymbol{B}_2 \\ \hline \boldsymbol{C}_1 & \boldsymbol{0} & \boldsymbol{D}_1 \\ \boldsymbol{C}_2 & \boldsymbol{D}_2 & \boldsymbol{0} \end{array}\right]. \tag{C.5}$$

It is evident from the above equation that no feedthrough terms must be allowed from the exogenous inputs $\boldsymbol{w}$ to the performance variables $\boldsymbol{z}$, and from the control input $\boldsymbol{u}$ to the measurements $\boldsymbol{y}$. The first restriction is fulfilled by the generalized plant $\boldsymbol{P}(z)$ presented in Fig. 4.2, but not the second. However, the plant $\boldsymbol{P}$ can be modified to satisfy the restrictions given for $\tilde{\boldsymbol{P}}$. In order to do that, a new set of measurements is defined by $\tilde{\boldsymbol{y}} = \boldsymbol{y} - \boldsymbol{D}_3\boldsymbol{u} = \boldsymbol{C}_2\boldsymbol{x} + \boldsymbol{D}_2\boldsymbol{w}$, where $\boldsymbol{D}_3$ denotes the feedthrough matrix from $\boldsymbol{u}$ to $\boldsymbol{y}$. Then, an optimal controller $\tilde{\boldsymbol{K}}(z)$ can be found for the modified plant with new output $\tilde{\boldsymbol{y}}(k)$. One can verify that the controller $\boldsymbol{K} = \tilde{\boldsymbol{K}}(\mathbf{I} + \boldsymbol{D}_3\tilde{\boldsymbol{K}})^{-1}$ is an $\mathcal{H}_2$ optimal controller for the original plant $\boldsymbol{P}$ with feedthrough term. The regularity of $(\mathbf{I} + \boldsymbol{D}_3\tilde{\boldsymbol{K}})^{-1}$ is ensured if the resulting feedback loop is well-posed. This is equivalent to the invertibility of $\mathbf{I} - \boldsymbol{D}_3\boldsymbol{D}_\mathrm{c}$, with $\boldsymbol{D}_\mathrm{c}$ being the feedthrough matrix of the controller. Since we limit our focus on strictly proper controllers, well-posedness of the control loop is always ensured. It is further assumed for $\tilde{\boldsymbol{P}}$ that the matrices $(\boldsymbol{C}_1\boldsymbol{D}_1)$, $(\boldsymbol{C}_2\boldsymbol{D}_2)$, $(\boldsymbol{B}_1^\mathrm{T}\boldsymbol{D}_2^\mathrm{T})^\mathrm{T}$, and $(\boldsymbol{B}_2^\mathrm{T}\boldsymbol{D}_1^\mathrm{T})^\mathrm{T}$ are of maximum rank. This implies that $\tilde{\boldsymbol{P}}$ does not contain any redundant inputs or outputs.

If the above requirements are met, the $\mathcal{H}_2$ optimal strictly proper controller is given by

$$\tilde{\boldsymbol{K}}(z) = \left[\begin{array}{c|c} \boldsymbol{A} - \boldsymbol{B}_2\boldsymbol{F} - \boldsymbol{L}\boldsymbol{C}_2 & \boldsymbol{L} \\ \hline -\boldsymbol{F} & \mathbf{0} \end{array}\right], \tag{C.6}$$

where

$$\boldsymbol{F} = \left(\boldsymbol{B}_2^\mathrm{T}\boldsymbol{P}\boldsymbol{B}_2 + \boldsymbol{D}_1^\mathrm{T}\boldsymbol{D}_1\right)^{-1}\left(\boldsymbol{B}_2^\mathrm{T}\boldsymbol{P}\boldsymbol{A} + \boldsymbol{D}_1^\mathrm{T}\boldsymbol{C}_1\right), \tag{C.7}$$

$$\boldsymbol{L} = \left(\boldsymbol{B}_1\boldsymbol{D}_2^\mathrm{T} + \boldsymbol{A}\boldsymbol{Q}\boldsymbol{C}_2^\mathrm{T}\right)\left(\boldsymbol{D}_2\boldsymbol{D}_2^\mathrm{T} + \boldsymbol{C}_2\boldsymbol{Q}\boldsymbol{C}_2^\mathrm{T}\right)^{-1}. \tag{C.8}$$

The matrices $\boldsymbol{P}$ and $\boldsymbol{Q}$ are the unique positive semi-definite solutions to the following discrete-time Riccati equations,

$$\begin{aligned} \boldsymbol{P} = \boldsymbol{A}^\mathrm{T}\boldsymbol{P}\boldsymbol{A} + \boldsymbol{C}_1^\mathrm{T}\boldsymbol{C}_1 - \left(\boldsymbol{C}_1^\mathrm{T}\boldsymbol{D}_1 + \boldsymbol{A}^\mathrm{T}\boldsymbol{P}\boldsymbol{B}_2\right)\left(\boldsymbol{D}_1^\mathrm{T}\boldsymbol{D}_1 + \boldsymbol{B}_2^\mathrm{T}\boldsymbol{P}\boldsymbol{B}_2\right)^{-1}\left(\boldsymbol{D}_1^\mathrm{T}\boldsymbol{C}_1 + \boldsymbol{B}_2^\mathrm{T}\boldsymbol{P}\boldsymbol{A}\right) \\ \text{with} \quad \boldsymbol{D}_1^\mathrm{T}\boldsymbol{D}_1 + \boldsymbol{B}_2^\mathrm{T}\boldsymbol{P}\boldsymbol{B}_2 > \mathbf{0}, \end{aligned} \tag{C.9}$$

and

$$\begin{aligned} \boldsymbol{Q} = \boldsymbol{A}\boldsymbol{Q}\boldsymbol{A}^\mathrm{T} + \boldsymbol{B}_1\boldsymbol{B}_1^\mathrm{T} - \left(\boldsymbol{B}_1\boldsymbol{D}_2^\mathrm{T} + \boldsymbol{A}\boldsymbol{Q}\boldsymbol{C}_2^\mathrm{T}\right)\left(\boldsymbol{D}_2\boldsymbol{D}_2^\mathrm{T} + \boldsymbol{C}_2\boldsymbol{Q}\boldsymbol{C}_2^\mathrm{T}\right)^{-1}\left(\boldsymbol{D}_2\boldsymbol{B}_1^\mathrm{T} + \boldsymbol{C}_2\boldsymbol{Q}\boldsymbol{A}^\mathrm{T}\right) \\ \text{with} \quad \boldsymbol{D}_2\boldsymbol{D}_2^\mathrm{T} + \boldsymbol{C}_2\boldsymbol{Q}\boldsymbol{C}_2^\mathrm{T} > \mathbf{0}. \end{aligned} \tag{C.10}$$

One can conclude from the above equations that the controller is composed of a unique $\mathcal{H}_2$ optimal state feedback law $\boldsymbol{F}$ in conjunction with a unique $\mathcal{H}_2$ optimal observer matrix $\boldsymbol{L}$.

C.3 Phasor Notation

The following short-hand notation, also known as complex exponential representation (CER) [69] or phasor notation, for harmonic functions is used in parts of this thesis. Any quantity $x(t)$ that exhibits a harmonic behavior over time can be written as

$$x(t) = \hat{x}\cos(\omega t + \varphi). \tag{C.11}$$

We define its complex equivalent as

$$\begin{aligned} x_{\mathrm{c}}(t) &:= \hat{x}\cos(\omega t + \varphi) + \mathrm{j}\,\hat{x}\sin(\omega t + \varphi) \\ &= \hat{x}\,\mathrm{e}^{\mathrm{j}(\omega t + \varphi)} \\ &= \hat{x}\,\mathrm{e}^{\mathrm{j}\varphi}\,\mathrm{e}^{\mathrm{j}\omega t} \\ &= \tilde{x}\,\mathrm{e}^{\mathrm{j}\omega t}. \end{aligned} \tag{C.12}$$

The original, time-dependent quantity $x(t)$ can be recovered by

$$x(t) = \Re\left\{x_c(t)\right\} = \Re\left\{\tilde{x}\,\mathrm{e}^{\mathrm{j}\omega t}\right\} = |\tilde{x}|\cos(\omega t + \angle\tilde{x}). \tag{C.13}$$

Integration and differentiation of $x(t)$ may be compactly represented as

$$\dot{x}(t) \Leftrightarrow \mathrm{j}\omega\tilde{x}, \tag{C.14}$$

and

$$\int x(t)\,\mathrm{d}t \Leftrightarrow -\mathrm{j}\frac{1}{\omega}\tilde{x}. \tag{C.15}$$

The time-average product of two harmonic quantities can be represented with the help of phasor notation as

$$\frac{1}{T_{\mathrm{p}}}\int_0^{T_{\mathrm{p}}} x(t)y(t)\,\mathrm{d}t = \overline{x(t)\cdot y(t)} = \frac{1}{2}\Re\left\{\tilde{x}\tilde{y}^*\right\}, \tag{C.16}$$

where the $*$ operator denotes conjugate complex, and $T_{\mathrm{p}} = \frac{2\pi}{\omega}$ is the periodic time.

C.4 Optimal Harmonic Vibration Control

Assuming that the location and frequency spectrum of some disturbance excitation is known, we want to compute the optimal actuator voltages to minimize the time-average kinetic energy of the smart panel. This can be done by expressing the energy in terms of the disturbance and control forces in a quadratic Hermitian form, see also [65, 145].

In steady-state harmonic motion, the plate displacement can be expressed in phasor notation as

$$\tilde{w}(x, y, \omega) = \sum_{i=1}^{\infty} W_i(x, y)\tilde{\eta}_i(\omega). \tag{C.17}$$

The modal displacements are in turn given by

$$\tilde{\eta}_i(\omega) = \frac{1}{\omega_i^2 - \omega^2 + \mathrm{j}2D_i\omega\omega_i}\left(\tilde{f}_i^{\mathrm{g,d}}(\omega) + \tilde{f}_i^{\mathrm{g,c}}(\omega)\right), \tag{C.18}$$

where $f_i^{\mathrm{g,d}}$ and $f_i^{\mathrm{g,c}}$ are the generalized disturbance and control forces of the ith mode, respectively. The last equation follows directly from (2.71) when the contributions of the piezo patches are neglected and the additional remarks made in App. A.5. The generalized control forces are given via the electromechanical coupling matrix $\boldsymbol{G}_{\mathrm{em}}$ as $f_i^{\mathrm{g,c}} = -\boldsymbol{G}_{\mathrm{em}}^{(i,:)}\boldsymbol{U}$, where $\boldsymbol{U}$ is the vector of actuator voltages.

The control objective is the time-average kinetic energy, which is given for a Kirchhoff plate as

$$\bar{E}_{\mathrm{kin}} = \frac{1}{2}\sum_{i=1}^{\infty}\frac{1}{T}\int_0^T \dot{\eta}_i^2(t)\,\mathrm{d}t \tag{C.19}$$

when the structural basis functions are normalized as in (2.47). For harmonic motion, this reads

$$\bar{E}_{\mathrm{kin}} = \frac{1}{2}\sum_{i=1}^{\infty}\frac{1}{2}\left|\dot{\tilde{\eta}}_i\right|^2 = \frac{1}{4}\dot{\tilde{\boldsymbol{\eta}}}^{\mathrm{H}}\dot{\tilde{\boldsymbol{\eta}}} = \frac{1}{4}\omega^2\tilde{\boldsymbol{\eta}}^{\mathrm{H}}\tilde{\boldsymbol{\eta}}. \tag{C.20}$$

By setting $1/(\omega_i^2 - \omega^2 + \mathrm{j}2D_i\omega\omega_i)\tilde{f}_i^{\mathrm{g,d}} =: \tilde{\eta}_i^{\mathrm{d}}$ and $-1/(\omega_i^2 - \omega^2 + \mathrm{j}2D_i\omega\omega_i)\boldsymbol{G}_{\mathrm{em}}^{(i,:)} =: \boldsymbol{b}_i^{\mathrm{T}}$, we have $\tilde{\eta}_i = \tilde{\eta}_i^{\mathrm{d}} + \boldsymbol{b}_i^{\mathrm{T}}\tilde{\boldsymbol{U}}$, or in matrix form

$$\tilde{\boldsymbol{\eta}}(\omega) = \tilde{\boldsymbol{\eta}}^{\mathrm{d}}(\omega) + \boldsymbol{B}\tilde{\boldsymbol{U}}(\omega). \tag{C.21}$$

The input matrix $\boldsymbol{B}$ can also be conveniently stated as $\boldsymbol{B} = -\boldsymbol{\Omega}\boldsymbol{G}_{\mathrm{em}}$, with $\boldsymbol{\Omega} = \bigoplus_{i=1}^{\infty} 1/(\omega_i^2 - \omega^2 + \mathrm{j}2D_i\omega\omega_i)$. With these notations, the energy can be expressed as

$$\bar{E}_{\mathrm{kin}} = \frac{1}{4}\omega^2\left[\left(\tilde{\boldsymbol{\eta}}^{\mathrm{d}} + \boldsymbol{B}\tilde{\boldsymbol{U}}\right)^{\mathrm{H}}\left(\tilde{\boldsymbol{\eta}}^{\mathrm{d}} + \boldsymbol{B}\tilde{\boldsymbol{U}}\right)\right] = \frac{1}{4}\omega^2\boldsymbol{e}^{\mathrm{H}}\boldsymbol{e}, \tag{C.22}$$

where $\boldsymbol{e} = \tilde{\boldsymbol{\eta}}^{\mathrm{d}} + \boldsymbol{B}\tilde{\boldsymbol{U}}$. The minimization of $\bar{E}_{\mathrm{kin}}$ can thus be interpreted as finding the minimum 2-norm solution to the system of equations $\boldsymbol{B}\tilde{\boldsymbol{U}} = -\tilde{\boldsymbol{\eta}}^{\mathrm{d}}$. The optimal control inputs are therefore given by

$$\tilde{\boldsymbol{U}}_{\mathrm{opt}} = -\boldsymbol{B}^{+}\tilde{\boldsymbol{\eta}}^{\mathrm{d}}. \tag{C.23}$$

The existence of a unique solution is guaranteed if $\boldsymbol{B}$ is of full column rank. This is identical to requiring that $\boldsymbol{G}_{\mathrm{em}}$ is of full column rank, which can be assumed satisfied for sensible actuator positioning.

D Appendix to Active Structural Acoustic Control

D.1 Simulation of Sound Radiation of a Baffled Plate

To illustrate the characteristics of a simple sound field, the plate configuration shown in Fig. 3.1 is simulated when excited at the shaker position. It is assumed that the plate is set in an infinite baffle, such that the Rayleigh integral is applicable. The amplitude of the point force is 1 N and will harmonically oscillate with either the first or second resonance frequency of the plate. Since only these two excitation frequencies are considered, it is justified to approximate the structural state of motion only by the first or second modal velocity, respectively. More precisely, we let $\dot{\tilde{w}}(\boldsymbol{x}, \omega_{\{1,2\}}) \approx \dot{\tilde{\eta}}_{\{1,2\}}(\omega_{\{1,2\}})W_{\{1,2\}}(\boldsymbol{x})$. The angle of the modal velocity phasor $\dot{\tilde{\eta}}$ shall be denoted by $\varphi_{\dot{\eta}}$. When $\varphi_{\dot{\eta}} = 0$, this implies that the plate is in undeformed state and crosses $z = 0$ from negative to positive values. The maximum positive deflection is reached for $\varphi_{\dot{\eta}} = {}^{\pi}/_{2}$, and the maximum deflection in negative direction for $\varphi_{\dot{\eta}} = {}^{-\pi}/_{2}$. These relationships are illustrated in Fig. D.1. At all time instants, the following conditions hold at the boundary layer between structure and fluid [69]: The z-component of the particle velocity adjacent to the plate surface is identical to the plate velocity, i.e. $\tilde{v}_z(x, y, 0, \omega) = \dot{\tilde{w}}(x, y, \omega)$, and the pressure phasor is 90° ahead of the velocity phasor, i.e. $\varphi_{\mathrm{f}} = {}^{\pi}/_{2}$.

It must be mentioned that although the approximation of resonant motion of lightly damped structures by the corresponding single modal velocity usually comes with negligible error, the neglected structural modes may significantly contribute to the structure-borne sound field. This comes from the fact that a structural mode with small modal amplitude may be a much better sound generator as another structural mode with higher amplitude. This will be further illustrated in this section by the concept of modal radiation efficiencies. Nevertheless, all figures in this section are produced by considering only the respective resonant mode, for simplicity and clarity of presentation.

We first consider the state of motion illustrated on the left side of Fig. D.1, $\varphi_{\dot{\eta}} = -\frac{\pi}{2}$. This phase angle implies that the particle velocity approaches zero near the plate surface and the pressure reaches its maximum positive value. The pressure field is illustrated for the first two resonance frequencies in Fig. D.2 at the normal distances 0.1, 2, and 4 m. It can be seen that positive and negative values of the same magnitude appear when exciting at second resonance, which conforms with the corresponding structural mode shape, and that the pressure values are about one magni-

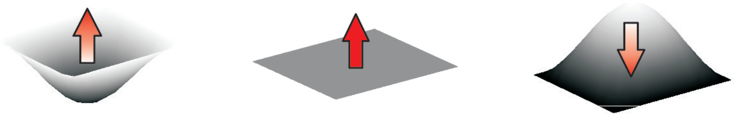

Figure D.1: Plate deflections of first bending mode for three different phasor angles; from left to right: $\varphi_{\dot{\eta}} = {}^{-\pi}/_{2}$, $\varphi_{\dot{\eta}} = 0$, $\varphi_{\dot{\eta}} = {}^{\pi}/_{2}$.

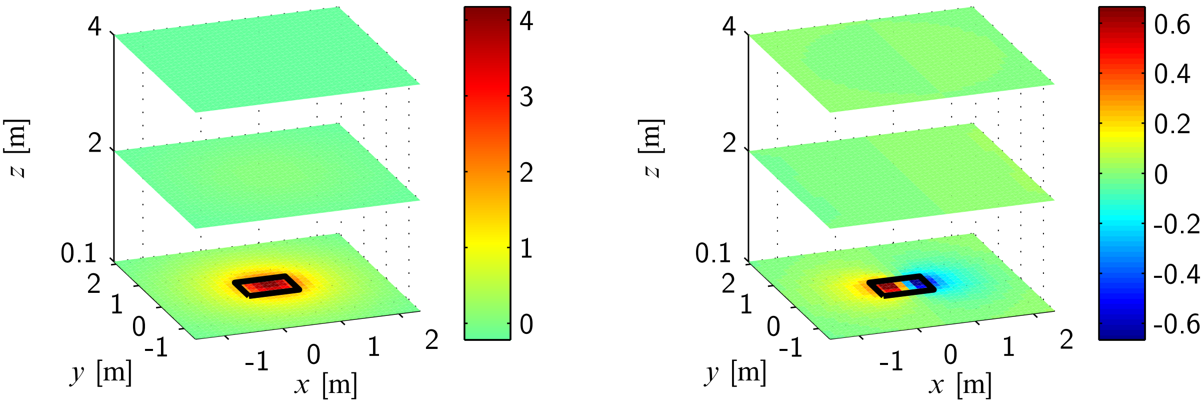

Figure D.2: Pressure field at first resonance (left) and second resonance (right) for $\varphi_{\dot{\eta}} = -\frac{\pi}{2}$ in Pa.

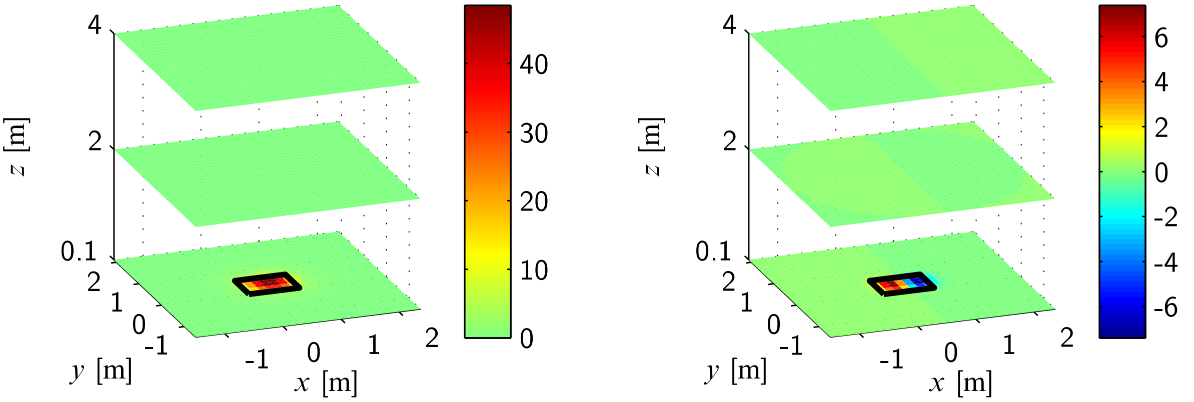

Figure D.3: z-Component of particle velocity field at first resonance (left) and second resonance (right) for $\varphi_{\dot{\eta}} = 0$ in mm/s.

tude smaller compared to the excitation at first resonance.

For $\varphi_{\dot{\eta}} = 0$, the plate and particle velocities reach their maximum and consequently, the pressure field close to the plate surface is at a minimum, as illustrated in Figs. D.3 and D.4, respectively. Another quarter of a period later, particle velocity is minimal and is about to reverse its flow direction from positive to negative values, see Fig. D.5.

An overall impression of the pressure and particle velocity fields can be gathered by considering their respective levels L_p and L_{v_z} [69]. The sound pressure level is defined as

$$L_\mathrm{p}(\boldsymbol{x}) = 20\,\mathrm{lg}\,\frac{p_\mathrm{RMS}(\boldsymbol{x})}{p_0}, \tag{D.1}$$

and the velocity level is given by

$$L_{\mathrm{v}_z}(\boldsymbol{x}) = 20\,\mathrm{lg}\,\frac{v_{z,\mathrm{RMS}}(\boldsymbol{x})}{v_0}. \tag{D.2}$$

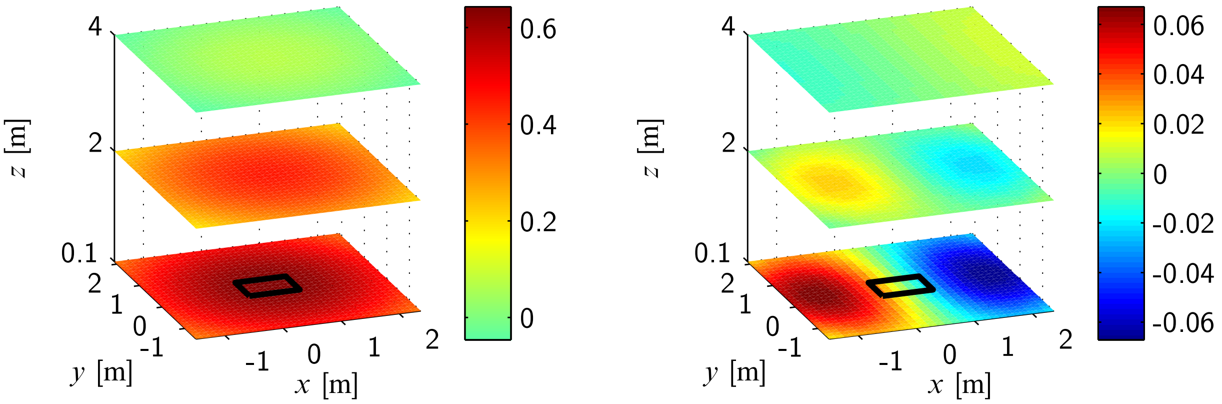

Figure D.4: Pressure field at first resonance (left) and second resonance (right) for $\varphi_{\dot{\eta}} = 0$ in Pa.

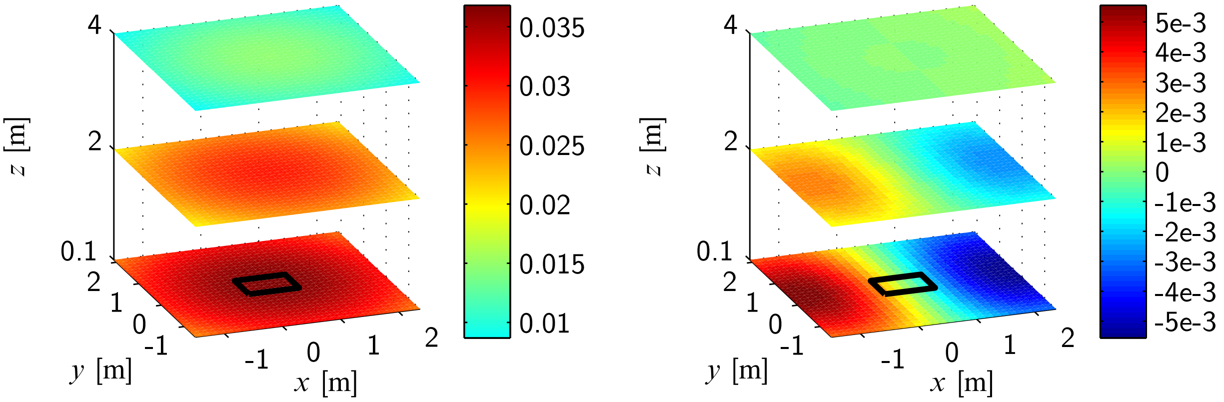

Figure D.5: z-Component of particle velocity field at first resonance (left) and second resonance (right) for $\varphi_{\dot{\eta}} = \frac{\pi}{2}$ in $^{\mathrm{mm}}/_{\mathrm{s}}$.

The RMS values in the above equations are normalized with respect to $p_0 = 2 \cdot 10^{-5}\,\mathrm{Pa}$ and $v_0 = 5 \cdot 10^{-8}\,\mathrm{m\,s^{-1}} \approx {}^{p_0}/_{Z_0}$. The pressure p_0 is commonly accepted as the lowest perceivable pressure fluctuation by human ear. The levels are shown in Figs. D.6 and D.7.

The particle velocity, and therefore also the sound intensity, are characterized by three-dimensional vector fields. Figure D.8 shows the intensity fields at first and second resonance at their respective maximum values. Here, the different characteristic sound-emission profiles can also be recognized.

It becomes obvious that the baffled plate is a much less effective sound radiator when vibrating at second than at first resonance. This is due to the mode shapes associated with the respective eigenfrequencies. At second resonance, the two characteristic domes vibrate in antiphase and lead to pressure and velocity fluctuations close to the plate surface which largely cancel out, as illustrated in Fig. D.9.
The effectivity of the different mode shapes to emit sound power can be quantified by the associated values of radiation efficiency. Values of radiation efficiencies for the first few bending modes

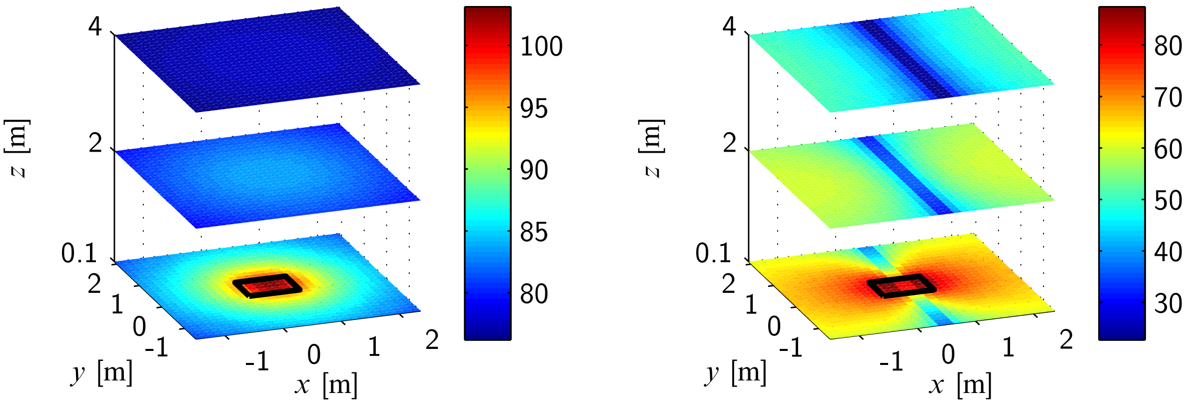

Figure D.6: Sound pressure level (in dB) at first resonance (left) and second resonance (right).

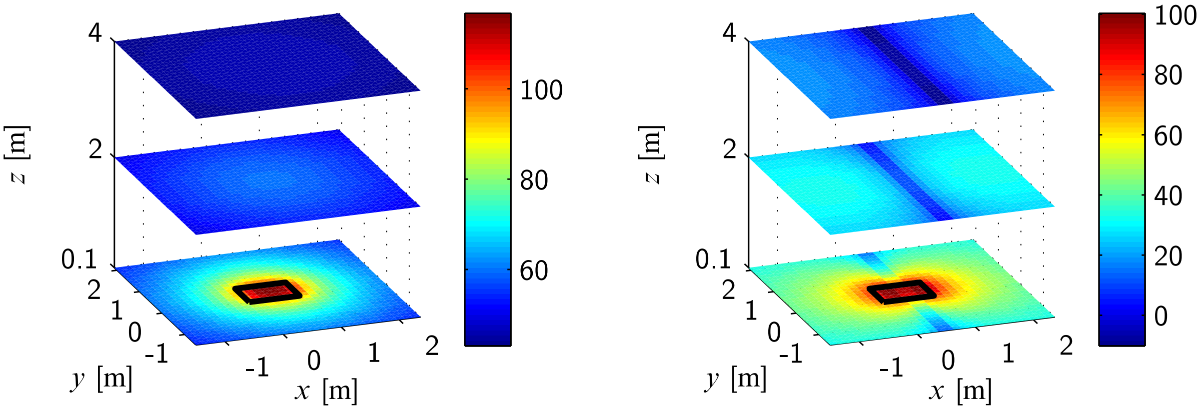

Figure D.7: z-Component of particle velocity level (in dB) at first resonance (left) and second resonance (right).

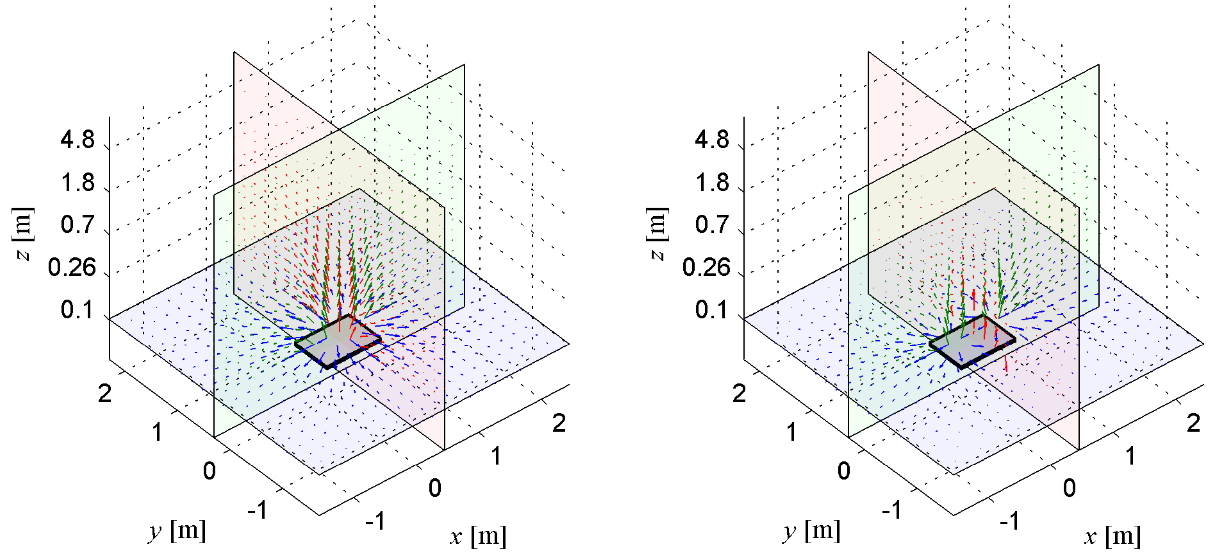

Figure D.8: Maximum intensity at first resonance (left) and second resonance (right) (different scales).

Figure D.9: Illustration of radiation cancellation.

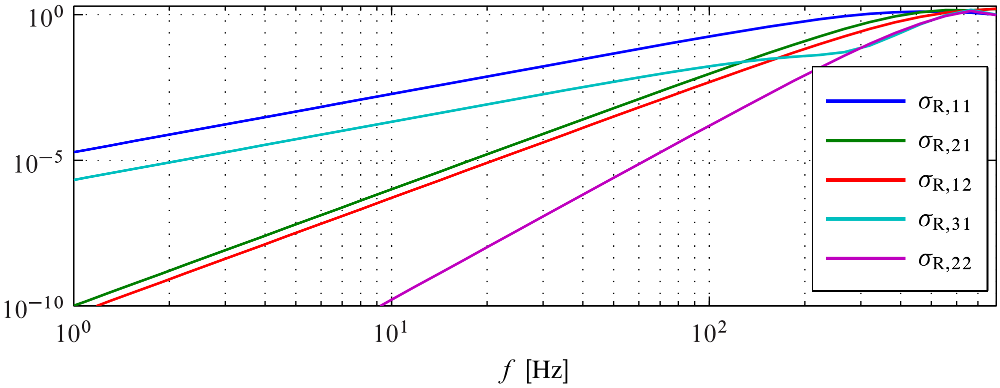

Figure D.10: Radiation efficiencies for the first five plate bending modes.

of the simply-supported baffled plate are plotted in Fig. D.10. The series expansion presented in [120] was used to produce these curves. It can be seen that at low frequencies, those bending modes are efficient radiators which have a net volume displacement, for example the (1,1)- and (3,1)-modes. These are characterized by two odd index numbers. The least effective radiators at low frequencies are those modes which are characterized by two even mode indices, like the (2,2)-mode. Here, radiation cancellation works best. With increasing frequency, all radiation efficiencies approach a value close to one. This is because increasing frequency implies increased phase velocity of the bending waves in the plate. Once this phase velocity approaches and exceeds the speed of sound, radiation cancellation is curbed. The frequency where the bending wave phase velocity equals the speed of sound is termed *coincidence frequency*. It can be calculated with knowledge of the dispersion relation of bending waves, $\rho h\omega^2 - Dk_{\mathrm{S}}^4 = 0$, see also (2.15). Acoustic waves are non-dispersive, i.e. their phase wave speed is independent of the wave frequency and is given by the speed of sound, $c_0 = {}^{\omega}\!/_{k_{\mathrm{A}}} = \text{const.}$, with the acoustic wave number k_{A}. Equality of phase speeds at some certain frequency implies that also the structural and acoustic wave numbers, k_{S} and k_{A}, must be equal. By equating these two quantities, the coincidence frequency ω_{c} can be calculated by

$$\omega_{\mathrm{c}} = \sqrt{\frac{\rho h}{D}} c_0^2. \tag{D.3}$$

For the plate of the acoustic demonstrator, the value of the coincidence frequency is 3.00 kHz.

The wave number ratio ${}^{k_{\mathrm{S}}}\!/_{k_{\mathrm{A}}}$ is of major significance for the sound radiation of baffled plates. It can be shown that bending waves characterized by $k_{\mathrm{S}} > k_{\mathrm{A}}$ produce *evanescent waves* in the sound field, which exponentially decay with increasing distance from the radiation source. These do not contribute to the emitted mean sound power. Only the *propagating waves*, which are caused by structural waves with $k_{\mathrm{S}} < k_{\mathrm{A}}$, cause a net energy transfer. One may consult [70] for a comprehensive treatment of this issue.

D.2 Optimal Harmonic Local and Global ASAC

For global control, the cost function is given by the time-average sound power,

$$\bar{P}(\omega) = \dot{\tilde{\boldsymbol{\eta}}}^{\mathrm{H}}(\omega)\boldsymbol{\Pi}(\omega)\dot{\tilde{\boldsymbol{\eta}}}(\omega) = \omega^2\tilde{\boldsymbol{\eta}}^{\mathrm{H}}(\omega)\boldsymbol{\Pi}(\omega)\tilde{\boldsymbol{\eta}}(\omega) \tag{D.4}$$

with the power transfer matrix $\boldsymbol{\Pi}(\omega)$, see Sec. 5.4. Employing (C.21), this equals

$$\bar{P} = \omega^2\left[\left(\tilde{\boldsymbol{\eta}}^{\mathrm{d}} + \boldsymbol{B}\tilde{\boldsymbol{U}}\right)^{\mathrm{H}}\boldsymbol{\Pi}\left(\tilde{\boldsymbol{\eta}}^{\mathrm{d}} + \boldsymbol{B}\tilde{\boldsymbol{U}}\right)\right]. \tag{D.5}$$

Minimizing $\bar{P}$ can therefore be interpreted as finding the optimal 2-norm solution to the system of equations $\boldsymbol{R}\boldsymbol{B}\tilde{\boldsymbol{U}} = -\boldsymbol{R}\tilde{\boldsymbol{\eta}}^{\mathrm{d}}$, where $\boldsymbol{R}$ is a Cholesky factor of $\boldsymbol{\Pi}$. The optimal solution is given by

$$\tilde{\boldsymbol{U}}_{\mathrm{opt}}^{\mathrm{global}} = -\left(\boldsymbol{R}\boldsymbol{B}\right)^{+}\boldsymbol{R}\tilde{\boldsymbol{\eta}}^{\mathrm{d}}. \tag{D.6}$$

The existence of a unique solution is guaranteed if $\boldsymbol{R}\boldsymbol{B}$ is of full column rank. This is identical to requiring that $\boldsymbol{G}_{\mathrm{em}}$ is of full column rank, which can be assumed satisfied for sensible actuator placement.

For optimal local control, the goal is to minimize the RMS sound pressure at a given location $\boldsymbol{x}$. For a baffled plane structure radiating into free space, the sound pressure at any point in the closed half space may be calculated by Rayleigh's integral formula (compare (5.11)),

$$\tilde{p}(\boldsymbol{x},\omega) = \frac{\mathrm{j}\omega\rho_0}{2\pi}\sum_{i=1}^{\infty}\underbrace{\iint_S W_i(\boldsymbol{x})\frac{\mathrm{e}^{-\mathrm{j}kR}}{R}\,\mathrm{d}S}_{=:x_i}\;\dot{\tilde{\eta}}_i = \frac{\mathrm{j}\omega\rho_0}{2\pi}\boldsymbol{x}^{\mathrm{T}}\dot{\tilde{\boldsymbol{\eta}}} = -\frac{\omega^2\rho_0}{2\pi}\boldsymbol{x}^{\mathrm{T}}\tilde{\boldsymbol{\eta}}. \tag{D.7}$$

The RMS sound pressure can be easily calculated by $p_{\mathrm{RMS}}(\boldsymbol{x},\omega) = {}^{1}/\!\sqrt{2}\,|\tilde{p}(\boldsymbol{x},\omega)|$. With the help of the last equation, the squared RMS pressure is expressed in terms of the modal displacements as follows,

$$\begin{aligned} p_{\mathrm{RMS}}^2(\boldsymbol{x},\omega) &= \frac{1}{2}\tilde{p}(\boldsymbol{x},\omega)\tilde{p}^*(\boldsymbol{x},\omega) \\ &= \frac{\omega^4\rho_0^2}{8\pi^2}\boldsymbol{x}^{\mathrm{T}}\tilde{\boldsymbol{\eta}}\boldsymbol{x}^{\mathrm{H}}\tilde{\boldsymbol{\eta}}^* \\ &= \frac{\omega^4\rho_0^2}{8\pi^2}\tilde{\boldsymbol{\eta}}^{\mathrm{H}}\underbrace{\boldsymbol{x}^*\boldsymbol{x}^{\mathrm{T}}}_{=:\boldsymbol{X}}\tilde{\boldsymbol{\eta}} \\ &= \frac{\omega^4\rho_0^2}{8\pi^2}\left(\tilde{\boldsymbol{\eta}}^{\mathrm{d}} + \boldsymbol{B}\tilde{\boldsymbol{U}}\right)^{\mathrm{H}}\boldsymbol{X}\left(\tilde{\boldsymbol{\eta}}^{\mathrm{d}} + \boldsymbol{B}\tilde{\boldsymbol{U}}\right) \qquad \text{(see (C.21))}. \end{aligned} \tag{D.8}$$

Since the square root is a monotonously increasing function, p_{RMS} is minimal when p_{RMS}^2 is minimal. Unlike the cases treated before, the Hermitian, positive semi-definite matrix $\boldsymbol{X}$ has n_{S}

columns (the number of incorporated mode shapes), but is of rank one. Writing its eigendecomposition as $\boldsymbol{X} = \boldsymbol{V}^{\mathrm{H}} \boldsymbol{\Lambda} \boldsymbol{V}$, the corresponding set of linear equations is

$$\boldsymbol{\Lambda}^{1/2} \boldsymbol{V} \boldsymbol{B} \tilde{\boldsymbol{U}} = -\boldsymbol{\Lambda}^{1/2} \boldsymbol{V} \tilde{\boldsymbol{\eta}}^{\mathrm{d}}. \tag{D.9}$$

This system is exactly solvable iff $\boldsymbol{\Lambda}^{1/2} \boldsymbol{V} \tilde{\boldsymbol{\eta}}^{\mathrm{d}} \in \operatorname{im}\{\boldsymbol{\Lambda}^{1/2} \boldsymbol{V} \boldsymbol{B}\}$ which is equal to the requirement

$$\operatorname{rank}\left\{\boldsymbol{\Lambda}^{1/2} \boldsymbol{V} \boldsymbol{B}\right\} = 1 \overset{!}{=} \operatorname{rank}\left(\boldsymbol{\Lambda}^{1/2} \boldsymbol{V} \boldsymbol{B} \middle| \boldsymbol{\Lambda}^{1/2} \boldsymbol{V} \tilde{\boldsymbol{\eta}}^{\mathrm{d}}\right). \tag{D.10}$$

Since $\boldsymbol{\Lambda}^{1/2} = \oplus\{\sqrt{\lambda_1}, 0, \ldots, 0\}$, it is easy to see that this is always satisfied, unless the first row of the product $\boldsymbol{V} \boldsymbol{B}$ is zero, i.e. $\boldsymbol{V}^{(1,:)} \boldsymbol{B} = \boldsymbol{0}$. The number of incorporated modes n_{S} is generally greater than the number of actuators n_{P}, which implies that $\boldsymbol{B} \in \mathbb{C}^{n_{\mathrm{S}} \times n_{\mathrm{P}}}$ indeed has a left null space. Strictly speaking, the number of structural modes is infinite. However, for a practical simulation model of limited order, it is unlikely that the actuators are positioned in such a way that the first row of $\boldsymbol{V}$ is part of the left null space of $\boldsymbol{B}$.
In case that (D.9) is solvable, the RMS pressure can be made zero by any $\tilde{\boldsymbol{U}}$ from the set

$$\tilde{\boldsymbol{U}}_{\mathrm{opt}}^{\mathrm{local}} = -\left(\boldsymbol{\Lambda}^{1/2} \boldsymbol{V} \boldsymbol{B}\right)^{+} \boldsymbol{\Lambda}^{1/2} \boldsymbol{V} \tilde{\boldsymbol{\eta}}^{\mathrm{d}} + \ker\left\{\boldsymbol{\Lambda}^{1/2} \boldsymbol{V} \boldsymbol{B}\right\}. \tag{D.11}$$

D.3 Radiation Modes of a Baffled Plate

Reconsider the spatial discretization of a baffled plate as in (5.22), $\bar{P} = \dot{\tilde{\boldsymbol{w}}}_{\mathrm{e}}^{\mathrm{H}} \boldsymbol{R} \dot{\tilde{\boldsymbol{w}}}_{\mathrm{e}}$. Applying the eigenvalue decomposition on $\boldsymbol{R}$, this can be rewritten as

$$\bar{P} = \dot{\tilde{\boldsymbol{w}}}_{\mathrm{e}}^{\mathrm{H}} \boldsymbol{V}^{\mathrm{H}} \boldsymbol{\Lambda} \boldsymbol{V} \dot{\tilde{\boldsymbol{w}}}_{\mathrm{e}} = \tilde{\boldsymbol{z}}^{\mathrm{H}} \boldsymbol{\Lambda} \tilde{\boldsymbol{z}}. \tag{D.12}$$

The orthonormal matrix $\boldsymbol{V}$ transforms the vector of structural velocities $\boldsymbol{w}_{\mathrm{e}}$ into a new vector $\boldsymbol{z}$, whose elements contribute to sound power independently. These transformed variables are given by a linear combination of the mutually orthogonal columns of $\boldsymbol{V}$, which define the so-called *radiation modes*. These mode shapes can be seen as orthonormal basis functions with respect to acoustic radiation. Since the matrix $\boldsymbol{R}$ is frequency dependent, the radiation modes are also frequency dependent, which is a major difference to the structural basis functions. The figures D.11 and D.12 show the first few radiation modes of a baffled plate at two different frequencies. The plate dimensions are identical to those of the acoustic demonstrator. The radiation modes are sorted in descending order according to their associated eigenvalues. It can be seen that the first radiation mode shape, which is the biggest contributor to sound power, resembles at low frequencies the movement of a rigid surface. For more information regarding radiation modes and their application in acoustic analysis and control, the reader is referred to [25, 33, 66].

D.4 Reformulation of the Direct Estimation Problem

To put the direct estimation problem into a more suitable form, the diag{·} operator must be expressed in terms of elementary operations. To this end, we consider the following equality for an

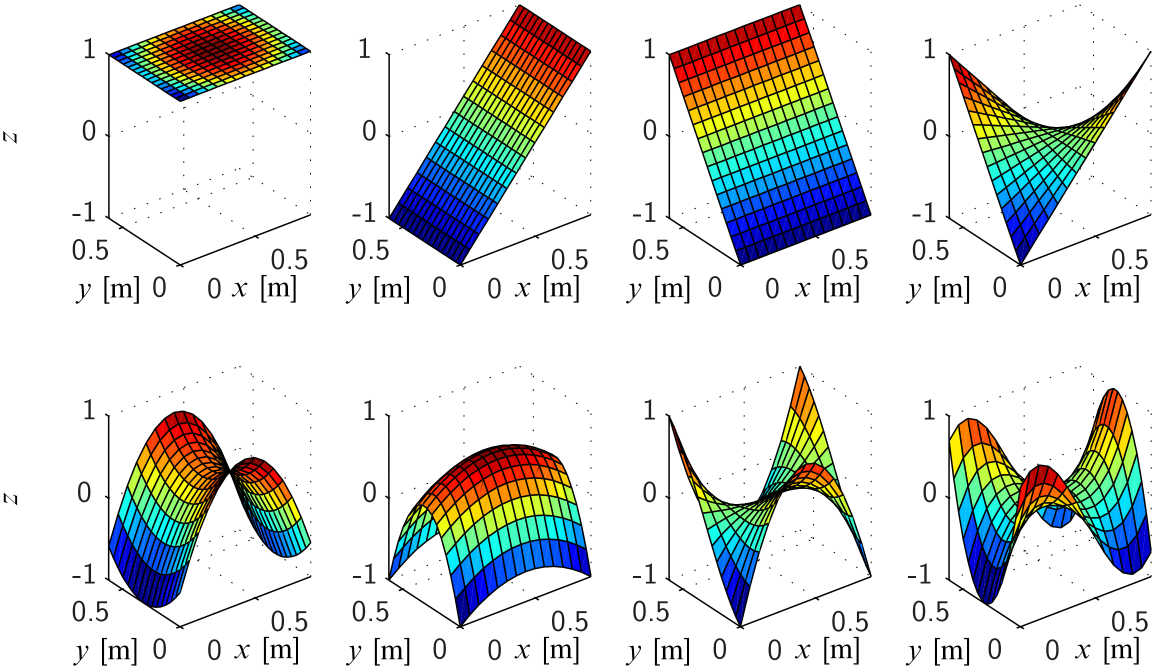

Figure D.11: First eight radiation mode shapes of a baffled plate at 10 Hz.

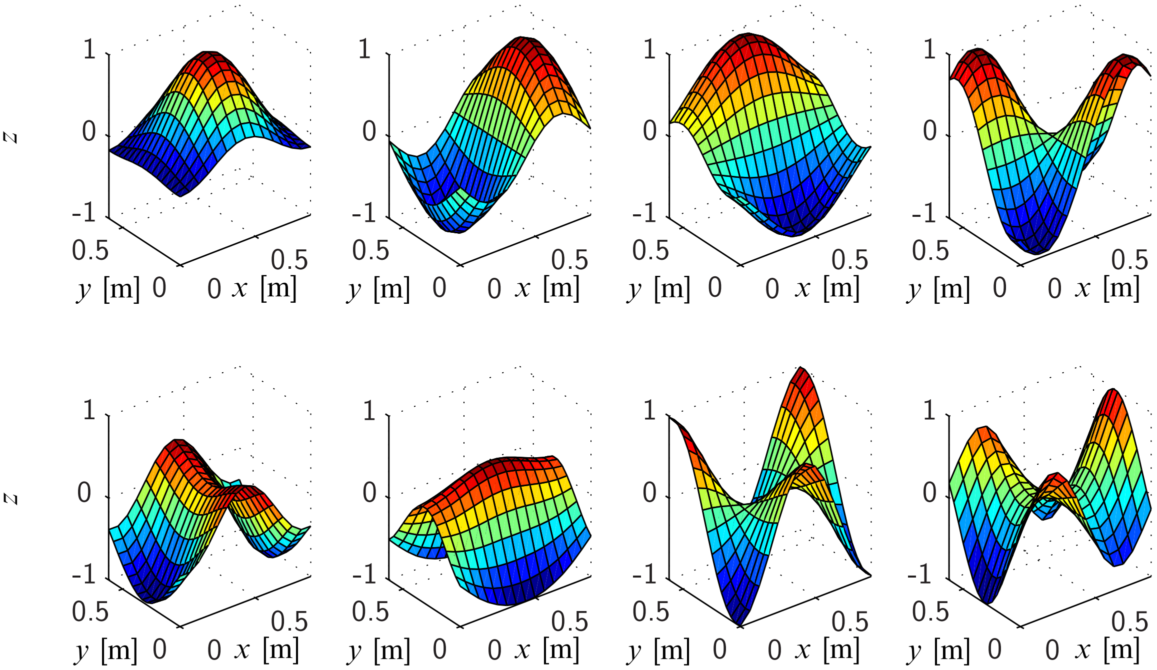

Figure D.12: First eight radiation mode shapes of a baffled plate at 500 Hz.

Hermitian matrix A of dimension $(M \times M)$,

$$\operatorname{diag}\{A\} = \sum_{i=1}^{M} e_i \underbrace{e_i^{\mathrm{T}} A e_i}_{=a_{ii}}, \tag{D.13}$$

with e_i being the ith column of the identity matrix of dimension M. This can be rewritten in matrix form as

$$\operatorname{diag}\{A\} = T_{\mathrm{D,H}} \operatorname{vech}\{A\}, \tag{D.14}$$

where the $\left(M \times \frac{M}{2}(M+1)\right)$ dimensional matrix $T_{\mathrm{D,H}} \in \{0,1\}$ has one non-zero entry in each row. The corresponding column indices are $(1, M+1, M(M-1)+1, M(M-1)(M-2)+1, \dots, \frac{M}{2}(M+1))$.
The operation vech$\{A\}$ can be restated as S_{H} vec$\{A\}$ with the $\left(\frac{M}{2}(M+1) \times M^2\right)$ dimensional binary matrix S_{H}. It also has one non-zero entry in each row and the corresponding column indices are $(1, 2, \dots, M, M+2, M+3, \dots, 2M, 2M+3, 2M+4, \dots, M^2)$.

Furthermore, in case of equation (5.31), the matrix A has the structure $A = X^{\mathrm{H}} \Pi X, \Pi \in \mathbb{C}^{n \times n}$. Thus,

$$\operatorname{diag}\left\{X^{\mathrm{H}} \Pi X\right\} = T_{\mathrm{D,H}}\, S_{\mathrm{H}} \operatorname{vec}\left\{X^{\mathrm{H}} \Pi X\right\}. \tag{D.15}$$

By making use of the identity vec$\{ACB\} = (B^{\mathrm{T}} \otimes A)vec\{C\}$, this gives

$$\operatorname{diag}\left\{X^{\mathrm{H}} \Pi X\right\} = T_{\mathrm{D,H}}\, S_{\mathrm{H}} \left(X^{\mathrm{T}} \otimes X^{\mathrm{H}}\right) \operatorname{vec}\{\Pi\}. \tag{D.16}$$

The vectorization vec$\{\Pi\}$ is related to the vech$\{\cdot\}$ operator by $S_{\mathrm{H,i}}$vech$\{\Pi\}$ = vec$\{\Pi\}$ with the binary matrix $S_{\mathrm{H,i}}$ of dimension $\left(n^2 \times \frac{n}{2}(n+1)\right)$. The final formulation is

$$\operatorname{diag}\left\{X^{\mathrm{H}} \Pi X\right\} = \underbrace{T_{\mathrm{D,H}}\, S_{\mathrm{H}}}_{=:T_1} \left(X^{\mathrm{T}} \otimes X^{\mathrm{H}}\right) \underbrace{S_{\mathrm{H,i}}}_{=:T_2} \operatorname{vech}\{\Pi\}. \tag{D.17}$$

The $(M \times M^2)$ dimensional binary matrix T_1 has one non-zero entry in each row at column indices $(1, M+2, 2M+3, \dots, M^2)$.

D.5 Transmission Zeros of the Structural Transfer Function

It is temporarily assumed that the outputs of the continuous-time, square structural transfer matrix G_{S} are modal displacements $\eta = (\eta_1, \dots, \eta_{n_{\mathrm{S}}})^{\mathrm{T}}$. A state space description of such a $G_{\mathrm{S}} \in \mathbb{C}^{n_{\mathrm{S}} \times n_{\mathrm{S}}}$ has the form

$$\begin{pmatrix} \dot{\eta} \\ \ddot{\eta} \end{pmatrix} = \begin{pmatrix} \mathbf{0} & \mathbf{I} \\ -K^{\mathrm{g}} & -D^{\mathrm{g}} \end{pmatrix} \begin{pmatrix} \eta \\ \dot{\eta} \end{pmatrix} + \underbrace{\begin{pmatrix} \mathbf{0} \\ \Phi_{\mathrm{A}}^{\mathrm{T}} \end{pmatrix}}_{=B} f, \tag{D.18a}$$

$$\eta = \underbrace{\begin{pmatrix} \mathbf{I} & \mathbf{0} \end{pmatrix}}_{C} \begin{pmatrix} \eta \\ \dot{\eta} \end{pmatrix}, \tag{D.18b}$$

where $\boldsymbol{K}^{\mathrm{g}}$ and $\boldsymbol{D}^{\mathrm{g}}$ are diagonal matrices containing information on the eigenfrequencies and the modal damping ratios, and all modes are assumed to be controllable. The system order n equals $2n_{\mathrm{S}}$, and the number of inputs and outputs is equal to the number of structural variables, $p = q = n_{\mathrm{S}}$. Furthermore, the product $\boldsymbol{CB}$ is zero. According to [168], the following inequality holds in general for a square proper system,

$$\#\,\text{transmission zeros} \leq n - 2p + \operatorname{rank}(\boldsymbol{CB}). \tag{D.19}$$

For the case at hand, this upper limit is equal to zero. This proofs that $\boldsymbol{G}_{\mathrm{S}}(s)$ can only have zeros at $s = 0$ when the outputs are modal velocities or accelerations.
The discretized version of $\boldsymbol{G}_{\mathrm{S}}(s)$, $\boldsymbol{G}_{\mathrm{S}}(z)$, does consequently have zeros at $z = 1$ and additional zeros inside the unit circle coming from the discretization process, which approach $z = -1$ for $T_{\mathrm{s}} \to 0$. Thus, $\boldsymbol{G}_{\mathrm{S}}(\mathrm{e}^{\mathrm{j}\omega})$ is ensured to be regular for all ω but zero for finite sampling.

In case that a spatial discretization is used, the outputs of $\boldsymbol{G}_{\mathrm{S}}$ are displacements at the sensor locations on the structure, or time derivatives of these quantities. Then theoretically, the system order n is unlimited, since there are infinitely many modes to be considered. Nevertheless, a band-limited model is used in every practical simulation setup, and then, the number of transmission zeros is again limited by (D.19).
In case that $\boldsymbol{G}_{\mathrm{S}}(z)$ has full normal rank, its rows still form a basis for the row space of $\boldsymbol{G}_{\mathrm{S},\infty}(\mathrm{e}^{\mathrm{j}\omega})$ but for a limited number of isolated points, which are given by the transmission zeros of $\boldsymbol{G}_{\mathrm{S}}$ on the unit circle. Thus, the considerations made for the spectral discretization in Sec. 5.6.3 can be analogously transferred to the case of spatial discretization.

D.6 Actuator and Sensor Placement

As pointed out in Sec. 5.6.3, the positioning of the actuators determines the influence of the spectral discretization on the discrepancy between the true and the identified acoustic FRFs $\boldsymbol{G}_{\mathrm{p}}$ and $\boldsymbol{G}_{\mathrm{v}}$. In case of spatial discretization, the error coefficients appearing in (5.54) are also functions of the sensor positions. This case is not treated here, but analog considerations apply.

An easy way to apply the guidelines mentioned in Sec. 5.6.3 is to superpose the mode shapes of the modes to be controlled and the first few adjacent modes. The actuator positions must reflect a compromise between achieving low controllability of the adjacent modes while preserving sufficient control authority over the modes to be controlled. In the present case, the frequency range from zero to 200 hertz, which comprises the first five lowly damped resonances of the acoustic demonstrator, shall be targeted by ASAC. These resonances are dominated by the plate dynamics. The additive superposition of the absolute values of the first five plate bending modes and of modes six to eight are shown in Fig. D.13. It can be judged from the selected actuator positions that a good compromise between control authority and control spillover can easily be found for the presented problem.

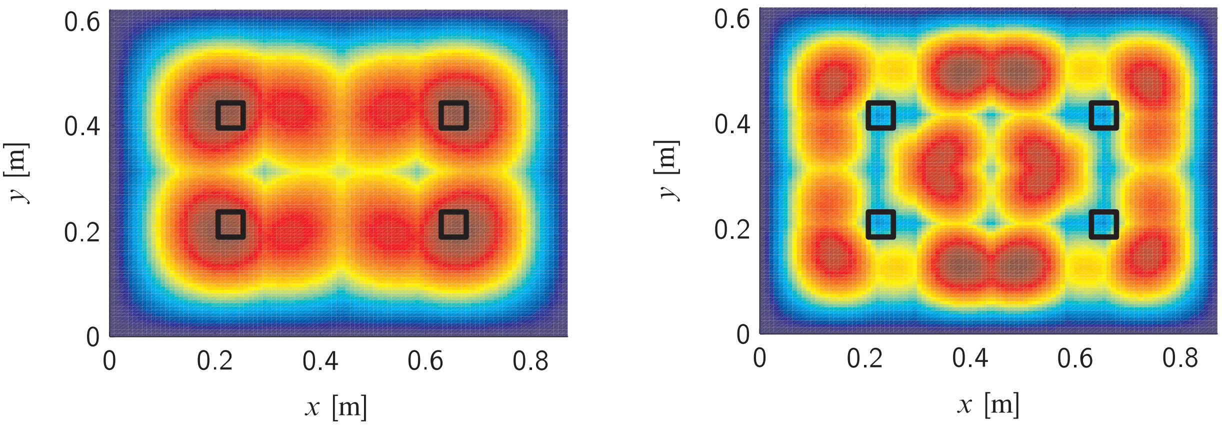

Figure D.13: Additive superposition of the magnitude of the first five plate mode shape functions (left) and modes six to eight (right). The selected actuator positions are indicated by rectangles.

D.7 Parametric Modeling Procedure

We consider minimization of the optimality measure $J = \|\Re\{\boldsymbol{We}\}\|_2^2$ (compare (5.62)) with respect to the parameters of a pth order MIMO ARX model[1] $\boldsymbol{\Xi}(z) = \boldsymbol{Q}^{-1}(z)\boldsymbol{R}(z)$, with

$$\begin{aligned} \boldsymbol{Q}(z) &= \mathbf{I} + \boldsymbol{Q}_1 z^{-1} + \cdots + \boldsymbol{Q}_p z^{-p} \quad \text{and} \\ \boldsymbol{R}(z) &= \boldsymbol{R}_0 + \boldsymbol{R}_1 z^{-1} + \cdots + \boldsymbol{R}_p z^{-p}. \end{aligned} \tag{D.20}$$

Pre-multiplying the model equation by $\boldsymbol{Q}(z)$ gives $\boldsymbol{Q}(z)\boldsymbol{\Xi}(z) = \boldsymbol{R}(z)$. Then, it can be seen that the frequency response of the model at $z_n := \mathrm{e}^{\mathrm{j}\omega_n T_\mathrm{s}}$ is implicitly given as

$$\boldsymbol{\Xi}(z_n) = -\boldsymbol{Q}_1\boldsymbol{\Xi}(z_n)z_n^{-1} - \cdots - \boldsymbol{Q}_p\boldsymbol{\Xi}(z_n)z_n^{-p} + \boldsymbol{R}_0 + \boldsymbol{R}_1 z_n^{-1} + \cdots + \boldsymbol{R}_p z_n^{-p}. \tag{D.21}$$

This equation is nonlinear in the model parameters, since it involves multiplications of matrices $\boldsymbol{Q}_i$ and FRF values $\boldsymbol{\Xi}(z_n)$, which in turn depend on the model parameters, too. This implies that the error vector $\boldsymbol{e} = \mathrm{vec}\{\Delta\boldsymbol{\Xi}_\Omega\}$ is also nonlinear in the model parameters, and the problem of minimizing the measure J with respect to $\boldsymbol{Q}_i$ and $\boldsymbol{R}_i$ is non-convex and must be solved iteratively. In order to generate starting values for the iterative minimization of the nonlinear least squares problem, (D.21) must be linearized. This can be easily done by replacing the model FRF values on the right hand side by the measured FRFs $\hat{\boldsymbol{\Xi}}(z_i)$, $i = 1, \ldots, N$,

$$\boldsymbol{\Xi}(z_n) \approx -\boldsymbol{Q}_1\hat{\boldsymbol{\Xi}}(z_n)z_n^{-1} - \cdots - \boldsymbol{Q}_p\hat{\boldsymbol{\Xi}}(z_n)z_n^{-p} + \boldsymbol{R}_0 + \boldsymbol{R}_1 z_n^{-1} + \cdots + \boldsymbol{R}_p z_n^{-p}. \tag{D.22}$$

The justification for this simplification is that if model parameters can be found such that the equation error of (D.22) is small, then the model FRF values and the measured FRF values are close. With the last equation, the error vector can be rewritten (see also [113]),

$$\boldsymbol{e} = \mathrm{vec}\left\{\hat{\boldsymbol{\Xi}}_\Omega - \boldsymbol{\Xi}_\Omega\right\} \approx \mathrm{vec}\left\{\hat{\boldsymbol{\Xi}}_\Omega - \boldsymbol{\Theta\Phi}\right\}, \tag{D.23}$$

---

[1] This type of model is also known as left matrix fraction description (LMFD).

with $\boldsymbol{\Theta} = (-\boldsymbol{Q}_1, \dots, -\boldsymbol{Q}_p, \boldsymbol{R}_0, \dots, \boldsymbol{R}_p)$ and

$$\boldsymbol{\Phi} = \left(\begin{array}{ccc} \hat{\boldsymbol{\Xi}}(z_1)z_1^{-1} & \dots & \hat{\boldsymbol{\Xi}}(z_N)z_N^{-1} \\ \vdots & & \vdots \\ \hat{\boldsymbol{\Xi}}(z_1)z_1^{-p} & \dots & \hat{\boldsymbol{\Xi}}(z_N)z_N^{-p} \\ \hline \mathbf{I}_{n_\mathrm{S}} & \dots & \mathbf{I}_{n_\mathrm{S}} \\ \mathbf{I}_{n_\mathrm{S}}z_1^{-1} & \dots & \mathbf{I}_{n_\mathrm{S}}z_N^{-1} \\ \vdots & & \vdots \\ \mathbf{I}_{n_\mathrm{S}}z_1^{-p} & \dots & \mathbf{I}_{n_\mathrm{S}}z_N^{-p} \end{array}\right). \tag{D.24}$$

In order to express the optimality measure in terms of the model parameters, it is expanded as follows,

$$\begin{aligned} J &= \|\Re\{\boldsymbol{W}\boldsymbol{e}\}\|_2^2 \\ &\approx \left\|\Re\left\{\boldsymbol{W}\operatorname{vec}\left\{\hat{\boldsymbol{\Xi}}_\Omega - \boldsymbol{\Theta}\boldsymbol{\Phi}\right\}\right\}\right\|_2^2 \\ &= \left\|\Re\left\{\boldsymbol{W}\operatorname{vec}\hat{\boldsymbol{\Xi}}_\Omega\right\} - \Re\left\{\boldsymbol{W}\operatorname{vec}\{\boldsymbol{\Theta}\boldsymbol{\Phi}\}\right\}\right\|_2^2 \\ &= \left\|\Re\left\{\boldsymbol{W}\operatorname{vec}\hat{\boldsymbol{\Xi}}_\Omega\right\} - \Re\left\{\boldsymbol{W}\left(\boldsymbol{\Phi}^\mathrm{T}\otimes\mathbf{I}_{n_\mathrm{S}}\right)\right\}\operatorname{vec}\boldsymbol{\Theta}\right\|_2^2 \\ &= \left\|\Re\left\{\boldsymbol{W}\operatorname{vec}\hat{\boldsymbol{\Xi}}_\Omega\right\} - \Re\left\{\boldsymbol{W}\tilde{\boldsymbol{\Phi}}\right\}\operatorname{vec}\boldsymbol{\Theta}\right\|_2^2. \end{aligned} \tag{D.25}$$

The last equation represents the squared error norm of the system of linear equations $\Re\{\boldsymbol{W}\tilde{\boldsymbol{\Phi}}\}\operatorname{vec}\boldsymbol{\Theta} = \Re\{\boldsymbol{W}\operatorname{vec}\hat{\boldsymbol{\Xi}}_\Omega\}$. Consequently, the solution is given by

$$\operatorname{vec}\boldsymbol{\Theta} = \Re\left\{\boldsymbol{W}\tilde{\boldsymbol{\Phi}}\right\}^+\Re\left\{\boldsymbol{W}\operatorname{vec}\hat{\boldsymbol{\Xi}}_\Omega\right\}. \tag{D.26}$$

The problem with the above solution is that the regression matrix $\Re\{\boldsymbol{W}\tilde{\boldsymbol{\Phi}}\}$ is generally not of full column rank, which implies that the parameters $\boldsymbol{\Theta}$ cannot be uniquely recovered from (D.26). To see this, the structures of the matrices $\boldsymbol{W}$ and $\tilde{\boldsymbol{\Phi}}$ are considered in more detail.
The weighting matrix $\boldsymbol{W} = \bigoplus_{n=1}^N \boldsymbol{W}_n$ is block-diagonal with N blocks of dimension $M \times n_\mathrm{S}^2$. The matrix $\tilde{\boldsymbol{\Phi}} = (\boldsymbol{\Phi}^\mathrm{T}\otimes\mathbf{I})$ is banded,

$$\tilde{\boldsymbol{\Phi}} = \left(\begin{array}{ccc|c|ccc} \hat{\boldsymbol{\Xi}}^\mathrm{T}(z_1)z_1^{-1}\otimes\mathbf{I} & \dots & \hat{\boldsymbol{\Xi}}^\mathrm{T}(z_1)z_1^{-p}\otimes\mathbf{I} & \mathbf{I}\otimes\mathbf{I} & \mathbf{I}\otimes\mathbf{I}z_1^{-1} & \dots & \mathbf{I}\otimes\mathbf{I}z_1^{-p} \\ \vdots & & \vdots & \vdots & \vdots & & \vdots \\ \hat{\boldsymbol{\Xi}}^\mathrm{T}(z_N)z_N^{-1}\otimes\mathbf{I} & \dots & \hat{\boldsymbol{\Xi}}^\mathrm{T}(z_N)z_N^{-p}\otimes\mathbf{I} & \mathbf{I}\otimes\mathbf{I} & \mathbf{I}\otimes\mathbf{I}z_N^{-1} & \dots & \mathbf{I}\otimes\mathbf{I}z_N^{-p} \end{array}\right). \tag{D.27}$$

It follows that the columns $pn_\mathrm{S}^2 + 1$ to $(p+1)n_\mathrm{S}^2$ of $\boldsymbol{W}\tilde{\boldsymbol{\Phi}}$, indicated by the vertical lines in the above equation, are given by the blocks of $\boldsymbol{W}$ itself,

$$\left(\boldsymbol{W}\tilde{\boldsymbol{\Phi}}\right)^{(:,pn_\mathrm{S}^2+1:(p+1)n_\mathrm{S}^2)} = \begin{pmatrix} \boldsymbol{W}_1 \\ \vdots \\ \boldsymbol{W}_N \end{pmatrix}. \tag{D.28}$$

The elements $\boldsymbol{W}_n$ of $\boldsymbol{W}$ where defined in (5.61) as $\boldsymbol{W}_n = \boldsymbol{T}(\boldsymbol{Q}^\mathrm{T}(\mathrm{j}\omega_n)\otimes\boldsymbol{Q}^\mathrm{H}(\mathrm{j}\omega_n))$ with some binary matrix $\boldsymbol{T}$. It can be shown by straightforward calculation that this formulation is equivalent to $\boldsymbol{W}_n = ((\boldsymbol{W}_n^1)^{\mathrm{T}}, \dots, (\boldsymbol{W}_n^M)^{\mathrm{T}})^{\mathrm{T}}$ where each row $\boldsymbol{W}_n^i$ is given by

$$\begin{aligned}\boldsymbol{W}_n^i &= \left(\boldsymbol{Q}^{(1,i)}(\mathrm{j}\omega_n)\left(\boldsymbol{Q}^{(:,i)}(\mathrm{j}\omega_n)\right)^{\mathrm{H}}, \dots, \boldsymbol{Q}^{(n_{\mathrm{S}},i)}(\mathrm{j}\omega_n)\left(\boldsymbol{Q}^{(:,i)}(\mathrm{j}\omega_n)\right)^{\mathrm{H}}\right)\\ &= \left(\boldsymbol{Q}^{(1,i)}\left(\boldsymbol{Q}^{(1,i)}\right)^*, \dots, \boldsymbol{Q}^{(1,i)}\left(\boldsymbol{Q}^{(n_{\mathrm{S}},i)}\right)^*, \dots, \boldsymbol{Q}^{(n_{\mathrm{S}},i)}\left(\boldsymbol{Q}^{(1,i)}\right)^*, \dots, \boldsymbol{Q}^{(n_{\mathrm{S}},i)}\left(\boldsymbol{Q}^{(n_{\mathrm{S}},i)}\right)^*\right).\end{aligned} \tag{D.29}$$

Thus, $\boldsymbol{W}_n^i$ usually contains n_{S}^2 different complex numbers and consequently, (D.28) can be expected to be of full column rank. However, the solution (D.26) uses only the real part of $\boldsymbol{W}\tilde{\boldsymbol{\Phi}}$ which also means considering only the real parts of (D.28) and (D.29). Taking the real part of the row vector $\boldsymbol{W}_n^i$ leads to repeated entries, since for example $\Re\{\boldsymbol{Q}^{(1,i)}\left(\boldsymbol{Q}^{(2,i)}\right)^*\}$ is identical to $\Re\{\boldsymbol{Q}^{(2,i)}\left(\boldsymbol{Q}^{(1,i)}\right)^*\}$, and so on. It is easy to see that $\Re\{\boldsymbol{W}_n^i\}$ contains only $\sum_{l=1}^{n_{\mathrm{S}}} l = (n_{\mathrm{S}}(n_{\mathrm{S}}+1))/2$ structurally different entries, and that the repeated entries appear at the same positions for every $i = 1, \dots, M$. This holds for every block $\boldsymbol{W}_n, n = 1, \dots, N$. Finally, it becomes clear that the submatrix (D.28) suffers from a structural loss of row rank of the order $n_{\mathrm{S}} - (n_{\mathrm{S}}(n_{\mathrm{S}}+1))/2$, and so does $\boldsymbol{W}\tilde{\boldsymbol{\Phi}}$.

In order to cope with this problem, it is proposed to look instead for the best real-valued solution to the problem $\min J' = \|\boldsymbol{W}\boldsymbol{e}\|_2^2$. This leads to the system of equations $\boldsymbol{W}\tilde{\boldsymbol{\Phi}}\operatorname{vec}\hat{\boldsymbol{\Theta}} = \boldsymbol{W}\operatorname{vec}\boldsymbol{\Xi}_{\Omega}$. The best real-valued solution to this problem is given by

$$\operatorname{vec}\boldsymbol{\Theta} = \left[\left(\boldsymbol{W}\tilde{\boldsymbol{\Phi}}\right)_{\mathrm{re}}\right]^+ \left(\boldsymbol{W}\operatorname{vec}\hat{\boldsymbol{\Xi}}_{\Omega}\right)_{\mathrm{re}}, \tag{D.30}$$

which replaces (D.26) to generate initial values for the optimization process. The problem of minimizing $\|\Re\{\boldsymbol{W}\boldsymbol{e}\}\|_2^2$ can then be iteratively solved by algorithms suitable for nonlinear least-squares problems, like trust-region methods, see for example [49].

Most optimization techniques employ some kind of information on the derivative of the cost function with respect to the optimization parameters, and this information is usually represented by the Jacobian matrix. The Jacobian may generally be approximated by finite-difference calculations. However, providing analytical expressions for the Jacobian both increases accuracy and speeds up computation. Providing the optimization algorithm with a user-supplied Jacobian matrix is therefore very desirable.

The optimization algorithm [49] is geared towards solving nonlinear least-squares problems of the type $\min_{\boldsymbol{x}} J = \|\boldsymbol{f}(\boldsymbol{x})\|_2^2$ and employs the first-order derivative of the vector-valued function $\boldsymbol{f}$ with respect to the optimization variables $\boldsymbol{x}$. For the case at hand, we have $\boldsymbol{f} = \Re\{\boldsymbol{W}\boldsymbol{e}(\boldsymbol{\Theta})\}$ and $\boldsymbol{x} = \operatorname{vec}\boldsymbol{\Theta}$. The required Jacobian matrix ${}^{\partial \boldsymbol{f}}/_{\partial \boldsymbol{x}}$ shall now be provided. To this end, the following general relationships for matrix derivatives will prove useful.

$$\begin{aligned}\frac{\partial \boldsymbol{A}(\boldsymbol{X})\boldsymbol{B}}{\partial \boldsymbol{X}} &= \left(\boldsymbol{B}^{\mathrm{T}} \otimes \mathbf{I}_k\right)\frac{\partial \boldsymbol{A}(\boldsymbol{X})}{\partial \boldsymbol{X}},\\ \frac{\partial \boldsymbol{A}\boldsymbol{B}(\boldsymbol{X})}{\partial \boldsymbol{X}} &= \left(\mathbf{I}_m \otimes \boldsymbol{A}\right)\frac{\partial \boldsymbol{B}(\boldsymbol{X})}{\partial \boldsymbol{X}},\end{aligned} \tag{D.31}$$

where $\boldsymbol{A} \in \mathbb{C}^{k\times l}$, and $\boldsymbol{B} \in \mathbb{C}^{l\times m}$. In the above equations, the derivative of a matrix with respect to another matrix is interpreted as $\frac{\partial \boldsymbol{A}(\boldsymbol{X})}{\partial \boldsymbol{X}} := \frac{\partial \operatorname{vec} \boldsymbol{A}(\boldsymbol{X})}{\partial \operatorname{vec} \boldsymbol{X}}$. Another useful relationship is

$$\frac{\partial \boldsymbol{C}^{-1}}{\partial \boldsymbol{C}} = -\left(\boldsymbol{C}^{\mathrm{T}} \otimes \boldsymbol{C}\right)^{-1} \tag{D.32}$$

for some regular $\boldsymbol{C}$.

Having these results in mind, one can calculate the Jacobian matrix ${}^{\partial \boldsymbol{f}}/_{\partial \boldsymbol{x}}$ as follows. Firstly, the vector function whose norm shall be minimized is rewritten as

$$\begin{aligned} \boldsymbol{f} &= \Re\left\{\boldsymbol{W}\boldsymbol{e}\right\} \\ &= \Re\left\{\boldsymbol{W} \operatorname{vec} \Delta \boldsymbol{\Xi}_{\Omega}\right\} \\ &= \frac{1}{2}\left(\boldsymbol{W} \operatorname{vec} \Delta \boldsymbol{\Xi}_{\Omega} + \boldsymbol{W}^{*} \operatorname{vec} \boldsymbol{\Xi}_{\Omega}^{*}\right) \\ &= \frac{1}{2}\left(\tilde{\boldsymbol{f}} + \tilde{\boldsymbol{f}}^{*}\right), \end{aligned} \tag{D.33}$$

and consequently

$$\frac{\partial \boldsymbol{f}}{\partial \boldsymbol{x}} = \frac{1}{2}\left(\frac{\partial \tilde{\boldsymbol{f}}}{\partial \boldsymbol{x}} + \frac{\partial \tilde{\boldsymbol{f}}}{\partial \boldsymbol{x}}^{*}\right). \tag{D.34}$$

We further have

$$\begin{aligned} \frac{\partial \tilde{\boldsymbol{f}}}{\partial \boldsymbol{x}} &= \left(1 \otimes \boldsymbol{W}\right) \frac{\partial \operatorname{vec} \Delta \boldsymbol{\Xi}_{\Omega}}{\partial \boldsymbol{x}} \\ &= \boldsymbol{W} \frac{\partial(\operatorname{vec} \hat{\boldsymbol{\Xi}}_{\Omega} - \operatorname{vec} \boldsymbol{\Xi}_{\Omega})}{\partial \boldsymbol{x}} \\ &= -\boldsymbol{W} \frac{\partial \operatorname{vec} \boldsymbol{\Xi}_{\Omega}}{\partial \boldsymbol{x}}. \end{aligned} \tag{D.35}$$

The derivative in the last equation can be alternatively expressed as

$$\frac{\partial \operatorname{vec} \boldsymbol{\Xi}_{\Omega}}{\partial \boldsymbol{x}} = \frac{\partial \operatorname{vec} \boldsymbol{\Xi}_{\Omega}}{\partial \operatorname{vec} \boldsymbol{\Theta}} = \frac{\partial \boldsymbol{\Xi}_{\Omega}}{\partial \boldsymbol{\Theta}} = \frac{\partial(\boldsymbol{\Xi}(z_1), \ldots, \boldsymbol{\Xi}(z_N))}{\partial(\boldsymbol{\Theta}_Q, \boldsymbol{\Theta}_R)}, \tag{D.36}$$

where the parameter matrix $\boldsymbol{\Theta}$ has been partitioned into $\boldsymbol{\Theta}_Q := (-\boldsymbol{Q}_1, \ldots, -\boldsymbol{Q}_p)$ and $\boldsymbol{\Theta}_R := (\boldsymbol{R}_0, \ldots, \boldsymbol{R}_p)$. Consequently, the derivative matrix is partitioned as

$$\frac{\partial \boldsymbol{\Xi}_{\Omega}}{\partial \boldsymbol{\Theta}} = \begin{pmatrix} \dfrac{\partial \boldsymbol{\Xi}(z_1)}{\partial \boldsymbol{\Theta}_Q} & \dfrac{\partial \boldsymbol{\Xi}(z_1)}{\partial \boldsymbol{\Theta}_R} \\ \vdots & \vdots \\ \dfrac{\partial \boldsymbol{\Xi}(z_N)}{\partial \boldsymbol{\Theta}_Q} & \dfrac{\partial \boldsymbol{\Xi}(z_N)}{\partial \boldsymbol{\Theta}_R} \end{pmatrix}. \tag{D.37}$$

We first calculate the blocks $\frac{\partial \boldsymbol{\Xi}(z_i)}{\partial \boldsymbol{\Theta}_Q} = \frac{\partial \boldsymbol{Q}^{-1}(z_i)\boldsymbol{R}(z_i)}{\partial \boldsymbol{\Theta}_Q}, i = 1, \dots, N$. Considering (D.31) and (D.32), one immediately has

$$\begin{aligned}
\frac{\partial \boldsymbol{\Xi}(z_i)}{\partial \boldsymbol{\Theta}_Q} &= \underbrace{\left(\boldsymbol{R}^{\mathrm{T}}(z_i) \otimes \mathbf{I}_{n_{\mathrm{S}}}\right)}_{=:\tilde{\boldsymbol{R}}(z_i)} \frac{\partial \boldsymbol{Q}^{-1}(z_i)}{\partial \boldsymbol{\Theta}_Q} \\
&= -\tilde{\boldsymbol{R}}(z_i)\Big(\underbrace{\boldsymbol{Q}^{\mathrm{T}}(z_i) \otimes \boldsymbol{Q}(z_i)}_{=:\hat{\boldsymbol{Q}}(z_i)}\Big)^{-1} \frac{\partial \boldsymbol{Q}(z_i)}{\partial \boldsymbol{\Theta}_Q} \\
&= -\tilde{\boldsymbol{R}}(z_i)\hat{\boldsymbol{Q}}^{-1}(z_i) \frac{\partial(\mathbf{I} + \boldsymbol{Q}_1 z_i^{-1} + \dots + \boldsymbol{Q}_p z_i^{-p})}{\partial(-\boldsymbol{Q}_1, \dots, -\boldsymbol{Q}_p)} \\
&= \tilde{\boldsymbol{R}}(z_i)\hat{\boldsymbol{Q}}^{-1}(z_i)\left(\mathbf{I}z_i^{-1}, \dots, \mathbf{I}z_i^{-p}\right).
\end{aligned} \tag{D.38}$$

For the blocks $\frac{\partial \boldsymbol{\Xi}(z_i)}{\partial \boldsymbol{\Theta}_R}$, one gets

$$\begin{aligned}
\frac{\partial \boldsymbol{\Xi}(z_i)}{\partial \boldsymbol{\Theta}_R} &= \left(\mathbf{I}_{n_{\mathrm{S}}} \otimes \boldsymbol{Q}^{-1}(z_i)\right) \frac{\partial \boldsymbol{R}(z_i)}{\partial \boldsymbol{\Theta}_R} \\
&= \Big(\underbrace{\mathbf{I}_{n_{\mathrm{S}}} \otimes \boldsymbol{Q}(z_i)}_{=:\tilde{\boldsymbol{Q}}(z_i)}\Big)^{-1} \frac{\partial \boldsymbol{R}(z_i)}{\partial \boldsymbol{\Theta}_R} \\
&= \tilde{\boldsymbol{Q}}^{-1}(z_i) \frac{\partial(\boldsymbol{R}_0 + \boldsymbol{R}_1 z_i^{-1} + \dots + \boldsymbol{R}_p z_i^{-p})}{\partial(\boldsymbol{R}_0, \dots, \boldsymbol{R}_p)} \\
&= \tilde{\boldsymbol{Q}}^{-1}(z_i)\left(\mathbf{I}, \mathbf{I}z_i^{-1}, \dots, \mathbf{I}z_i^{-p}\right).
\end{aligned} \tag{D.39}$$

Using the expressions (D.38) and (D.39) in (D.37), the partial derivative $\frac{\partial \tilde{f}}{\boldsymbol{x}}$ can be computed. The derivative $\frac{\partial \tilde{f}^*}{\partial \boldsymbol{x}}$ can be easily stated, since it is clear that (D.34) is real. Thus, one has

$$\frac{\partial \tilde{f}^*}{\partial \boldsymbol{x}} = \left(\frac{\partial \tilde{f}}{\partial \boldsymbol{x}}\right)^* \overset{\text{(D.34)}}{\Longrightarrow} \frac{\partial f}{\partial \boldsymbol{x}} = \Re\left\{\frac{\partial \tilde{f}}{\partial \boldsymbol{x}}\right\}. \tag{D.40}$$

Once the final parameters of the ARX model $\boldsymbol{\Xi}(z) = \boldsymbol{Q}(z)^{-1}\boldsymbol{R}(z)$ are found, the model can be converted to into state space form either by the FD-ERA algorithm or by directly composing the state space matrices from the parameter matrices $\boldsymbol{Q}_i$ and $\boldsymbol{R}_i$ in observable canonical form. Both methods are described in full detail in [113]. The canonical state space form obtained from a pth order ARX model with n_{S} outputs has order $p \cdot n_{\mathrm{S}}$, but this may not be a minimal realization.

D.8 Modal Filter Design

As outlined in Sec. 5.6.2, there are two common methods for calculating the modal filter matrix $\boldsymbol{T} \in \mathbb{R}^{n_{\mathrm{S}} \times n_{\mathrm{sensors}}}$. The first method simply takes the elements of $\boldsymbol{T}$ as the values of the n_{S} eigenfunctions at the n_{sensors} sensor positions. The problem with modal filter design in this case is that the eigenfunctions of the undamped plate-cavity system can be calculated (see Sec. 2.5), but these are not equal to the mode shapes of the system with damping, because the coupled system cannot be described by Caughey damping. The mode shapes of the coupled system are therefore complex-valued. Strictly speaking, a perfect static modal filter cannot be designed for the acoustic demonstrator.

Simulations as well as experiments show that a second method for modal filter design gives better results than the first one in this case. The idea is to optimize the modal filter weights such that the FRFs from some given inputs to the filter outputs closely match desired FRFs. The desired reference FRFs can be constructed solely from knowledge of the damping ratios of the conjugate-complex pole pairs and their corresponding eigenfrequencies. In case that acceleration sensors are used, a reference FRF for each mode is given as the frequency response of a second order system of the form

$$G_{\mathrm{ref},i}(z) = \mathcal{Z}_{T_\mathrm{s}} \left\{ \frac{K_i s^2}{\frac{1}{\omega_i^2} s^2 + \frac{2D_i}{\omega_i} s + 1} \right\}, \qquad i = 1, \ldots, n_\mathrm{S}, \tag{D.41}$$

where D_i and ω_i are the damping ratio and eigenfrequency of the ith mode. The $\mathcal{Z}$ operator symbolizes bilinear transform to the discrete time domain with sampling rate T_s. The gains of the modal filters at infinity may be adjusted by the parameters K_i. Furthermore, let the transfer functions from the structural inputs $\boldsymbol{u}$ to the set of sensors $\boldsymbol{y}_\mathrm{S}$ be given by $\boldsymbol{H}$, i.e. $\boldsymbol{y}_\mathrm{S}(z) = \boldsymbol{H}(z)\boldsymbol{u}(z)$.

Now, consider the case when there is only one input. The goal shall be to minimize for each filter $\|\boldsymbol{T}_i \boldsymbol{H}_\Omega - \boldsymbol{g}_{i,\Omega}\|_2^2$, where $\boldsymbol{T}_i$ is the ith row of $\boldsymbol{T}$,

$$\boldsymbol{H}_\Omega = \left(\boldsymbol{H}(\mathrm{e}^{\mathrm{j}\omega_1}), \ldots, \boldsymbol{H}(\mathrm{e}^{\mathrm{j}\omega_N})\right), \qquad \text{and} \qquad \boldsymbol{g}_{i,\Omega} = \left(G_{\mathrm{ref},i}(\mathrm{e}^{\mathrm{j}\omega_1}), \ldots, G_{\mathrm{ref},i}(\mathrm{e}^{\mathrm{j}\omega_N})\right). \tag{D.42}$$

The number of relevant frequencies N must not be less than the number of sensors, since $\boldsymbol{H}_\Omega$ is required to be of full row rank for a unique solution. Then, this is a standard least-squares problem, which may be solved immediately for the best real-valued solution by $\boldsymbol{T}_i^\mathrm{T} = [(\boldsymbol{H}_\Omega^\mathrm{T})_\mathrm{re}]^+ (\boldsymbol{g}_{i,\Omega}^\mathrm{T})_\mathrm{re}$ and is treated in more detail in [155]. Thus, in case of only one input, the gains K_i may be freely assigned for each filter.

In case of several inputs, the reference transfer functions from every input to the output of the ith modal filter are also given by D.41, but this time, only one gain may be freely assigned and the gains for all other inputs are implicitly determined but unknown. In order to cope with this problem, it is proposed to modify the procedure presented in [155] as follows. Firstly, the matrix $\boldsymbol{H}_\Omega$ and the vector $\boldsymbol{g}_{i,\Omega}$ are redefined for n_u inputs,

$$\begin{aligned} \boldsymbol{H}_\Omega &= \left(\boldsymbol{H}_1(\mathrm{e}^{\mathrm{j}\omega_1}), \ldots, \boldsymbol{H}_1(\mathrm{e}^{\mathrm{j}\omega_N}), \boldsymbol{H}_2(\mathrm{e}^{\mathrm{j}\omega_1}), \ldots, \boldsymbol{H}_2(\mathrm{e}^{\mathrm{j}\omega_N}), \ldots, \boldsymbol{H}_{n_u}(\mathrm{e}^{\mathrm{j}\omega_1}), \ldots, \boldsymbol{H}_{n_u}(\mathrm{e}^{\mathrm{j}\omega_N})\right) \\ &= (\boldsymbol{H}_{1,\Omega}, \boldsymbol{H}_{2,\Omega}, \ldots, \boldsymbol{H}_{n_u,\Omega}), \end{aligned} \tag{D.43}$$

where $\boldsymbol{H}_l$ is the lth column of the FRF matrix $\boldsymbol{H}$, and

$$\begin{aligned} \boldsymbol{g}_{i,\Omega} &= \left(G_{\mathrm{ref},i}(\mathrm{e}^{\mathrm{j}\omega_1}), \ldots, G_{\mathrm{ref},i}(\mathrm{e}^{\mathrm{j}\omega_N}), \kappa_{i,1} G_{\mathrm{ref},i}(\mathrm{e}^{\mathrm{j}\omega_1}), \ldots, \kappa_{i,1} G_{\mathrm{ref},i}(\mathrm{e}^{\mathrm{j}\omega_N}), \right. \\ &\qquad \left. \ldots, \kappa_{i,n_u-1} G_{\mathrm{ref},i}(\mathrm{e}^{\mathrm{j}\omega_1}), \ldots, \kappa_{i,n_u-1} G_{\mathrm{ref},i}(\mathrm{e}^{\mathrm{j}\omega_N})\right) \\ &= (\boldsymbol{g}_{i,1,\Omega}, \kappa_{i,1}\boldsymbol{g}_{i,1,\Omega}, \ldots, \kappa_{i,n_u-1}\boldsymbol{g}_{i,1,\Omega}) \\ &= (\boldsymbol{g}_{i,1,\Omega}, \boldsymbol{g}_{i,2,\Omega}, \ldots, \boldsymbol{g}_{i,n_u,\Omega}). \end{aligned} \tag{D.44}$$

The $n_u - 1$ unknown constants $\kappa_{i,l}$ adjust the gains of the reference functions for the inputs $2, \ldots, n_\mathrm{u}$ for mode i. The optimization problem is now to minimize the error of the following system of equations,

$$\begin{aligned} \boldsymbol{T}_i \boldsymbol{H}_{1,\Omega} &= \boldsymbol{g}_{i,1,\Omega}, \\ \boldsymbol{T}_i \boldsymbol{H}_{2,\Omega} &= \kappa_{i,1} \boldsymbol{g}_{i,1,\Omega}, \\ &\vdots \\ \boldsymbol{T}_i \boldsymbol{H}_{n_u,\Omega} &= \kappa_{i,n_u-1} \boldsymbol{g}_{i,1,\Omega}. \end{aligned} \tag{D.45}$$

The unknown constants $\kappa_{i,l}$ are now included in the vector of optimization variables by rearranging (D.45) as

$$\underbrace{(\boldsymbol{T}_i, \kappa_{i,1}, \kappa_{i,2}, \ldots, \kappa_{i,n_u-1})}_{=:\tilde{\boldsymbol{T}}_i} \underbrace{\begin{pmatrix} \boldsymbol{H}_{1,\Omega} & \boldsymbol{H}_{2,\Omega} & \boldsymbol{H}_{3,\Omega} & \cdots & \boldsymbol{H}_{n_u,\Omega} \\ \boldsymbol{0} & -\boldsymbol{g}_{i,1,\Omega} & \boldsymbol{0} & \cdots & \boldsymbol{0} \\ \vdots & & \ddots & & \vdots \\ \boldsymbol{0} & \cdots & \boldsymbol{0} & -\boldsymbol{g}_{i,1,\Omega} & \boldsymbol{0} \\ \boldsymbol{0} & \cdots & \cdots & \boldsymbol{0} & -\boldsymbol{g}_{i,1,\Omega} \end{pmatrix}}_{=:\tilde{\boldsymbol{H}}_\Omega} = \underbrace{(\boldsymbol{g}_{i,1,\Omega}, \boldsymbol{0}, \boldsymbol{0}, \ldots, \boldsymbol{0})}_{=:\tilde{\boldsymbol{g}}_{i,\Omega}}. \tag{D.46}$$

In case that $\tilde{\boldsymbol{H}}_\Omega$ is of full row rank, the minimum real-valued 2-norm solution for the above problem is given for each $i = 1, \ldots, n_\mathrm{S}$ by $\tilde{\boldsymbol{T}}_i^\mathrm{T} = [(\tilde{\boldsymbol{H}}_\Omega^\mathrm{T})_\mathrm{re}]^+ (\tilde{\boldsymbol{g}}_{i,\Omega}^\mathrm{T})_\mathrm{re}$. The sought modal filter coefficients are given by the first n_sensors elements of $\tilde{\boldsymbol{T}}_i$.

Before the transformation matrix $\boldsymbol{T}$ can be computed by the above equations, the positions of the sensors must be selected. The positioning of the 13 accelerometers on the plate of the acoustic demonstrator is done such that they are preferably placed at the nodes of mode shape functions which are adjacent to those to be detected. Additional degrees of freedom can be used to minimize the condition number of $\boldsymbol{T}$, which reduces the sensitivity of the modal filters to errors in sensor positioning. The selected design for the model of the acoustic demonstrator achieves a condition number very close to one. One may consult [107] or [174] for further details.

D.9 Modeling of Acoustically Induced Vibration

The theoretical model of the acoustic demonstrator which was derived in Ch. 2 allows for the plate to be excited by arbitrary pressure distributions. Acoustically induced vibration by a source outside the cavity can be included in the model by finding its equivalent surface pressure distribution. This is the focus of this appendix. The presentation follows closely the one presented in Chapter 6 of [70].

Momentarily, the structure is assumed to be rigid. Given an acoustic source, the complex incident pressure distribution which would be measured on the structural surface S if the structure was removed shall be denoted by $\tilde{p}_i(\boldsymbol{x}, \omega), \boldsymbol{x} \in S$. The associated normal particle velocity is denoted by $\tilde{v}_i(\boldsymbol{x}, \omega)$. These pressure and velocity distributions are altered by the presence of the structure.

More specifically, the normal velocity on S must then be zero. This can be thought of as an imaginary surface moving with velocity $\dot{\tilde{w}}(\boldsymbol{x},\omega) = -\tilde{v}_i(\boldsymbol{x},\omega)$. The general expression for the surface pressure caused by structural velocity shall be given by the linear relation

$$\tilde{p}_\mathrm{S}(\boldsymbol{x},\omega) = \iint_S Z_\mathrm{rad}(\boldsymbol{x},\boldsymbol{x}_\mathrm{S},\omega)\dot{\tilde{w}}(\boldsymbol{x},\omega)\,\mathrm{d}S, \tag{D.47}$$

where Z_rad denotes some distributed radiation impedance. It is actually given by Green's function $G(\boldsymbol{x},\boldsymbol{x}_\mathrm{S},\omega)$, where $\boldsymbol{x} \in S$, compare (5.1). The pressure distribution on S in the presence of the rigid structure, the so-called blocked pressure, is then given by

$$\tilde{p}_\mathrm{bl} = \tilde{p}_i + \tilde{p}_\mathrm{S} = \tilde{p}_i - \iint_S Z_\mathrm{rad}\tilde{v}_i\,\mathrm{d}S. \tag{D.48}$$

In the special case of a plane wave incident on a baffled structure, one has $\tilde{p}_\mathrm{bl} = 2\tilde{p}_i$, see [70]. Now, the sound field of the rigid structure is superimposed with that of the flexible structure. This implies that an additional surface pressure component appears which is caused by the structural movement,

$$\tilde{p} = \tilde{p}_\mathrm{bl} + \tilde{p}_\mathrm{rad} = \tilde{p}_\mathrm{bl} + \iint_S Z_\mathrm{rad}\dot{\tilde{w}}\,\mathrm{d}S. \tag{D.49}$$

The structural velocity can in turn be calculated from the distributed structural impedance Z_S and the total surface pressure,

$$\dot{\tilde{w}}(\boldsymbol{x},\omega) = \iint_S Z_\mathrm{S}^{-1}(\boldsymbol{x},\boldsymbol{x}_\mathrm{S},\omega)\tilde{p}(\boldsymbol{x},\omega)\,\mathrm{d}S \quad \Leftrightarrow \quad \tilde{p}(\boldsymbol{x},\omega) = \iint_S Z_\mathrm{S}(\boldsymbol{x},\boldsymbol{x}_\mathrm{S},\omega)\dot{\tilde{w}}(\boldsymbol{x},\omega)\,\mathrm{d}S, \tag{D.50}$$

where Z_S^{-1} denotes the structural admittance function. It is assumed in the above equation that the mapping on the left hand side is bijective such that the inverse mapping exists[2]. It is further noted that Z_S is determined solely by structural properties, whereas Z_rad represents the properties of the acoustic environment. Using the right hand side of (D.50) in (D.49) results in

$$\iint_S (Z_\mathrm{S} - Z_\mathrm{rad})\dot{\tilde{w}}\,\mathrm{d}S = \tilde{p}_\mathrm{bl}, \tag{D.51}$$

from which $\dot{\tilde{w}}$ can be determined. The sought quantity $\tilde{p}$, which replaces the acoustical excitation by an equivalent pressure distribution, is then obtained by using the result in the right side of (D.50).

The considered case in Sec. 5.10 is the excitation of the baffled plate of the acoustic demonstrator by an incident plane wave. Since the plate is assumed to be set in an infinite baffle, it holds $\tilde{p}_\mathrm{bl}(\boldsymbol{x},\omega) = 2\tilde{p}_i(\boldsymbol{x},\omega)$. Furthermore, one usually has for engineering structures vibrating in air $Z_\mathrm{S} \gg Z_\mathrm{rad}$, which implies together with equation (D.51) and the right side of (D.50) that $\tilde{p} \approx \tilde{p}_\mathrm{bl}$. Thus, the acoustical excitation by a plane wave of complex amplitude $\tilde{p}_i(\boldsymbol{x},\omega)$ may be approximated by an equivalent plate surface pressure $\tilde{p}(\boldsymbol{x},\omega) = 2\tilde{p}_i(\boldsymbol{x},\omega)$. In case that the plane wave is normally incident on the structure, the pressure distribution is uniform, i.e. $\tilde{p}(\boldsymbol{x},\omega) \approx 2\tilde{p}_i(\omega)\,\forall \boldsymbol{x} \in S$.

---

[2] If this is not the case, one may insert the left side of (D.50) into (D.49) to get an implicit expression for $\tilde{p}$.

Bibliography

[1] Agüero, J. C.; Goodwin, G. C.; van den Hof, P. M. J. A virtual closed loop method for closed loop identification. *Automatica*, 47(8):1626–1637, 2011.

[2] Ahn, Hyo-Sung. Exact Maximum Singular Value of a Complex Interval Matrix. *IEEE Transactions on Automatic Control*, 53(9):2165–2170, 2008.

[3] Al-Bassyiouni, M. *Active Control of Sound Transmission into Three-Dimensional Enclosures*. PhD thesis, University of Maryland, College Park, 2004.

[4] Albertos, P.; Sala, A. *Iterative Identification and Control: Advances in Theory and Applications*. Springer, London, 2002.

[5] Alvin, K. F.; Park, K. C. Second-Order Structural Identification Procedure via State-Space-Based System Identification. *AIAA Journal*, 32(2):397–406, 1994.

[6] Alvin, K. F.; Peterson, L. D.; Park, K. C. Extraction of Normal Modes and Full Modal Damping from Complex Modal Parameters. *AIAA Journal*, 35(7):1187–1194, 1997.

[7] Andersen, H. H.; Hojbjerre, M.; Sorensen, D.; Erikson, P. S. *Linear and graphical models for the multivariate complex normal distribution*, volume 101 of *Lecture Notes in Statistics*. Springer, 1995.

[8] Antony, J. *Design of experiments for engineers and scientists*. Butterworth-Heinemann, Amsterdam, 2010.

[9] Balas, M. J. Active Control of Flexible Systems. *Journal of Optimization Theory and Applications*, 25(3):415–436, 1978.

[10] Balas, M. J. Direct Velocity Feedback Control of Large Space Structures. *Journal of Guidance and Control*, 2(3):252–255, 1979.

[11] Balas, M. J. Distributed Parameter Feedback Control with Finite Dimensional Controllers: Recent Results. In *IEEE International Conference on Circuits and Computers (ICCC), Port Chester, NY*, pages 429–433, 1980.

[12] Balas, M. J. Finite Element Models and Feedback Control of Flexible Aerospace Structures. In *Joint Automatic Control Conference, San Francisco, CA*, 1980.

[13] Banks, H. T.; Smith, R. C.; Wang, Y. *Smart Material Structures: Modeling, Estimation and Control*. Research in Applied Mathematics. Wiley, Chichester, 1996.

[14] Barenthin, M.; Bombois, X.; Hjalmarsson, H.; Scorletti, G. Identification for control of multivariable systems: Controller validation and experiment design via LMIs. *Automatica*, 44:3070–3078, 2008.

[15] Baumann, W. T. Active suppression of acoustic radiation from impulsively excited structures. *Journal of the Acoustical Society of America*, 90(6):3202–3208, 1991.

[16] Baumann, W. T. Active structural acoustic control of broadband disturbances. *Journal of the Acoustical Society of America*, 92(4):1998–2005, 1992.

[17] Bayard, D. S. Statistical Plant Set Estimation Using Schroeder-Phased Multisinusoidal Input Design. In *American Control Conference, Chicago, IL*, pages 2988–2995, 1992.

[18] Bayard, D. S.; Chiang, R. Y. A Frequency Domain Approach to Identification, Uncertainty Characterization and Robust Control Design. In *32nd Conference on Decision and Control. San Antonio, TX*, pages 2266–2271, 1993.

[19] Bayard, D. S.; Chiang, R. Y. Identification, Uncertainty Characterization and Robust Control Synthesis Applied to Large Flexible Structures Control. *International Journal of Robust and Nonlinear Control*, 8:97–112, 1998.

[20] Bayard, D. S.; Yam, Y. Frequency Domain Identification for Robust Control Design. In Smith, R. S., editor, *The modeling of uncertainty in control systems*, volume 192 of *Lecture Notes in Control and Information Sciences*, pages 303–335. Springer, Berlin, 1994.

[21] Bazanella, A. S.; Gevers, M.; Mišković, L. Closed-loop identification of MIMO systems: a new look at identifiability and experiment design. *European Journal of Control*, 16(3):228–239, 2010.

[22] Benninger, N. F. *Analyse und Synthese linearer Systeme mit Hilfe neuer Strukturmaße*. PhD thesis, Technische Hochschule Karlsruhe, Karlsruhe, 1987.

[23] Berkhoff, A. P. Sensor scheme design for active structural acoustic control. *Journal of the Acoustical Society of America*, 108(3):1037–1045, 2000.

[24] Berkhoff, A. P. Piezoelectric Sensor Configuration for Active Structural Acoustic Control. *Journal of Sound and Vibration*, 246(1):175–183, 2001.

[25] Berkhoff, A. P. Broadband radiation modes: Estimation and active control. *Journal of the Acoustical Society of America*, 111(3):1295–1305, 2002.

[26] Berkhoff, A. P. Identification and Control of Acoustic Radiation Modes. In *Proceedings of Mechatronics, Twente, Netherlands*, pages 1397–1406, 2002.

[27] Berkhoff, A. P. A technique for improved stability of adaptive feedforward controllers without detailed uncertainty measurements. *Smart Materials and Structures*, 21(6):1–12, 2012.

[28] Berkhoff, A. P.; Sarajlic, E.; Cazzolato, B. S.; Hansen, C. H. Inverse and Reciprocity Methods for Experimental Determination of Radiation Modes. In *8th International Congress on Sound and Vibration, Hong Kong, China*, pages 1629–1636, 2001.

[29] Bin, L.; Yugang, L.; Xuegang, Y.; Shanglian, H. Maximal Modal Force Rule for Optimal Placement of Point Piezoelectric Actuators for Plates. *Journal of Intelligent Material Systems and Structures*, 11(512-515), 2000.

[30] Blevins, R. D. *Formulas for Natural Frequency and Mode Shape*. Krieger, Malabar, Florida, reprint edition, 2001.

[31] Bohlin, T. *Practical grey-box process identification: Theory and applications*. Advances in Industrial Control. Springer, London, 2006.

[32] Bombois, X. *Connecting Prediction Error Identification and Robust Control Analysis: a new framework*. PhD thesis, Université Catholique de Louvain, Leuven, 2000.

[33] Borgiotti, G. V.; Jones, K. E. Frequency independence property of radiation spatial filters. *Journal of the Acoustical Society of America*, 96(6):3516–3524, 1994.

[34] Boyd, S.; Vandenberghe, L. *Convex Optimization*. Cambridge Univ. Press, Cambridge, 2004.

[35] Brillinger, D. R. *Time series: Data analysis and theory*. Society for Industrial and Applied Mathematics, Philadelphia, Pa., 1981.

[36] Brogliato, B.; Egeland, O.; Lozano, R.; Maschke, B. *Dissipative Systems Analysis and Control: Theory and Applications*. Communications and Control Engineering. Springer, London, 2nd edition, 2007.

[37] Bruant, I.; Gallimard, L.; Nikoukar, Shahram. Optimal piezoelectric actuator and sensor location for active vibration control, using genetic algorithm. *Journal of Sound and Vibration*, (329):1615–1635, 2010.

[38] Bruant, I.; Proslier, L. Optimal Location of Actuators and Sensors in Active Vibration Control. *Journal of Intelligent Material Systems and Structures*, 16:197–206, 2005.

[39] Bultheel, A.; van Barel, M.; Rolain, Y.; Pintelon, R. Numerically Robust Transfer Function Modeling From Noisy Frequency Domain Data. *IEEE Transactions on Automatic Control*, 50(11):1835–1839, 2005.

[40] Burg, K.; Haf, H.; Wille, F.; Meister, A. *Partielle Differentialgleichungen und funktionalanalytische Grundlagen: Höhere Mathematik für Ingenieure, Naturwissenschaftler und Mathematiker*. Vieweg+Teubner Verlag, Wiesbaden, 5. edition, 2010.

[41] Cavallo, A.; de Maria, G.; Natale, C.; Pirozzi, S. Gray-Box Identification of Continuous-Time Models of Flexible Structures. *IEEE Transactions on Automatic Control*, 15(5):967–981, 2007.

[42] Cavallo, A.; de Maria, G.; Natale, C.; Pirozzi, S. *Active Control of Flexible Structures: From Modeling to Implementation*. Advances in Industrial Control. Springer, London, 2010.

[43] Cazzolato, B. S. *Sensing Systems for Active Control of Sound Transmission into Cavities*. PhD thesis, University of Adelaide, Adelaide, 1999.

[44] Charon, W. Practical Design and Verification of LQG Controllers as Applied to Active Structures. *Journal of Intelligent Material Systems and Structures*, 8:960–985, 1997.

[45] Chen, J.; Gu, G. *Control-Oriented System Identification: An $\mathcal{H}_\infty$ Approach*. Wiley, New York, NY, 2000.

[46] Clark, R. L.; Saunders, W.; Gibbs, G. P. *Adaptive Structures: Dynamics and Control*. A Wiley Interscience publication. Wiley, New York, NY, 1998.

[47] Clausert, H.; Wiesemann, G. *Grundgebiete der Elektrotechnik 1: Gleichstromnetze, Operationsverstärkerschaltungen, elektrische und magnetische Felder*. Oldenbourg, München, 9. edition, 2005.

[48] Codrons, B. *Process Modelling for Control: A Unified Framework Using Standard Black-box Techniques*. Advances in Industrial Control. Springer-Verlag, London, 2005.

[49] Coleman, T. F.; Li, Y. An Interior, Trust Region Approach for Nonlinear Minimization Subject to Bounds. *SIAM Journal on Optimization*, 6:418–445, 1996.

[50] Crandall, S. H.; Karnopp, D. C.; Kurtz, E. F.; Pridmore-Brown, D. C. *Dynamics of Mechanical and Electromechanical Systems*. McGraw-Hill, 1968.

[51] Crassidis, J. L.; Baz, A.; Wereley, N. $\mathcal{H}_\infty$ Control of Active Constrained Layer Damping. *Journal of Vibration and Control*, 6:113–136, 2000.

[52] Curtain, R. F.; Zwart, H. J. *An Introduction to Infinite-Dimensional Linear Systems Theory*, volume 21 of *Texts in Applied Mathematics*. Springer, New York, 1995.

[53] Datta, S.; Chaudhuri, B.; Chakraborty, D. Partial pole placement with minimum norm controller. In *49th IEEE Conference on Decision and Control (CDC 2010), Atlanta, USA*, 2010.

[54] Davison, E. J.; Wang, S. H. Properties and Calculation of Transmission Zeros of Linear Multivariable Systems. *Automatica*, 10(6):643–658, 1974.

[55] de Callafon, R. *Feedback Oriented Identification for Enhanced and Robust Control: a fractional approach applied to a wafer stage*. PhD thesis, Technische Universiteit Delft, Delft, 1998.

[56] de Vries, D. K.; van den Hof, P. M. J. Quantification of Uncertainty in Transfer Function Estimation: a Mixed Probabilistic-Worst-case Approach. *Automatica*, 31:543–557, 1995.

[57] Deutscher, J. *Zustandsregelung verteilt-parametrischer Systeme*. Springer, Dordrecht, 2012.

[58] Dhuri, K. D.; Seshu, P. Multi-objective optimization of piezo actuator placement and sizing using genetic algorithm. *Journal of Sound and Vibration*, (323):495–514, 2009.

[59] Douma, S. G. *From data to performance: System identification uncertainty and robust control design*. PhD thesis, Technische Universiteit Delft, Delft, 2006.

[60] Douma, S. G.; van den Hof, P. M. J. Relations between uncertainty structures in identification for robust control. *Automatica*, 41:439–457, 2005.

[61] Douma, S. G.; van den Hof, P. M. J.; Bosgra, O. H. Controller tuning freedom under plant identification uncertainty: double Youla beats gap in robust stability. *Automatica*, 39:325–333, 2003.

[62] Du, H.; Zhang, N.; Nguyen, H. Mixed $\mathcal{H}_2/\mathcal{H}_\infty$ control of tall buildings with reduced-order modelling technique. *Structural Control and Health Monitoring*, 15:64–89, 2007.

[63] Du, J. T.; Li, W. L.; Liu, Z. G.; Xu, H. A.; Ji, Z. L. Acoustic analysis of a rectangular cavity with general impedance boundary conditions. *Journal of the Acoustical Society of America*, 130(2):807–817, 2011.

[64] Dullerud, G. E. *Control of Uncertain Sampled Data Systems*. Systems & Control: Foundations & Applications. Birkhäuser, Boston, 1996.

[65] Elliott, S. J. *Signal Processing for Active Control*. Signal Processing and its Applications. Academic Press, San Diego, CA, 2001.

[66] Elliott, S. J.; Johnson, M. E. Radiation modes and the active control of sound power. *Journal of the Acoustical Society of America*, 94(4):2194–2204, 1993.

[67] Evans, L. C. *Partial differential equations*, volume 19 of *Graduate Studies in Mathematics*. American Math. Soc., Providence, RI, 2. edition, 2010.

[68] Fahrmeir, L.; Hamerle, A., editor. *Multivariate statistische Verfahren*. de Gruyter, Berlin, 1984.

[69] Fahy, F. *Foundations of Engineering Acoustics*. Academic Press, Amsterdam, 2. edition, 2001.

[70] Fahy, F.; Gardonio, P. *Sound and Structural Vibration: Radiation, Transmission and Response*. Academic Press, Amsterdam, 2. edition, 2007.

[71] Fahy, F. J. *Sound Intensity*. E & FN Spon, London, 2. edition, 1995.

[72] Fang, B.; Kelkar, A. G.; Joshi, S. M.; Pota, H. R. Modelling, system identification, and control of acoustic-structure dynamics in 3-D enclosures. *Control Engineering Practice*, 12:989–1004, 2004.

[73] Francis, B. A. *A Course in $\mathcal{H}_\infty$ Control Theory*, volume 88 of *Lecture Notes in Control and Information Sciences*. Springer, Berlin, 1987.

[74] Franke, D. *Systeme mit örtlich verteilten Parametern: Eine Einführung in die Modellbildung, Analyse und Regelung*. Springer, Berlin, 1987.

[75] Fuller, C. R.; Elliott, S. J.; Nelson, P. A. *Active Control of Vibration*. Academic Press, London, 1996.

[76] Garulli, A., editor. *Robustness in identification and control*, volume 245 of *Lecture Notes in Control and Information Sciences*. Springer, London, 1999.

[77] Gawronski, W. K. *Advanced Structural Dynamics and Active Control of Structures*. Mechanical Engineering Series. Springer-Verlag, New York, 2004.

[78] Gevers, M. Identification for Control: From Early Achievements to the Revival of Experiment Design. *European Journal of Control*, 11:335–352, 2005.

[79] Gevers, M.; Bazanella, A. S.; Bombois, X.; Mišković, L. Identification and the Information Matrix: How to Get Just Sufficiently Rich? *IEEE Transactions on Automatic Control*, 54(12):2828–2840, 2009.

[80] Gevers, M.; Bombois, X.; Codrons, B.; Scorletti, G.; Anderson, B. D. O. Model validation for control and controller validation in a prediction error identifcation framework —Part II: illustrations. *Automatica*, 39:417–427, 2003.

[81] Gevers, M.; Bombois, X.; Codrons, B.; Scorletti, G.; Anderson, B. D. O. Model validation for control and controller validation in a prediction error identifcation framework—Part I: theory. *Automatica*, 39:403–415, 2003.

[82] Gevers, M.; Mišković, L.; Bonvin, D.; Karimi A. Identification of multi-input systems: variance analysis and input design issues. *Automatica*, 42(4):559–572, 2006.

[83] Gibbs, G. P.; Clark, R. L.; Cox, D. E.; Vipperman, J. S. Radiation modal expansion: Application to active structural acoustic control. *Journal of the Acoustical Society of America*, 107(1):332–339, 2000.

[84] Goodwin, G. C.; Braslavsky, J. H.; Seron, M. M. Non-stationary stochastic embedding for transfer function estimation. *Automatica*, 38:47–62, 2002.

[85] Goodwin, G. C.; Salgado, M. A stochastic embedding approach for quantifying uncertainty in the estimation of restricted complexity models. *International Journal of Adaptive Control and Signal Processing*, 3(4), 1989.

[86] Goodwin, G. C.; Welsh, J. S. Singularity Issues in Closed Loop Identification. In Goodwin, G. C.; Anderson, B. D. O., editor, *Model Identification and Adaptive Control*, pages 27–52. Springer, London, 2001.

[87] Gross, D.; Hauger, W.; Schröder, J.; Wall, W. *Technische Mechanik 2: Elastostatik*. Springer-Verlag, Berlin, Heidelberg, 11. edition, 2011.

[88] Gugercin, S.; Antoulas, A. C.; Zhang, H. P. An Approach to Identification for Robust Control. *IEEE Transactions on Automatic Control*, 48(6):1109–1115, 2003.

[89] Guillaume, P.; Pintelon, R.; Schoukens, J. Accurate Estimation of Multivariable Frequency Response Functions. In *13th Triennal IFAC World Congress, San Francisco, CA*, pages 423–428, 1996.

[90] Güney, M.; Eşkinat, E. Optimal actuator and sensor placement in flexible structures using closed-loop criteria. *Journal of Sound and Vibration*, (312):210–233, 2008.

[91] Günnewig, J. *Optimierte Aktive Schwingungsdämpfung von Leichtbaustrukturen*. PhD thesis, RWTH Aachen, Aachen, 2000.

[92] Gupta, V.; Sharma, M.; Thakur, N. Optimization Criteria for Optimal Placement of Piezoelectric Sensors and Actuators on a Smart Structure: A Technical Review. *Journal of Intelligent Material Systems and Structures*, 21:1227–1243, 2010.

[93] Hać, A.; Liu L. Sensor and Actuator Location in Motion Control of Flexible Structures. *Journal of Sound and Vibration*, 167(2):239–261, 1993.

[94] Hagedorn, P.; DasGupta, A. *Vibrations and Waves in Continuous Mechanical Systems*. Wiley, Chichester, 2007.

[95] Hagood, N. W.; Chung, W. H.; von Flotow, A. Modelling of Piezoelectric Actuator Dynamics for Active Structural Control. *AIAA-90-1087-CP*, pages 2242–2256, 1990.

[96] Hakvoort, R. G. *System Identification for Robust Process Control: Nominal Models and Error Bounds*. PhD thesis, Technische Universiteit Delft, Delft, 1994.

[97] Hakvoort, R. G.; van den Hof, P. M. J. Identification of Probabilistic System Uncertainty Regions by Explicit Evaluation of Bias and Variance Errors. *IEEE Transactions on Automatic Control*, 42(11):1516–1528, 1997.

[98] Halim, D.; Reza Moheimani, S. O. An optimization approach to optimal placement of collocated piezoelectric actuators and sensors on a thin plate. *Mechatronics*, 13:27–47, 2003.

[99] Haniš, T.; Hromčík, M. Optimal Sensors Placement and Elimination of Undesirable Mode Shapes. In *European Control Conference (ECC). Budapest, Hungary*. 2009.

[100] Hansen, C. H.; Snyder, S. D. *Active Control of Noise and Vibration*. Taylor & Francis, London, 1996.

[101] Hering, E.; Modler, K.-H. *Grundwissen des Ingenieurs*. Carl Hanser Verlag, München, 14. edition, 2007.

[102] Herold, S. *Simulation des dynamischen und akustischen Verhaltens aktiver Systeme im Zeitbereich*. PhD thesis, TU Darmstadt, Darmstadt, 2003.

[103] Hindi, H.; Seong, C. -Y; Boyd, S. Computing Optimal Uncertainty Models from Frequency Domain Data. In *41st Conference on Decision and Control. Las Vegas, NV*, pages 2898–2905, 2002.

[104] Hiramoto, K.; Doki, H.; Obinata, G. Optimal Sensor/Actuator Placement for Active Vibration Control Using Explicit Solution of Algebraic Riccati Equation. *Journal of Sound and Vibration*, (229):1057–1075, 2000.

[105] Hjalmarsson, H. From experiment design to closed-loop control. *Automatica*, 41:393–438, 2005.

[106] Hjalmarsson, H.; Gevers, M.; de Bruyne, F. For Model-based Control Design, Closed-loop Identification Gives Better Performance. *Automatica*, 32(12):1659–1673, 1996.

[107] Hubbard, J. E. *Spatial Filtering for the Control of Smart Structures: An Introduction*. Springer-Verlag, 2010.

[108] IEEE. Standard on Piezoelectricity, Nr. 176-1978, 1978.

[109] Iorga, L.; Baruh, H.; Ursu, I. $\mathcal{H}_\infty$ Control with μ-analysis of a Piezoelectric Actuated Plate. *Journal of Vibration and Control*, 15(8):1143–1171, 2009.

[110] Isermann, R.; Münchhof, M. *Identification of Dynamic Systems: An Introduction with Applications*. Springer-Verlag, Berlin, Heidelberg, 2011.

[111] Janda, O.; Liebig, B.; Lange, H.; Konigorski, U.; Koch, A. Design and Hardware Implementation of a Controller for Active Damping of a Smart Structure. In *14th Adaptronic Congress, Darmstadt*, 2011.

[112] Jian, K.; Friswell, M. I. Distributed Modal Sensors for Rectangular Plate Structures. *Journal of Intelligent Material Systems and Structures*, 18:939–948, 2007.

[113] Juang, J. -N. *Applied System Identification*. Prentice Hall, Englewood Cliffs, NJ, 1994.

[114] Junkins, J. L.; Kim, Y. *Introduction to Dynamics and Control of Flexible Structures*. AIAA Education Series. American Institute of Aeronautics and Astronautics Inc, Washington, D.C, 1993.

[115] Kammeyer, K.-D; Kroschel, K. *Digitale Signalverarbeitung*. Vieweg + Teubner, Wiesbaden, 7. edition, 2009.

[116] Klose, S. *Systemtheoretische Analyse und Entwurf der modalen Eigendynamik von flexiblen Balken mit variablem Querschnittsverlauf auf Basis des örtlichen Eigenwertproblems*. PhD thesis, TU Darmstadt, Darmstadt, 2012.

[117] Kuhnen, K.; Krejci, P. Compensation of complex hysteresis and creep effects in piezoelectrically actuated systems: A new Preisach modeling approach. *IEEE Transactions on Automatic Control*, 54(3):537–550, 2009.

[118] Leleu, S.; Abou-Kandil, H.; Bonnassieux, Y. Piezoelectric Actuators and Sensors Location for Active Control of Flexible Structures. In *17th IEEE Instrumentation and Measurement Technology Conference. Baltimore, MD, USA*, volume 2, pages 813–825. 2000.

[119] Li, F.; de Oliviera, M.; Skelton, R. E. Integrating Information Architecture and Control or Estimation Design. *SICE Journal of Control, Measurement, and System Integration*, 2(1):120–128, 2008.

[120] Li, W. L. An Analytical Solution for the Self- and Mutual Radiation Resistances of a Rectangular Plate. *Journal of Sound and Vibration*, 245(1):1–16, 2001.

[121] Litz, L. *Reduktion der Ordnung linearer Zustandsraummodelle mittels modaler Verfahren*. PhD thesis, Technische Hochschule Karlsruhe, Karlsruhe, 1979.

[122] Ljung, L. Model Validation and Model Error Modeling: Report No.: 2125. http://www.control.isy.liu.se/publications/ (09.07.2012), 1999.

[123] Ljung, L. *System identification: Theory for the user*. Prentice Hall Information and System Sciences Series. Prentice Hall PTR, Upper Saddle River NJ, 2. edition, 1999.

[124] Ljung, L. Model Error Modelling and Control Design: Report no.: 2220. http://www.control.isy.liu.se/publications/ (09.07.2012), 2000.

[125] Ljung, L. Estimating Linear Time-Invariant Models of Nonlinear Time-varying Systems. *European Journal of Control*, 7:203–219, 2001.

[126] Lückel, J.; Müller, P. C. Analyse von Steuerbarkeits-, Beobachtbarkeits- und Störbarkeitsstrukturen linearer, zeitinvarianter Systeme. *Regelungstechnik*, 23:163–171, 1975.

[127] Lunze, J. *Regelungstechnik 1*. Springer, Berlin, 8. edition, 2010.

[128] Luo, Z. -H; Guo, B. -Z; Morgul, O. *Stability and Stabilization of Infinite Dimensional Systems with Applications*. Communications and Control Engineering. Springer, London, 1999.

[129] Markert, R. *Strukturdynamik*. Skript zur Vorlesung, Fachgebiet Strukturdynamik, TU Darmstadt, 2006.

[130] Mayer, D. *Regelung und Identifikation aktiver mechanischer Strukturen mit adaptiven digitalen Filtern*. PhD thesis, TU Darmstadt, Darmstadt, 2003.

[131] Meirovitch, L. *Dynamics and Control of Structures*. A Wiley Interscience publication. Wiley, New York, 1990.

[132] Meirovitch, L. *Principles and Techniques of Vibrations*. Prentice-Hall, Upper Saddle, NJ, 1997.

[133] Meirovitch, L.; Öz, H. An Assessment of Methods for the Control of Large Space Structures. In *Joint Automatic Control Conference, Denver, CO*, pages 34–41, 1979.

[134] Meirovitch, L.; Öz, H. Observer Modal Control of Dual-Spin Flexible Spacecraft. *Journal of Guidance and Control*, 2(2):101–110, 1979.

[135] Meirovitch, L.; Öz, H. Active Control of Structures by Modal Synthesis. In Leiphold, H. H. E., editor, *Structural Control*, pages 505–521. North-Holland Publishing, Amsterdam, 1980.

[136] Meirovitch, L.; Öz, H. Modal-Space Control of Large Flexible Spacecraft Possessing Ignorable Coordinates. *Journal of Guidance and Control*, 3(6):569–577, 1980.

[137] Melz, T. *Entwicklung und qualifikation modularer Satellitensysteme zur adaptiven Vibrationskompensation an mechanischen Kryokühlern*. PhD thesis, TU Darmstadt, Darmstadt, 2002.

[138] Milanese, M., editor. *Bounding Approaches to System Identification*. Plenum Press, New York, NY, 1996.

[139] Milanese, M.; Taragna, M. Optimality, Approximation, and Complexity in Set Membership $\mathcal{H}_\infty$ Identification. *IEEE Transactions on Automatic Control*, 47(10):1682–1690, 2002.

[140] Milanese, M.; Taragna, M. $\mathcal{H}_\infty$ set membership identification: A survey. *Automatica*, 41:2019–2032, 2005.

[141] Mišković, L.; Karimi, D.; Bonvin. Closed-loop identification of multivariable systems: With or without excitation of all references? *Automatica*, 44(8):2048–2056, 2008.

[142] Montazeri, A.; Posthan, J.; Yousefi-Koma, A. Design and Analysis of Robust Minimax LQG Controller for an Experimental Beam Considering Spill-Over Effect. *IEEE Transactions on Control Systems Technology*, 19(5):1251–1259, 2011.

[143] Moore, B. Principal Component Analysis in Linear Systems: Controllability, Observability, and Model Reduction. *IEEE Transactions on Automatic Control*, 26(1):17–32, 1981.

[144] Morris, K. Linear-Quadratic Optimal Actuator Location. *IEEE Transactions on Automatic Control*, 56(1):113–124, 2011.

[145] Nelson, P. A.; Elliott, S. J. *Active Control of Sound*. Academic Press, San Diego, CA, 1992.

[146] Obinata, G.; Anderson, B. D. O. *Model Reduction for Control System Design*. Communications and Control Engineering. Springer, London, 2001.

[147] Oppenheim, A. V.; Weinstein, C. J. Effects of finite register length in digital filtering and the fast Fourier transform. *Proceedings of the IEEE*, 60(8):957–976, 1972.

[148] Paeschke, L. *Strukturoptimierung adaptronischer Systeme unter regelungstechnischen Aspekten*. Master thesis, Fachgebiet Regelungstechnik und Mechatronik, TU Darmstadt, 2010.

[149] Pan, J.; Sum, K. S. On acoustic and structural modal cross-couplings in plate-cavity systems. *Journal of the Acoustical Society of America*, 107(4):2021–2038, 2000.

[150] Papadimitriou, C. Optimal sensor placement methodology for parametric identification of structural systems. *Journal of Sound and Vibration*, (278):923–947, 2004.

[151] Petersen, I. R.; Pota, H. R. Minimax LQG optimal control of a flexible beam. *Control Engineering Practice*, 11:1273–1287, 2003.

[152] Pintelon, R.; Schoukens, J. *System identification: A Frequency Domain Approach*. IEEE Press, New York, 2001.

[153] Preumont, A. *Mechatronics: Dynamics of Electromechanical and Piezoelectric Systems*. Springer Netherlands, 2006.

[154] Preumont, A. *Vibration Control of Active Structures: An Introduction*, volume 179 of *Solid Mechanics and its Applications*. Springer, Berlin, 3. edition, 2011.

[155] Preumont, A.; François, A.; de Man, P.; Piefort, V. Spatial filters in structural control. *Journal of Sound and Vibration*, 265(1):61–79, 2003.

[156] Preumont, A.; Seto, K. *Active Control of Structures*. John Wiley, Chichester, 2008.

[157] Rantzer, A. On the Kalman-Yakubovich-Popov lemma. *Systems & Control Letters*, 28:7–10, 1996.

[158] Rao, S. S. *Vibration of Continuous Systems*. Wiley, Hoboken, NJ, 2007.

[159] Reinelt, W.; Garulli, A.; Ljung, L. Comparing different approaches to model error modelling in robust identification. *Automatica*, 38:787–803, 2002.

[160] Reinelt, W.; Ljung, L.; Garulli, A. Model Error Modeling in Robust Identification: Report No.: 2353. http://www.control.isy.liu.se/publications/ (09.07.2012), 2001.

[161] Roppenecker, G. *Zeitbereichsentwurf linearer Regelungen: Grundlegende Strukturen und eine allgemeine Methodik ihrer Parametrierung*. Methoden der Regelungs- und Automatisierungstechnik. Oldenbourg, München, Wien, 1990.

[162] Saberi, A.; Chen, B. M.; Sannuti, P. *$\mathcal{H}_2$ Optimal Control*. Prentice Hall International Series in Systems and Control Engineering. Prentice Hall, London, 1995.

[163] Schlake, J. C. *Modellbildung, Systemanalyse und Reglerentwurf örtlich verteilter Systeme basierend auf numerischen Approximationsmodellen*. PhD thesis, TU Darmstadt, Darmstadt, 2011.

[164] Schoukens, J.; Renneboog, J. Modeling the noise influence after a discrete Fourier transform. *IEEE Transactions on Instrumentation and Measurement*, 35(3):278–286, 1986.

[165] Söderström, T.; Wang, L.; Pintelon, R.; Schoukens, J. Can errors-in-variables systems be identified from closed-loop experiments? *Automatica*, 49:681–684, 2013.

[166] Sethi, V.; Song, G. Optimal Vibration Control of a Model Frame Structure Using Piezoceramic Sensors and Actuators. *Journal of Vibration and Control*, 11:671–684, 2005.

[167] Skelton, R. E. Model error concepts in control design. *International Journal of Control*, 49(5):1725–1753, 1989.

[168] Skogestad, S.; Postlethwaite, I. *Multivariable Feedback Control: Analysis and Design*. Wiley, Chichester, 2. edition, 2005.

[169] Smith, R. S., editor. *The modeling of uncertainty in control systems: Proceedings of the 1992 Santa Barbara workshop*, volume 192 of *Lecture Notes in Control and Information Sciences*. Springer, Berlin, 1994.

[170] Sánchez-Peña, R. S.; Puig Cayuela, V.; Quevedo Casín, J., editor. *Identification and Control: The Gap between Theory and Practice*. Springer-Verlag, London, 2007.

[171] Sánchez-Peña, R. S.; Sznaier, M. *Robust Systems: Theory and Applications*. Adaptive and Learning Systems for Signal Processing, Communications, and Control. Wiley, New York, NY, 1998.

[172] Snyder, S. D.; Tanaka, N. Calculating total acoustic power output using modal radiation efficiencies. *Journal of the Acoustical Society of America*, 97(3):1702–1709, 1995.

[173] Spurk, J. H. *Strömungslehre: Einführung in die Theorie der Strömungen*. Springer, Berlin, 4. edition, 1996.

[174] Stein, L.; Konigorski, U. Design of Modal Filters Exact on Maximal Spaces of Functions. In *7th Vienna Conference on Mathematical Modelling, MATHMOD, Vienna, Austria*, 2012.

[175] Stenman, A.; Tjärnström, F. A Nonparametric Approach to Model Error Modelling: Report no.: 2230. http://www.control.isy.liu.se/publications/ (09.07.2012), 2000.

[176] Stölting, H.-D; Kallenbach, E. *Handbuch Elektrische Kleinantriebe*. Hanser, München, 3. edition, 2006.

[177] Storm, R. *Kompendium Maschinenakustik: Band 2, Maschinenakustische Grundgleichung*. 3. edition, 2008.

[178] Strang, G. *Introduction to Linear Algebra*. Wellesley-Cambridge Press, Wellesley, MA, 4. edition, 2009.

[179] Sum, K. S.; Pan, J. A study of the medium frequency response of sound field in a panel-cavity system. *Journal of the Acoustical Society of America*, 103(3):1510–1519, 1998.

[180] Tanaka, N.; Sanada, T. Modal control of a rectangular plate using smart sensors and smart actuators. *Smart Materials and Structures*, 16:36–46, 2007.

[181] Tøffner-Clausen, S. *System identification and robust control: A case study approach*. Advances in Industrial Control. Springer, London, 1996.

[182] Tsai, M. C. On Discrete Spectral Factorizations – A Unify Approach. *IEEE Transactions on Automatic Control*, 38(10):1563–1567, 1993.

[183] van Brunt, B. *The Calculus of Variations*. Springer-Verlag, New York, NY, 2010.

[184] van de Wal, M.; de Jager, B. A review of methods for input/output selection. *Automatica*, 37:487–510, 2001.

[185] van den Boom, T. *MIMO System Identification for* $\mathcal{H}_\infty$ *Robust Control*. PhD thesis, Technische Universiteit Eindhoven, Eindhoven, 1992.

[186] van den Hof, P. M. J.; Schrama, R. J. P. Identification and Control - Closed-loop Issues. *Automatica*, 31(12):1751–1770, 1995.

[187] Verboven, P. *Frequency-Domain System Identification for Modal Analysis*. PhD thesis, Vrije Universiteit Brussel, Brussels, 2002.

[188] Veres, S. M.; Wall, D. S. *Synergy and Duality of Identification and Control*, volume 10 of *Systems and Control Series*. Taylor & Francis, London, 2000.

[189] Wahlberg, B.; Ljung, L. Hard Frequency-Domain Error Bounds from Least-Squares Like Identification Techniques. *IEEE Transactions on Automatic Control*, 37(7):900–912, 1992.

[190] Wang, B. -T; Fuller, C. R. Near-field pressure, intensity, and wave-number distributions for active structural acoustic control of plate radiation: Theoretical analysis. *Journal of the Acoustical Society of America*, 92(3):1489–1496, 1992.

[191] Wang, X. Deterministic-Statistical Analysis of a Structural-Acoustic System. *Journal of Sound and Vibration*, (330):4827–4850, 2011.

[192] Wernholt, E.; Gunnarsson, S. Analysis of Methods for Multivariable Frequency Response Function Estimation in Closed Loop. In *46th IEEE Conference on Decision and Control. New Orleans, LA*, pages 4881–4888. 2007.

[193] Weyer, T. *Entwurf selbsteinstellender elektromechanischer Tilger*. PhD thesis, TU Braunschweig, Braunschweig, 2007.

[194] Widrow, B.; Walach, E. *Adaptive Inverse Control*. Prentice Hall Information and System Sciences Series. Prentice Hall PTR, Upper Saddle River, NJ, 1996.

[195] Xie, S. L.; Zhang, X. N.; Zhang, J. H.; Hu, L. $\mathcal{H}_\infty$ Robust Vibration Control of a Thin Plate Covered with a Controllable Constrained Damping Layer. *Journal of Vibration and Control*, 10:115–133, 2004.

[196] Yang, J. *An Introduction to the Theory of Piezoelectricity*, volume 9 of *Advances in Mechanics and Mathematics*. Springer Science + Business Media Inc, Boston, MA, 2005.

[197] Zhou, K.; Doyle, J. C.; Glover, K. *Robust and Optimal Control*. Prentice Hall, Upper Saddle River, NJ, 1996.

Author's Publications

[1] Janda, O.; Kartzow, F.; Schewe, L. Simultane Optimierung von Tilgerparametern an einem Stabwerk. In *36. Jahrestagung für Akustik (DAGA), Berlin, Germany*, pages 289-290, 2010.

[2] Kurch, M.; Atzrodt, H.; Kartzow, F.; Schewe, L.; Janda, O. On Model Order Reduction for Parameter Optimisation of Vibration Absorbers. In *10th International Conference on Recent Advances in Structural Dynamics (RASD), Southampton, England*, 2010.

[3] Janda, O.; Konigorski, U. Identification and Robust Active Damping of a Flexible Structure. In *4th WSEAS Conference on Engineering Mechanics, Structures and Engineering Geology (EMESEG), Corfu, Greece*, pages 508-516, 2011.

[4] Janda, O.; Liebig, B.; Lange, H.; Konigorski, U.; Koch, A. Design and Hardware Implementation of a Controller for Active Damping of a Smart Structure. In *14th Adaptronic Congress, Darmstadt, Germany*, 2011.

[5] Stein, G. L.; Janda, O.; Konigorski, U. Identification of Power Transfer Matrices. In *39. Jahrestagung für Akustik (DAGA), Merano, Italy*, pages 1363-1366, 2013.

[6] Janda, O.; Stein, G. L.; Heuss, O.; Konigorski, U. Identification of Power Transfer Matrices for Active Structural Acoustic Control. In *20th International Congress on Sound & Vibration (ICSV), Bangkok, Thailand*, 2013.